Sea ice response to anthropogenic pollution: an experimental and modelling study

Royal Holloway, University of London

Thesis submitted for the degree of Doctor of Philosophy

Amelia Ann Marks

Declaration of authorship

I Amelia Ann Marks hereby declare that this thesis and the work presented in it is entirely my own. Where I have consulted the work of others, this is always clearly stated.

Signed:

Date:

“There is no question that climate change is happening; the only arguable point is what part humans are playing in it.” *David Attenborough*

Acknowledgements

There are many people I would like to thank for their help and support, without whom this thesis would not have been possible. Firstly I would like to thank my supervisor, Martin King, for his support and guidance throughout this work. I would also like to thank other people involved in the project. A further huge thank you must go to Jerry Morris for his great help with construction and set up of the sea ice simulator. I would also like to thank those involved in the Dome C fieldwork including, but not limited to, Alasdair MacArthur for guidance on using equipment and Corrado Fragiacomo for help in the field.

Secondly, I would like to thank those who have provided funding towards the PhD. Including, Royal Holloway for providing funding for my fees and maintenance throughout this work. The Earth Science's department research committee for helping fund papers, fieldwork and conferences. And finally, COMNAP and PNRA for providing funding for fieldwork at Dome C, Antarctica, which was an incredible experience.

Finally I would like to thank all my friends and family for their support. To my fellow PhD students for ensuring regular tea/lunch/coffee breaks and while I'm on tea breaks, I would like to thank "The Hub" for providing an escape from the office and having potentially the world's best cheesecake! To the fellow survivors of Caddy Close thanks for the highly informative late night conversations. My sister, Rachel, thanks for your support, friendship, and for doing a PhD first. Lastly, to Peter, thank you.

Abstract

Anthropogenic pollution can be entrained from the atmosphere into snow and sea ice where it causes increased absorption of solar radiation. Black carbon accounts for 85% of absorption by impurities in snow and sea ice. Increased absorption causes decreased snow and sea ice albedo, which has climatic consequences, and decreased light penetration, which affects photobiology and photochemistry of snow and sea ice. To investigate the effects of black carbon on sea ice two methods are utilised; radiative-transfer modelling and laboratory experiments with artificial sea ice. Firstly, radiative-transfer calculations are undertaken using the TUV (tropospheric ultraviolet-visible)-snow model, showing black carbon is most influential when concentrated in a surface 5 cm layer of a snow-free melting sea ice, which could exacerbate sea ice melting rates. A thin snow layer over sea ice (<5 cm) will "disguise" black carbon in sea ice, although times of year when sea ice is snow-free correspond with times of largest solar radiation, further exacerbating melt rates. Secondly, to validate the TUV-snow model, a sea ice simulator has been developed which creates sea ice in 2 tonne tanks, replicating polar temperatures, illumination conditions, seawater salinity, fabric of sea ice and ocean energy balance. Results from the response of the simulated sea ice to black carbon are compared to radiative-transfer calculations in order to validate the model. To recreate measurements of the artificial sea ice reflectance, using the TUV-snow model, the black carbon mass-ratio in the top layer of sea ice must be reduced by a factor of three in the model, compared to that added to the artificial ice. Two reasons are suggested for this; different absorption cross-section of black carbon added to the ice or mobilisation of black carbon from the artificial sea ice surface. The results presented in this thesis greatly improve understanding of the effects of black carbon in sea ice on albedo and light penetration depths, and are of use to climate modellers investigating global climatic effects of black carbon.

Contents

Acknowledgements 3

Abstract 4

Glossary 31

1 Introduction **34**

1.1 Effects of anthropogenic pollution 37

1.1.1 Direct radiative-forcing 38

1.1.2 Cloud effects 39

1.2 The effects of anthropogenic pollution on snow and sea ice 41

1.2.1 Albedo effect 43

1.2.2 Effects on light penetration 45

1.3 Methods to access snow and sea ice response to anthropogenic pollution 46

1.3.1 Fieldwork 46

1.3.2 Radiative-transfer modelling 47

1.3.2.1 Radiative-transfer theory 48

1.3.2.2 Review of previous radiative-transfer modelling of black carbon in snow and sea ice 50

1.3.3 Experiments on artificial snow and sea ice 52

1.3.4 Remote sensing 53

1.3.5 Anisotropic reflectance of Polar surfaces 54

1.4 Aims of the thesis 55

1.4.1 Thesis overview 56

2 The effects of black carbon and HULIS distribution on ablating Antarctic sea ice optical properties: Light penetration, albedo and PAR **57**

2.1 Introduction 57

2.2 The TUV-snow radiative-transfer model 60

2.2.1 Model overview 60
2.2.1.1 Absorption and scattering cross-section 61
2.2.1.2 The asymmetry parameter 62
2.2.2 Addition of absorbing impurities in snow/sea ice to the TUV-snow model 62
2.2.3 Defining model parameters 64
2.2.3.1 Number of streams 65
2.2.3.2 Cloud optical depth 67
2.2.3.3 Under-ice albedo 69
2.2.4 Calculating changes in albedo, *e*-folding depth and PAR with increasing black carbon and HULIS uniformly distributed throughout the sea ice using the TUV-snow model 70
2.2.5 Modeling change in albedo with variation in black carbon and HULIS distribution 72
2.3 Results 73
2.3.1 The effect of black carbon and HULIS on sea ice surface albedo 73
2.3.2 Variation in *e*-folding depth with increasing mass-ratio of black carbon and HULIS in sea ice 76
2.3.3 Variation in PAR with increasing black carbon and HULIS mass-ratio 79
2.3.4 The effect of black carbon and HULIS distribution in sea ice on surface albedo reponse 83
2.3.4.1 Effect of increasing black carbon and HULIS in a top layer of varying thickness 84
2.3.4.2 Effect of increasing black carbon and HULIS in a 1 cm layer in sea ice 87
2.4 Discussion 89
2.4.1 The effects of black carbon versus HULIS 90
2.4.2 Comparison with previous modelling of albedo changes due to black carbon 91
2.4.3 Effects of black carbon and HULIS on photobiological processes 92
2.4.4 How is black carbon and HULIS likely to be distributed in sea ice? 94
2.4.5 Model limitations and potential future progression 97
2.5 Conclusions 99

3 The effects of additional black carbon on Arctic sea ice surface albedo: Variation with sea ice type and snow cover 101

3.1 Introduction 101

3.2 Method 103

3.2.1 Using the TUV-snow model to calculate scattering and absorption cross-sections 104

3.2.2 Calculating albedo in sea ice and snow with increasing black carbon in sea ice 115

3.3 Results 118

3.3.1 Variation in albedo with increasing black carbon content in first year and multi-year sea ice 118

3.3.2 Effect of snow cover and type on the influence of black carbon in sea ice on surface albedo 121

3.4 Discussion 123

3.4.1 Absorption cross-sections of snow and sea ice 124

3.4.2 Variation in the impact of black carbon with sea ice type 126

3.4.3 The role of snow and snow type in the influence of black carbon in sea ice on surface albedo 128

3.4.4 Potential limitations in the model and future research possibilities 129

3.5 Conclusions 132

4 Dependence of snow and sea ice type on the response of albedo and light penetration depth (*e*-folding-depth) to increasing black carbon 134

4.1 Introduction 134

4.2 Method 136

4.3 Results 138

4.3.1 Response of albedo to increasing black carbon in optically thick snow and sea ice 139

4.3.2 Albedo response to increasing black carbon for snow/sea ice with a thickness of 1, 0.5 and 0.25 or 0.1 m 148

4.3.3 Response of *e*-folding depth to increasing black carbon in optically thick snow and sea ice 151

4.3.4 Response of *e*-folding depth to increasing black carbon in a snow/sea ice with a thickness of 1, 0.5 and 0.25 or 0.1 m 156

4.4 Discussion 159
4.4.1 The role of scattering cross-section in determining snow and sea ice response to black carbon 159
4.4.2 The response of snow versus sea ice 160
4.4.3 "Optically thick snow and sea ice" 161
4.4.4 The impact of climate change 162
4.4.5 Model limitations and sensitivity 162
4.5 Conclusions 163

5 Initial experiments with a sea ice simulator 164
5.1 Introduction 164
5.2 Sea ice simulator design and development 166
5.2.1 Creating polar temperatures 167
5.2.2 Creating an artificial ocean 169
5.2.2.1 Housing an ocean 170
5.2.2.2 Creating seawater salinity 173
5.2.2.3 Replicating ocean energy balance 175
5.2.2.4 Replicating ocean circulation 175
5.2.3 Creating natural illumination 176
5.3 Development of techniques for measuring sea ice physical and optical properties 177
5.3.1 Measuring sea ice reflectance 178
5.3.2 Measuring sea ice *e*-folding depth 183
5.3.3 Measuring temperature profiles 186
5.3.4 Determining sea ice properties by ice coring 186
5.4 Preliminary results 190
5.4.1 Change in reflectance of freezing sea ice 190
5.4.2 Change in temperature of freezing sea ice 192
5.4.3 Initial *e*-folding depth measurements 194
5.4.4 Ice core measurements 195
5.5 Discussion 198
5.5.1 How realistic is the simulated ice? 198
5.5.2 Limitations of the sea ice simulator 201
5.6 Conclusions 203

6 Artificial sea ice reflectance response to increased black carbon, for evaluation of the TUV-snow model 205

6.1 Introduction 205

6.2 Experimental determination of the effect of black carbon on reflectance of artificial sea ice 206

6.2.1 Experimental method 207

6.2.1.1 Sea ice simulator set up and ice growth 207

6.2.1.2 Making black carbon solutions 208

6.2.2 Experimental results 209

6.2.2.1 Measured nadir reflectance of clean bottom ice 210

6.2.2.2 Measured *e*-folding depth of bottom clean ice 212

6.2.2.3 Measured reflectance with the addition of a top, black carbon bearing, ice layer 214

6.2.2.4 Ice core data 215

6.3 Evaluation of the TUV-snow model 225

6.3.1 Evaluation method 225

6.3.2 Evaluation results 228

6.3.3 Initial TUV-snow model fit (fits A and B) 228

6.3.4 Deriving scattering and absorption cross-section from albedo and *e*-folding depth data 231

6.3.5 Comparison of measured reflectance of artificial sea ice to model results using derived scattering and absorption cross-section values (Fits C–G) 234

6.4 Discussion 238

6.4.1 Reasons for reduced black carbon mass-ratio to produce fit between modelled and measured reflectance 239

6.4.1.1 Black carbon properties 239

6.4.1.2 Black carbon mobilisation 241

6.4.1.3 Asymmetry parameter 242

6.4.1.4 Layer thickness 243

6.4.1.5 Uncertainty in derived scattering and absorption cross-section 245

6.4.1.6 Uncertainty in added black carbon mass-ratio 246

6.4.2 How realistic is the simulated scenario? 246

6.4.2.1 Effects on ice properties 246
6.4.2.2 Presence of other absorbing impurities 247
6.4.3 Suggestions for future research 248
6.5 Conclusions 249

7 Validation of a Gonio Radiometirc Spectrometer System for measuring Polar surface BRDF (HDRF) 250
7.1 Introduction 251
7.2 Reflectance terminology 255
7.3 HDRF measurements at Dome C 256
7.3.1 GRASS equipment design 256
7.3.2 Acquiring HDRF measurements with GRASS 259
7.3.2.1 Raw measurement collection 259
7.3.2.2 Raw measurement processing to generate HDRF plots 260
7.3.3 HDRF measurement location 266
7.3.4 Snow physical properties from snow pits 270
7.4 Results 270
7.4.1 Variation in polar plots of HDRF of individual sites 271
7.4.2 A spatially averaged HDRF polar contour plot of a Dome C snow surface 278
7.5 Discussion 281
7.5.1 Comparison to previous Dome C measurements 281
7.5.2 Accuracy and precision of HDRF measurements using GRASS . 285
7.5.2.1 Geometrical accuracy 285
7.5.2.2 Effect of varying optic lens cone of acceptance and radiance collector zenith angle position 288
7.5.2.3 Atmospheric conditions 290
7.5.2.4 Spectralon reference panels 291
7.6 Conclusions 291

8 Concluding remarks 293
8.1 Introduction 293
8.2 Key conclusions 293
8.3 The importance of black carbon in sea ice in the global climate system 298
8.4 Future research potential 298

8.4.1 Black carbon concentrations and distribution in sea ice 299
8.4.1.1 Fieldwork 299
8.4.1.2 Remote sensing 300
8.4.2 Incorporating the effects of black carbon in sea ice in to global climate models 300
8.4.3 More realistic sea ice simulation 301
8.5 Final conclusions 302

A Data for chapter 4 for albedo/*e*-folding depth response to black carbon for different snow/sea ice thicknesses 326

B Supplementary data for chapter 6 for ice cores taken before and after the addition of a black carbon bearing layer 331

C Supplementary data for chapter 7 for HDRF measurements from individual snow sites at Dome C 339

List of Figures

1.1 Radiative forcing factors defined by the IPCC report 2013, radiative-forcing by black carbon is highlighted. Credit: IPCC (2013). 35
1.2 Black carbon sources and climatic effects, based on Bond et al. (2013). 36
1.3 Black carbon effects and associated climatic forcing, credit: Bond et al. (2013). 38
1.4 Solar radiation spectrum at the top and bottom of the atmosphere compared to a black body, credit: Global Warming Art. 39
1.5 The role of anthropogenic pollutants in decreasing albedo and light penetration depth in snow and sea ice. A) Clean snow/sea ice; longer *e*-folding depths and larger albedo. B) Snow/sea ice with impurities; shorter *e*-folding depths and smaller albedo. 42
1.6 Methods of entrainment of black carbon into sea ice. 43
1.7 Photo of ablating Antarctic sea ice showing the difference in albedo between sea ice/snow and ocean. Sea ice has a noticeably much higher albedo than the surrounding open ocean. 44
1.8 Absorption and scattering of photons in A) sea ice and B) snow. In sea ice and snow scattering occurs at air-ice boundaries and absorption occurs as photons travel through ice. 49
1.9 The effect of snow anisotropic reflectance on satellite albedo measurements. 54

2.1 Overview of the structure of layers in the TUV-snow model showing division of the atmosphere and snow/sea ice into layers, not to scale. . 61

2.2 A comparison of absorption cross-sections, of black carbon in ice, air and brine (salinity 30 ppt) (left hand side). All black carbon cross sections were calculated using Mie theory using a black carbon proxy of Warren and Wiscombe (1980). HULIS in ice absorption is taken from Hoffer et al. (2006). Absorption cross-section of ice (right hand side) is taken from Warren and Wiscombe (1980), (note different scales). Sparse markers are used for clarity, with a marker every 50 data points. 64
2.3 Effect of changing stream number on calculated albedo. 66
2.4 Effect of changing stream number on calculated e-folding depth. 67
2.5 Calculated snow surface albedo with solar zenith angle for different cloud optical depths. 68
2.6 Variation in sea ice surface albedo with change in under-ice albedo. . . 69
2.7 Comparison between flat plate and spherical irradiance. 71
2.8 Effect of increasing black carbon mass-ratio (1–1024 ng g^{-1}) on sea ice albedo at wavelengths 300–700 nm. 73
2.9 Effect of increasing HULIS mass-ratio (1–1024 ng g^{-1}) on sea ice albedo at wavelengths 300–700 nm. 75
2.10 Calculated *e*-folding depth versus black carbon mass-ratio at wavelengths from 300–700nm under isotropic solar radiation conditions. 77
2.11 Calculated *e*-folding depth versus HULIS mass-ratio at wavelengths from 300–700 nm under isotropic solar radiation conditions. 79
2.12 Relative PAR with depth through sea ice with an increasing mass-ratio of black carbon. The numbers on the graph are the PAR *e*-folding depth for the corresponding mass-ratio of black carbon (the depth required to reduce PAR by $\frac{1}{e}$). The PAR *e*-folding depth is larger for smaller black carbon mass-ratios. 80
2.13 PAR at the base of a 1 m thick ablating sea ice for different solar zenith angles (0, 25, 36, 45, 53, 60, 72, 84 and 90°) and black carbon mass-ratios. 81
2.14 Relative PAR with depth through sea ice with an increasing mass-ratio of HULIS. The numbers on the graph are the PAR *e*-folding depth for the corresponding mass-ratio of HULIS (the depth required to reduce PAR by $\frac{1}{e}$). The PAR *e*-folding depth is slightly larger for smaller HULIS mass-ratios. 82

2.15 PAR at the base of a 1 m thick ablating sea ice for different solar zenith angles (0, 25, 36, 45, 53, 60, 72, 84 and 90°) and HULIS mass-ratios. . 83
2.16 Albedo with increasing black carbon mass-ratio in a top surface layer of varying thickness at A) 400 nm and B) 600nm. C) and D) show columnar density of black carbon at C) 400 nm and D) 600 nm. 85
2.17 Albedo with increasing HULIS mass-ratio in a surface layer in the sea ice of varying thickness at A) 300 nm and B) 400 nm and change in albedo with columnar density of HULIS at C) 300 nm and D) 400 nm. 87
2.18 Albedo with black carbon in a 1cm layer moved down in the sea ice in 10 cm intervals at A) 400 nm and B) 600 nm. 88
2.19 Albedo with HULIS in a 1cm layer moved down in the sea ice at a wavelength of 300 nm. 89
2.20 Black carbon ratio which will reduce PAR at the base of a 1 m thick ablating sea ice to the light compensation point below which algal accumulation will not occur, for different solar zenith angles (0, 25, 36, 45, 53, 60, 72, 84 and 90°). 93
2.21 Variation in sea ice surface albedo with different sea ice thickness and under ice albedo. Solid lines show surface albedo with an under-ice albedo of 0.01 and dashed lines show surface albedo for a under-ice albedo of 0.99. 99

3.1 Albedo data for selected snow and sea ice from Grenfell and Maykut (1977). The figure number of Grenfell and Maykut (1977) from which data is extracted from is also shown. 105
3.2 The *e*-folding depth (m) data for selected snow and sea ice from Grenfell and Maykut (1977). The figure number of Grenfell and Maykut (1977) from which data is extracted from is also shown. 106
3.3 Calculated albedo and *e*-folding depth for different σ_{scatt} values and black carbon mass-ratios at 400 nm wavelength. The measured albedo and e-folding depth for wet snow at a wavelength of 400 nm is shown as a dashed line. The intersection of the calculated albedo/*e*-folding depth with the measured albedo/e-folding depth for each black carbon mass-ratio provides a potential absorption and scattering cross-section value. 108

3.4 Interpolation of albedo and *e*-folding depth data for wet snow from Grenfell and Maykut (1977). Intersection provides unique values for scattering and absorption cross-section for the ice at that wavelength. The intersection was calculated every 25 nm from wavelengths from 400–700 nm, only every 100 nm is shown for clarity. 109

3.5 Interpolation of albedo and *e*-folding depth data for dry snow from Grenfell and Maykut (1977). Intersection provides unique values for scattering and absorption cross-section for the ice at that wavelength. The intersection was calculated every 25 nm from wavelengths from 400–700 nm, only every 100 nm is shown for clarity. 110

3.6 Interpolation of albedo and *e*-folding depth data for first year sea ice from Grenfell and Maykut (1977). Intersection provides unique values for scattering and absorption cross-section for the ice at that wavelength. The intersection was calculated every 25 nm from wavelengths from 400–700 nm, only every 100 nm is shown for clarity. 111

3.7 Interpolation of albedo and *e*-folding depth data for multi-year sea ice from Grenfell and Maykut (1977). Intersection provides unique values for scattering and absorption cross-section for the ice at that wavelength. The intersection was calculated every 25 nm from wavelengths from 400–700 nm, only every 100 nm is shown for clarity. 112

3.8 Calculated $\sigma_{\text{scatt}}(\lambda)$, in granular white sea ice, blue sea ice, wet snow and dry snow. Dashed lines show the average wavelength independent scattering cross section for each snow and sea ice type. 113

3.9 Calculated $\sigma^{+}_{\text{abs}}(\lambda)$, in granular white sea ice, blue sea ice, wet snow and dry snow. Error bars show the average difference in $\sigma^{+}_{\text{abs}}(\lambda)$ values through making small changes to the data fit for obtaining these values. $\sigma^{+}_{\text{abs}}(\lambda)$ is per kg of sea ice. 114

3.10 Sea ice and snow configurations modelled (not to scale). 116

3.11 Flow diagram of method from deriving absorption and scattering cross-section values from the data of Grenfell and Maykut (1977) to calculate the albedo response of sea ice to increased black carbon and the effect of snow. 118

3.12 A) Albedo with increasing additional black carbon content from 1 to 1024 $ng\ g^{-1}$, evenly distributed in the top 5 cm of 155 cm of typical first year sea ice. B) Albedo with increasing black carbon content from 1 to 1024 $ng\ g^{-1}$, evenly distributed in the top 5 cm layer of 155 cm of a typical multi-year sea ice. 120
3.13 Albedo of snow surface at 500 nm with different thicknesses of snow cover overlying sea ice. C) dry snow on first year ice, D) wet snow on first year ice, E) dry snow on the multi-year ice, F) wet snow on multi-year ice. 122
3.14 Albedo of snow surface at 700 nm with different thicknesses of snow cover overlying sea ice. C) dry snow on first year ice, D) wet snow on first year ice, E) dry snow on the multi-year ice, F) wet snow on multi-year ice. 123
3.15 Absorption cross-sections for common impurities found in sea ice. Sea ice algae and sediment absorption from Light et al. (1998). HULIS absorption from Hoffer et al. (2006). Black carbon absorption calculated by Mie theory, as described in chapter 2. 124
3.16 Comparison of measured albedo by Grenfell and Maykut (1977) (dashed line) with albedo modelled in the study presented here (markers and solid line). 131

4.1 Albedo with increasing absorption cross-section (bottom x-axis) and black carbon mass-ratio (top x-axis) for different snow types; cold polar snow (red), windpacked snow (green) and melting snow (blue). 140
4.2 Relative change in albedo and *e*-folding depth. Each line shows a typical albedo or *e*-folding depth for a particular snow or sea ice type, taken as the mid-value for that snow or sea ice. 142
4.3 Albedo of snow with increasing mass-ratio of black carbon (absorption cross-section) and scattering cross-section, at wavelengths 300, 400, 550 and 700 nm and snow densities of 0.2, 0.4, 0.6 g cm^{-3}. 144
4.4 Albedo with increasing absorption cross-section (bottom x-axis) and black carbon mass-ratio (top x-axis) for different sea ice types; multi-year ice (red), first-year ice (green) and melting ice (blue). 146

4.5 Sea ice albedo with increasing mass-ratio of black carbon (absorption cross-section) and scattering cross-section, at wavelengths 300, 400, 550 and 700 nm and sea ice densities of 0.7, 0.8, 0.9 g cm^{-3}. 147
4.6 Thickness sensitivity study showing albedo of three snow types (cold polar snow, windpacked snow and melting snow) with increasing black carbon mass-ratio (absorption cross-section) for snow thicknesses of 0.1, 0.5, 1 and 10 m. 149
4.7 Albedo of three types of sea ice (multi-year ice, first-year ice and melting ice) with increasing black carbon mass-ratio (absorption cross-section) for sea ice thicknesses of 0.25, 0.5, 1 and 10 m. 150
4.8 Change in *e*-folding depth with increasing black carbon mass-ratio (absorption cross-section) for different snow types; cold polar snow, windpacked snow and melting snow. 152
4.9 Change in *e*-folding depth with increasing black carbon mass-ratio (absorption cross-section) for different sea ice types; multi-year ice, first-year ice and and melting ice. 153
4.10 Snow *e*-folding depth with increasing mass-ratio of black carbon (absorption cross-section) and scattering cross-section, at wavelengths 300, 400, 550 and 700 nm and snow densities of 0.2, 0.4, 0.6 g cm^{-3}. 154
4.11 Change in sea ice *e*-folding depth with increasing mass-ratio of black carbon (absorption cross-section) and scattering cross-section, at wavelengths 300, 400, 550 and 700 nm and densities of 0.7, 0.8, 0.9 g cm^{-3}. 155
4.12 Change in *e*-folding depth of snow with increasing black carbon mass-ratio (absorption cross-section) for snow thicknesses of 0.1, 0.5, 1 and 10 m. 157
4.13 Sea ice *e*-folding depth with increasing black carbon mass-ratio (absorption cross-section) for sea ice thicknesses of 0.25, 0.5, 1 and 10 m. 158
4.14 Grain size effects on surface albedo. A) Medium/small grain size results in a larger scattering cross-section as there are more air-ice interfaces in the same snow volume. More photons are scattered back out of medium resulting in higher albedo. B) Larger grain size results in smaller scattering cross-section as there are fewer air-ice interfaces. Fewer photons are scattered back out of medium resulting in lower albedo. 160

5.1 Set up of the sea ice simulator in a cold store. Sea ice is grown in the 2000 L tank placed on wooden pallets. A UV steriliser, filter and pump are contained in a heated wooden cabinet (to left of photo, shown uncovered), the roles of which are explained in section 5.2.2. Fluorescent lights above the tank provide illumination, as described in section 5.2.3. A fan above the tank blows cold air over the water surface, aiding freezing. 167
5.2 Cold store used to house the sea ice simulator which can be temperature controlled down to –25°C. 168
5.3 Air flow in the cold store including flow of cold air along floor of container and fan to blow cold air on to the water surface to increase heat flow from the water and aid freezing. 169
5.4 Set up of the artificial ocean including the tank with pipes running around base (1), chiller unit (2) and pump, UV steriliser and filter in a heated wooden cabinet (3). 170
5.5 Space Blanket insulation surrounding 2000 L polyethylene tank placed on wooden pallets 171
5.6 Unistrut frame surrounding 2000 L tank (covered in black neoprene) providing extra structural support. 172
5.7 Cross-section through tank wall showing layers of neoprene, polystyrene insulation, unistrut and the wooden boards surrounding the tank. . . . 173
5.8 Measured salinity (PSU) obtained from known concentration of Tropic Marine in tap water and pure water. 174
5.9 Daylight simulation and ultraviolet fluorescent lights providing isotropic shortwave illumination. 176
5.10 Set-up of sea ice simulator for measuring sea ice properties. Thermocouples to measure temperature profile through ice and water shown, not at exact depths. Fibre optic inserted into drilled hole to measure *e*-folding depth. Fibre optic fixed above ice surface to measure nadir reflectance. UV and visible lights above ice provide isotropic shortwave illumination. 178
5.11 Spectralon panel placed on ice surface for reference measurement in same location as ice surface radiance measurements taken. 179
5.12 Laser on Spectralon panel showing viewing footprint of optic lens to find correct location for the Spectralon panel. 180

5.13 Effect on reflectance measurements with having one white side panel missing for access. Uncertainty bars show ± one standard deviation of five measurement repeats. 181
5.14 Typical raw sea ice surface non-saturated and saturated intensity spectra taken for reflectance measurements. Peaks are caused by atomic transitions of mercury in the fluorescent light source. 182
5.15 Set up of fibre optic for measuring *e*-folding depth down one hole with a diffusing disk placed around fibre optic at the ice surface to ensure any light entering the drilled hole was isotropic. 183
5.16 Comparison of *e*-folding depth measurements taken using six individual fibre optics frozen in the ice at different depths (A) versus a single optic placed in a hole gradually drilled in the ice (B). 184
5.17 Comparison of *e*-folding depth measurements taken using six individual fibre optics technique versus a single fibre optic, at 500 nm. 185
5.18 Taking ice cores using a low speed and high torque drill attached to an ice corer. 188
5.19 Tool to remove ice cores from corer, the top metal disk is attached to the corer and the bottom metal disk is wound down to extract the ice core from the corer. 188
5.20 Change in ice surface during freezing and ice growth up to ∼40 cm, diffusing boards removed. 190
5.21 Change in reflectance of ice during ice growth at a wavelength of 500 nm. Error bars show variation with three repeat measurements. 191
5.22 Nadir sea ice surface reflectance at wavelengths from 350 to 650 nm for optically thick simulated ice. 192
5.23 Example of temperature profiles measured during ice growth. Dashed lines show estimated ice depth. 193
5.24 Change in daily ice thickness estimated from temperature profiles. . . . 194
5.25 Example of *e*-folding depth measurements taken from three holes drilled through the ice. Depth of first measurement set to 0 cm. 195
5.26 Representative example of ice core data from three cores including measured temperature, salinity and density and derived brine salinity, brine density, percent brine and percent air. Data from all ice cores taken is shown in chapter 6 and Appendix B. 197

5.27 Comparison of measured sea ice simulator ice reflectance to albedo values of sea ice measured in the field by Grenfell and Maykut (1977)(*).199
5.28 Segment of base of ice core showing transition from columnar ice (left) to platelet/granular ice (right). 201
5.29 Cross-section through ice grown in the tank to show irregular thickness of the base of the ice due to extended growth at the sides of the tank and around the teflon tube containing the thermocouples. The ice is ∼5 cm thicker in these areas. 202

6.1 Measured daily nadir reflectance at a wavelength of 500 nm of the clean bottom layer of ice before the black carbon bearing layer is added for each run. Error bars show one standard deviation of three measurements taken each day. A line is added to show where reflectance becomes constant with increased ice growth. 210
6.2 Measured reflectance versus wavelength of clean bottom layer of ice before black carbon bearing layer added for each run. Error bars show one standard deviation of five measurements taken on consecutive days. A smoothing spline (dashed line) is fitted to the measurements to remove noise. 211
6.3 Measured *e*-folding depth of the bottom clean ice layer before the black carbon bearing layer is added for each run (1–4) at wavelengths 350–650 nm, every ∼25 nm (wavelengths chosen to eliminate peaks in spectra as described in chapter 5). Some wavelengths are missing due to poor fitting of intensity data. 213
6.4 Artificial sea ice surface reflectance versus wavelength with black carbon in a 5 cm surface layer of ice in mass-ratios of 75 ng g^{-1}, 150 ng g^{-1} and 300 ng g^{-1}. 0 ng g^{-1} represents a blank run where just artificial seawater was added to the sea ice surface. Reflectance data presented every ∼10 nm, gaps at certain wavelengths occur due to peaks in intensity spectra. 215

6.5 **Run 1 before layer added** Physical ice properties for bottom "clean" ice layer before additional layer added for run 1. Temperature, density and salinity are measured from core sections, while brine salinity, brine density and brine and air volume are derived from equations of Cox and Weeks (1983). Photo of the ice core is also shown. 218

6.6 **Run 1 after layer added** Physical ice properties for bottom "clean" ice layer and additional layer added for run 1. Temperature, density and salinity are measured from core sections, while brine salinity, brine density and brine and air volume are derived from equations of Cox and Weeks (1983). Photo of the ice core is also shown. 219

6.7 **Run 2 before layer added** Physical ice properties for bottom "clean" ice layer before additional black carbon bearing layer added for run 2. Temperature, density and salinity are measured from core sections, while brine salinity, brine density and brine and air volume are derived from equations of Cox and Weeks (1983). Photo of the ice core is also shown. 220

6.8 **Run 3 before layer added** Physical ice properties for bottom "clean" ice layer before additional black carbon bearing layer added for run 3. Temperature, density and salinity are measured from core sections, while brine salinity, brine density and brine and air volume are derived from equations of Cox and Weeks (1983). Photo of the ice core is also shown. 221

6.9 **Run 3 after layer added** Physical ice properties for bottom "clean" ice layer and additional black carbon bearing layer for run 3. Temperature, density and salinity are measured from core sections, while brine salinity, brine density and brine and air volume are derived from equations of Cox and Weeks (1983). Photo of the ice core is also shown. 222

6.10 **Run 4 before layer added** Physical ice properties for bottom "clean" ice layer before additional black carbon bearing layer added for run 4. Temperature, density and salinity are measured from core sections, while brine salinity, brine density and brine and air volume are derived from equations of Cox and Weeks (1983). Photo of the ice core is also shown. 223

6.11 **Run 4 after layer added** Physical ice properties for bottom "clean" ice layer and additional black carbon bearing layer for run 4. Temperature, density and salinity are measured from core sections, while brine salinity, brine density and brine and air volume are derived from equations of Cox and Weeks (1983). Photo of the ice core is also shown 224

6.12 Fits A and B: Comparison between measured and modelled (dashed lines) reflectance of simulated sea ice surface due to black carbon in a 5 cm surface layer in concentrations of 0 ng g^{-1}, 75 ng g^{-1}, 150 ng g^{-1} and 300 ng g^{-1}. Fit A shows a fit where the scattering cross-section for the top and bottom layer is varied between each run to obtain the best fit. Fit B shows a fit where the scattering cross-section of the top and bottom layer are kept constant between each run. 230

6.13 Wavelength dependent absorption cross-section derived from reflectance and *e*-folding depth data from runs 1 to 4 for the "clean" bottom ice layer. A smooth line is added to guide the eye. Values for run 4 are too small to plot clearly. 232

6.14 Scattering cross-section derived from reflectance and *e*-folding depth data from runs 1 to 4, for the "clean" bottom ice layer. A straight line is added for the average scattering cross-section for each run. Error bars show ± 1SD of all scattering cross-section values. Missing values occur where fit between reflectance and *e*-folding depth data gave a poor fit for absorption and scattering cross-section values as the absorption cross-section at these wavelengths was very low. 233

6.15 Fits C and D: Comparison between measured and calculated (dashed lines) reflectance of simulated sea ice surface due to black carbon in a 5 cm surface layer in concentrations of 0 ng g^{-1}, 75 ng g^{-1}, 150 ng g^{-1} and 300 ng g^{-1}. Derived absorption by impurities is added to the top and bottom layer, and the bottom layer is fitted with the derived scattering cross-section. Fit C shows a fit where the scattering cross-section for the top layer is varied between each run to obtain the best fit. Fit D shows a fit where the scattering cross-section of the top layer is kept constant between each run. 235

6.16 Fits E and F: Comparison between measured and calculated (dashed lines) reflectance of simulated sea ice surface due to black carbon in a 5 cm surface layer. Black carbon in the surface layer in the model is reduced, as shown, to achieve a better fit. Derived absorption by impurities is added to the top and bottom layer, and the bottom layer is fitted with the derived scattering cross-section. Fit E shows a fit where the scattering cross-section for the top layer is varied between each run to obtain the best fit, as shown. Fit F shows a fit where the scattering cross-section of the top layer is kept constant between each run, as shown. 237

6.17 Fit G: Comparison between measured and calculated (dashed lines) reflectance of simulated sea ice surface due to black carbon in a 5 cm surface layer. Black carbon in the surface layer is decreased to obtain a better fit. Derived absorption by impurities is added to the top and bottom layer, and the bottom layer is fitted with the derived scattering cross-section. Scattering cross-section of the top layer is between fits E and F, being within reasonable limits, but also varying to provide an accurate representation of measured values. 238

6.18 Modelled reflectance values, based on the same parameters for fit G but full black carbon mass-ratios used for each run (0, 75, 150 and 300 ng g^{-1} respectively) with a black carbon absorption cross-section of $\sim$10 m^2 g^{-1} and 6 m^2 g^{-1}. Measured reflectance values also shown with $\pm$1 SD uncertainty bars. 240

6.19 Absorption cross-section of black carbon in ice for different size black carbon particles at a wavelength of 600 nm, derived by Mie calculation. 241

6.20 Example of rough ice surface to which the 75 L of black carbon bearing seawater was added, this could cause deviations from a flat 5 cm layer of $\pm$1 cm. 243

6.21 Comparison between calculated and measured reflectance for runs 1–4. Modelling is based on the parameters for fit G, although black carbon mass-ratios in the top layer of 0, 75, 150 and 300 ng g^{-1} are used for runs 1–4 respectively. The top layer is modelled as 4, 5 and 6 cm thick to understand the role of top layer thickness in calculated reflectance values. 244

6.22 Comparison between calculated and measured reflectance for runs 1–4. Modelling is based on fit G (see table 6.4). The bottom layer is modelled as 35, 40 and 45 cm thick to understand the role of bottom layer thickness in calculated reflectance values. 245

6.23 Comparison between absorption spectra derived for "clean" ice from each run compared to chlorophyll absorption from Bricaud et al. (2004). The values for run 4 are too small to plot clearly. 248

7.1 Location of Concordia base (Dome C) in Antarctica (adapted from CDIAC (http://cdiac.ornl.gov/trends/co2/ice_core_co2.html)). 252

7.2 Technique used by Hudson et al. (2006) to measure BRDF of snow. Surface radiance was measured from the top of a tower. For each angle examined a different snow surface was observed. 253

7.3 A picture of GRASS: radiance collectors are attached to three arms spaced 15° apart, a further radiance collector is attached at nadir to record surface radiance. On top of the structure there is an integrating sphere to measure downwelling irradiance. The arms of GRASS can be rotated 360° to record surface radiance at all azimuth angles. 254

7.4 Definition of angles required for BRDF measurements, where ϕ_i is the azimuth angle of incident light, θ_i is the zenith angle of incidence light, ϕ_r is the azimuth viewing angle and θ_r is the zenith viewing angle. . . 255

7.5 Example of a radiance collector consisting of an optical lens attached to fibre optic, both of which are fastened to the GRASS frame via a bracket at the desired viewing zenith angle (Photo courtesy of K. D'Souza). . . 257

7.6 Set up of electrical equipment attached to GRASS, including coupling of fibre optics to multiplexer, connection to VSWIR spectrometer and connection to a Toughbook used to control GRASS, which can function in cold Polar temperatures. 259

7.7 Variation in raw intensity signal, at 800 nm, recorded from the tungsten-halogen lamp across all days and for all radiance collectors during the intercalibration. "Radiance collector number" refers to a specific azimuth and zenith angle where x.1 is for the smallest zenith angle and x.4 is the largest. 3.x, 4.x and 5.x refers to different azimuth angles. 4.0 is the nadir radiance collector. 261

7.8 Variation in the three repeats of the nadir radiance collector raw intensity signal at 800 nm during the intercalibration and day-to-day variation, relative standard deviation of measurements averages 3.1%. 262

7.9 Examples of change in raw downwelling irradiance signal at 500 nm during a measurement sequence. Site 6 shows very little variation while site 7 shows more variation in downwelling irradiance. The corrected data corrects for the steps which appear in the non corrected data due to rotating GRASS every 16 measurements, shown as dashed lines. 264

7.10 Example layout of polar plot with each dot representing a radiance collector at a different azimuth/zenith angle. The radius of the plot represents zenith angle (the centre 0°, the edge 60°) and the circumference represents azimuth values (shown on the figure). The solar principle plane runs from 0–180° with the sun positioned at 180°. The HDRF values for each radiance collector are linearly interpolated to form the polar plots in this chapter. 265

7.11 Typical Dome C conditions- clear skies and flat snow surface with small sastrugi. Photo taken from top of the "American Tower" from which the measurements by Hudson et al. (2006) were taken. 266

7.12 Map of the location of the measurement transect at Dome C running along the little used access road running from the base to the American Tower (Torre) (Image adapted from PNRA). 268

7.13 Location of ∼100 m transect over which GRASS measurements were taken. The transect runs parallel to a little used access "road" running from the main base to the "American tower" from which this photo was taken. The recent disturbed snow was due to tracked vehicles moving GRASS and ancillary equipment into position. 269

7.14 Example of snow pit ∼1×1×1 m dug after HDRF measurements were complete to measure snow grain size and type, density, temperature and penetration. 270

7.15 HDRF polar plots at 600 nm from each of the eight sites with site longitude and latitude (±5 m), average solar zenith angle, weather, surface conditions, selected snow pit data (snow stratigraphy, snow density and grain size) and a photo of each site. The solar principle plane is marked roughly on the photos as a dashed line. On the polar plots the solar principle plane runs from top to bottom with the sun at the base of the plots. 275

7.16 Comparison between reflected and non-reflected spatially averaged HDRF polar plot at 600 nm. Polar plot is made symmetrical in the right hand plot by reflecting and averaging across the solar principal plane. 279

7.17 Representative polar plots from HDRF averaged across all eight sites at wavelengths 400–1600 nm. Average solar zenith angle was 58.2±5.9°(1SD). Note different colour scale for each plot. 280

7.18 Comparison between BRF measurements by Hudson et al. (2006) (A) and BRF measurements from GRASS presented here (B) at a wavelength of 1000 nm (BRF approximates to HDRF at near infrared wavelengths). Relative difference (%) between plots A and B is shown in plot C. . . . 284

7.19 Variation in the viewing footprint of the nadir radiance collector as GRASS is rotated into four, 90° of azimuth apart, positions, shown as solid circles. Lengths show deviation of the viewing footprint from the centre, averaging 6.8 cm. The dashed circles show distance, each being 5 cm apart. 286

7.20 Variation in the viewing footprint of all radiance collectors on GRASS at different viewing azimuth/zenith angles, with the GRASS frame in one position only (no rotation). 287

7.21 Variation in the viewing footprint of all optics on GRASS (relative standard deviation (%)). 288

7.22 Variation in the viewing footprint of all radiance collectors on GRASS with the radiance collectors with different viewing zenith angle separation (10 and 15°) and different cone of acceptance (2 and 8°). 290

A.1 Data of albedo of snowpacks for different black carbon mass-ratios and snow thickness. 327

A.2 Albedo data for three different types of sea ice with increasing mass-ratio of black carbon and different sea ice thickness 328
A.3 Data for *e*-folding depth (m) of snow for different snow types, black carbon mass-ratio and snow thickness. 329
A.4 Data for *e*-folding depth (m) of three sea ice types for different sea ice thickness and black carbon mass-ratio 330

B.1 **Run 1 before layer added** Physical ice properties for bottom "clean" ice layer before additional layer added for run 1. Temperatue, density and salinity are measured from core sections, while brine salinity, brine density and brine and air volume are derived from equations of Cox and Weeks (1983). Photo of the ice core is also shown 332
B.2 **Run 1 after layer added** Physical ice properties for bottom "clean" ice layer and additional layer added for run 1. Temperature, density and salinity are measured from core sections, while brine salinity, brine density and brine and air volume are derived from equations of Cox and Weeks (1983). Photo of the ice core is also shown 333
B.3 **Run 2 before layer added** Physical ice properties for bottom "clean" ice layer before additional black carbon bearing layer added for run 2. Temperature, density and salinity are measured from core sections, while brine salinity, brine density and brine and air volume are derived from equations of Cox and Weeks (1983). Photo of the ice core is also shown 334
B.4 **Run 3 before layer added** Physical ice properties for bottom "clean" ice layer before additional black carbon bearing layer added for run 3. Temperature, density and salinity are measured from core sections, while brine salinity, brine density and brine and air volume are derived from equations of Cox and Weeks (1983). Photo of the ice core is also shown 335
B.5 **Run 3 after layer added** Physical ice properties for bottom "clean" ice layer and additional black carbon bearing layer for run 3. Temperature, density and salinity are measured from core sections, while brine salinity, brine density and brine and air volume are derived from equations of Cox and Weeks (1983). Photo of the ice core is also shown 336

B.6 **Run 4 before layer added** Physical ice properties for bottom "clean" ice layer before additional black carbon bearing layer added for run 4. Temperature, density and salinity are measured from core sections, while brine salinity, brine density and brine and air volume are derived from equations of Cox and Weeks (1983). Photo of the ice core is also shown 337

B.7 **Run 4 after layer added** Physical ice properties for bottom "clean" ice layer and additional black carbon bearing layer for run 4. Temperature, density and salinity are measured from core sections, while brine salinity, brine density and brine and air volume are derived from equations of Cox and Weeks (1983). Photo of the ice core is also shown 338

C.1 HDRF polar plots at wavelengths of 400, 800, 1000, 1200, 1400 and 1600 nm for site 1. The sun is at the base of each plot 340

C.2 HDRF polar plots at wavelengths of 400, 800, 1000, 1200, 1400 and 1600 nm for site 2. The sun is at the base of each plot 341

C.3 HDRF polar plots at wavelengths of 400, 800, 1000, 1200, 1400 and 1600 nm for site 3. The sun is at the base of each plot 342

C.4 HDRF polar plots at wavelengths of 400, 800, 1000, 1200, 1400 and 1600 nm for site 4. The sun is at the base of each plot 343

C.5 HDRF polar plots at wavelengths of 400, 800, 1000, 1200, 1400 and 1600 nm for site 5. The sun is at the base of each plot 344

C.6 HDRF polar plots at wavelengths of 400, 800, 1000, 1200, 1400 and 1600 nm for site 6. The sun is at the base of each plot 345

C.7 HDRF polar plots at wavelengths of 400, 800, 1000, 1200, 1400 and 1600 nm for site 7. The sun is at the base of each plot 346

C.8 HDRF polar plots at wavelengths of 400, 800, 1000, 1200, 1400 and 1600 nm for site 8. The sun is at the base of each plot 347

C.9 Downwelling data at 500 nm recorded from the integrating sphere on top of GRASS during the course of a measurement sequence, for all sites not included in chapter 7. 348

List of Tables

2.1 Summary of calculations completed where black carbon/HULIS is evenly distributed throughout the sea ice. 72
2.2 Summary of calculations completed where black carbon and HULIS is unevenly distributed in the sea ice. 72
2.3 Power law coefficients for relating e-folding depth to mass-ratio of black carbon, for wavelengths 300–600 nm, and over the mass-ratio range of black carbon listed. Uncertainties are ±1 standard deviation and calculated from fitting power law curves to figure 2.10. 78

3.1 Properties and measurement conditions of the snow and sea ice used in the study presented here. Measurement date, sky conditions, solar zenith angle and density are all from Grenfell and Maykut (1977). . . 107
3.2 Calculated $\sigma^{+}_{\text{scatt}}$, in granular white sea ice, blue sea ice, wet snow and dry snow. Error values show the average difference in calculated $\sigma^{+}_{\text{scatt}}$ values through making small changes to the data fit for obtaining these values. 113
3.3 Variation in derived σ_{scatt} and σ^{+}_{abs} of the blue sea ice and granular white sea ice from variation of the asymmetry parameter, g, at a wavelength of 550 nm. 115

4.1 Properties of snow and sea ice types studied. Optical and physical properties are based on work by Grenfell and Maykut (1977); Perovich (1990); Timco and Frederking (1996); Perovich (1996); Gerland et al. (1999); Fisher et al. (2005); King et al. (2005); France (2008); France et al. (2011); Marks and King (2013). 136
4.2 Level structure utilised for layers of snow/sea ice with different thicknesses and for the atmosphere. 138

5.1 Wavelengths of non-saturated and saturated spectra used to calculate reflectance. 182
5.2 Coefficients for polynomial function $F_1(T)$. 189

6.1 Black carbon mass-ratio in 75 L of seawater placed in 5 cm surface layer for each "run". The black carbon solution added to each 15 L of seawater is thoroughly mixed and the solutions in each of the five 15 L tubs are mixed with each other during addition to the top of the clean ice. 209
6.2 Ice thickness deduced from temperature data and core data when 5 cm layer has frozen at ice surface for each run. 216
6.3 Average ice physical properties of bottom layer and top black carbon bearing layer for each run (1–4). 217
6.4 Values of parameters used for each fit (A–G) including scattering cross-section used for the top, black carbon bearing layer, σ_{scatt}^{top}, the bottom clean ice layer, σ_{scatt}^{bottom}, mass-ratio of black carbon used in the TUV-snow model, $BC_{modelled}$, and if absorption by impurities other than black carbon, σ_{abs}^{+}, for the top and bottom layer was included. The asymmetry parameter, g, value is kept constant at 0.95 for each fit, as is the density and ice thickness for each fit. 228
6.5 Average scattering cross-section values of bottom "clean" ice layer for runs 1 to 4. 233
6.6 Variation in absorption cross-section ($cm^2\ kg^{-1}$) and scattering cross-section ($m^2\ kg^{-1}$) owing to variation in the asymmetry parameter at 400 nm. 242
6.7 Average ice properties measured from all ice cores before and after the addition of the 5 cm black carbon bearing ice layer. 247

7.1 Key to snow pit data including symbols for snow grain types, terms for measured snow grain size and snow hardness/penetration terms for snow penetrated using the tools described. 276

8.1 Summary table of the effects of impurities on albedo and *e*-folding depth.297

GLOSSARY

Absorption cross-section- Measure for the probability of an absorption process.

Albedo- True albedo is a measure of the upwelling irradiance from the whole hemisphere divided by downwelling irradiance from the whole hemisphere. However albedo is commonly reported as total upwelling flat plate irradiance divided by total downwelling flat plate irradiance and it is this value that is reported as albedo in the thesis. The difference between these two values under diffuse conditions is negligible. In the thesis the albedo is expressed mono chromatically rather than as a broadband albedo.

Anisotropic reflectance- Reflectance from a surface at different viewing angles is unequal.

Asymmetry parameter- Describes proportion of radiation scattered into the forward and backward direction, varies from -1 (all backward scattered) to 1 (all forward scattered).

Bidirectional Reflectance Distribution Function (BRDF)- Describes the ratio of incident light at a particular azimuth and zenith angle to the ratio of reflected light at a particular azimuth and zenith angle.

Bidirectional Reflectance Factor (BRF)- Ratio of upwelling light from a target surface to the upwelling light from a Lambertian surface under identical viewing and illumination geometries.

Black carbon- Formed in flames and emitted directly to atmosphere, very strong UV and visible light absorption (>5 m^2 g^{-1}), temperatures of vaporisation of 4000 K, aggregate morphology, insoluble in water/organic solvents.

Broadband- Light at multiple wavelengths

Diffuse radiation- Light that has undergone at least one scattering event.

***e*-folding depth-** Light decays exponentially through a medium, the *e*-folding depth is the depth over which light intensity reduces to $\frac{1}{e}$ (37%).

Goniometer- Device used to precisely measure angles.

Gonio Radiometric Spectrometer System- Goniometer system used to measure HDRF of target surfaces.

Hemispherical Directional Reflectance Factor (HDRF)- The field measurable quantity describing the ratio of surface radiance at a particular viewing and azimuth angle compared to the reflectance of a perfect Lambertian reflector (Spectralon panel) under identical viewing and illumination geometries.

Humic Like Substances (HULIS)- A class of organic molecules in atmospheric aerosol particles similar to terrestrial and aquatic humic substances.

Irradiance- The flux of radiant energy per unit area.

Isotropic radiation- Radiation intensity in all directions is equal.

Lambertian reflectance- Light reflectance from a surface is equal in all directions.

Mass ratio- The mass of black carbon per mass of snow/sea ice, expressed as ng of black carbon per g of snow/sea ice.

Mie scattering- Describes scattering by spheres using Mie's solution to Maxwell's equations. Maxwell's equations describe how electric and magnetic fields are generated and altered by each other and by charges and currents.

Mono-chromatic- Light at one wavelength

Nadir- 0° of zenith.

Optically thick- Minimum thickness of a medium where the surface albedo is independent of the underlying medium, thus a further increase in thickness of the medium has no effect on the albedo.

Photosynthetically Active Radiation (PAR)- Visible light- wavelengths 400–700 nm, used by photosynthetic algae.

Radiance- The flux of radiation subtending a solid angle in a given direction from a source.

Radiative forcing- The difference of radiant energy (sunlight) received by the Earth and energy radiated back to space. Quantified in units of Wm^{-2}.

Radiative transfer- Energy transfer through a medium in the form of electromagnetic radiation. Radiation is affected by absorption, emission, and scattering processes.

Reflectance- Upwelling radiance divided by downwelling radiance over a discrete angle.

Scattering cross-section- A hypothetical area which describes the likelihood of light or other radiation being scattered by a particle.

Single scattering albedo- Ratio of scattering optical depth to the total optical depth (scattering + extinction) of the atmosphere. Dimensionless quantity ranging from 0 to 1.

Spherical irradiance- Light passing through a point from all directions.

TUV-snow- Total Ultraviolet Visible- snow radiative transfer model used for radiative transfer calculations.

Chapter 1

Introduction

There is unequivocal evidence that the Earth's climate is warming and 95% certainty that human activities are resulting in rapid climate change (IPCC, 2013). A main contributor towards the climate change is anthropogenic pollution. Forms of anthropogenic pollutants and their associated radiative-forcing are summarised in figure 1.1, including aerosols and greenhouse gases. Where radiative-forcing is a change in net global energy balance, with a negative forcing causing cooling, and a positive forcing causing warming. The main focus of this thesis will be the climatic impacts of anthropogenic aerosols, in particular black carbon, which is highlighted in figure 1.1. Figure 1.1 shows that only black carbon out of all atmospheric aerosols has a positive radiative-forcing, thus is the only aerosol that has an overall warming effect on climate. Black carbon is defined by Bond et al. (2013) as a specific carbonaceous material with unique properties, which is formed in flames and emitted directly to the atmosphere. The unique properties are: very strong UV and visible light absorption (e.g. >5 m^2 g^{-1} at 550 nm (Bond and Bergstrom, 2006)), temperatures of vapourisation near 4000 K (Schwarz et al., 2006), aggregate morphology (Medalia and Heckman, 1969), and insoluble in water and common organic solvents (Fung, 1990). No other substance that has such a strong light absorption per unit mass is present in the atmosphere in significant quantities (Bond et al., 2013), consequently black carbon has wide ranging climatic effects, summarised in section 1.1, which make it potentially the second greatest contributor to global warming (Jacobson, 2001; Ramanathan and Carmichael, 2008; Bond et al., 2013).

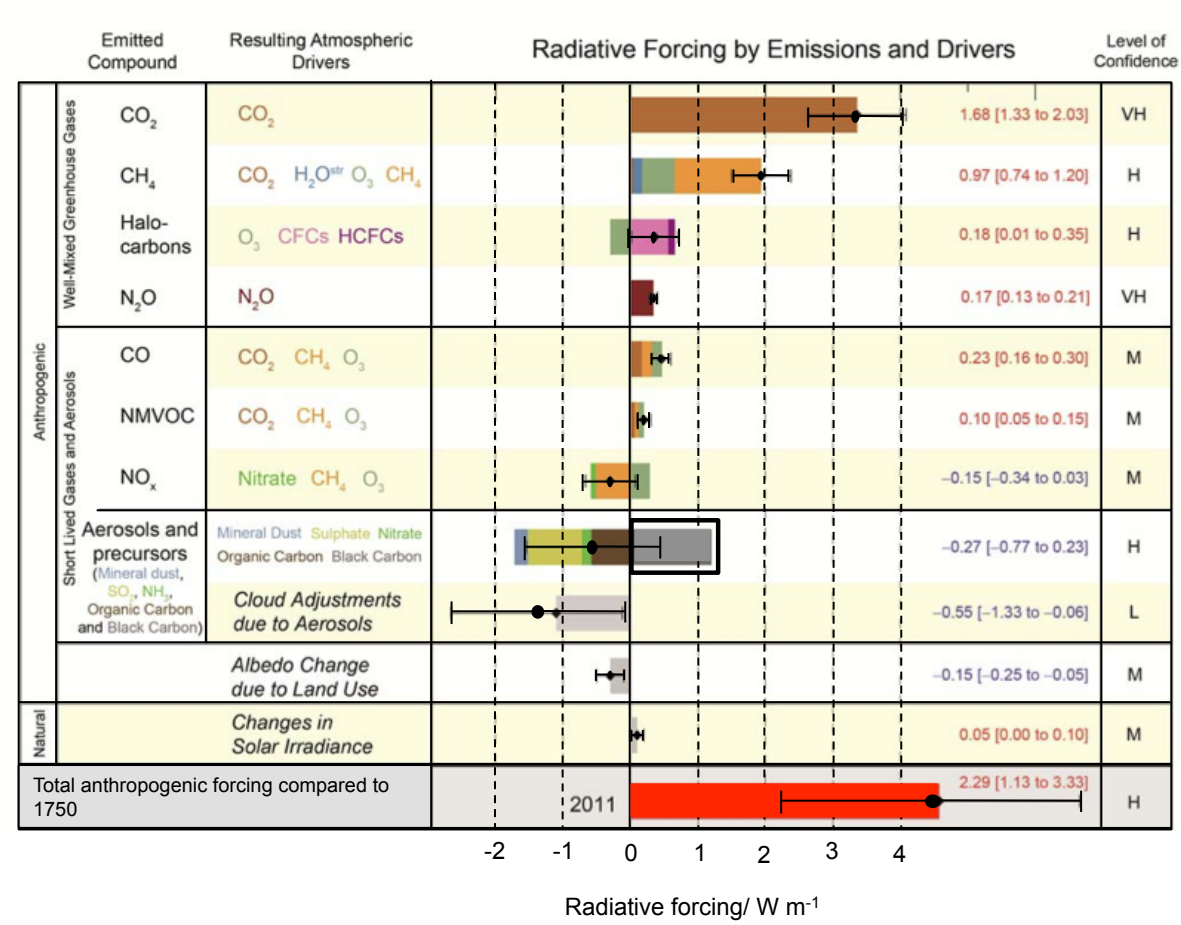

Figure 1.1 *– Radiative forcing factors defined by the IPCC report 2013, radiative-forcing by black carbon is highlighted. Credit: IPCC (2013).*

Sources of atmospheric black carbon and its climatic effects are summarised in figure 1.2. The largest global sources of black carbon are open burning of forests/savannahs, solid fuels burnt for cooking and heating and vehicle emissions. Global emissions for the year 2000 were 7500 Gg BC yr^{-1} (with 90% uncertainty limits ranging 2000–29000 Gg BC yr^{-1}). 4800 Gg BC was from energy related burning and 2800 Gg was from open biomass burning (Bond et al., 2013). Ramanathan and Carmichael (2008) state that uncertainty in published estimates for black carbon emissions is a factor of 2–5 on regional scales and at least ±50% on global scales. Other species co-emitted with black carbon include sulphur-containing particles; organic aerosols and compounds and nitrogen oxides, along with greenhouse gases (Bond et al., 2013). Black carbon has a residence time in the atmosphere of ∼1 week (Rhode et al., 1972) as it is relatively chemically inert, only being removed by wet or dry deposition. At high altitudes its lifetime is slightly longer (4–30 days) (Williams et al., 2002).

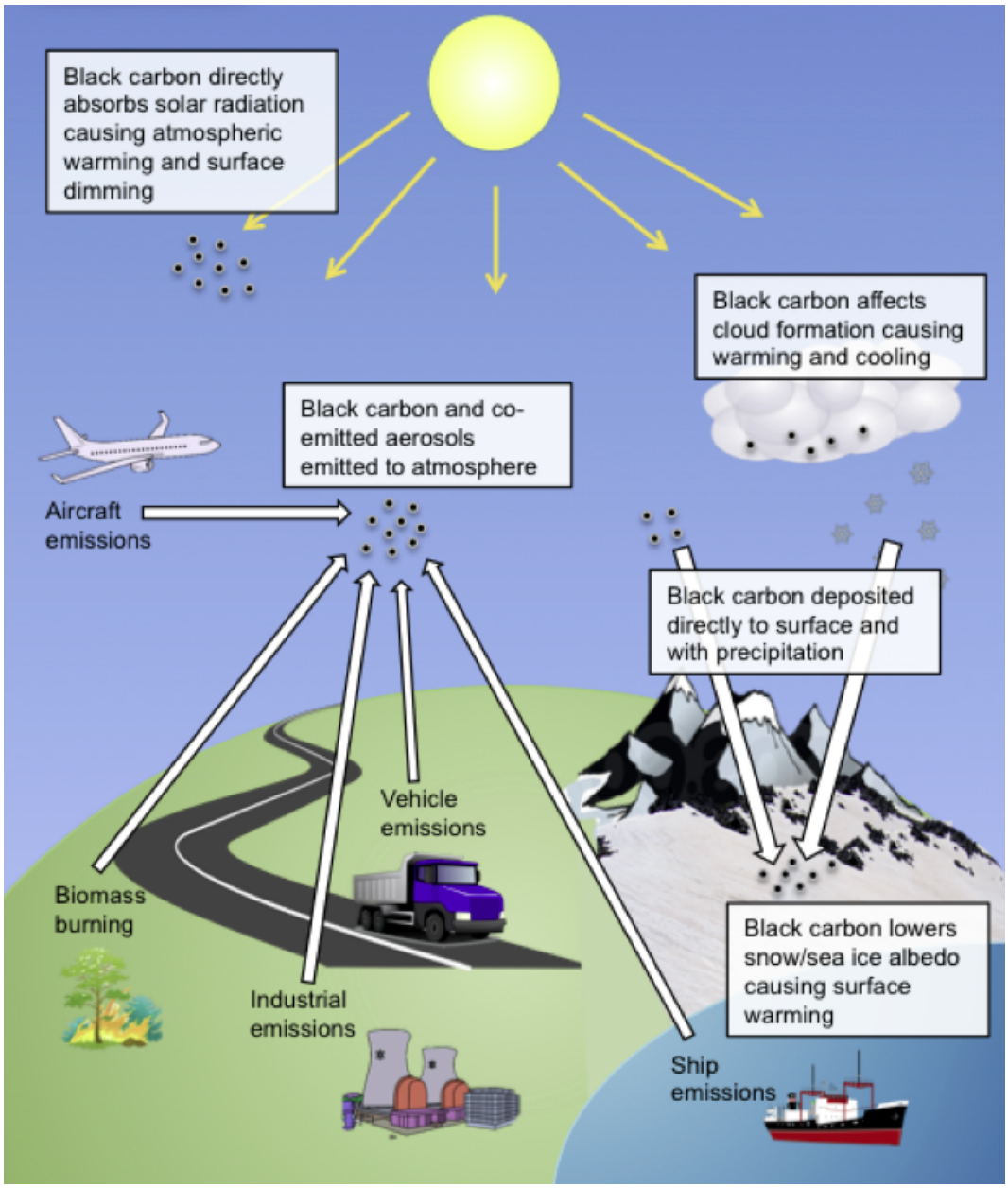

Figure 1.2 *– Black carbon sources and climatic effects, based on Bond et al. (2013).*

To understand global distribution of black carbon, models are used based on measurements from in-situ observations and remote sensing. The most quantitative and widespread data set for determining black carbon in the atmosphere is ground based measurements by AERONET (AErosol RObotic NETwork), a network of ground-based sun photometers which measure atmospheric aerosol properties providing continuous measurements of aerosol optical depth. The AeroCom project (Aerosol Comparisons between observation and models) (Kinne, 2006; Schulz et al., 2006) aimed to evaluate how well global aerosol models predict black carbon concentrations in the atmosphere, a review of the project is provided by Koch et al. (2009) finding that models are generally under-predicting atmospheric black carbon concentrations. Average global aerosol optical

depth attributable to black carbon from the AeroCom project is 0.0212, compared to typical total aerosol optical depth values for Europe of 0.17 (Meij et al., 2012). However, black carbon aerosol optical depth is highly variable across the globe with highest atmospheric concentrations of black carbon occurring in the northern hemisphere over eastern Europe, China and central Africa (Schulz et al., 2006).

Section 1.1 will examine effects of anthropogenic pollution, specifically black carbon, with section 1.2 particularly focussing on effects of black carbon in snow and sea ice which will be the focus of the thesis. Section 1.3 will describe methods to assess black carbon's impact on snow/sea ice and section 1.4 will provide an overview of the aims of the thesis.

1.1 Effects of anthropogenic pollution

The climatic effects of black carbon have been reviewed in detail by Highwood and Kinnersley (2006); Ramanathan and Carmichael (2008) and Bond et al. (2013), stating that black carbon could be the second greatest contributor to global warming after carbon dioxide (CO_2) and may be as important as CO_2 in melting of snowpacks and glaciers.

There are three key climatic effects of black carbon, shown in figure 1.2:

- Direct radiative-forcing
- Cloud effects
- Effects on snow and sea-ice

The associated climatic forcing of each of these three effects is shown in figure 1.3. Total climate forcing by black carbon is +0.65 W m^{-2} (90% certainty within 0.03–1.1 W m^{-2}) (Bond et al., 2013). Of particular interest for the study presented in this thesis is the radiative-forcing caused by black carbon in sea ice which has a low level of scientific understanding (LOSU).

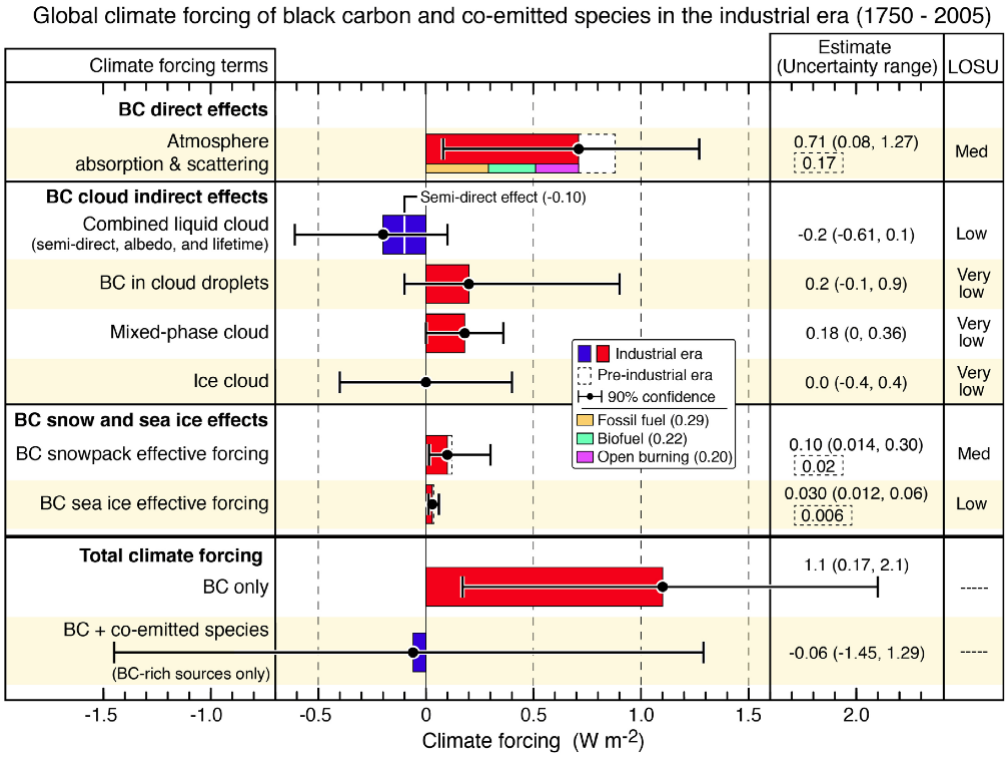

Figure 1.3 *– Black carbon effects and associated climatic forcing, credit: Bond et al. (2013).*

1.1.1 Direct radiative-forcing

Black carbon present in the atmosphere directly absorbs solar radiation. The solar radiation spectrum is shown in figure 1.4. Increased absorption of solar radiation causes a decreased planetary albedo and warming of the atmosphere, changing top of atmosphere energy balance. The amount of sunlight reaching the Earth's surface is thus reduced causing a surface dimming (Ramanathan and Carmichael, 2008; Bond et al., 2013). Direct radiative-forcing is a product of black carbon emissions, black carbon atmospheric lifetime, black carbon mass absorption cross-section and radiative-forcing per unit absorption optical depth (forcing efficiency). The effect was first described by Haywood and Shine (1995) and has been extensively studied since (e.g. Chung et al. (2005); Jacobson et al. (2005); Haywood and Ramaswamy (1998)). As a result direct radiative-forcing is the best quantified of the black carbon climate effects causing an annual mean forcing of 0.88 W m^{-2} (90% uncertainty range: 0.17 —1.48 W m^{-2}), although locally larger; up to +10 W m^{-2} over parts of Asia (Bond et al., 2013). The surface dimming effect caused by direct radiative-forcing results in a surface negative radiative-forcing of −3−−4 W m^{-2} (Ramanathan

and Carmichael, 2008). Chung et al. (2005) state that the direct radiative-forcing caused by black carbon is 70% of that caused by CO_2 and is greater than that caused by CH_4. The estimates of direct radiative-forcing are obtained from models of black carbon abundance and location. Direct radiative-forcing causes a surface warming concentrated in the northern hemisphere where black carbon atmospheric concentrations are highest, the response is greatest during winter and early spring (Chung et al., 2005; Bond et al., 2013).

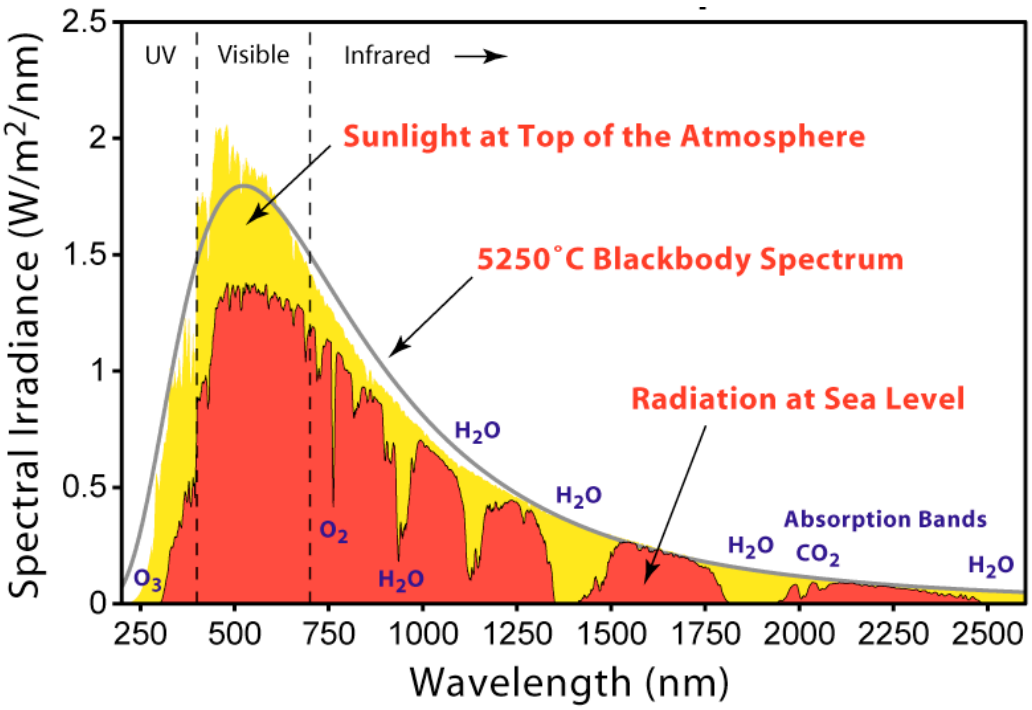

Figure 1.4 *– Solar radiation spectrum at the top and bottom of the atmosphere compared to a black body, credit: Global Warming Art.*

1.1.2 Cloud effects

Black carbon influences cloud properties via complex and diverse processes. The cloud effects are the largest source of uncertainty in quantifying black carbon's role in the climate system (Bond et al., 2013). The best estimate of the climate forcing owing to black carbon cloud effects is positive, $+0.23$ W m^{-2}, with substantial uncertainty (-0.47 to $+1.0$ W m^{-2} 90% uncertainty range). Clouds can be affected in four ways by black carbon causing both a positive and negative radiative-forcing, as seen in figure 1.3:

- Semi-direct effects including changes to the vertical temperature structure of the atmosphere which could shift cloud distributions

- Liquid (warm) cloud effects including changes in number concentration of liquid cloud droplets, changes in cloud albedo and lifetime of liquid (warm) clouds
- Changes in phase partitioning and precipitation in mixed phase clouds
- Changes in ice particle number concentration affecting ice (cold) clouds

A review of the semi-direct effects of black carbon (and other atmospheric aerosols) on cloud cover is covered by Koch and Genio (2010), who describe several possible effects depending on the situation of black carbon in the atmosphere. If black carbon is embedded within a cloud layer cloud cover is decreased as cloud droplets evaporate due to warming by black carbon absorbing radiation (Hansen et al., 1997; Ramanathan et al., 2001b). Atmospheric aerosols situated below cloud can enhance convection and cloud cover, while atmospheric aerosols above a cloud stabilise the underlying layer increasing certain cloud types but reducing others. Overall there is a net negative surface radiative-forcing due to the semi-direct effect.

Black carbon has two competing indirect effects on cloud droplet number in liquid clouds: firstly it increases aerosol number concentration, increasing cloud droplet concentration and thus cloud formation causing negative forcing; secondly black carbon particles act as sites to collect soluble material, reducing cloud droplet number concentration, resulting in positive radiative-forcing (Kristjansson, 2002).

The cloud lifetime effect in liquid clouds is due to the presence of increased aerosol concentration resulting in more and smaller droplets which collide less efficiently, potentially leading to longer cloud lifetimes thus greater cloud reflectivity. The certainty in this effect is very low, and forcing could be positive or negative, global climate models use a negative forcing (Koch and Genio, 2010).

Absorption of black carbon within cloud droplets decreases cloud albedo leading to the formation of "brown clouds" which heats clouds and dissipates them, causing a 0.2 W m^{-2} surface forcing (Bond et al., 2013) . Conversely, Twomey (1974) suggested higher droplet concentration due to particles like black carbon in the atmosphere can enhance cloud albedo, known as the "Twomey effect".

In mixed phase clouds (liquid and ice) black carbon can act as ice nuclei increasing ice formation and fall out causing a positive radiative-forcing of $+0.18$ W m^{-2} (± 0.18 W m^{-2} with 90% certainty) (Bond et al., 2013)

For ice clouds black carbon both increases and decreases ice nuclei and cirrus cloud lifetime depending on a variety of factors. Different modelling suggests either a positive or negative forcing of 0 ± 0.4 W m^{-2}.

1.2 The effects of anthropogenic pollution on snow and sea ice

The focus of the study presented in this thesis will be effects of black carbon in snow and, in particular, sea ice. Entrainment of anthropogenic pollutants into snow and sea ice causes increased absorption of incident solar radiation, which is widely reported to decrease surface albedo, exacerbating melting, (e.g. Chýlek et al. (1983); Warren (1984); Warren and Wiscombe (1985); Clarke and Noone (1985); Ledley and Thompson (1986); Warren and Clarke (1990); Light et al. (1998); Grenfell et al. (2002); Jacobson (2004); Flanner et al. (2007); Doherty et al. (2010); Reay et al. (2012); France et al. (2012); Goldenson et al. (2012); Holland et al. (2012); Bond et al. (2013)) and shorten light penetration depths or *e*-folding depths (the depth of snow or sea ice over which light intensity reduces to $\frac{1}{e}$($\sim$37%)), which although is not as important for climatic effects, can affect photochemical and photobiological processes that occur in snow and sea ice (e.g. Reay et al. (2012); France et al. (2012)). The effects on albedo and light penetration are shown in figure 1.5 and discussed in sections 1.2.1 and 1.2.2 respectively. 80% of light absorption due to impurities in snow is due to black carbon (Doherty et al., 2010). Although nearly all aerosols (except sulphate and sea salt) exert a positive radiative-forcing when incorporated into surface layers of pure snow and sea ice as multiple scattering within snow and sea ice enables small mass-ratios of impurities to absorb large amounts of radiation (Warren and Wiscombe, 1980), described in further detail in section 1.3.2.1 . Doherty et al. (2010) show non-black carbon constituents in Arctic snow are mainly brown carbon and dust with most absorption by non-black carbon components due to brown carbon. HULIS (HUmic Like Substances) has also been found to be a common absorbing constituent of snow (e.g. Voisin et al. (2012); France et al. (2012)). Light et al. (1998) suggest sediment and algae are common absorbing impurities in sea ice.

Anthropogenic pollutants can be entrained into snow through wet and dry deposition.

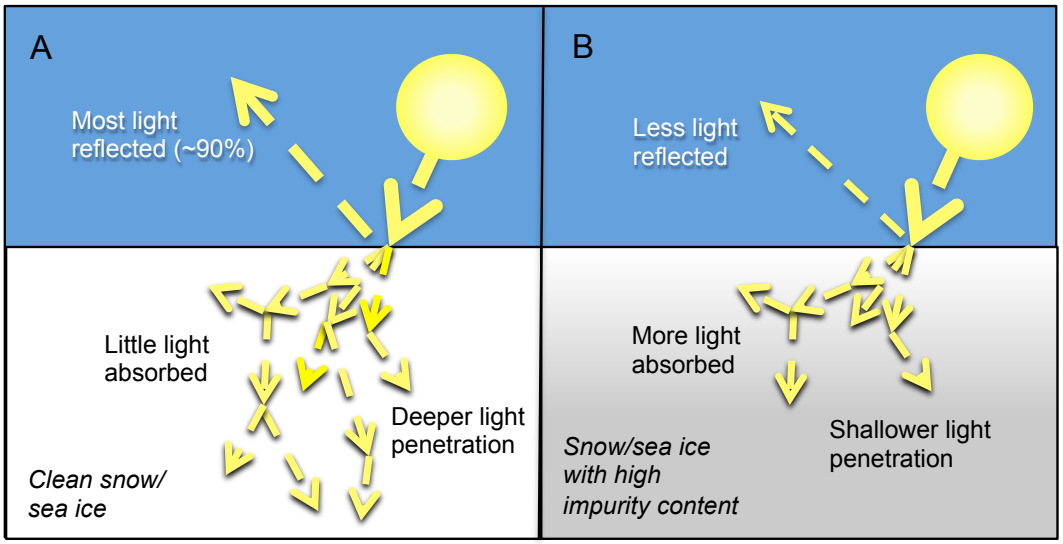

Figure 1.5 *– The role of anthropogenic pollutants in decreasing albedo and light penetration depth in snow and sea ice. A) Clean snow/sea ice; longer e-folding depths and larger albedo. B) Snow/sea ice with impurities; shorter e-folding depths and smaller albedo.*

Anthropogenic pollutant entrainment into sea ice is more diverse and is summarised in figure 1.6. Black carbon is predominately entrained into sea ice, like snow, through wet and dry atmospheric deposition (Jacobson, 2004). In the case of wet deposition black carbon will be deposited onto sea ice with snow fall. When the snow melts some black carbon will be left behind on the sea ice surface. In Antarctica seawater may inundate snow overlying sea ice leading to formation of "snow-ice" (Massom et al., 2001), which will include any black carbon originally in the snow. Black carbon may also enter sea ice, to a lesser degree, directly from seawater (Dittmar, 2008), and from sediment inclusions including black carbon where sea ice forms over shallow ocean shelves (Masiello, 1998; Middelburg et al., 1999). The process by which black carbon is entrained into the sea ice will affect its distribution in the sea ice, explored in chapter 2. Although sea ice is predominately snow covered the times of year corresponding to a snow-free sea ice coincide with the times of largest solar radiation, thus black carbon in the sea ice has greater effect.

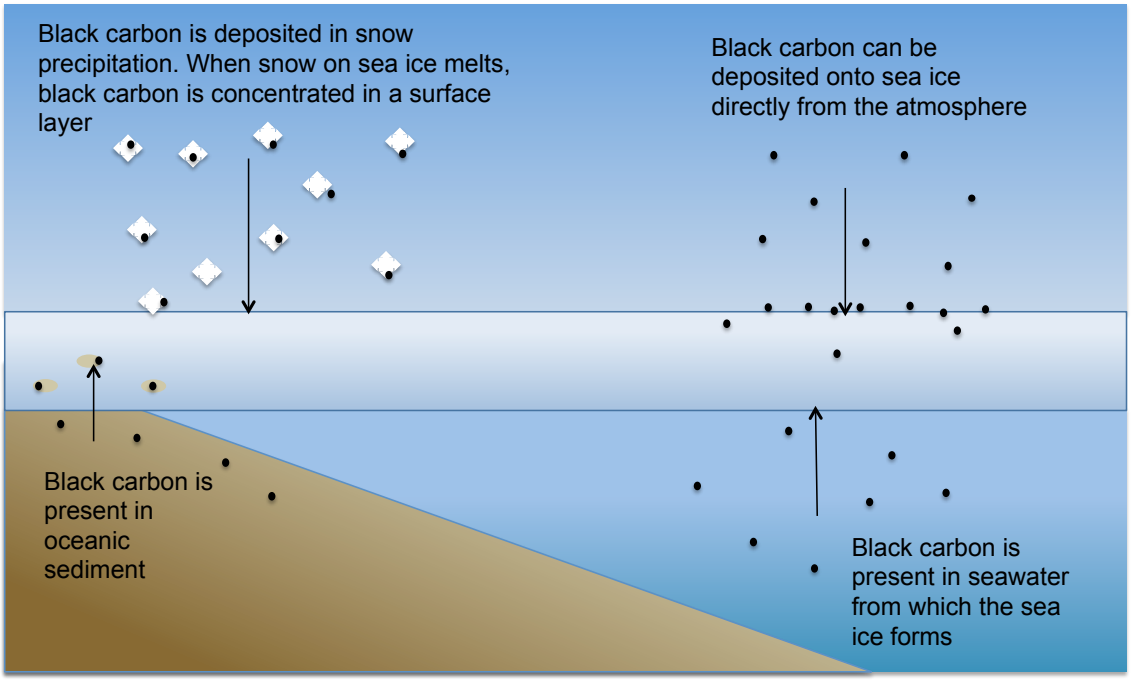

Figure 1.6 *– Methods of entrainment of black carbon into sea ice.*

1.2.1 Albedo effect

The incorporation of black carbon and other anthropogenic pollutants into snow and sea ice lowers albedo through increased absorption of downwelling solar radiation, which causes warming of the snow/sea ice resulting in increased melting, depicted in figure 1.5 (e.g. Chýlek et al. (1983); Warren (1984); Warren and Wiscombe (1985); Clarke and Noone (1985); Warren and Clarke (1990); Hansen and Nazarenko (2004); Flanner et al. (2007); Doherty et al. (2010); Reay et al. (2012)). Snow and sea ice have a natural cooling effect on the planet due to their high albedo, thus a loss of snow and sea ice owing to melting causes a drastic decrease in planetary albedo, as the high surface albedo of the snow/sea ice is replaced with the low surface albedo of rock/ocean, an effect demonstrated by figure 1.7. Decreased planetary albedo causes increased planetary temperatures which feeds back to further snow/sea ice melting. Black carbon may be a main contributing factor towards unprecedented snow and sea ice decline in the Northern hemisphere. Annual mean Arctic sea ice extent has decreased by 3.5–4.1% per decade from 1979–2012 with summer extent decreasing by 9.4–13.6% per decade. Northern hemisphere snow cover has decreased since the mid 20^{th} century by 1.6% per decade for March and April and 11.7% for June from 1967–2012 (IPCC, 2013) .

Figure 1.7 *– Photo of ablating Antarctic sea ice showing the difference in albedo between sea ice/snow and ocean. Sea ice has a noticeably much higher albedo than the surrounding open ocean.*

Clarke and Noone (1985) and Warren and Wiscombe (1985) were the first to show there was enough black carbon present in the Arctic snow to affect climate while Hansen and Nazarenko (2004) and Jacobson (2004) were the first to produce model studies on the climate forcing due to change in albedo caused by black carbon in snow and sea ice. Hansen and Nazarenko (2004) suggest a climate forcing of +0.3 W m^{-2} due to black carbon in snow in the northern hemisphere also suggesting black carbon in snow is twice as effective as CO_2 at altering global surface air temperature. The estimate of Hansen and Nazarenko (2004) is higher than recent estimates. Section 1.3.2 reviews radiative-transfer modelling work investigating the effects of black carbon in snow and sea ice. The effects of black carbon on snow are much more widely reported than black carbon in sea ice, which will be the focus of this thesis.

The 2013 IPCC report quantifies the radiative-forcing from black carbon on snow and sea ice as +0.04 W m^{-2} (95% uncertainty limits 0.02–0.09 W m^{-2}) with low confidence. Bond et al. (2013) suggest the forcing due to black carbon in snow is 0.035 W m^{-2} (0.01–0.09 W m^{-2}) and due to black carbon in melting snow free sea ice is 0.012 W m^{-2} (0.008–0.017 W m^{-2}).

1.2.2 Effects on light penetration

Anthropogenic pollutants can also decrease light penetration depths in snow and sea ice, as shown in figure 1.5. Although decreasing light penetration depths are not as important for climate, it is important for photobiology and photochemistry occurring in the snow and sea ice, although this has been far less reported than the albedo effects.

Sea ice forms an important habitat for photosynthetic algae, which provide a concentrated primary food source for polar organisms (Lizotte, 2001; Thomas and Dieckmann, 2002; Mock and Thomas, 2005). The algae, which typically occur at maximum concentrations in the bottom few centimetres of sea ice (Perovich, 2006), require photosynthetically active radiation (visible light, wavelengths 400–700 nm, PAR) to photosynthesise. A reduction in light penetration depth (*e*-folding depth), due to black carbon, will reduce PAR at the base of the sea ice. Sea ice algae are highly adapted to low light conditions, and can quickly respond to a reduction in light, (Raven et al., 2000; McMinn and Ryan, 2003; Mangoni et al., 2009; Arrigo et al., 2010) however small values of PAR limit algae growth (Welch and Bergmann, 1989; Cota and Sullivan, 1990; Mundy et al., 2005). PAR is the limiting factor to algae growth for most of the year (Saenz, 2011). Black carbon may reduce PAR at the sea ice base. The effect of black carbon in sea ice at reducing *e*-folding depth and PAR has not previously been quantified, although dissolved and particulate organic matter have been shown to significantly attenuate sea ice PAR and UVR transmission (Belzile et al., 2000).

Both snow and sea ice are photochemically active, with sunlit snow and ice playing an important role in the processing of atmospheric species and having a significant effect on the overlying atmospheric chemistry. Snow photochemistry is reviewed in detail by Grannas et al. (2007). Black carbon in snow and sea ice may alter photochemical processes. The effects on photochemistry in snow due to increasing black carbon mass-ratios were examined by France et al. (2012) and Reay et al. (2012). Reay et al. (2012) showed that doubling black carbon concentrations decreased depth-integrated production rates of NO_2 and OH to ∼70% and ∼65% respectively for solar zenith angles greater than 60° and black carbon concentrations greater than 8 ng g^{-1}. The effects of black carbon on sea ice photochemistry have not been investigated.

1.3 Methods to access snow and sea ice response to anthropogenic pollution

Section 1.3 will explore different methods to constrain potential impacts of black carbon on snow and sea ice and review previous work including; fieldwork to measure black carbon, radiative-transfer modelling and experiments with artificial snow and sea ice.

1.3.1 Fieldwork

Fieldwork has been carried out to assess concentrations of black carbon in snow, and to a much less extent sea ice. Black carbon concentrations in snow have been measured using three different filter based methods. Firstly the thermo-optical method, or similar variations (Chýlek et al., 1987; Cachier and Pertuisot, 1994; Lavanchy et al., 1999; Xu et al., 2006; Jenk et al., 2006; Hagler et al., 2007a,b; Legrand and Puxbaum, 2007; Ming et al., 2008; Forsström et al., 2009; Ming et al., 2009; Thevenon et al., 2009; Xu et al., 2009a,b; Hadley et al., 2010). The thermo-optical method involves a stepwise combustion of material on a filter. There are two variations of the thermo-optic method: the IMPROVE (Interagency Monitoring of Protected Visual Environments) method (Chow et al., 1993), known as Total Optical Reflectance (TOR) which measures changes in light reflectance through the stepwise combustion process; and the NIOSH (National Institute of Occupational Safety and Health) method (Birch and Cary, 1996) referred to as Total Optical Transmission (TOT) which measures changes in light transmission during the combustion process to derive the black carbon concentration. A comparison between the two methods is provided in detail in Chow et al. (2001).

Secondly, the laser-induced incandescence method is used to detect refractory black carbon mass with a Single Particle Soot Photometer (SP2) (McConnell et al., 2007; McConnell and Edwards, 2008). A sample filter containing black carbon is heated to vaporisation temperatures ($\sim$4000 K) with an infrared intracavity laser, then incandescence proportional to refractory black carbon mass is detected to deduce the concentration of black carbon on the filter.

Thirdly, optical analysis of black carbon concentrations on filters is completed using

an integrating-plate spectrophotometer (Clarke and Noone, 1985) and later using an improved method with an ISSW Spectrophotometer, which incorporates an integrating sandwich and an integrating sphere (Grenfell et al., 2011; Doherty et al., 2010). The ISSW Spectrophotometer creates multiple reflections through the filter sample through sandwiching the sample between the output from an integrating sphere and a diffusing plate, enhancing the absorption by the filter. The method uses the wavelength-dependence of the measured light absorption on the filter to calculate the black carbon concentration (Doherty et al., 2010). This method is advantageous as the absorption cross-section is directly measured compared to other methods where a mass is obtained.

Measured concentrations of Arctic black carbon from the above studies are mostly from snow surfaces in March/April/May on snow that has not experienced melting. Black carbon values range from 3 ng g^{-1} on the Arctic ocean (∼85–90°N) (Doherty et al., 2010) to 31 ng g^{-1} at Abisko, Sweden (∼68.3°N) (Clarke and Noone, 1985). Measurements of black carbon in sea ice are extremely limited. A few cores taken by Doherty et al. (2010) suggest the black carbon content of a snow free melting sea ice granular surface layer is similar to that of the snow that previously covered it, averaging 8 ng g^{-1} (3–15 ng g^{-1}) (Doherty et al., 2010). This black carbon concentration in sea ice would cause an albedo reduction of 0.01–0.028 and an estimated global annual radiative-forcing of 0.012 W m^{-2} (Bond et al., 2013). The results from Doherty et al. (2010) also suggest that black carbon is concentrated at the surface of sea ice, although their results are not conclusive. Black carbon in Arctic sea ice was also measured at a few sites by Grenfell et al. (2005) finding an average value of 5.5 ng g^{-1}, however there was a large degree of uncertainty in the method used owing to the presence of other transparent particles in the sea ice, which may have obscured black carbon particles.

Fieldwork is limited by expense and safety and also only enables investigation of small, accessible areas of the planet.

1.3.2 Radiative-transfer modelling

Radiative-transfer modelling of the effects of black carbon on snow and sea ice is highly advantageous as a large range of lateral and temporal parameters can be

explored. Section 1.3.2 will first discuss the theory behind radiative-transfer modelling (section 1.3.2.1) and then go on to review previous radiative-transfer modelling of the effects of black carbon on snow and sea ice (section 1.3.2.2).

1.3.2.1 Radiative-transfer theory

Radiative-transfer describes the propagation of electromagnetic radiation (photons) through a medium. Photons are affected by absorption, emission, and scattering processes; they are lost through absorption, created by emission and are redistributed through scattering. The medium through which photons travel will have specific absorption, scattering and emission properties.

In the case of snow and sea ice only absorption and scattering processes are important at shortwave wavelengths. The optical properties of snow are reviewed in detail by Warren (1982) and the optical properties of sea ice are reviewed by Perovich (2003a). Snow consists of ice grains surrounded by air, while sea ice consists of pure ice with brine and air pockets. In clean snow absorption of photons may occur as photons travel trough the ice, while in clean sea ice absorption occurs as photons travel through ice and brine. Absorption by air is considered negligible (Perovich, 1996). Scattering occurs due to inhomogeneities in the snow or sea ice. In clean snow and sea ice scattering occurs predominately at air-ice boundaries between snow grains or due to trapped air bubbles in sea ice. The ice-brine refractive index is much less than ice-air, thus in sea ice scattering by brine pockets is much less than air pockets (Perovich, 2003a). The scattering cross-section is a function of grain size; scattering cross-section is inversely proportional to grain size (Kokhanovsky and Zege, 2004). Additional impurities in snow and sea ice, such as black carbon, are considered to only absorb radiation and not contribute to scattering. The absorption and scattering of photons in snow and sea ice is summarised in figure 1.8

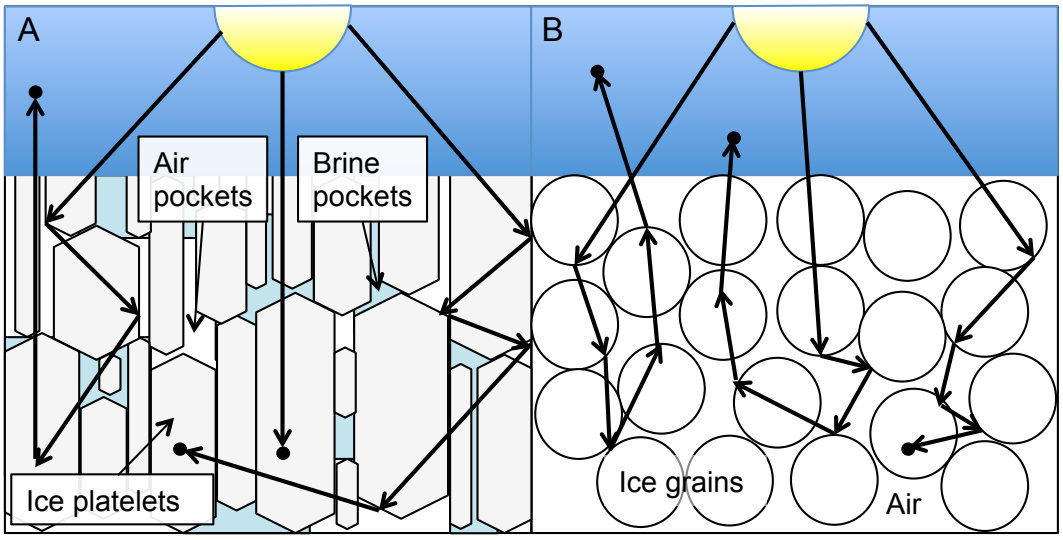

Figure 1.8 *– Absorption and scattering of photons in A) sea ice and B) snow. In sea ice and snow scattering occurs at air-ice boundaries and absorption occurs as photons travel through ice.*

Radiative-transfer modelling of the atmosphere and snow/sea ice uses a plane parallel approximation, which assumes variations in the atmosphere, clouds, snow and sea ice are much more dramatic in the vertical direction over horizontal. Thus any horizontal variations in optical properties are ignored and radiative properties only depend on vertical structure. The curvature of the Earth is also ignored in a plane parallel approximation, although it can be fixed by a pseudo-spherical correction (Petty, 2006).

All radiative-transfer models use a solver to numerically solve the radiative-transfer equation. Solvers include, but are not limited to; an Eddington approximation, discrete ordinate method, delta-Eddington method and a Monte Carlo method.

The simplest form of a radiative-transfer model is the two stream approximation which divides radiative-transfer into an upwelling hemisphere and a downwelling hemisphere and assumes intensity is constant within each hemisphere, thus radiation propagates into two discrete directions. Two-stream approximation captures the essence of the radiative transfer of light and is commonly utilised in global circulation models and weather forecasting models. A simple two stream approximation can be used to explain common observations such as the colour and brightness of the sky and clouds, scattering in milk causing the white appearance and the darkening of wet sand (**?**). A common plane parallel radiative-transfer code based on the two stream approximation is the Eddington-approximation (Petty, 2006). The delta-Eddington

model (Joseph et al., 1976) is an improvement of the Eddington approximation for highly asymmetric phase functions by combining the two stream approximation with a Dirac delta function. Other radiative transfer codes based on the two stream approximation include Quadrature and Hemispheric constant models.

The Monte Carlo method looks at the individual trajectories of large numbers of photons through a medium based on the statistical properties of the photons. The statistical probably of scattering and absorption of the photons in the medium is determined from albedo and phase functions. The Monte Carlo method differs from other radiative transfer models and is beneficial as it can handle non plane-parallel conditions. However, a draw back of Monte Carlo models is the vast numbers of photons which have to be modelled in order to obtain statistically relevant results (Petty, 2006).

The most widely used plane parallel radiative transfer code is the discrete ordinates method (DISORT) dscribed in detail by Stamnes et al. (1988). The DISORT code is a generalisation of the Eddington approximation (two stream method) to include a large number of individual streams in each hemisphere with each one representing a different direction (Petty, 2006).

In this thesis the Tropospheric Ultraviolet Visible (TUV)-snow radiative-transfer model (Lee-Taylor and Madronich, 2002) is used to investigate the effects of black carbon on snow and sea ice. The TUV-snow model is a one-dimensional coupled atmosphere-snow/sea ice radiative-transfer model using the DISORT code, which is described in detail in chapter 2, section 2.2.

1.3.2.2 Review of previous radiative-transfer modelling of black carbon in snow and sea ice

Radiative-transfer modelling of the effects of black carbon on snow albedo is extensive. Early work by Chýlek et al. (1983); Warren (1984); Warren and Wiscombe (1985); Clarke and Noone (1985), demonstrated that black carbon in snow could act as a possible radiative-forcing component, with a reduction in snow albedo of 1–3% (Clarke and Noone, 1985). More recently models have progressed into looking at the global radiative-forcing due to black carbon in snow. Bond et al. (2013) provides a comparison of models of possible radiative-forcing due to black carbon in snow

by Hansen and Nazarenko (2004); Jacobson (2004); Hansen et al. (2005, 2007); Flanner et al. (2007, 2009); Koch et al. (2009); Rypdal et al. (2009); Skeie et al. (2011); Wang et al. (2011), with the suggested forcing ranging from 0.024 W m^{-2} (Skeie et al., 2011) to 0.16 W m^{-2} (Hansen and Nazarenko, 2004) for present day forcing, showing a fair degree of uncertainty.

Conversely to snow, very limited radiative-transfer modelling has been conducted into the effects of black carbon on the albedo of sea ice (Ledley and Thompson, 1986; Light et al., 1998; Grenfell et al., 2002; Jacobson, 2004; Holland et al., 2012; Goldenson et al., 2012). Although sea ice optical properties have been investigated (Perovich, 2006; Grenfell and Maykut, 1977; Perovich, 1998a; Perovich et al., 1998b, 2002; Perovich, 2003a; Light et al., 2008).

Ledley and Thompson (1986) showed that soot deposition on sea ice following a nuclear disaster could significantly decrease Arctic sea ice albedo, resulting in decreased sea ice thickness and potential ice free conditions in summer. Ledley and Thompson (1986) used a one-dimensional thermodynamic sea ice model to examine the change in sea-ice albedo due to smoke-fall following a nuclear war, investigating how varying the time of year and duration of smoke-fall changes the effect on sea ice. They suggest that smoke-fall would have a serious impact on sea ice, with the largest perturbations occurring with spring smoke-fall.

Light et al. (1998) focused their radiative-transfer study on the effects of included sediment particles on the albedo of a multi-year frozen sea ice. Using a structural optical model in combination with a four-stream radiative-transfer model they investigated the effects of sediment particle mass-ratio, vertical distribution and particle size, on sea ice albedo and compared the albedo change caused by sediment particles to the albedo change caused by one mass-ratio of black carbon, suggesting 150 ng g^{-1} of soot within sea ice can lead to a 30% decrease in sea ice surface albedo.

Jacobson (2004) used a one-dimensional radiative-transfer calculation under direct solar conditions with a solar zenith angle of 72° to investigate change in albedo with mass-ratios of 0, 25, 100, 250 and 500 ng g^{-1} of black carbon in sea ice. Jacobson (2004) suggest 25 ng g^{-1} of black carbon can reduce sea ice albedo by 2.1% at a wavelength of 550 nm.

Grenfell et al. (2002) collected mass-ratios of soot in snow and sea ice samples

during the Surface Heat Budget of the Arctic Ocean (SHEBA) experiment. They concluded the soot mass-ratios found in sea ice could modify the melt cycle of snow-free sea ice through acceleration of summer ablation. Using a multilayer four-stream radiative-transfer model they investigated effects of varying mass-ratios and vertical distribution of soot on albedo, between wavelengths of 350–2750 nm. Grenfell et al. (2002) report a 1% albedo decrease for an increase in black carbon mass-ratio from 0–100 ng g^{-1} in the top 1cm layer of their sea ice.

Black carbon in sea ice has very recently been added to a few global climate models; Goldenson et al. (2012) used the Community Earth System Model Version 1 (CESM1) to model the forcing due to black carbon and dust in snow and sea ice, and Holland et al. (2012) utilised the Community Climate System Model 4 to investigate the impact of melt ponds and aerosols (black carbon and dust) on Arctic sea ice. Goldenson et al. (2012) suggest black carbon could cause a decrease in Arctic sea ice thickness of 0.34 m in September, while Holland et al. (2012) conclude that black carbon and dust causes an annual average 0.2 W m^{-2} increase in shortwave absorption in Arctic sea ice over the 20th century, which could decrease Summer sea ice area by 0.5 million km^2.

Detailed knowledge on the effects of black carbon on sea ice is still very limited. The work presented in this thesis will use radiative-transfer calculations to better constrain the effects of black carbon on sea ice albedo and light penetration depths including; a detailed study of effects of different black carbon distribution in sea ice, the effects of snow cover over sea ice and the response of different types of sea ice e.g. multi-year ice versus first year ice. The results from the radiative-transfer calculations are presented in chapters 2–4.

1.3.3 Experiments on artificial snow and sea ice

Extensive radiative-transfer modelling has been carried out on the effects of black carbon on snow albedo, and to a much lesser extent the effects of black carbon on sea ice. Although models are highly advantageous they are limited by a need for validating to ensure the models represents reality. Validation can be conducted in the field although this is difficult to achieve, artificial snow and sea ice can also be used for model validation.

Radiative-transfer models of pure-snow albedo have been validated by measurements

(Wiscombe and Warren, 1980; Grenfell et al., 1994; Jacobson, 2004). A study by Brandt et al. (2011) found good agreement between theory and measured albedo reduction owing to one mass-ratio of black carbon (2500 ng g^{-1}) in snow. Validation of model predictions of reduction in snow albedo owing to a range of black carbon mass-ratios (0–1700 ng g^{-1}) and snow grain sizes (55, 65, 110 μm) has been conducted by Hadley and Kirchstetter (2012) using artificial snow. The results of Hadley and Kirchstetter (2012) are used to validate the Snow, Ice and Aerosol radiation (SNICAR) model (Flanner et al., 2007) which is used in the 2013 IPCC report (IPCC, 2013).

Validation of models for the effects of black carbon on sea ice has not been undertaken previously and will be investigated in chapters 5 and 6 of this thesis through generation of artificial sea ice using a sea ice simulator.

1.3.4 Remote sensing

Satellite borne instruments are used to remotely measure planetary albedo providing information about expansive and inaccessible areas of the planet (e.g. Brest and Goward (1987), Wielicki et al. (2005)). There is potential for black carbon mass-ratios in snow and sea ice to be derived from albedo measurements from satellites (Warren, 2012; Painter et al., 2012). The European Space Agency and Norwegian Space Centre black carbon PRODEX project was set up to develop an approach to use Earth observation by satellites for black carbon monitoring. A test site was set up in Svalbard where simultaneous satellite and field measurements of spectral reflectance were acquired. Satellite data was taken from Terra MODIS and ENVISAT MERIS. Snow samples were also taken at the field site to determine the fraction of black carbon and other organic/lithogenic material. Initial results show that a model would be required to determine between various materials present in the snow, which is currently in development. Remote sensing would enable large scale monitoring of Polar black carbon, however Warren (2012) also highlight the following limitations to obtaining black carbon concentrations in snow for satellite observations: difficulties determining snow from thin cloud layers over snow, which may also contain black carbon e.g. Arctic haze, and effects of the anisotropic reflectance of snow, discussed in detail in the subsequent section, 1.3.5.

1.3.5 Anisotropic reflectance of Polar surfaces

Polar snow and sea ice surfaces do not reflect light isotropically; reflectance varies with viewing and illumination angle. Most satellite sensors measure reflectance at a few viewing angles, which tend to be close to nadir, and over a limited field of view. Rather than directly measuring surface albedo, which should include radiance from the whole hemisphere, an effect demonstrated by figure 1.9.

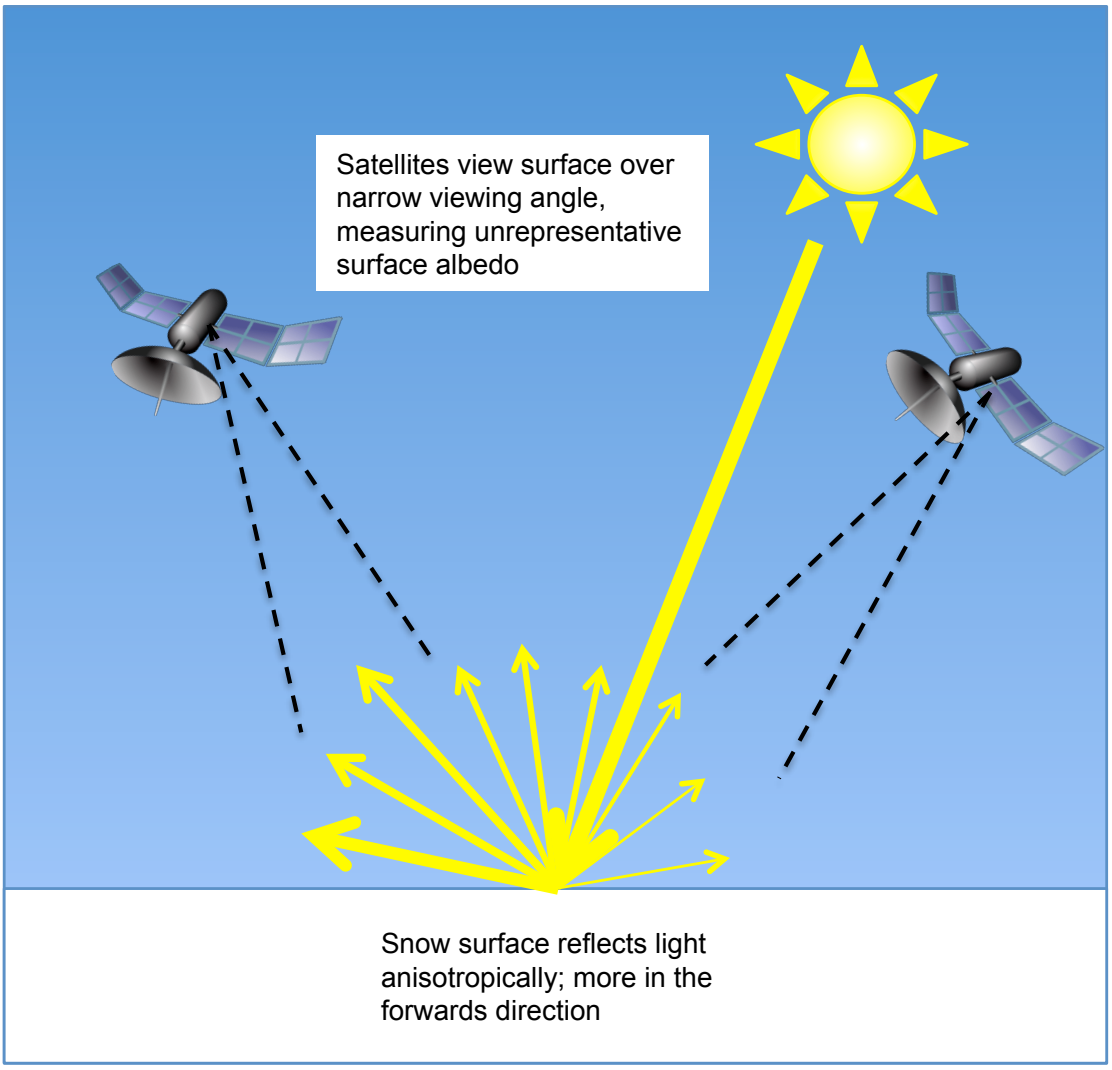

Figure 1.9 *– The effect of snow anisotropic reflectance on satellite albedo measurements.*

Algorithms are required to convert the satellite reflectivity measurements to a measurement of albedo accounting for the anisotropic reflectance of snow. The algorithms require ground-based measurements of the anisotropic reflectance; commonly described by a bi-directional reflectance distribution factor (BRDF), described in further detail in chapter 7 and measured in the field as a hemispherical directional reflectance factor (HDRF). BRDF is the ratio of incident light at a known zenith, θ_i, and azimuth,

ϕ_i, angle, to radiance reflected at a known observational zenith and azimuth angle (Nicodemus et al., 1977). Deserts and permanent snow fields are often used as ground calibration sites to take BRDF measurements as they are spatially homogeneous and temporally stable (e.g. Angal et al. (2011); Teilleta et al. (2001)). Middleton and Mungal (1952) were the first to measure the anisotropic reflectance of snow surfaces and Warren (1982) reviews early attempts at measuring snow anisotropic reflectance, demonstrating that snow forward scatters incident solar radiation and that BRDF of snow depends on grain size (e.g. Kuhn (1985); Dozier et al. (1988); Aoki and Fukabori (2000); Painter and Dozier (2004); Peltoniemi et al. (2005)). Snow surface features have also been shown to have an important effect on measured BRDF, e.g. sastrugi (Warren et al., 1998) and surface roughness (Peltoniemi et al., 2005). The BRDF of snow has been measured in several localities (e.g. Warren et al. (1998); Hudson et al. (2006); Aoki and Fukabori (2000); Painter and Dozier (2004); Peltoniemi et al. (2005)) using different techniques including ground based field goniometers and measuring from a tall tower. Measurements of BRDF have also been conducted under laboratory conditions (Dumont et al., 2010) and BRDF of snow has been modelled (e.g. Leroux et al. (1999); Dozier et al. (1988)). Chapter 7 of this thesis will include surface measurements of BRDF (measured as an HDRF) at Dome C, Antarctica which has been identified as a ideal calibration site for satellite measurements (Six et al., 2004).

1.4 Aims of the thesis

The aim of this thesis will be to examine the effects of black carbon on sea ice albedo and light penetration depths using a combination of radiative-transfer modelling and laboratory measurements on simulated sea ice. Research into potential effects of black carbon on sea ice are very limited which is surprising seeing as sea ice is a fundamental component of the Earth's climate system and, covering up to 7% of the Earth's surface, is one of Earth's largest biomes (Dieckmann and Hellmer, 2010). To investigate the effects of black carbon on sea ice radiative-transfer modelling using the TUV-snow model (described in chapter 2) is carried out. Radiative-transfer modelling is highly advantageous as a wide range of parameters can be examined. However, radiative-transfer models require validation to ensure results represent reality. To

validate the TUV-snow model experiments looking at effects of black carbon will be conducted on artificially grown sea ice using a sea ice simulator. The thesis will finally look at the anisotropic reflectance of snow surfaces measured at Dome C, Antarctica, with reference to measuring black carbon concentrations in snow and sea ice using remote sensing by satellites.

1.4.1 Thesis overview

Chapters 2–4 will investigate the response of sea ice to anthropogenic pollution, particularly black carbon, using the TUV-snow model.

Chapter 2 will introduce the TUV-snow model and investigate the albedo, light penetration and PAR propagation response of an ablating Antarctic sea ice to increased black carbon and HULIS, including an investigation of how black carbon distribution affects the response.

Chapter 3 will progress into looking at the response of Arctic sea ice to increasing black carbon and also investigate the degree to which a snow cover over sea ice will mitigate the albedo response of increased black carbon in sea ice.

Chapter 4 will further develop the work of chapters 2 and 3 through a thorough investigation of how the albedo and light penetration depth of snow and sea ice with different optical properties responds to increased black carbon.

Chapters 5 and 6 move onto developing the use of a sea ice simulator to generate artificial sea ice with the aim to compare the response of laboratory sea ice to results from TUV-snow.

Chapter 5 is a technical chapter explaining the design and development of the sea ice simulator, with preliminary results.

Chapter 6 will develop the use of the sea ice simulator to better understand and constrain the response of sea ice to black carbon. Results from the sea ice simulator are then compared to model results in order to validate the TUV-snow model.

Chapter 7 will investigate the anisotropic reflectance of snow surfaces through describing results from fieldwork measuring HDRF of snow surfaces at Dome C.

Chapter 2

The effects of black carbon and HULIS distribution on ablating Antarctic sea ice optical properties: Light penetration, albedo and PAR

2.1 Introduction

In the following chapter the impact of two common impurities, black carbon and HULIS (HUmic LIke Substances) on the albedo and light penetration depth of an ablating Antarctic sea ice will be addressed. As discussed in chapter 1, a decreased albedo due to light absorbing impurity content in sea ice will exacerbate sea ice melting, while decreased light penetration depths or *e*-folding depths (the distance over which light intensity reduces to $\frac{1}{e}$ of its initial value) due to impurities can influence photobiological processes and photochemistry within the ice. Black carbon has commonly been reported to decrease albedo of snow and sea ice (e.g. Chýlek et al. (1983); Warren (1984); Clarke and Noone (1985); Warren and Wiscombe (1985); Light et al. (1998); Warren and Clarke (1990); Grenfell et al. (2002); Hansen and Nazarenko (2004); Jacobson (2004); Solomon et al. (2007); Flanner et al. (2007); Doherty et al. (2010); Reay et al. (2012)), however, Doherty et al. (2010) suggest that up to 40% of light absorption by impurities in snow samples collected in the Arctic is due to other light-absorbing impurities. Voisin et al. (2012) suggest that HULIS may

contribute to additional absorption.

Previous calculations on the effects of black carbon on albedo of sea ice have all focussed on multi-year Arctic sea ice (Light et al., 1998; Grenfell et al., 2002; Jacobson, 2004). Light et al. (1998); Grenfell et al. (2002) and Jacobson (2004) suggest for an increase in black carbon from 1–100 ng g^{-1} of black carbon in the sea ice, at a 500 nm wavelength, albedo will decrease to 73%, 99% and 92% of the original albedo value. However each of these studies uses different distributions of black carbon, thus intercomparison is difficult. The study presented here is based on the field and initial radiative-transfer modelling study of King et al. (2005) for snow-free ablating first year sea ice in Terra Nova Bay, Antarctica. Study of the response of a snow-free ablating sea ice to black carbon/HULIS has not been previously undertaken and is beneficial as melting sea ice coincides with times of the year when solar radiation (heat energy) is greatest. Thus, absorption of solar radiation by impurities will be increased and melting exacerbated. Ablating sea ice will also have different optical properties to multi-year ice, so the response to impurities may be different. The effects of HULIS on the albedo of sea ice have not been previously determined for any sea ice type although HULIS has been shown to effect snow albedo (eg. France et al. (2011)).

The potential effect of black carbon and HULIS on light penetration through an ablating first year ice has also never been investigated. Decreased light penetration due to impurities in sea ice will influence propagation of Photosynthetically Active Radiation (PAR). Available PAR is critical for photobiological processes in sea ice. For example, in Antarctica the sea ice habitat constitutes 5% of total annual primary production in the region of the Southern Ocean influenced by sea ice, sea ice algae are the primary source of food for krill, which are a main source of food for squid, penguins, seals and baleen whales (Lizotte, 2001). These photosynthetic sea ice algae, which are found concentrated at the sea ice base (Perovich, 2006), require PAR for photosynthesis. The need to study the effect of impurities on PAR propagation through sea ice is apparent, yet to all knowledge the effect of black carbon and HULIS on PAR propagation has not previously been quantified. Dissolved and particulate organic matter have been shown to significantly attenuate sea ice PAR and UVR transmission (Belzile et al., 2000).

Chapter 2 will also investigate the effect of impurity distribution on albedo response.

The method of impurity entrainment into sea ice will effect its distribution within the ice. Black carbon and HULIS can be entrained into sea ice through wet and dry atmospheric deposition (Jacobson, 2004). Wet deposition occurs where black carbon and HULIS is deposited onto sea ice with snow fall, when the snow melts some black carbon or HULIS will be left behind on the sea ice surface. In Antarctica, seawater may inundate snow overlying sea ice leading to formation of "snow-ice" (Massom et al., 2001), which will include any black carbon and HULIS originally in the snow. Black carbon and HULIS may also enter sea ice directly from seawater (Dittmar, 2008), and from sediment inclusions including black carbon/HULIS where sea ice forms over shallow ocean shelves (Masiello, 1998; Middelburg et al., 1999). Both Light et al. (1998) and Grenfell et al. (2002) investigated how particle distribution within the sea ice affects albedo, however Light et al. (1998) only investigated layers of sediment particles. Grenfell et al. (2002) investigated the sea ice albedo change with a 1 cm layer at the top of the ice pack with varying black carbon concentrations (0–1000 ng g^{-1}) and albedo change with a different thickness layer (0.1–10 cm) with the same total black carbon mass, suggesting that the largest changes in albedo occur when soot is concentrated near the surface. The study of Grenfell et al. (2002) was based on multi-year Arctic sea ice, the response of ablating Antarctic sea ice may be different. The effect of HULIS distribution on albedo has not previously been determined. In this chapter the albedo effect of two scenarios will be presented. Firstly, black carbon and HULIS at the sea ice surface. Black carbon and HULIS may be distributed in just a surface layer, particularly if the black carbon/HULIS is entrained in the sea ice during the formation of snow-ice, during snow melt or by direct deposition. Secondly, black carbon and HULIS in a layer at depth in the sea ice. An anomalously high black carbon/HULIS mass-ratio in a layer in the sea ice could occur due to a sediment layer in the sea ice or a high black carbon/HULIS bearing snow layer that is turned into snow-ice.

The influence of black carbon and HULIS on albedo and light penetration depth (*e*-folding depth) will be calculated using the Tropospheric Ultraviolet visible (TUV)-snow radiative-transfer model described in section 2.2. The radiative-transfer calculations presented here can be divided into two sections. The results from which could be used to determine the climatic and biological importance of black carbon and HULIS in ablating Antarctic sea ice.

1. Calculations quantifying the reduction in albedo, light penetration depth and PAR in sea ice due to increasing black carbon and HULIS uniformly distributed throughout sea ice.
2. Calculations to investigate the effects of black carbon and HULIS distribution on sea ice surface albedo.

2.2 The TUV-snow radiative-transfer model

2.2.1 Model overview

The Tropospheric Ultraviolet Visible (TUV)-snow model (Lee-Taylor and Madronich, 2002) is a one-dimensional coupled atmosphere-snow/sea ice radiative-transfer model using the DISORT code (Stamnes et al., 1988) discussed in chapter 1. The model is a modification of the TUV atmospheric model (Madronich and Flocke, 1998). Snow layers were added at the base of the TUV model by Lee-Taylor and Madronich (2002), with the optical properties of the snow/sea ice being described in a similar manner to cloud in the TUV model but with absorption and scattering cross-sections relevant to snow or sea ice. The TUV-snow model uses plane parallel approximation, described in chapter 1, thus assumes the atmosphere and snow/sea ice vary only vertically and not horizontally. There is a pseudospherical correction for large solar zenith angles. The atmosphere and snow/sea ice can be divided into a series of "layers" , as seen in figure 2.1 showing a schematic overview of the TUV-snow model. Each layer in the model has its own optical properties defined by a scattering cross-section, absorption cross-section, asymmetry parameter (g) and a density. These parameters are subsequently defined in sections 2.2.1.1 and 2.2.1.2 respectively. "Levels" divide each layer and the irradiance at each level in the model can be calculated as a function of upwelling irradiance, I_{up}, and downwelling irradiance, I_{down}, which are determined from the optical properties of the above and below layer. The TUV-snow model is advantageous as it doesn't require detailed microphysical knowledge of the sea ice, but simply bulk properties describing light scattering and light absorption. Using calculated values of upwelling and downwelling irradiance at each defined level properties such as albedo and e-folding depths can be calculated as described in section 2.2.4.

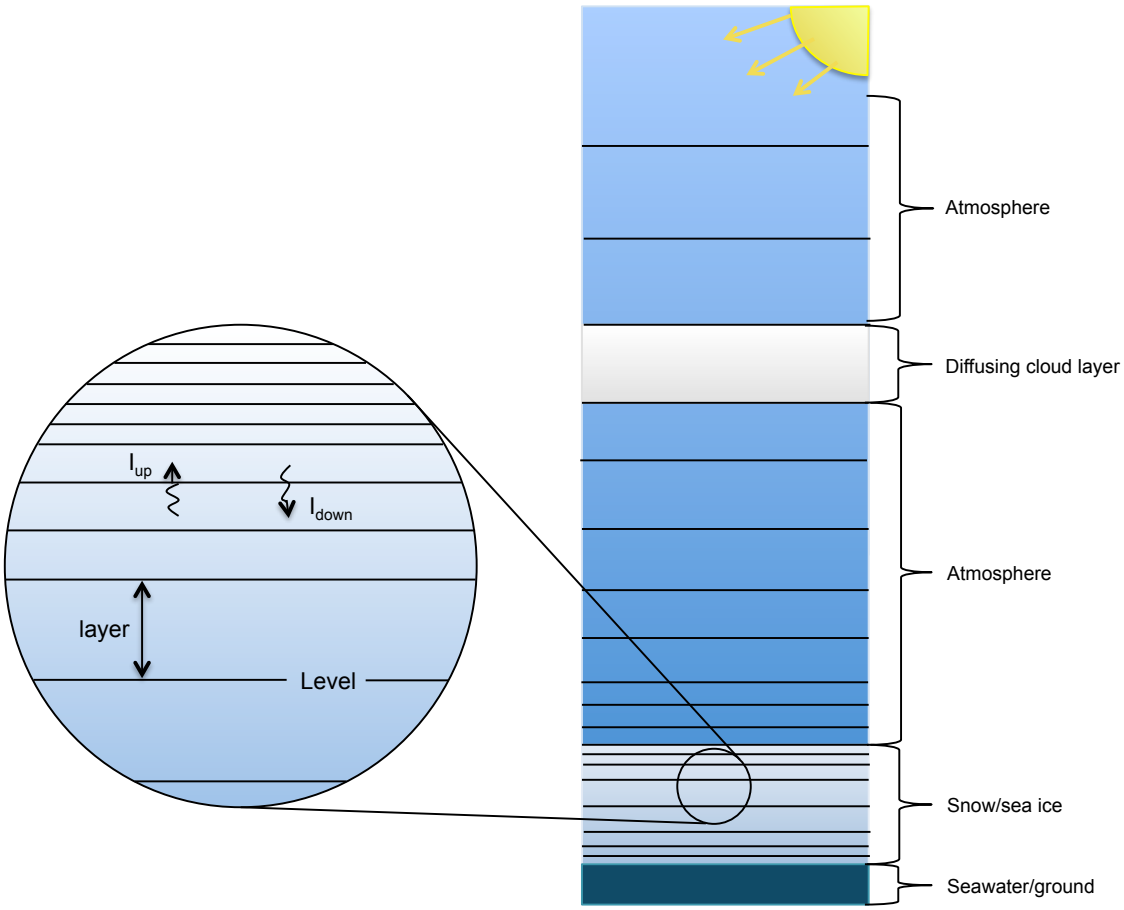

Figure 2.1 *– Overview of the structure of layers in the TUV-snow model showing division of the atmosphere and snow/sea ice into layers, not to scale.*

The TUV-snow model has been applied previously for radiative-transfer calculations in sea ice (King et al., 2005) and has also been used to derive physical and optical properties from field data (i.e. *e*-folding depth and albedo) and predict changes to snow optical properties for radiative-transfer calculations in snow (Fisher et al., 2005; Beine et al., 2006; France et al., 2007, 2010a,b, 2011, 2012). The model has been shown to be accurate in laboratory experiments with photolysis of compounds in artificial snow (Phillips and Simpson, 2005).

2.2.1.1 Absorption and scattering cross-section

The absorption cross-section, σ_{abs}, is a hypothetical area which describes the probability of light being absorbed by a particle, with the units $cm^2\ kg^{-1}$ (Petty, 2006). The absorption cross-section of pure ice which is used in the modelling with the TUV-snow model in this thesis is taken from Warren and Brandt (2008) and is shown in figure 2.2. The absorption cross-section of ice is small and very wavelength dependent,

increasing steadily at wavelengths greater than 400 nm. The absorption cross-section of added impurities is described in section 2.2.2. The scattering cross-section, σ_{scatt}, is a hypothetical area describing the probability of light being scattered by a particle (Petty, 2006). The scattering cross-section has the units $m^2\ kg^{-1}$.

2.2.1.2 The asymmetry parameter

The asymmetry parameter, g, describes the angular redistribution of radiation after a scattering event into the forwards or backwards hemisphere (Petty, 2006). For a large number of scattered photons the asymmetry parameter can be interpreted as the average value of $\cos\theta$, where θ is the scattering angle. The asymmetry parameter will therefore be a value between 1 and –1. A value of $g>0$ implies that photons in the medium are preferentially scattered into the forwards hemisphere while a value of $g<0$ implies photons are preferentially scattered into the backwards hemisphere. A value of $g=0$ implies perfect isotropic scattering; there is equal likelihood of a photon being scattered into the forward or backward direction (Petty, 2006). In the case of snow and sea ice, the particle size means g is in the range of 0.8–1.0, meaning snow and sea ice are predominately forwards scattering (Warren and Wiscombe, 1980).

2.2.2 Addition of absorbing impurities in snow/sea ice to the TUV-snow model

The response of snow/sea ice to increased black carbon and HULIS can be evaluated using the TUV-snow model. Black carbon/HULIS are added into the snow/sea ice model as an absorbing impurity. It is assumed black carbon and HULIS only contribute to the absorption and not scattering. The total absorption cross-section of snow/sea ice, σ_{abs}, at a wavelength, λ, is due to absorption cross-section of ice, σ_{abs}^{ice}, and absorption cross-section of impurities, σ_{abs}^{+}, which is dependant on the mass-ratio (ng of impurity per g of snow or sea ice) of the impurity in ice or snow $[impurity]$, defined by equation 2.1:

$$\sigma_{abs}(\lambda) = \sigma_{abs}^{ice}(\lambda) + \sigma_{abs}^{+}(\lambda)[impurity] \tag{2.1}$$

The absorption cross-section for small, insoluble impurities is determined by Mie scattering theory, using the method outlined by Warren and Brandt (2008). Mie scattering theory describes scattering and absorption of electromagnetic radiation by homogeneous spheres and is based on a solution to "Maxwell's equations" derived by Gustav Mie. To calculate the absorption spectra for black carbon in ice a Mie Scattering code MieCalc1.3 was used, which is an internet based programme for Mie calculations based on Bohren (1986). The calculation requires the refractive index of the medium, the refractive index of the particle, the imaginary index of refraction for the particle, the wavelength over which the calculation should be undertaken and the possible diameter range for the particle. For black carbon in ice the wavelength independent refractive index of black carbon particles is 1.8–0.5i, with a diameter of 0.2 μm and density of 1 g m^{-3} (Clarke and Noone, 1985; Warren and Brandt, 2008). The wavelength dependant refractive index of the surrounding ice was taken from Warren and Brandt (2008), shown on figure 2.2 (right axis). MieCalc1.3 calculates absorption efficiencies, Q_{ab}, which can be converted to an absorption cross-section σ_{ab}, using equation 2.2, (Petty, 2006), where ρ is a density of 1 g cm^{-3} and d is a diameter of 0.2 μm. Values for the absorption cross-section of black carbon in ice obtained from the Mie calculation are shown in figure 2.2. The absorption spectra for black carbon in brine is also shown, which is very similar as the refractive indexes for brine and ice are similar. Figure 2.2 also shows black carbon in air, which would be the case for snow calculations. The absorption cross-section for HULIS, also shown in figure 2.2, was taken from Hoffer et al. (2006) figure 5.

$$\sigma_{ab} = \left(\frac{3}{(2\rho d)} \right) Q_{ab} \tag{2.2}$$

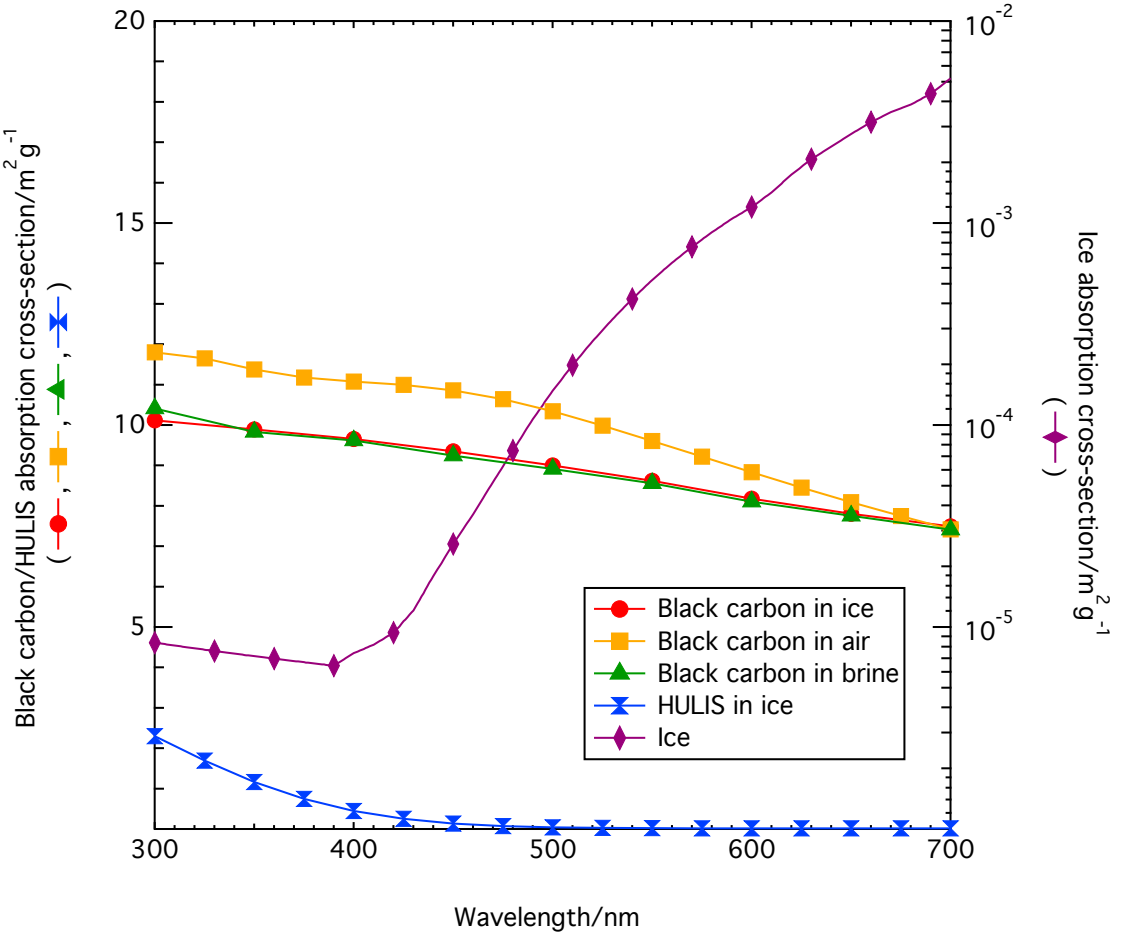

Figure 2.2 *– A comparison of absorption cross-sections, of black carbon in ice, air and brine (salinity 30 ppt) (left hand side). All black carbon cross sections were calculated using Mie theory using a black carbon proxy of Warren and Wiscombe (1980). HULIS in ice absorption is taken from Hoffer et al. (2006). Absorption cross-section of ice (right hand side) is taken from Warren and Wiscombe (1980), (note different scales). Sparse markers are used for clarity, with a marker every 50 data points.*

2.2.3 Defining model parameters

For the radiative-transfer modelling presented in this chapter optical properties of sea ice included a wavelength-independent scattering cross-section, σ_{scatt}, of 0.15 m^2 kg^{-1} (King et al., 2005) and a wavelength-independent asymmetry factor of g = 0.95 (Mobley et al., 1998). The sea ice was 1 m thick with a density of 0.9 g cm^{-3} and was split into 110 levels with 1 cm levels from 0 (the sea ice base) to 99 cm and 1 mm levels from 99 to 100 cm (the sea ice surface). Under ice albedo was set at 0.1 (see section 2.2.3.3). The Earth-Sun distance was 1 AU, corresponding to a nominal date set to 03/04/99. The atmosphere was aerosol free with an ozone column of 300 Dobson units. The atmosphere was split into 80 levels with 1 m levels from 1–10

m, 10 m levels from 10–100 m, 100 m levels from 100–1000 m, 1 km levels from 1–10 km, and 2 km levels from 10–90 km. The model employed eight streams (see section 2.2.3.1) and a pseudo-spherical correction (Lee-Taylor and Madronich, 2002). For the calculations of *e*-folding depth and albedo, irradiance at the surface of the sea ice was isotropic. Isotropic solar radiation at the surface of the sea ice was achieved by placing cumulus clouds in the model at an altitude of 1 km, with an optical depth of 16 (see section 2.2.3.2), an asymmetry parameter of 0.85 and a single scattering albedo (ratio of scattering efficiency to total extinction efficiency) of 0.9999. Isotropic solar radiation conditions were chosen as the albedo of sea ice and snow varies with solar zenith angle (e.g. Hubley (1955)) under direct conditions. Isotropic illumination removes this solar zenith angle dependence allowing calculation of the changes in albedo, *e*-folding depth and relative changes in PAR owing to increasing or decreasing black carbon content only and not due to the solar zenith angle. Calculations of light penetration depth, PAR and surface albedo were determined at wavelengths between 300 and 700 nm at 1 nm intervals.

2.2.3.1 Number of streams

The number of streams used in the TUV-snow model defines the accuracy of the modelling. Less streams is quicker, while a larger number of streams means the model is more accurate but slower. To ascertain the optimum stream number radiative-transfer calculations were carried out using stream numbers of 2, 4, 8, 16 and 32 in the TUV-snow model. A snowpack with a scattering cross-section of 25 m^2 kg^{-1} a density of 0.4 g cm^{-3}, a *g* value of 0.89 and a black carbon content of 20 ng g^{-1} was used. Zenith angle was set to 60° and direct conditions were used by setting the cloud optical depth to 0. Earth-sun distance was 1 AU. The albedo and *e*-folding depth of the snowpack was calculated over wavelengths 280–800 nm. Figure 2.3 shows the effect of changing stream number on calculated albedo at wavelengths 280–800 nm while figure 2.4 shows the effect of changing stream number on calculated *e*-folding depth at wavelengths of 300 and 450 nm.

From figures 2.3 and 2.4 it can be noted that a difference in the calculated albedo and *e*-folding depth is only observed at 2 streams. For the modelling presented here 8 streams will be used, as this provides the optimum balance between computational

time and accuracy.

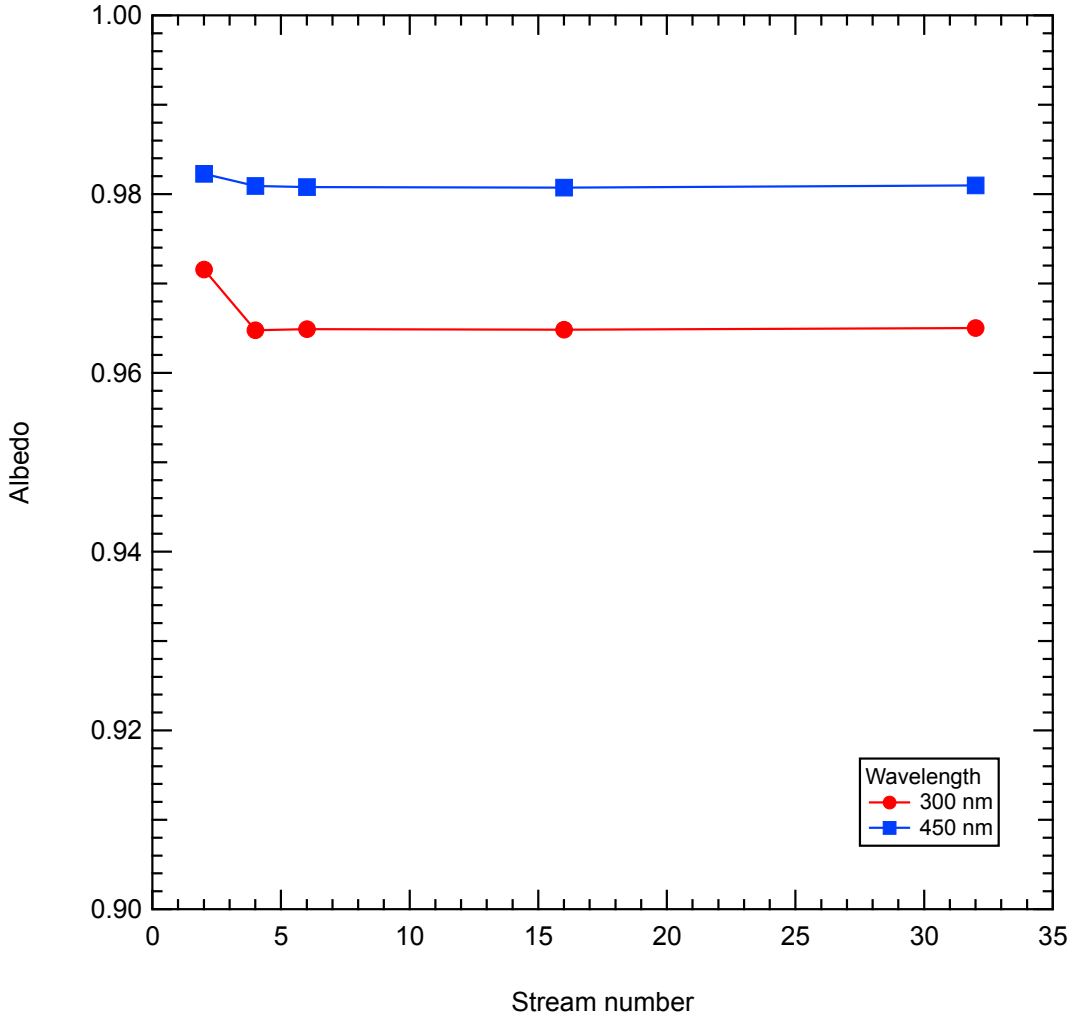

Figure 2.3 *– Effect of changing stream number on calculated albedo.*

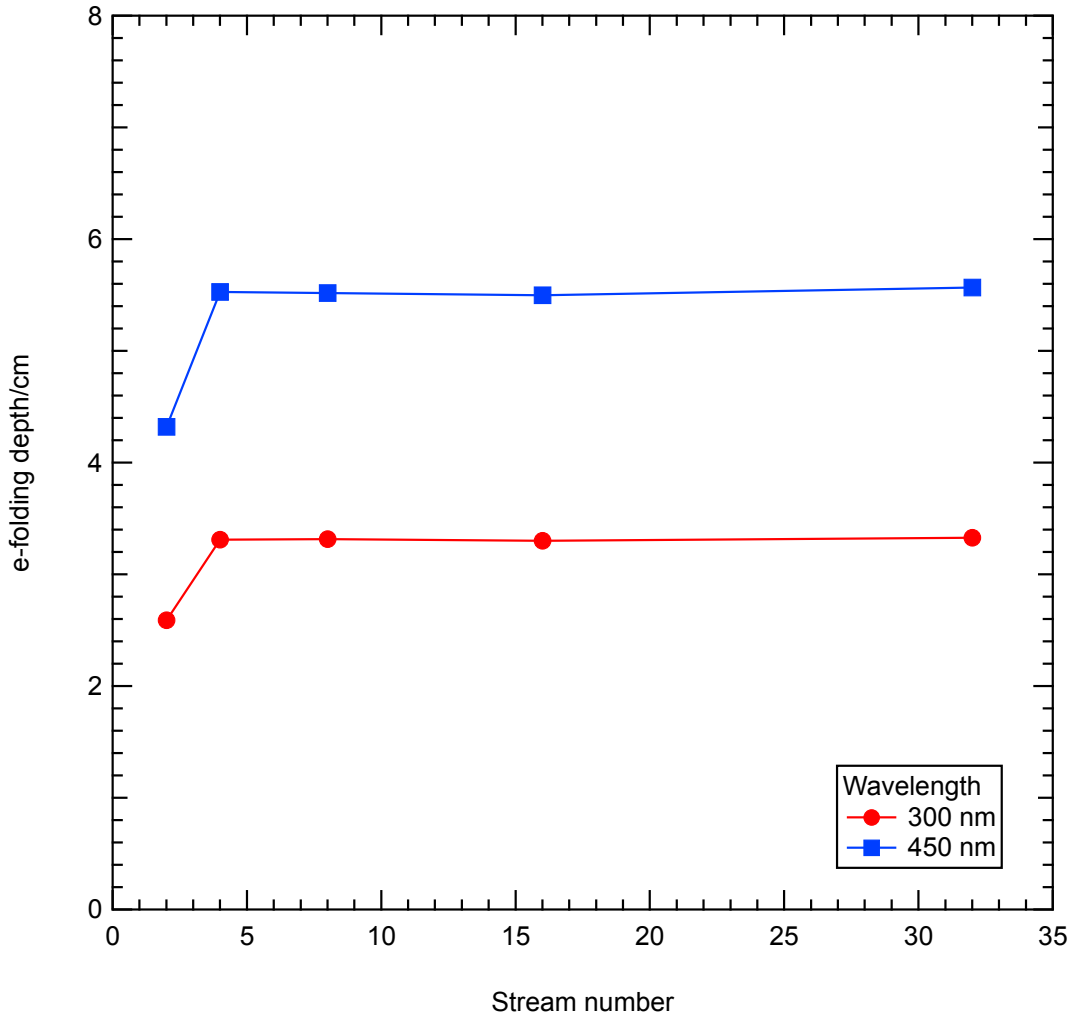

Figure 2.4 *– Effect of changing stream number on calculated e-folding depth.*

2.2.3.2 Cloud optical depth

The cloud optical depth is a measure of loss of light intensity owing to scattering by a cloud layer, and defines how isotropic the light reaching the snow/sea ice surface will be. Increasing the cloud optical depth increases the degree of scattering occurring in the cloud layer, with a cloud optical depth of 0 corresponding to direct light.

Isotropic conditions are defined as where light intensity from each direction is equal, compared to direct conditions where all light comes from one direction. Under isotropic conditions albedo and *e*-folding depth are independent of solar zenith angle. Under direct solar conditions the albedo of the surface is dependent upon solar zenith angle.

To ascertain the cloud optical depth required to produce isotropic sky conditions

the radiative-transfer calculations were carried out using the TUV-snow model. The same parameters were used as for determining an optimum stream number in section 2.2.3.1 and the snowpack used had the same properties. Snow surface albedo was calculated at solar zenith angles of 90, 84, 78, 72, 66, 60, 53, 45, 36, 25 and 0° and at cloud optical depths of 2, 4, 8, 16, 32, 64 and 128. Figure 2.5 shows the snow surface albedo at different solar zenith angles and for different cloud optical depths. As cloud optical depth increases albedo becomes more constant with solar zenith angle as radiation becomes more isotropic. By a cloud optical depth of 16 albedo is constant with solar zenith angle and isotropic conditions are achieved.

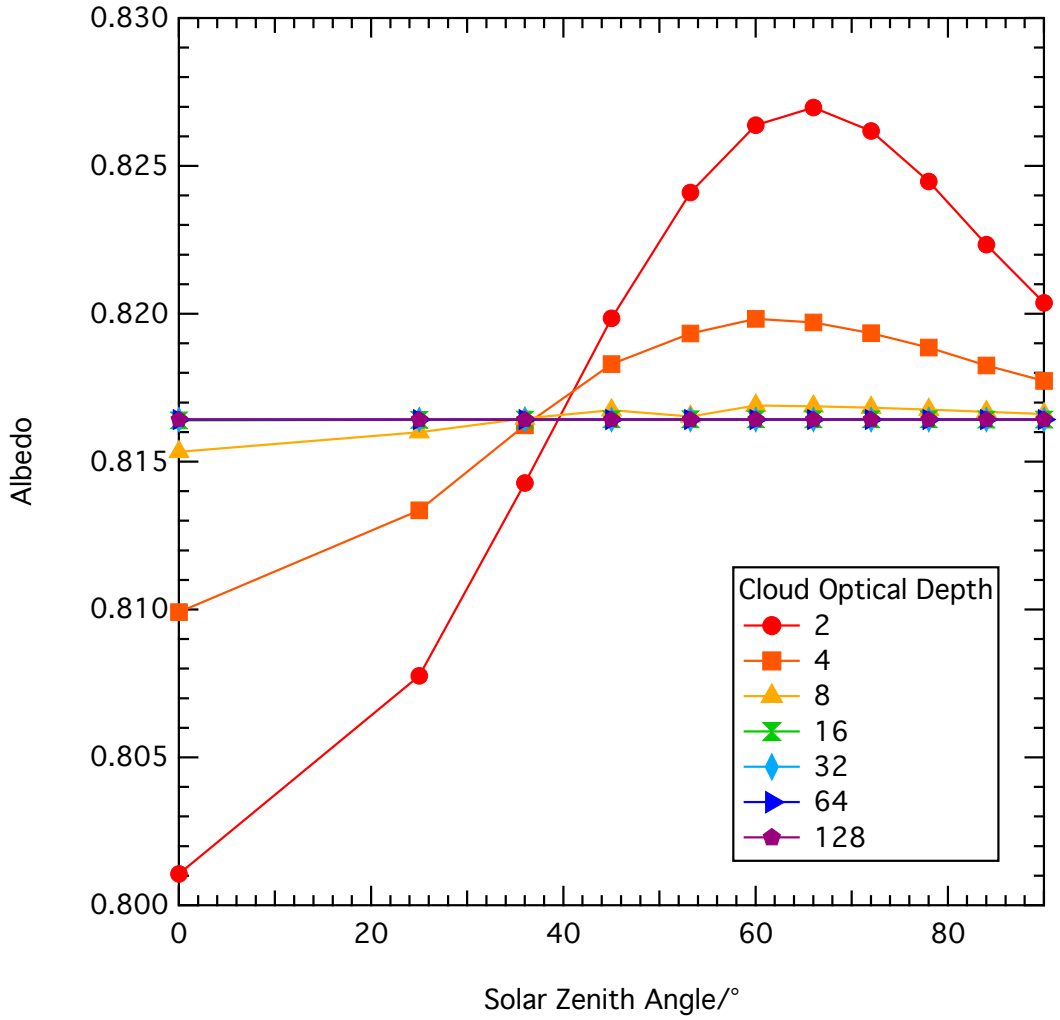

Figure 2.5 *– Calculated snow surface albedo with solar zenith angle for different cloud optical depths.*

2.2.3.3 Under-ice albedo

The albedo of the layer under the ice is set as a wavelength independent value of 0.1, representing a value close to ocean albedo (Payne, 1972). Figure 2.6 shows how the albedo of a 1 m thick clean sea ice (with the properties outlined in section 2.2.3) changes with variation in under ice albedo from 0.02–0.12 showing that there is negligible effect on the surface albedo with small changes in under ice albedo and therefore using a value of 0.1 is suitable.

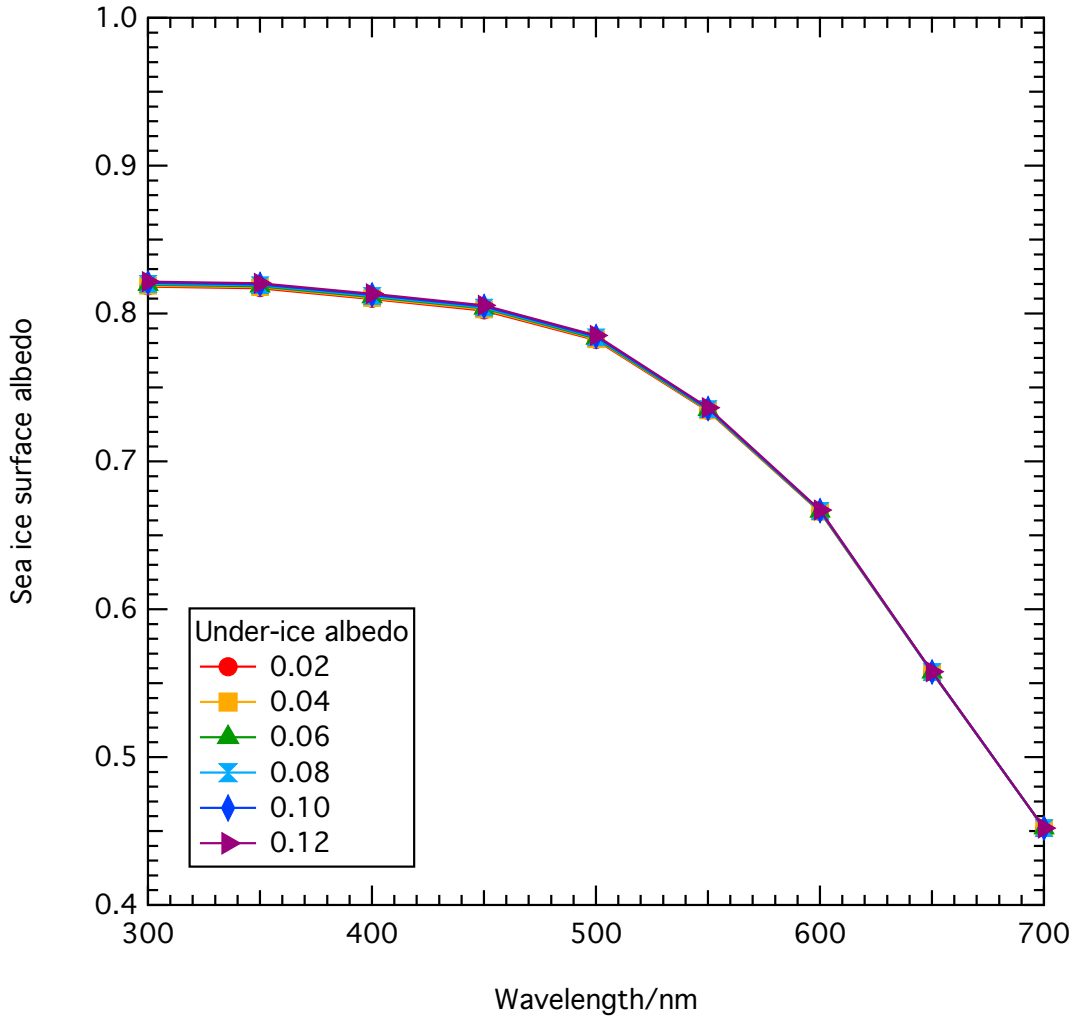

Figure 2.6 – *Variation in sea ice surface albedo with change in under-ice albedo.*

2.2.4 Calculating changes in albedo, *e*-folding depth and PAR with increasing black carbon and HULIS uniformly distributed throughout the sea ice using the TUV-snow model

Changes in the measurable optical properties of the ablating sea ice (*e*-folding depth, PAR and albedo) were calculated for black carbon and HULIS mass-ratios of 1, 2, 4, 8, 16, 32, 64, 128, 256, 512 and 1024 ng g^1, homogeneously distributed through the sea ice. For completeness mixing ratios of black carbon up to 1024 ng g^{-1} have been included as Doherty et al. (2010) reported snow black carbon mass-ratios up to ∼500 ng g^{-1}. Although mass-ratios of black carbon above 100 ng g^{-1} would be considered extremely large and the two larger mass-ratios, 512 and 1024 ng g^{-1}, have only been included for completeness. Albedo is calculated in this work as the ratio of upwelling irradiance to the downwelling irradiance at the sea ice surface. The *e*-folding depth, is the distance (normal to the sea ice surface) over which light intensity, I, at depth z, will reduce to $\frac{1}{e}$ (∼37%) of the original value, $I_{z'}$, calculated using equation 2.3. Where I_z is the downwelling irradiance at depth z, z' is a reference depth, and $I_{z'}$ is the reference downwelling irradiance, taken at z'.

$$\frac{I_z}{I_{z'}} = e^{-\left(\frac{(z-z')}{e}\right)} \tag{2.3}$$

To calculate the *e*-folding depth the irradiance at the depths 30, 40, 50 and 60 cm were calculated, with reference irradiance at a depth of 30 cm. The irradiance values were then fitted to equation 2.3. In an optically thick snow or sea ice *e*-folding depths are asymptotic, as light intensity contiually reduces by $\frac{1}{e}$ (∼37%), thus will reach zero at infinity. Where "optically thick" describes a sea ice or snowpack which is of sufficient thickness to be uninfluenced by the albedo of a layer beneath it. However, in the work described here the *e*-folding depths described are not asymptotic as the sea ice is not optically thick.

PAR as a function of depth through the sea ice was calculated through integrating "flat plate" monochromatic irradiances, I(λ), from 400 to 700 nm at each of the 110 levels through the sea ice, using equation 2.4.

$$PAR = \int_{400nm}^{700nm} I(\lambda) d\lambda \tag{2.4}$$

PAR at each depth was then expressed as a ratio to the PAR calculated at the surface to provide a relative measurement of PAR attenuation with depth, i.e. $\left(\frac{PAR_z}{PAR_{z=0}}\right)$. PAR was calculated with a "flat plate" geometry under isotropic conditions, as opposed to a spherical or point irradiance used in photochemistry, to enable comparison with other biological studies (e.g Bjorn (2007)). Figure 2.7 shows a comparison between flat plate and spherical irradiance.

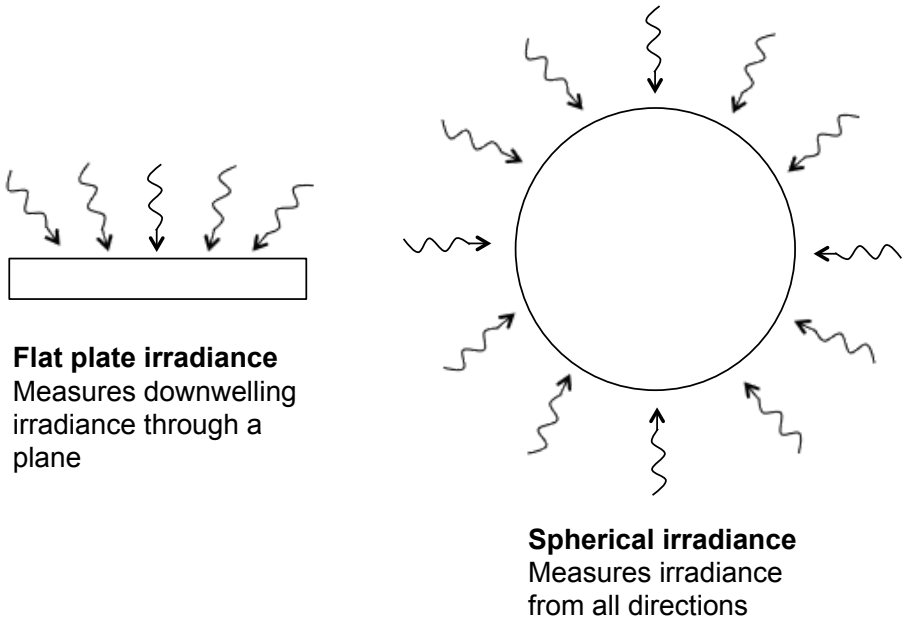

Figure 2.7 *– Comparison between flat plate and spherical irradiance.*

A second calculation allowed absolute values of PAR at the base of the sea ice to be calculated for solar zenith angles 0, 25, 36, 45, 53, 60, 72, 84 and 90° with clear skies. Clear sky conditions were achieved by removing the diffusing cloud layer from the radiative-transfer calculations described earlier in section 2.2.3.2. PAR at the sea ice base is examined as sea ice algae tend to be concentrated at the base of sea ice.

Table 2.1 provides a summary of the calculations described above.

Impurity	Impurity distribution	Sky conditions	Calculated optical properties
Black carbon	Homogeneous	Isotropic	Albedo, *e*-folding depth, relative PAR
HULIS	Homogeneous	Isotropic	Albedo, *e*-folding depth, relative PAR
Black carbon	Homogeneous	Clear	PAR at sea ice base
HULIS	Homogeneous	Clear	PAR at sea ice base

Table 2.1 *– Summary of calculations completed where black carbon/HULIS is evenly distributed throughout the sea ice.*

2.2.5 Modeling change in albedo with variation in black carbon and HULIS distribution

To investigate the effects of the vertical distribution of black carbon and HULIS on surface albedo, firstly, albedo at the surface of the sea ice was calculated with black carbon and HULIS only present in a surface layer of the sea ice of varying thickness. The black carbon or HULIS bearing layer was modelled with thicknesses of 0.1, 1, 10, 50 and 100 cm and concentrations of 1, 2, 4, 8, 16, 32, 64, 128, 256, 512 and 1024 ng g^{-1} of black carbon or HULIS in each layer thickness. The remaining sea ice, below the black carbon or HULIS bearing layer was clean.

Secondly, surface albedo was calculated as a function of the depth of a 1 cm layer of sea ice containing black carbon or HULIS. The 1 cm layer was placed in the sea ice described in section 2.2.3 at depths of 0, 10, 20, 30, 40, 50, 60, 70, 80 and 90 cm, and black carbon or HULIS in the layer had concentrations of 1, 2, 4, 8, 16, 32, 64, 128, 256, 512 and 1024 ng g^{-1}.

The effects of black carbon and HULIS distribution on *e*-folding depths could not be determined as calculations of *e*-folding depth require the impurity to be homogeneously distributed throughout the sea ice.

Table 2.2 provides a summary of the calculations described above.

Impurity	Impurity distribution	Sky conditions	Calculated optical properties
Black carbon	Within top layer of 0.1, 1, 10, 50 and 100 cm thickness	Isotropic	Albedo
HULIS	Within top layer of 0.1, 1, 10, 10, 50 and 100 cm thickness	Isotropic	Albedo
Black carbon	Within 1 cm layer at depths of 0, 10, 20, 30, 40, 50, 60, 70, 80 and 90 cm in to ice	Isotropic	Albedo
HULIS	Within 1 cm layer at depths of 0, 10, 20, 30, 40, 50, 60, 70, 80 and 90 cm in to ice	Isotropic	Albedo

Table 2.2 *– Summary of calculations completed where black carbon and HULIS is unevenly distributed in the sea ice.*

2.3 Results

The results section will report the effects of black carbon and HULIS pollution on albedo, then *e*-folding depth and propagation of PAR and finally report variation in albedo of sea ice with black carbon and HULIS distribution in the ice.

2.3.1 The effect of black carbon and HULIS on sea ice surface albedo

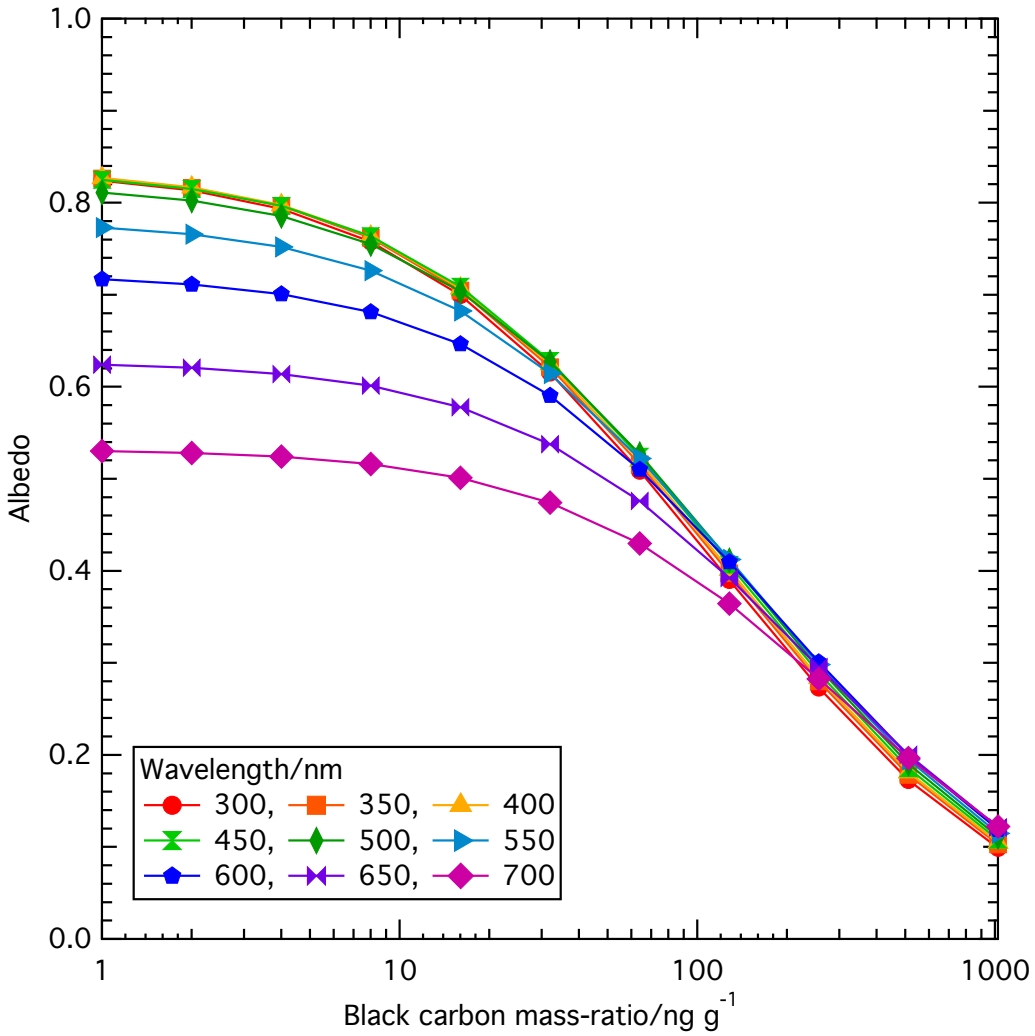

Figure 2.8 *– Effect of increasing black carbon mass-ratio (1–1024 ng g^{-1}) on sea ice albedo at wavelengths 300–700 nm.*

Figure 2.8 shows surface albedo of sea ice as a function of increasing mass-ratio of black carbon, for wavelengths 300–700 nm. As the mass-ratio of black carbon increases, albedo decreases at all wavelengths, with an 86% decrease in albedo (from

0.81 to 0.11) at a wavelength of 500 nm with black carbon mass-ratio increase of 1 to 1024 ng g^{-1}, and a 7% decrease in albedo for a more realistic black carbon mass-ratio increase of 1 to 8 ng g^{-1}. For black carbon mass-ratios between 16–1024 ng g^{-1} a doubling of black carbon appears to cause an absolute decrease in albedo of ∼0.1 for wavelengths from 300–500 nm. The response of the albedo of sea ice to black carbon is wavelength dependent. At small mass-ratios of black carbon, <8 ng g^{-1}, albedo is largest at shorter wavelengths, and albedo is strongly wavelength dependant. For black carbon mass-ratios greater than 100 ng g^{-1}, there is little variation in albedo with wavelength and when black carbon is >512 ng g^{-1} albedo is smallest at shorter wavelengths. The observed trend is due to a change from ice dominated absorption of solar radiation to black carbon dominated absorption; similar behaviour has previously been seen in snowpacks (Reay et al., 2012). Figure 2.2 displays the absorption cross-sections of ice and black carbon particles in ice used for these calculations. The absorption cross-section of black carbon is a factor of $\sim 10^4$–10^6 larger than the absorption cross-section of ice per unit mass (note different scales used in figure 2.2). The absorption cross-section of ice is strongly wavelength dependent, whereas the absorption cross-section of black carbon is not. Thus as the mass-ratio of black carbon increases in sea ice the absorption of light by black carbon becomes increasingly more important than absorption of light by ice. As a result the wavelength dependence of albedo decreases and the wavelength with the largest albedo changes from shorter to longer wavelengths as black carbon mass-ratio increases.

Figure 2.9 shows the response of sea ice albedo to increasing mass-ratio of HULIS at wavelengths 300–700 nm. At wavelengths from 300 to 450 nm the surface albedo of sea ice decreases with increasing mass-ratio of HULIS with a 31% decrease (from 0.83 to 0.57) at a wavelength of 400 nm across the whole HULIS mass-ratio range examined (1–1024 ng g^{-1}), and a 0.5% decrease in albedo from 1 to 8 ng g^{-1}. The albedo response is less extreme as wavelength increases from 300–450 nm, as the absorption cross-section of HULIS is largest at shorter wavelengths. At 300 nm with an increase in HULIS from 1 to 100 ng g^{-1} there is a decrease from 0.84 to 0.66 (78.6% of the albedo at 1 ng g^{-1}) . At a wavelength of 450 nm, with an increase in HULIS from 1 to 100 ng g^{-1}, there is a decrease in albedo from 0.84 to 0.82 (97.6% of the albedo at 1 ng g^{-1}). At wavelengths above 500 nm there is no significant

albedo response to increasing HULIS in the sea ice. The wavelength dependence of the response can be explained through figure 2.2, which shows the absorption cross-section of HULIS is much larger at shorter wavelengths, decreasing to near 0 cm^2 kg^{-1} by 500 nm, explaining the lack of response for wavelengths longer than 500 nm. As HULIS mass-ratio increases the wavelength dependence of the result becomes larger. For wavelengths from 300–450 nm the response of sea ice albedo to increasing HULIS is non-linear. For example, at a wavelength of 400 nm, with a doubling of HULIS mass-ratio from 50–100 ng g^{-1} sea ice albedo decreases from 0.81 to 0.79 (97.5% of the albedo value at 50 ng g^{-1}) . While with a doubling of HULIS mass-ratio from 100 to 200 ng g^{-1} albedo decreases from 0.79 to 0.75 (94.9% of the albedo value at 100 ng g^{-1}).

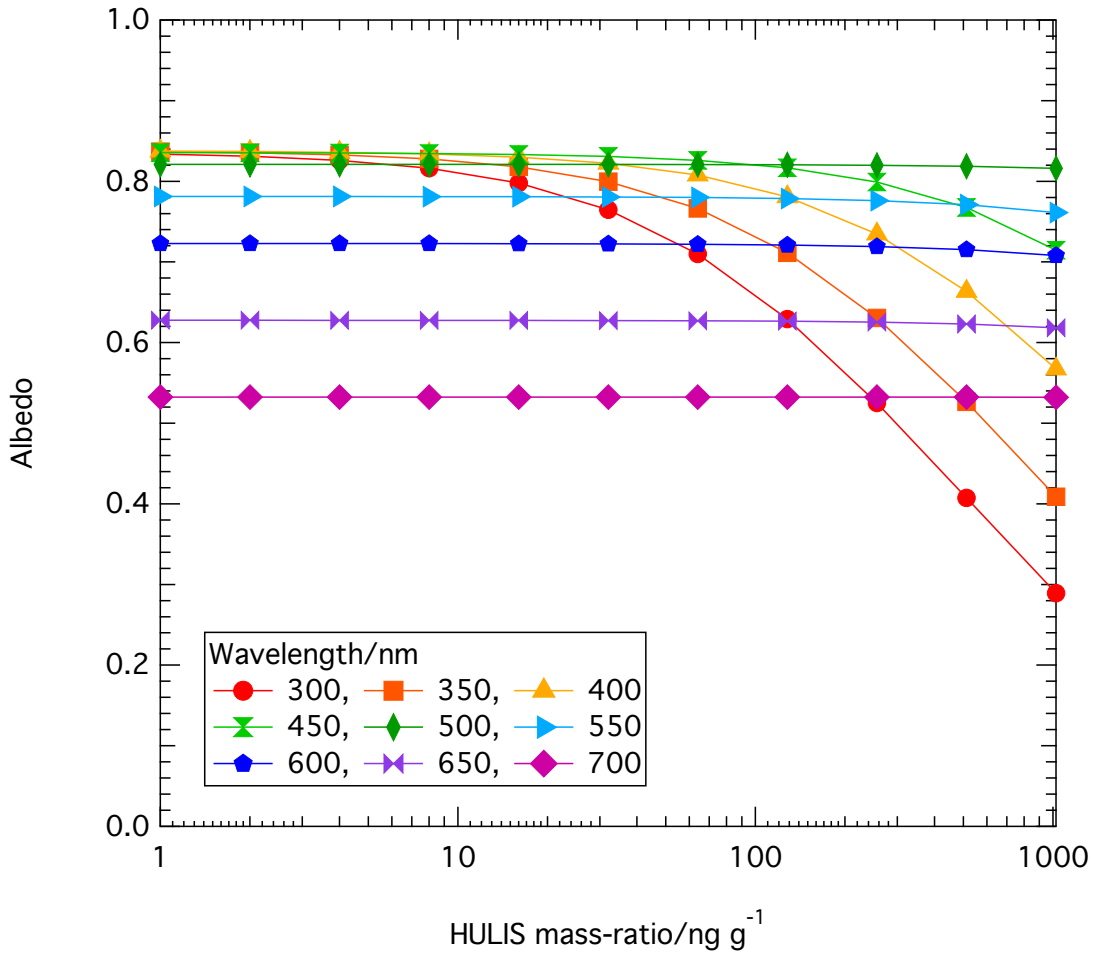

Figure 2.9 *– Effect of increasing HULIS mass-ratio (1–1024 ng g^{-1}) on sea ice albedo at wavelengths 300–700 nm.*

2.3.2 Variation in *e*-folding depth with increasing mass-ratio of black carbon and HULIS in sea ice

The response of *e*-folding depth with increasing mass-ratio of black carbon at wavelengths 300–700 nm is plotted in Figure 2.10. With increasing mass-ratio of black carbon the *e*-folding depth rapidly decreases, with an overall 91% decrease (from 68.1 cm to 6.01 cm) at a wavelength of 500 nm across the whole black carbon mass-ratio range examined (1–1024 ng g^{-1}), and a 15% decrease in *e*-folding depth from 1 to 8 ng g^{-1}. At small mass-ratios of black carbon, <100 ng g^{-1}, shorter wavelengths, <450 nm, have the largest *e*-folding depths and there is large variation in *e*-folding depth with wavelength. As the mass-ratio of black carbon increases, to over 100 ng g^{-1}, the variation in *e*-folding depth with wavelength becomes significantly less and there is a switch to longer wavelengths, >600 nm, having larger e-folding depths. The trend, as for albedo, is due to a change from ice absorption dominating light absorption to the black carbon absorption dominating light absorption as the mass-ratio of black carbon increases.

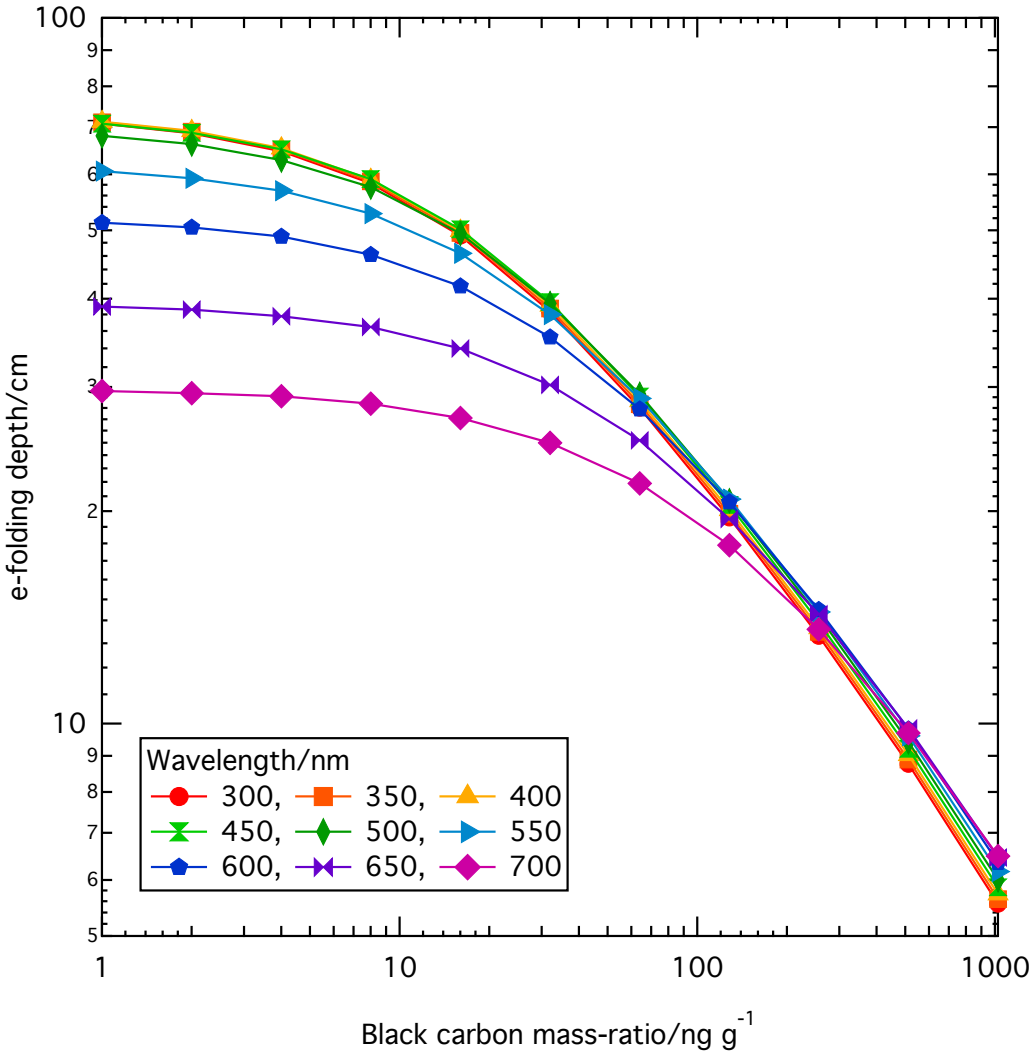

Figure 2.10 *– Calculated e-folding depth versus black carbon mass-ratio at wavelengths from 300–700nm under isotropic solar radiation conditions.*

The variation of *e*-folding depth with black carbon mass-ratio follows a simple power law over wavelengths 300–650 nm, as shown in equation 2.5.

$$\epsilon = \alpha[BC]^{-\beta} \tag{2.5}$$

α and β are empirical constants, ϵ is *e*-folding depth and $[BC]$ denotes the mass-ratio of black carbon. The power law relationship, displayed in equation 2.5, is valid for wavelengths shorter than 650 nm and for black carbon mass-ratios over 32 ng g^{-1}. The curves in Figure 2.10, with wavelengths in the range 300–600 nm, were fitted to equation 2.5. The values determined for α and β are shown in table 2.3. The exponent, β, at all wavelengths was ~0.4. Thus for a 10% increase in black carbon

mass-ratio, *e*-folding depth will reduce to 97% ($1.1^{-0.4}$) of its initial value. The factor with which it changes is independent of the actual value of $[BC]$.

Wavelength/nm	α/cm g$^{\beta}$ ng$^{-\beta}$	β	**Valid BC mass-ratio range/ng g^{-1}**
300	179.3±7.8	0.4066±0.0018	32-1024
350	180.1±7.9	0.4045±0.019	32-1024
400	180.7±8.0	0.4022±0.019	32-1024
450	179.8±8.2	0.3961±0.020	32-1024
500	170.6±8.4	0.3760±0.022	32-1024
550	179.6±8.2	0.3995±0.016	64-1024
600	177.6±6.3	0.4028±0.011	128-1024

Table 2.3 *– Power law coefficients for relating e-folding depth to mass-ratio of black carbon, for wavelengths 300–600 nm, and over the mass-ratio range of black carbon listed. Uncertainties are ±1 standard deviation and calculated from fitting power law curves to figure 2.10.*

Figure 2.11 shows the response of the *e*-folding depth to increasing mass-ratio of HULIS at wavelengths 300–700 nm. Similarly to the albedo response (figure 2.9), there is a clear wavelength dependance to the *e*-folding depth response due to the absorption cross-section of HULIS (figure 2.2). At wavelengths from 300–450 nm *e*-folding depth of sea ice clearly decreases with increasing mass-ratio of HULIS. At a wavelength of 400 nm there is an overall 55% decrease (from 74.1 cm to 33.6 cm) across the whole HULIS mass-ratio range examined (1–1024 ng g^{-1}), and a 0.5% decrease in *e*-folding depth from 1 to 8 ng g^{-1}. Similarly to albedo the response decreases as wavelength increases. At 300 nm with an increase in HULIS mass-ratio from 1 to 100 ng g^{-1} there is a decrease from 73.4 cm to 43.9 cm (59.8% of the *e*-folding depth at 1 ng g^{-1}). At 450 nm with an increase in HULIS from 1 to 100 ng g^{-1} there is a decrease from 73.4 cm to 70.0 cm (95.4% of the *e*-folding depth at 1 ng g^{-1}). At wavelengths above 500 nm there is no significant *e*-folding depth response to increasing HULIS in the sea ice as HULIS absorption above 500 nm is negligible.

For wavelengths from 300–450 nm the sea ice *e*-folding depth response to increasing HULIS is non-linear, similar to the albedo response. At a wavelength of 400 nm, with a doubling of HULIS mass-ratio from 50–100 ng g^{-1} sea ice *e*-folding depth decreases from 68.7 cm to 64.3 cm (93.6% of the albedo value at 50 ng g^{-1}). While with a doubling of HULIS mass-ratio from 100 to 200 ng g^{-1} albedo decreases from 64.3 cm to 57.0 cm (88.6% of the albedo value at 100 ng g^{-1}).

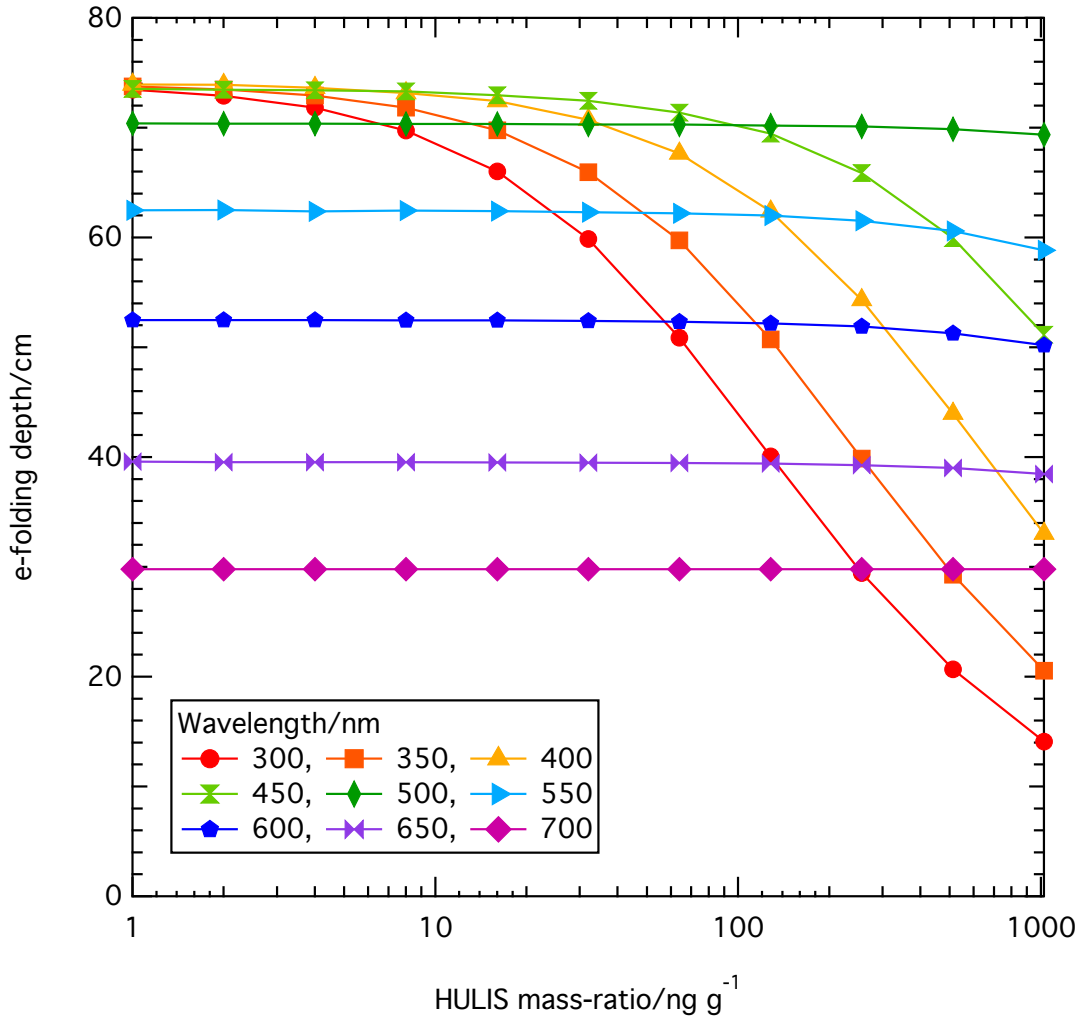

Figure 2.11 *– Calculated e-folding depth versus HULIS mass-ratio at wavelengths from 300–700 nm under isotropic solar radiation conditions.*

2.3.3 Variation in PAR with increasing black carbon and HULIS mass-ratio

Figure 2.12 shows PAR at a depth, z, relative to the PAR at the surface, as a function of different mass-ratios of black carbon. Relative PAR, $\left(\frac{PAR_z}{PAR_{z=0}}\right)$, decreases exponentially with depth into the sea ice, under isotropic illumination of the surface. At the smallest mass-ratio of black carbon considered, 1 ng g^{-1}, 11% of the PAR incident on the sea ice surface reaches the base of the sea ice, however for a black carbon mass-ratio of 256 ng g^{-1} PAR at the base of the sea ice has decreased to less than 0.1% of the PAR incident on the surface. PAR decreases more rapidly with depth as the mass-ratio of black carbon increases, shown by PAR *e*-folding depths shown on figure 2.12, these values are the depth required to reduce relative PAR to $\frac{1}{e}$ (∼37%) of the initial value.

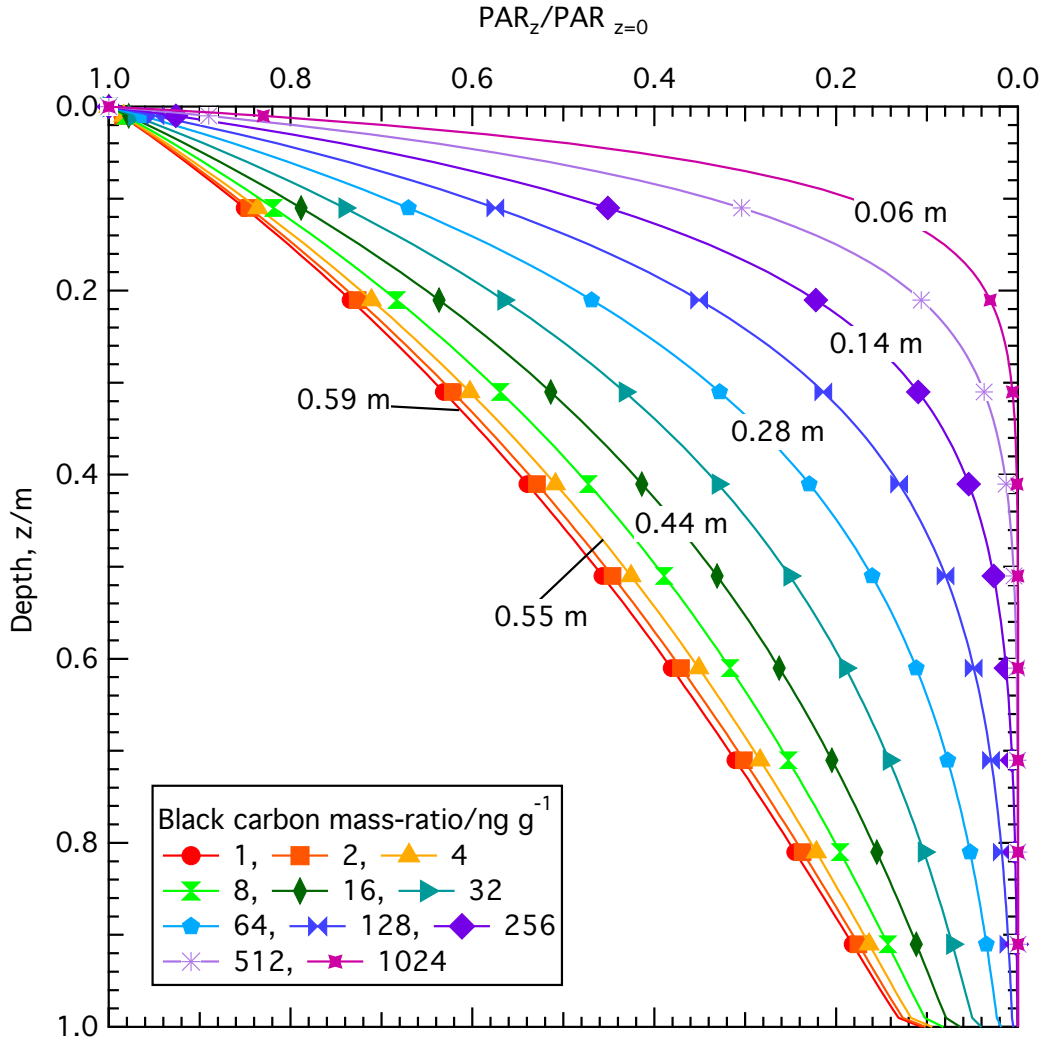

Figure 2.12 *– Relative PAR with depth through sea ice with an increasing mass-ratio of black carbon. The numbers on the graph are the PAR e-folding depth for the corresponding mass-ratio of black carbon (the depth required to reduce PAR by $\frac{1}{e}$). The PAR e-folding depth is larger for smaller black carbon mass-ratios.*

Figure 2.13 shows absolute values of PAR at the base of the sea ice as a function of solar zenith angle (0, 25, 36, 45, 53, 60, 72, 84 and 90°) and black carbon mass-ratio, under clear sky illumination conditions. Obviously values of PAR are larger for smaller solar zenith angles as surface solar irradiance is larger. At a solar zenith angle of 60° PAR decreases from 1.08 to 0.05 μmol photon m^{-2} s^{-1} with a black carbon mass-ratio increase from 1 to 128 ng g^{-1} (4.9% of the PAR value at 1 ng g^{-1}). While, at a solar zenith angle of 84° PAR decreases from 0.132 to 0.006 over the same black carbon mass-ratio increase (4.5% of the PAR value at 1 ng g^{-1}). Therefore the variation in the relative effect of black carbon on PAR at the sea ice base with solar zenith angle appears negligible.

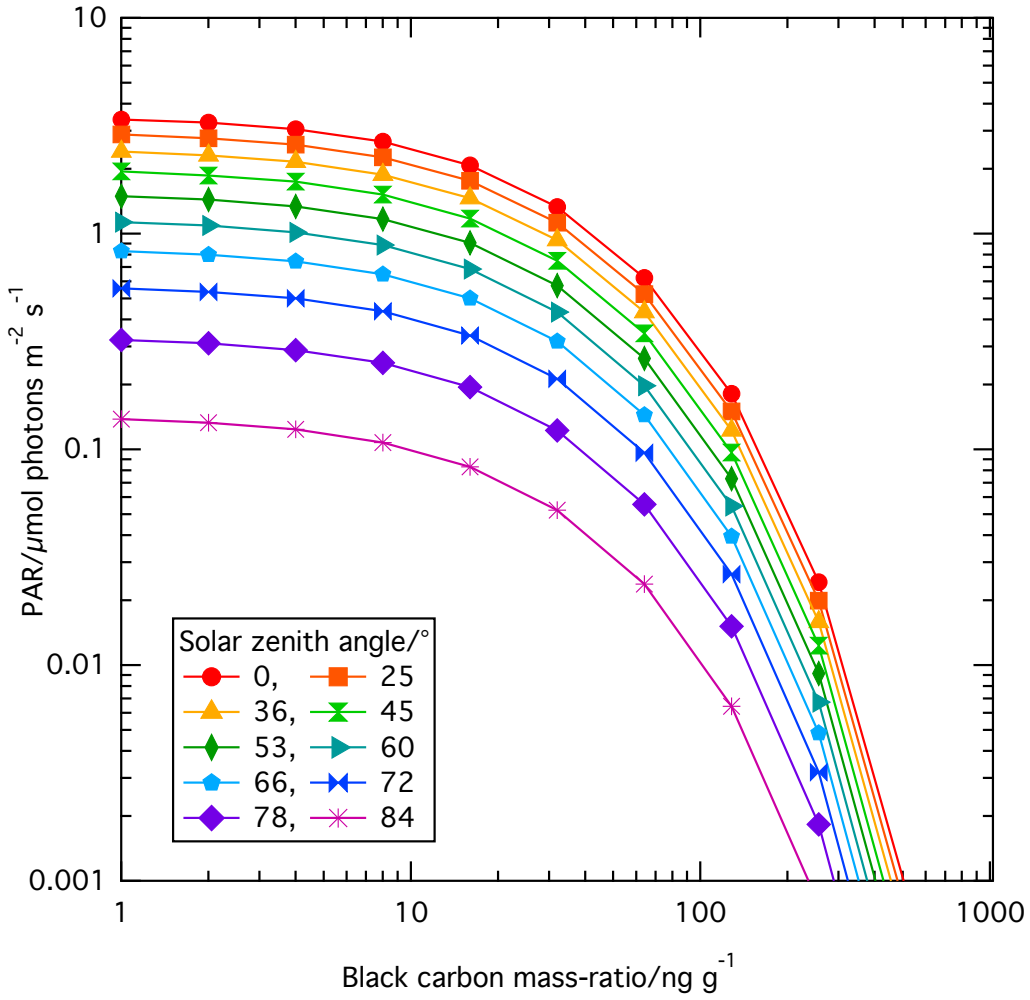

Figure 2.13 *– PAR at the base of a 1 m thick ablating sea ice for different solar zenith angles (0, 25, 36, 45, 53, 60, 72, 84 and 90°) and black carbon mass-ratios.*

Variation in relative PAR through 1m of sea ice with increasing HULIS mass-ratio is shown in figure 2.14. Relative PAR is very similar at HULIS mass-ratios from 1–256 ng g^{-1} and decreases only slightly at HULIS concentrations of 512 and 1024 ng g^{-1}. Figure 2.14 also shows PAR *e*-folding depths for mass-ratios of HULIS of 1, 128 and 1024 ng g^{-1}. The PAR *e*-folding depth only decreases by 9 cm over the entire HULIS mass-ratio examined (1 to 1024 ng g^{-1}).

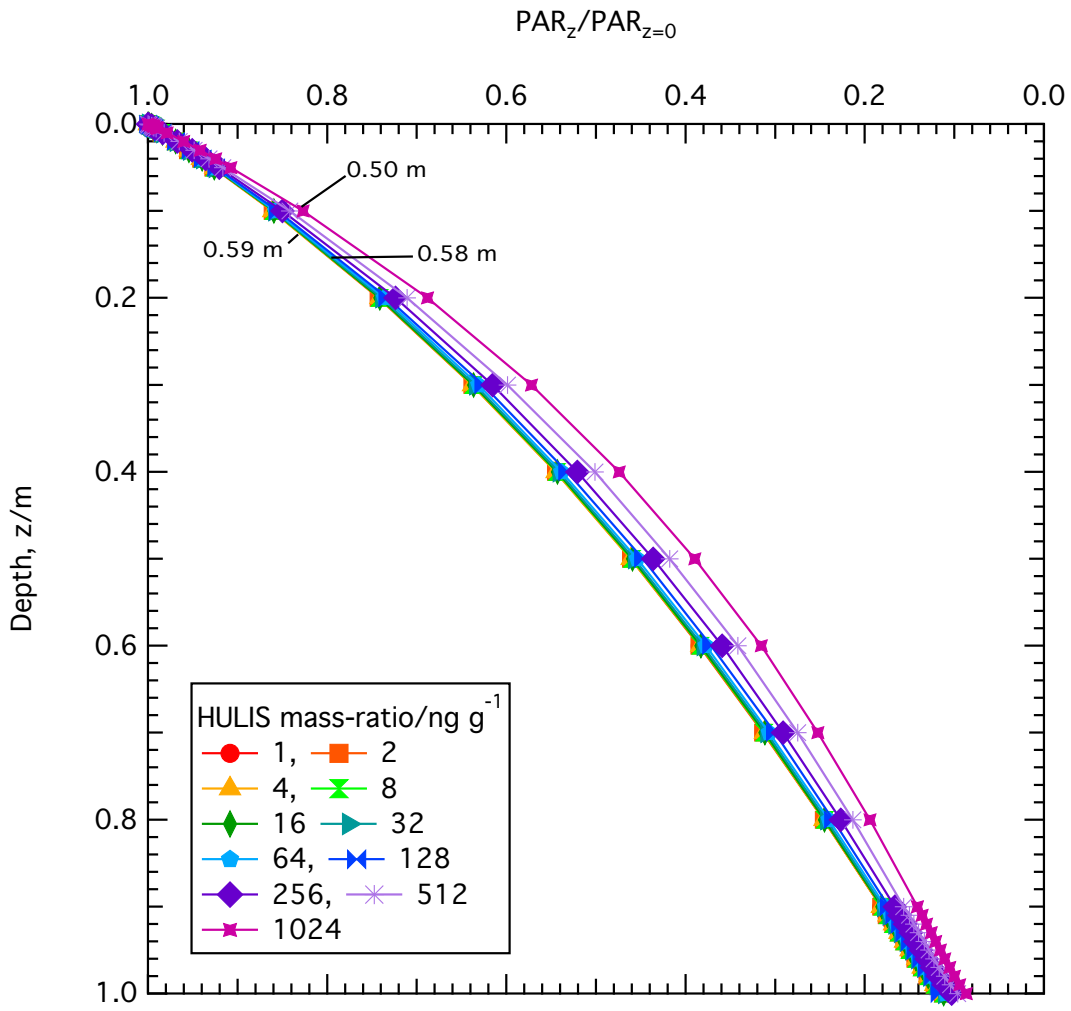

Figure 2.14 *– Relative PAR with depth through sea ice with an increasing mass-ratio of HULIS. The numbers on the graph are the PAR e-folding depth for the corresponding mass-ratio of HULIS (the depth required to reduce PAR by $\frac{1}{e}$). The PAR e-folding depth is slightly larger for smaller HULIS mass-ratios.*

Figure 2.15 shows variation in PAR at the base of a 1m thick sea ice at different solar zenith angles and HULIS mass-ratios. Unsurprisingly PAR is largest at the smallest solar zenith angle where solar irradiation is greatest. There is only a very small change in PAR at the base of the 1m thick sea ice with increasing mass-ratio of HULIS. At a solar zenith angle of 60° PAR decreases from 1.53 to 1.08 μmol photon m^{-2} s^{-1} with a HULIS mass-ratio increase from 1 to 1024 ng g^{-1} (70.6% of the PAR value at 1 ng g^{-1}). While, at a solar zenith angle of 84° PAR decreases from 0.184 to 0.129 μmol photon m^{-2} s^{-1} over the same HULIS mass-ratio increase (70.1% of the PAR value at 1 ng g^{-1}). Again the variation in the relative effect of HULIS on PAR with solar zenith angle appears to be negligible.

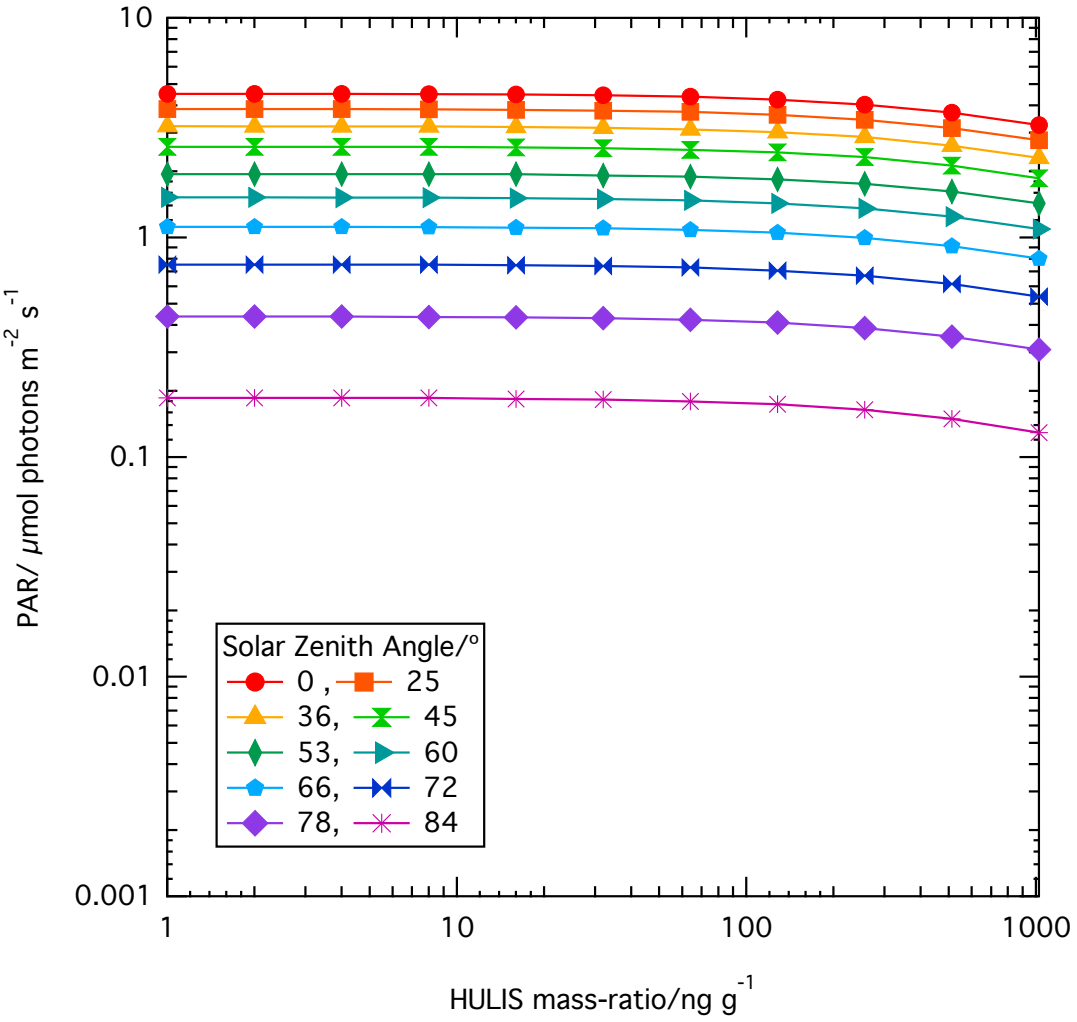

Figure 2.15 *– PAR at the base of a 1 m thick ablating sea ice for different solar zenith angles (0, 25, 36, 45, 53, 60, 72, 84 and 90°) and HULIS mass-ratios.*

The results presented in figures 2.13 and 2.15 would only occur under clear sky conditions, and for a 1 m thick ablating sea ice; the results are very sensitive to changes in ice thickness and atmospheric conditions, e.g. clouds, aerosol.

2.3.4 The effect of black carbon and HULIS distribution in sea ice on surface albedo reponse

The effects of black carbon and HULIS distribution on albedo with black carbon or HULIS in a surface layer and in a layer at different depths in the sea ice will be reported separately.

2.3.4.1 Effect of increasing black carbon and HULIS in a top layer of varying thickness

Figure 2.16 shows surface albedo, for wavelengths of 400 nm (A and C) and 600 nm (B and D), with black carbon just present in a surface layer of varying thickness in the sea ice (0.1 cm–100 cm) and the rest of the 1 m thick sea ice contains no impurities (data for wavelengths of 300–500 nm showed very similar results to 400 nm). At a wavelength of 400 nm a 0.1 cm layer at the surface of the ice containing black carbon has limited effect on surface albedo even at the maximum black carbon concentration modelled of 1024 ng g^{-1}, with only a 3.5% albedo decrease from 1–1024 ng g^{-1} of black carbon. A 1 cm layer has a greater effect, with a 28% albedo decrease from 1–1024 ng g^{-1}; this is not surprising as a 0.1 cm layer with a certain black carbon concentration will contain a factor of 10 less total black carbon than a 1 cm layer with the same black carbon concentration. Figures 2.16 A and B thus represent a total increase in black carbon mass with increasing layer thickness. Figures 2.16 C and D conversely show albedo plotted against the columnar density of black carbon in the surface layer. Columnar density, $\rho_{columnar}$, is defined by equation 2.6. Where $[BC]$ is the black carbon mass-ratio, d is the layer thickness and ρ is the sea ice density. Columnar density provides a means of comparing total black carbon mass in the layers.

$$\rho_{columnar} = [BC]d\rho \tag{2.6}$$

Figures 2.16 C and D demonstrate more equitably how the thickness of a black carbon bearing layer effects surface albedo, rather than just how the total amount of black carbon in a layer effects surface albedo. Two regimes can be noted in figures 2.16 C and D. Firstly, for thin layers (0.1, 1, 10 cm), on the left hand side of the graph, it appears that layer thickness does not influence surface albedo. At thicknesses of 0.1–10 cm albedo decreases steadily along the same curve with increasing columnar density of black carbon, with no clear difference between thicknesses of the black carbon layer, apart from a larger decrease in albedo; although the larger albedo decrease is to be expected due to the greater black carbon amount present. However on the right hand side, with thicknesses above 10 cm, a second regime occurs as albedo no longer decreases along the same curve, instead there are distinct curves for

10, 50 and 100 cm each showing a more gradual decrease in albedo with increasing black carbon amount. For a columnar density of black carbon of 1×10^4 ng cm^{-2} and a wavelength of 400 nm the albedo for a 10, 50 and 100 cm thick black carbon bearing layer is 0.60, 0.68 and 0.74 respectively. Therefore for the same black carbon total mass the albedo is considerably less when the black carbon is concentrated in a thinner surface layer. The effect occurs because black carbon concentrated at the surface has a greater chance of absorbing photons entering the sea ice before the photons are scattered back out the ice.

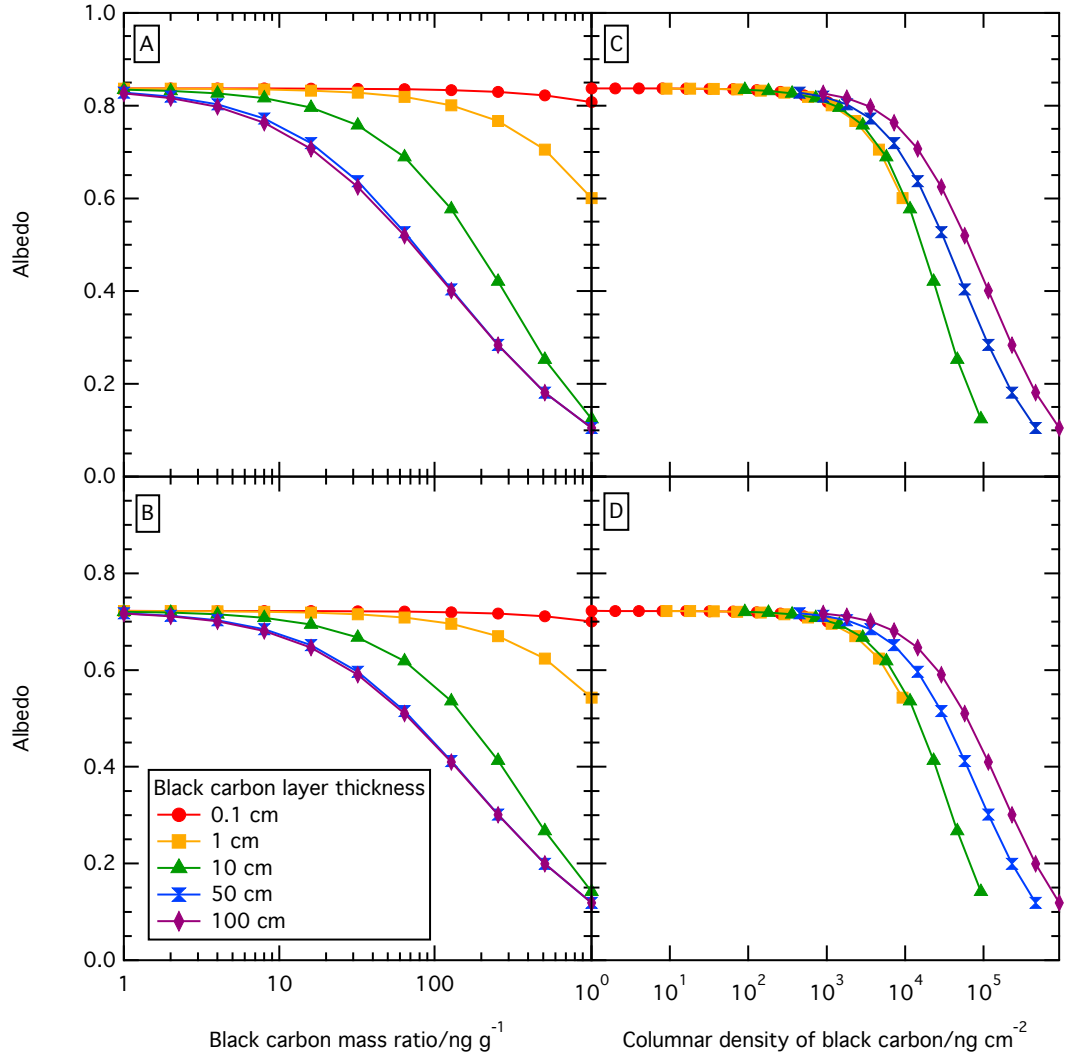

Figure 2.16 *– Albedo with increasing black carbon mass-ratio in a top surface layer of varying thickness at A) 400 nm and B) 600nm. C) and D) show columnar density of black carbon at C) 400 nm and D) 600 nm.*

Figure 2.17 shows the surface albedo of sea ice with HULIS placed in a surface layer of varying thickness (0.1 cm–100 cm) and the rest of the 1 m thick sea ice containing no impurities. The surface albedo at wavelengths of 300 nm (A) and 400 nm (B) is

shown. As seen before in figure 2.9 the shorter wavelength of 300 nm is much more responsive to HULIS additions than a wavelength of 400 nm, as the HULIS absortion cross-section is much larger at 300 nm . At wavelengths of 300 and 400 nm HULIS in only a 0.1 cm layer appears to have very limited effect on albedo. For example at a wavelength of 300 nm albedo only decreases from 0.84 to 0.83 with a HULIS increase from 1 to 100 ng g^{-1} in a 0.1 cm layer (99.3% of the albedo value at 1 ng g^{-1}). At a wavelength of 400 nm HULIS also seems to have limited effect at 1 cm, with albedo also only decreasing to 99.3% of the albedo at 1 ng g^{-1} over the same mass-ratio increase. The effect of HULIS in a 1 cm layer is greater at 300 nm. At both 300 and 400 nm wavelengths there is very little difference between the albedo response with HULIS in a 50 cm surface layer and HULIS in a 100 cm surface layer. As for black carbon, graphs A and B represent a total increase in HULIS mass-ratio with increasing layer thickness. Graphs C and D of figure 2.17 show albedo plotted against the columnar density of HULIS in the surface layer. Similarly to black carbon the graphs fall into two regimes with depths of 0.1, 1 and 10 cm (to the left of the graph) all lying on the same curve. 50 and 100 cm (to the right of the graph) lie on separate curves suggesting that for the same total HULIS mass-ratio surface albedo will be less when the HULIS is more concentrated near the surface. For example, for a columnar density of HULIS of 1 x 10^4 ng cm^{-2} the albedo for a 10, 50 and 100 cm thick HULIS bearing layer at 300 nm is 0.76, 0.79 and 0.81 respectively. Again HULIS concentrated in a surface layer has an increased probability of absorbing photons entering the sea ice.

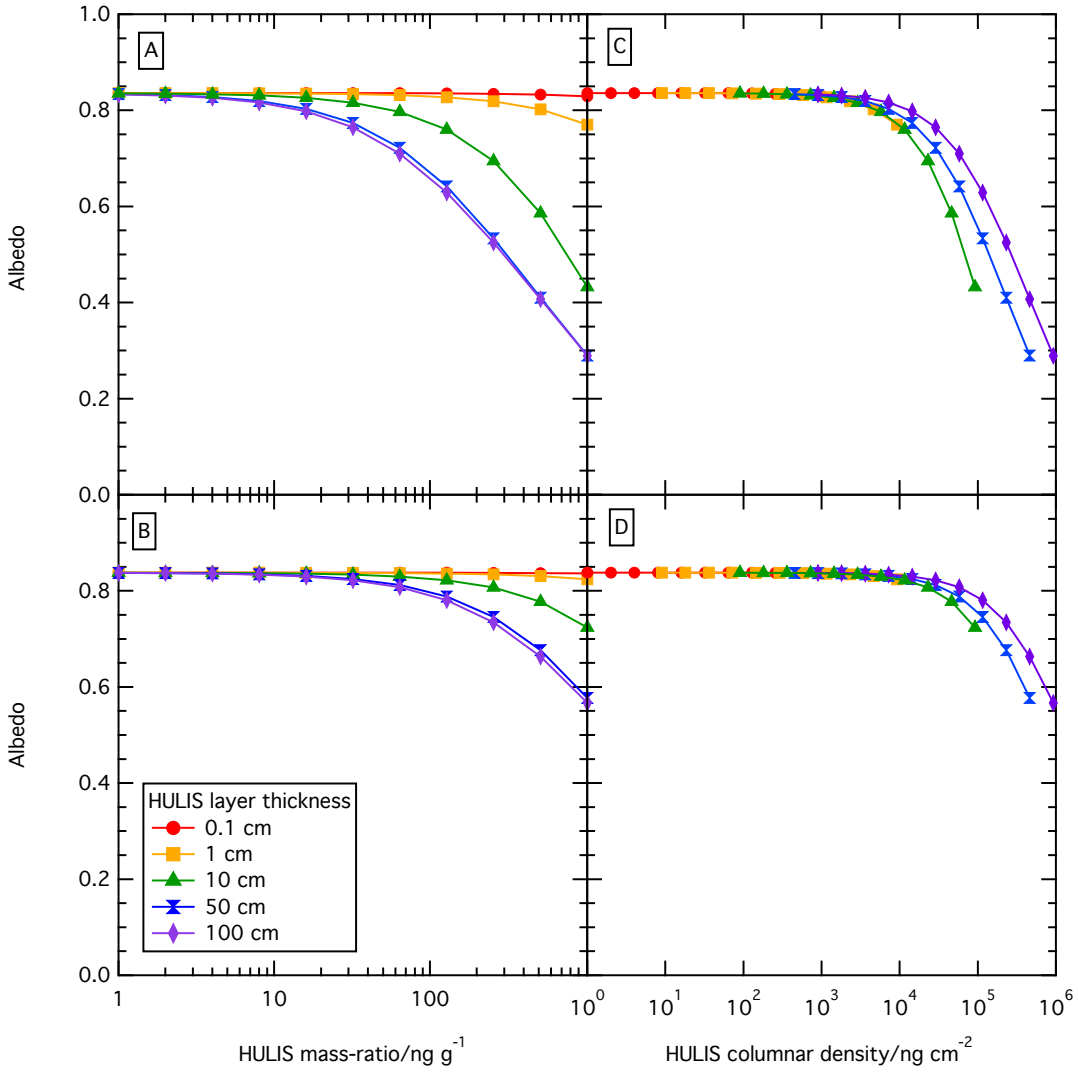

Figure 2.17 *– Albedo with increasing HULIS mass-ratio in a surface layer in the sea ice of varying thickness at A) 300 nm and B) 400 nm and change in albedo with columnar density of HULIS at C) 300 nm and D) 400 nm.*

2.3.4.2 Effect of increasing black carbon and HULIS in a 1 cm layer in sea ice

Figure 2.18 demonstrates the effect on sea ice surface albedo of placing a 1 cm layer with varying black carbon mass-ratio at different depths in the sea ice. At all depths black carbon mass-ratio in a thin surface layer does not strongly affect the albedo until a black carbon mass-ratio, >10 ng g^{-1}, as is also suggested by figure 2.16. The deeper the black carbon layer the less effect increasing black carbon has on albedo because black carbon situated deeper in the sea ice has less chance of absorbing photons entering the sea ice before the photons are scattered back out. The greatest change in albedo occurs when the black carbon bearing layer is moved down between the two shallowest depths considered of 0 and 10 cm; a 10% increase in surface albedo occurs

at a wavelength of 400 nm and 11% for 600 nm, at a black carbon concentration of 1024 ng g^{-1}. The increase in albedo is much less at a more realistic black carbon mass-ratio of 4 ng g^{-1}, where only a 0.03% increase in albedo occurs at 400 nm and 0.04% at 600 nm over the same depth change. The black carbon bearing layer still appears to have a slight effect on surface albedo as deep as 80 cm, although at 90 cm the effect the layer has is negligible.

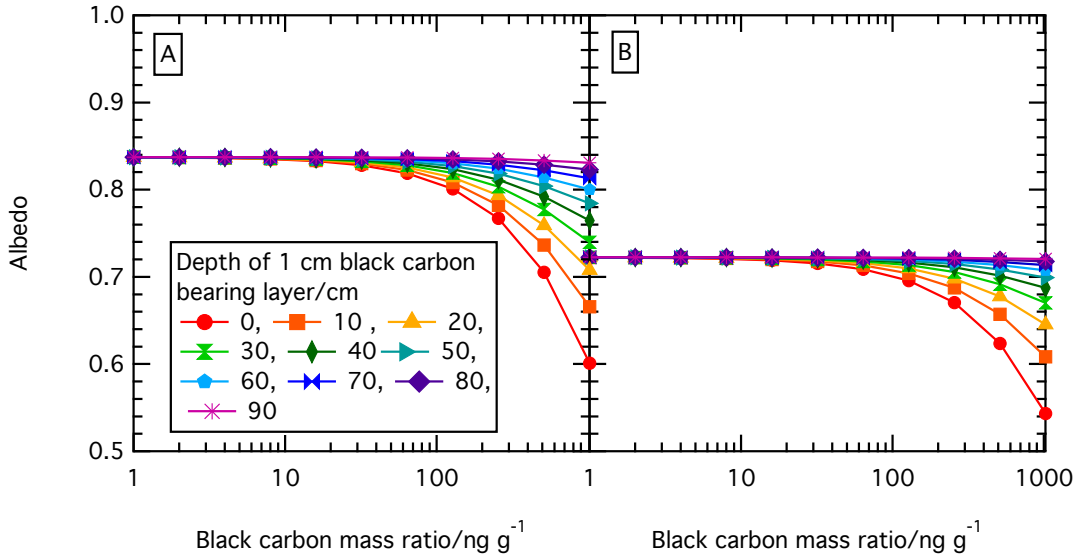

Figure 2.18 *– Albedo with black carbon in a 1cm layer moved down in the sea ice in 10 cm intervals at A) 400 nm and B) 600 nm.*

Figure 2.19 shows the response of sea ice surface albedo to a 1cm thick layer of HULIS placed at various depths in the sea ice from the surface to 90 cm depth in 10 cm increments. HULIS in a 1 cm layer has limited effect on surface albedo at all depths with HULIS mass-ratio less than 100 ng g^{-1}, as suggested by figure 2.17. For a HULIS mass-ratio greater than 100 ng g^{-1} the 1 cm HULIS layer has greatest effect when it is situated in a surface layer (0 cm). For example, for an increase in HULIS from 100 to 1000 ng g^{-1} with HULIS in a 1 cm layer at the sea ice surface (0 cm) albedo decreases from 0.83 to 0.77. With the layer at 50 cm albedo decreases from 0.83 to 0.82 over the same HULIS mass-ratio increase. As for black carbon, the change in HULIS layer position has greatest effect at shallow depths, for example at a HULIS mass-ratio of 500 ng g^{-1} when the HULIS layer is at the surface (0 cm) albedo is 0.80, and when the layer is at 40 cm the albedo is 0.82, a 2.5% increase in albedo between 0 and 40 cm. At a depth of 80 cm the albedo is 0.83, a 1.0% increase between 40 and 80 cm.

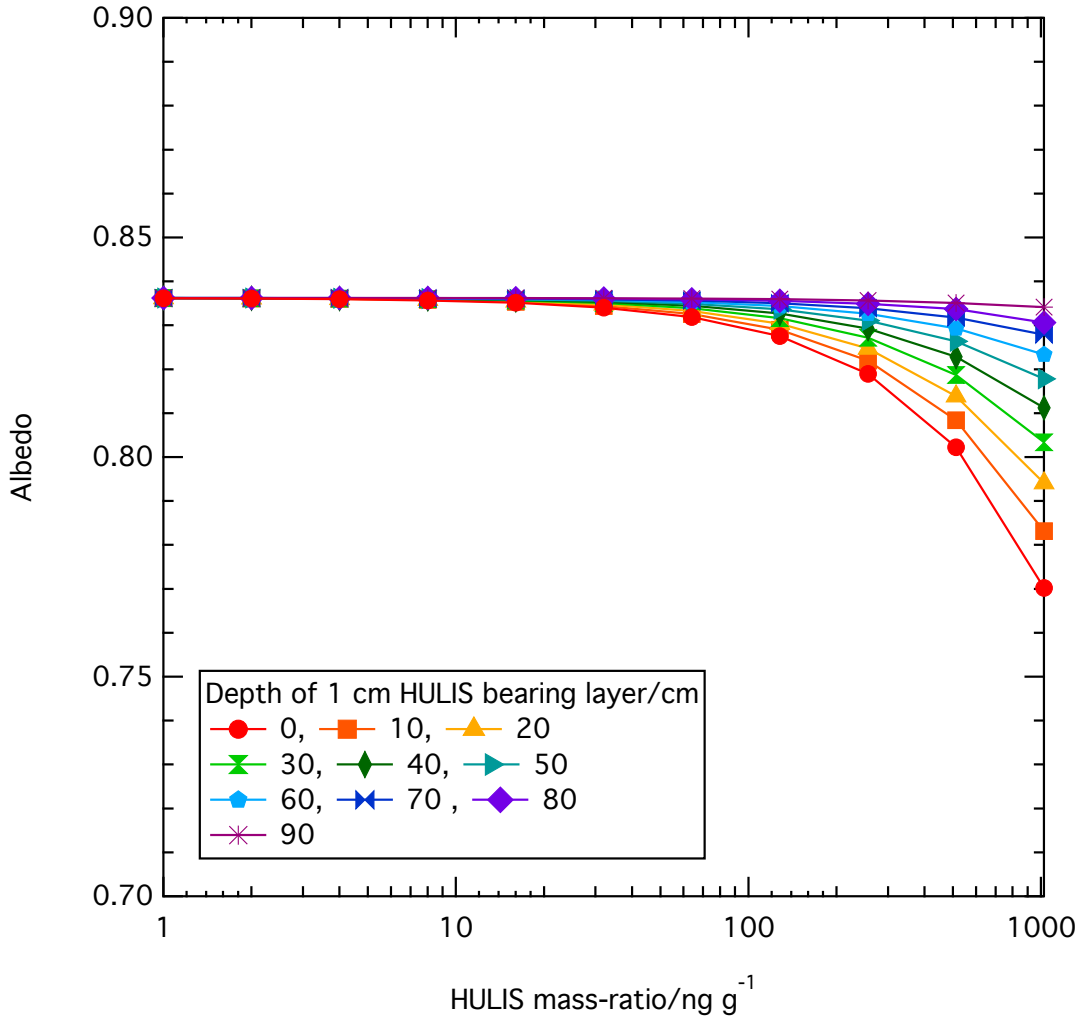

Figure 2.19 *– Albedo with HULIS in a 1cm layer moved down in the sea ice at a wavelength of 300 nm.*

2.4 Discussion

The discussion section will focus on a comparison of the effects of black carbon versus the effects of HULIS. The results presented here will then be compared to previous modelling of effects of black carbon on sea ice albedo by Light et al. (1998), Ledley and Thompson (1986), Jacobson (2004) and Grenfell et al. (2002). Black carbon and HULIS effect on photobiological processes will be discussed and how black carbon and HULIS are most likely to be distributed in sea ice will also be considered. Finally model limitations and potential progression of the work presented in this chapter will be discussed

2.4.1 The effects of black carbon versus HULIS

Chapter 2 has considered the effects of two common absorbing impurities, black carbon and HULIS, on sea ice albedo and *e*-folding depths. The results show that black carbon consistently has a much larger impact than HULIS on both these factors. For example, when the impurity is evenly distributed in the sea ice with an increase in black carbon and HULIS from 1–100 ng g^{-1} at a wavelength of 400 nm, albedo decreases from 0.83 to 0.44 (53% of the original albedo value) for black carbon and from 0.84 to 0.79 (94% of the original albedo value) for HULIS from the albedo value at 1 ng g^{-1}. The *e*-folding depth decreases from 70.5 to 23.0 cm (32.6% of the original *e*-folding depth) for black carbon and from 73.8 cm to 64.0 cm (86.7% of the original *e*-folding depth) for HULIS over the same mass-ratio increase. For HULIS a surface layer needs to be greater than 10 cm thick before it has a noticeable effect on albedo while with black carbon a 0.1–1 cm layer has an effect. A layer containing HULIS greater than ∼60 cm deep has negligible effect on albedo while with black carbon a layer up to ∼90 cm deep influences albedo.

The greater effect observed by black carbon on albedo and light penetration depths can be explained by the absorption cross-section of black carbon and HULIS (figure 2.2). Black carbon has a much larger absorbing cross-section than HULIS. At a wavelength of 300 nm black carbon has a 5 times larger absorption cross-section while at a wavelength of 600 nm black carbon has a 800 times larger absorption cross-section than HULIS. Highlighting the wavelength dependence of HULIS absorption cross-section. The absorption spectrum of black carbon does not vary significantly with wavelength. The absorption cross-section of HULIS is conversely highly wavelength dependent with absorption peaking at 300 nm and significantly decreasing to 500 nm where absorption approaches 0 cm^2 kg^{-1}.

A significantly larger mass-ratio of HULIS would be required to have the same effect as black carbon, and HULIS will only impact shorter wavelengths (>450 nm). HULIS absorption could be important for photochemical processes occurring within the sea ice which require UV radiation. For example, in snow samples at Barrow, Alaska Beine et al. (2011) suggest that HULIS accounts for 50% of total light absorption in the photochemically active region (300–450 nm).

2.4.2 Comparison with previous modelling of albedo changes due to black carbon

Light et al. (1998), Grenfell et al. (2002) and Jacobson (2004) each report effects of black carbon on multi-year Arctic sea ice optical properties. Light et al. (1998) focused their radiative-transfer study on the effects of included sediment particles on the albedo of sea ice. Using a structural optical model in combination with a four-stream radiative-transfer model they investigated the effects of sediment particle mass-ratio, vertical distribution and particle size, on sea ice albedo and compared the change in albedo caused by sediment particles to the change in albedo caused by one mass-ratio of soot. The sea ice described by Light et al. (1998) is a multi-year frozen Arctic sea ice, this will have very different optical properties to the ablating first year seasonal sea ice utilised in the study presented here. Jacobson (2004) used a one-dimensional radiative-transfer calculation under direct solar conditions, with a solar zenith angle of 72°, to investigate change in albedo with mass-ratios of 0, 25, 100, 250 and 500 ng g^{-1} of black carbon in sea ice, using similar sea ice properties to Light et al. (1998). Grenfell et al. (2002) measured mass-ratios of soot in snow and sea ice samples during the Surface Heat Budget of the Arctic Ocean (SHEBA) experiment, obtaining an average value of 5.5 ng g^{-1} for sea ice in the Arctic Ocean. They concluded the soot mass-ratios found in sea ice could modify the melt cycle of snow-free sea ice through acceleration of summer ablation. Using a multilayer four-stream radiative-transfer model they investigated effects of varying mass-ratios and vertical distribution of soot on albedo, between wavelengths of 350–2750 nm.

The potential changes in albedo reported by Light et al. (1998), Grenfell et al. (2002) and Jacobson (2004) vary from those reported here and from each other. For an increase from 1–100 ng g^{-1} of black carbon in the sea ice figure 2.8 suggests a relative albedo decrease of 44% would occur at a 500 nm wavelength. However Light et al. (1998) report a relative albedo decrease of 27% at 500 nm and Jacobson (2004) report a decrease of only 8% for the same black carbon change, while Grenfell et al. (2002) only report a 1% decrease in albedo, for the same increase in black carbon mass-ratio in the top 1cm layer of their sea ice. The differences between calculated albedo changes with black carbon that occur in literature could to be due to variations in sea ice type modelled. However, each of these studies distributes black carbon

differently in the sea ice, which makes intercomparison more difficult. Light et al. (1998) evenly distributed black carbon throughout the sea ice, similarly to the work presented here, while the 1% decrease in albedo reported by Grenfell et al. (2002) has black carbon placed in only a 1 cm surface layer. The results presented here suggest a 4% decrease in albedo when black carbon is situated in a 1 cm surface layer for a black carbon increase from 1–100 ng g^{-1}, at a wavelength of 500 nm. Overall the decrease in albedo reported in this chapter appears to be higher than previous literature has reported, which is likely to be due to the different sea ice types investigated.

2.4.3 Effects of black carbon and HULIS on photobiological processes

Increasing black carbon and HULIS in sea ice limits light penetration, and thus propagation of PAR into sea ice, which could affect photobiological processes. For example, PAR availability is, for the majority of the year, the greatest factor limiting photosynthetic sea ice algae growth (Welch and Bergmann, 1989; Cota and Sullivan, 1990; Mundy et al., 2005; Saenz, 2011). Primary production in Antarctic sea ice constitutes 5% of total annual primary production in the region of the Southern Ocean influenced by sea ice (Lizotte, 2001). A decrease in primary production decreases food sources for larger organisms, affecting the entire Polar food web. Sea ice algae are the primary source of food for krill, which are a main source of food for squid, penguins, seals and baleen whales (Lizotte, 2001).

The light compensation point defines the light intensity where respiration and photosynthesis rate is equal and net algae growth is zero. Above the point net primary production is greater than zero and thus algae accumulate in their environment. Measured light compensation points for sea ice algae vary from 0.18 μmol photon m^{-2} s^{-1} (Cota, 1985) to $\sim$2 μmol photon m^{-2} s^{-1} (McMinn et al., 2000). The light compensation point will vary with temperature and algae type (Kirk, 2000).

Figure 2.20 shows the black carbon mass ratio that would cause PAR at the base of the sea ice to decrease to the light compensation point, below which algae will no longer accumulate in sea ice for different solar zenith angles. The black carbon mass-ratios for light compensation points of 0.18 and 2.0 μmol photon m^{-2} s^{-1} are shown.

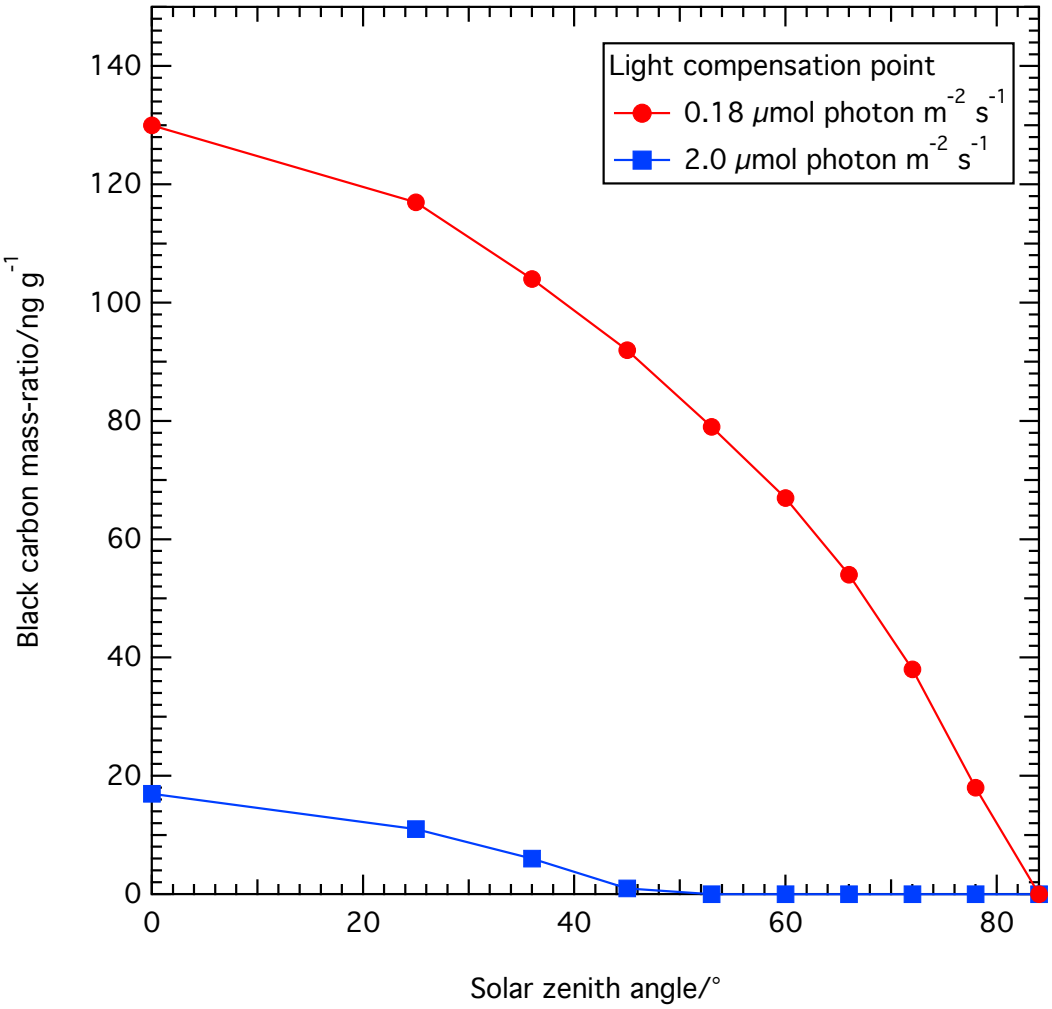

Figure 2.20 *– Black carbon ratio which will reduce PAR at the base of a 1 m thick ablating sea ice to the light compensation point below which algal accumulation will not occur, for different solar zenith angles (0, 25, 36, 45, 53, 60, 72, 84 and 90°).*

From figure 2.20 it can be suggested black carbon in sea ice is likely to be most detrimental during autumn and spring months when solar zenith angle is larger, therefore affecting the length of the sea ice algae growing season. For the lower light compensation point examined of 0.18 μmol photon m^{-2} s^{-1} black carbon mass-ratios need to be less than 50 ng g^{-1} to reduce the PAR to the light compensation point at solar zenith angles larger than ~65°, the black carbon required to reduce PAR to the light compensation point largely decreases with a increased light compensation point. For a light compensation point of 2 μmol photon m^{-2} s^{-1} less than 1 ng g^{-1} is required to reduce PAR to the light compensation point.

For PAR at the base of the sea ice to be at the light compensation point the HULIS mass-ratio required is highly zenith angle dependent. For a light compensation point

of 0.18 μmol photon m^{-2} s^{-1}, the point only occurs for a zenith angle of 84° with a HULIS mass-ratio of 63 ng g^{-1}, for all other zenith angles the mass-ratio of HULIS would have to exceed 1024 ng g^{-1} which is unrealistic. For a light compensation point of 2 μmol photon m^{-2} s^{-1}, the point only occurs for a zenith angle of 45° with a HULIS mass-ratio of 744 ng g^{-1}, for smaller zenith angles the mass-ratio of HULIS would have to exceed 1024 ng g^{-1} and for larger zenith angles the mass-ratio is less than 1 ng g^{-1}.

2.4.4 How is black carbon and HULIS likely to be distributed in sea ice?

In section 2.3.4 the results from radiative-transfer calculations investigating how black carbon and HULIS distribution in sea ice will affect surface albedo are presented. In section 2.4.4 the possible ways in which black carbon and HULIS could be entrained in sea ice and thus be distributed within the sea ice will be reviewed. Although literature is available on sources and distribution of black carbon, information for HULIS is far more limited. In the modelling presented here a number of different scenarios have been presented with the black carbon and HULIS situated in different thickness layers in different regions of the sea ice, first of all in a layer of increasing depth at the top of the sea ice and secondly in a constant depth layer moved down in the sea ice.

The first scenario, where black carbon and HULIS are entrained in the upper part of sea ice, could occur due to; direct dry deposition of black carbon and HULIS on to sea ice following, for example, a forest fire, black carbon/HULIS deposition from meltwater as snow melts or during the formation of “snow-ice” as is subsequently described.

Black carbon and HULIS can be entrained into sea ice directly from the atmosphere through wet and dry deposition. Jacobson (2004) base their modelling on suggesting that soot in snow and sea ice comes from 98% precipitation and only 2% from dry deposition. Grenfell et al. (2002) base part of their modelling on assuming the black carbon is situated in the top 1 cm of ice, due to melting of an overlying 1–2 m of snow; although most soot would be carried away with melt water, a portion may be left behind and deposited in the upper layers of sea ice. However Grenfell et al. (2002)

based their study just on Arctic snow and sea ice, the situation for Antarctic snow and sea ice is likely to be highly different. Antarctica is a wet snow-ice system where a greater precipitation of snow on a thinner layer of sea ice, compared to the Arctic, causes seawater to flood the snow, causing melting followed by freezing, creating new "snow-ice" (Massom et al., 2001). As a result any black carbon present in the snow will be reincorporated in to the sea ice. It is estimated by Jeffries et al. (2001) that snow-ice makes up 12–36% of total ice mass in autumn and winter. When the black carbon from snow is incorporated into the sea ice all of the black carbon will enter the sea ice, which is different therefore from the Arctic where most black carbon in snow will be carried away in meltwater. However, in Antarctica there is less black carbon in snow, with Warren and Clarke (1990) reporting values of only 0.1–0.3 ng g^{-1} near the south pole. Chýlek et al. (1987) report slightly higher values from the Ross Ice Shelf of 2.5 ng g^{-1}, but that is still considerably lower than Arctic values which range from 23 ng g^{-1} collected by at Barrow, Alaska, to as high as 45.5 ng g^{-1} collected at Alert, Canada (Clarke and Noone, 1985). Therefore in the Antarctic there will be a smaller concentration of black carbon over a greater depth at the top of the sea ice, compared to the Arctic where a higher concentration of black carbon will be distributed into a thinner layer at the top of the sea ice. Values for HULIS concentrations in snow are very limited. Voisin et al. (2012) suggest mass-ratios of 1-10 ng g^{-1} in Arctic snow, stating that the values would be expected to be lower in Antarctica. France et al. (2012) suggest values in the range of 1200–1500 ng g $^{-1}$ for Arctic snow, which is considerably higher.

In rare circumstances a large deposition of black carbon can occur due to a large black carbon producing event, an idea studied by Ledley and Thompson (1986) who examine the effect of sootfall following a nuclear war on sea ice. Other large black carbon producing events include forest fires, for example in 2004 there was a large increase in Arctic atmospheric black carbon due to burning of the Boreal forests in North America (Law and Stohl, 2007). These large black carbon producing events would result in an anonymously high amount of dry deposition of black carbon on the sea ice surface over a relatively short time period which would have a short term severe detrimental effect on the sea ice albedo. Indeed Ledley and Thompson (1986) suggest the Arctic could be sea ice free in winter after such an event, due to the extreme albedo decrease and associated sea ice melting.

The second scenario presented, where black carbon and HULIS was found in layers within the sea ice could occur due to entrainment of sediment layers in the sea ice, which includes a component of black carbon and HULIS, or due to an anomalously high black carbon/HULIS polluted layer in a snow pack that is subsequently turned into snow-ice as described above. Black carbon and HULIS can also be entrained through sediment inclusions in sea ice, which occurs where sea ice forms over shallow ocean shelves. The effect of sediment inclusions on sea ice albedo is studied in great detail by Light et al. (1998). The mass of organic carbon stored in ocean sediments is $\sim$ 160 Tg year^{-1} (Hedges and Keil, 1995) with black carbon making up about 6% of the carbon, and up to 50% at some sites (Masiello, 1998). It is suggested that up to 50% of Arctic sea ice may have sediment inclusions (Larssen et al., 1987; Pfirman et al., 1989; Nurnberg et al., 1994; Eicken et al., 2000, 2005). Giani et al. (2010) suggest that HULIS makes up to 17% of total sedimentary organic matter on shallow continental shelves. Sediment inclusions could occur uniformly distributed through the sea ice or as layers.

Black carbon and HULIS was also modelled evenly distributed through the entire sea ice, which could result from black carbon/HULIS being entrained from the seawater the sea ice forms from. Unlike black carbon, HULIS is water soluble so will dissolve in oceans. Suman et al. (1997) suggest an approximate flux of 8.4 $\times$ 10^{17} μmol per year of black carbon to oceans from all sources, with Masiello (1998) suggesting that residence times of black carbon in the water column will range from 2,400 to 13,900 years. During this time black carbon is stored as a constituent of marine dissolved organic carbon (DOC), with black carbon making up 4–22% of deep marine DOC (Masiello, 1998), and 0.9–2.6% of shallow marine DOC (Dittmar, 2008). Marine DOC is one of the biggest carbon pools with 700 Gt of carbon storage (Hedges et al., 1997). Data on HULIS concentrations in seawater are limited, Krivácsy et al. (2008) report HULIS mass-ratios in marine air of 0.40 μg m^{-3} making up 19% of water-soluble organic carbon. Black carbon and HULIS entrainment from seawater would result in an even deposition of black carbon and HULIS throughout the sea ice. Although entrainment through this method is likely to result in a lower concentration than through surface entrainment, it could still potentially be enough to cause an effect on albedo and light penetration depths. Black carbon and HULIS from seawater is likely to be more important in Antarctica where lower concentrations of atmospheric

black carbon and HULIS are reported.

Taking all possible forms of black carbon and HULIS entrainment into consideration black carbon and HULIS is most likely to be found in trace amounts throughout the sea ice due to emplacement from the seawater from which it forms and through sediment inclusions. However the effect of the black carbon and HULIS from seawater and sediment is likely to be negligible compared to entrainment from snow meltwater and snow-ice formation, which will lead to black carbon and HULIS concentrated near the surface. Therefore the most realistic scenario of those modelled is shown in figures 2.16 and 2.17 with black carbon/HULIS situated in a 1 cm surface layer, which provides a realistic model of Antarctic sea ice at the end of the season. Regarding previous literature where black carbon was also distributed differently in each study, the most realistic is the Grenfell et al. (2002) study where black carbon was also situated in a 1 cm surface layer. The black carbon and HULIS concentrated at a surface layer is also where black carbon and HULIS will have most effect on the albedo, potentially exacerbating melting rates.

2.4.5 Model limitations and potential future progression

In the calculations undertaken there are several issues which introduce uncertainty, these include; the absorption spectra of ice, black carbon and HULIS, the optical properties of black carbon and HULIS, depth of the sea ice modelled and the field data used to perform the calculations.

The values used for the refractive index, size and density of black carbon in the calculations were based on calculations by Warren and Wiscombe (1980, 1985) these are critiqued by (Bohren, 1986). Bohren (1986) firstly suggest the refractive index which Warren and Wiscombe (1985) use of $1.8 \pm 0.5i$, has a factor of 5 uncertainty in the imaginary part (Roesler and Faxvog, 1980). Secondly Bohren (1986) argues that all soot particles are assumed to be spherical but plate-like particles would be twice as absorbing as spherical particles. Thirdly the porosity of the carbon particles is unknown, with porous particles having a larger light absorption cross-section than dense particles. The black carbon absorption cross-section should be used with caution, however for the calculations to be undertaken some properties of the black carbon must be assumed. Recent work by France et al. (2012) demonstrates the absorption

cross-section calculated using values from Warren and Wiscombe (1980) and Warren and Wiscombe (1985) and also used here, agrees with measured absorption cross-section of black carbon reviewed by Bond and Bergstrom (2006). The properties of HULIS were reviewed by Graber and Rudich (2006) who suggest that atmospheric HULIS may differ considerably to terrestrial and aquatic HULIS e.g. smaller molecular weight and greater surface activity. Similarly to black carbon the error caused by uncertainty in the properties of HULIS is likely to be low.

The radiative-transfer calculations presented here were based on field data, and a radiative-transfer modelling study of King et al. (2005) for ablating sea ice in Terra Nova Bay, Antarctica, which was taken to be representative of all sea ice in that locality. The results presented here for change in albedo with mass-ratio of black carbon are different to those previously reported in literature (Light et al., 1998; Grenfell et al., 2002; Jacobson, 2004). These previous results reported also differ from each other. The differences in results may be due to differences in the ice properties used, although, due to differences in black carbon distribution in each study, intercomparison is difficult. The outcome of calculations may be highly sensitive to small adjustments in sea ice properties, thus the results presented here are only relevant to the sea ice at Terra Nova Bay, Antarctica. The albedo and *e*-folding depths reported are sea ice depth dependent as the sea ice utilised is not optically thick i.e. the value of the calculated albedo will be affected by sea ice depth. Figure 2.21 shows sea ice surface albedo for a range of sea ice thicknesses with different under ice albedo. From figure 2.21 the thickness of sea ice required for the albedo to be independent of the underlying medium can be determined. For the sea ice presented here a depth of over 10 m would be required for the sea ice to be optically thick which would be entirely unrealistic of an ablating Antarctic sea ice. For greater model certainty more field data on properties of different types of sea ice are required to observe how the effects on *e*-folding depth, PAR and albedo with increasing black carbon vary due to sea ice type/thickness. Furthermore accurate data on black carbon mass-ratios and macrostructural distribution in sea ice are required. The results presented here are for snow-free ablating sea ice, however sea ice is predominately snow covered and a snow cover may “mask” impurities in sea ice, a topic which will be explored in chapter 3.

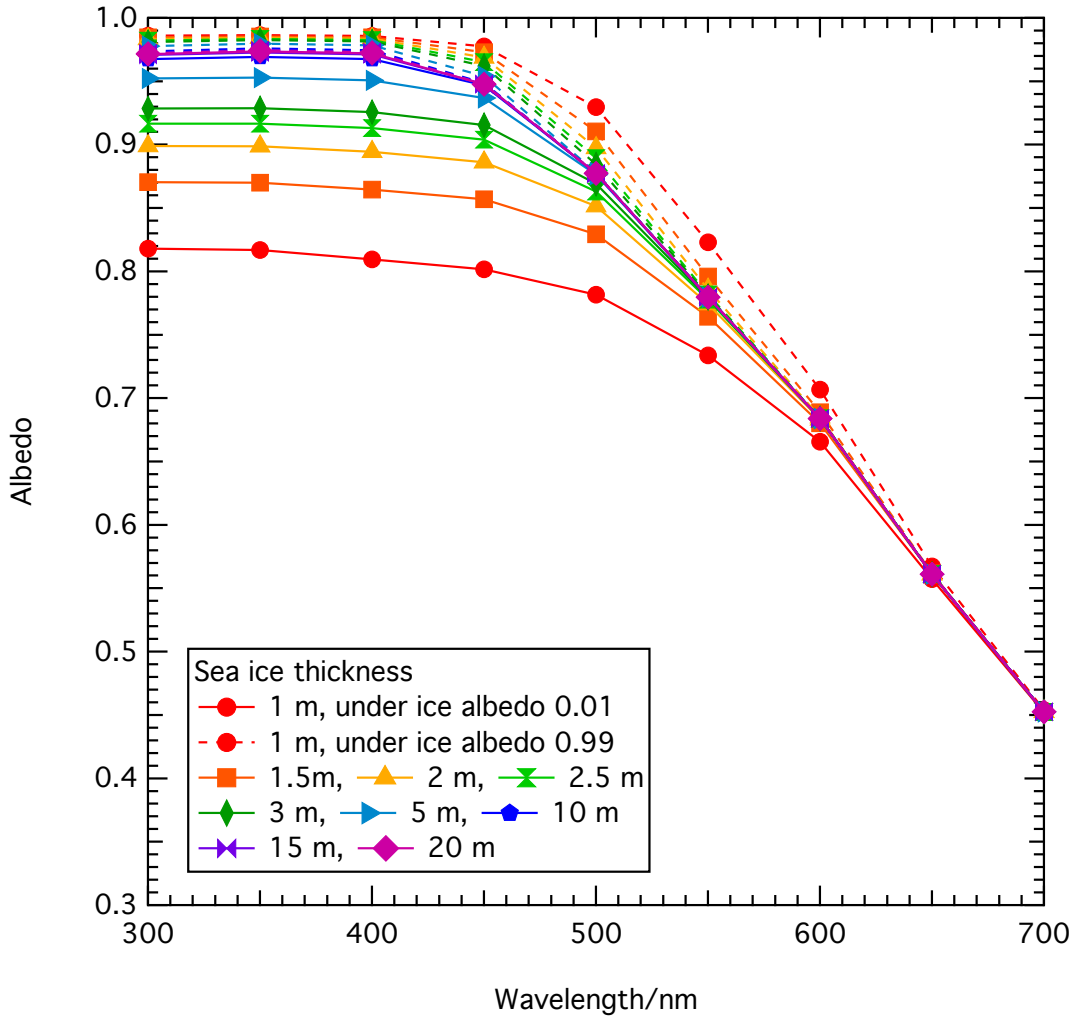

Figure 2.21 *– Variation in sea ice surface albedo with different sea ice thickness and under ice albedo. Solid lines show surface albedo with an under-ice albedo of 0.01 and dashed lines show surface albedo for a under-ice albedo of 0.99.*

2.5 Conclusions

Overall the results of chapter 2 suggest the effects of black carbon and HULIS are likely to be more important for climate than biology, as an unrealistic black carbon mass ratio is required to reduce light levels within the sea ice to below the light compensation point for algae, while a relatively small amount of black carbon can have an influence on albedo. The radiative-transfer modelling presented in chapter 2 shows that black carbon impurities have a much greater effect than HULIS on albedo and *e*-folding depths of an ablating Antarctic sea ice. With an increase in black carbon/HULIS from 1–100 ng g^{-1}, at a wavelength of 400 nm, albedo decreases from 0.83 to 0.44 (53% of the original albedo value) for black carbon and from 0.84 to 0.79

(94% of the original albedo value) for HULIS. The *e*-folding depth decreases from 70.5 to 23.0 cm (32.6% of the original *e*-folding depth) for black carbon and from 73.8 cm to 64.0 cm (86.7% of the original *e*-folding depth) for HULIS over the same mass-ratio increase. Black carbon is much more absorbing than HULIS; 5 times more absorbing at shorter wavelengths and up to 800 more times absorbing at longer wavelengths. HULIS absorption cross-section is also much more wavelength dependant, being much larger at shorter wavelengths (<500 nm). Therefore HULIS absorption may still be important at shorter wavelengths where it may influence photochemistry. The distribution of impurities within the sea ice affects the albedo response. Black carbon and HULIS have a greater effect on albedo of sea ice when they are concentrated at the surface of the sea ice, however black carbon in a 1 cm layer can affect the albedo down to 90 cm deep and down to 50 cm deep for HULIS. Black carbon and HULIS are most likely to be distributed in sea ice as a concentrated surface layer due to black carbon entrainment following overlying snow melt, but may also be found throughout the sea ice due to entrainment from the sea water from which it forms. The study presented here was for a first year Antarctic, snow-free, ablating sea ice. A snow cover over sea ice may diminish the effects of impurities in sea ice which will be explored in chapter 3. Different sea ice types may also respond differently to impurities, an idea which will be explored in chapters 3 and 4.

Chapter 3

The effects of additional black carbon on Arctic sea ice surface albedo: Variation with sea ice type and snow cover

---

The work presented in chapter 3 has been published as; A. Marks & M. King (2013). The effects of additional black carbon on the albedo of Arctic sea ice: variation with sea ice type and snow cover. The Cryosphere, 7, 1193–1204. All radiative-transfer calculations and data analysis were carried out by myself, with guidance provided by my supervisor, Martin King.

3.1 Introduction

In chapter 2 the effect of two common impurities (black carbon and HUmic Like Substances (HULIS)) on an ablating Antarctic sea ice albedo was calculated using the TUV-snow radiative-transfer model. The results from chapter 2 suggest that different sea ice types may respond differently to impurities, although this was difficult to ascertain as study intercomparison is limited by differences in black carbon distribution. This chapter will explore the difference in albedo response of a first year and multi-year Arctic sea ice to black carbon. In this chapter black carbon will be distributed in

the top 5 cm of the sea ice, as chapter 2 suggested that this was most likely for an Arctic sea ice. Having black carbon distributed in the same way in both the first and multi-year sea ice will enable comparison of their albedo response. Different sea ice types will exhibit different physical and optical properties, including light scattering, absorption and density, which will affect the surface albedo of sea ice and thus impact the extent to which black carbon will affect the albedo of the sea ice. Chapter 2 showed that black carbon was a dominating light absorbing impurity, thus this chapter will only focus on black carbon.

The results of chapter 2, and indeed previous literature, are limited to snow-free sea ice. However, sea ice is predominately snow covered. The role of black carbon in sea ice on the albedo of an overlying snow will also be explored in this chapter. Snow on sea ice is commonly up to a few tens of centimetres thick (Weeks, 2010). Light penetrates snow and the underlying sea ice (e.g. King and Simpson (2001); King et al. (2005)), thus the optical properties of sea ice (i.e. black carbon content) will strongly influence the surface albedo of the snow. Where a thin snow cover is present black carbon in sea ice may lower the albedo of the overlying snow surface, leading to increased snow melting. The effect of black carbon in sea ice on the albedo of a thin overlying snow cover needs to be fully understood in order to understand the degree to which black carbon in sea ice may be climatically important. Warren and Wiscombe (1980) showed that 2 cm liquid equivalent of snow with a grain radius of 50 μm (20 cm new, fluffy snow) and 8 cm liquid equivalent of snow with a grain radius of 200 μm (20 cm fine grained, old snow) is enough for albedo to be semi-infinite or "optically thick"; the albedo is negligibly effected by an increase in the snowpack thickness(within 1 % of the albedo of an infinitely thick snowpack). France et al. (2011) demonstrate a snowpack needs to be greater than 3–4 *e*-folding depths ($\sim$ 10–20 cm) before it is optically thick enough for its albedo to be uninfluenced by the underlying surface. However, France et al. (2011) were simulating snow on a dark surface and the case of snow on sea ice will be different. Warren and Wiscombe (1980) and Brandt et al. (2005) briefly consider the effect of snow on the albedo of sea ice with Brandt et al. (2005) suggesting that just 3 cm of snow on sea ice may be optically thick and therefore black carbon in sea ice would no longer be detectible in the albedo of the snow surface.

The radiative-transfer modelling in this chapter will be based on field data from

Grenfell and Maykut (1977). Using a technique developed by Lee-Taylor and Madronich (2002), and described in section 3.2.1, unique values of the cross-section of absorption by impurities and the scattering cross-section can be derived for a snow or sea ice from albedo and *e*-folding depth data. The derived parameters can subsequently be utilised in the TUV-snow radiative-transfer model (as described in chapter 2). Derivation of the absorption cross-section by impurities also enables estimation of the mass-ratio of black carbon present in a snow/sea ice. To establish the extent that black carbon in sea ice may be climatically important mass-ratios found in sea ice need to be acquired. Data on typical black carbon concentrations in sea ice is very limited (Doherty et al., 2010; Grenfell et al., 2002), although is much more readily available for snow (e.g Clarke and Noone (1985); Doherty et al. (2010)).

In chapter 3 absorption and scattering cross-sections are derived for two Arctic sea ice types; a granular white ice and a blue ice, and two Arctic snow types; dry snow and wet snow, from albedo and *e*-folding depth data collected by Grenfell et al. (2002). Using the TUV-snow model, with the derived scattering and absorption cross-sections, chapter 3 has two aims:

1. Establish the response of the surface albedo of a first year versus a multi-year Arctic sea ice to an increased black carbon content.

2. Quantify the change in albedo of snow-covered sea ice with increasing black carbon in the sea ice. The change in the albedo of the snow covered sea ice will be quantified as a function of snow depth, snow type, sea ice type and amount of black carbon in the sea ice – an effect which has not previously been quantified.

3.2 Method

The method section will be split into two sections. Firstly, a section describing how the TUV-snow model can be used to derive scattering and absorption cross-sections for a snow and sea ice, describing the process for the two snow types (wet and dry) and two sea ice types (blue ice and granular white ice) used in this chapter. Secondly, the derived scattering and absorption cross-sections will be used to determine the response of a multi-year and first year Arctic sea ice to increased surface black carbon

and establish the degree to which a wet and dry snow cover affects this response.

3.2.1 Using the TUV-snow model to calculate scattering and absorption cross-sections

In chapter 2, section 2.2, the TUV-snow radiative-transfer model is described. In chapter 2 the model was used to calculate albedo and *e*-folding depth of sea ice using a known scattering and absorption cross-section of the sea ice. The TUV-snow model can also be used to ascertain the scattering cross-section, $\sigma_{\text{scatt}}(\lambda)$, and the cross-section of absorption by impurities, $\sigma^{+}_{\text{abs}}(\lambda)$, of a snow/sea ice, if the albedo, *e*-folding depth, density and asymmetry parameter, g, are known. The technique was first used, and is described, by Lee-Taylor and Madronich (2002). Values of albedo and *e*-folding depth for a snow/sea ice are interpolated to find unique values of, $\sigma_{\text{scatt}}(\lambda)$, and $\sigma^{+}_{\text{abs}}(\lambda)$ which satisfy the measured albedo and liquid equivalent *e*-folding depth values. The method is henceforth described for the snow and sea ice studied in this chapter.

In the radiative-transfer modelling presented in this chapter $\sigma_{\text{scatt}}(\lambda)$ and $\sigma^{+}_{\text{abs}}(\lambda)$ are calculated from albedo and *e*-folding depth data from Grenfell and Maykut (1977). Grenfell and Maykut (1977) conducted measurements of light extinction coefficient (reduction in flux within a scattering medium, wavelengths 400–800 nm) and albedo (wavelengths 400–1000 nm) for melt ponds, snow on sea ice, and bare sea ice on first year sea ice near Point Barrow, Alaska, and on multi-year ice near Fletcher's Ice Island in the Beaufort Sea. The *e*-folding depth, ϵ, is related to extinction coefficient, κ, by equation 3.1.

$$\epsilon = \frac{1}{\kappa} \tag{3.1}$$

From the data of Grenfell and Maykut (1977) values of $\sigma_{\text{scatt}}(\lambda)$, and $\sigma^{+}_{\text{abs}}(\lambda)$ are calculated for a blue ice, a granular white ice, a dry snow and a wet snow. These snow and sea ice types are chosen as data is available for their albedo and *e*-folding depths. The albedo and *e*-folding depths of the snow and sea ice used from Grenfell and Maykut (1977) are shown in figures 3.1 and 3.2 respectively.

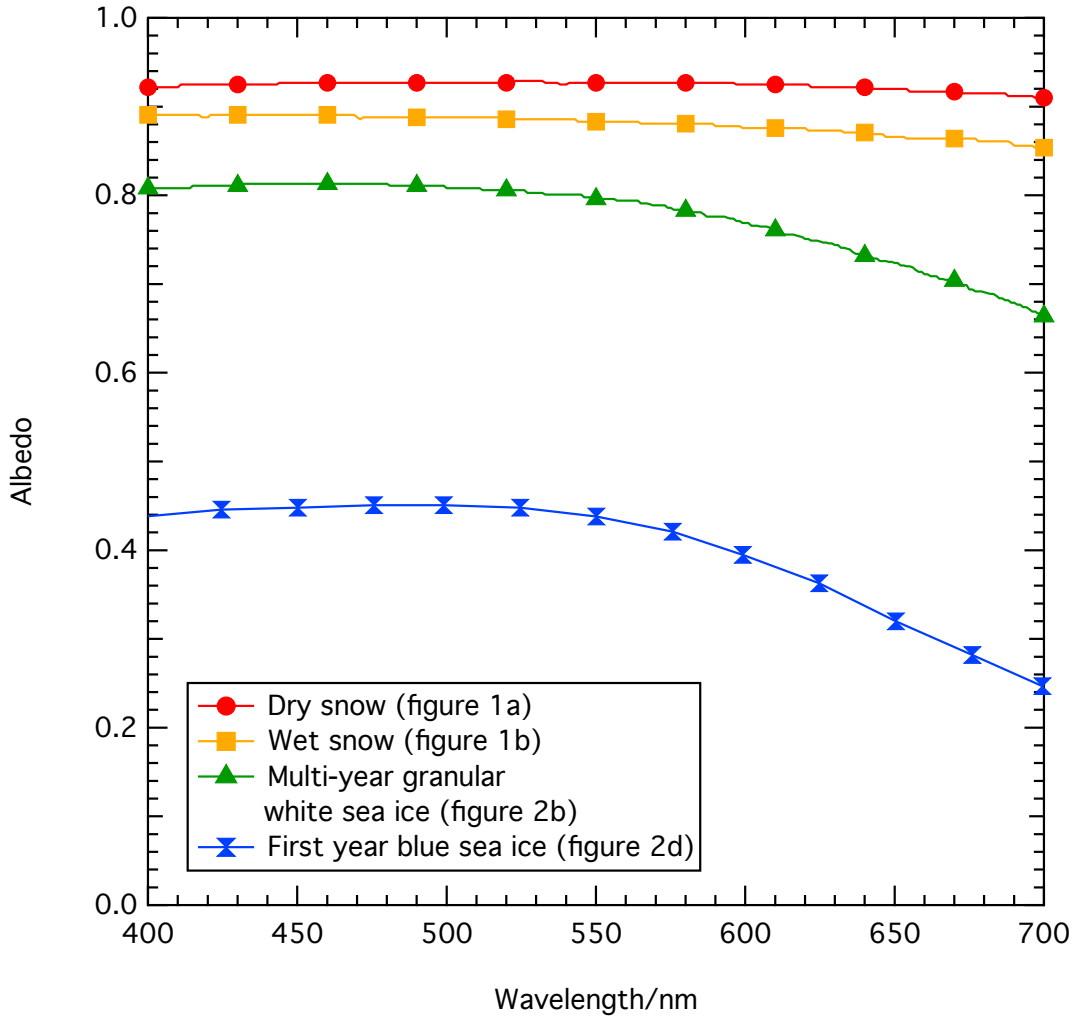

Figure 3.1 *– Albedo data for selected snow and sea ice from Grenfell and Maykut (1977). The figure number of Grenfell and Maykut (1977) from which data is extracted from is also shown.*

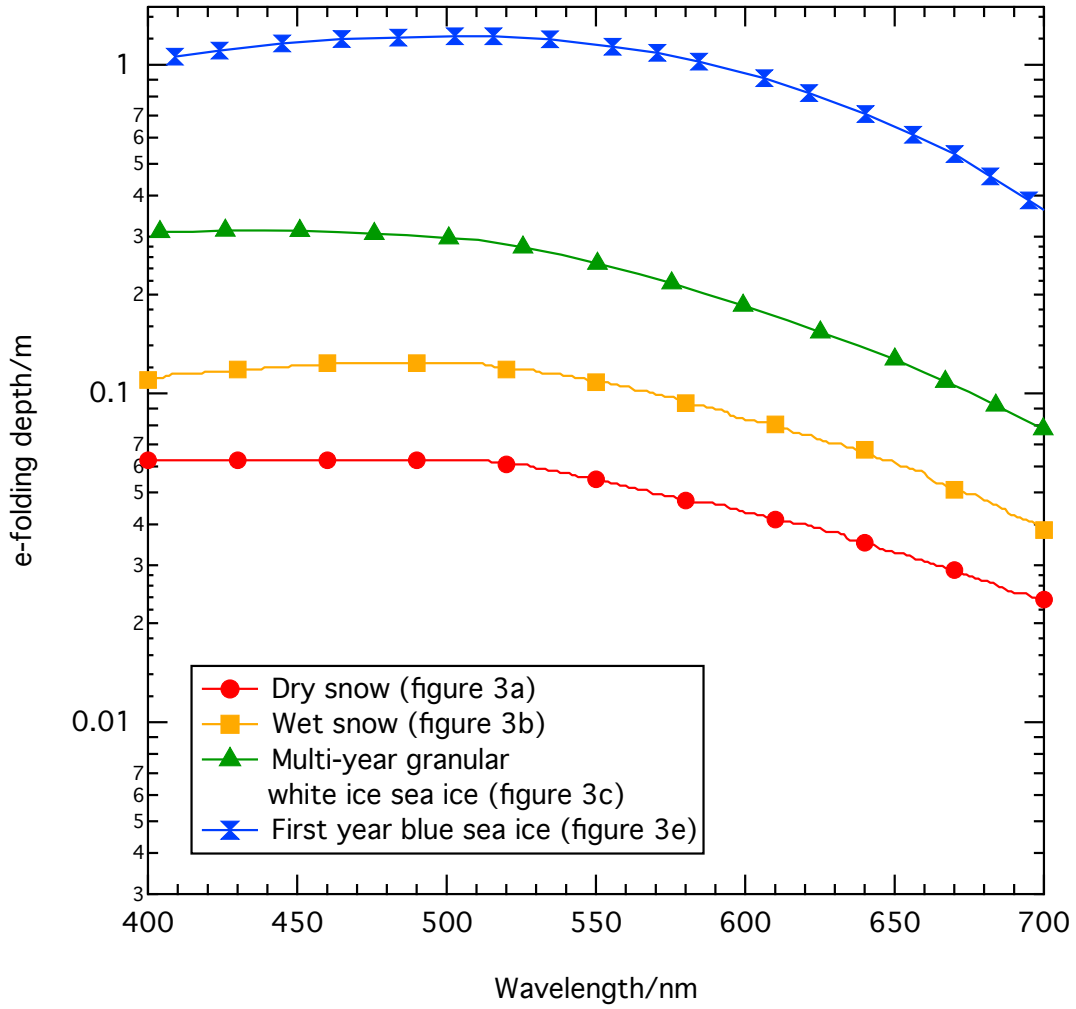

Figure 3.2 *– The e-folding depth (m) data for selected snow and sea ice from Grenfell and Maykut (1977). The figure number of Grenfell and Maykut (1977) from which data is extracted from is also shown.*

To calculate $\sigma_{\text{scatt}}(\lambda)$, and $\sigma^{+}_{\text{abs}}(\lambda)$ for a snow/sea ice the TUV-model is used to calculate the albedo and *e*-folding depths for a range of σ_{scatt}, and σ^{+}_{abs} at wavelengths from 400–700 nm. A particular mass-ratio of black carbon in snow or sea ice will exhibit a unique absorption cross-section, thus the σ^{+}_{abs} is entered as a black carbon mass-ratio. The link between absorption cross-section and the mass-ratio of black carbon is shown in equation 3.2. Where, σ^{+}_{abs} is the absorption cross-section owing to light absorbing impurities, σ_{BC} is the absorption cross-section for black carbon and [BC] is the black carbon mass-ratio. For these calculations black carbon is assumed to have a wavelength independent absorption cross-section of 10 $\text{m}^2\ \text{g}^{-1}$ thus an absorption cross-section of $10\text{m}^2\ \text{g}^{-1}$ corresponds to an absorption cross-section of black carbon of 1 $\text{ng}\ \text{g}^{-1}$

$$[\mathrm{BC}] = \frac{\sigma^{+}_{\mathrm{abs}}}{\sigma_{\mathrm{BC}}}, \tag{3.2}$$

Black carbon is assumed to only contribute to absorption, not scattering, thus an increase in black carbon is analogous to increased absorption by impurities. For each snow/sea ice the TUV-snow model was set up with the sky conditions, measurement date (used to calculate Earth-Sun distance), sea ice/snow density and solar zenith angle described by Grenfell and Maykut (1977); the values are shown in table 3.1. The sea ice/snow was modelled as 1.5 m thick, with 24 layers (Grenfell and Maykut (1977) state sea ice thickness averaged ∼1.5 m). The atmosphere was aerosol free.

Snow/sea ice Type	**Measurement date**	**Sky conditions**	**Solar Zenith angle/°**	**Density/ g cm^{-3}**
Blue Sea Ice	15 Jun 1972	Clear	50	0.9
Granular White Sea Ice	1 Jul 1974	Clear	65	0.5
Dry Snow	20 Jun 1972	Clear	50	0.4
Wet Snow	20 Jun 1972	Isotropic	50	0.47

Table 3.1 *– Properties and measurement conditions of the snow and sea ice used in the study presented here. Measurement date, sky conditions, solar zenith angle and density are all from Grenfell and Maykut (1977).*

Figure 3.3 shows calculated albedo and *e*-folding depths over a given range of of σ_{scatt} and black carbon mass-ratio for the wet snow at a wavelength of 400 nm. Where the black carbon mass-ratio corresponds to a particular absorption cross-section of impurities ($\sigma^{+}_{\mathrm{abs}}$), according to equation 3.2. Figure 3.3 also shows the measured albedo and *e*-folding depth by Grenfell and Maykut (1977) for the wet snow at a wavelength of 400 nm as a dashed line. The intersection between the calculated and measured values of albedo and *e*-folding depth (circled on figure 3.3) provides potential σ_{scatt} and $\sigma^{+}_{\mathrm{abs}}$ (calculated from the mass-ratio of black carbon) values for the snow/sea ice which would exhibit the measured albedo *or* *e*-folding depth of the wet snow. The σ_{scatt} and $\sigma^{+}_{\mathrm{abs}}$ intersection values are then plotted and interpolated for both albedo and *e*-folding depth. The intersection between the albedo and *e*-folding depth curve gives unique σ_{scatt}, and $\sigma^{+}_{\mathrm{abs}}$ values which satisfy both the measured albedo *and* *e*-folding depth.

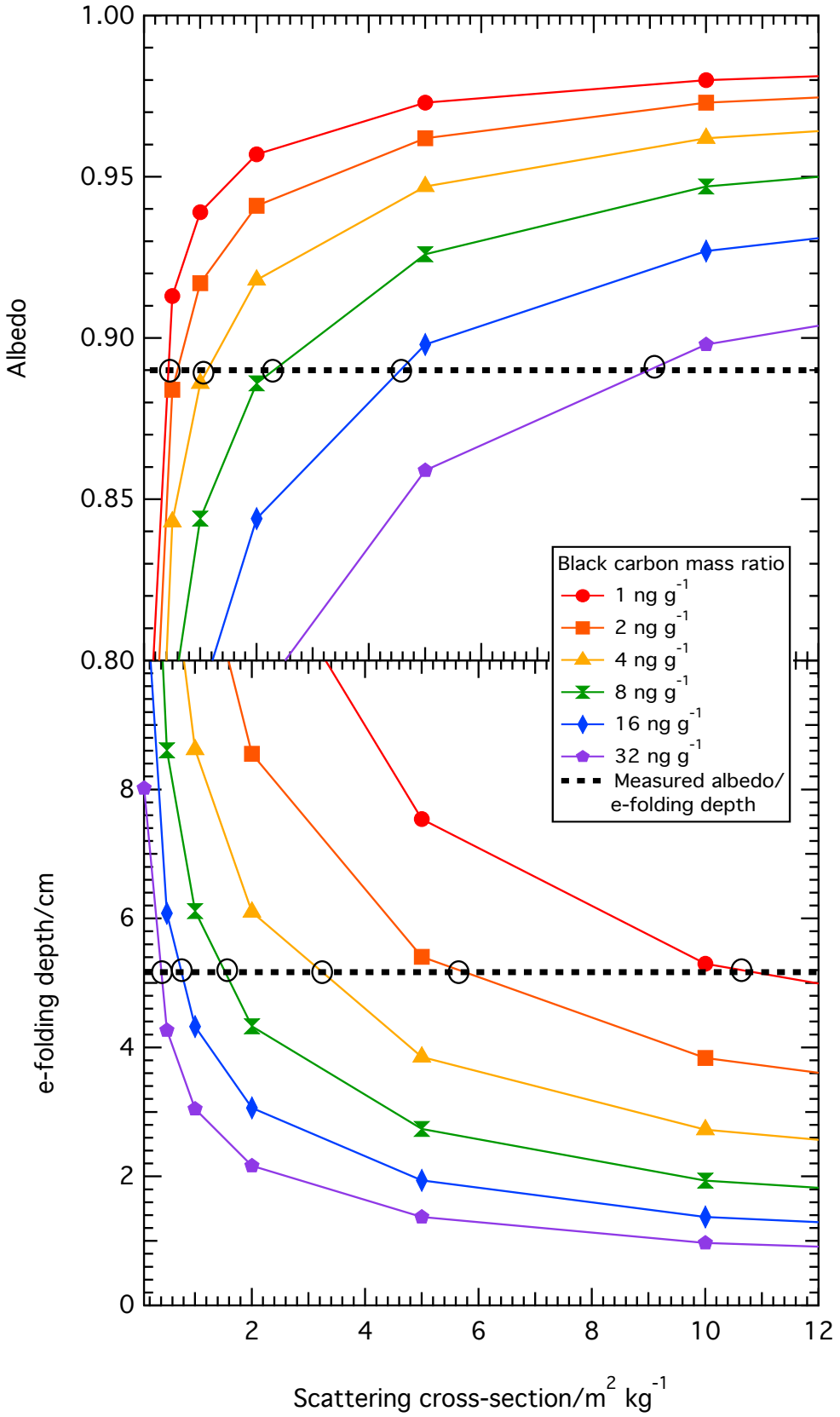

Figure 3.3 *– Calculated albedo and e-folding depth for different σ_{scatt} values and black carbon mass-ratios at 400 nm wavelength. The measured albedo and e-folding depth for wet snow at a wavelength of 400 nm is shown as a dashed line. The intersection of the calculated albedo/e-folding depth with the measured albedo/e-folding depth for each black carbon mass-ratio provides a potential absorption and scattering cross-section value.*

Figure 3.4 shows the interpolation for the wet snow; where the circled points on figure 3.3 form the markers in figure 3.4 for the lines at 400 nm (red lines). Figure 3.5 shows the same interpolation for the dry snow, figure 3.6 shows the interpolation for the first year sea ice and figure 3.7 shows the interpolation for the multi-year ice at wavelengths of 400, 500, 600 and 700 nm for each snow/sea ice. The intersection between the interpolated albedo and *e*-folding depth curve at each wavelength provides a unique σ_{scatt}, and σ^{+}_{abs} value which satisfies both the measured albedo and *e*-folding depth of the snow/sea ice.

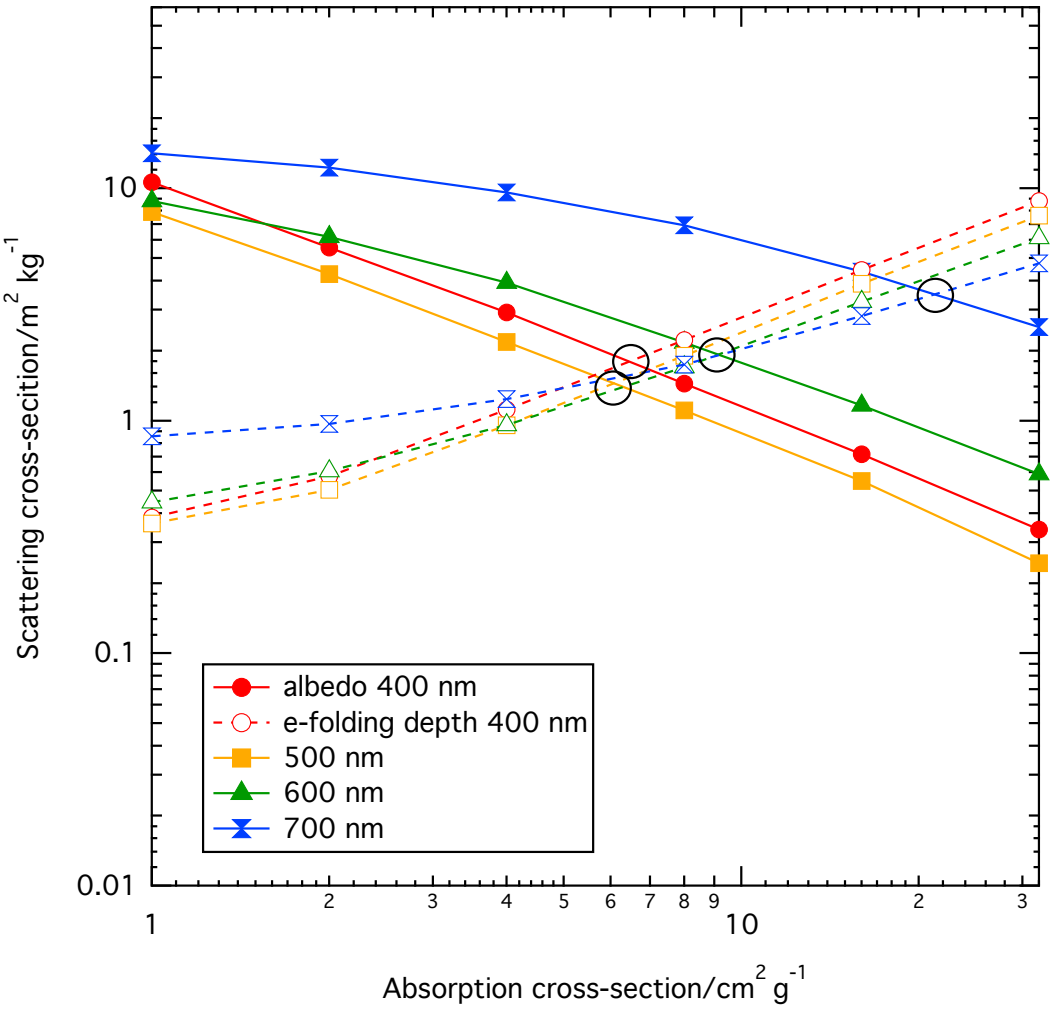

Figure 3.4 *– Interpolation of albedo and e-folding depth data for wet snow from Grenfell and Maykut (1977). Intersection provides unique values for scattering and absorption cross-section for the ice at that wavelength. The intersection was calculated every 25 nm from wavelengths from 400–700 nm, only every 100 nm is shown for clarity.*

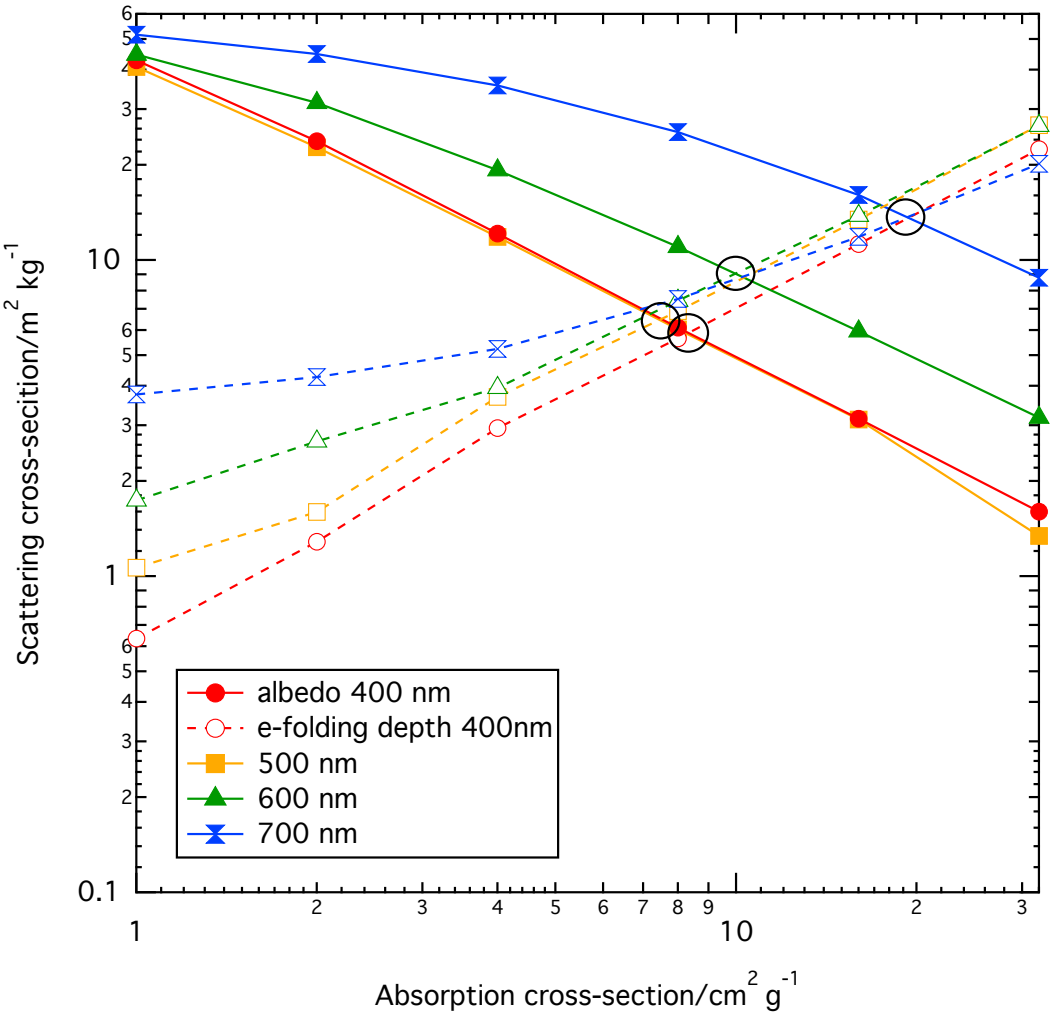

Figure 3.5 *– Interpolation of albedo and e-folding depth data for dry snow from Grenfell and Maykut (1977). Intersection provides unique values for scattering and absorption cross-section for the ice at that wavelength. The intersection was calculated every 25 nm from wavelengths from 400–700 nm, only every 100 nm is shown for clarity.*

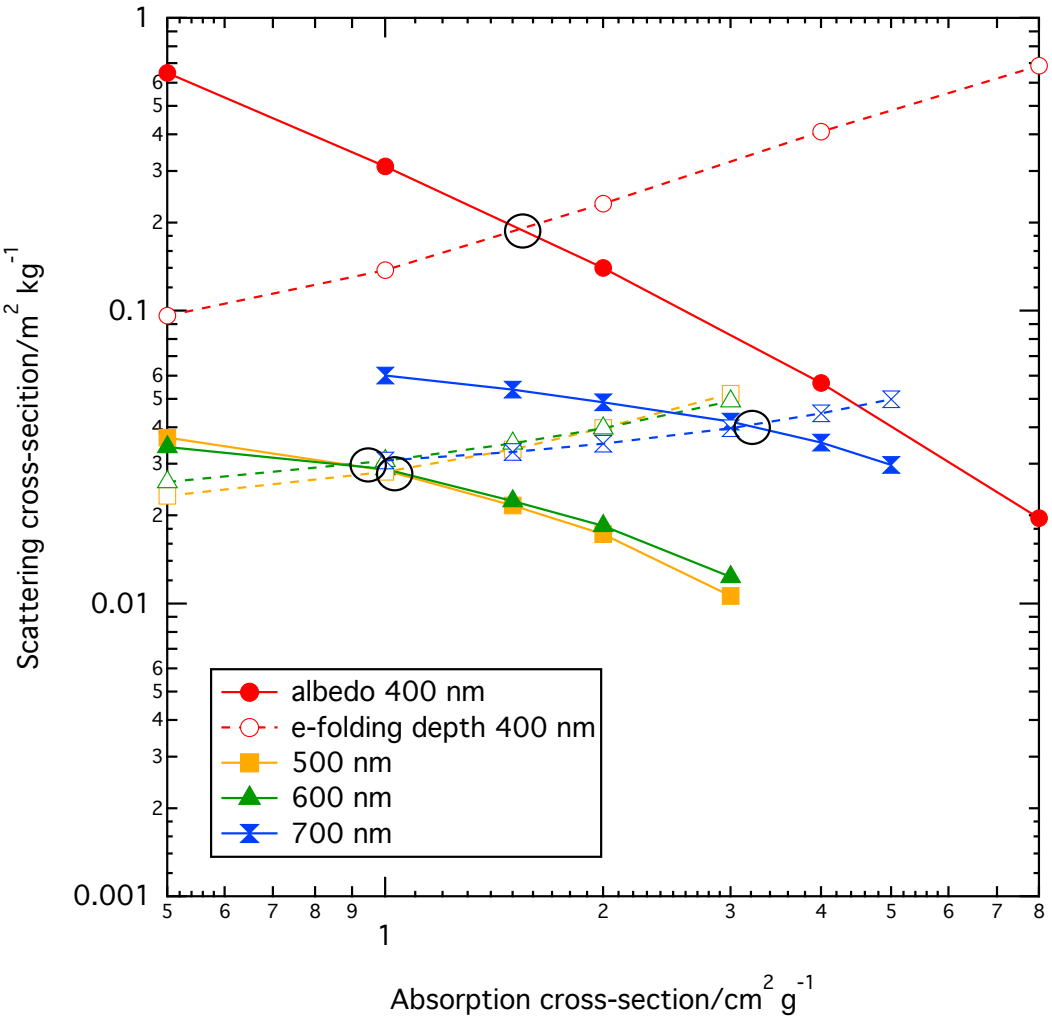

Figure 3.6 *– Interpolation of albedo and e-folding depth data for first year sea ice from Grenfell and Maykut (1977). Intersection provides unique values for scattering and absorption cross-section for the ice at that wavelength. The intersection was calculated every 25 nm from wavelengths from 400–700 nm, only every 100 nm is shown for clarity.*

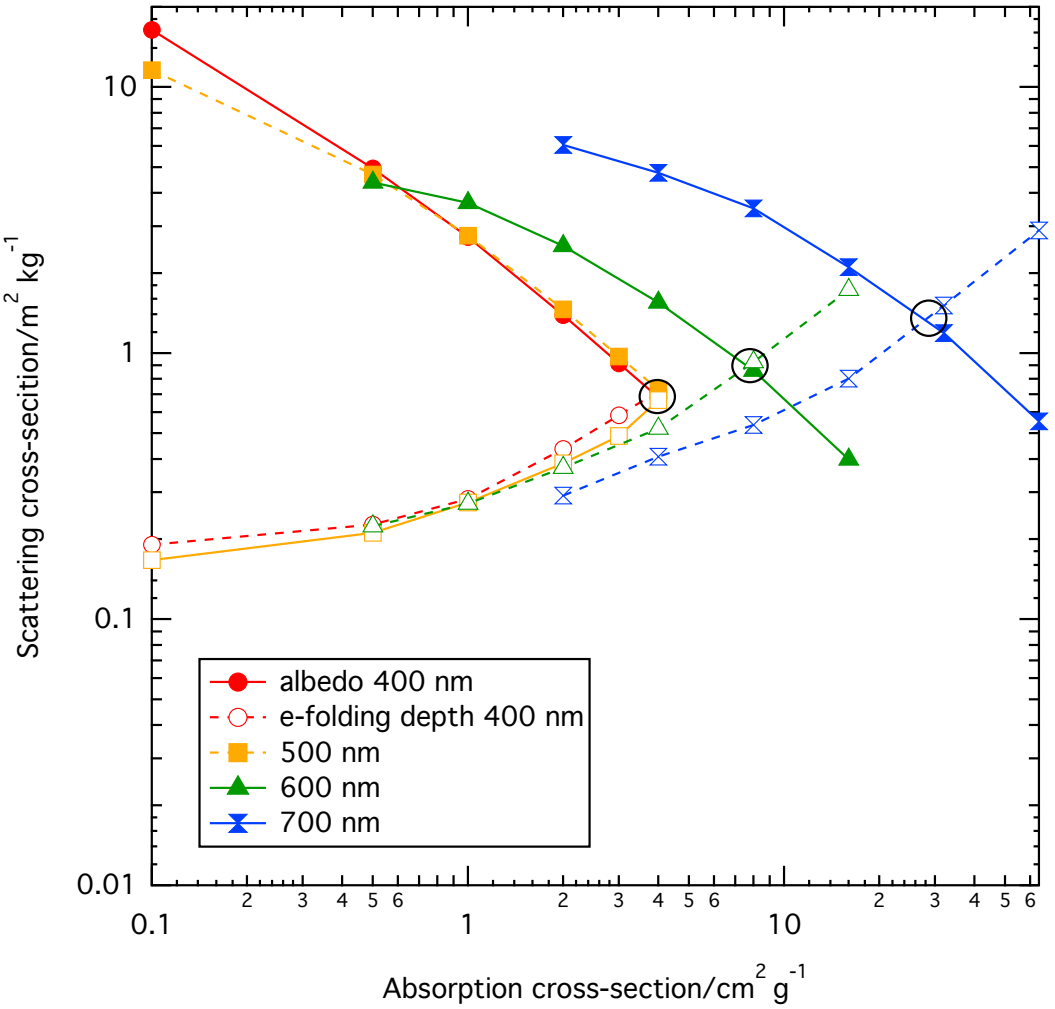

Figure 3.7 *– Interpolation of albedo and e-folding depth data for multi-year sea ice from Grenfell and Maykut (1977). Intersection provides unique values for scattering and absorption cross-section for the ice at that wavelength. The intersection was calculated every 25 nm from wavelengths from 400–700 nm, only every 100 nm is shown for clarity.*

The calculated value of $\sigma_{\text{scatt}}(\lambda)$ for each sea ice and snow type, shown in figure 3.8 is approximately wavelength independent, as also suggested by Lee-Taylor and Madronich (2002).

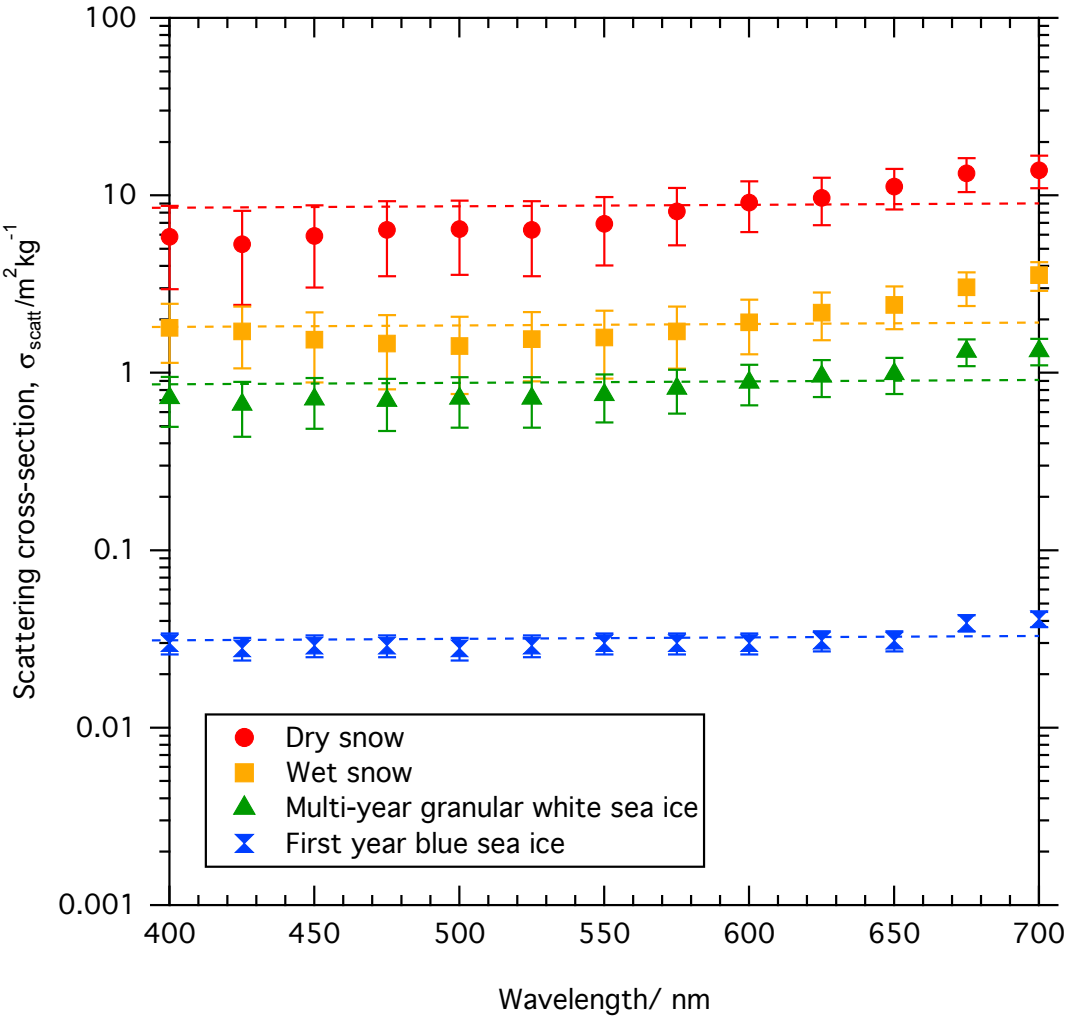

Figure 3.8 *– Calculated $\sigma_{scatt}(\lambda)$, in granular white sea ice, blue sea ice, wet snow and dry snow. Dashed lines show the average wavelength independent scattering cross section for each snow and sea ice type.*

Table 3.2 shows the average scattering cross-section values for each snow and sea ice type.

Snow/sea ice type	$\sigma_{\mathbf{scatt}}/\mathbf{m^2\ kg^{-1}}$
Blue Sea Ice	0.03±0.003
Granular White Sea Ice	0.87±0.079
Dry Snow	8.35±1.09
Wet Snow	1.99±0.23

Table 3.2 *– Calculated σ^{+}_{scatt}, in granular white sea ice, blue sea ice, wet snow and dry snow. Error values show the average difference in calculated σ^{+}_{scatt} values through making small changes to the data fit for obtaining these values.*

The calculated $\sigma^{+}_{abs}(\lambda)$ values for each sea ice and snow type were wavelength dependent, these are shown in figure 3.9. The intersections on figures 3.6, 3.7, 3.5, and 3.4 and

thus the derived values of $\sigma_{scatt}(\lambda)$ and $\sigma_{abs}(\lambda)$ may be sensitive to the initial fit to the reflectivity and *e*-folding depth data, propagating the uncertainty results in the error bars in figure 3.9.

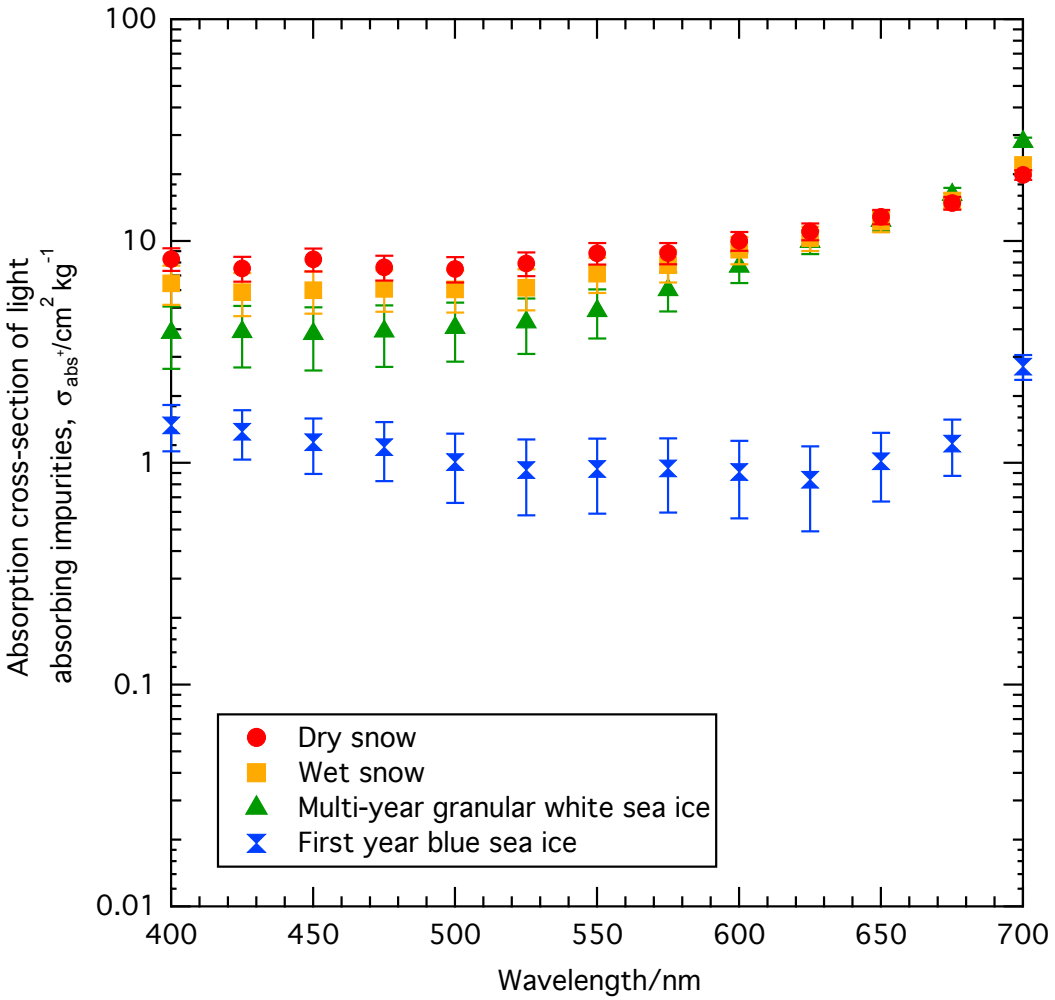

Figure 3.9 – *Calculated $\sigma^{+}_{abs}(\lambda)$, in granular white sea ice, blue sea ice, wet snow and dry snow. Error bars show the average difference in $\sigma^{+}_{abs}(\lambda)$ values through making small changes to the data fit for obtaining these values. $\sigma^{+}_{abs}(\lambda)$ is per kg of sea ice.*

The asymmetry parameter, g, was held constant in this study at a value of 0.95 for the sea ice and 0.89 for snow. It is not always possible to find a unique solution for $\sigma_{scatt}(\lambda)$, $\sigma^{+}_{abs}(\lambda)$ *and* g. Adopting the approach of Lee-Taylor and Madronich (2002), g, was held constant and σ_{scatt} and σ^{+}_{abs} varied. France et al. (2012) undertook a sensitivity study of changing g by ± 0.05, as this covers the possible variation in the asymmetry parameter suggested by Warren and Wiscombe (1980), over the wavelengths utilised in this study. France et al. (2012) found the value of σ_{scatt} and σ^{+}_{abs} to be relatively insensitive to the value of g for a snowpack in Barrow, Alaska. Repeating a

similar study to France et al. (2012) for the blue sea ice and granular white sea ice yields the values presented in table 3.3. Table 3.3 shows σ^{+}_{abs} is insensitive to changes in g and σ_{scatt} only slightly varies.

Asymmetry	**Blue sea ice**		**Granular white sea ice**	
Parameter, g	$\sigma_{\text{scatt}}/\text{m}^2\text{kg}^{-1}$	$\sigma^{+}_{\text{abs}}/\text{cm}^2\text{kg}^{-1}$	$\sigma_{\text{scatt}}/\text{m}^2\text{kg}^{-1}$	$\sigma^{+}_{\text{abs}}/\text{cm}^2\text{kg}^{-1}$
0.945	0.027	1.037	0.665	4.272
0.95	0.03	1.037	0.726	4.272
0.955	0.034	1.035	0.814	4.272

Table 3.3 *– Variation in derived σ_{scatt} and σ^{+}_{abs} of the blue sea ice and granular white sea ice from variation of the asymmetry parameter, g, at a wavelength of 550 nm.*

3.2.2 Calculating albedo in sea ice and snow with increasing black carbon in sea ice

The calculated scattering and absorption cross-sections are subsequently utilised in the TUV-snow radiative-transfer model to quantify, firstly, the albedo response of increasing black carbon in a 5 cm surface layer of a 155 cm thick multi-year and first year Arctic sea ice. The first year sea ice modelled consists of just the blue ice. The multi-year sea ice consists of the blue ice with a 5 cm surface layer of the granular white sea ice. Grenfell and Maykut (1977) state that the melting multi-year sea ice observed in the Arctic basin was typically bluish-white in colour (similar to the first year blue ice) with a decomposed layer at the surface ranging from 2–15 cm thick (the granular white ice layer).

Secondly, the TUV-snow model is used to quantify the effect of wet and dry snow layers on the albedo of the multi-year and first year sea ice with increasing black carbon in the sea ice. The albedo of an optically thick layer of snow on sea ice will only be influenced by the optical properties of snow. However, the albedo of a thin layer of snow will be influenced by the optical properties of the sea ice below it. Snow coverings of 0.5, 1, 2, 5, and 10 cm of the dry and wet snow were added to both the multi-year and first year sea ice.

A summary of the snow and sea ice formations modelled is shown in figure 3.10. Black carbon mass-ratios of 0, 1, 2, 4, 8, 16, 32, 64, 128, 256, 512, 1024 ng g^{-1} were used. Note the black carbon is additional to any already present. Therefore total light

absorption in the layer containing additional black carbon is represented by Eq. (3.3).

$$\sigma_{\text{abs}}(\lambda) = \sigma^{\text{ice}}_{\text{abs}}(\lambda) + \sigma^{+}_{\text{abs}}(\lambda) + \sigma^{\text{BC}}_{\text{abs}}(\lambda)[BC] \tag{3.3}$$

Where, $\sigma^{\text{ice}}_{\text{abs}}(\lambda)$ is the absorption cross-section for pure ice per unit mass of ice (taken from Warren and Brandt (2008)), $\sigma^{+}_{\text{abs}}(\lambda)$ is the absorption cross-section due to light absorbing impurities already present in the snowpack, or sea ice, per unit mass of snow/sea ice, as calculated in section 3.2.1, $\sigma^{\text{BC}}_{\text{abs}}(\lambda)$ is absorption by additional black carbon (as described in chapter 2, section 2.2.2) per unit mass of black carbon, $[BC]$ is the mass-ratio of black carbon and λ is the wavelength of light.

Additional black carbon was placed in only a 5 cm layer at the top of the sea ice. Chapter 2 suggested black carbon is most likely to be concentrated in a surface layer as atmospheric deposition and surface snow melt concentrate black carbon at the top of the sea ice. The sea ice below the uppermost 5 cm layer had no additional black carbon, and the snow layer, where present, was also modelled with no additional black carbon.

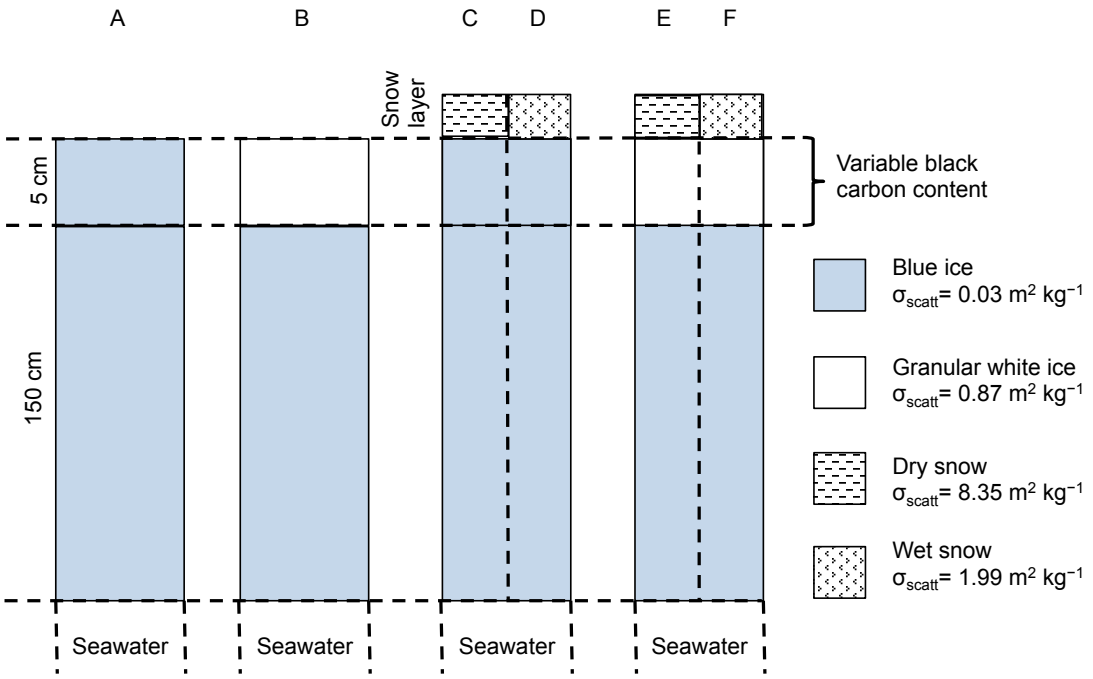

Figure 3.10 *– Sea ice and snow configurations modelled (not to scale).*

Changes in the albedo of the sea ice surface with a variation in black carbon mass-ratio in a 5 cm surface layer of the sea ice were calculated, in the same manner as in chapter 2; as the ratio of upwelling to downwelling surface irradiance $\left(\frac{\text{Irr}_{\text{up}}}{\text{Irr}_{\text{down}}}\right)$.

All calculations were undertaken at wavelengths 400–700 nm (the range measured by Grenfell and Maykut (1977)), using an eight-stream radiative-transfer calculation with a pseudo-spherical correction (Lee-Taylor and Madronich, 2002). The atmosphere had an ozone column of 300 Dobsons with no aerosol. A wavelength independent under-ice albedo was used of 0.1 and the Earth–Sun distance was set to 1 AU. Isotropic sky conditions were used throughout the work by placing cumulus clouds in the model at a 1 km altitude, with an optical depth of 32, an asymmetry parameter of 0.85 and a single scattering albedo of 0.9999. Isotropic sky conditions were used to calculate surface albedo independent of solar zenith angle. The albedo of sea ice and snow depend on the solar zenith angle but are not dependant on the absolute irradiance of incident radiation. The work presented in chapter 3 is the first time the TUV-snow model has been configured to a coupled atmosphere-snow-sea ice system.

Figure 3.11 shows an overview of the stages described in the method to firstly derive scattering and absorption cross-sections for snow and sea ice. And secondly use the derived scattering and absorption cross-sections to calculate the response of sea ice to increased black carbon and the effects of snow cover.

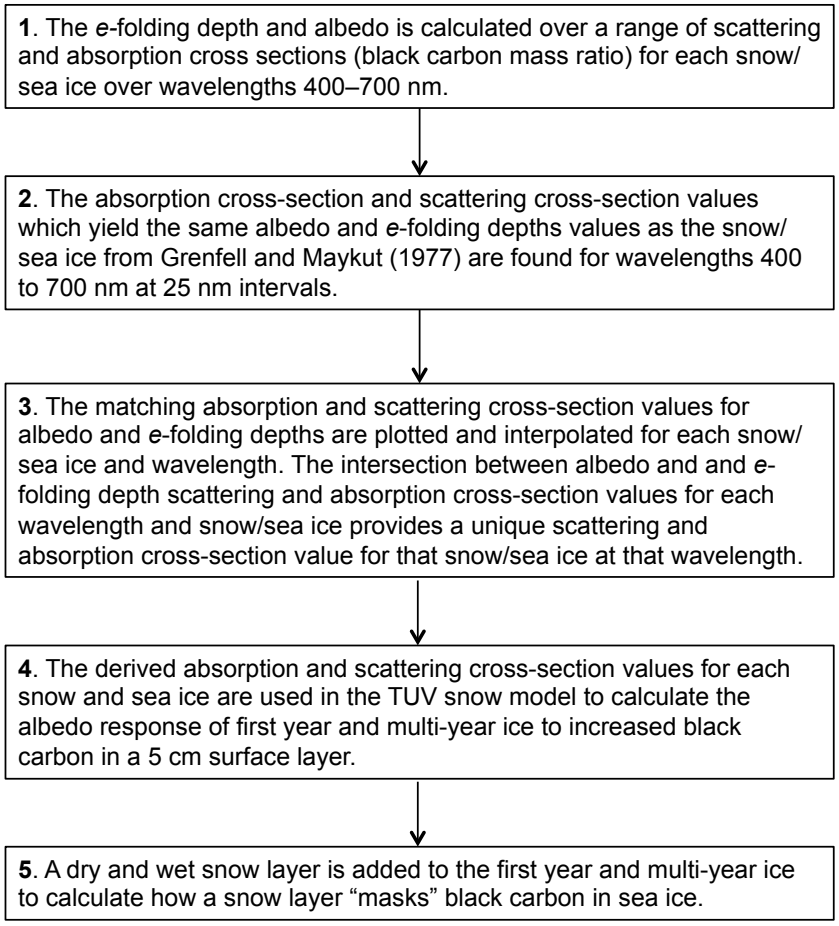

Figure 3.11 *– Flow diagram of method from deriving absorption and scattering cross-section values from the data of Grenfell and Maykut (1977) to calculate the albedo response of sea ice to increased black carbon and the effect of snow.*

3.3 Results

The results section will describe how the effect on surface albedo of additional black carbon in a surface layer of sea ice varies with sea ice type (section 3.3.1) and snow cover (section. 3.3.2).

3.3.1 Variation in albedo with increasing black carbon content in first year and multi-year sea ice

Figure 3.12 shows the surface albedo of the first year and multi-year sea ice at wavelengths 400–700 nm with additional black carbon, ranging from 1–1024 ng g^{-1}, in a top 5 cm layer. For both sea ice types as black carbon content increases the albedo decreases. For a wavelength of 500 nm and a black carbon increase from 1 to 8 ng g^{-1},

albedo decreases to 98.7 % of the initial value for first year sea ice, and decreases to 99.7 % of the initial value in the multi-year sea ice. While for an increase in black carbon from 1 to 1024 ng g^{-1}, the whole range examined, albedo decreases to 25.3% of the initial value for first year ice and decreases to 59.1% of the original value for multi-year ice over the same black carbon mass-ratio range. Thus the albedo of first year sea ice is more sensitive to additional black carbon than the multi-year sea ice.

The decrease in albedo with increasing mass-ratio of black carbon is non-linear in both the first year and multi-year ice. For example, in the first year ice (figure 3.12A) a doubling of additional black carbon from 2 to 4 ng g^{-1} leads to a decrease in albedo to 99.7% of the albedo value at 2 ng g^{-1}, but a doubling of additional black carbon from 512 to 1024 ng g^{-1} results in a decrease in albedo to 54 % of the albedo value at 512 ng g^{-1}. For the multi-year ice (figure 3.12B) a doubling of black carbon from 2 to 4 ng g^{-1} leads to a decrease in albedo to 99.9 %, but a doubling from 512 to 1024 ng g^{-1} leads to a decrease in albedo to 79%, at a wavelength of 500 nm. Similar behaviour was observed and explained in chapter 2. As black carbon mass-ratio increases the wavelength dependence of the albedo decreases in both the first year and multi-year ice, as albedo moves from an ice dominated to a black carbon dominated regime as discussed in chapter 2, section 2.3.1.

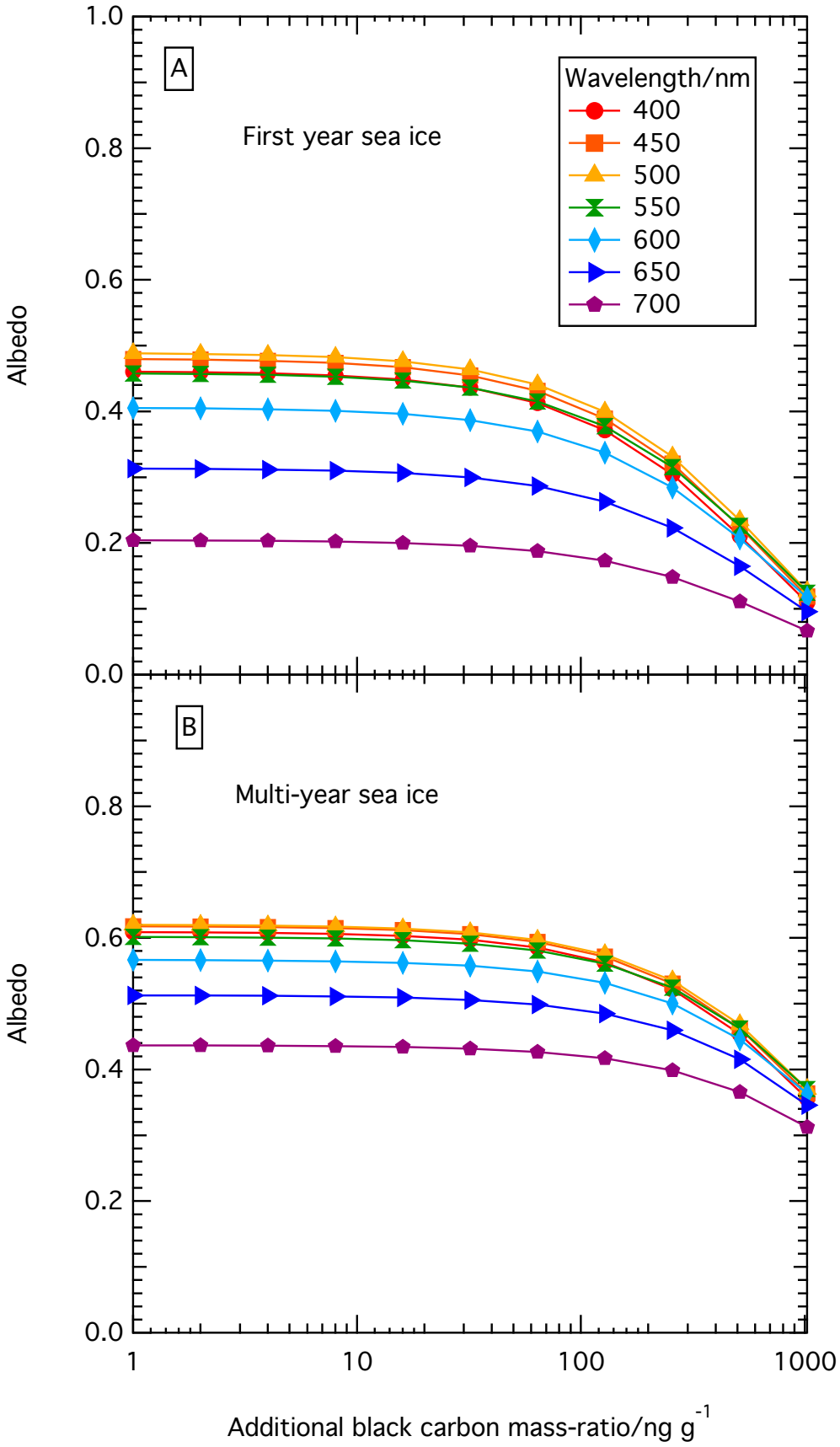

Figure 3.12 *– A) Albedo with increasing additional black carbon content from 1 to 1024 ng g^{-1}, evenly distributed in the top 5 cm of 155 cm of typical first year sea ice. B) Albedo with increasing black carbon content from 1 to 1024 ng g^{-1}, evenly distributed in the top 5 cm layer of 155 cm of a typical multi-year sea ice.*

3.3.2 Effect of snow cover and type on the influence of black carbon in sea ice on surface albedo

Figures 3.13 and 3.14 show surface albedo with snow cover over sea ice between 0 and 10 cm thick as a function of additional mass-ratio of black carbon in sea ice, at wavelengths of 500 nm and 700 nm respectively (wavelengths of 400 and 600 nm showed very similar results to 500 nm). An optically thick snow layer on sea ice (1 m thick) is also shown in figures 3.13 and 3.14 for comparative purposes. The addition of a thin layer (0.5 cm) of snow on sea ice drastically increases the surface albedo. A layer of 2–5 cm of snow is effectively enough to mask any change in albedo owing to additional black carbon in sea ice. However, it is not thick enough to be wholly responsible for surface albedo. The asymptotic *e*-folding depths of the wet and dry snowpacks are 12 cm and 6 cm, at a wavelength of 500 nm, previously it has been shown that a snowpack needs to be greater than 3–4 *e*-folding depths before it is optically thick enough to be uninfluenced by the underlying layer (e.g. France et al. (2011)).

Figures 3.13 and 3.14 show dry snow has a much greater impact on mitigating the effect of black carbon in sea ice on surface albedo than wet snow. The dry snow has a higher albedo than the wet snow so the difference between the sea ice albedo and snow albedo is larger and thus more effective. The greater effect of dry snow is most noticeably observed with the addition of a layer of snow of 0.5 cm thickness. With an increase in snow thickness from 5 to 10 cm of dry snow there is only a very small change in albedo. For the same wet snow addition there is still a noticeable difference in the albedo calculated, suggesting a greater thickness of wet snow would be required for the snow layer to be optically thick. The increase in surface albedo owing to the addition of snow to sea ice is greater for the first year ice than the multi-year ice. The initial albedo of the first year ice is lower than the albedo of the multi-year ice, due to the presence of a surface granular layer on the multi-year ice. The surface granular layer provides a more scattering medium which has a higher albedo. Therefore a larger change in albedo occurs with the addition of snow.

The snow has a greater effect at a wavelength of 700 nm, figure 3.14, compared to 500 nm, figure 3.13 as the albedo of sea ice is more wavelength dependant than the albedo of snow, shown in figure 3.1. The albedo of sea ice is lowest at 700 nm, thus

the difference between the snow and sea ice albedo is largest at 700nm, so the snow covering has a greater effect.

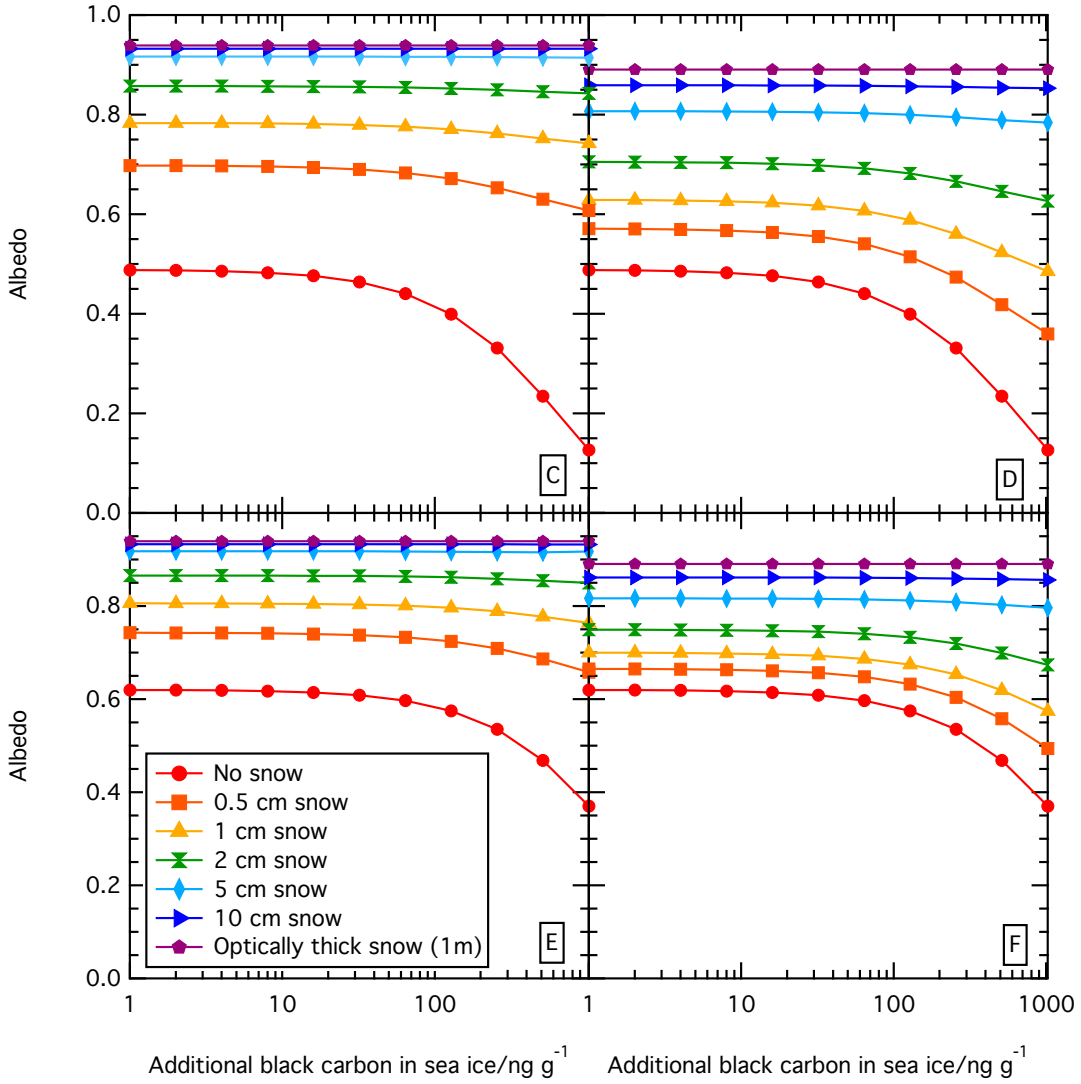

Figure 3.13 *– Albedo of snow surface at 500 nm with different thicknesses of snow cover overlying sea ice. C) dry snow on first year ice, D) wet snow on first year ice, E) dry snow on the multi-year ice, F) wet snow on multi-year ice.*

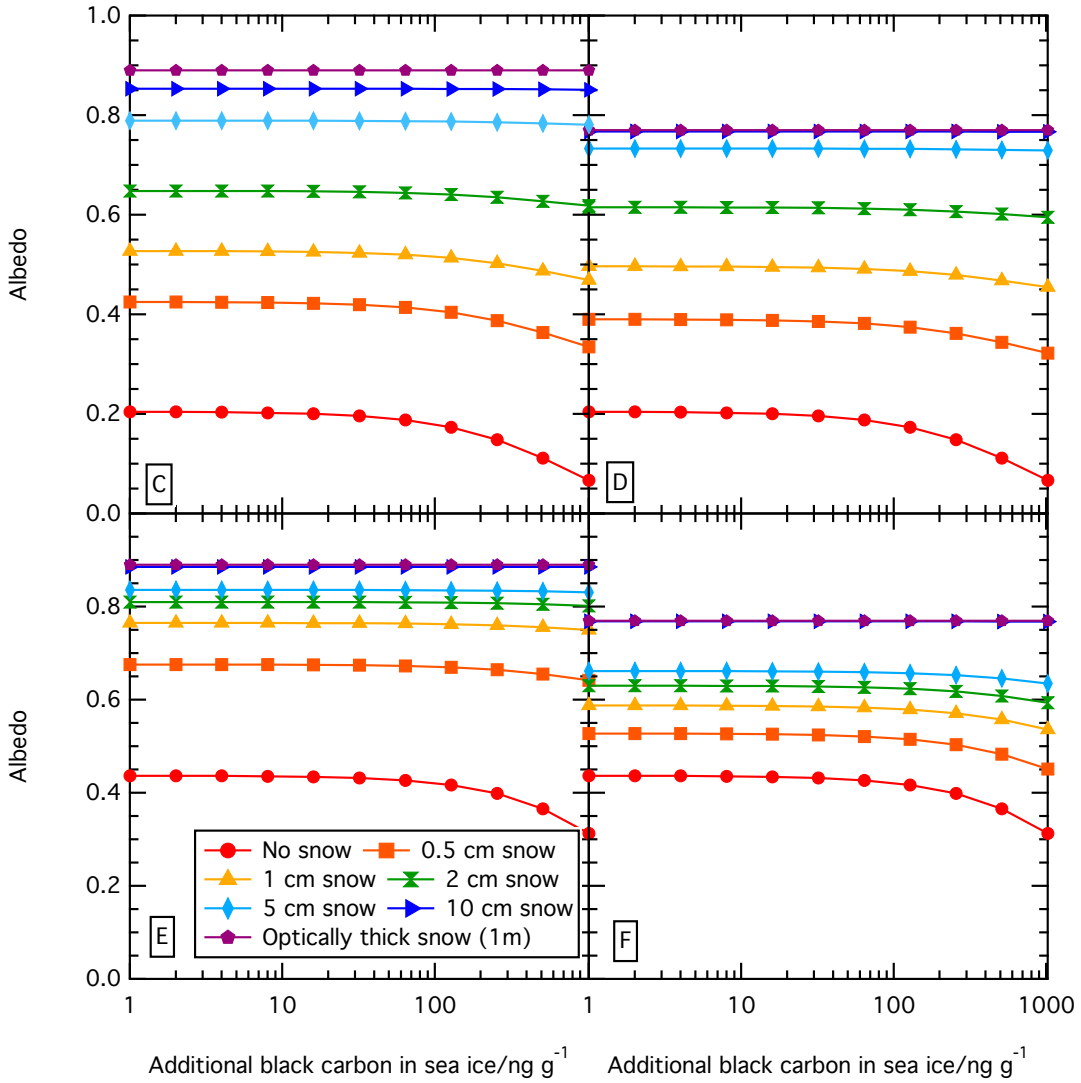

Figure 3.14 *– Albedo of snow surface at 700 nm with different thicknesses of snow cover overlying sea ice. C) dry snow on first year ice, D) wet snow on first year ice, E) dry snow on the multi-year ice, F) wet snow on multi-year ice.*

3.4 Discussion

The following discussion will focus on the light absorbing impurities in the sea ice, the response of albedo to black carbon depending on sea ice type, the effect of snow cover and finishes with a discussion on the limitations and potential progression of the work.

3.4.1 Absorption cross-sections of snow and sea ice

Figure 3.9 shows the absorption cross-sections for the light absorbing impurities, σ^{+}_{abs}, in the snow types (wet and dry) and sea ice types (blue ice and granular white ice) determined from the albedo and extinction coefficient data of Grenfell and Maykut (1977). Figure 3.9 shows variation with wavelength to be reasonably flat, but with a slight increase with longer wavelengths. The lack of a strong wavelength dependance may be interpreted as consistent with black carbon being the dominant light absorbing impurity. The absorption cross-section of black carbon is shown in figure 3.15 along with other common light absorbing impurities.

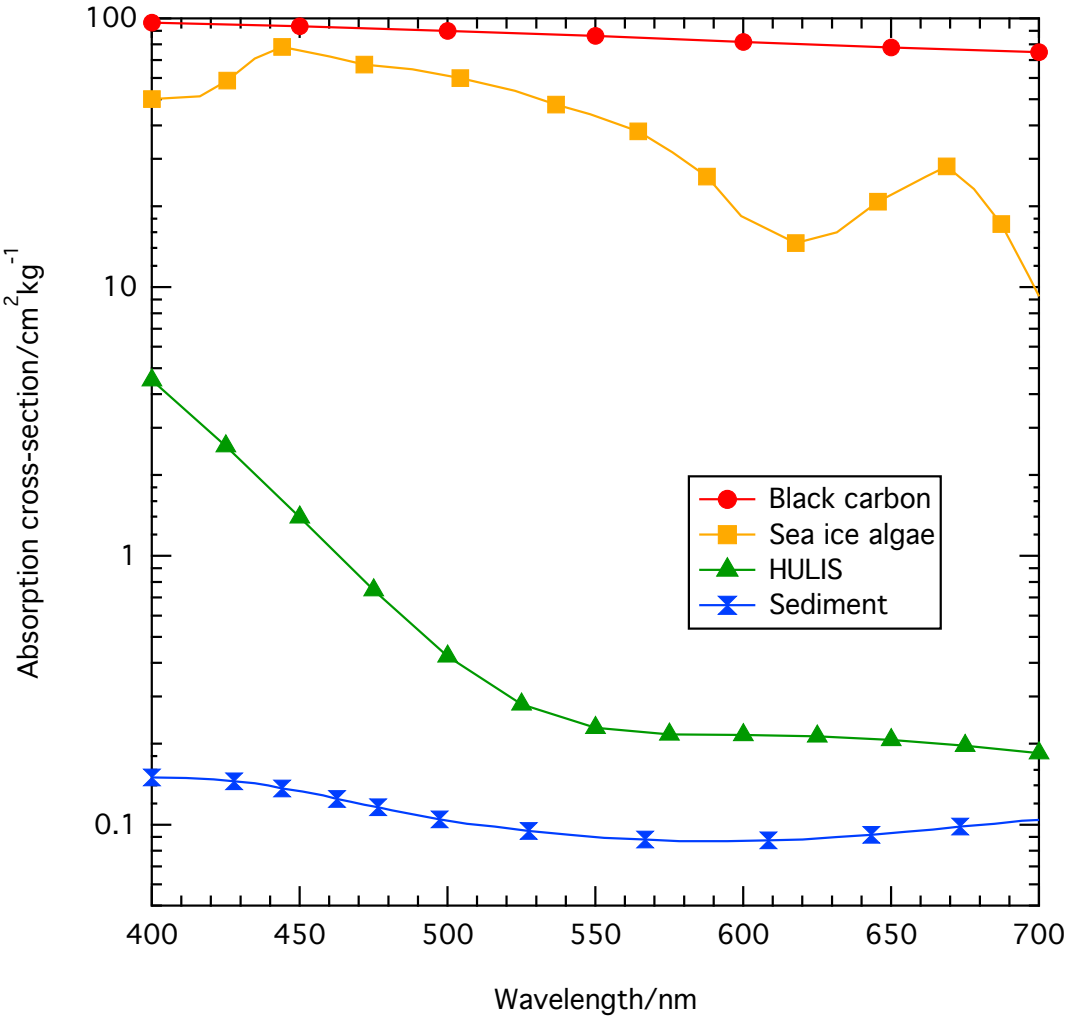

Figure 3.15 *– Absorption cross-sections for common impurities found in sea ice. Sea ice algae and sediment absorption from Light et al. (1998). HULIS absorption from Hoffer et al. (2006). Black carbon absorption calculated by Mie theory, as described in chapter 2.*

The mass-ratio of black carbon in each sea ice and snow type can be estimated from

the data in figure 3.9 using equation 3.4 as described in France et al. (2012) and Reay et al. (2012).

$$[\mathrm{BC}] = \frac{\sigma^{+}_{\mathrm{abs}}}{\sigma_{\mathrm{BC}}}, \tag{3.4}$$

Where, $\sigma^{+}_{\mathrm{abs}}$ is the absorption cross-section owing to light absorbing impurities over the wavelength range 400–600 nm in figure 3.9, σ_{BC} is the absorption cross-section for black carbon ($\sim$10 m^2 g^{-1}, and shown in Figure 3.15), and [BC] is the black carbon mass-ratio. Only the wavelengths 400–600 nm are used as absorption increases above 600 nm which is inconsistent with black carbon (potential causes for this are discussed at the end of this section).

Using equation 3.4 the following mass-ratio of black carbon is derived for each snow and sea ice type. The granular white ice has an estimated equivalent black carbon mass-ratio of 48 ng g^{-1}, the blue sea ice has 11.1 ng g^{-1}, the wet snow has 63 ng g^{-1} and the dry snow has 83 ng g^{-1}. Although not improbable, these values are large compared to previous literature reporting black carbon values in snow and sea ice. Clarke and Noone (1985) report typical black carbon mass-ratios in Arctic snow, ranging from 23 ng g^{-1} at Barrow, Alaska, to 45.5 ng g^{-1} at Alert, Canada. Grenfell et al. (2002) report values of black carbon mass-ratio in Arctic sea ice of 5.5 ng g^{-1}. Figure 6c of Warren and Wiscombe (1980) shows they required 300 ng g^{-1} of black carbon to reproduce the albedo of the snow presented by Grenfell and Maykut (1977), and suggest that the large black carbon mass-ratio may be due to pollution from the T3 camp. Note 3 on page 2732 of Warren and Wiscombe (1980) suggests that a value of 150 ng g^{-1} is actually more accurate based on a more realistic density of the black carbon absorber. The mass-ratio of black carbon in the snow presented by Warren and Wiscombe (1980) is still approximately twice the values presented here. To explain the different black carbon mass-ratio calculated by Warren and Wiscombe (1980) compared to those presented in chapter 3 requires comparison of the two techniques. The calculations presented here use the same optical properties of the black carbon as note 3 in Warren and Wiscombe (1980) and further adopted by Warren (1982). The radiative-transfer calculations of Warren and Wiscombe (1980) reproduce the albedo data of Grenfell and Maykut (1977) only, whereas the work presented here reproduces the albedo and light penetration data. The work of Warren and Wiscombe (1980) uses an assumption of grain size based on absorption by ice

only at a wavelength of 900 nm, assuming no absorption by impurities at 900 nm. The radiative-transfer calculation employed here requires no knowledge of grain size. Thus the radiative-transfer calculation presented here may be a truer representation of the equivalent mass-ratio of black carbon as it is more constrained by experimental data, reproduces albedo and light penetration data and does not require assumption of grain size. The black carbon concentrations presented here are still high and

In the work presented here it is likely that not all absorption by light absorbing impurities is due to black carbon, and other light absorbing impurities are present. Doherty et al. (2010) conclude that 40% of the light absorption in their filtered snow and sea ice samples was due to species other than black carbon. The presence of other light absorbing impurities could explain the increase in absorption cross-section observed at longer wavelengths. Other light absorbing impurities present in sea ice and snow could include sediments, atmospheric dust, algae and HUmic LIke Substances (HULIS) (e.g. Light et al., 1998; France et al., 2012). The absorption cross-section of each of these is also shown in figure 3.15. France et al. (2012) suggest algae as a possibility for the increase in absorption they observe at longer wavelengths. Figure 3.15 shows how ice algae absorption increases at wavelengths 600–650 nm. However, ice algae absorption also peaks at wavelengths from 400–500 nm and decreases from 650–700 nm; trends that are not seen in the absorption cross-section in figure 3.9. The absorption of sediments and atmospheric dust are also shown in figure 3.15 (where atmospheric dust is assumed to have identical optical properties to sediments) these steadily increase from 550 to 700 nm. Thus, there may also be sediment or dust in the snow and sea ice studied.

3.4.2 Variation in the impact of black carbon with sea ice type

Figure 3.12 shows that the albedo of the sea ice surface is surprisingly insensitive to *additional* black carbon mass-ratios under 100 ng g^{-1} added to the top 5 cm of the sea ice. Although this is *additional* black carbon to black carbon already present and the albedo of the sea ice is sensitive to absolute changes in black carbon mass ratios of 1–100 ng g^{-1}. The impact of additional black carbon on surface albedo is dependant on the sea ice type, with first year sea ice showing a more sensitive response to black carbon than the multi-year sea ice. First year ice will typically be thinner than multi-

year ice, thus exacerbated melting will be more influential in causing sea ice decline.

Similar differences in the effect of black carbon on surface albedo with sea ice type are observed in previous modelling of black carbon in sea ice, as described in chapter 2, section 2.4.2. Light et al. (1998) suggest for an increase from 0 to 100 ng g^{-1} of black carbon in the sea ice albedo will decrease to 73 % of the original value, at a wavelength of 500 nm. While Grenfell et al. (2002) only report a decrease in albedo to 99 % of the original value for an increase from 0 to 100 ng g^{-1} of black carbon. The results of chapter 2 suggest that albedo would decrease to 66% of the original albedo value for an ablating Antarctic sea ice. While calculations presented here suggest a decrease in albedo to 96 % for multi-year ice and 91 % for first year ice for an additional black carbon increase from 0–100 ng g^{-1}. The greatest albedo difference is therefore observed in the modelling of chapter 2, where a scattering cross-section of 0.15 m^2 kg^{-1} is used. Light et al. (1998) model a sea ice with scattering cross-section values of 0.654, 1.46, 0.96 $m^2\,kg^{-1}$ in three layers from the top, 0.05, 0.2, 2.6 m thick respectively. These values compare with a scattering cross-section used by Grenfell et al. (2002) of 0.3 m^2 kg^{-1} in the upper 4 cm, and 0.0375 m^2 kg^{-1} for the lower 150 cm. Compared to the scattering cross-sections used in this chapter of 0.03 m^2 kg^{-1} for blue ice and 0.87 m^2 kg^{-1} for granular white ice. The multi-year ice consists of the granular white ice on top of a blue ice, while the first year ice is just blue ice. The granular white ice has larger values for the scattering and absorption cross-section than the blue ice.

The results presented here suggest that a large value of the scattering cross-section may result in black carbon having less effect on albedo, a concept explored in chapter 4. However, as different studies distribute the black carbon in different positions in the sea ice comparability between studies is limited; Grenfell et al. (2002) place black carbon in a surface 1 cm layer, Light et al. (1998) distributed black carbon in a 10 cm layer in the sea ice, in chapter 2 the black carbon was evenly distributed in the sea ice and in the work presented here black carbon is situated in a 5 cm surface layer.

3.4.3 The role of snow and snow type in the influence of black carbon in sea ice on surface albedo

Previous research into the effects of black carbon on surface albedo of sea ice has focussed on snow free conditions typical of late and early periods in the sea ice season, e.g. Light et al. (1998) mention their study only being valid during the ablation season when snow cover is eliminated. However, sea ice is predominately snow covered. Figure 3.13 demonstrates the extent even a thin snow cover (< 1 cm) can diminish the effect black carbon in the sea ice has on the surface albedo. Figure 3.13 shows that additional black carbon in the sea ice changes the snow surface albedo with up to 5 cm of snow and the snow is not optically thick until the snow is over 10 cm thick. A snow/sea ice is defined as optically thick when increasing its thickness does not result in a change in surface reflectivity. France et al. (2011) state optically thick was typically when the snow thickness is three to four *e*-folding depths but for snow on sea ice a practical definition of optically thick appears to be approximately one *e*-folding depth of snow. The difference can be rationalised as optical thickness for land based snowpacks occurs where there is no change in surface albedo with increasing snow thickness owing to the influence of a dark ground surface. Whereas, for snow on sea ice the albedo difference between snow and sea ice is much smaller than the difference between dark soil and snow. The albedo of optically thick snow (1 m thick) is also shown on figure 3.13 for comparison. Brandt et al. (2005) suggest from their results studying albedo of Antarctic sea ice that a snow covering of 3 cm, or in some cases just 1 cm, can be classed as optically thick snow. The results presented here agree that a thin snow covering will greatly increase the albedo, but a snow cover greater than 3 cm would be needed to be described as optically thick.

Figure 3.13 also shows how the influence of black carbon in sea ice on surface albedo is affected by the type of snow cover. Dry snow has a greater effect at mitigating the impact of black carbon in sea ice on surface albedo compared to wet snow. The dry snow has a smaller *e*-folding depth (figure 3.2) and a larger scattering cross-section. Thus a smaller thickness is required to be optically thick.

To understand the degree to which black carbon in sea ice may affect surface albedo knowledge of snow depth over sea ice and its variation seasonally and spatially is essential. Snow depth measurements over sea ice have been reported both from

ground measurements (e.g. Warren et al., 1999; Massom et al., 2001) and more recently through satellite and airborne measurements (e.g Kanagaratnam et al., 2007; Kwok and Cunningham, 2008; Kwok et al., 2011; Galin et al., 2012). Two studies provide an overview of snow thickness over sea ice. Warren et al. (1999) present a comprehensive data set of Arctic Ocean snow cover from measurements of snow depth and density collected over 37 years at the Soviet drifting stations, while Massom et al. (2001) review snow thickness and snow type of Antarctic snow on sea ice, using data collected over 10 years. Arctic sea ice is mostly free of snow during the second half of July and all of August. During these months black carbon in sea ice would affect surface albedo. Snow thickness reaches a maximum in the Arctic in May with an average depth of 34.4 cm (Warren et al., 1999). In Antarctica mean snow thickness varies both seasonally and regionally due to differences in precipitation regimes and the age of the underlying ice (Massom et al., 2001). In March, in East Antarctica, 20 % of the sea ice is predominately snow free, and less than 10 % of the snow cover is thicker than 10 cm. By August (winter), snow thickness is typically 10–20 cm, but 10 % of the sea ice remains snow free (Massom et al., 2001). Snow on sea ice would appear to predominately mask the effects of black carbon in sea ice. However, the effect of black carbon on albedo of sea ice is important for a few months of the year, in both the Antarctic and Arctic. These months would be following a period of snow melt over sea ice where black carbon may be concentrated onto the sea ice surface from meltwater (Grenfell et al., 2002). Doherty et al. (2010) measured spatial variation of black carbon through sea ice cores taken on sea ice in the southern Canadian basin suggesting black carbon is concentrated near the surface following snowmelt. Further work on the distribution of black carbon in sea ice would be useful. The months of bare sea ice would also coincide with higher surface irradiance owing to smaller solar zenith angles, so melting may be exacerbated, as more radiation is absorbed by black carbon.

3.4.4 Potential limitations in the model and future research possibilities

The work presented here has several limitations: firstly, the method for obtaining scattering and absorption cross-sections of sea ice and snow; secondly, the absorption spectra and physical characteristics of the black carbon as discussed in chapter 2, and thirdly, the age of the field data on which these data are based.

There is a source of uncertainty in the method for obtaining the absorption and scattering cross-sections from *e*-folding depth and albedo data (e.g. Lee-Taylor and Madronich, 2002; King et al., 2005; France et al., 2011, 2012). Figure 3.9 has error bars for the calculated values of absorption cross-section for light absorbing impurities, $\sigma^{+}_{\mathrm{abs}}(\lambda)$, and table 3.2 shows estimates of uncertainty for the calculated scattering cross-section, σ_{scatt}, values. The uncertainty bars on Figure 3.9 represent the range of values of $\sigma^{+}_{\mathrm{abs}}(\lambda)$ that are derived from an optimal fit of the albedo and extinction coefficient data from Grenfell and Maykut (1977), while holding the asymmetry parameter, g, and density constant. All values of σ_{scatt} are within 13 % and the majority of $\sigma^{+}_{\mathrm{abs}}(\lambda)$ values are within 10 %. Figure 3.16 shows a comparison between our modelled albedo and the original albedo measured by Grenfell and Maykut (1977) for each snow and sea ice type. A reasonable fit between the albedo for each snow/sea ice type is observed, with all modelled albedo being within 10 % of the measured value and the two snows being within 2 % of the measured albedo.

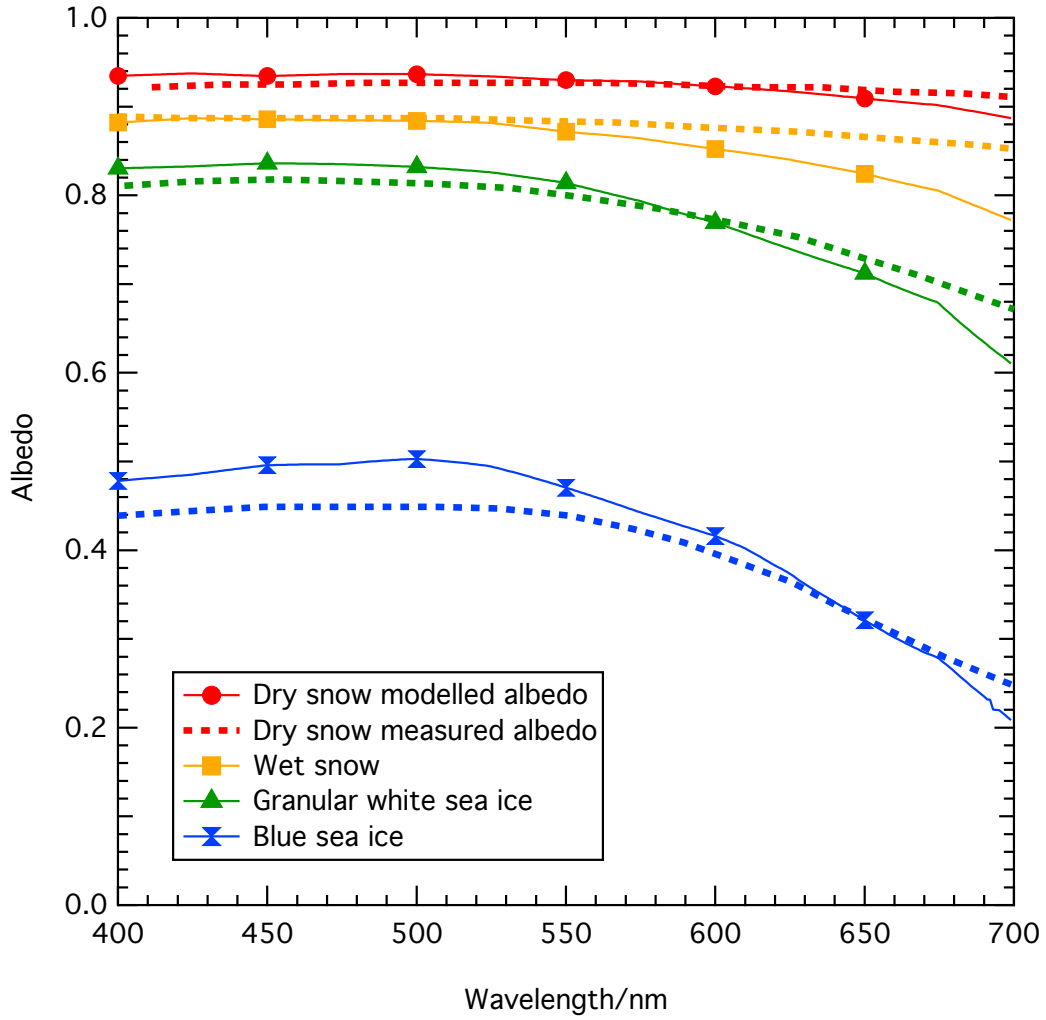

Figure 3.16 *– Comparison of measured albedo by Grenfell and Maykut (1977) (dashed line) with albedo modelled in the study presented here (markers and solid line).*

The calculation to obtain values of $\sigma^{+}_{\text{abs}}(\lambda)$ and σ_{scatt} assumes all light absorbing impurities are due to black carbon. In reality impurities are likely to include other substances, for example HULIS, dust, sediment and marine algae that would contribute to absorption in the sea ice. The very large value of the absorption cross-section of black carbon compared to other substances often results in black carbon being the dominant absorbing impurity. The black carbon properties used for our calculations (refractive index, size and density) are taken to be a standard proxy for black carbon and are based on calculations by Warren and Wiscombe (1980, 1985). As discussed in chapter 2, Bohren (1986) reviewed uncertainties in the black carbon "proxy". France et al. (2012) recently demonstrated a good correlation between their black carbon absorption cross-section (used in chapters 2 and 3) and the experimentally measured absorption cross-section of black carbon reviewed by Bond and Bergstrom (2006).

The optical properties of the sea ice and snow in this chapter are based on a field study of snow and sea ice from the 1970s (Grenfell and Maykut, 1977). The black carbon content of the sea ice may not be representative of present day sea ice. The study of Grenfell et al. (2002) refers to one location on the sea ice, north of Barrow, Alaska, which may have been slightly polluted, explaining the relatively high black carbon mass-ratios reported. Thus the results in this chapter must be interpreted within this caution. However, the Grenfell and Maykut (1977) study is exceptional in the quality and amount of data it produced. To derive σ_{scatt} and $\sigma^{+}_{\text{abs}}(\lambda)$ for the work in this chapter required monochromatic measurements of reflectivity, and light penetration, over a wide range of wavelengths, sea ice types and snow types. Such a large dataset recorded in one study makes it an ideal dataset. Confidence in using the Grenfell and Maykut (1977) study also comes from the work of Lee-Taylor and Madronich (2002). Lee-Taylor and Madronich (2002) also calculated scattering and absorption cross-sections of the snowpacks reported in Grenfell and Maykut (1977) along with more modern studies of other snowpacks. The values obtained in the Lee-Taylor and Madronich (2002) study suggest they can potentially be considered contemporary with the present century. However, the black carbon content of the snow derived from the work by Grenfell and Maykut (1977) does appear large compared to the study of Doherty et al. (2010).

Chapter 3 has shown that different sea ice types respond differently to black carbon, it thus follows that different snow types will also respond differently. Chapter 4 will progress the work of chapter 3 to investigate how a large range of different snow and sea ice types respond to black carbon.

3.5 Conclusions

Absorption and scattering cross-sections were derived for a blue ice, a granular white ice, and dry and wet snow from field data from Grenfell and Maykut (1977). The absorption cross-section suggests black carbon is the dominating absorbing impurity with estimated black carbon mass-ratios of 48 ng g^{-1} for the granular white ice, 11.1 ng g^{-1} for the blue ice, 63 ng g^{-1} for wet snow and 83 ng g^{-1} for dry snow. Estimated black carbon mass-ratios are larger than previously reported suggesting the presence of a secondary absorbing impurity which is likely to be atmospheric

dust/sediment. The derived absorption and scattering cross-sections were used in radiative-transfer calculations showing that a first year Arctic sea ice albedo is more responsive to black carbon additions than multi-year sea ice. For an addition of 8 ng g^{-1} from 1 ng g^{-1} of black carbon in multi-year year sea ice albedo decreases to 99.7 % of the original value, compared to an albedo decrease to 98.7 % for the same black carbon mass ratio increase in first year sea ice. The first year sea ice is a less scattering environment than the multi-year sea ice. Thus, a less scattering sea ice environment may be more responsive to additional black carbon, an effect which will be investigated in chapter 4. The effect on the albedo of snow overlying sea ice due to black carbon in the sea ice was determined. A 0.5 cm layer of snow greatly diminishes the effect of black carbon in sea ice on snow surface albedo. A 2–5 cm layer (less than half the *e*-folding depth of snow) is enough to mask any change in surface albedo owing to additional black carbon in the sea ice, but not thick enough to ignore the underlying sea ice. For snow on sea ice a practical definition of optically thick appears to be approximately one *e*-folding depth of snow. Although the effects of black carbon in sea ice are limited to when snow cover is below 2–5 cm, black carbon is still very important in the sea ice system. As soon as snow is thin enough for black carbon in the sea ice to affect surface albedo it will exacerbate snow melting leading to longer snow free conditions, and greater sea ice melting. The period of the year when sea ice is snow free coincides with the smallest solar zenith angles, i.e. when the solar radiation is greatest, so the influence of black carbon will be larger.

Chapter 4

Dependence of snow and sea ice type on the response of albedo and light penetration depth (e-folding-depth) to increasing black carbon

---

4.1 Introduction

Snow and sea ice varies extensively both laterally and temporally in terms of thickness, density and grain size which causes variation in the optical and physical properties of snow and sea ice, providing characteristic types of snow and sea ice. Chapters 2 and 3 have alluded to different snow and sea ice types showing different albedo and e-folding depth responses to increased black carbon, which will be investigated in this chapter. Warren (1982) and Hadley and Kirchstetter (2012) show that for a given amount of light absorbing impurity a greater reduction in albedo for coarse-grained snow than for fine-grained snow is achieved. Using the model of Warren and Wiscombe (1980), Warren (1982) calculated the effect of volcanic ash on the albedo of snow with grain sizes of 100 and 1000 μm. The ash caused a greater reduction in albedo for the large grained snow. Hadley and Kirchstetter (2012) showed that artificial snow with three different grain sizes responded differently to black carbon additions, with a more coarse grained snow showing a greater albedo response. Figure S4 in the supplementary information of Reay et al. (2012) shows e-folding

depth with increasing black carbon for four different, yet similar, snowpacks at Barrow Alaska; a hard snowpack, soft snowpack, inland snow and snow on sea ice. The soft snowpack was slightly more responsive than the other three snowpacks raising the question if the *e*-folding depth of different snowpacks would also respond differently to black carbon. Zatko et al. (2013) calculated *e*-folding depths of Antarctic and Greenland ice sheets considering the effect of increasing mass-ratio of black carbon and grain size independently of each other. Figure 3C of Zatko et al. (2013) shows the decrease in actinic flux with depth in a snowpack is dependent on snow grain size, with a larger decrease observed for smaller grain sizes and figure 3B demonstrates the decreasing *e*-folding depth with increasing mass-ratio of black carbon.

A detailed study exploring the effect of different types of snow and sea ice on the variation of albedo and *e*-folding depth with black carbon has not previously been attempted. The work presented here expands on the work by Reay et al. (2012) to considering a much larger variety of snowpacks and includes sea ice, while the work of Zatko et al. (2013) is very different to the work presented here, which explores the change in albedo and *e*-folding depth with increasing mass-ratio of black carbon as a function of scattering cross-section (i.e. grain size). The work of Warren (1982) was limited to two hypothetical types of snow and a few concentrations of light absorbing impurity. The work of Hadley and Kirchstetter (2012) was limited to snow only.

Presented in chapter 4 for the first time are radiative-transfer calculations to quantify how the albedo and *e*-folding depth of three different types of snow (cold polar snow, windpacked snow and melting snow) and three different types of sea ice (multi-year sea ice, first-year sea ice and melting sea ice) respond to increasing black carbon. Different types of snow and sea ice may be optically characterised by a scattering-cross section, mass density and asymmetry parameter. Variation in these parameters will result in different albedo and *e*-folding depths and different responses in these measurements to black carbon. To all knowledge a systematic study of the response of albedo and *e*-folding depth to black carbon as a function of snow and sea ice type has not been undertaken.

4.2 Method

The response of albedo and *e*-folding depth to increased black carbon for the three different snow and sea ice types (cold polar snow, windpacked snow, melting snow, multi-year sea ice, first-year sea ice and melting sea ice) were calculated using the TUV-snow radiative-transfer model, as described in chapter 2. Each snow and sea ice type was characterised by different scattering cross-sections. The range of values of the scattering cross-section, density and asymmetry parameter, g, used to describe the snow/sea ice types are shown in table 4.1. The values of density and scattering cross-section chosen cover a wide range of possible types of snow and sea ice.

Snow/sea ice type	**Scattering cross-section /m^2 kg^{-1}**	**Density /g cm^{-3}**	**Asymmetry parameter (g)**
Cold polar snow	15–25	0.2–0.6	0.89
Windpacked snow	5–10	0.2–0.6	0.89
Melting snow	0.5–2	0.2–0.6	0.89
Frozen multi-year sea ice	0.5–1	0.7–0.95	0.98
Frozen first-year sea ice	0.1–0.2	0.7–0.95	0.98
Melting sea ice	0.01–0.05	0.7–0.95	0.98

Table 4.1 *– Properties of snow and sea ice types studied. Optical and physical properties are based on work by Grenfell and Maykut (1977); Perovich (1990); Timco and Frederking (1996); Perovich (1996); Gerland et al. (1999); Fisher et al. (2005); King et al. (2005); France (2008); France et al. (2011); Marks and King (2013).*

As previously described, albedo was calculated as the ratio of upwelling, I_{up}, to downwelling, I_{down}, irradiance at the surface of the snow/sea ice $\left(\frac{I_{up}}{I_{down}}\right)$. The *e*-folding depth was calculated, in the same manner as chapter 2, using equation 4.1, as the distance over which irradiance within the snow/sea ice will reduce to $\frac{1}{e}$ (∼37%) of the original value.

$$\frac{I_z}{I_{z'}} = e^{-\left(\frac{(z-z')}{\epsilon}\right)} \tag{4.1}$$

Where ϵ is *e*-folding depth, I_z is the downwelling irradiance at thickness z, z' is a reference thickness, and $I_{z'}$ is the reference downwelling irradiance, at z'.

Albedo and *e*-folding depth of the different types of snow/sea ice were calculated for

mass-ratios of black carbon from 1 to 1024 ng g^{-1} (1, 2, 4, 8, 16, 32, 64, 128, 256, 512 and 1024 ng g^{-1}). Black carbon was assumed to be evenly distributed throughout the snow/sea ice in order to allow calculations of the effects of black carbon on *e*-folding depth. Black carbon was also assumed to be the only absorbing impurity. The absorption spectrum for black carbon in ice was the same as used in chapters 2 and 3.

Snow and ice thicknesses of 10 m, 1 m, 0.5 m and 0.25 m (for sea ice) and 0.1 m (for snow) were used. A snow and sea ice with an unrealistic thickness of 10 m was studied to ensure a response of albedo and *e*-folding depth to increased black carbon with snow or sea ice that is independent of the underlying medium (optically thick snow/ice), which is useful to enable comparisons to be made.

The atmosphere and snow or sea ice are split into levels in the model, table 4.2 describes the structure of levels for each snow and sea ice thickness modelled. Calculations were undertaken at wavelengths 300–800 nm, using an eight-stream model with a pseudo-spherical correction (Lee-Taylor and Madronich, 2002). The atmosphere had an ozone column of 300 Dobsons with no atmospheric loading of aerosol and was formed of 80 uneven levels (also shown in table 4.2). A wavelength-independent under-snow or sea ice albedo of 0.1 was used and the Earth-Sun distance was set to 1 AU. Isotropic sky conditions were used by placing cumulus clouds in the model at a 1 km altitude, with an optical thickness of 16, an asymmetry parameter of 0.85 and a single scattering albedo of 0.9999. Isotropic conditions were used so that albedo could be calculated independent of solar zenith angle. Light penetration depth through the snow or sea ice was calculated in the asymptotic zone for optically thick snow/sea ice.

Snow/sea ice thickness/m	Number of levels	Level structure
0.1	25	1 mm increments from 0–1 cm 1 cm increments from 1–9 cm 1 mm increments from 9.5 to 10 cm
0.25	40	1 mm increments from 0–1 cm 1 cm increments from 1–24 cm 1 mm increments from 24.5 to 25 cm
0.5	38	1 mm increments from 0–1 cm 1 cm increments from 1–10 cm 10 cm increments from 10 to 40 cm 1 cm increments from 40–49 1 mm increments from 49–50 cm
1	30	1 cm increments from 1–10 cm 10 cm increments from 10–90 cm 1 cm increments from 95 to 99 cm 1 mm increments from 99–100 cm
10	47	1 cm increments from 1–10 cm 10 cm increments from 10–90 cm 1m increments from 100 to 900 cm 10 cm increments from 900–990 cm 1 mm increments from 990–1000 cm
Atmosphere (90 km thick)	80	10 m increments from 10–100 m 100 m increments from from 100–1000 m 1 km increments from 1–10 km 2 km increments from 10–90 km

Table 4.2 *– Level structure utilised for layers of snow/sea ice with different thicknesses and for the atmosphere.*

4.3 Results

The results section will examine the response of snow and sea ice albedo to increasing black carbon as a function of the type of snow and sea ice and secondly the response of *e*-folding depth to the same changes in black carbon mass-ratio and snow and sea ice type. In the results section relative changes in albedo and *e*-folding depth owing to a specific mass-ratio of black carbon for different snow and sea ice types will be examined, to enable comparison between different snow and sea ice types. The change in albedo and *e*-folding depth is reported relative to an albedo and *e*-folding depth calculated with a black carbon mass-ratio of 1 ng g^{-1}. The relative change can be expressed mathematically for albedo as, $\frac{A_{BC=1}-A_{BC=x}}{A_{BC=1}}$, and as, $\frac{\epsilon_{BC=1}-\epsilon_{BC=x}}{\epsilon_{BC=1}}$, for *e*-folding depth, where $A_{BC=x}$ is albedo at a black carbon mass-ratio of x ng g^{-1} and $\epsilon_{BC=x}$ is an *e*-folding depth at a black carbon mass-ratio of x ng g^{-1}.

4.3.1 Response of albedo to increasing black carbon in optically thick snow and sea ice

The albedo of snow is very sensitive to both the mass-ratio of black carbon and snow type, as shown in figure 4.1. Figure 4.1 shows the calculated albedo of snow as a function of black carbon (increasing absorption cross-section of light absorbing impurity) for the three snowpacks (cold polar snow, windpacked snow and melting snow), at a wavelength of 550 nm and a snow density of 0.4 g cm^{-3}, for an optically thick snow. Studying optically thick snow and sea ice (10 m of snow/sea ice) is important in order to be able to fairly compare different snow/sea ice types without having any thickness effect. The shaded areas represent the albedo values calculated for the range of scattering cross-sections in table 4.1. A melting snowpack shows a considerably larger change in albedo due to additions of black carbon than a windpacked snow and a cold polar snow shows the smallest change.

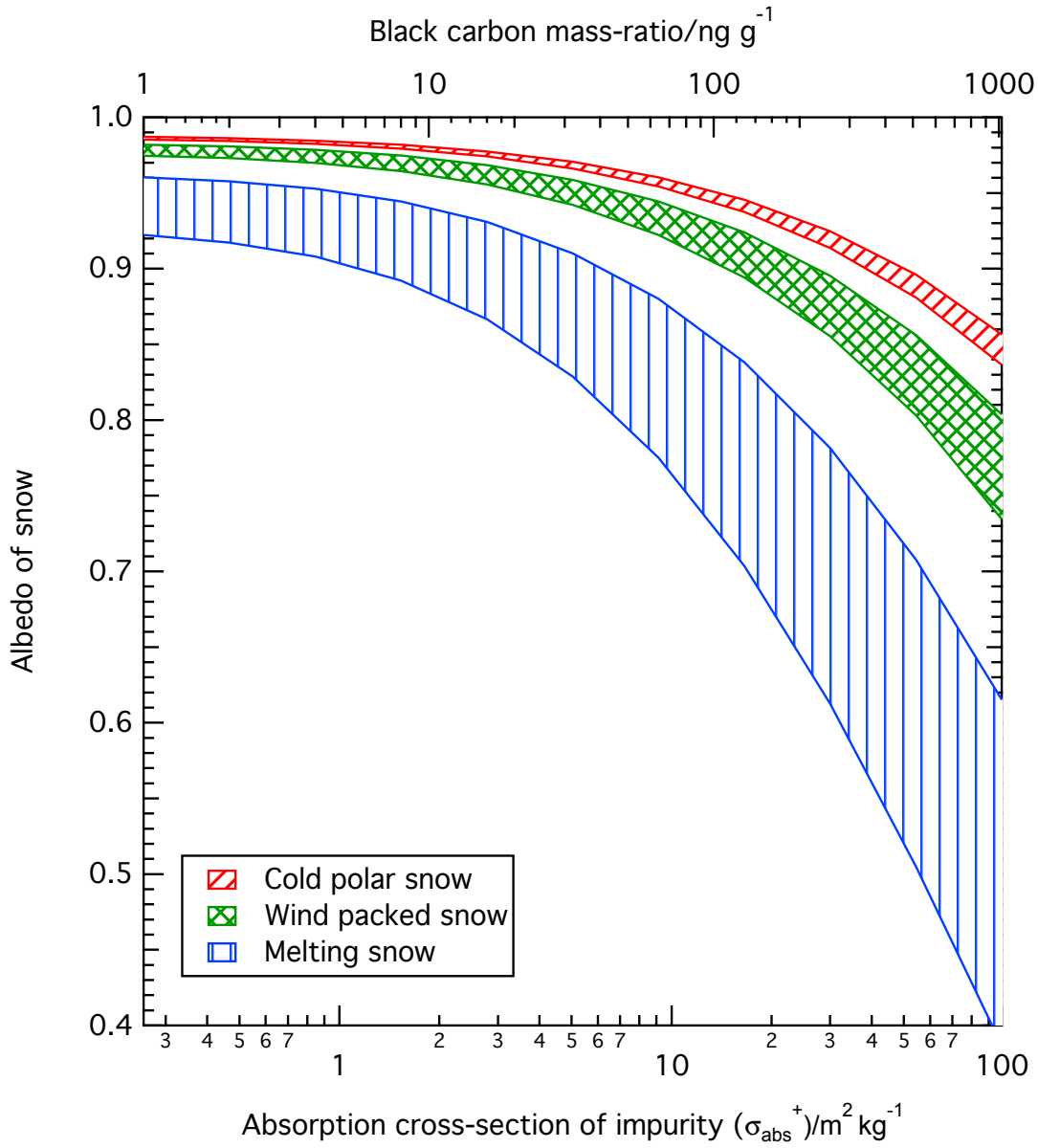

Figure 4.1 *– Albedo with increasing absorption cross-section (bottom x-axis) and black carbon mass-ratio (top x-axis) for different snow types; cold polar snow (red), windpacked snow (green) and melting snow (blue).*

Figure 4.2A shows the relative change in albedo with increasing mass-ratio of black carbon for a mid-range snow and sea ice, of each type examined. The values in figure 4.2A are derived using the mid albedo values from each shaded area representing a different snow/sea ice type in figures 4.1 and 4.4, over the black carbon mass-ratio range examined. The relative change in albedo is different for the three snowpacks. The relative change as a function of increasing black carbon for a melting snowpack is a factor of ~3.5 larger than the relative change in albedo as a function of increased black carbon for a cold polar snowpack. Mathematically the above ratio is expressed in equation 4.2.

$$s = \frac{\frac{A_{BC=1} - A_{BC=x}}{A_{BC=1}}_{melting}}{\frac{A_{BC=1} - A_{B=x}}{A_{BC=1}}_{coldpolar}} \tag{4.2}$$

The equivalent ratio is ∼1.2 for a windpacked snow relative to a cold polar snowpack. The sensitivity is a weak function of mass-ratio of black carbon and the values of 3.5 and 1.2 are useful approximations. Accurate numbers can be determined from figure 4.2 A. For example, for an addition of black carbon from 1 to 50 ng g^{-1} the relative decrease in cold polar snow albedo is 3%, for windpacked snow it is 4% and for melting snow the decrease is to 11%.

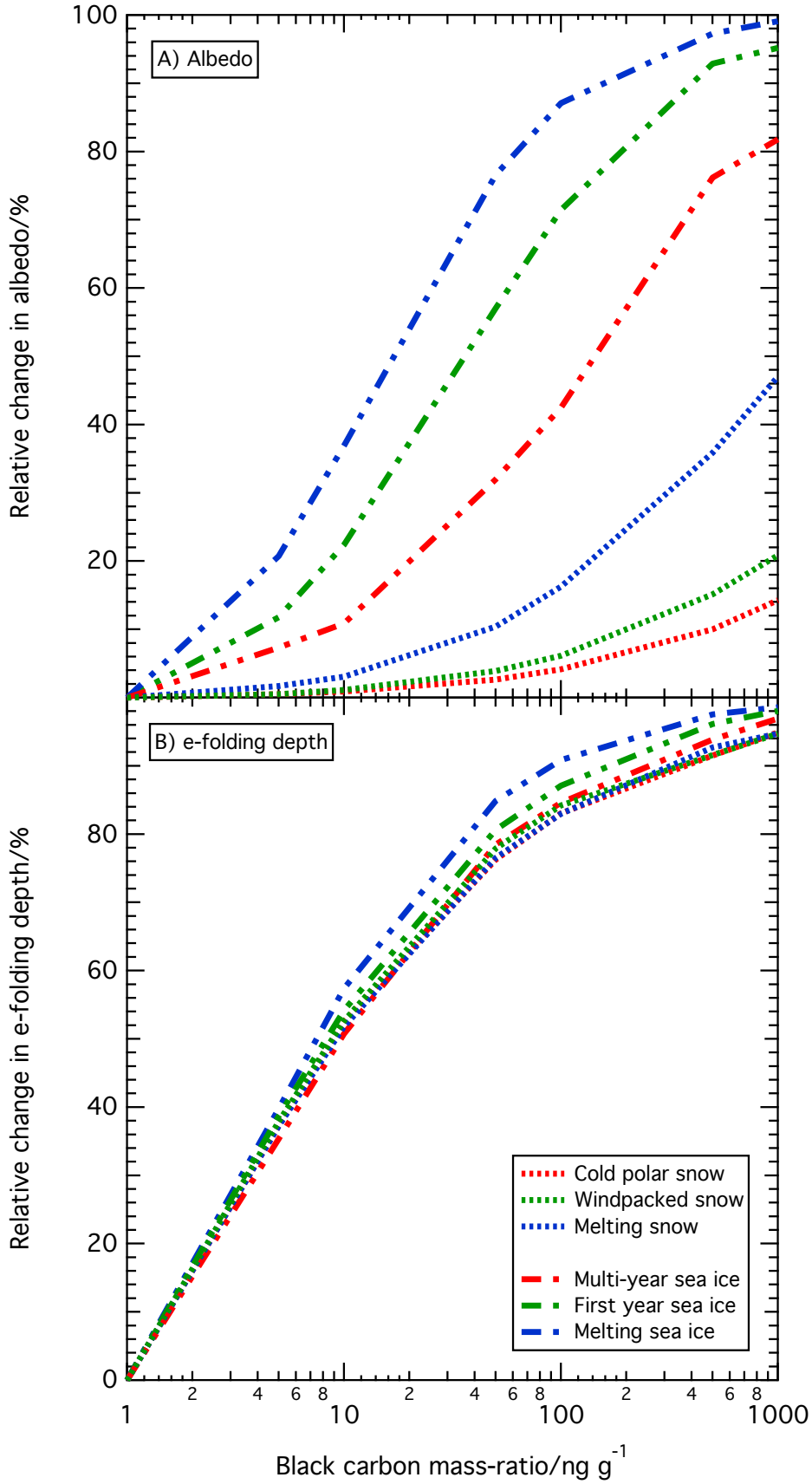

Figure 4.2 *– Relative change in albedo and e-folding depth. Each line shows a typical albedo or e-folding depth for a particular snow or sea ice type, taken as the mid-value for that snow or sea ice.*

Figure 4.3 shows a more detailed variation of snow albedo as a function of the scattering cross-section range examined for snow (0.5–25 m^2 kg^{-1}) and black carbon mass-ratio (absorption cross-section) at snow densities of 0.2, 0.4 and 0.6 g cm^{-3} and at wavelengths of 300, 400, 550 and 700 nm rather than the example cases of scattering cross-section highlighted in figure 4.1. Figure 4.3 demonstrates that the relationships shown in figure 4.1 are very similar to those at wavelengths of 300–550 nm. A wavelength of 700 nm in figure 4.3 exhibits different features to the shorter wavelengths which is due to increased absorption by ice at longer wavelengths (as shown in figure 2.2). Unsurprisingly at all wavelengths albedo is largest for larger scattering cross-sections (i.e. cold polar snow) as demonstrated by Warren (1982).

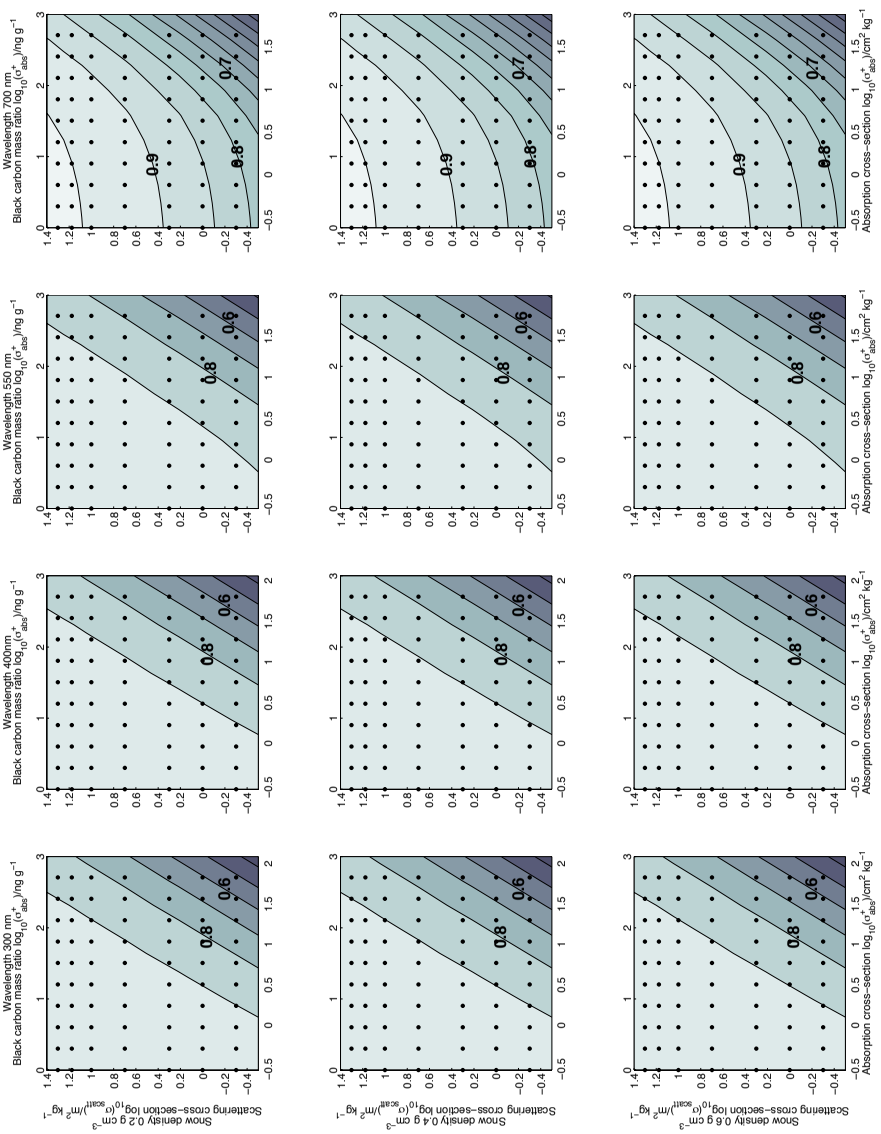

Figure 4.3 *– Albedo of snow with increasing mass-ratio of black carbon (absorption cross-section) and scattering cross-section, at wavelengths 300, 400, 550 and 700 nm and snow densities of 0.2, 0.4, 0.6 g cm^{-3}.*

Figure 4.4 shows the albedo of sea ice as a function of increasing mass-ratio of black carbon (increasing absorption cross-section of snowpack impurity) for the multi-year sea ice, first year ice, and melting sea ice at a wavelength of 550 nm and a sea ice density of 0.8 g cm^{-3}. Figure 4.4, similarly to figure 4.1 for the albedo of snow, shows that the albedo of sea ice is sensitive to the amount of black carbon and type of sea ice. The melting sea ice shows the largest change in albedo due to additions of black carbon and the multi-year sea ice has the smallest change. Figure 4.2A shows the relative change in albedo with increasing mass-ratio of black carbon is different for the three sea ice. The relative change in albedo as a function of increasing black carbon for a melting ice is a factor of $\sim$2.2 larger than the relative change in albedo as a function of increased black carbon for a multi-year ice (applying equation 4.2). The equivalent ratio is $\sim$1.6 for a first-year ice relative to a multi-year ice. For example, for an increase of black carbon from 1 to 50 ng g^{-1} in multi-year sea ice the relative decrease in albedo is 30%, compared to a decrease of 76% for melting sea ice.

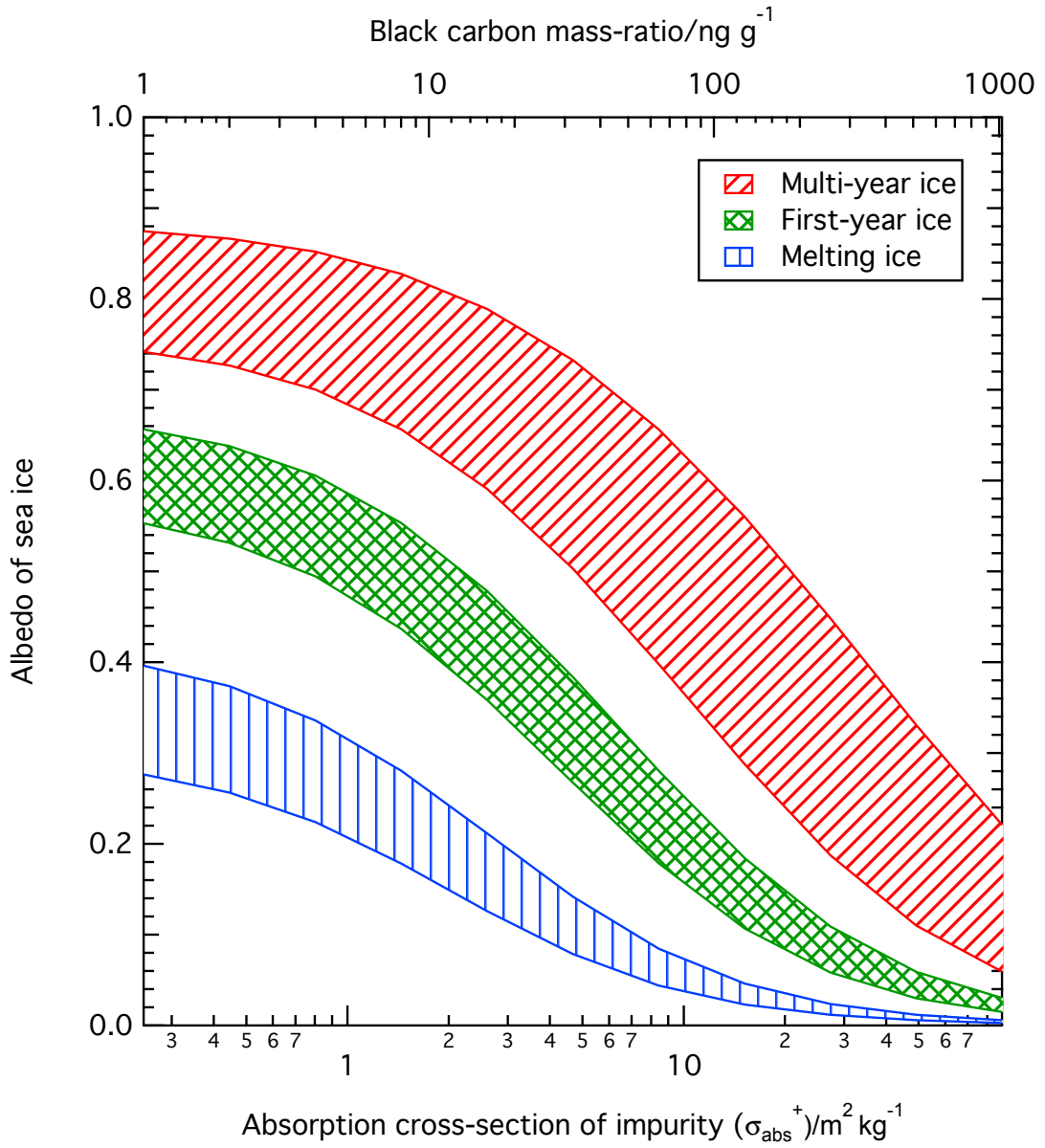

Figure 4.4 *– Albedo with increasing absorption cross-section (bottom x-axis) and black carbon mass-ratio (top x-axis) for different sea ice types; multi-year ice (red), first-year ice (green) and melting ice (blue).*

The albedo of sea ice at wavelengths of 300, 400, 550 and 700 nm as a function of the entire scattering cross-section range examined for sea ice (0.01–1 m^2 kg^{-1}) and black carbon mass-ratio (absorption cross-section) at sea ice densities of 0.7, 0.8 and 0.9 g cm^{-3} is shown in figure 4.5. The results are very similar to figure 4.3 for snow albedo, with density having no effect on albedo, as expected, and wavelengths from 300–550 nm showing similar results, with a more pronounced effect at a wavelength of 700 nm. Albedo is obviously largest for the larger scattering cross-sections (i.e. multi-year sea ice).

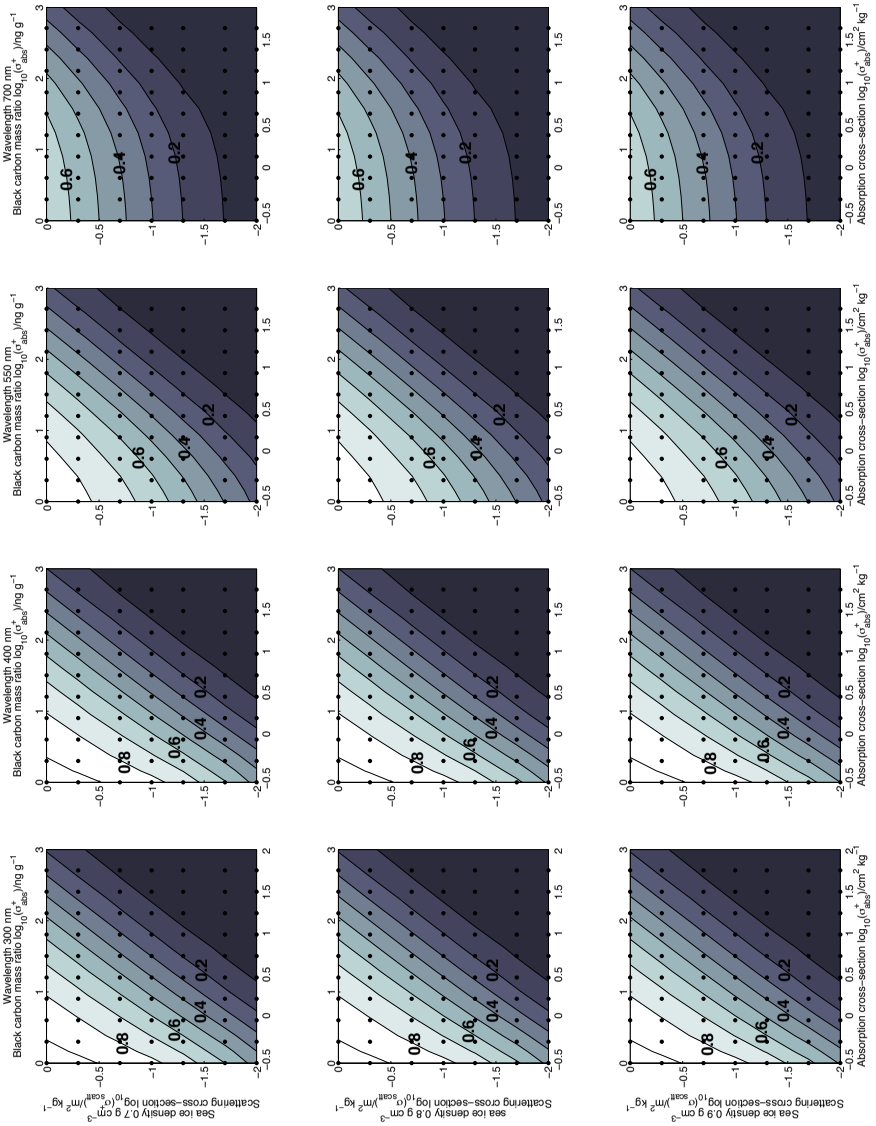

Figure 4.5 *– Sea ice albedo with increasing mass-ratio of black carbon (absorption cross-section) and scattering cross-section, at wavelengths 300, 400, 550 and 700 nm and sea ice densities of 0.7, 0.8, 0.9 g cm^{-3}.*

4.3.2 Albedo response to increasing black carbon for snow/sea ice with a thickness of 1, 0.5 and 0.25 or 0.1 m

The results presented in section 4.3.1 are for a 10 m thick snow/sea ice, in reality this is likely to be an unrealistic thickness for most scenarios. The thickness of 10 m was chosen so that the snow and sea ice was optically thick, thus changes in albedo and *e*-folding depth were independent of the underlying surface and snow or sea ice with small scattering cross-section values could be compared with larger scattering cross-section values. In order to understand the dependence of the results on thickness the calculations were repeated with more realistic thicknesses of 0.1m (for snow), 0.25 m (for sea ice) and 0.5 m and 1 m for snow and sea ice. Figures 4.6 and 4.7 show the albedo of the three different types of snow and sea ice respectively as a function of black carbon (absorption cross-section) and thickness, at a constant wavelength of 550 nm and a constant density of 0.4 g cm^{-3} for the snow and 0.8 g cm^{-3} for the sea ice. The albedo of the snow, figure 4.6, is much less sensitive to thickness than sea ice, figure 4.7. The windpacked snow and cold polar snow show negligible thickness dependance because these are already optically thick owing to their large scattering cross-section. However, the melting snow is thickness dependent up to a snow thickness of $\sim$50 cm. Decreased thickness of the melting snow reduces the relative change in albedo with increasing mass-ratio of black carbon compared to the optically thick case. Albedo of all sea ice types, shown in figure 4.7, is dependent on thickness. Reducing the thickness reduces the relative change in albedo for increasing black carbon. For mass-ratios of black carbon less than 100 ng g^{-1} sea ice albedo increases as the sea-ice thickness increases. The difference in dependence on thickness for snow and sea ice is due to the fact that snow is optically thick at a much shallower thickness than sea ice owing to the larger scattering cross-section of snow relative to sea ice. The results presented in figures 4.6 and 4.7 are dependent on the underlying medium. For the calculations presented here the underlying medium had a wavelength independent albedo of 0.1 to crudely represent soil or seawater (Payne, 1972; Dickinson, 1983).

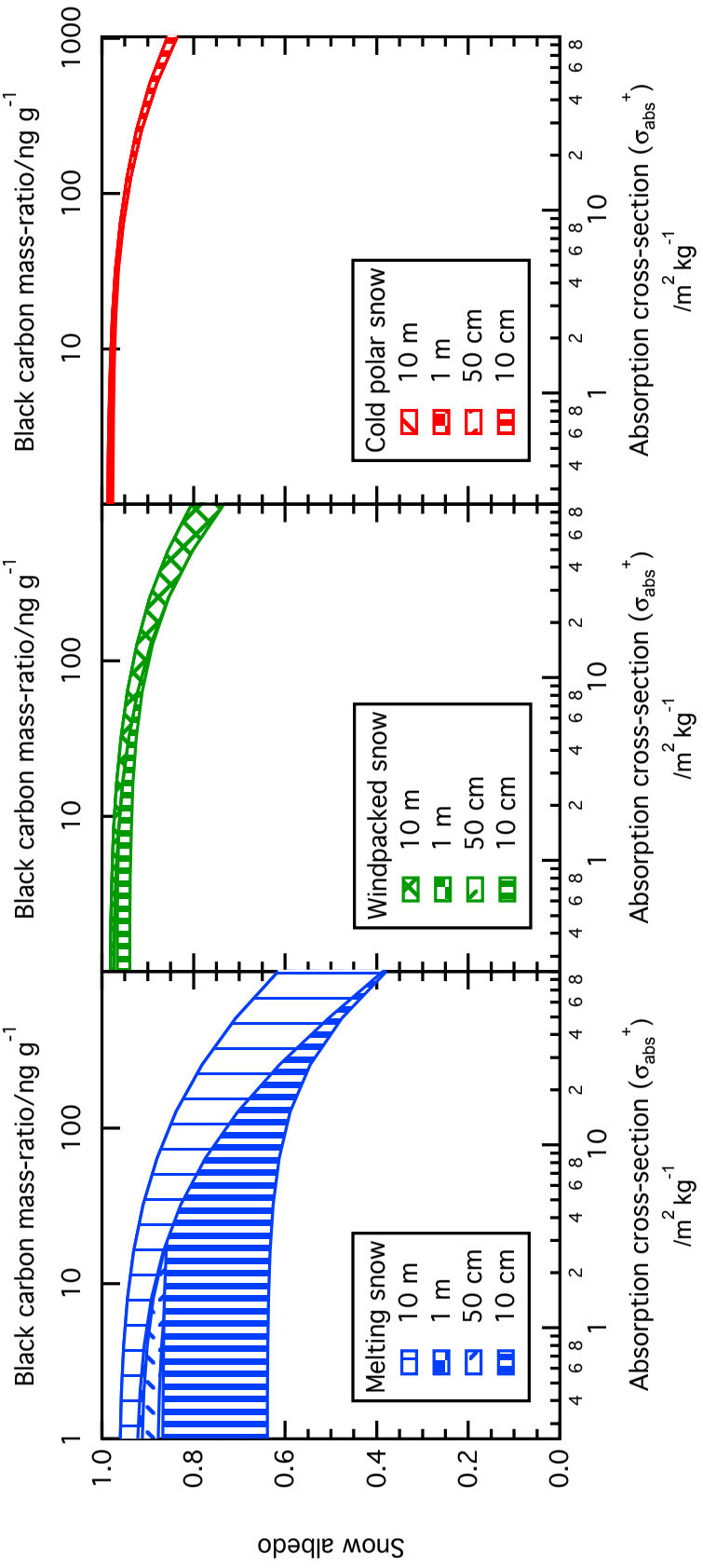

***Figure 4.6** – Thickness sensitivity study showing albedo of three snow types (cold polar snow, windpacked snow and melting snow) with increasing black carbon mass-ratio (absorption cross-section) for snow thicknesses of 0.1, 0.5, 1 and 10 m.*

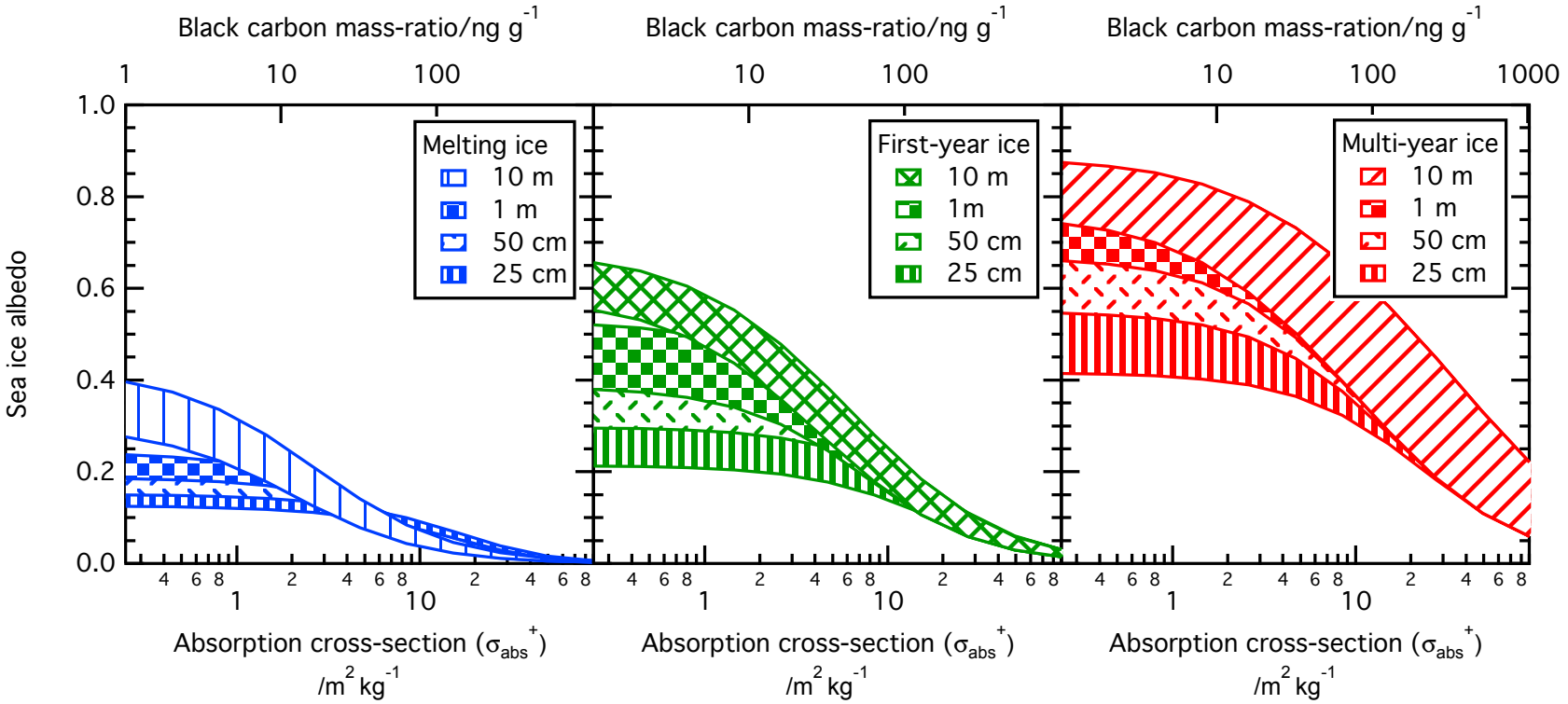

Figure 4.7 *– Albedo of three types of sea ice (multi-year ice, first-year ice and melting ice) with increasing black carbon mass-ratio (absorption cross-section) for sea ice thicknesses of 0.25, 0.5, 1 and 10 m.*

4.3.3 Response of *e*-folding depth to increasing black carbon in optically thick snow and sea ice

Figure 4.8 shows the *e*-folding depth of snow with increasing mass-ratio of black carbon (increasing absorption cross-section) for the three snowpacks at a wavelength of 550 nm and a snow density of 0.4 g cm^{-3}. Figure 4.9 shows variation in sea ice *e*-folding depth with increasing absorption cross-section (black carbon) for the three types of sea ice with a density of 0.8 g cm^{-3}. Both figures 4.8 and 4.9 show there is a large change in the *e*-folding depth with increasing mass-ratio of black carbon which is different for each snow and sea ice type. However, as shown in figure 4.2 B the relative change in *e*-folding depth is effectively the same for different types of snow or sea ice. The relative change in *e*-folding depth as a function of increasing black carbon for a melting snow and a windpacked snow is approximately the same as the relative change in *e*-folding depth as a function of increased black carbon for a cold polar snow. Thus although the absolute change in *e*-folding depth is different for each snow type the relative change is almost the same, in contrast to albedo. The relative decrease in *e*-folding depths with increased mass-ratio of black carbon, shown in figure 4.2 B is again similar for the three sea ice types considered (although slightly more difference is observed between the sea ice types than the three snowpacks considered).

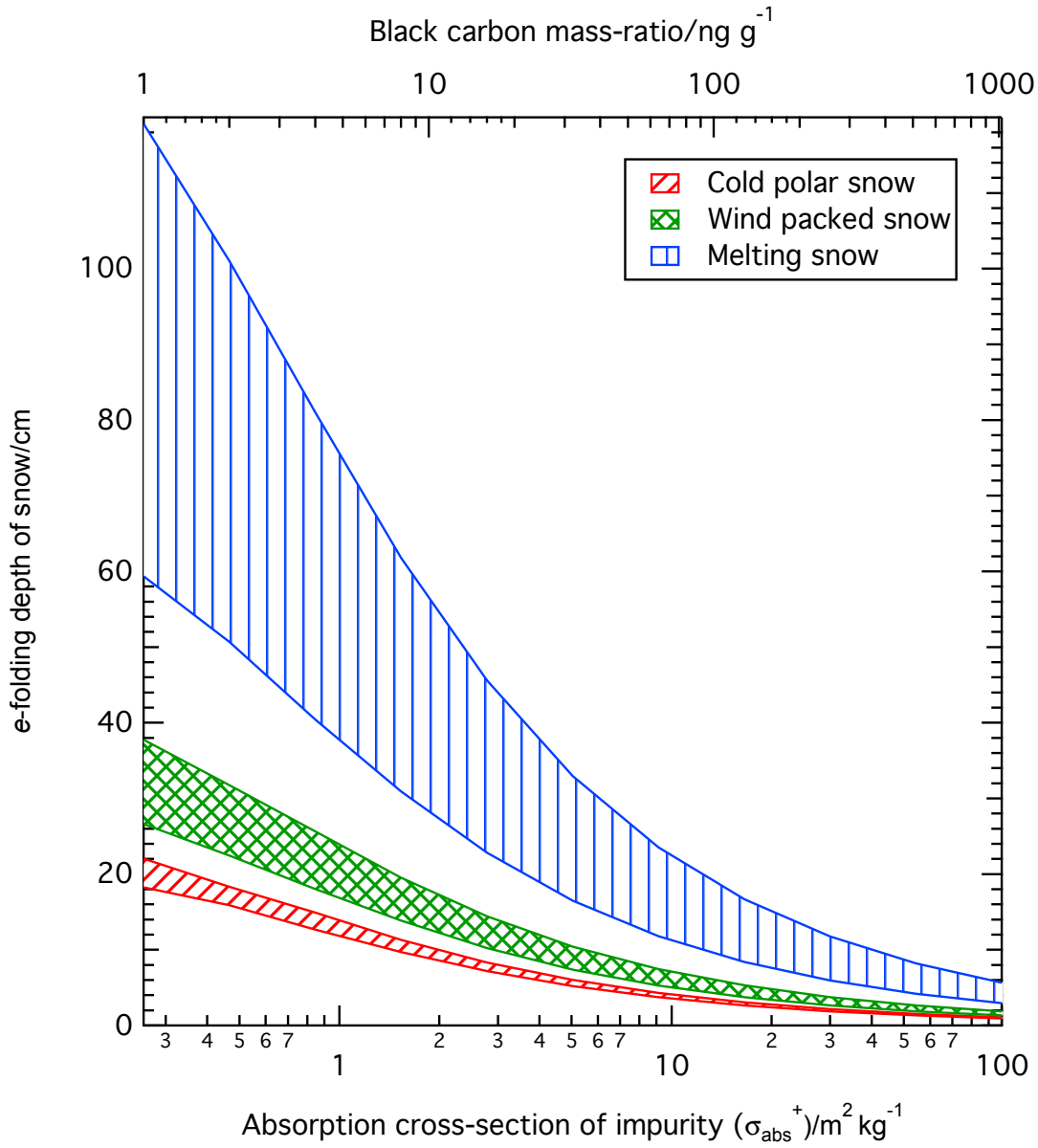

Figure 4.8 *– Change in e-folding depth with increasing black carbon mass-ratio (absorption cross-section) for different snow types; cold polar snow, windpacked snow and melting snow.*

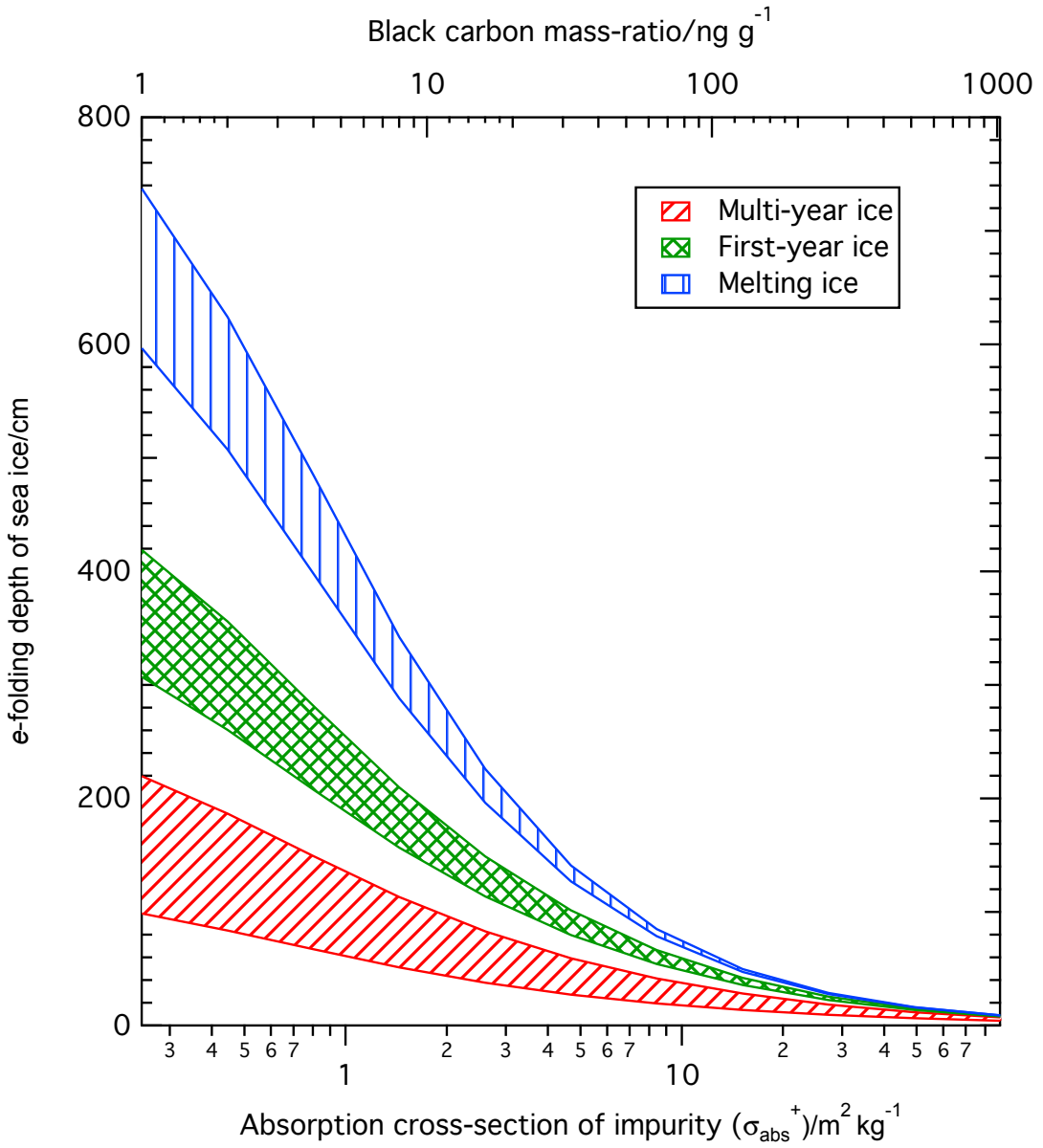

Figure 4.9 *– Change in e-folding depth with increasing black carbon mass-ratio (absorption cross-section) for different sea ice types; multi-year ice, first-year ice and and melting ice.*

Figures 4.10 and 4.11 show snow and sea ice *e*-folding depth at wavelengths of 300, 400, 550 and 700 nm as a function of the entire scattering cross-section range examined for the snow and sea ice (0.01–1 m^2 kg^{-1}) and black carbon mass-ratio range (absorption cross-section) at snow densities of 0.2, 0.4 and 0.6 g cm^{-3} and sea ice densities of 0.7, 0.8 and 0.9 g cm^{-3}. Density obviously affects *e*-folding depth, with a more dense snow/sea ice having slightly shorter *e*-folding depths (Warren, 1982). Wavelengths from 300–550 nm show similar results to figures 4.8 and 4.9 with a more pronounced effect at a wavelength of 700 nm. At all wavelengths *e*-folding depth is shortest for larger scattering cross-sections (i.e. cold polar snow/multi-year sea ice).

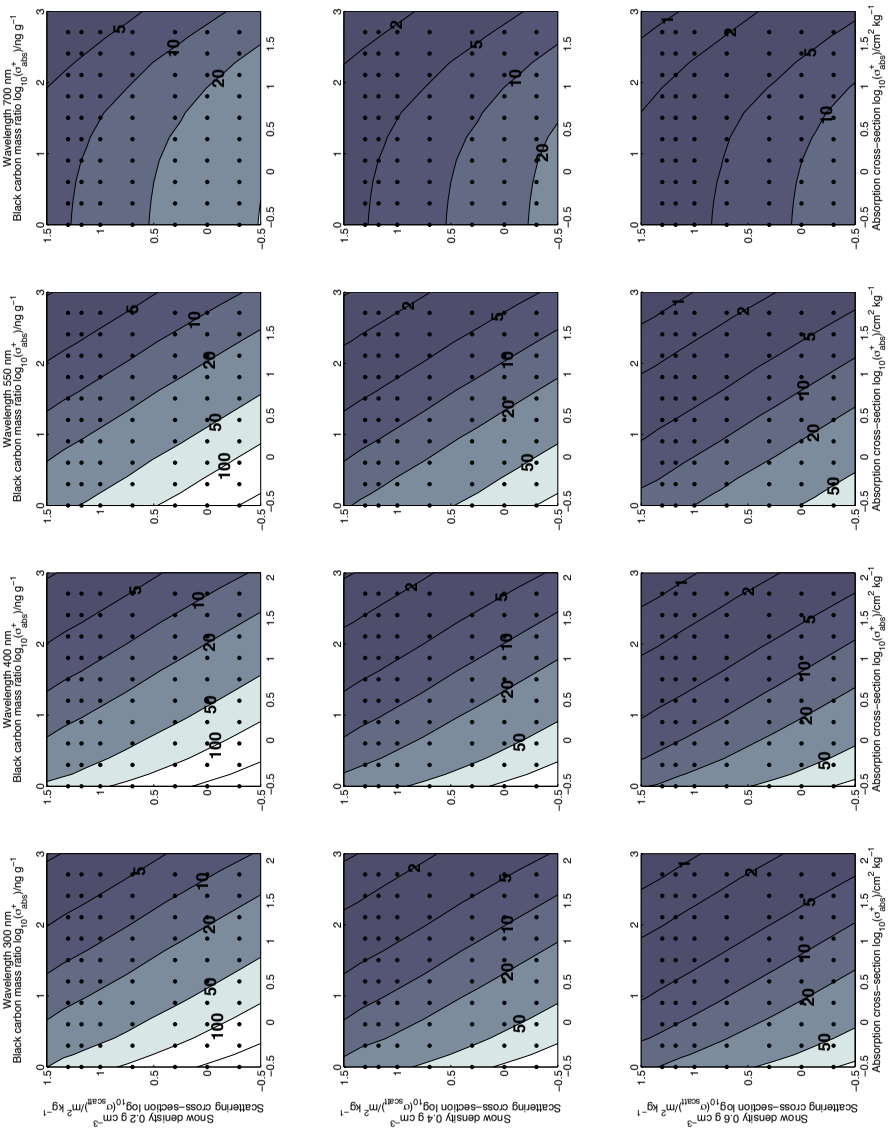

Figure 4.10 *– Snow e-folding depth with increasing mass-ratio of black carbon (absorption cross-section) and scattering cross-section, at wavelengths 300, 400, 550 and 700 nm and snow densities of 0.2, 0.4, 0.6 g cm^{-3}.*

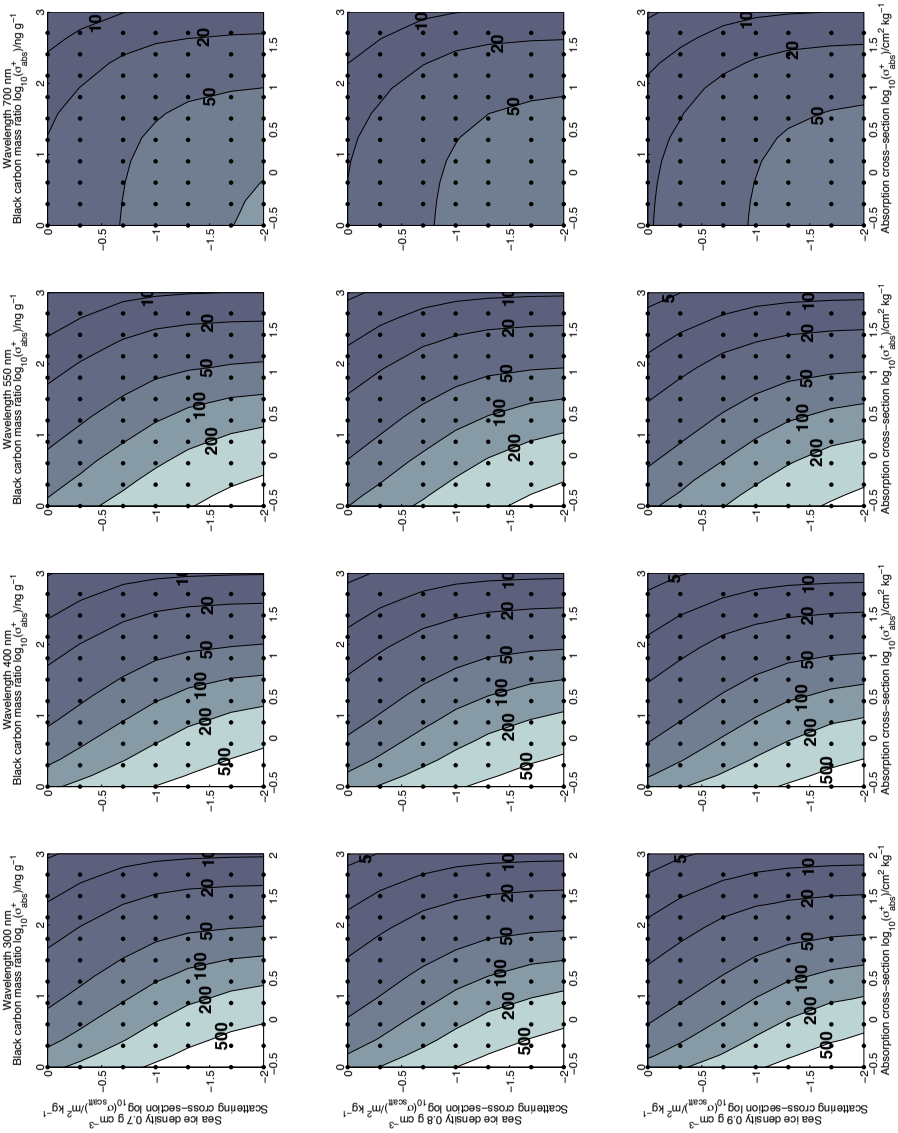

Figure 4.11 *– Change in sea ice e-folding depth with increasing mass-ratio of black carbon (absorption cross-section) and scattering cross-section, at wavelengths 300, 400, 550 and 700 nm and densities of 0.7, 0.8, 0.9 g cm^{-3}.*

4.3.4 Response of *e*-folding depth to increasing black carbon in a snow/sea ice with a thickness of 1, 0.5 and 0.25 or 0.1 m

The sensitivity of *e*-folding depth to different thicknesses of snow and sea ice (0.1, 0.25, 0.5, 1 and 10 m) is shown in figures 4.12 and 4.13 respectively. Conversely to the variation of albedo, the variation of *e*-folding depth with black carbon for different snow and sea ice types is very sensitive to the thickness of the snow/sea ice. The *e*-folding depth is more sensitive to thickness because the *e*-folding depth calculation uses light intensity values within the snow/sea ice, the values of which are more likely to be affected by the albedo of the underlying layer than the surface albedo would be as the scattering that dominates albedo mainly occurs in the top few centimetres of the snow or sea ice. Figure 4.12 shows that for the variation of *e*-folding depth with increasing black carbon mass ratio, melting snow is most sensitive to thickness, but all snow types are sensitive up to a black carbon mass-ratio of $\sim$100 ng g^{-1}, where the black carbon dominates the absorption of light within the snow or ice (Reay et al., 2012). The *e*-folding depth of sea ice, figure 4.13, is more sensitive to thickness than snow, with large variations in *e*-folding depth observed with different sea ice thicknesses. The most sensitive sea ice is the melting ice. Figures 4.12 and 4.13 demonstrate that as the mass-ratio of black carbon increases the value of *e*-folding depth for the different snow/sea ice types trend to a similar value of *e*-folding depth as the dominant loss of photons in the snow and sea ice becomes absorption by black carbon. The plots shown in figures 4.12, 4.13, 4.6 and 4.7 are designed to demonstrate the snow/sea ice thickness effect, for clarity the data used to plot these graphs is shown in appendix A

Although the absolute values of albedo and *e*-folding depth may vary with thickness, it is important to consider that the trend for a medium with a larger scattering cross-section to be less responsive to black carbon still exists.

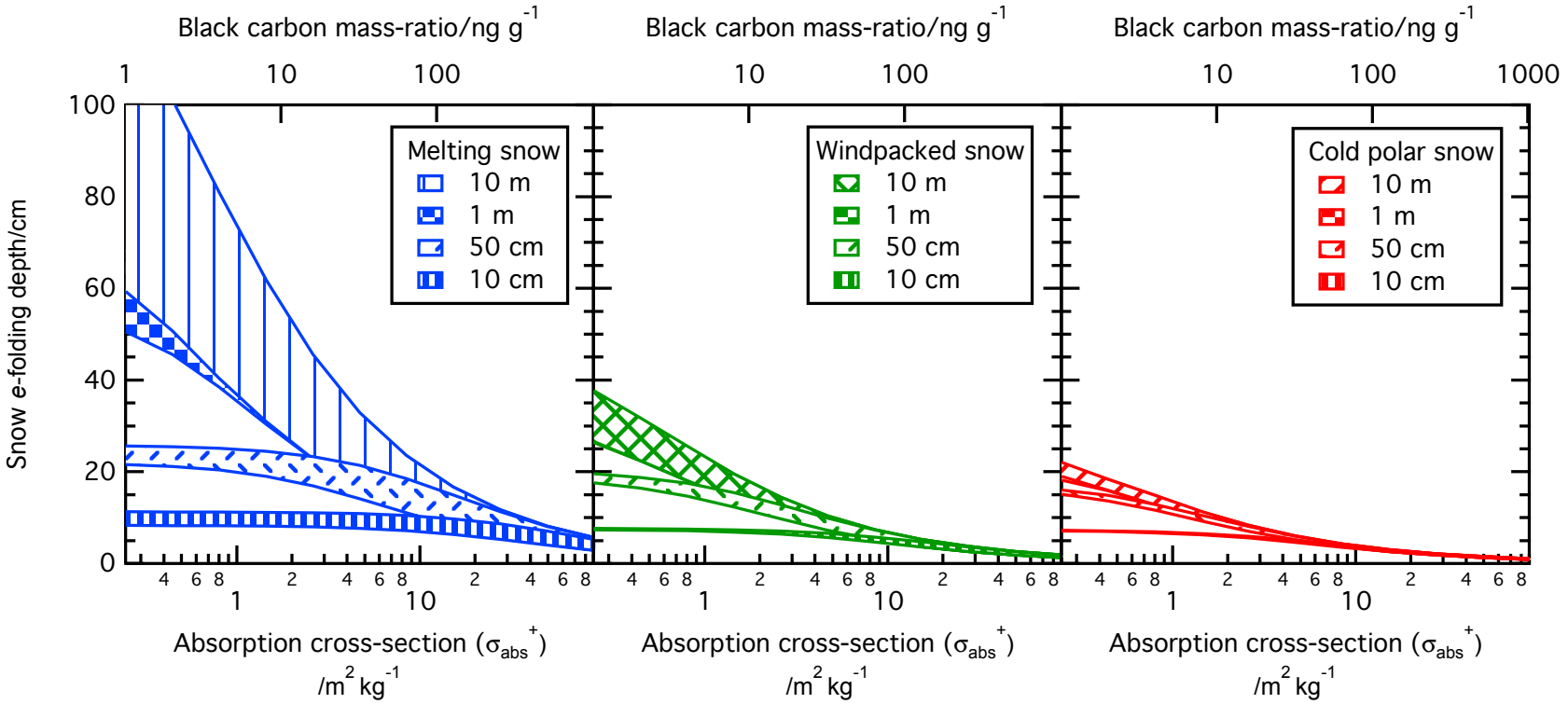

Figure 4.12 *– Change in e-folding depth of snow with increasing black carbon mass-ratio (absorption cross-section) for snow thicknesses of 0.1, 0.5, 1 and 10 m.*

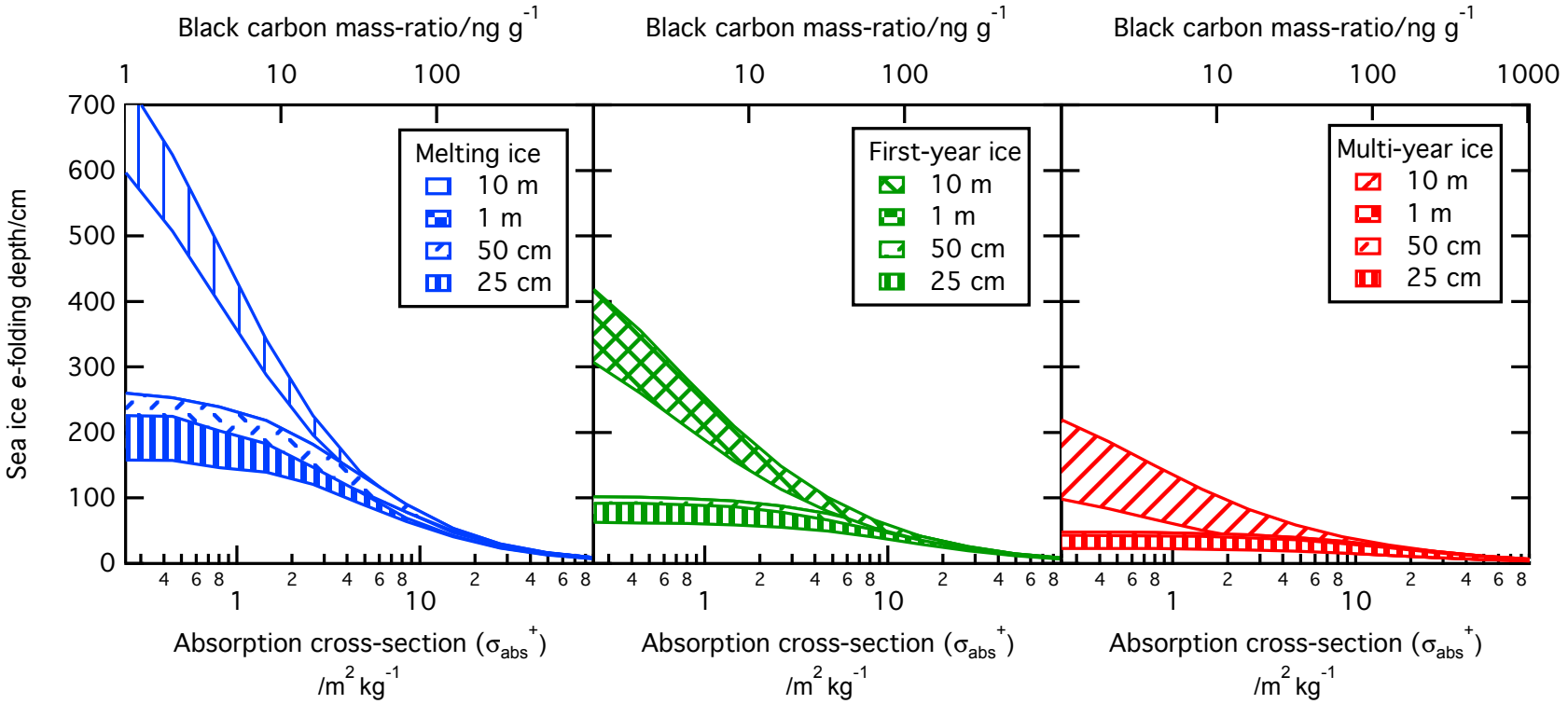

Figure 4.13 *– Sea ice e-folding depth with increasing black carbon mass-ratio (absorption cross-section) for sea ice thicknesses of 0.25, 0.5, 1 and 10 m.*

4.4 Discussion

The calculations presented here show that the response of albedo and *e*-folding depth of snow and sea ice to black carbon is dependent on the snow or sea ice type, which is dependent on the scattering cross-section of the snow or sea ice. While it is not surprising that the albedo and light penetration depth are dependent on scattering cross-section, by picking scattering cross-section values to represent realistic snow and sea ice types it has enabled quantification of the different response of snow and sea ice types. The values presented could be used for simple energy balance climate models.

The discussion will initially focus on how snow and sea ice scattering cross-section affects the albedo and *e*-folding depth response to increasing black carbon, then examine the response of snow versus sea ice. The discussion section will also include an examination of how climate change is leading to changes in snow and sea ice types commonly observed and the effect this will have on the response to black carbon. Finally model limitations and sensitivity will be discussed.

4.4.1 The role of scattering cross-section in determining snow and sea ice response to black carbon

Figures 4.1, 4.2A and 4.4 show that a snow and sea ice with a large scattering cross section, e.g. cold polar snow and multi-year ice, show a smaller change in albedo owing to additions of black carbon than the snow or sea ice with a smaller scattering cross-section. Warren (1982) and Aoki et al. (2003) stated that albedo of a snowpack decreases as grain size of that snowpack increases, with Kokhanovsky and Zege (2004) demonstrating that scattering cross-sections of snow may be inversely proportional to grain size of snow. Warren (1982) explains this phenomenon as photons are scattered at air-ice interfaces and absorbed passing through ice. The effect of the dependance of albedo on grain size is demonstrated in figure 4.14. In a snow or sea ice with a larger scattering cross-section (smaller grain size) a photon propagates less far through a snowpack before it is scattered out, so it has less opportunity to be absorbed by any black carbon in the sea ice or snow before it exits the snow or sea ice, thus the albedo is higher. Although the work here demonstrates

the known result that an increase in scatttering cross-section (typically smaller grain size for snow) results in smaller changes to albedo owing to an increase in black carbon than for a smaller scattering cross-section (typically a larger grain size), this is the first time, to all knowledge, the effect has been calculated in detail for three characteristic snowpacks and sea ice. The factor by which *e*-folding depths decrease with increasing mass-ratio of black carbon is almost independent of the type of snow or sea ice.

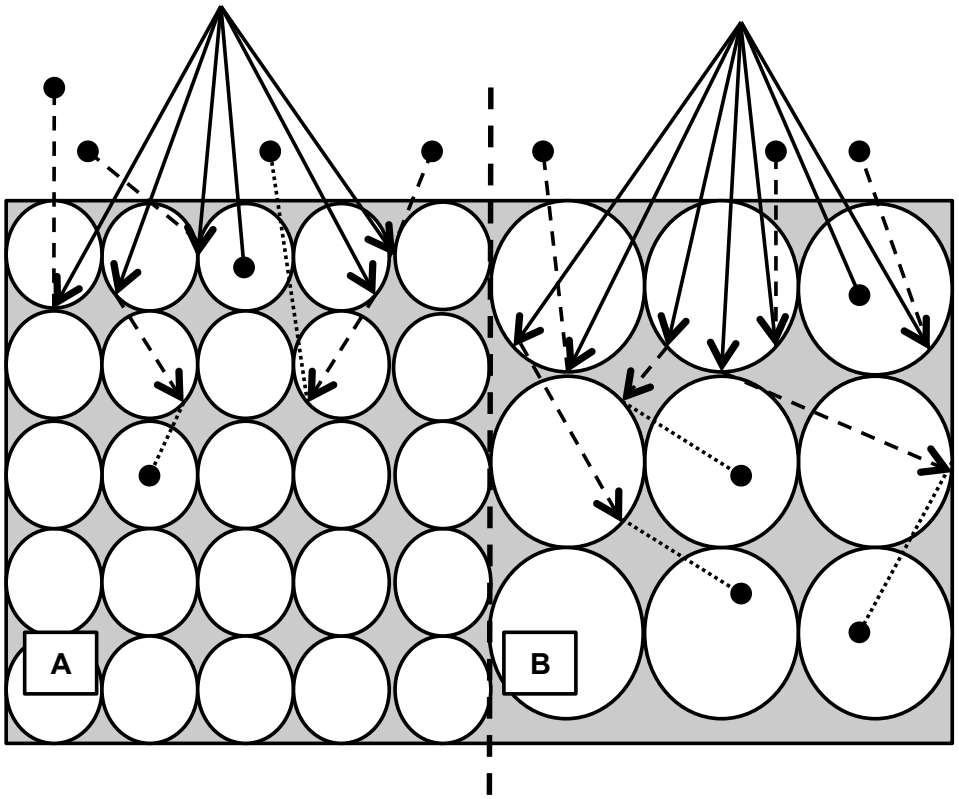

Figure 4.14 *– Grain size effects on surface albedo. A) Medium/small grain size results in a larger scattering cross-section as there are more air-ice interfaces in the same snow volume. More photons are scattered back out of medium resulting in higher albedo. B) Larger grain size results in smaller scattering cross-section as there are fewer air-ice interfaces. Fewer photons are scattered back out of medium resulting in lower albedo.*

4.4.2 The response of snow versus sea ice

Calculations of the response of albedo of both snow and sea ice to increased black carbon enables comparison between how the two mediums respond. The albedo of sea ice is far more responsive to additions of black carbon than the albedo of snow, as briefly suggested by Bond et al. (2013). Snow has a larger scattering cross-section than sea ice, therefore as explained in section 4.4.1, sea ice is more responsive to black

carbon. For example, according to figures 4.1 and 4.4, for a first-year sea ice and a windpacked snow, there is a relative decrease in albedo of 57% and 4% respectively, with a black carbon increase from 1 to 50 ng g^{-1}. The different albedo response of snow and sea ice to increased black carbon is clearly shown in figure 4.2A.

As noted in section 4.3.3 the *e*-folding depth is sensitive to the mass-ratio of black carbon and the type of snow or sea ice; but the relative change in *e*-folding depth is practically insensitive to the type of snow or sea ice type owing to two contrasting effects. A more scattering snow or sea ice will be less responsive to black carbon as photons entering the snow/sea ice are more likely to be scattered out before penetrating into the snow pack thus decreasing the *e*-folding depth. In a less scattering snow pack black carbon is more effective so photons will be absorbed by black carbon which also has the effect of reducing *e*-folding depth. For example, figures 4.8 and 4.9 show that for a windpacked snow compared to a first-year sea ice a relative change in *e*-folding depth to 22% and 20% of the original *e*-folding depth respectively occurs, for a black carbon increase from 1 to 50 ng g^{-1}. Researchers studying photobiology and photochemistry of snow and sea ice who require light penetration information can use figure 4.2 as a rough rule to calculate how a change in black carbon may change the light penetration depth of solar radiation.

4.4.3 "Optically thick snow and sea ice"

For some of the calculations presented here a thickness of 10 m is used to ensure optically thick snow and sea ice is achieved and thus the snow/sea ice is independent of the underlying medium to enable comparison between snow and sea ice types. France et al. (2011) report that a snowpack is optically thick after 3–4 *e*-folding depths. For the majority of snowpacks examined here the snow would be optically thick at about 1 m.

However, for snow with a very small scattering cross-section (<1 m^2 kg^{-1}) or small black carbon mass-ratio (<5 ng g^{-1}), the thickness at which optically thick occurs increases to over 2 m (but less than 10 m). In the case of sea ice optically thick would occur before a thickness of 5 m, increasing to 10 m for the small densities, scattering cross-section (<0.025 m^2 kg^{-1}) or black carbon mass-ratios (<5 ng g^{-1}). For all optical properties in the work in this chapter the 10 m thickness is sufficient

for the optically thick approximation.

4.4.4 The impact of climate change

The 2013 IPCC report describes potential changes that may occur to snow cover and sea ice as a result of climate change. There has been a significant decrease in Arctic sea ice extent equating to –3.8% a decade, with Antarctica showing no statistically significant trend (IPCC, 2013). The most noticeable change in the Arctic is the decrease in summer sea ice extent (–13.7% a decade), which has lead to a decrease in multi-year sea ice in favour of first-year sea ice (IPCC, 2013). As shown here, first-year ice is more responsive to black carbon additions than the multi-year ice, which could potentially exacerbate sea ice melting. Furthermore as first-year ice transforms into melting ice it becomes even more responsive to black carbon additions, further exacerbating sea ice melting.

The case for snow is slightly more complicated. Since the early 20^{th} century snow covered area in the northern hemisphere has declined in spring and summer but not substantially in winter. Generally there has been a decrease in old multi-year, compacted or windblown snow and an increase in cold polar snow in some areas, or an increase in wet melting snow in areas where a decrease in snow covered area occurs (IPCC, 2013). An increase in melting snow will lead to snow which is more responsive to black carbon, further exacerbating melting. Conversely, an increase in cold polar snow will result in snow which is less responsive to black carbon.

4.4.5 Model limitations and sensitivity

The calculations presented here show the effects that changes in scattering cross-section of snow and sea ice have on the e-folding depth and albedo response to increased mass-ratio of black carbon. The calculations assumed the asymmetry parameter, g, and the optical properties of black carbon were unchanged with snow and sea ice type. The effect of changing these properties is considered to be secondary to the effect of changing black carbon mass-ratio, scattering cross-section and density. Uncertainties in the optical properties of the particulate black carbon used for calculations were discussed in chapter 2.

The value of the asymmetry parameter, g, was 0.89 for snow (Warren and Wiscombe, 1980) and 0.98 for sea ice (Mobley et al., 1998). Warren and Wiscombe (1980) show using exact Mie calculations for wavelengths less than 1000 nm g is practically invariant with wavelength ($g \approx 0.89$) for snow. Mobley et al. (1998) calculated asymmetry parameters for sea ice from Mie calculations that gave a range from 0.96 to 0.99, based on air bubble content, with a lower bubble content giving a higher g value, the most likely value is 0.98. The values we use here are therefore commonly reported as the most likely values for snow/sea ice at the wavelengths investigated. Small changes in g (± 0.005) have very little effect on the albedo and e-folding depths reported, as shown by France et al. (2012) for snow and chapter 3 for sea ice. The effects of changing g by larger amounts is investigated in chapter 6, section 6.4.1.3.

4.5 Conclusions

The response of albedo of snow and sea ice to increased mass-ratios of black carbon is dependent on the type of snow and sea ice. A snow or sea ice with a large scattering cross-section, e.g. a cold polar snow or a multi-year sea ice, is less responsive to black carbon than a melting snow or sea ice. The relative change in albedo owing to increasing black carbon is less in snow than sea ice. For an increase of black carbon from 1 to 50 ng g^{-1} a relative change in albedo of 76% occurs for melting sea ice compared to 30% for multi-year ice, 11% for melting snow and 3% for cold polar snow. In the case of e-folding depth the snow and sea ice type has very little effect on the relative response due to increased black carbon. Current climate change is leading to a decrease in multi-year sea ice and an increase in first-year/melting sea ice, which would be more responsive to black carbon, potentially exacerbating sea ice melting rates.

Chapter 5

Initial experiments with a sea ice simulator

The work presented in this chapter explains the set up and design of the sea ice simulator and initial results from measuring simulated sea ice properties. The initial design of the sea ice simulator was by Martin King, although I was also involved in aspects of the design. The building of components for the sea ice simulator was principally done by our science engineer, Jerry Morris. I undertook testing of all components, evolving methods for growing realistic sea ice and measuring of sea ice properties.

5.1 Introduction

Chapters 2–4 have described results from radiative-transfer calculations using the TUV-snow model to investigate the effects of anthropogenic pollution, mainly black carbon, on snow and sea ice albedo and light penetration depth. The TUV-snow model is highly advantageous as a vast range of parameters can be explored through knowledge of only the bulk physical and optical properties of the snow/sea ice. However, to increase certainty in the TUV-snow model it must be validated to show it accurately represents reality. The TUV-snow model has been shown to be accurate in lab experiments with snow by Phillips and Simpson (2005) but has never been validated for sea ice. Ideally, validation would be carried out in the field. However, field excursions on sea ice are expensive, often highly dangerous and limited to the

accessible sea ice. To validate the TUV-snow model for sea ice a sea ice simulator has been developed allowing replication of a natural sea ice environment under controlled conditions with real ice. Chapters 5 and 6 will describe initial experiments with the Royal Holloway sea ice simulator. The purpose of this chapter, chapter 5, is to describe the sea ice simulator design and development and describe results from initial ice growth experiments, which can be used to characterise the sea ice being grown in the simulator. Chapter 6 will move on to experiments investigating how simulated sea ice responds to black carbon, results from which can be used for TUV-snow model validation.

Sea ice simulators have previously been developed around the world on a variety of scales for different applications. Large scale sea ice simulators include the United States Cold Regions Research and Engineering Laboratory (CRREL) Ice Engineering Facility, the Arctic Environmental Test Basin in Germany, the Aalto University Ice Tank, Finland and the Sea ice Environmental Research Facility (SERF) at the University of Manitoba, Canada. The Ice Engineering Facility at CRREL consists of an inside refrigerated towing tank filled with artificial seawater measuring 37 × 9 × 2.4 m, the lowest temperature achievable is –24°C, with ice able to grow to 2–15 cm thick. The facility is used to study mechanical behaviour of sea ice, study ice structural interactions and measure ice floes (e.g. Arcone et al. (1986); Swift et al. (1992); Beaven et al. (1995); Shen et al. (2004); Buist et al. (2011)). The Arctic Environmental Test Basin is an indoor ice tank measuring 30 × 6 × 1.2 m where temperatures down to –15°C can be created. The facility includes both wave makers and current generators and is used to study Arctic marine biology and chemistry (e.g.Krembs et al. (2001); Mock et al. (2002); Tison et al. (2002); Papadimitriou et al. (2003)). The Interdisciplinary Ice Tank Experiment (INTERICE I, II and III) used the Arctic Environmental Test Basin (e.g. Eicken et al. (1998); Haas et al. (1999)). The Aalto University Ice Tank is an indoor multipurpose basin (40 × 40 m), mainly used for ice model scale tests, it also includes a wave generator (e.g. Polach et al. (2013)). The Sea Ice Environmental Research Facility is a new outdoor seawater pool measuring 18.3 × 9.1 × 26 m and holding 380 m^3 of seawater, which is used to carry out mesocosm-scale studies (e.g. Isleifson et al. (2012); Hare et al. (2013)).

Medium-scale sea ice simulators include Perovich and Grenfell (1981) who formed sea ice in a cylindrical insulated tank measuring 0.61 m (high) × 0.95 m (diameter) at

temperatures of $-10 - -37^{\circ}$C to investigate the optical properties of a young sea ice. Weissenberger and Grossmann (1998) investigated the role of water circulation and wave action for incorperation of phytoplankton and bacteria using a 3 m^3 tank filled with sea water and placed in a deep freeze room.

Small-scale simulators involve only a few litres of seawater in a small container. Grossmann and Gleitz (1993) investigated microbial responses to sea-ice formation using 11 L of seawater in a plastic vessel with a magnetic stirrer, placed in a cold room at –5°C. Light et al. (2009) investigated hydrohalite in sea ice by placing NaCl solutions in insulated buckets in a cold room.

The scale of the simulator is directly related to the purpose it is required for. To investigate the effects of black carbon on sea ice albedo and light penetration depths a medium scale sea ice simulator will be utilised. The simulator is the first UK based medium scale sea ice simulator. The development of the sea ice simulator is described in this chapter, including the initial design to replicate the sea ice environment and the development of methods used to characterise the simulated ice's physical and optical properties.

5.2 Sea ice simulator design and development

The sea ice simulator is designed to replicate a natural sea ice environment as near as possible. To achieve this there are several key factors which the simulator must replicate:

- Polar temperatures
- The ocean (including seawater chemistry, circulation and energy balance)
- "Natural" shortwave illumination

Section 5.2 will describe how each of these concepts were addressed to create an artificial environment replicating the natural world. Figure 5.1 shows an overall photo of the sea ice simulator. The components shown in figure 5.1 will be explained in the subsequent sections.

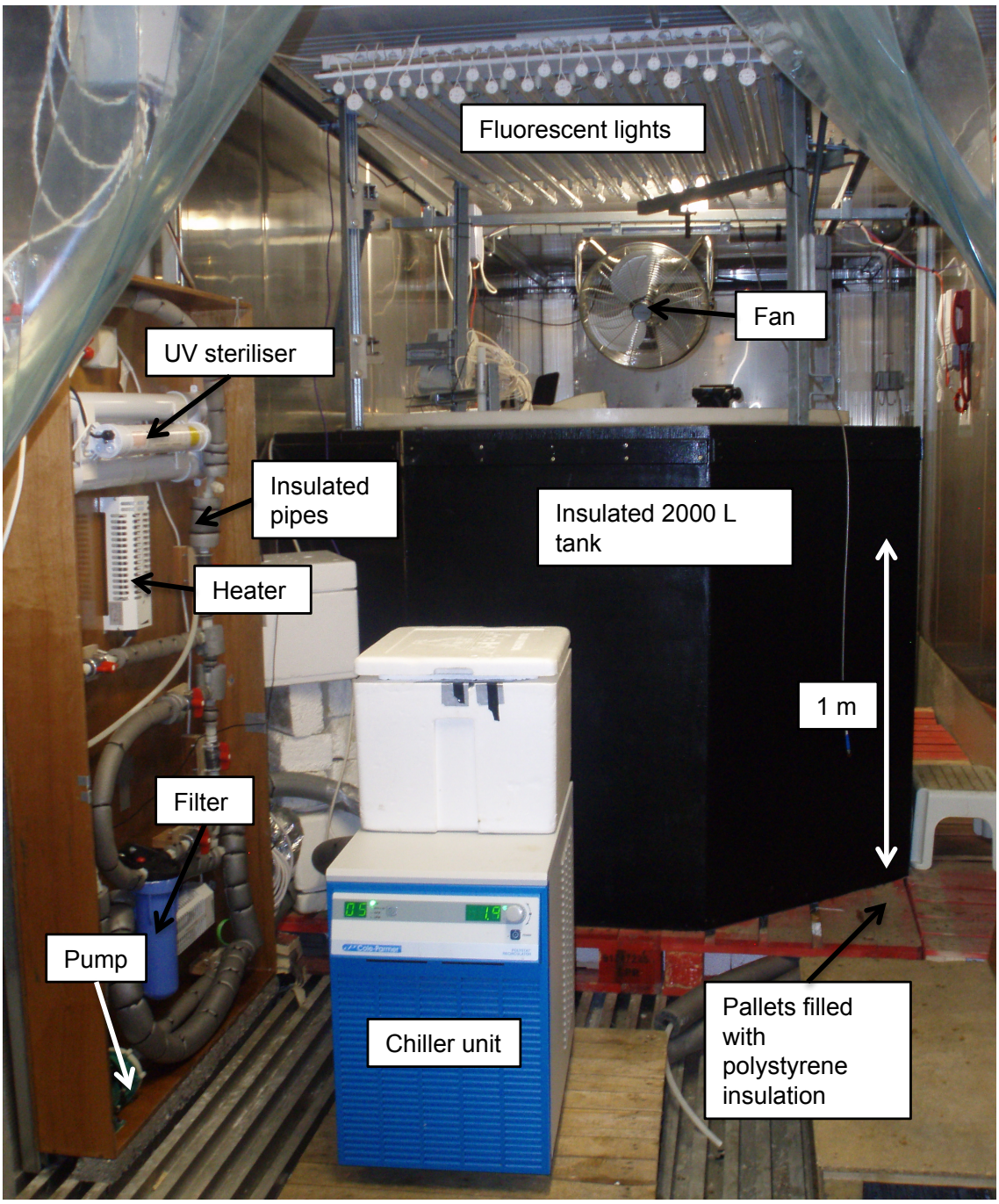

Figure 5.1 *– Set up of the sea ice simulator in a cold store. Sea ice is grown in the 2000 L tank placed on wooden pallets. A UV steriliser, filter and pump are contained in a heated wooden cabinet (to left of photo, shown uncovered), the roles of which are explained in section 5.2.2. Fluorescent lights above the tank provide illumination, as described in section 5.2.3. A fan above the tank blows cold air over the water surface, aiding freezing.*

5.2.1 Creating polar temperatures

The sea ice simulator is housed in a Daikin cold store (11.95d × 2.56h × 2.29w m), shown in figure 5.2, which has a stainless steel interior and an aluminium flooring.

Figure 5.2 *– Cold store used to house the sea ice simulator which can be temperature controlled down to –25°C.*

The cold store can be temperature controlled from 25°C to –25° C. Cold air is blown along the floor from the compressor end of the container housing the condensing unit. An air fan attached to the ceiling, shown in figure 5.1, blows air at the water surface, increasing flow of warm air away from the water surface to help freezing. The air flow around the container is shown in figure 5.3. To create sea ice the cold store was set to a temperature of –18°C, normally the temperature inside the container was a few °C above the set temperature (~ -15°C) due to the presence of heat producing components inside the container.

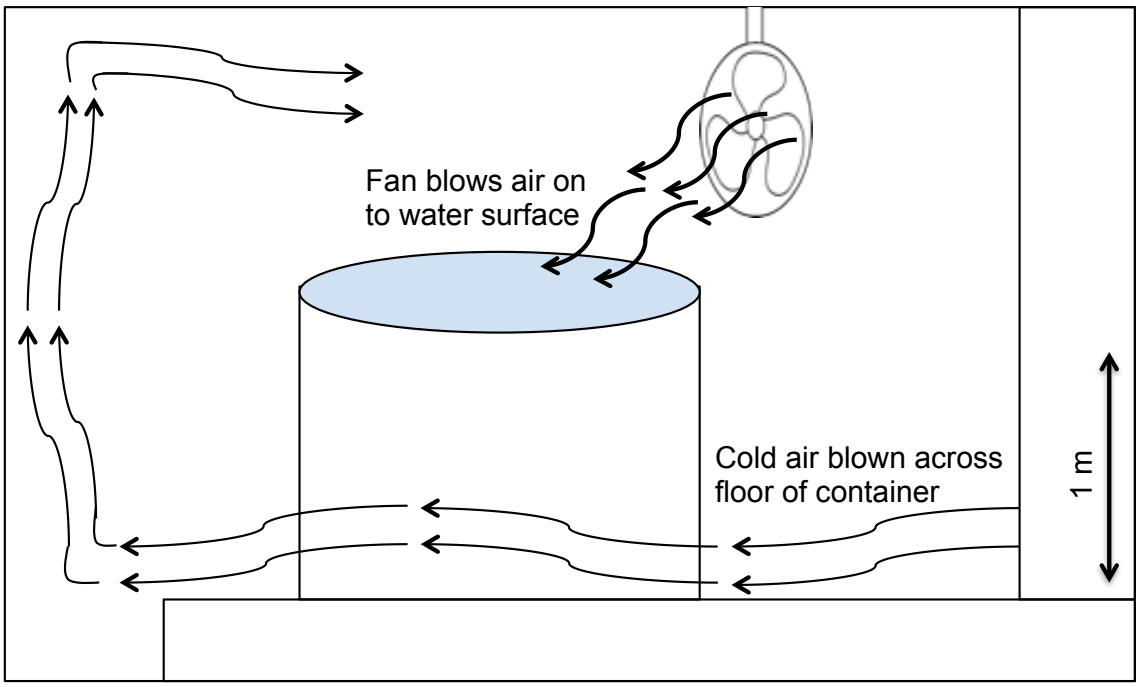

Figure 5.3 *– Air flow in the cold store including flow of cold air along floor of container and fan to blow cold air on to the water surface to increase heat flow from the water and aid freezing.*

5.2.2 Creating an artificial ocean

The following sections will describe developing a container to make sea ice, making seawater, ensuring a correct ocean energy balance is achieved and replicating ocean circulation. The schematic drawing and photos of figure 5.4 show an overview of the set up of the artificial ocean which will be subsequently described.

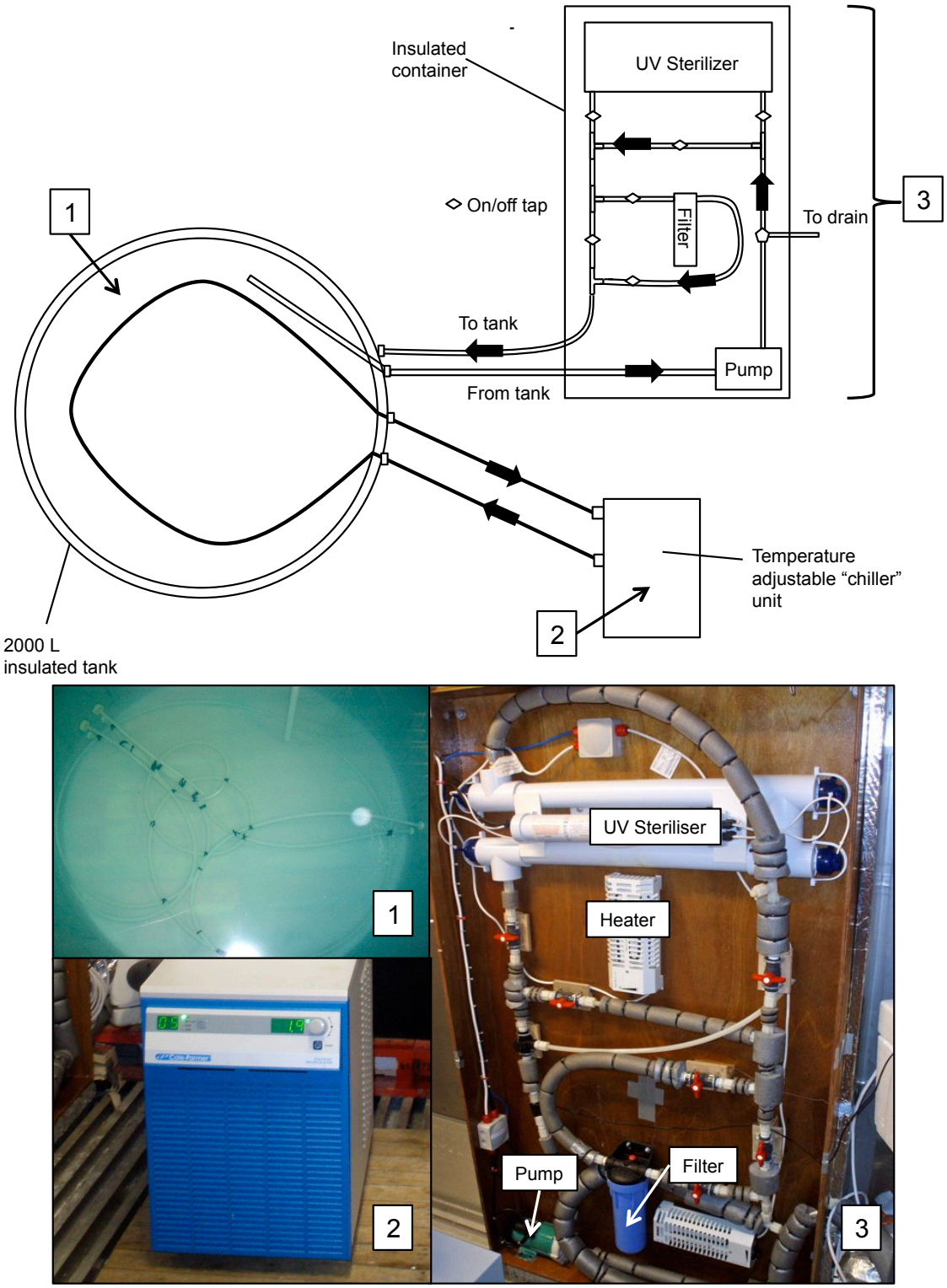

Figure 5.4 *– Set up of the artificial ocean including the tank with pipes running around base (1), chiller unit (2) and pump, UV steriliser and filter in a heated wooden cabinet (3).*

5.2.2.1 Housing an ocean

In the cold store sea ice is grown in a 2000 L polyethylene cylindrical white plastic tank (1.32 m high × 1.39 m diameter). Following the approach adopted by Perovich

and Grenfell (1981) a cylindrical design is utilised to help avoid stress build-up at particular locations. The tank is placed on wooden pallets filled with polystyrene and expanding foam to insulate the base of the tank. In the initial test design the tank was covered around the sides with "Space Blanket" insulation to stop freezing down the sides of the tank and represent a continuous ocean, as shown in figure 5.5.

Figure 5.5 *– Space Blanket insulation surrounding 2000 L polyethylene tank placed on wooden pallets*

Following successful initial tests the Space Blanket was later replaced with more permanent insulation including a 1 cm layer of black neoprene surrounding the tank sides. A metal "Unistrut" frame was developed around the tank to improve structural integrity by evenly applying stress to the tank, shown in figure 5.6.

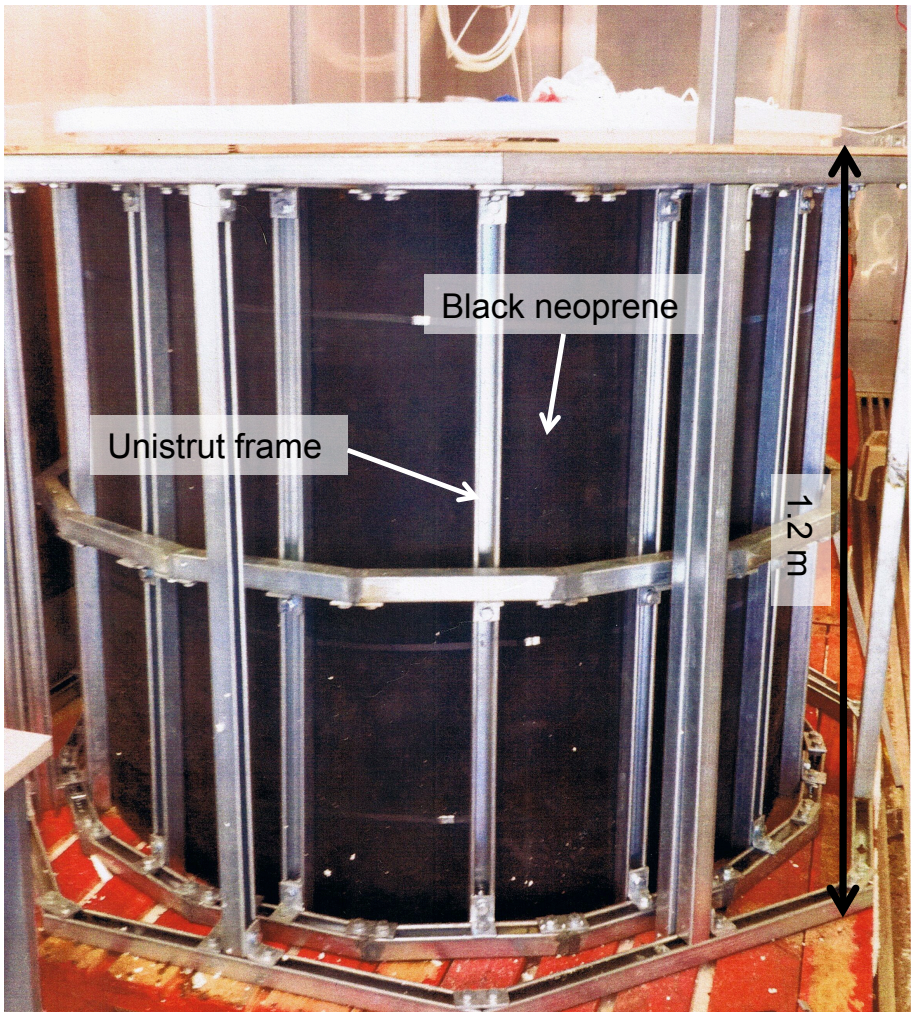

Figure 5.6 *– Unistrut frame surrounding 2000 L tank (covered in black neoprene) providing extra structural support.*

Wooden boards are fixed around the Unistrut structure with polystyrene insulation fitting between the wooden boards and the tank. The wood was then painted black with waterproof, mould resistant, paint as seen in figure 5.1. A cross-section through the tank wall is shown in figure 5.7 showing the positions of the polyethylene tank, polystyrene insulation, neoporene, Unistrut frame and surrounding wooden boards.

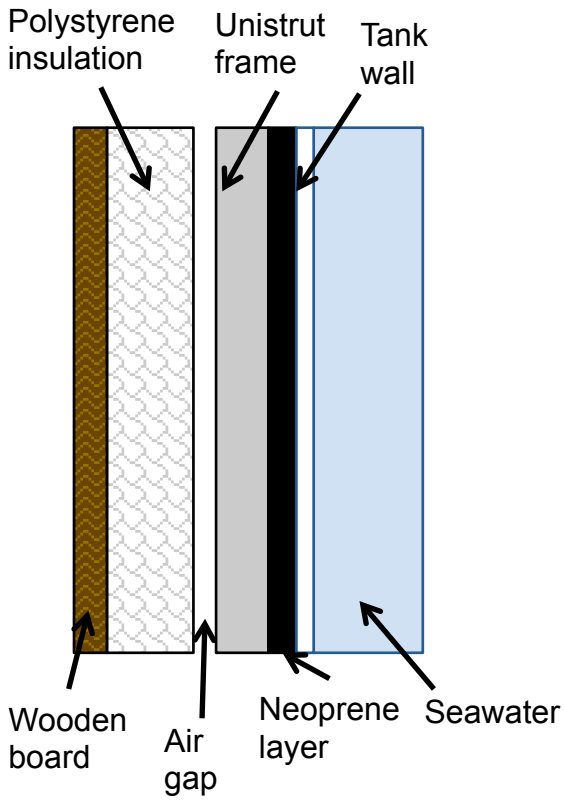

Figure 5.7 *– Cross-section through tank wall showing layers of neoprene, polystyrene insulation, unistrut and the wooden boards surrounding the tank.*

5.2.2.2 Creating seawater salinity

To create seawater, tap water was mixed with Tropic Marine. Tropic Marine is a synthetic sea salt mixture containing over 70 elements in the natural concentrations of the ocean. Atkinson and Bingman (1997) analysed the elemental composition of several commercial synthetic sea salt mixtures, including Tropic Marine, in comparison to typical tropical seawater. Major cations and anions of Tropic Marine were within 10% of seawater. Previous investigations with sea ice simulators have used NaCl solutions to create artificial seawater e.g. Perovich and Grenfell (1981), Haas et al. (1999), Tison et al. (2002) and Light et al. (2009) or most commonly synthetic sea salt mixtures e.g. Krembs et al. (2001), Mock et al. (2002), Papadimitriou et al. (2003) and Hare et al. (2013). Rarely, natural seawater is used e.g. Grossmann and Gleitz (1993), however this was a very small scale biological experiment. The use of Tropic Marine provides a very good approximation of seawater which is suitable for investigating effects of black carbon on sea ice.

Average Arctic ocean salinity is around 31–32 Practical salinity units (PSU) (Boyer

et al., 2013). The practical salinity scale, units PSU, was defined by Dauphinee et al. (1981) and adopted by UNESCO (United Nations Educational, Scientific and Cultural Organisation) as a standard measure for seawater salinity.

To ascertain the concentration of Tropic Marine required for a salinity of 31–32 PSU know masses of Tropic Marine were added to a known volume of tap water. Solutions were also made up with pure water to test if tap water affected salinity. The salinity of each solution was measured using a Fisher Scientific seawater refractometer. Figure 5.8 shows the measured salinity of each solution. For a seawater salinity of 31–32 PSU in the 2000 L tank 74 kg of Tropic Marine is required. Figure 5.8 shows there is negligable difference between tap water and pure water; thus tap water is used in the simulator as it is far easier to obtain in the large quantities required.

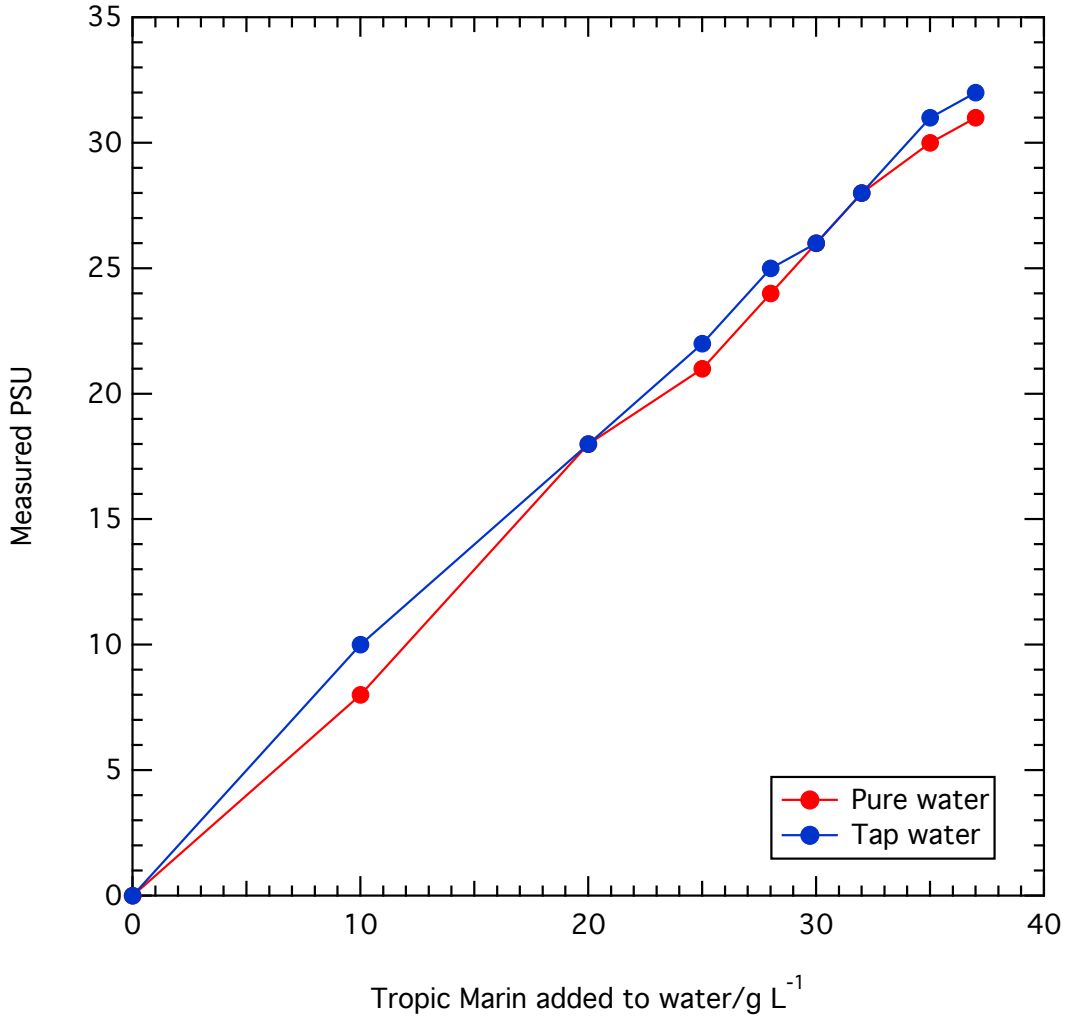

Figure 5.8 *– Measured salinity (PSU) obtained from known concentration of Tropic Marine in tap water and pure water.*

To prevent algae growth in the artificial seawater it is pumped through a UV steriliser,

shown in figure 5.4. The water is also pumped through a 10 μm filter to remove any particulate impurities, also shown in figure 5.4. Tropic Marine also includes limited nitrate and phosphate, required for algae growth.

5.2.2.3 Replicating ocean energy balance

Sea ice formation in the simulator needs to replicate natural formation, thus a correct heat balance must be created. Naturally where sea ice forms the air temperature is lower than ocean temperature, causing cooling and freezing of the ocean surface (Eicken, 2003). To ensure ice only forms at the tank surface, the sides and base of the tank are insulated as discussed in section 5.2.2.1. A pipe is also run around the bottom of the tank, shown in figure 5.4, picture 1, connected to a NESLAB Merlin M150 chiller unit shown in figure 5.4, picture 2. The chiller unit contains a 50% water and 50% clear glycol solution which is pumped around the pipe at the base of the tank in a closed system at a constant temperature, above freezing, warming the water at the base of the tank to prevent freezing and help even ice growth. The method of a closed loop system to heat the bottom of the tank in a sea ice simulator is also used by Hare et al. (2013).

5.2.2.4 Replicating ocean circulation

Natural seawater is continuously circulating around an ocean. To create circulation within the tank an Iwaki MD-10 pump circulates water at $\sim$10 L min^{-1} pumping water out near the edge of the base of the tank as seen in figure 5.4 and returning it through a tube to the centre of the base. Circulation of water prevents stratification of the water below the ice. The pump and the filter and UV steriliser, mentioned previously, are all housed in a wooden container containing electric heaters to prevent the seawater flowing through the pipes in the container from freezing. The pipes are also all insulated with foam. A uncovered photo of the container is shown in figure 5.4, photo 3. Taps on the pipes can control the flow of water through various components in the container. During ice formation the wooden container is covered in 5 cm thick foam insulation.

5.2.3 Creating natural illumination

Illumination replicating shortwave solar wavelengths (350–650 nm) is required for investigations of black carbon effects on reflectance and *e*-folding depth. As both reflectance and *e*-folding depth are relative measurements, the absolute intensity of the radiation is unimportant. Illumination is provided, as shown in figure 5.9, with a set of twenty Daystar daylight simulation fluorescent tubes and five sun-bed ultraviolet tube lights. These are placed directly above the tank to provide a isotropic illumination source. The light was further diffused by white boards placed around the edges of the tank. Using a isotropic light source is easier to replicate using the TUV-snow model during the model validation process in chapter 6. Furthermore if a beam of light is used instead of a isotropic source then light will scatter away as it enters the medium, lowering albedo, while if all the sample is illuminated by a isotropic source, albedo will be higher.

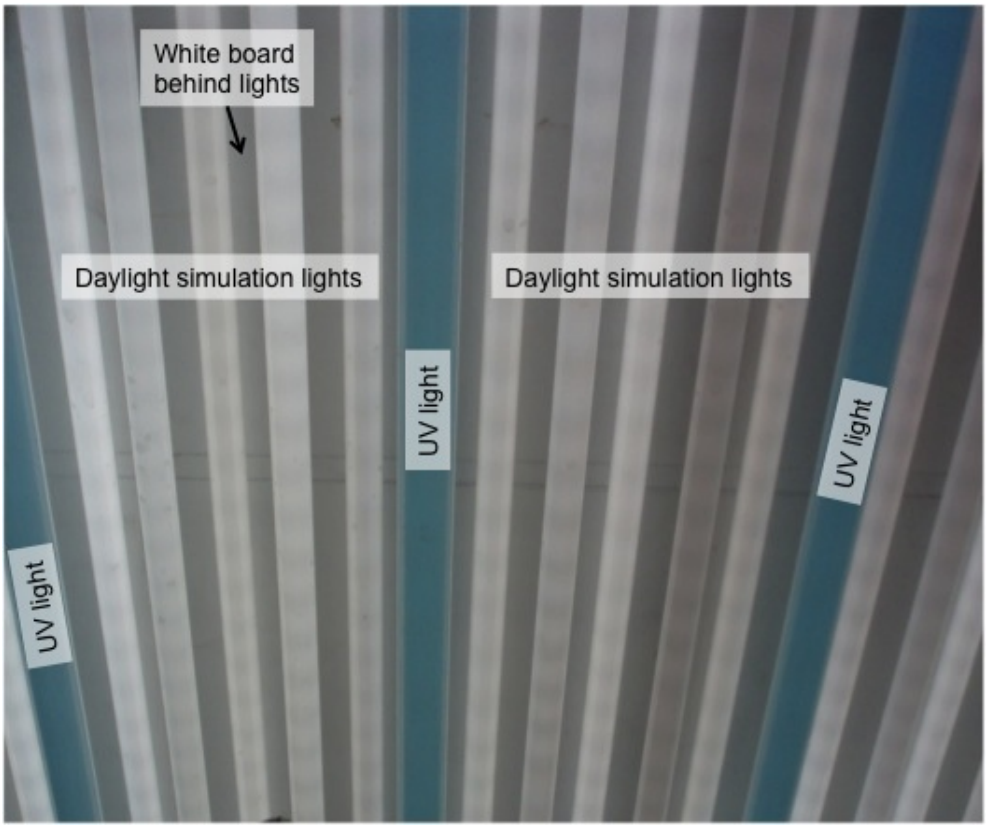

Figure 5.9 *– Daylight simulation and ultraviolet fluorescent lights providing isotropic shortwave illumination.*

5.3 Development of techniques for measuring sea ice physical and optical properties

To form ice in the sea ice simulator the simulator is set up as shown in figure 5.1 and the temperature in the cold store set to an air temperature of -18°C (achieving ~ -15°C inside the store). Ice forms at the surface after ∼24 hours with 30–40 cm forming after three weeks. To use the simulated sea ice for validation of the TUV-snow radiative-transfer model the sea ice physical and optical properties must be characterised. The set up of the sea ice simulator for measuring temperature, nadir reflectance and light *e*-folding depth is shown in figure 5.10. The procedures for measuring each of these properties and for measuring the sea ice salinity and density via ice cores are outlined in the subsequent sections. Temperature and the reflectance of the ice was measured regularly during ice growth. The *e*-folding depth was measured once the ice reflectance had become constant with time; usually when ice thickness approximated 30–40 cm. Ice cores were taken once all other measurements were complete as this affected the ice surface.

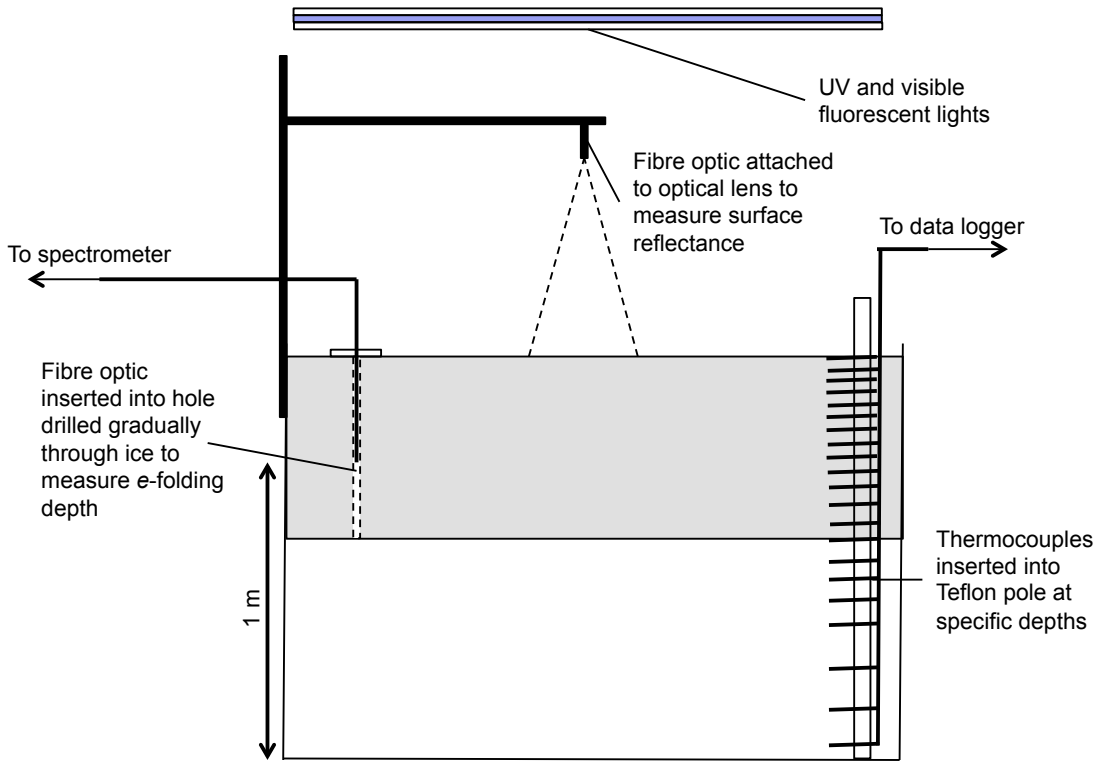

Figure 5.10 *– Set-up of sea ice simulator for measuring sea ice properties. Thermocouples to measure temperature profile through ice and water shown, not at exact depths. Fibre optic inserted into drilled hole to measure e-folding depth. Fibre optic fixed above ice surface to measure nadir reflectance. UV and visible lights above ice provide isotropic shortwave illumination.*

5.3.1 Measuring sea ice reflectance

To measure sea ice reflectance the radiance of light from the sea ice surface measured at nadir is ratioed to the radiance from a reference Lambertian reflector at nadir (a Spectralon panel). Spectralon reference panels are designed to be perfect Lambertian reflectors. A true Lambertian reflector reflects 100% of incident light equally in all directions. In reality the Spectralon panel used in these experiments deviates slightly away from being a true Lambertian reflector, with deviations of up to 8% (Sandmeier et al., 1998). Before surface radiance measurements are taken the fluorescent lights were left on for at least an hour to allow them to warm up to provide a steady light intensity. Radiance was measured via a 400 μm xsr fibre optic coupled to an Ocean Optics USB 2000 spectrometer and connected to a toughbook computer where Ocean Optics software was used to measure light intensity spectra. The Ocean Optics spectrometer measured wavelengths from 200–1000 nm with a resolution of 4 nm at a wavelength of 500 nm. The fibre optic was situated $\sim$40 cm above the sea ice

surface at nadir, focussed on the sea ice surface. Initially the area of the field of view of the fibre optic was only 1.8 cm^2 and therefore did not contain a representative area of the sea ice. A ∼7.0 cm^2 circular Spectralon reference panel was used to ratio these initial sea ice radiance measurements to.

To cover a more representative sample of the ice surface an optical lens was attached to the fibre optic as shown in figure 5.10. The optical lens provides a view footprint covering an area ∼315 cm^2. To calculate reflectance using the optical lens a larger Spectralon panel was required (25×25 cm). The panel was positioned on a perspex tray with adjustable legs and a circular spirit level to ensure the panel was flat, as shown in figure 5.11

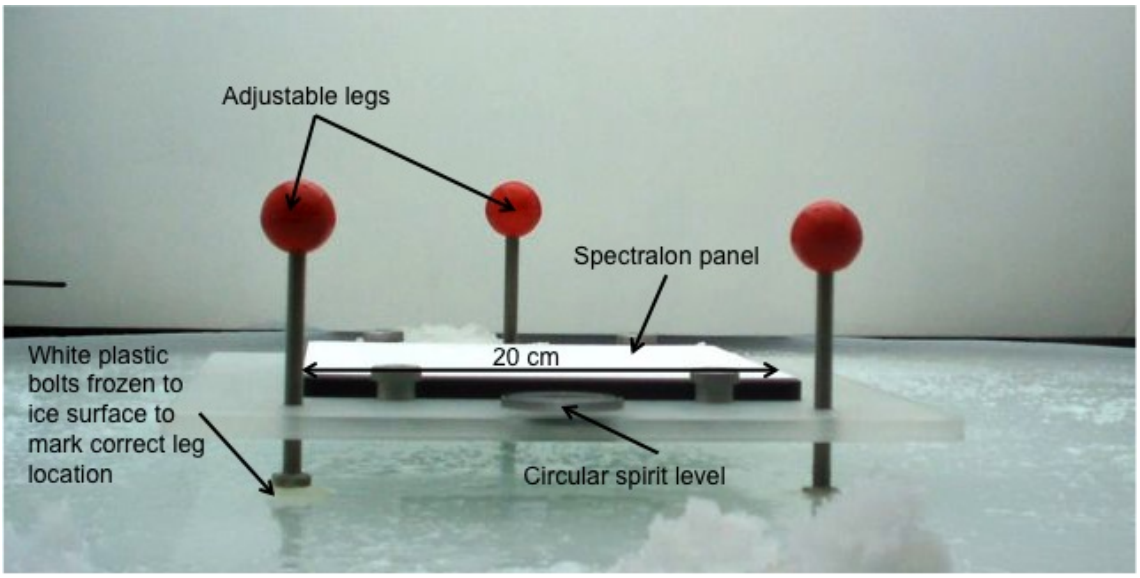

Figure 5.11 *– Spectralon panel placed on ice surface for reference measurement in same location as ice surface radiance measurements taken.*

The radiance of the ice surface was measured three times with a reference measurement taken between each ice intensity measurement. The panel was placed in the same location that the ice surface radiance was measured. To ensure the optical lens was centred on the Spectralon panel a laser was shone down the optic on to the sea ice surface and the panel positioned so the entire laser light was on the panel, as shown in figure 5.12.

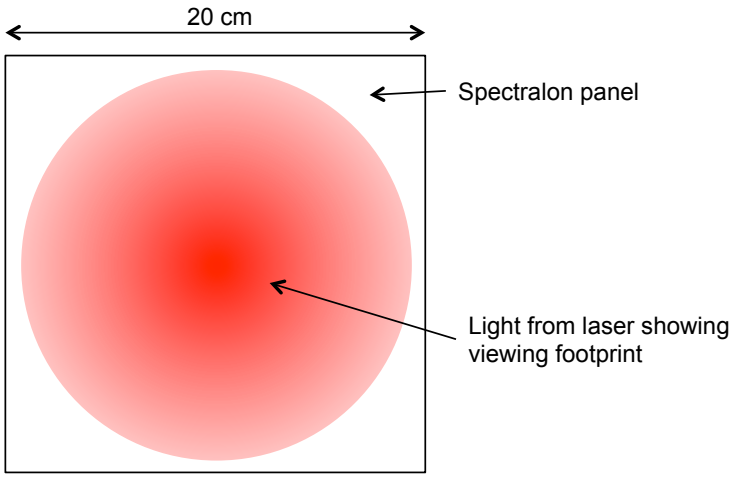

Figure 5.12 *– Laser on Spectralon panel showing viewing footprint of optic lens to find correct location for the Spectralon panel.*

The correct panel location was then marked with white plastic bolts frozen onto the ice to ensure the panel was placed in the same location everyday. Radiance measurements of the ice and panel were taken three times daily to enable calculation of a standard deviation of the reflectance. Integration times were used which gave both saturated and non-saturated spectra (a typical saturated and non-saturated spectra is shown in figure 5.14) to provide a better signal:noise ratio at wavelengths with low light intensities. Dark measurements were taken at the end of the measurements to correct for electrical noise by placing a cap over the optical lens to stop light entering. Reflectance measurements of both the ice and the Spectralon reference panel were taken with white panels in place surrounding the sides of the tank to provide a isotropic environment. One side of the tank did not have a side panel in place to allow access to the ice to remove the Spectralon reference panel. Figure 5.13 shows the effect on the reflectance measurements through having all the panels in place and with one panel missing, showing there is no difference outside uncertainty.

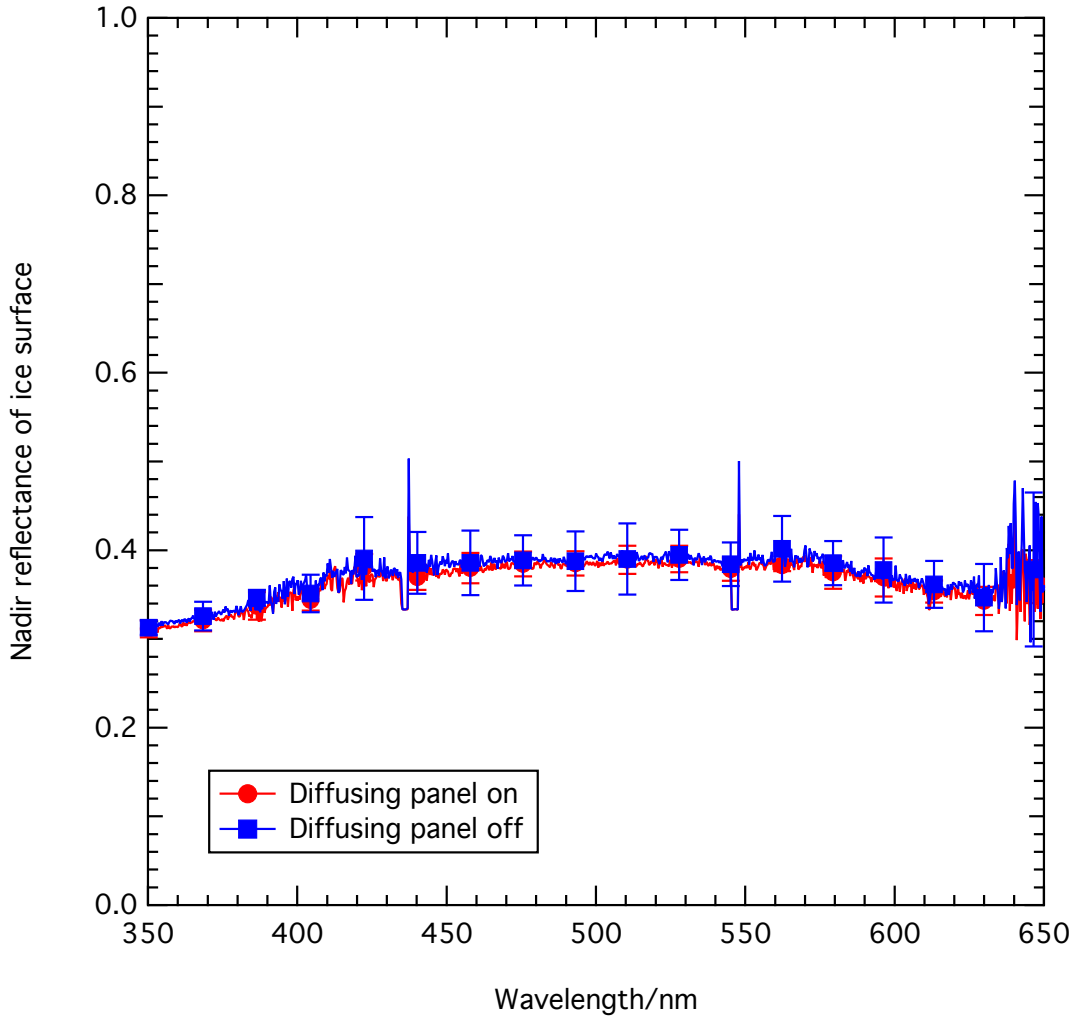

Figure 5.13 *– Effect on reflectance measurements with having one white side panel missing for access. Uncertainty bars show ± one standard deviation of five measurement repeats.*

To obtain nadir reflectance measurements from the raw radiance of the ice and panel measurements, the dark spectra are first deducted from both the saturated and non-saturated spectra for the ice and Spectralon panel surface radiance measurements. A second dark deduction for noise is made by deducting the average intensity of the first 100 pixels, wavelengths 179–216 nm, (where there should be no light) from all wavelengths for the ice and Spectralon panel measurements. Figure 5.14 shows a typical non-saturated and saturated spectra recorded from the ice. The spectra contain sharp peaks due to emission by the fluorescent lights. Reflectance was calculated at ∼10 nm intervals using the saturated and non-saturated values as shown in table 5.1. Wavelength intervals occurring where there was a distinct peak in the spectra were ignored, to reduce noise in derived reflectance values, hence the missing wavelengths in table 5.1. At each wavelength a dark-corrected saturated

or non-saturated ice surface radiance measurement was divided by the corresponding saturated or non-saturated reference Spectralon panel radiance measurement to derive a reflectance measurement. The procedure is completed for each of the three intensity measurement repeats providing three reflectance measurements, the average and standard deviation of which is then calculated providing an indictation of uncertainty.

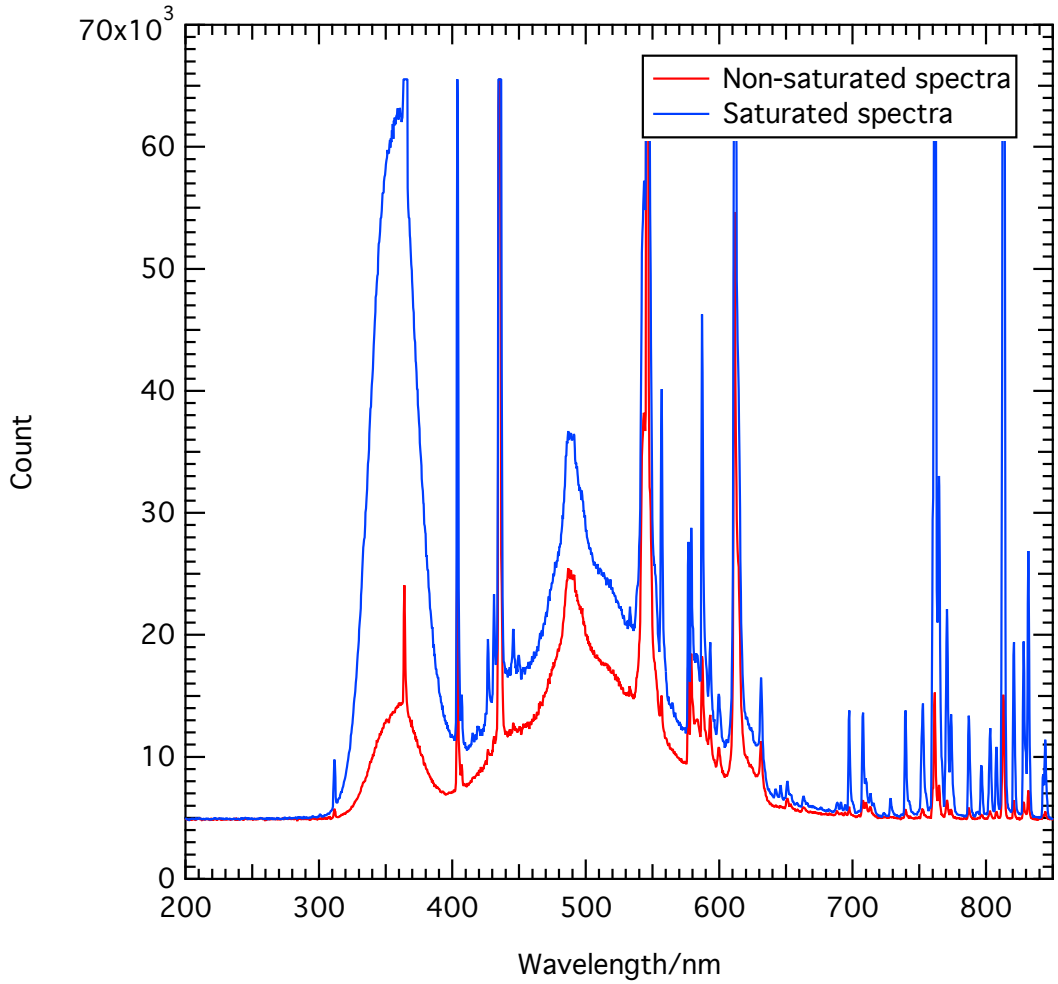

Figure 5.14 *– Typical raw sea ice surface non-saturated and saturated intensity spectra taken for reflectance measurements. Peaks are caused by atomic transitions of mercury in the fluorescent light source.*

Saturated wavelengths/nm	300, 310, 320, 330, 340, 350, 640, 660 670, 680, 720, 730, 750, 760, 780, 790
Non-saturated wavelengths/nm	370, 380, 390, 400, 420, 430, 450, 460 470, 480, 490, 500, 510, 520, 530, 540 560, 570, 600, 620, 630

Table 5.1 *– Wavelengths of non-saturated and saturated spectra used to calculate reflectance.*

5.3.2 Measuring sea ice *e*-folding depth

Measurements of the sea ice *e*-folding depth were initially conducted by freezing six fibre optics into the ice at specific depths (0, 2, 4, 6, 8, 10 cm) shown in figure 5.16 A. Light intensity through each fibre optic was measured and ratioed to the intensity recorded by the shallowest fibre optic. The fibre optics were first intercalibrated by placing all fibre optics at a depth of 6 cm into the water and recording the intensity from each fibre. Results using this "6 optic" method are shown in figure 5.17, the results using this method were consistently poor with the data showing weak trends; light would be expected to decrease exponentially into a medium. The *e*-folding depths calculated using this technique have a very large degree of uncertainty. The 6 optic method requires intercalibration of the optics, although several attempts were made at doing this under different conditions all results were poor, it is likely that the noise from using different optics results in poor quality data.

An alternative method for measuring *e*-folding depth was developed where *e*-folding depth is measured by drilling a single hole gradually through the ice in ∼5 cm increments. At each depth drilled the same fibre optic was inserted into the hole and the light intensity measured three times via an Ocean Optics spectrometer connected to a Panasonic Toughbook. A diffusing disk was placed around the fibre at the ice surface to ensure any light leaking down the drilled hole was isotropic, as shown in figure 5.15.

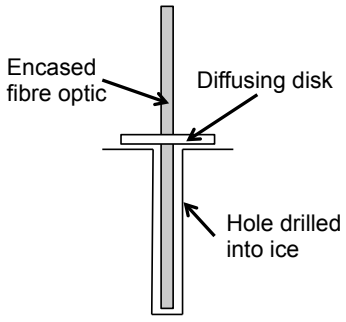

Figure 5.15 *– Set up of fibre optic for measuring e-folding depth down one hole with a diffusing disk placed around fibre optic at the ice surface to ensure any light entering the drilled hole was isotropic.*

Non-saturated and saturated light intensity spectra were recorded at each depth, three times, with different integration times used for different depths into the sea ice. Simultaneously to the light intensity in the hole being measured, the light intensity

of another fibre optic inside a teflon pot (to create isotropic conditions) at the ice surface was measured, to account for any change in the intensity of the fluorescent lights. The new "1 optic" set up for *e*-folding depth measurements is shown in figure 5.16 B.

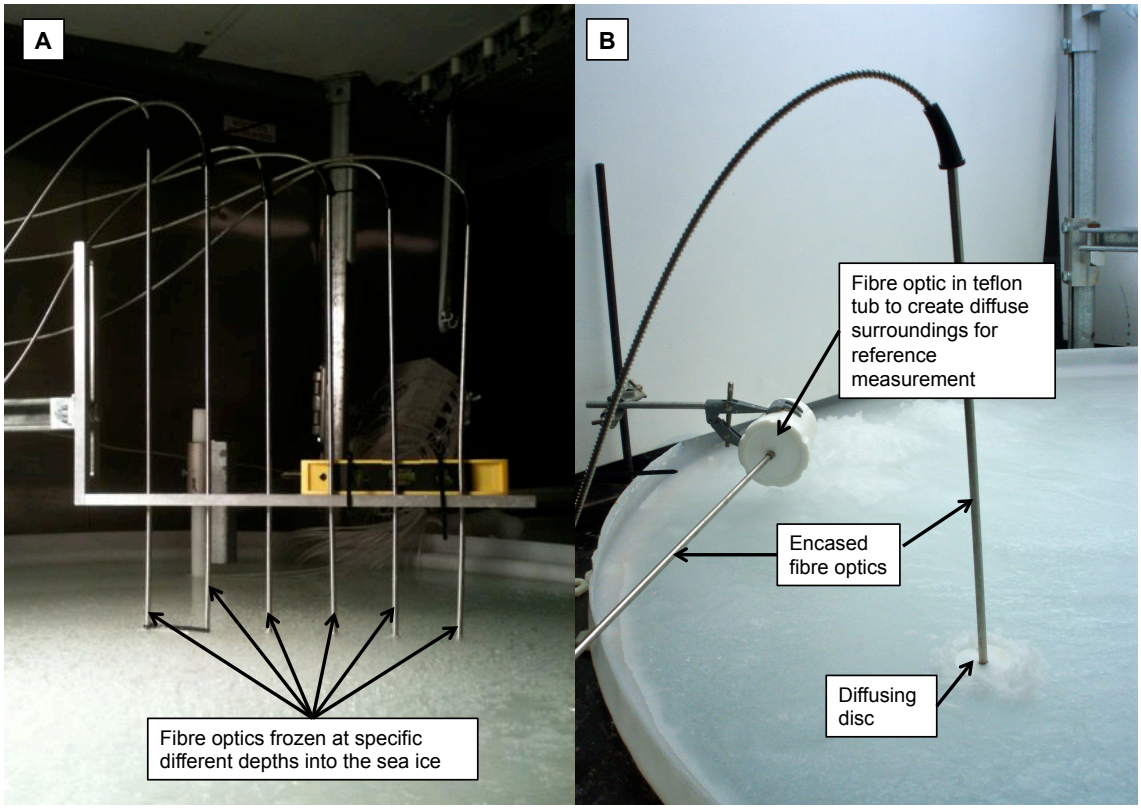

Figure 5.16 *– Comparison of e-folding depth measurements taken using six individual fibre optics frozen in the ice at different depths (A) versus a single optic placed in a hole gradually drilled in the ice (B).*

Figure 5.17 shows that results using the "1 optic" technique show a more consistently decreasing light intensity through the ice with a more consistent *e*-folding depth of 24–31 cm, compared to the large variation in *e*-folding depth calculated using the "six optic" technique. However, there is still a fair amount of spread around the exponential fit, although this improves with later measurements as human error is reduced (for example see figure 5.25). The single optic technique is advantageous as it eliminates the need for the fibre optic intercalibration, as only one fibre optic is required.

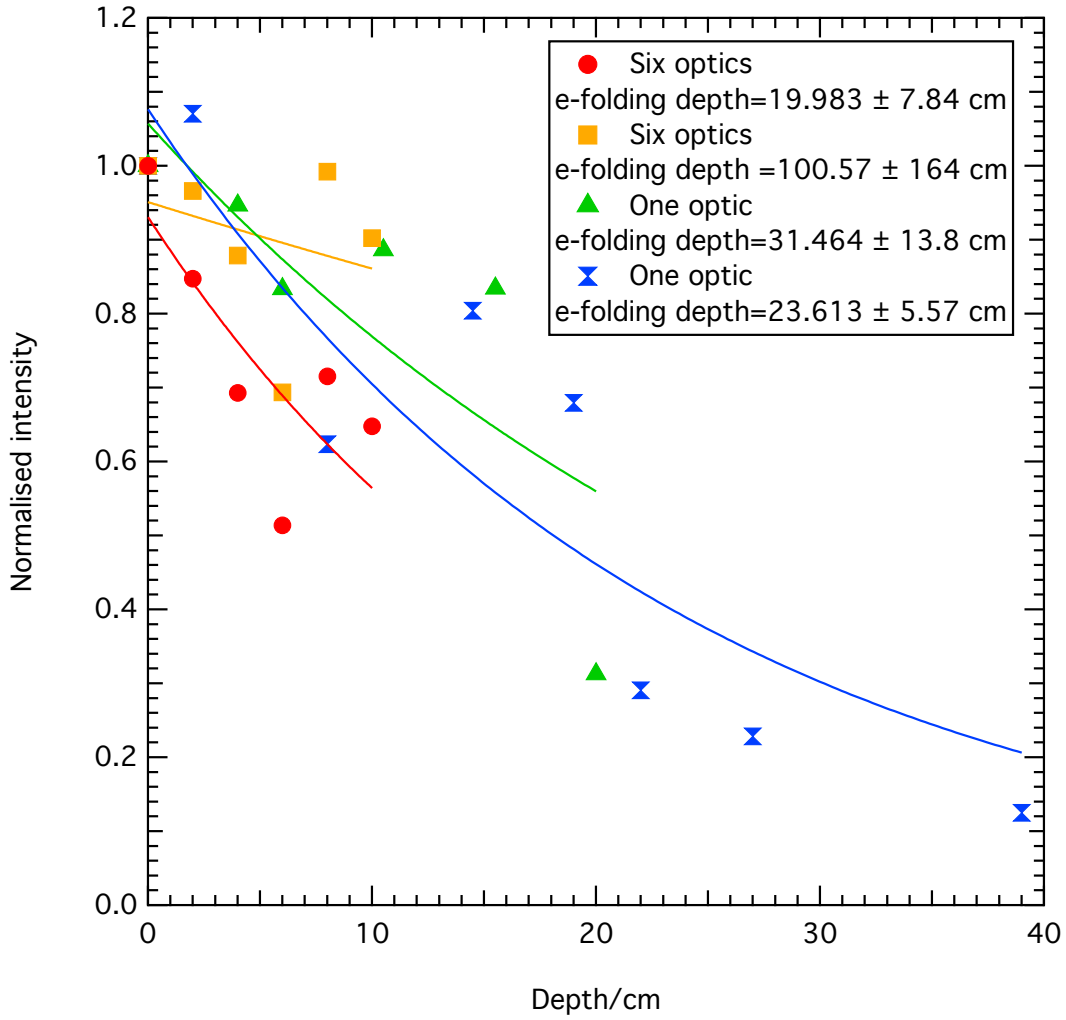

Figure 5.17 *– Comparison of e-folding depth measurements taken using six individual fibre optics technique versus a single fibre optic, at 500 nm.*

To calculate *e*-folding depth from the raw measurements of intensity at each depth firstly dark measurements taken at each integration time are deducted from all intensity measurements. A second dark deduction is carried out by deducting the average intensity of the first 100 pixels from all wavelengths. Light intensity at each depth is divided by the reference light intensity to account for any variation in light intensity from fluorescent lights, as demonstrated by equation 5.1. The referenced measurement at each depth, I_z, is then divided by the intensity at the first depth, $I_{z'}$, to derive relative intensity measurements, $\frac{I_z}{I_{z'}}$. Relative intensity measurements, $\frac{I_z}{I_{z'}}$, are plotted against depth measurements, z, (where the depth of the first measurement, z' is set to 0). An exponential fit is then fitted to the data. To calculate *e*-folding depth equation 5.2 is applied which can be rearranged to form equation 5.3, where ϵ is the *e*-folding depth, I_z is intensity at a specific depth, $I_{z'}$ is intensity at the shallowest depth, z is a

specific depth and z' is the shallowest depth.

$$I_z = \frac{I_{raw(z)} - I_{dk1} - I_{dk2}}{I_{ref}} \tag{5.1}$$

For each *e*-folding depth measurement light intensity was measured down three separate holes and *e*-folding depth calculated for each hole individually providing an indication of data consistency and uncertainty.

$$\frac{I_z}{I_{z'}} = e^{-\left(\frac{(z-z')}{\epsilon}\right)} \tag{5.2}$$

$$\epsilon = \frac{(z-z')}{-ln\left(\frac{I_z}{I_{z'}}\right)} \tag{5.3}$$

5.3.3 Measuring temperature profiles

Temperature profiles through the sea ice are recorded regularly during ice growth by a series of thermocouples, as used by Rabus and Echelmeyer (2002); Johnston and Timco (2002); Nomurai et al. (2006). Thermocouples are inserted into a teflon pole at depths of –1, 0, 1, 2, 3, 4, 5, 6, 7, 8, 11, 14, 17, 20, 23, 26, 29, 32, 35, 38, 43, 48, 58, 68, 78, 88, 98, 108, 118, 122 cm into the water (where –1 cm is 1 cm above the water surface), as shown in figure 5.10. The thermocouples are then frozen in place during ice formation. All thermocouples are wired to a control box which is connected to a data logger to measure the temperature of each thermocouple.

Thermocouple calibration and intercalibration was carried out prior to installation by inserting the thermocouples into a glycol/water bath of known temperature from 0—20°C and recording the temperature registered by each thermocouple. Corrections were then applied to account for differences between measured and actual temperature.

5.3.4 Determining sea ice properties by ice coring

Measurement of physical properties of sea ice is important to enable characterisation of the ice grown in the simulator to ensure it is realistic of natural sea ice. Physical properties measured include density, salinity and temperature from which brine salinity,

brine density and brine and air volume can be derived from equations presented by Cox and Weeks (1983). The density of sea ice is a product of the brine and air volume. Pure ice has a density of $\sim$1.0 g cm^{-3}. A sea ice with a high air volume will decrease density while increased brine volume will increase overall density. Sea ice density typically ranges from 0.72–0.94 g cm^{-3} (Timco and Frederking, 1996). The bulk salinity of the sea ice is a function of the brine volume and brine salinity. When sea ice freezes only pure water enters the ice matrix with salts left behind in brine pockets in the sea ice. Over time the brine drains out of the ice into the underlying seawater, lowering the bulk ice salinity (Eicken, 2003). The temperature of the ice will affect the brine salinity and freezing rates. As the temperature of the sea ice decreases, the freezing point of the brine is reached so pure water in the brine freezes resulting in a more saline, and consequently more dense, remaining brine, which will have a lower freezing point (Eicken, 2003).

Salinity and density of the sea ice was measured by taking cores of the ice, allowing characterisation of the sea ice. The corer design is shown in figure 5.18 and is based on a CRREL report on design of ice augers for shallow ice depth by Rand and Mellor (1985). The corer is a hollow cylindrical plastic tube with 3 cm internal diameter and walls 0.5 cm thick with helical groves around the sides to enable removal of ice from the drilled core. The cutting end of the corer is caped with stainless steel with a series of teeth to cut the ice. The top end of the corer attaches to a high torque and low speed drill. After a core was drilled through the ice it was immediately removed from the corer. To remove the core the top end of the corer is removed and a metal arm is inserted, shown in figure 5.19. The top end of this is fixed in place and the core can then be wound out the corer. Once removed the core is measured and photographed and then divided into $\sim$5 cm sections and its length and width accurately measured. Division of ice cores into sections was done quickly to minimise brine drainage, as suggested by Eicken et al. (2010). Each ice section was placed in a pre-weighed teflon tub and the mass recorded allowing the sea ice mass and hence density to be determined. Each sample was then left to melt and the salinity of the melted sample was measured using a seawater refractometer.

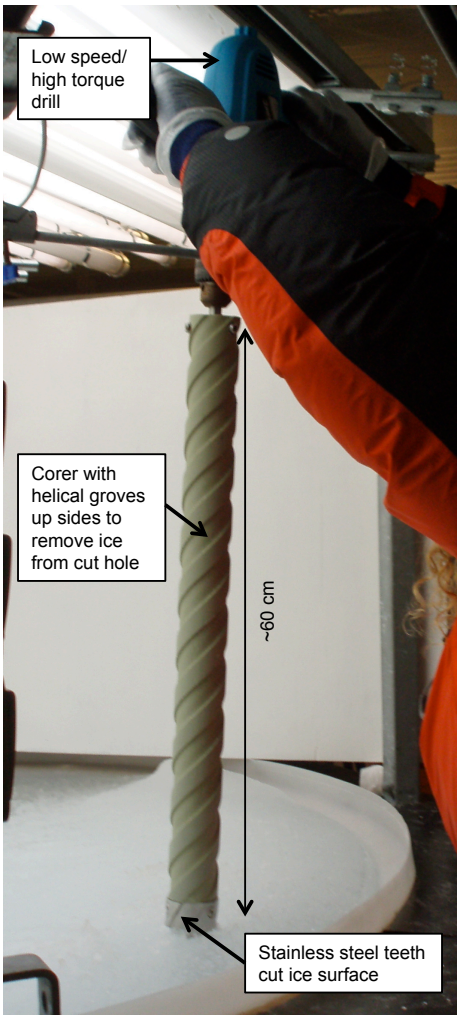

Figure 5.18 *– Taking ice cores using a low speed and high torque drill attached to an ice corer.*

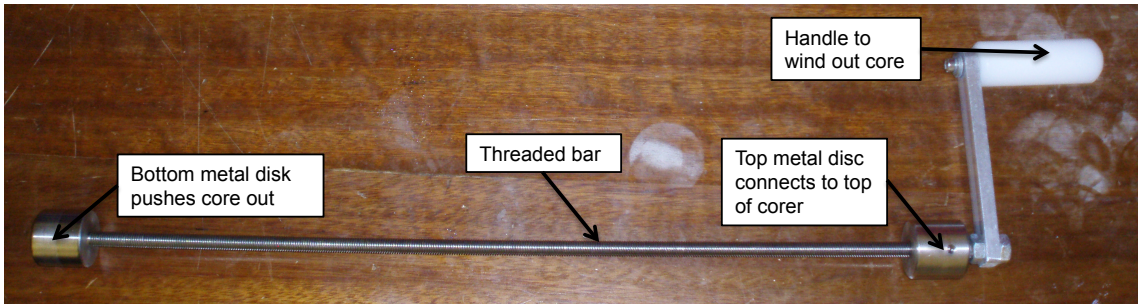

Figure 5.19 *– Tool to remove ice cores from corer, the top metal disk is attached to the corer and the bottom metal disk is wound down to extract the ice core from the corer.*

Cox and Weeks (1983) derived a series of equations for deriving air and brine volume fractions, brine salinity and brine density from knowledge of sea ice temperature, salinity and density.

To calculate the volume fraction of air, $\frac{V_a}{V}$, equation 5.4 is applied, where T is temperature, ρ is the density of the sea ice, ρ_i is the density of pure ice (determined by equation

5.5), S_{si} is the sea ice salinity and $F_2(T)$ and $F_1(T)$ are empirical polynomial functions where: $F_i(T) = a_i + b_i T + c_i T^2 + d_i T^3$, which is based on phase relations. Table 5.2 lists the coefficients required for the calculations from –22.9°C to –2°C. Above –2°C the derived data become increasingly inaccurate.

$$\frac{V_a}{V} = 1 - \frac{\rho}{\rho_i} + \rho S_{si} \frac{F_2(T)}{F_1(T)} \tag{5.4}$$

$$\rho_i = 0.917 - 1.403 \times 10^{-4} T \tag{5.5}$$

Table 5.2 – *Coefficients for polynomial function $F_1(T)$.*

$\mathbf{a_1}$	$\mathbf{b_1}$	$\mathbf{c_1}$	$\mathbf{d_1}$
–4.732	–22.45	–0.6397	–0.0174
$\mathbf{a_2}$	$\mathbf{b_2}$	$\mathbf{c_2}$	$\mathbf{d_2}$
0.08903	–0.01763	-5.33×10^{-4}	-8.801×10^{-6}

Using the volume fraction of air, $\frac{V_a}{V}$, the volume fraction of brine, $\frac{V_b}{V}$, can be calculated using equation 5.6

$$\frac{V_b}{V} = \left(1 - \frac{V_a}{V}\right) \frac{\rho_i S_{si}}{F_1(T) - \rho_i S_{si} F_2(T)} \tag{5.6}$$

The salinity of brine, S_b, can be determined by equation 5.7, where T is temperature of the sea ice.

$$S_b = \left(1 - \frac{54.11}{T}\right)^{-1} \times 1000, \tag{5.7}$$

The density of brine, ρ_b, can then be determined by equation 5.8

$$\rho_b = 1 + 8 \times 10^{-4} S_b \tag{5.8}$$

Application of the above equations enables the ice developed in the sea ice simulator to be well characterised.

5.4 Preliminary results

Section 5.4 will describe initial results from measurements of change in reflectance and temperature of growing sea ice and *e*-folding depth measurements and salinity and density measurements from ice cores taken after ice has grown to 30–40 cm thick.

5.4.1 Change in reflectance of freezing sea ice

Figure 5.20 shows photos taken during ice growth (white boards removed), showing that the largest change in reflectance occurs within the first few days of ice growth, however photos are of limited use to show true changes in reflectance.

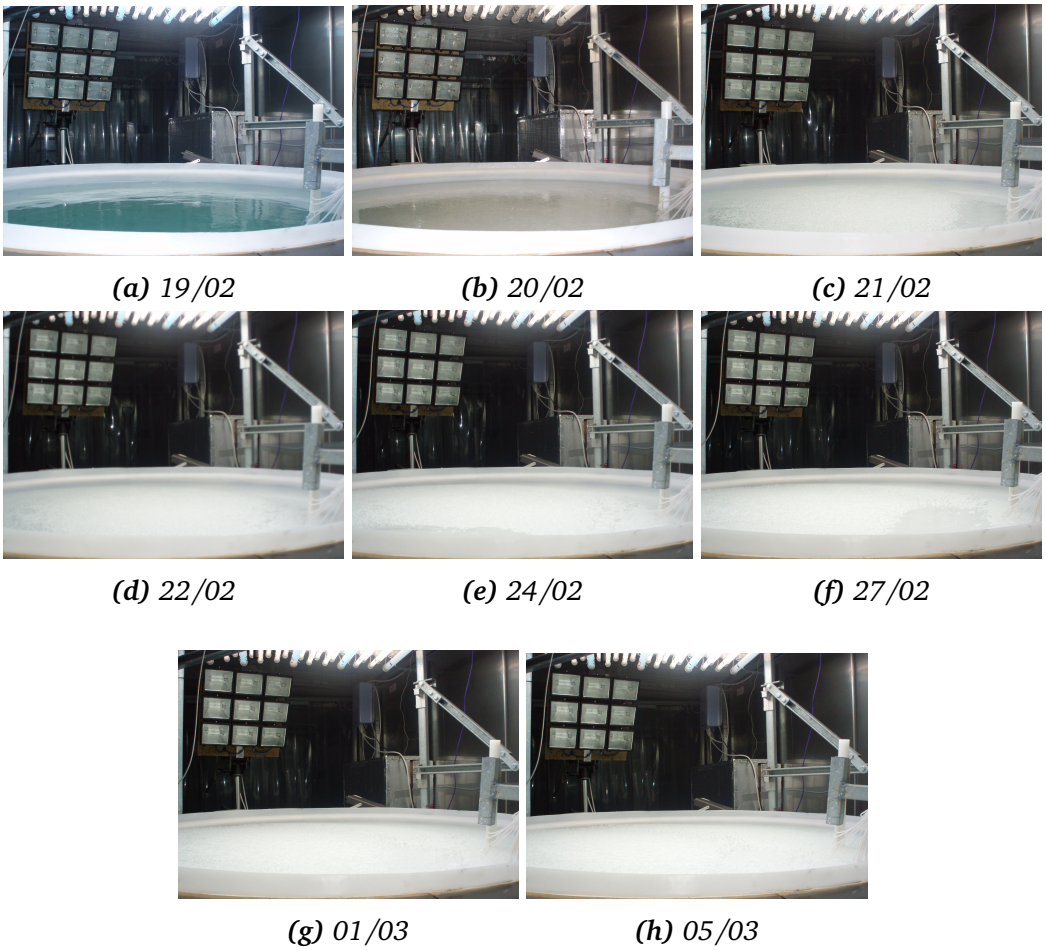

(a) *19/02* ***(b)*** *20/02* ***(c)*** *21/02*

(d) *22/02* ***(e)*** *24/02* ***(f)*** *27/02*

(g) *01/03* ***(h)*** *05/03*

Figure 5.20 *– Change in ice surface during freezing and ice growth up to ∼40 cm, diffusing boards removed.*

Figure 5.21 shows an example of the daily reflectance measured during sea ice growth over 18 days, at a wavelength of 500 nm.

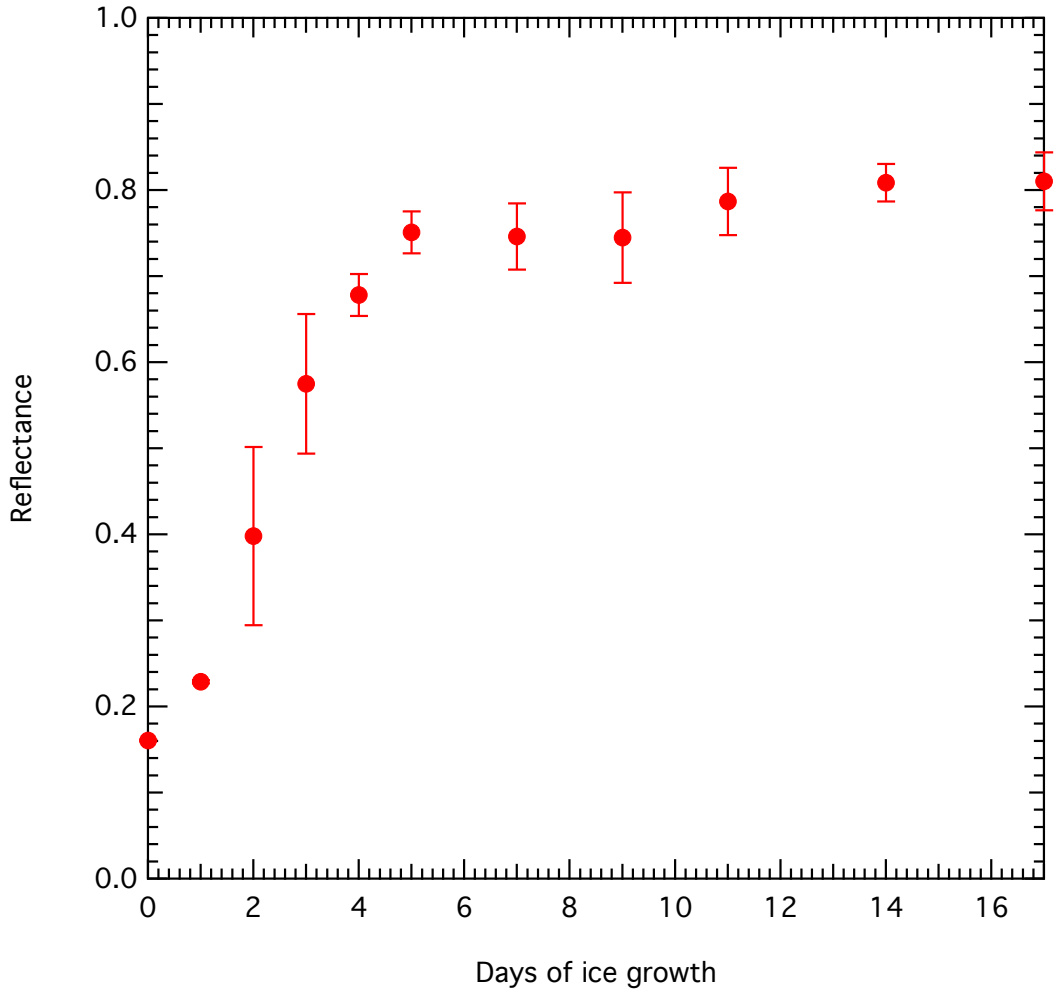

Figure 5.21 *– Change in reflectance of ice during ice growth at a wavelength of 500 nm. Error bars show variation with three repeat measurements.*

Figure 5.21 shows that reflectance increases for the first ∼10 days of freezing before plateauing around 0.8. At this stage the ice is still growing but reflectance becomes independent of ice thickness, so the ice has reached "optical thickness", at this stage *e*-folding depth measurements can be taken. The uncertainty bars on figure 5.21 represent one standard deviation of the three repeated measurements of reflectance, calculated from the three repetitions.

Figure 5.22 shows the average reflectance from days when the reflectance measurements have plateaued, across wavelengths 350 to 700 nm. Figure 5.22 shows reflectance peaks at around 500 nm while the smallest reflectance values are observed at longer wavelengths. As seen in chapters 2 to 4 this shape is consistent with sea ice reflectance and will be discussed further in the discussion section 5.5.1.

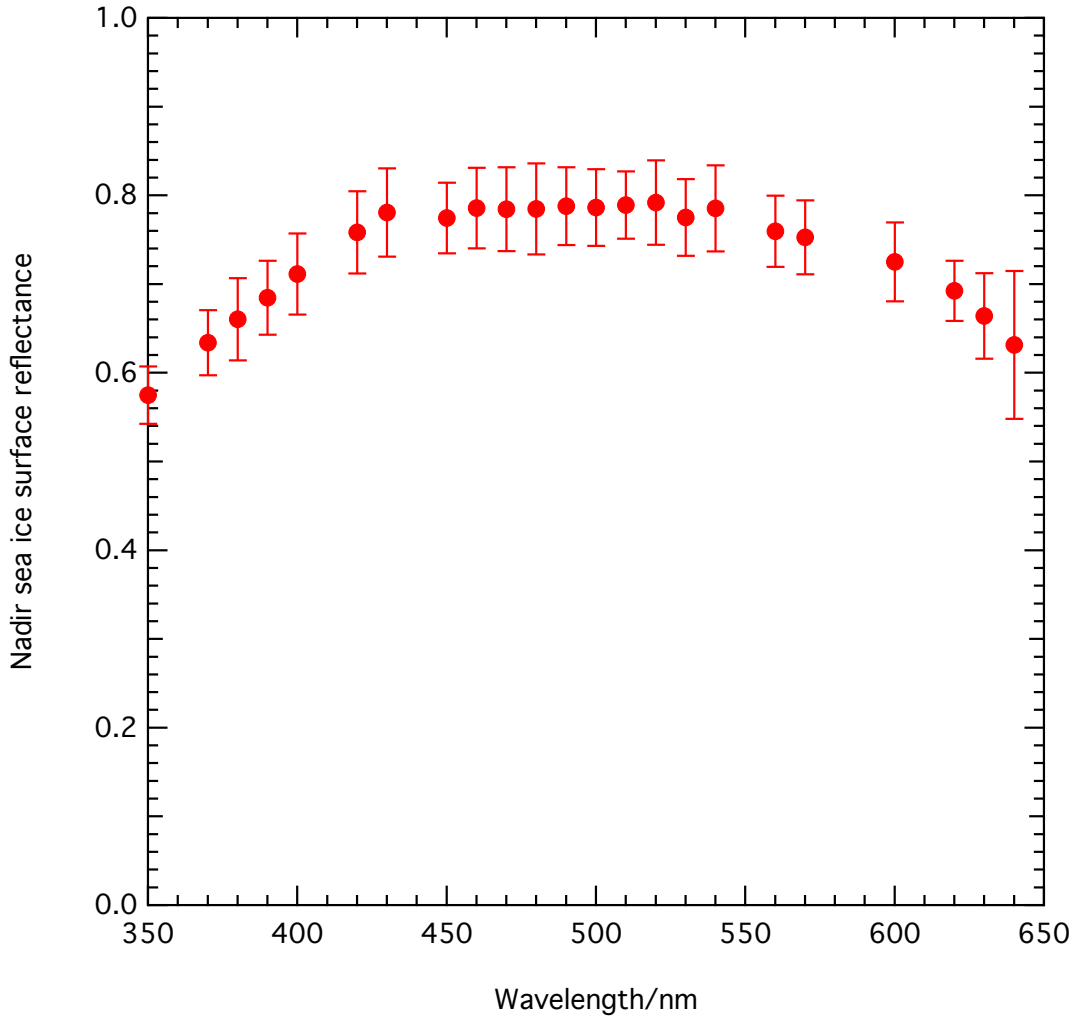

Figure 5.22 *– Nadir sea ice surface reflectance at wavelengths from 350 to 650 nm for optically thick simulated ice.*

5.4.2 Change in temperature of freezing sea ice

Figure 5.23 shows an example of temperature profiles taken during ice growth. Day 0 shows no ice in the tank with a constant temperature through the tank. As ice grows the temperature at the surface decreases, with temperature linearly increasing through the ice until a temperature of ∼–2° where temperature becomes constant with depth, showing a clear ice-water boundary and thus providing an indication of depth (shown as the dashed lines on figure 5.23). Over time the ice surface temperature gradually decreases reaching a minimum of ∼–15°. The water temperature also decreases slightly with time from ∼–2° to –4°. Overall, the difference between the ice surface temperature and the ice base temperature becomes larger, resulting in a steeper temperature gradient within the ice.

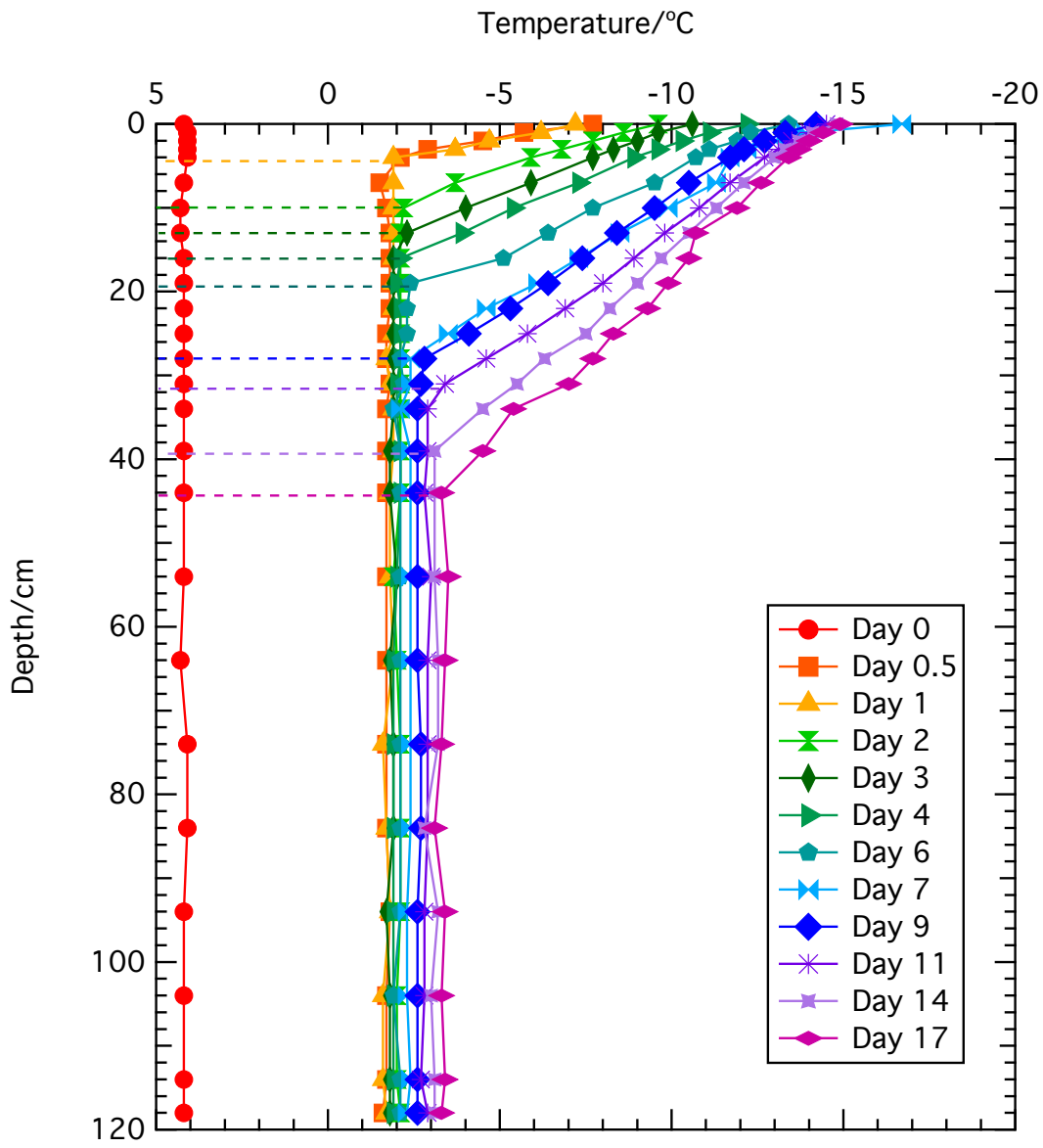

Figure 5.23 *– Example of temperature profiles measured during ice growth. Dashed lines show estimated ice depth.*

Figure 5.24 shows the estimated ice thickness from the temperature profiles. Thickness increases linearly with a slight slow down in growth rate with time.

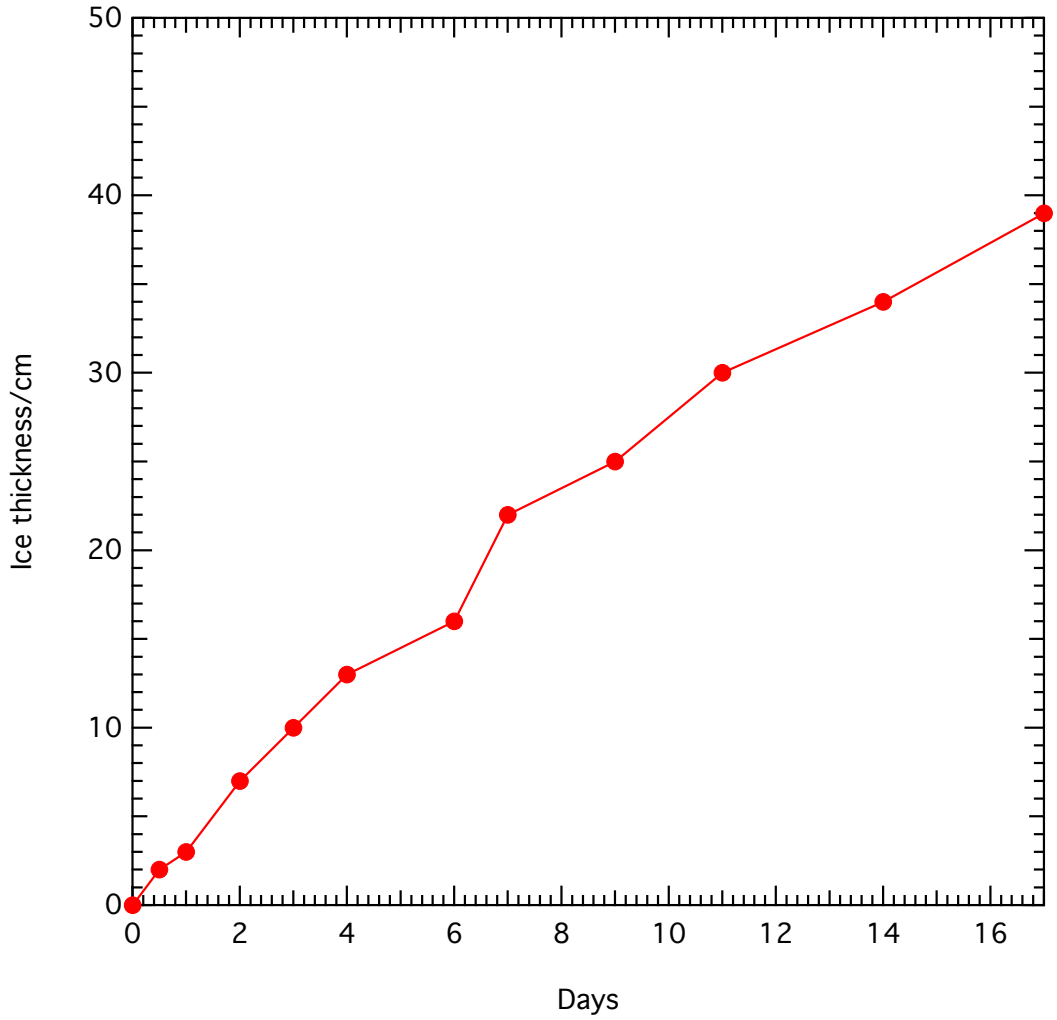

Figure 5.24 *– Change in daily ice thickness estimated from temperature profiles.*

5.4.3 Initial *e*-folding depth measurements

An example of *e*-folding depth measurements from three separate holes drilled through the ice are shown in figure 5.25. Each marker on the graphs represent a depth where a measurement was taken. Figure 5.25 shows that light intensity decreases exponentially through the sea ice as expected. An exponential fit to the intensity values is shown in figure 5.25. The *e*-folding depth of each of the three holes is shown in figure 5.25 averaging at 13 cm. A good level of agreement in *e*-folding depth occurs between the three holes drilled, with a standard deviation of 1 cm.

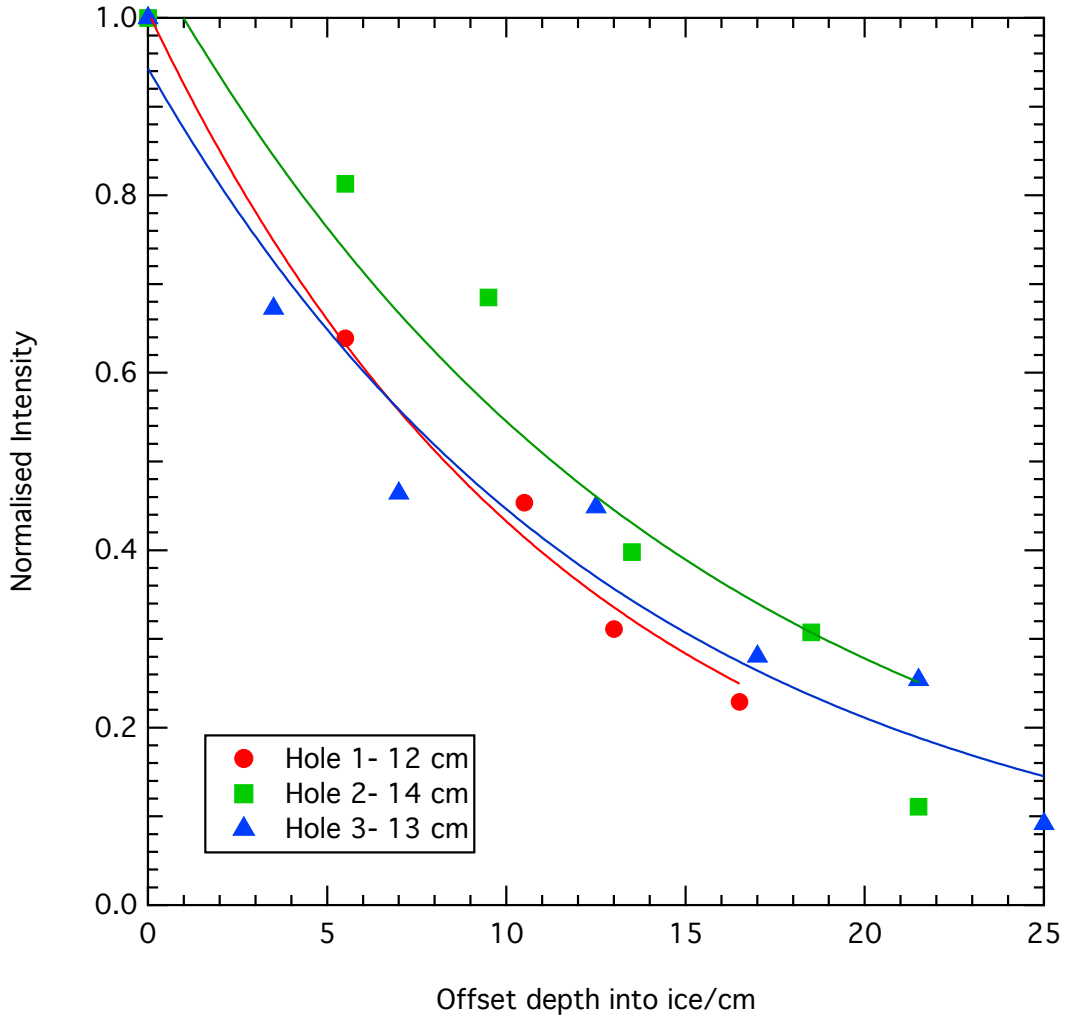

Figure 5.25 *– Example of e-folding depth measurements taken from three holes drilled through the ice. Depth of first measurement set to 0 cm.*

5.4.4 Ice core measurements

Figure 5.26 shows example data from a core, including measured temperature, density, salinity and derived brine salinity, brine density, percentage brine and percentage air using the equations in section 5.3.2. A photo of the core is also shown to the left of the plots. Temperature decreases linearly through the cores. Density does not appear to show any particular trends through the cores ranging from 0.85–0.95 g cm^{-1}. Salinity is greatest at the top and bottom of the cores peaking at 10–12 PSU with the centre of the cores being 6–8 PSU. Similarly the percentage brine increases at the ice base and at the surface. Brine salinity and brine density decreases gradually through the ice, with brine salinity ranging from 160–200 PSU at the surface to ∼80 PSU at the base and brine density ranging from ∼1.15 g cm^{-1} at the surface to ∼1.05 g cm^{-3} at

the base. The percentage air is inversely proportional to the density.

The cores taken of the ice show a specific structure. The surface of the ice is granular and white for the top centimetre. The centre of the core shows columnar ice and at the base there is a slushy layer.

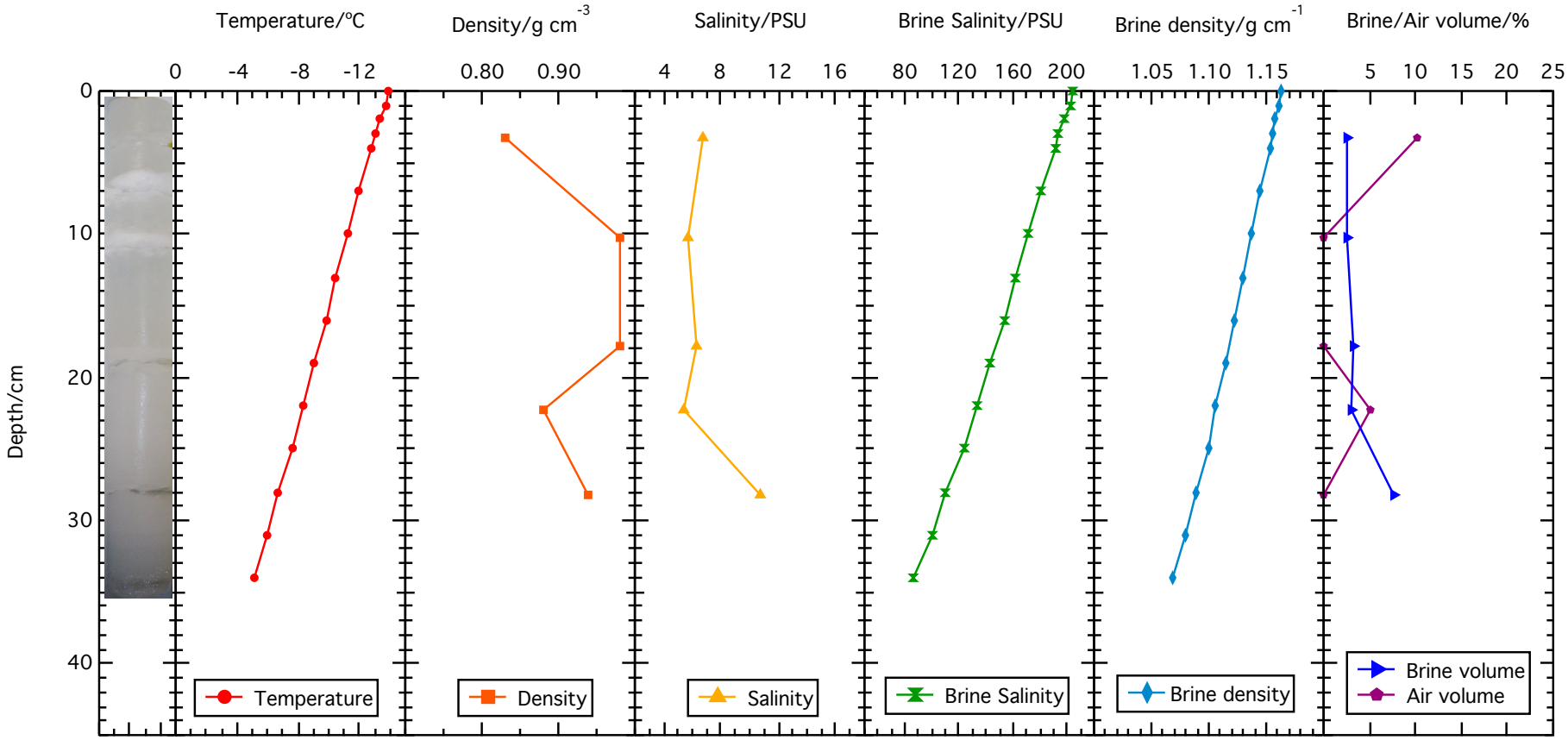

Figure 5.26 *– Representative example of ice core data from three cores including measured temperature, salinity and density and derived brine salinity, brine density, percent brine and percent air. Data from all ice cores taken is shown in chapter 6 and Appendix B.*

5.5 Discussion

The discussion section will review how comparable the ice grown in the sea ice simulator is to natural sea ice, followed by the limitations of a sea ice simulator.

5.5.1 How realistic is the simulated ice?

The sea ice simulator is designed to replicate natural sea ice growth in a controlled environment. Section 5.5.1 will review how the measured parameters of the sea ice compare to field measurements of sea ice.

Temperature profiles from the simulated sea ice show a linear increase in temperature from the surface to the ice base, this has been commonly reported (e.g. Eicken (2003); Perovich et al. (1998b)). Eicken (2003) also suggest that at typical winter temperatures ice would take ∼1 month to form 50 cm, this is a similar growth rate to that observed in the simulator. Nakawo and Sinha (1981) measured growth rates in Arctic first year sea ice reporting that in the first month of ice growth, growth is approximately linear reaching 40–50 cm in a month. Subsequent growth rate gradually slows down reaching ∼1.7 m in 6 months. In the ice grown in the simulator ice growth appears linear with a slight decrease in growth rate with time.

The albedo of various Arctic sea ice types were reported by Grenfell and Maykut (1977). Figure 5.27 shows a comparison of the average optically thick reflectance of the sea ice simulator ice in comparison to the albedos reported by Grenfell and Maykut (1977). The albedo of the simulated ice is considerably higher than a first year ice resembling an albedo closer to a multi-year ice. Brandt et al. (2005) state that “frost flowers” often form on thin ice exposed to cold air which has a similar albedo increasing effect as a thin snow layer. A similar process is occurring in the simulated ice, causing a slightly higher albedo than would be expected for a first year ice. Brandt et al. (2005) report change in albedo of growing snow-free sea ice suggesting an increase from 0.15 for 5 cm of ice to ∼0.4 for 40 cm of ice. These values are slightly lower than for the thin ice in the simulator which will again be due to the presence of the granular surface layer.

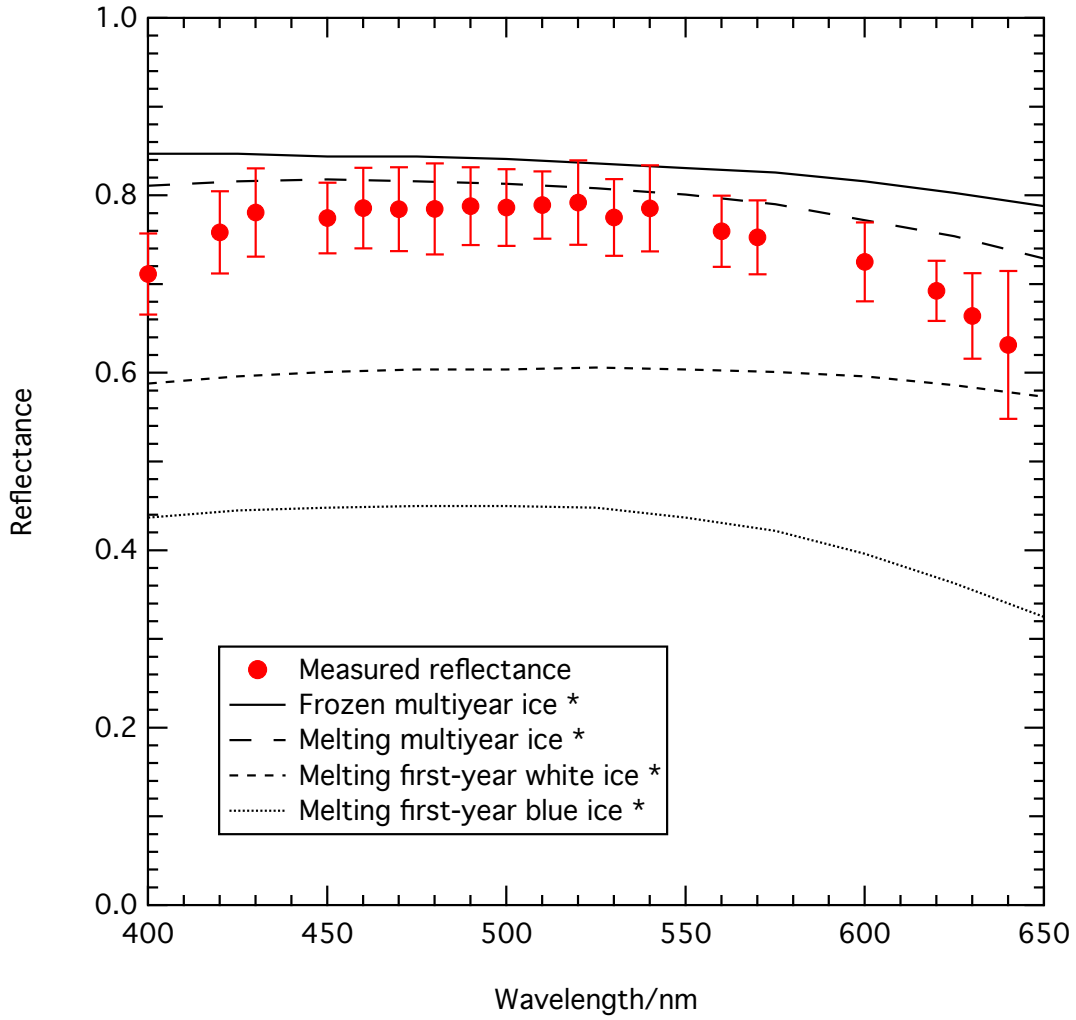

Figure 5.27 *– Comparison of measured sea ice simulator ice reflectance to albedo values of sea ice measured in the field by Grenfell and Maykut (1977)(*).*

Typical *e*-folding depths of sea ice at around 500 nm range from ∼1 m for a first year blue ice to ∼35 cm for a multi-year granular white ice (Grenfell and Maykut, 1977). Calculated *e*-folding depths for the simulated ice range from 10–35 cm, which are fairly short for sea ice, although not entirely unrealistic. The short *e*-folding depths calculated for the simulated ice may suggest the ice is highly scattering compared to a more natural sea ice, or that an absorbing impurity is present causing decreased *e*-folding depths, this will be investigated in chapter 6. A further explanation for the short *e*-folding depths could be due to the ice not being truly optically thick thus light reflected from the bottom of the tank maybe affecting the *e*-folding depth measurements; this will need to be accounted for when replicating the ice using the TUV-snow model.

Typical sea ice densities are reviewed by Timco and Frederking (1996) reporting first

year sea ice densities in the range 0.84 to 0.94 g cm^{-3}, the density of sea ice created in the simulator ranged from 0.85 to 0.95 g cm^{-3}, thus being in the range of natural ice. Weeks and Lee (1958) measured sea ice density profiles through first-year ice on the Labrador coast, USA showing no clear systematic variation in density with depth. Similarly Perovich et al. (1998b) measured density profiles through Arctic first year sea ice showing no clear variation with depth which is also observed in the simulated sea ice.

Figure 5.26 shows salinity data from example cores, each showing a distinctive “C” shape with a higher salinity seen at the base and top of the cores. Malgrem et al. (1927) studied salinity of first-year ice also showing a characteristic “C” shape to the sea ice salinity profile. The shape of the salinity profile, explained by Eicken (2003), is due to a combination of salt segregation, gravity drainage and brine expulsion. Salt segregation occurs as salt ions are rejected from the sea ice during growth as the ice cools, due to the phase relations in sea ice described by Assur (1960). As sea ice freezes the salts dissolved in the sea water are not incorporated into the ice but instead remain in a brine, as the sea ice cools, more water in the brine freezes thus the brine freezing point decreases as it becomes increasingly saline. At a temperature of –8.2°C the brine becomes supersaturated of sodium sulphate, which results in precipitation of the salt. Other salts become supersaturated as the brine becomes increasingly saline with decreasing temperature. As ice grows the salt ions are rejected from the ice at the ice-water interface. Salt segregation is the most important controlling factor in controlling the sea ice salinity in first year ice (Eicken, 2003). Gravity drainage occurs as sea ice is cooled from above resulting in more saline brine in the upper layers of the ice. The cooler brine in the upper layers of sea ice is replaced by warmer, lower salinity brine and seawater from lower layers, in a convective exchange. Brine expulsion occurs due to a build up of pressure during ice growth in pores causing brine to be expelled into the upper layers of ice and onto the surface, resulting in a higher surface salinity (Eicken, 2003). The ice was drilled through daily to relieve underlying pressure to limit brine expulsion on to the surface. A combination of brine expulsion, causing higher surface salinity and gravity drainage resulting in higher brine salinity near the water-ice interfaces causes the typical "C" shape in the salinity profiles observed.

The typical structure of a first year sea ice is described by Eicken (2003) showing a

granular surface layer, overlying columnar ice with granular/platelet ice at the ice-water boundary. The structure described by Eicken (2003) is similar to that observed in ice cores of the simulated ice. The surface of the simulated ice has a clear granular texture, and at the base there is a slushy platelet layer. Figure 5.28 shows a photo of a bottom section of a core showing the transition from columnar ice to granular/platelet ice at the base of the core.

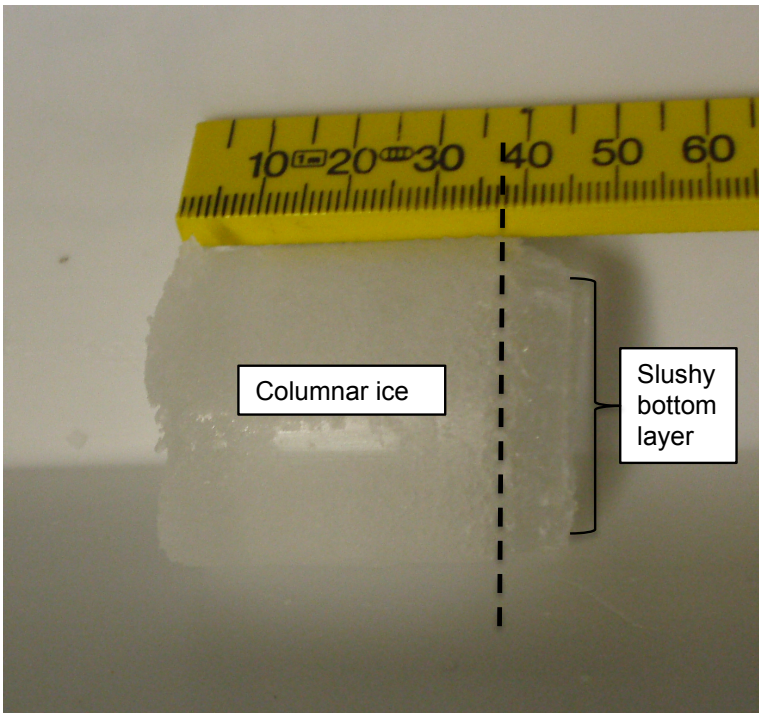

Figure 5.28 *– Segment of base of ice core showing transition from columnar ice (left) to platelet/granular ice (right).*

Overall the sea ice simulator creates a realistic sea ice, recreating typical growth rates, salinity and temperature profiiles, reflectance and *e*-folding depths of a first year sea ice.

5.5.2 Limitations of the sea ice simulator

Although the simulator creates a near realistic sea ice environment, as with all simulators, there are limitations in the degree to which a "natural" sea ice environment can be created. In section 5.5.2 the following limitations are discussed; light intensity, uneven ice growth, hyper-saline seawater, surface brine expulsion and reflectance measurements.

The fluorescent lights used for the study provide shortwave illumination representative

of isotropic sunlight. However the intensity of the illumination is not representative of solar intensities. For measurements of albedo and *e*-folding depth absolute radiance of the light source is unimportant as these measurements rely on a ratio of light intensities. The simulator aims to create a isotropic light source using the fluorescent tubes and a series of white boards, this is clearly not a perfect isotropic environment (as light intensity is not equal from all directions) but is a good approximation of one. Importantly the fluorescent lights provide even illumination across the sea ice surface.

Although the sides of the tank are insulated ice growth across the tank is not quite linear with slightly thicker ice (∼5 cm) around the edges of the tank (∼5 cm from the sides) and around the teflon pole which the thermocouples were inserted into, as shown in figure 5.29. Unfortunately the thicker ice areas could not be rectified but is unimportant as reflectance measurements were taken in the same place, away from the sides of the tank.

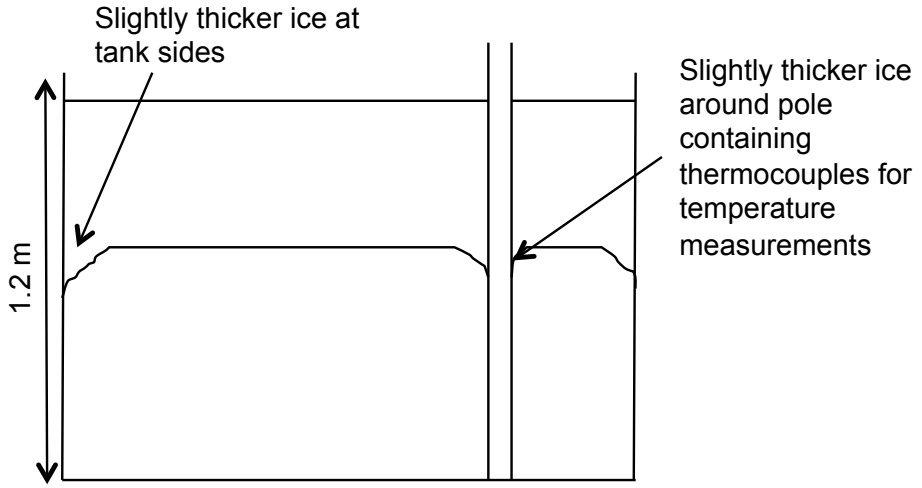

Figure 5.29 *– Cross-section through ice grown in the tank to show irregular thickness of the base of the ice due to extended growth at the sides of the tank and around the teflon tube containing the thermocouples. The ice is ∼5 cm thicker in these areas.*

As sea ice in the simulator grows the seawater below the ice increases in salinity. In nature the seawater below ice is commonly hyper-saline, representing reality. However, as the simulator is a closed system the build up of hyper-saline brine beneath the sea ice eventually stops ice growth and the water becomes unrealistically saline. Although not a major problem for the experiments as the ice still reaches 30–40 cm thick, to stop this occurring a secondary tank could be attached to the first tank and fresher water could be circulated around the base to keep the salinity of the water slightly lower,

so it doesn't inhibit ice formation. Engineering constraints prevented the adoption of this measure.

The reflectance measurements reported here are a measure of radiance from the ice surface measured at nadir compared to a Lambertian reflector (Spectralon panel) at nadir. These measurements approximate to albedo which is a measure of the upwelling irradiance from the whole hemisphere divided by downwelling irradiance from the whole hemisphere, compared to reflectance which is the ratio between upwelling and downwelling irradiance only measured at nadir. To compare the nadir reflectance measurements to true albedo an assumption must be made that sea ice is also a Lambertian reflector, which is the case under isotropic conditions, which are used. Under direct light conditions sea ice reflectance shows small deviations away from being a Lambertian reflector, mainly at high viewing zenith angles. Arnold et al. (2002) suggest under direct conditions nadir reflectance is 5–40% smaller. For wavelengths 500–1000 nm, under direct conditions, the ratio between nadir reflectance and albedo approximates to 1 (0.95). The anisotropic reflectance of polar surfaces will be explored in chapter 7.

As sea ice grows in the simulator pools of hyper-saline brine tended to form on the sea ice surface. Although surface brine expulsion is a natural process as sea ice grows, the degree to which this originally occurred in the sea ice simulator was unrealistic. Owing to high build up of pressure in the underlying water in the simulator as the ice grew brine was being expelled onto the surface. To alleviate this problem the ice was drilled through daily to relieve the underlying pressure. It was ensured this was done away from the reflectance measurement area. Relieving the pressure meant that surface reflectance measurements were more stable and also stopped high pressure building in the tank which may have caused splitting.

5.6 Conclusions

Realistic sea ice can be simulated in the Royal Holloway sea ice simulator through recreating polar temperatures, "natural" shortwave illumination and an artificial ocean. Salinity profiles taken from cores of the simulated ice show a "C" shaped profile characteristic of a first year ice. Ice nadir reflectance measurements (which approximate

to albedo) of the simulated ice are slightly higher than field measurements of first year ice due to the presence of a granular surface layer. Measurements of *e*-folding depth are slightly shorter than field measurements suggesting a highly scattering simulated ice or that the bottom of the tank is influencing *e*-folding depth measurements. The sea ice simulator can be used in combination with the measured physical and optical properties of the simulated ice to investigate how the simulated ice responds to black carbon to validate the TUV-snow radiative-transfer model used in previous chapters, this will be explored in chapter 6.

Chapter 6

Artificial sea ice reflectance response to increased black carbon, for evaluation of the TUV-snow model

6.1 Introduction

The TUV-snow model utilised in chapters 2–4 has enabled exploration of the effects of black carbon over a wide range of conditions, including different snow and sea ice types with individual optical and physical properties. However, as with all models, the TUV-snow is limited by a need for evaluation to ensure the calculations produced by the model represent reality. To achieve evaluation, model results must be compared with empirical evidence. In the case of the TUV-snow model, the model has been previously evaluated for photochemistry in snow by Phillips and Simpson (2005) who compared results from the TUV-snow model to the direct photolysis of 2-nitrobenzaldehyde, within artificial snow. The TUV-snow model reproduced the depth-integrated photolysis rate coefficients within the standard deviation of experiments ($\sim$10%). The TUV-snow model has not been evaluated before for sea ice or for the effects of black carbon in snow or sea ice.

To the author's knowledge laboratory or field studies examining the effects of black carbon on reducing sea ice albedo have not been carried out. However, Hadley and Kirchstetter (2012) carried out successful laboratory experiments on artificial snow investigating the effects of black carbon on snow reflectance. The results from Hadley

and Kirchstetter (2012) were used to validate the Snow, Ice and Aerosol radiation (SNICAR) model (Flanner et al., 2007) used in the 2013 IPCC report (IPCC, 2013).

Chapter 6 will explore the evaluation of the TUV-snow model for black carbon in sea ice using the sea ice simulator described in chapter 5. Black carbon is added to a 5 cm layer of sea ice created in the simulator in mass-ratios of 75, 150 and 300 ng g^{-1} and the decrease in sea ice reflectance is measured. The results are then compared to a calculated decrease in reflectance for the same black carbon mass-ratio increase in sea ice with the same optical and physical properties as the artificial sea ice, using the TUV-snow model. Relatively large mass ratios of black carbon are used so the change in the sea ice reflectance due to black carbon additions can be measured with higher accuracy. The results presented in this chapter represent the first attempt to evaluate a model examining the effects of black carbon on sea ice reflectance.

6.2 Experimental determination of the effect of black carbon on reflectance of artificial sea ice

To evaluate the TUV-snow model measurements of change in reflectance due to black carbon in mass-ratios of 0, 75, 150 and 300 ng g^{-1} in a 5 cm layer of artificial sea ice, created in the sea ice simulator was measured. The results are then compared to a calculated change in reflectance due to black carbon using the TUV-snow model, for sea ice with the same optical and physical properties as the artificial sea ice. Black carbon is placed within a 5 cm surface layer of the artificial ice to replicate black carbon entrainment into sea ice following melting of overlying snow as described by Grenfell et al. (2002) and Doherty et al. (2010). Section 6.2 will describe the set up of the sea ice simulator and the method used to measure the change in reflectance due to black carbon in artificial sea ice and then provide all experimental results. Section 6.3 will then move onto the evaluation of the TUV-snow model. Throughout chapter 6 the term “experimental” refers to experiments with artificial sea ice using the sea ice simulator described in chapter 5, with results being referred to as “measured” values. The term “modelled” refers to calculations using the TUV-snow radiative-transfer model, the results from which are referred to as “calculated” values.

6.2.1 Experimental method

The method section will describe the experimental set up to measure reflectance of artificial sea ice owing to black carbon in a 5 cm surface layer.

6.2.1.1 Sea ice simulator set up and ice growth

To create an artificial sea ice environment to measure the effects of black carbon on sea ice reflectance the sea ice simulator was set up as described in chapter 5. Before freezing commenced 75 L (which equates to 5 cm depth) of artificial sea water was drained off the tank and contained in five 15 L tubs which were consequently kept in complete darkness, at room temperature, until required, when black carbon was added to them. Sea ice was grown in the simulator for three weeks producing sea ice with a thickness of 30–40 cm. Temperature and nadir reflectance of the ice were measured daily during growth and light penetration depth (*e*-folding depth) was measured at the end of ice growth along with physical measurements from ice cores, including salinity and density from which brine salinity and brine and air volume can be derived. Methods for measuring nadir reflectance, *e*-folding depth and obtaining ice core data are described in chapter 5 (sections 5.3.1, 5.3.2 and 5.3.4 respectively). An aqueous solution of black carbon of known concentration was then added to the 75 L of artificial seawater originally removed, a process described in section 6.2.1.2. The 75 L of seawater containing black carbon is poured on to the surface of the ice forming a 5 cm black carbon bearing layer. The black carbon bearing seawater is pre-cooled to prevent extensive melting of the underlying sea ice when poured onto the surface. The new 5 cm layer of black carbon bearing seawater was left to freeze for three days and the reflectivity of the new sea ice surface measured daily over a week. The sea ice was then cored and density and salinity measured to record the physical ice structure before and after the black carbon bearing layer was added so sea ice with the same physical properties could be recreated using the TUV-snow model during the model evaluation phase. After ice cores were taken the ice in the simulator was melted by raising the temperature of the cold store to $\sim$+2° (a relatively cool temperature was used for defrosting to prevent algae growth). Once melted the artificial seawater was filtered through a 1 μm Purtex 10 inch depth filter to remove major black carbon particulates. The 1 μm filter will also remove particles <1 μm present in the simulator

as particles will become charged and thus attached to the filter. Any black carbon left would be diluted by the rest of the seawater so its concentration would become negligible (black carbon in the top 5 cm layer will be diluted by a factor of 27 in all the seawater). The whole process of forming ice and adding a black carbon bearing layer was subsequently repeated with different black carbon mass-ratios. Black carbon mass-ratios of ∼75 ng g^{-1}, ∼150 ng g^{-1} and ∼300 ng g^{-1} were placed in a 5 cm layer at the surface of the ice. A blank run was also completed where just seawater (containing no black carbon) was placed on the surface of the ice. Thus, in total, 4 different "runs" were completed each with a different black carbon mass-ratio (∼0, 75, 150 and 300 ng g^{-1} of black carbon respectively), the exact mass-ratios used are detailed in table 6.1.

6.2.1.2 Making black carbon solutions

Black carbon is added, in an aqueous solution, to the 75 L of artificial seawater originally removed from the sea ice simulator tank then added in a 5 cm layer on top of the clean sea ice forming a bottom "clean" ice layer and a top black carbon bearing layer. The black carbon in the aqueous solution is "atmospherically representative" i.e. particle diameter <0.8 μm. To make the black carbon solutions a method is adopted and adapted from Clarke (1982) who required atmospherically representative black carbon to create reference filters for measuring black carbon mass-ratios in snow samples. Firstly ∼10 g of a commercially produced standard black carbon was added to 1000 ml of pure water and isopropanol in 4:1 ratio. The isopropanol aids dispersal of the black carbon in the solution. The solution is placed in an ultrasonic bath for at least 2 hours to ensure the black carbon is fully dispersed in the solution and to break up any conglomerated lumps. The solution is first suction filtered through 2 μm Nuclepore membrane filters and then through 0.8 μm Nuclepore filters to remove larger particles and ensure the final stock solution is representative of atmospheric black carbon. A coarse filter is used first to prevent clogging of the second filter by larger particles. To find the concentration of the filtered black carbon in the final stock solution three clean beakers are heated at 90°C in an oven to remove any residual water. The beakers are removed from the oven and covered with tin foil and left to cool to room temperature, then accurately weighted. 500 ml of the twice-filtered black carbon solution is added to each beaker and replaced in the oven at 90°C.

When the solution has fully evaporated (taking 24–48 hours) and beakers cooled, the beakers with black carbon residual are weighed using highly accurate scales. The mass of black carbon in 500 ml of solution can then be determined and thus the mass-ratio of black carbon in the solution. Three beakers are used so that a standard deviation in the mass-ratio can be derived to provide a measurement of uncertainty. Two black carbon stock solutions were made:

- Solution 1- black carbon mass-ratio 46 $\pm$ 11 μg g^{-1}
- Solution 2- black carbon mass-ratio 11 $\pm$ 1.5 μg g^{-1}

Specific amounts of solutions 1 and 2 were mixed with the 75 L of artificial sea water removed from the tank to give overall black carbon mass-ratios detailed in table 6.1. The black carbon mass-ratios approximate to 0, 75, 150 and 300 ng g^{-1}, these approximate values will be used for the rest of the chapter.

Run number	**Black carbon solution added to 15 L of seawater**	**Black carbon mass-ratio in 5 cm surface layer/ng g^{-1}**
1	0 ml	0
2	25 ml solution 1 added to each 15 L tub	76.7±18.3
3	50 ml solution 1 added to each 15 L tub	153.4±36.7
4	100 ml solution 1 added to 3 15 L tubs, 410 ml solution 2 added to 2 other 15 L tubs	305.0±61.8

Table 6.1 *– Black carbon mass-ratio in 75 L of seawater placed in 5 cm surface layer for each "run". The black carbon solution added to each 15 L of seawater is thoroughly mixed and the solutions in each of the five 15 L tubs are mixed with each other during addition to the top of the clean ice.*

6.2.2 Experimental results

The results section provides reflectance and *e*-folding depths of the clean bottom layer of ice and ice core data from cores taken before and after the top black carbon bearing layer is added for each run (1–4). These results enable physical and optical characterisation of the ice for each run for subsequent modelling. Change in reflectance due to the addition of black carbon to the artificial sea ice is also presented, which will be compared to calculations from the TUV-snow model in section 6.3.

6.2.2.1 Measured nadir reflectance of clean bottom ice

The nadir reflectance of the ice was measured daily as ice grew, after approximately two weeks the ice reflectance became constant with time, as shown in figure 6.1.

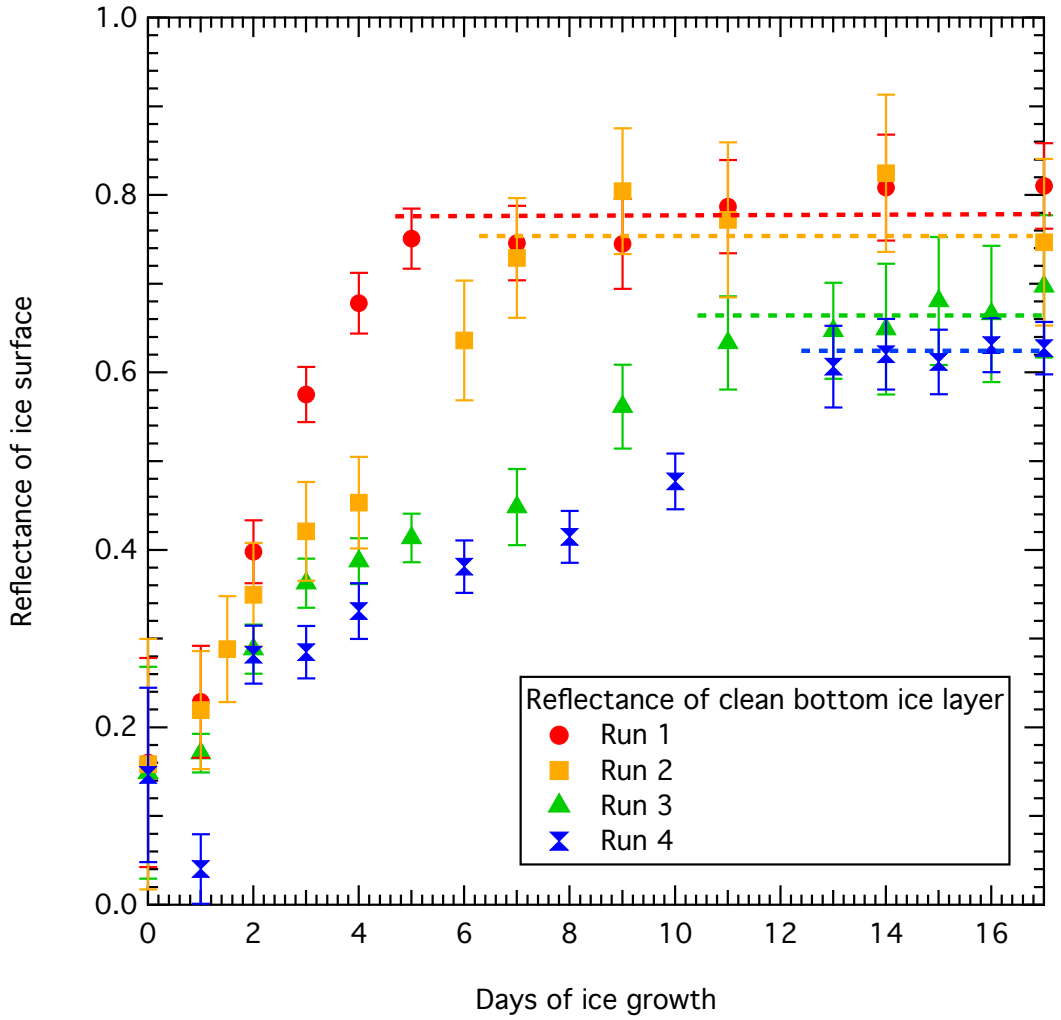

Figure 6.1 *– Measured daily nadir reflectance at a wavelength of 500 nm of the clean bottom layer of ice before the black carbon bearing layer is added for each run. Error bars show one standard deviation of three measurements taken each day. A line is added to show where reflectance becomes constant with increased ice growth.*

Figure 6.2 shows the nadir reflectance of the clean bottom ice layer before the black carbon layer is added for runs 1–4. Reflectance values shown on figure 6.2 are the average of 5 days of reflectance measurements taken when ice reflectance was constant with time (the ice had reached optical thickness). The data is fitted with a smoothing spline formulated by Reinsch (1967) (dashed lines) and error bars show one standard deviation of reflectivity from the 5 days of reflectance measurements.

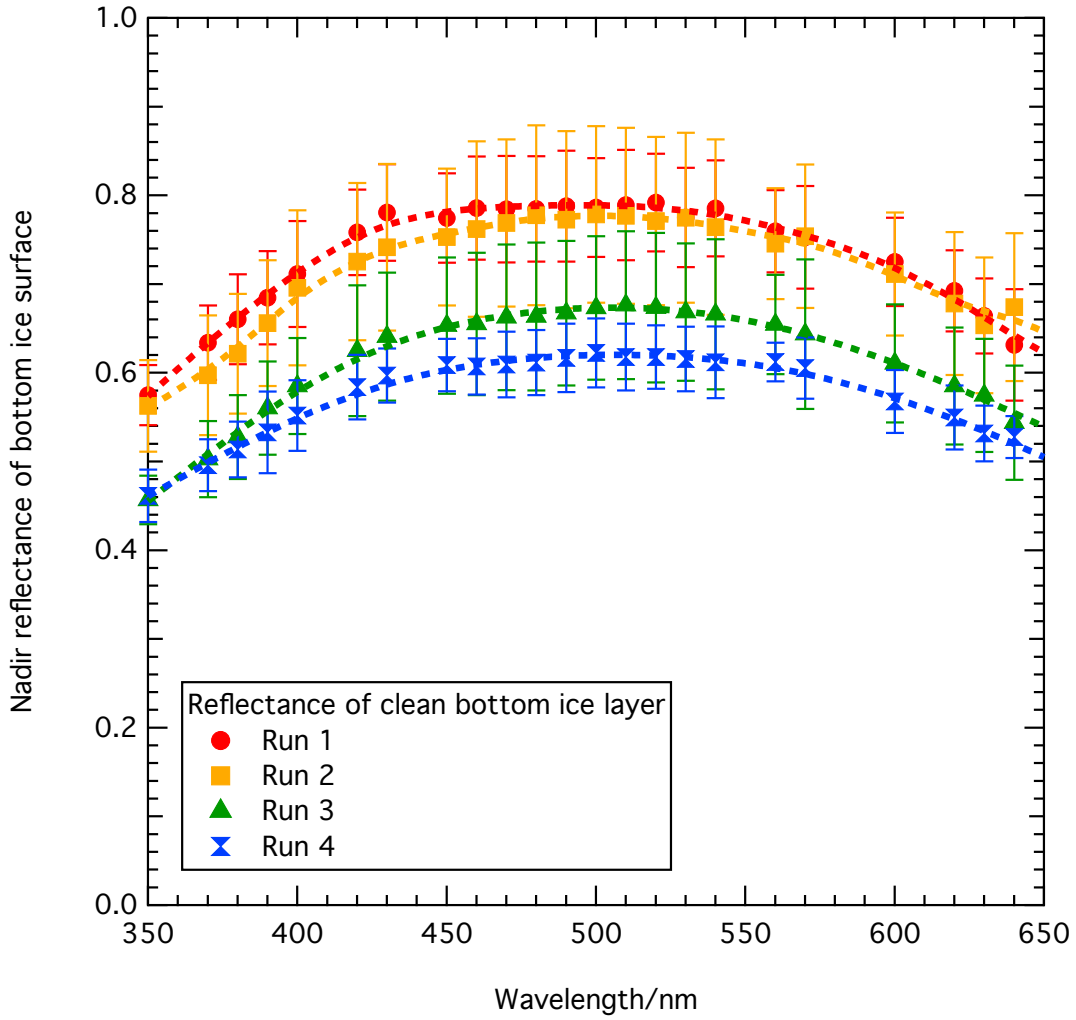

Figure 6.2 *– Measured reflectance versus wavelength of clean bottom layer of ice before black carbon bearing layer added for each run. Error bars show one standard deviation of five measurements taken on consecutive days. A smoothing spline (dashed line) is fitted to the measurements to remove noise.*

For all runs the nadir reflectance of the ice is clearly wavelength dependent peaking at values around 500 nm. The reflectance of the bottom clean ice layer is very similar at all wavelengths for the first two runs, runs 1 and 2, being easily within error of each other. The reflectance is lower at all wavelengths for runs 3 and 4, which are also within error of each other. The ice grown in each run has different physical properties, discussed in section 6.2.2.4, the lower reflectance in runs 3 and 4 could be attributed to a less scattering or more absorbing ice, as discussed in chapter 4.

6.2.2.2 Measured *e*-folding depth of bottom clean ice

Figure 6.3 shows the *e*-folding depth of the clean bottom layer of ice for each run before black carbon was added. The data was obtained and analysed using the method described in chapter 5 section 5.3.2. For each run the *e*-folding depth was measured down three holes drilled into the ice. The values on figure 6.3 show the average *e*-folding depth for the three holes at each wavelength. The uncertainty bars on the graph show the standard deviation in *e*-folding depth between the results from the three holes drilled. An exponential fit of the intensity data used to derive the *e*-folding depth (as described in chapter 5 section 5.3.2) that had an uncertainty (one standard deviation) larger than the resulting *e*-folding depth was rejected. Thus there is a lack of uncertainty bars for the *e*-folding depth at some wavelengths. The *e*-folding depth data is fitted with a smoothing spline to remove noise, as the variation in *e*-folding depth with wavelength is expected to be a smoothly varying function, this is shown as the dashed line on figure 6.3.

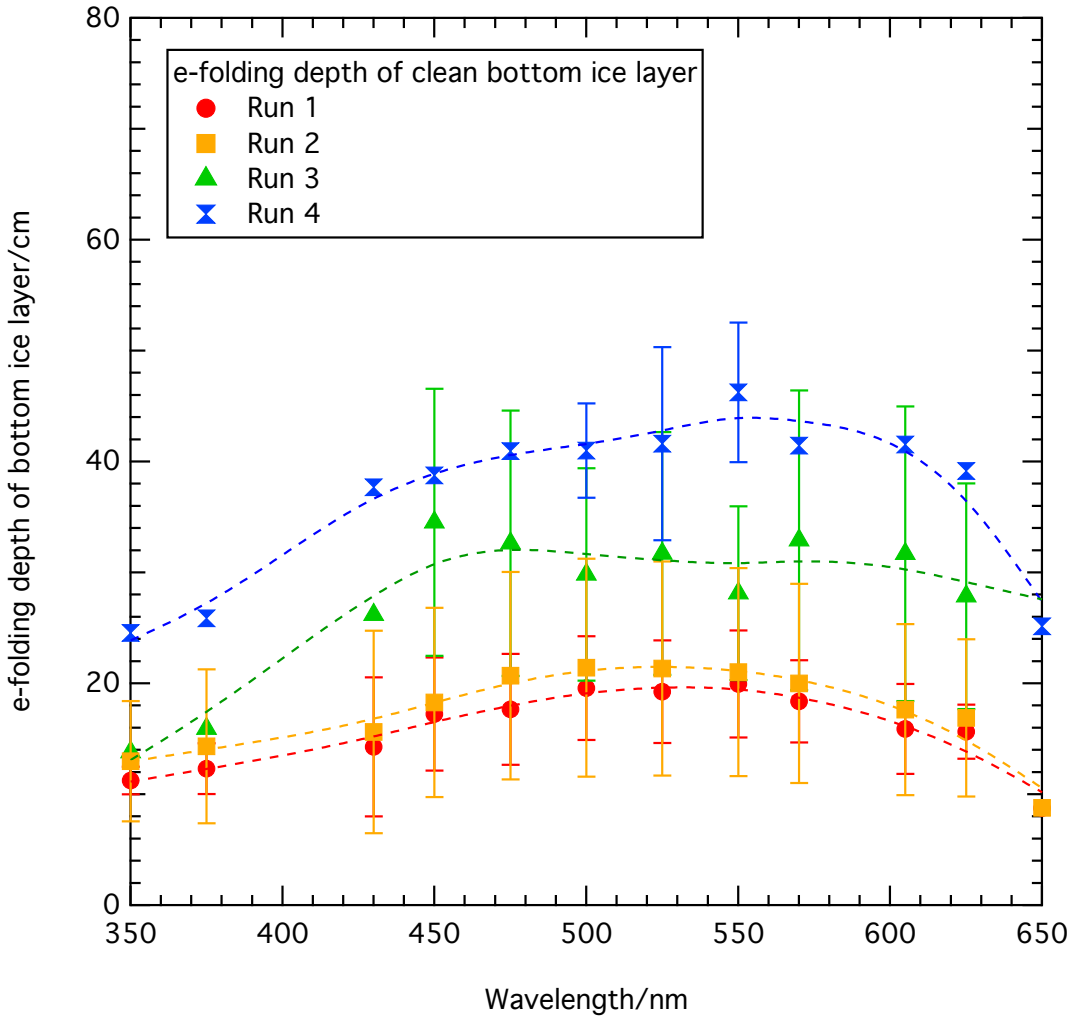

Figure 6.3 *– Measured e-folding depth of the bottom clean ice layer before the black carbon bearing layer is added for each run (1–4) at wavelengths 350–650 nm, every ~25 nm (wavelengths chosen to eliminate peaks in spectra as described in chapter 5). Some wavelengths are missing due to poor fitting of intensity data.*

Similarly to the reflectance data the *e*-folding depth of the clean ice is clearly wavelength dependent with the longest values observed around 550 nm for all runs. Again, runs 1 and 2 show very similar *e*-folding depths, well within uncertainty limits of each other. Run 3, and particularly run 4, show significantly longer *e*-folding depths. The increased *e*-folding depth for runs 3 and 4 can be attributed to a less scattering or less absorbing ice. At the end of run 2 the UV lights were left on continuously to eliminate the need to warm up the lights before taking measurements, this could have killed any algal life present in the sea water and thus decreased absorption and increased the *e*-folding depths.

6.2.2.3 Measured reflectance with the addition of a top, black carbon bearing, ice layer

Figure 6.4 shows the reflectance of the ice surface with black carbon mass-ratios of 75 ng g^{-1} (Run 2), 150 ng g^{-1} (Run 3) and 300 ng g^{-1} (Run 4) in a 5 cm layer at the sea ice surface in comparison to an added layer containing no black carbon (Run 1). Reflectance decreases at all wavelengths as black carbon mass-ratio increases. At 500 nm reflectance decreases to 97% of the reflectance of clean ice (Run 1) for an addition of 75 ng g^{-1}, to 90% for an addition of 150 ng g^{-1} compared to clean ice and to 79% for an addition of 300 ng g^{-1} compared to clean ice.

The *e*-folding depth of the ice after the black carbon layer was added was not measured as the ice was no longer a homogeneous medium.

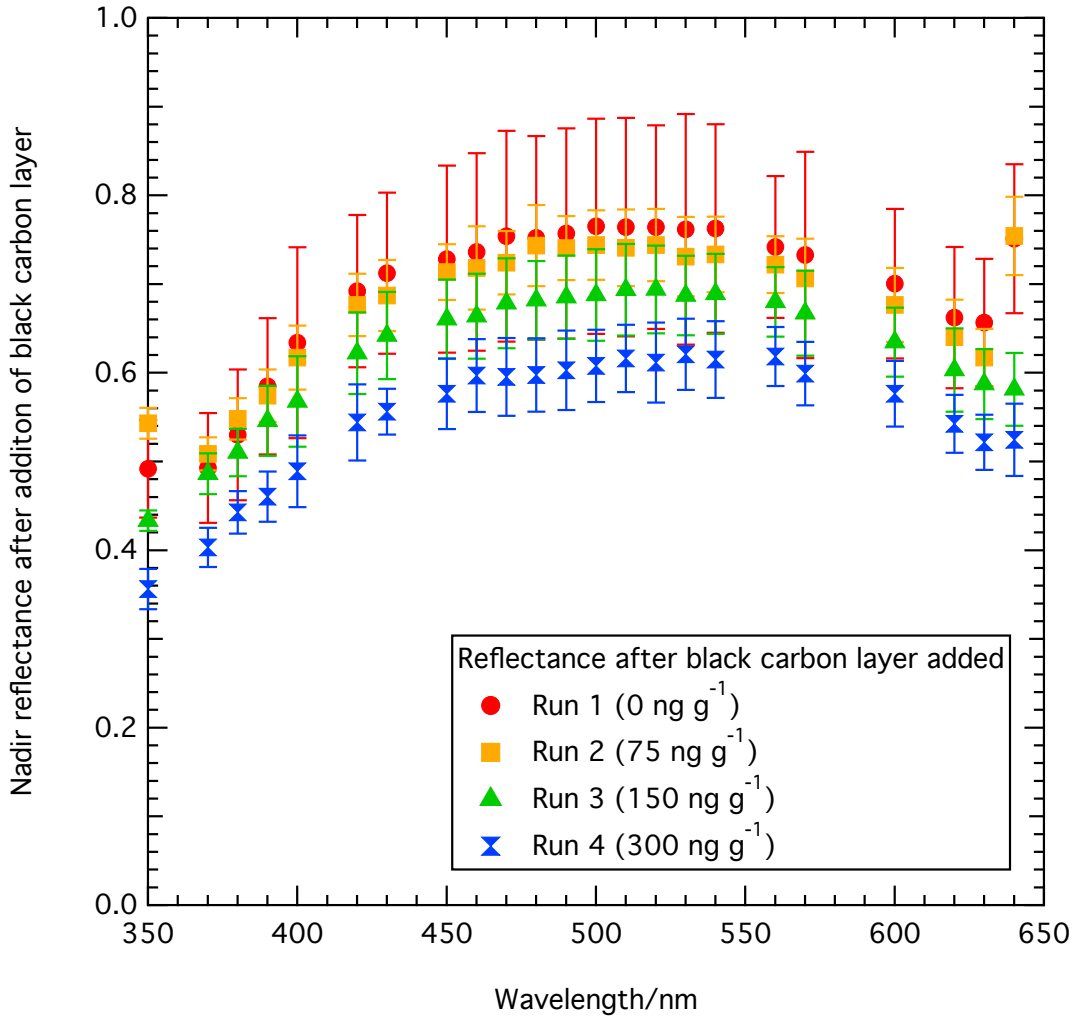

Figure 6.4 *– Artificial sea ice surface reflectance versus wavelength with black carbon in a 5 cm surface layer of ice in mass-ratios of 75 ng g^{-1}, 150 ng g^{-1} and 300 ng g^{-1}. 0 ng g^{-1} represents a blank run where just artificial seawater was added to the sea ice surface. Reflectance data presented every ∼10 nm, gaps at certain wavelengths occur due to peaks in intensity spectra.*

6.2.2.4 Ice core data

For each run (1–4) two ice cores were drilled of both the clean ice before the black carbon bearing layer was added and after the black carbon layer was added and frozen. Temperature, density and salinity of the cores were measured. The temperature is measured with an uncertainty of ±0.5°, the salinity has a uncertainty of ±0.5 PSU and density has an estimated uncertainty of 15%. Brine salinity, brine density and brine/air volume was derived from equations by Cox and Weeks (1983) as described in chapter 5, section 5.3.4. Figures 6.5–6.11, show the ice physical data from one of the cores taken from before and after the black carbon layer is added for each run

respectively, including a photo of each core. Note that the data for run 2 after the black carbon layer is added is missing. Data from the other two ice cores taken for each run (before and after the black carbon layer is added) are included in appendix B. There is a fair difference between cores taken of the same ice which shows there is lateral variability in the ice.

The temperature of the ice steadily decreases through the ice for all runs, while the density shows little correlation between runs and through cores varying from 0.8 to 1 g cm^{-3}. The salinity profile through the ice typically shows a "C" shape with higher salinity at top and bottom, as discussed in chapter 5. Where the additional black carbon bearing layer has been added the salinity is particularly high at the top of the ice core. Brine volume also shows a "C" shape with a greater brine volume observed in the top layers of the ice after the additional layer is added. Brine salinity and brine density both steadily decrease through the cores for each run. Air volume appears to be variable through cores and between runs.

The thickness of the ice can be deduced from both the ice cores and temperature data, shown in table 6.2, as described in chapter 5. The ice core data typically shows ice thickness ∼8 cm less than the temperature data, there are two reasons for this. Firstly, ice could be slightly thicker around the thermocouples as the teflon tube to which they are inserted acts as a conductor of heat away from the water. Secondly, ice cores may not record a bottom "slushy" section of ice and thus not represent the whole depth. Where the reflectance and *e*-folding depth measurements are taken the ice depth is most likely to be between the depth deduced from temperature and core data, also shown in table 6.2 as an "estimated thickness".

Run number	**Thickness from temperature data/cm**	**Thickness from cores/cm**	**Estimated thickness/cm**
1	49	40	45
2	55	–	51
3	44	34	39
4	43	36	40

Table 6.2 *– Ice thickness deduced from temperature data and core data when 5 cm layer has frozen at ice surface for each run.*

Table 6.3 shows the average ice physical properties of the upper black carbon bearing layer and the bottom layer for each run. These properties can be used for characterising the ice enabling modelling of ice with the same physical properties. The top layer

of the ice is typically more saline with a greater brine and air volume, and is also considerably colder than the bottom layer. The density shows no particular correlation between the top and bottom layer ranging from 0.91 to 1.0. The data for all variables between runs appears similar with no particular trends. A more detailed discussion of how the top ice layer effects the overall ice properties is given in section 6.4.2.1.

Property	**Run 1**		**Run 2**		**Run 3**		**Run 4**	
	Bottom	**Top**	**Bottom**	**Top**	**Bottom**	**Top**	**Bottom**	**Top**
Density/g cm^{-3}	0.91	0.92	0.91	–	0.92	1.00	0.95	0.93
Salinity/PSU	8	16	8	–	6	9	7	17
Temperature/°	-9.9	-12.2	-10.5	–	-9.8	-14.1	-10.8	-13.3
Brine salinity/PSU	154	184	161	–	152	207	154	197
Brine Volume/%	4.3	6.9	4.2	–	3.3	3.7	3.8	6.8
Air Volume/%	2.4	2.4	3.1	–	2.2	3.7	2.1	3.3

Table 6.3 *– Average ice physical properties of bottom layer and top black carbon bearing layer for each run (1–4).*

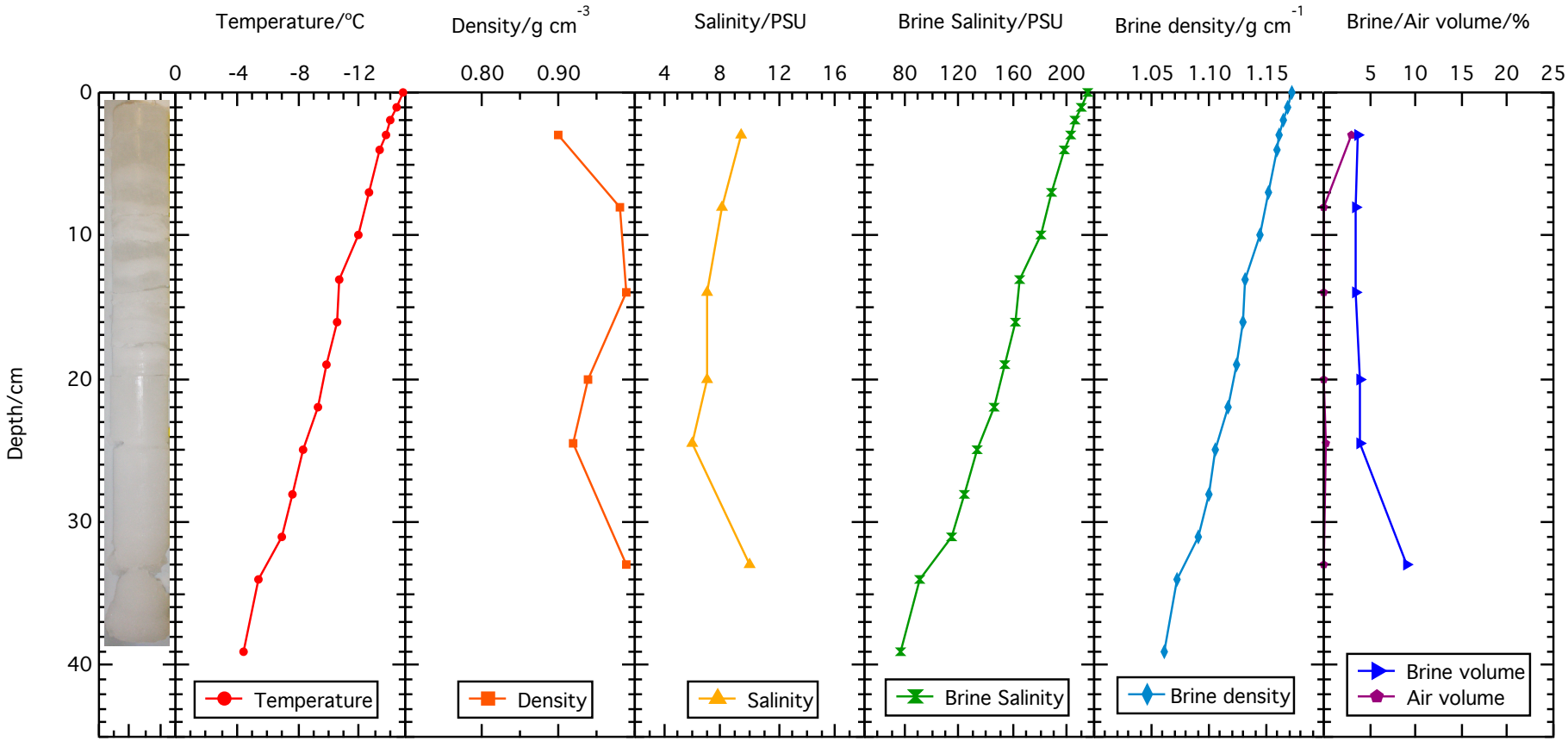

***Figure 6.5* – Run 1 before layer added** *Physical ice properties for bottom "clean" ice layer before additional layer added for run 1. Temperature, density and salinity are measured from core sections, while brine salinity, brine density and brine and air volume are derived from equations of Cox and Weeks (1983). Photo of the ice core is also shown.*

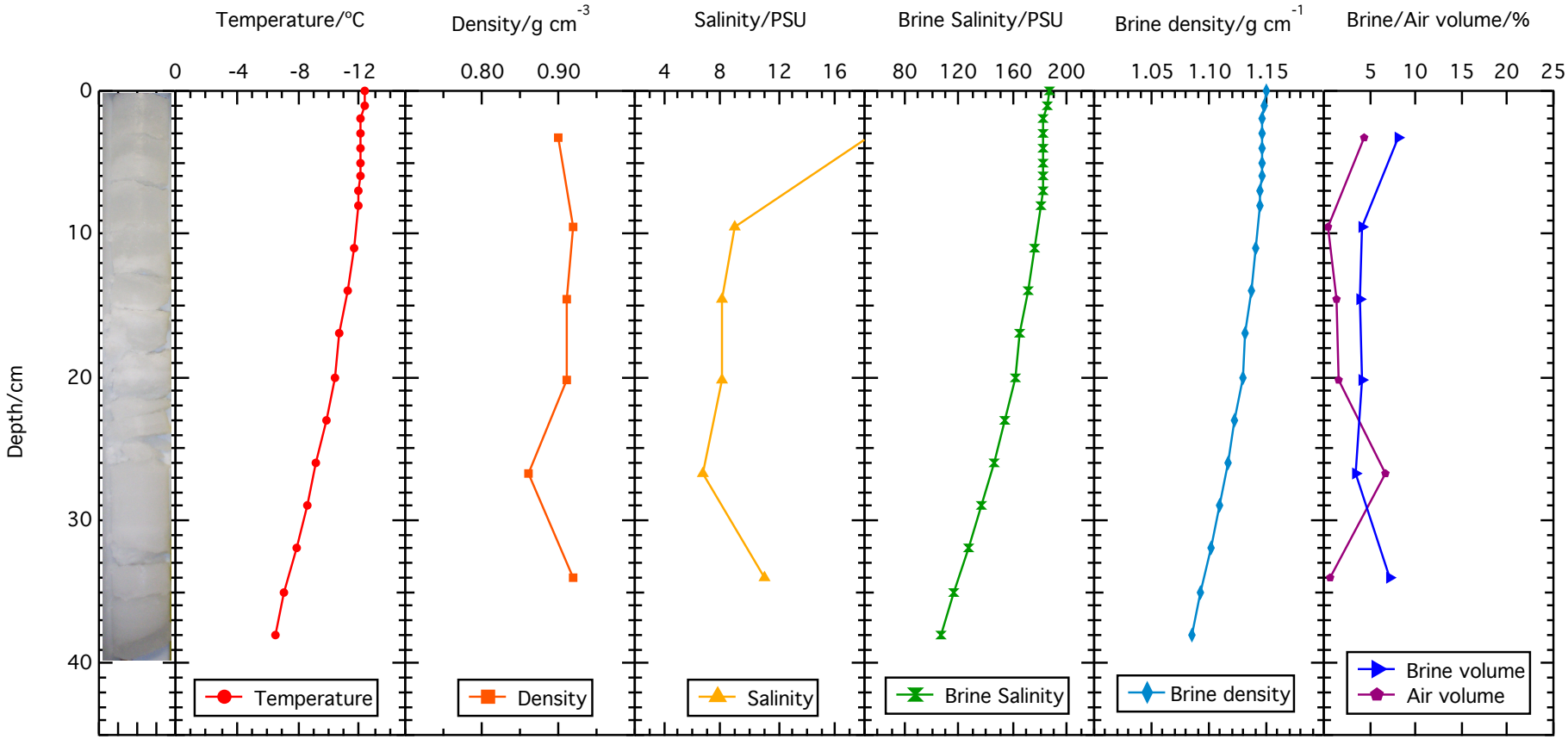

***Figure 6.6* – Run 1 after layer added** *Physical ice properties for bottom "clean" ice layer and additional layer added for run 1. Temperature, density and salinity are measured from core sections, while brine salinity, brine density and brine and air volume are derived from equations of Cox and Weeks (1983). Photo of the ice core is also shown.*

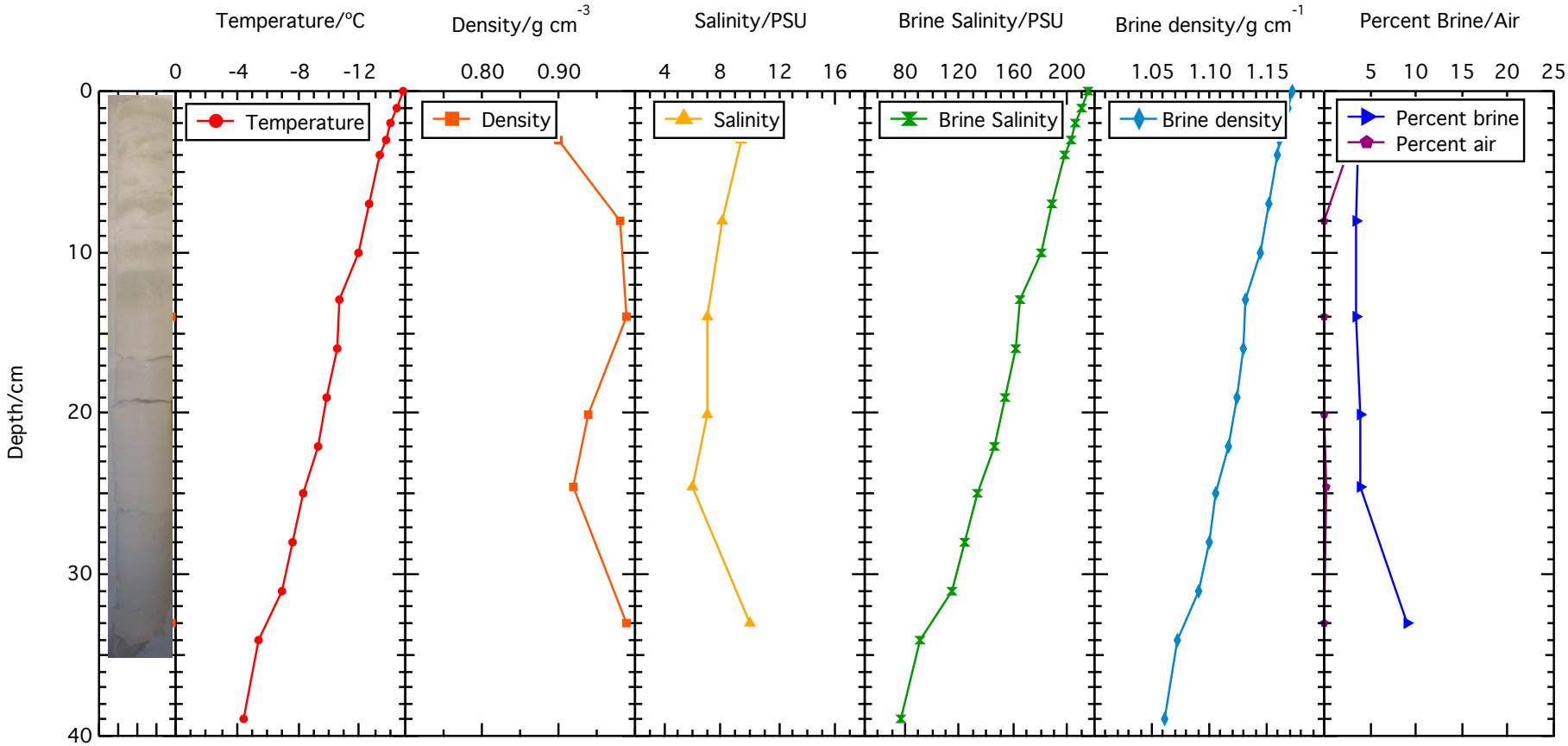

Figure 6.7 – **Run 2 before layer added** *Physical ice properties for bottom "clean" ice layer before additional black carbon bearing layer added for run 2. Temperature, density and salinity are measured from core sections, while brine salinity, brine density and brine and air volume are derived from equations of Cox and Weeks (1983). Photo of the ice core is also shown.*

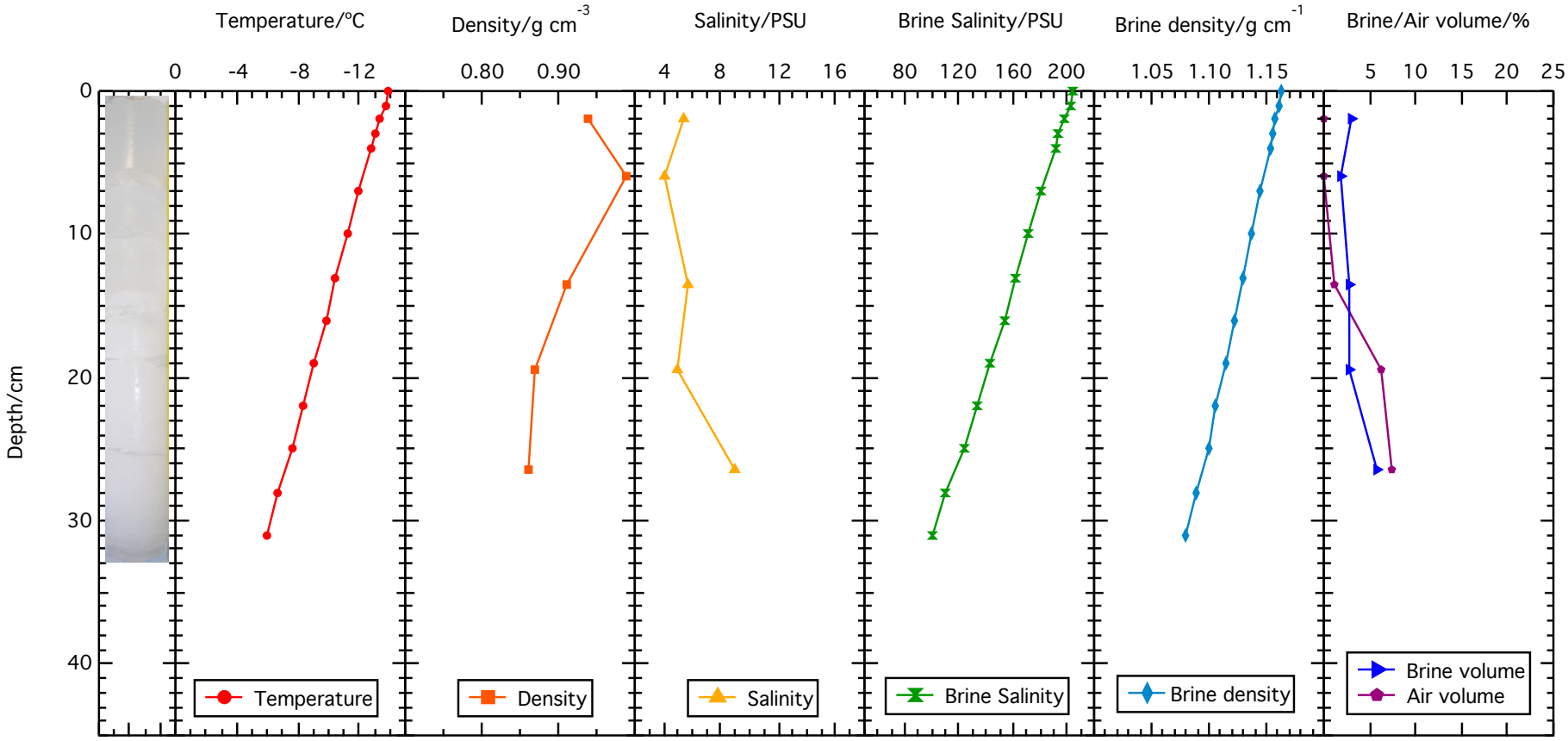

Figure 6.8 **– Run 3 before layer added** *Physical ice properties for bottom "clean" ice layer before additional black carbon bearing layer added for run 3. Temperature, density and salinity are measured from core sections, while brine salinity, brine density and brine and air volume are derived from equations of Cox and Weeks (1983). Photo of the ice core is also shown.*

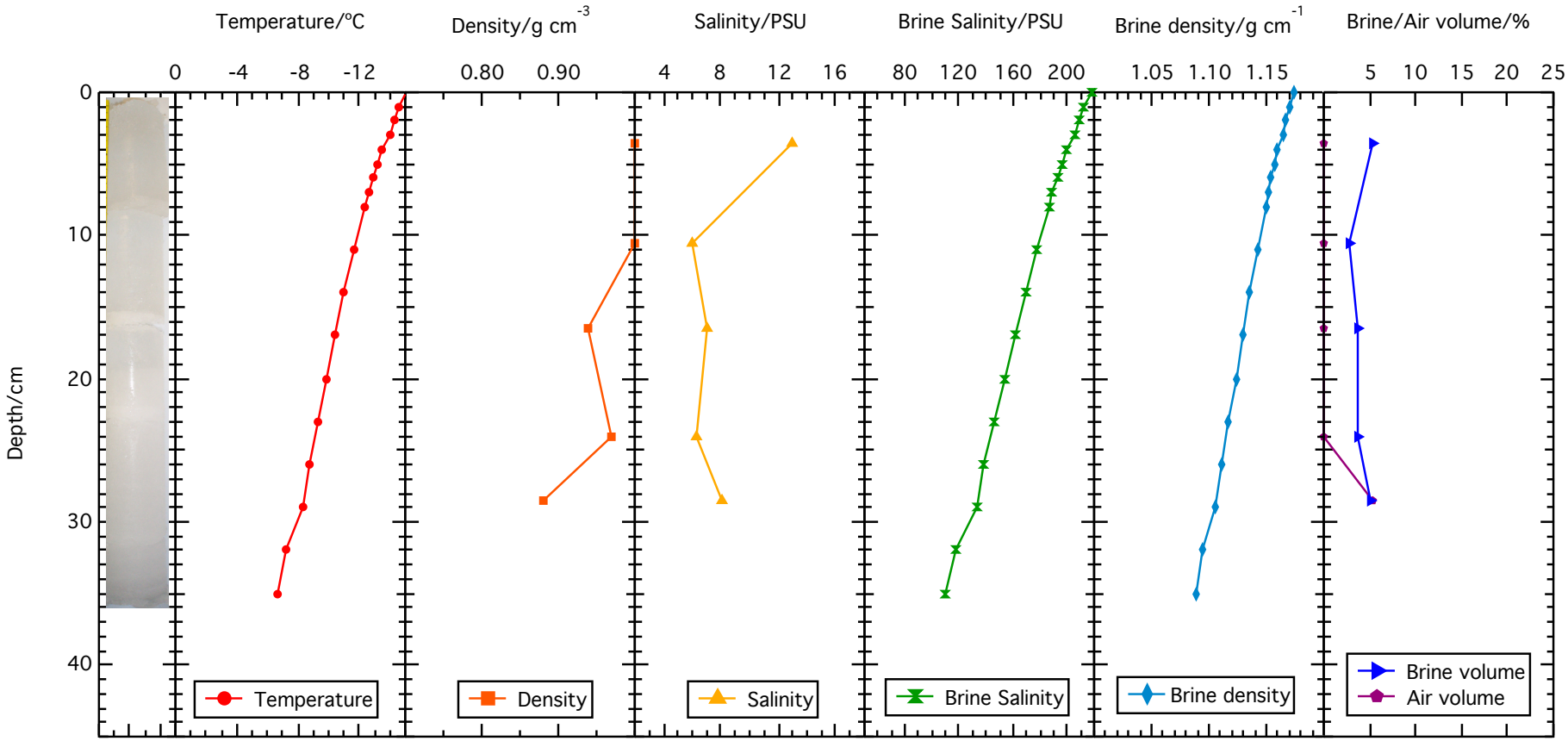

***Figure 6.9* – Run 3 after layer added** *Physical ice properties for bottom "clean" ice layer and additional black carbon bearing layer for run 3. Temperature, density and salinity are measured from core sections, while brine salinity, brine density and brine and air volume are derived from equations of Cox and Weeks (1983). Photo of the ice core is also shown.*

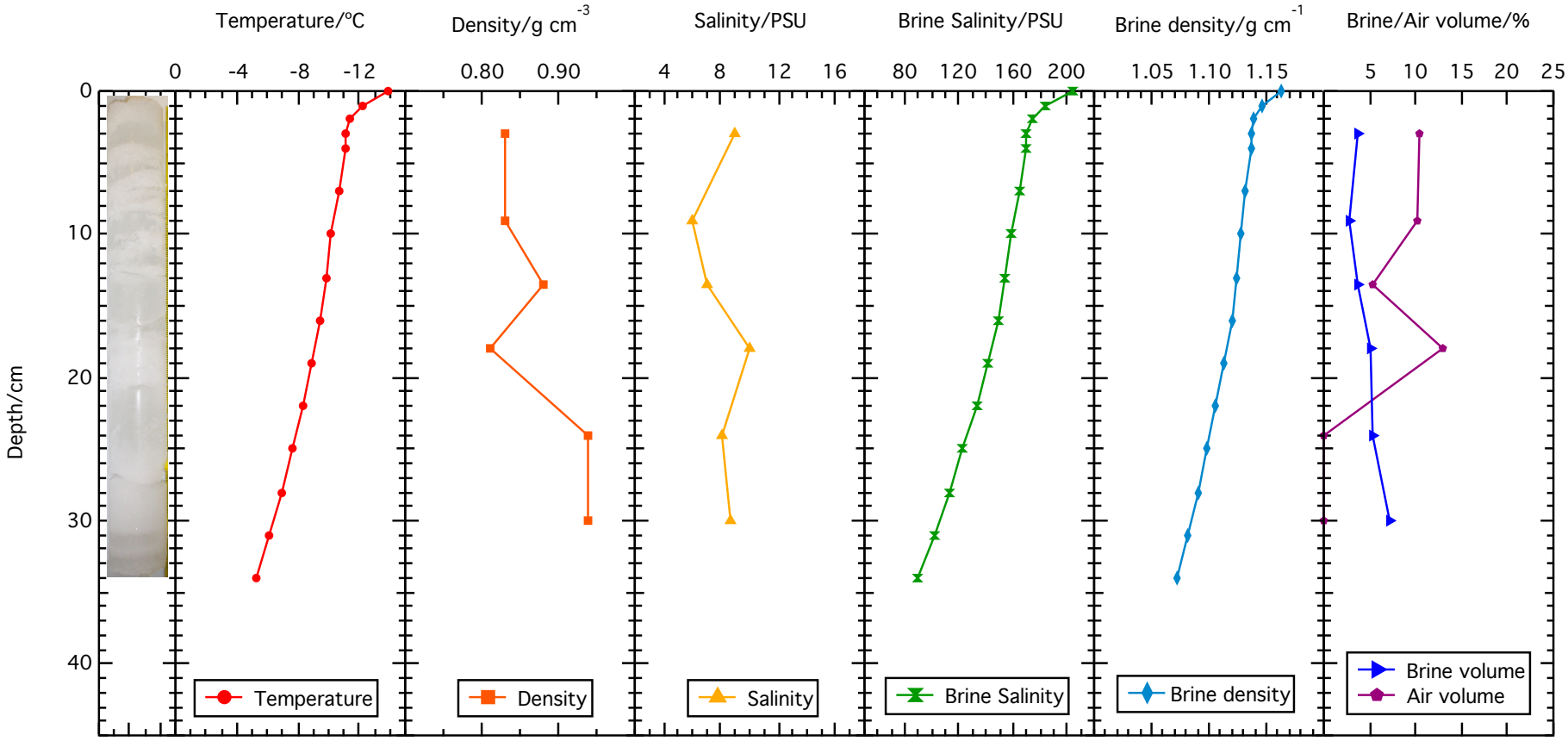

Figure 6.10 – **Run 4 before layer added** *Physical ice properties for bottom "clean" ice layer before additional black carbon bearing layer added for run 4. Temperature, density and salinity are measured from core sections, while brine salinity, brine density and brine and air volume are derived from equations of Cox and Weeks (1983). Photo of the ice core is also shown.*

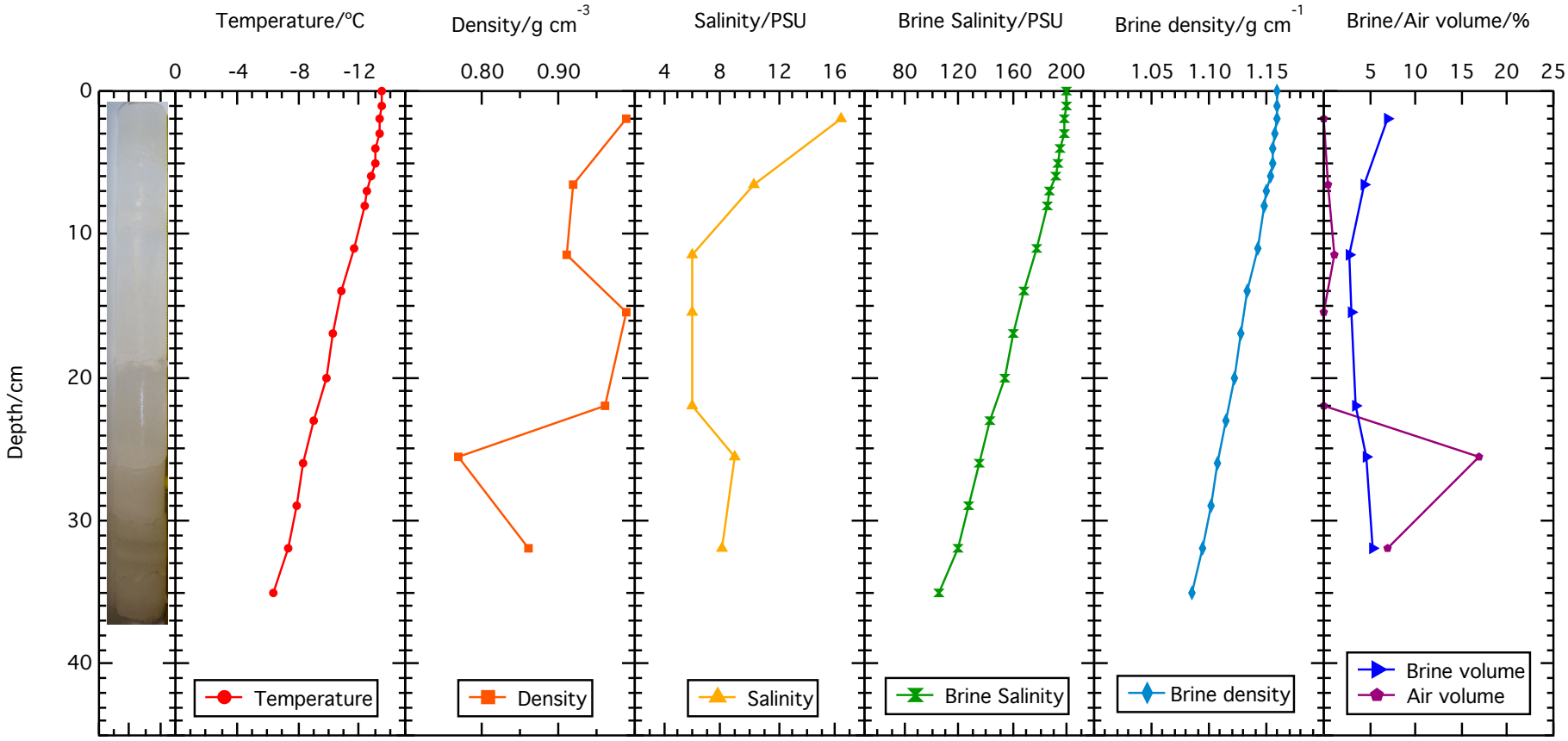

Figure 6.11 – **Run 4 after layer added** *Physical ice properties for bottom "clean" ice layer and additional black carbon bearing layer for run 4. Temperature, density and salinity are measured from core sections, while brine salinity, brine density and brine and air volume are derived from equations of Cox and Weeks (1983). Photo of the ice core is also shown*

6.3 Evaluation of the TUV-snow model

6.3.1 Evaluation method

To carry out evaluation of the TUV-snow model the results of variation in reflectance with black carbon in a top 5 cm layer of the artificial sea ice are compared to a calculated change in reflectance due to black carbon in sea ice calculated using the TUV-snow model. Section 6.3 will begin with a simple comparison between measurements of the change in reflectance due to black carbon, and calculations using the TUV-snow model, where the value of the scattering cross-section of the ice in the model is adjusted to achieve an optimum fit between the calculated and measured values. Following this, a more detailed evaluation is carried out where the properties of the simulated ice are deciphered from *e*-folding depth and reflectance data in a similar manner to chapter 3, this method accounts for any absorption present in the "clean" ice.

To initially model the artificial sea ice a 40 cm layer of clean ice (i.e. pure ice with no other absorbing impurities) and an upper 5 cm layer of clean ice with black carbon in concentrations of 0, 75, 150 and 300 ng g^{-1} was used. The same black carbon absorption spectrum was used as for radiative-transfer calculations in chapters 2–4 (based on Mie calculations with a wavelength independent refractive index of spherical black carbon particles of 1.8±0.5i, a diameter of 0.2 μm and density of 1 g m^{-3} (Warren and Wiscombe, 1985, 1980)). The value for the asymmetry parameter, g, was set to 0.95 as Mobley et al. (1998) state that g values for ice range from 0.95 to 0.99 depending on bubble content. The average air bubble content for the ice across all runs (measured from ice cores) was 3.84% (±1.93%), this counts as a bubble-rich ice, according to Mobley et al. (1998), thus a g value of 0.95 is used. The under ice albedo was set to the reflectance measured when the tank was filled with seawater, when no ice was present. The density of the top and bottom ice layer for each run is set to the density measured from ice cores as shown in table 6.3. Illumination conditions in the TUV-model were made isotropic, to match conditions in the simulator, by placing a cloud layer with an optical thickness of 32, a height of 1 km, an asymmetry parameter of 0.85 and a single scattering albedo of 0.9999. Albedo and *e*-folding depth measurements are independent of illumination intensity

so modelling with a diffusing cloud layer is acceptable. For the initial fit the scattering cross-section of both the ice layers (the 40 cm bottom clean ice layer (σ_{scatt}^{bottom}), and the top 5cm black carbon bearing layer (σ_{scatt}^{top})) was varied to achieve the best fit between modelled and measured data. The best fit was achieved through trial and error by modelling a range of black carbon and scattering cross-section values to see which produced a reflectance profile that was closest (judged by eye) to the measured reflectance, then systematically making small changes to these values to obtain to closer fit. The above method produces fits A and B as described below.

Following the initial fit of measured and calculated values a more precise fit is carried out where absorption and scattering cross-section values as a function of wavelength for the bottom "clean" ice layer are derived from reflectance and *e*-folding depth data (see section 6.3.4). Using the derived scattering and absorption cross-sections, calculations with the TUV-snow model were repeated, using the same set up as for the initial fit described above. However, the 40 cm bottom "clean" ice layer was set to have the absorption and scattering cross-section values described in section 6.3.4. For the top 5 cm black carbon bearing layer the same absorption as the bottom layer was used plus additional absorption due to the black carbon, the scattering value (σ_{scatt}^{top}) was varied from 0.01 to 1 m^2 kg^{-1}, the range for sea ice, as described in chapter 4 and by Perovich (1990, 1996), Mobley et al. (1998) and King et al. (2005) to obtain the best fit, this method produces fits C–G described below.

To produce an optimum fit between measured and modelled values of reflectance seven different fits are produced (A–G), with fit G providing the optimum fit. In each successive fit a parameter is adjusted to better recreate the artificial sea ice, as described below. These parameters include the scattering cross-section of the top (σ_{scatt}^{top}) and bottom (σ_{scatt}^{bottom}) layer, the black carbon mass-ratio modelled in the top layer ($BC_{modelled}$) and presence of other absorbing impurities (σ_{abs}^{+}) in both the bottom and top layer. Other parameters, for example, g value, ice thickness and black carbon absorption cross-section were not varied but the effect of varying these parameters is examined in the discussion, section 6.4. Table 6.4 summarises the values used for σ_{scatt}^{top}, σ_{scatt}^{bottom}, $BC_{modelled}$ and if σ_{abs}^{+} for the top and bottom layer was included for each fit, which will be presented in the results section 6.3.2.

Fits A and B Initial fit using the TUV-snow model with same scattering cross-section in top and bottom layer, no extra impurities added. Fit A uses a different

scattering cross-section for each run, while Fit B uses the same scattering cross-section for each run

Fits C and D Fit including derived impurity absorption cross-section for top and bottom layer, and derived scattering cross-section for the bottom layer. Scattering of the top, black carbon bearing layer, is adjusted within reasonable limits to provide the best recreation of the artificial sea ice. Fit C has a different scattering cross-section for the top layer for each run (1–4), while fit D uses the same scattering cross-section for the top layer for each run for comparison

Fits E, F and G Fit with reduced black carbon in the top layer to obtain a better fit. Again fit E has a different scattering cross-section for the top layer for each run, while fit F shows the same scattering cross-section. Fit G, for an optimum fit, shows a compromise between fits E and F with a small range of scattering cross-section in the top layer.

Fit	Run number	σ_{scatt}^{top}	σ_{scatt}^{bottom}	$[BC]_{modelled}$	σ_{abs}^{+}?
A	Run 1	0.5	0.5	0	Not included
	Run 2	0.8	0.8	75	Not included
	Run 3	0.9	0.9	150	Not included
	Run 4	1.4	1.4	300	Not included
B	Run 1	0.5	0.5	0	Not included
	Run 2	0.5	0.5	75	Not included
	Run 3	0.5	0.5	150	Not included
	Run 4	0.5	0.5	300	Not included
C	Run 1	0.01	0.315	0	Included
	Run 2	0.5	0.235	75	Included
	Run 3	1.0	0.115	150	Included
	Run 4	1.0	0.126	300	Included
D	Run 1	0.1	0.315	0	Included
	Run 2	0.1	0.235	75	Included
	Run 3	0.1	0.115	150	Included
	Run 4	0.1	0.126	300	Included
E	Run 1	0.02	0.275	0	Included
	Run 2	0.05	0.235	30	Included
	Run 3	0.4	0.115	50	Included
	Run 4	0.2	0.126	100	Included
F	Run 1	0.2	0.275	0	Included
	Run 2	0.2	0.235	30	Included
	Run 3	0.2	0.115	40	Included
	Run 4	0.2	0.126	100	Included
G	Run 1	0.1	0.275	0	Included
	Run 2	0.1	0.235	30	Included
	Run 3	0.3	0.115	40	Included
	Run 4	0.2	0.126	100	Included

Table 6.4 *– Values of parameters used for each fit (A–G) including scattering cross-section used for the top, black carbon bearing layer, σ_{scatt}^{top}, the bottom clean ice layer, σ_{scatt}^{bottom}, mass-ratio of black carbon used in the TUV-snow model, $BC_{modelled}$, and if absorption by impurities other than black carbon, σ_{abs}^{+}, for the top and bottom layer was included. The asymmetry parameter, g, value is kept constant at 0.95 for each fit, as is the density and ice thickness for each fit.*

6.3.2 Evaluation results

6.3.3 Initial TUV-snow model fit (fits A and B)

The calculated reflectance using the TUV-snow model for the initial fit (fits A and B) where the bottom layer is assumed to contain no absorbing impurities and the top layer is assumed to only have black carbon as an absorbing impurity, is shown

in figure 6.12. The scattering cross-section of both the ice layers (the bottom 40 cm clean ice layer, and the top 5 cm black carbon bearing layer) was varied to achieve the best fit between modelled and measured data in fit A and kept constant in Fit B.

Figure 6.12 initially suggests a fairly good fit between modelled and measured data, particularly at wavelengths from 450 nm to 550 nm. Below 450 nm and above 550 nm the modelled reflectance is higher than the measured, which is particularly prominent at the shorter wavelengths. It is important to note the lower reflectance at shorter and longer wavelengths occurs at all black carbon mass-ratios including run 1 (0 ng g^{-1} black carbon in top layer) suggesting the presence of a further absorbing impurity present in the "clean" ice that absorbs at wavelengths 350–450 nm and 550–650 nm, a concept examined in section 6.3.4.

In figure 6.12 the same scattering cross-section was used for both the "clean" bottom 40 cm layer of ice and the 5 cm, black carbon bearing, top layer of ice. For fit A, for each run a different scattering cross-section was used. 0.5 m^2 kg^{-1} was used for run 1, 0.8 m^2 kg^{-1} for run 2, 0.9 m^2 kg^{-1} for run 3 and 1.4 m^2 kg^{-1} for run 4. These values are not unrealistic, however 1.4 m^2 kg^{-1} would be a very large value for sea ice. The variation in scattering cross-sections used is surprisingly large, although slight variation would be expected with each new ice growth. Furthermore, the scattering cross-section increases with each run, a gradually higher scattering cross-section required to produce a fit suggests the change in reflectance caused by the additions of black carbon measured for the ice is less than is calculated by the TUV-snow model. Fit B in figure 6.12 shows the modelled versus measured reflectance if the scattering cross-section for the ice is kept constant at 0.5 m^2 kg^{-1} (the scattering cross-section that fits run 1 in fit A). Although a good fit is achieved for 0 ng g^{-1} (run 1), the other calculated reflectances are all too low, with this becoming worse as black carbon mass-ratio increases. To better understand the absorption and scattering cross-sections of the simulated ice, reflectance and *e*-folding depth data can be used to derive these values, as discussed in section 6.3.4.

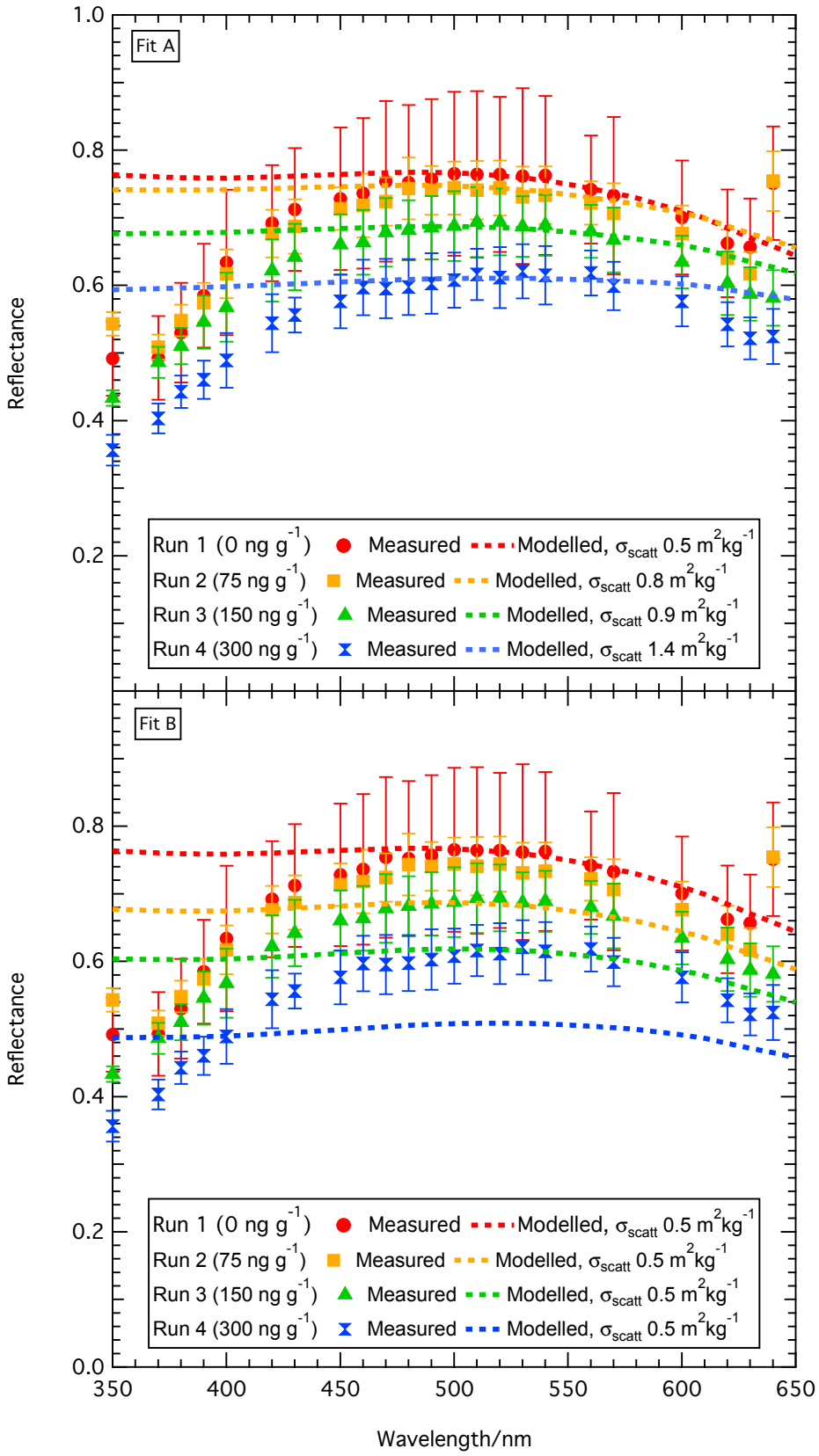

Figure 6.12 *– Fits A and B: Comparison between measured and modelled (dashed lines) reflectance of simulated sea ice surface due to black carbon in a 5 cm surface layer in concentrations of 0 ng g^{-1}, 75 ng g^{-1}, 150 ng g^{-1} and 300 ng g^{-1}. Fit A shows a fit where the scattering cross-section for the top and bottom layer is varied between each run to obtain the best fit. Fit B shows a fit where the scattering cross-section of the top and bottom layer are kept constant between each run.*

6.3.4 Deriving scattering and absorption cross-section from albedo and *e*-folding depth data

The initial fit (fits A and B) described in section 6.3.3 alludes to there being an absorbing impurity present in the clean ice which causes the decreased reflectance observed at longer and shorter wavelengths. Using the method described in chapter 3 and used by Lee-Taylor and Madronich (2002) the albedo and *e*-folding depth data of the clean ice below the black carbon layer can be used to derive a scattering and absorption cross-section for the clean ice and thus determine the presence of absorbing impurities present in the "clean" ice.

Using the same method described in detail in chapter 3, the reflectance (figure 6.2) and *e*-folding depth (figure 6.3) data for the bottom clean ice layer from each run (before black carbon is added to the surface) are fitted to obtain unique scattering and absorption cross-section values as a function of wavelength. The derived absorption cross-section values for the bottom ice for each run, shown in figure 6.13, are highly wavelength dependent. Figure 6.13 clearly shows there is either a small amount of light absorbing impurity with a large absorbing cross-section or a large amount with a weak absorption cross-section at wavelengths from 350 to 450 nm, present in the "clean" ice. The presence of an absorbing impurity, other than black carbon, which absorbs at wavelengths from 350 to 450 nm explains the bad fit of data in the initial fit of data with the TUV-snow model, figure 6.12, (fits A and B) at shorter wavelengths. The derived absorption cross-section for each run is fairly similar, decreasing slightly with increased run number. The slightly decreased absorption with increased run number is congruent with the increase in *e*-folding depth observed in figure 6.3. However the difference in the *e*-folding depth with run number observed is more extreme than the derived difference in absorption cross-section, and the decrease in absorption cross-section does not agree with the decrease in reflectance values observed in figure 6.2; increased absorption cross-section would lower reflectance. Therefore, it is also likely that a variation in the scattering cross-section is a main contributing factor to the different *e*-folding depths and reflectance values observed for the "clean" bottom ice layer for different run numbers.

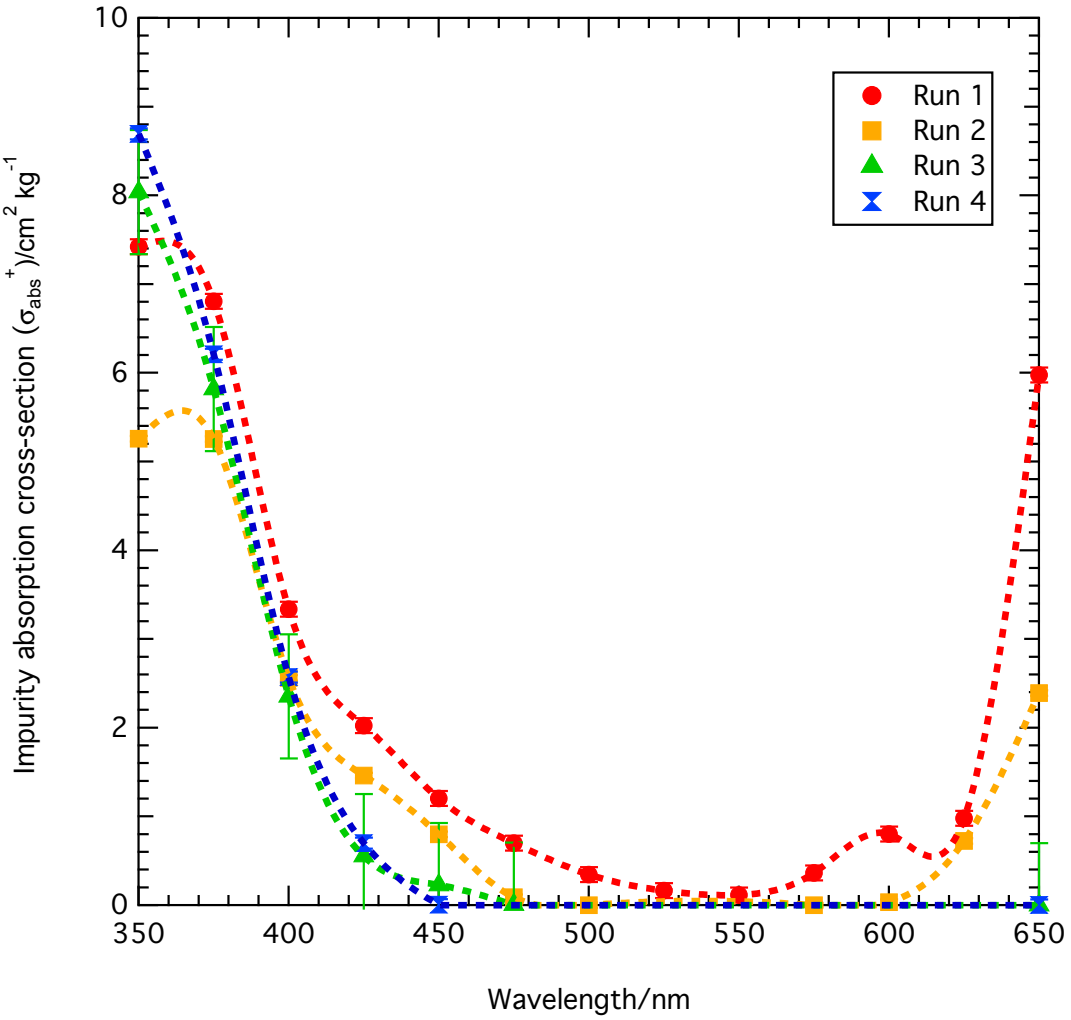

Figure 6.13 *– Wavelength dependent absorption cross-section derived from reflectance and e-folding depth data from runs 1 to 4 for the "clean" bottom ice layer. A smooth line is added to guide the eye. Values for run 4 are too small to plot clearly.*

Figure 6.14 shows the derived scattering cross-section for runs 1 to 4 for the bottom "clean" ice layer, also derived using the method described in chapter 3. Conversely to the absorption cross-section the scattering cross-section is not wavelength dependant with perhaps only a slight decrease in scattering cross-section at shorter wavelengths seen in runs 1 and 2. The decreased scattering cross-section values at shorter wavelengths could be attributed to different lights (UV versus visible) used to provide intensities at these wavelengths. As in chapter 3, scattering cross-section is thus assumed to be wavelength independent, yielding the values in table 6.5.

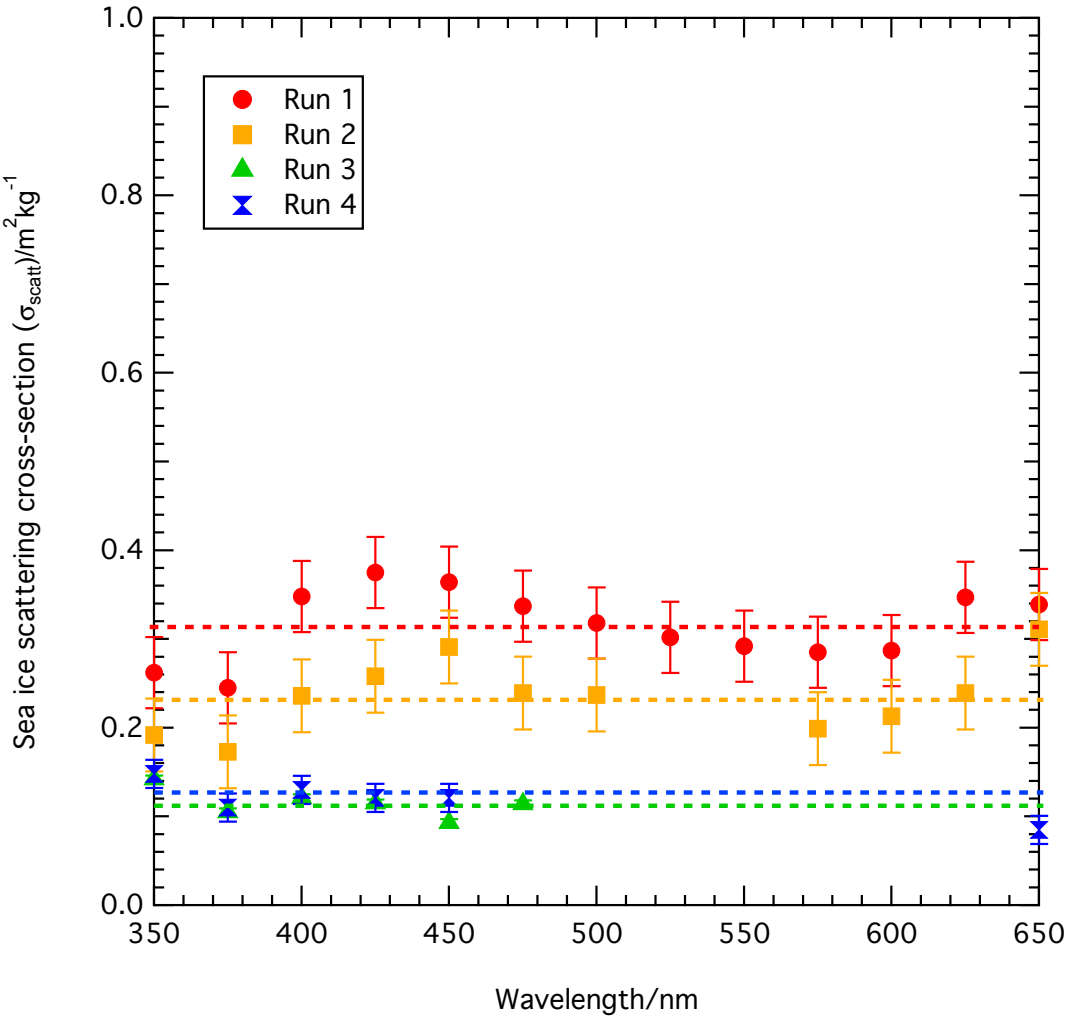

Figure 6.14 *– Scattering cross-section derived from reflectance and e-folding depth data from runs 1 to 4, for the "clean" bottom ice layer. A straight line is added for the average scattering cross-section for each run. Error bars show ± 1SD of all scattering cross-section values. Missing values occur where fit between reflectance and e-folding depth data gave a poor fit for absorption and scattering cross-section values as the absorption cross-section at these wavelengths was very low.*

Run number	**Scattering cross-section /m^2 kg^{-1}±1SD**
1	0.315±0.040
2	0.235±0.041
3	0.115±0.004
4	0.126±0.016

Table 6.5 *– Average scattering cross-section values of bottom "clean" ice layer for runs 1 to 4.*

6.3.5 Comparison of measured reflectance of artificial sea ice to model results using derived scattering and absorption cross-section values (Fits C–G)

Using the scattering and absorption cross-sections derived in section 6.3.4 calculations with the TUV-snow model in section 6.3.3 were repeated. The bottom layer had the derived scattering and absorption cross-section for the applicable run number, and the top, black carbon bearing layer, had the same absorption cross-section as the bottom layer for that run plus absorption by black carbon. The scattering cross-section of the top layer was varied between runs within reasonable limits to recreate the artificial ice in fit C and kept constant in fit D. The calculated reflectance for each run is shown in figure 6.15 for fits C and D.

In fit C the fit between the modelled and measured reflectance is fair. For 0 ng g^{-1} (run 1) the shape of the fit is very good at all wavelengths, however reflectance values at all wavelengths are slightly higher than measured values. For 75 ng g^{-1} (run 2) the shape of the fit is good for wavelengths from 450 to 550 nm, with the calculated and measured reflectance values being very similar. At shorter and longer wavelengths the fit is poorer, particularly at short wavelengths where the calculated values are significantly higher than the measured values. At 150 ng g^{-1} and 300 ng g^{-1} the shape of the calculated values poorly fits the measured values, at mid wavelengths from 450 to 550 nm the calculated reflectance values are lower than measured values, while at longer and shorter wavelengths the calculated values are significantly higher than measured values, again this is particularly true at the shortest wavelengths. The incorrect shape of the fits observed for 75, 150 and 300 ng g^{-1} (runs 2–4) could have two causes, firstly the absorption cross-section values used are incorrect or the scattering values used in the top or bottom ice layer are too high thus the absorption in the ice is less effective, as discussed in chapter 4. It is noticeable that the scattering cross-section of the upper 5 cm layer required to achieve a fit substantially increases from runs 1–4, from 0.01 m^2 kg^{-1} to 1.0 m^2 kg^{-1}, this is the difference between a melting ice and a frozen multiyear ice, there is no particular reason why this would occur, and thus may be inaccurate.

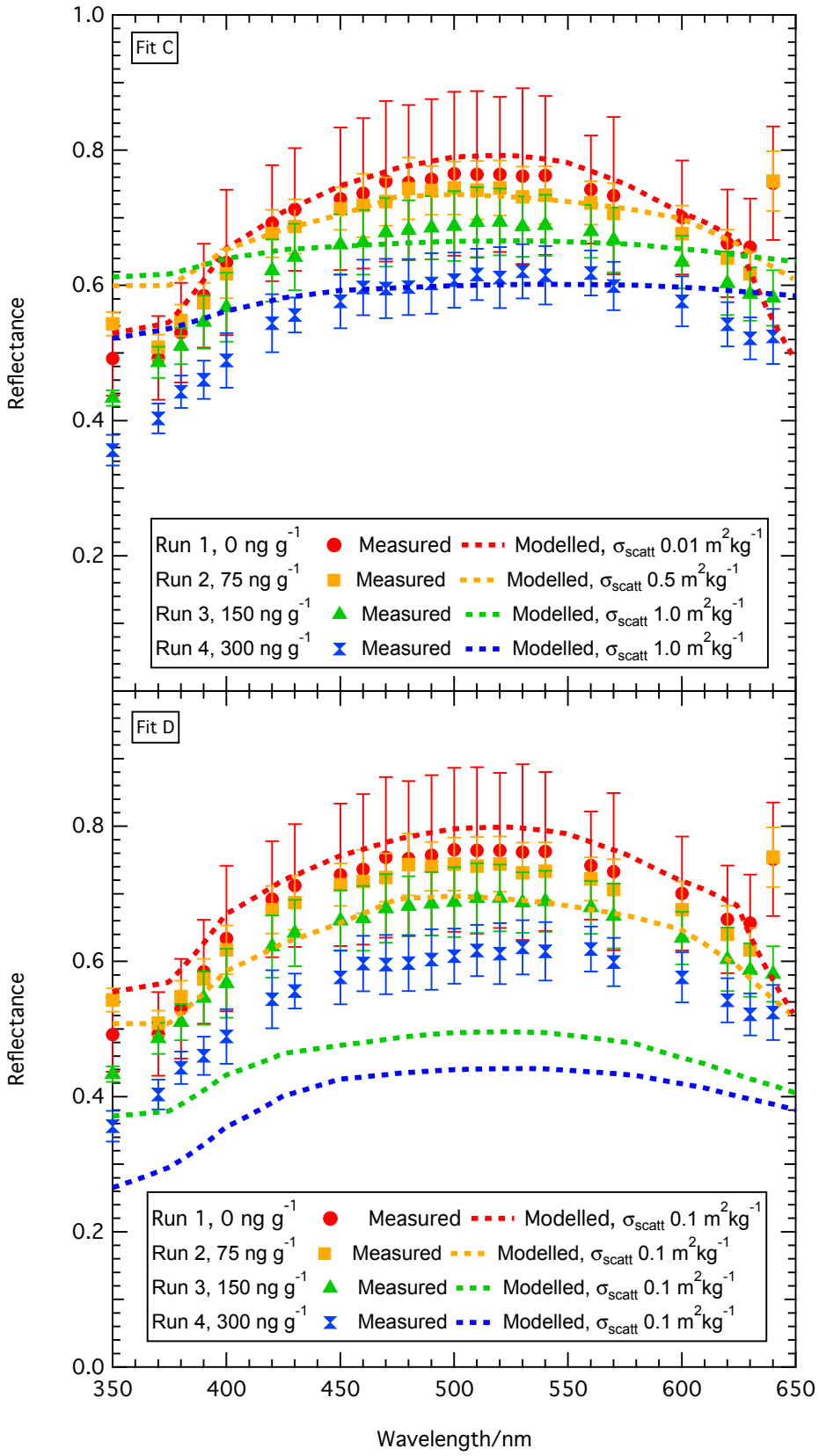

Figure 6.15 *– Fits C and D: Comparison between measured and calculated (dashed lines) reflectance of simulated sea ice surface due to black carbon in a 5 cm surface layer in concentrations of 0 ng g^{-1}, 75 ng g^{-1}, 150 ng g^{-1} and 300 ng g^{-1}. Derived absorption by impurities is added to the top and bottom layer, and the bottom layer is fitted with the derived scattering cross-section. Fit C shows a fit where the scattering cross-section for the top layer is varied between each run to obtain the best fit. Fit D shows a fit where the scattering cross-section of the top layer is kept constant between each run.*

Figure 6.15 fit D shows a comparison between modelled and measured reflectance using the same, more realistic, scattering cross-section value of 0.1 m^2 kg^{-1} for the top 5 cm layer for all runs. Although none of the calculated values are the same as the measured values, for each run, the shapes of the calculated reflectance curves are much more representative than fit C.

The low reflectance values for runs 2, 3 and 4 in fit D at all wavelengths using the same scattering cross-section suggests the absorption cross-section at all wavelengths used in the TUV-snow model is too large. The only way a smaller absorption cross-section at all wavelengths can be achieved is by reducing the amount of black carbon modelled in the top layer. Figure 6.16 shows a fit between modelled and measured reflectance values where the black carbon mass-ratio in the top layer is significantly reduced to obtain an optimum fit (fits E and F). In fit E the scattering cross-section in the top layer is varied while in fit F it is kept constant. In both fits E and F the modelled values of reflectance fit within the error of measured values at all wavelengths. The variation in scattering cross-section in fit E is much less than fit C but still varies by a factor of 20, which seems unrealistic. However, if the upper layer scattering cross-section is kept constant, as in fit F, although the fit is still within error, it is not as good as fit E and black carbon for run 3 has to be further reduced. To reach a compromise between fits E and F figure 6.17 shows a similar fit to fits E and F but the scattering cross-section in the top ice layer is only varied by a factor of 3 and within the limits of the scattering cross-section of the bottom ice layer, thus likely to be realistic of the artificial ice (fit G). Fit G is good at all wavelengths and well within the uncertainty of measured reflectance values.

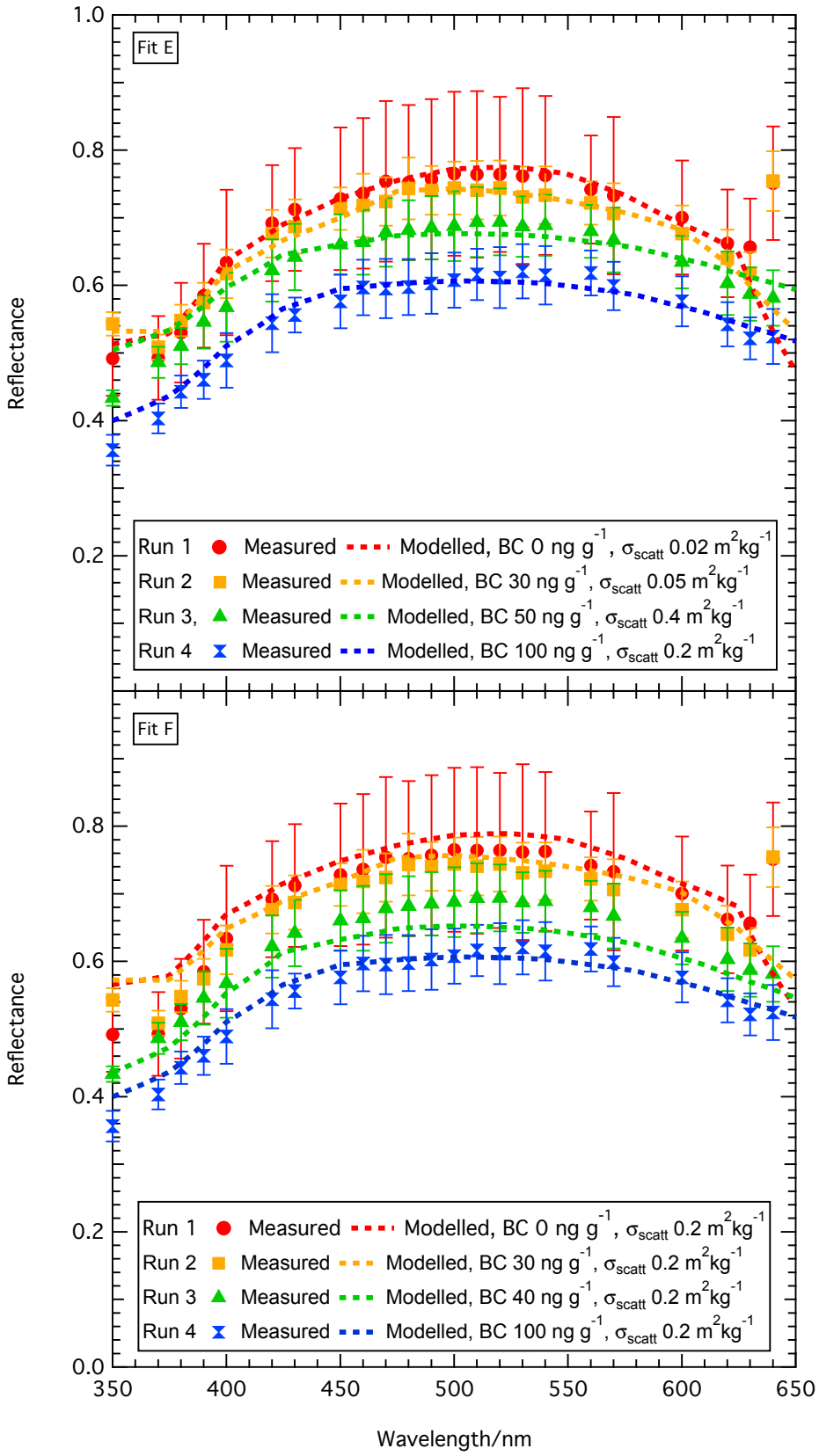

Figure 6.16 *– Fits E and F: Comparison between measured and calculated (dashed lines) reflectance of simulated sea ice surface due to black carbon in a 5 cm surface layer. Black carbon in the surface layer in the model is reduced, as shown, to achieve a better fit. Derived absorption by impurities is added to the top and bottom layer, and the bottom layer is fitted with the derived scattering cross-section. Fit E shows a fit where the scattering cross-section for the top layer is varied between each run to obtain the best fit, as shown. Fit F shows a fit where the scattering cross-section of the top layer is kept constant between each run, as shown.*

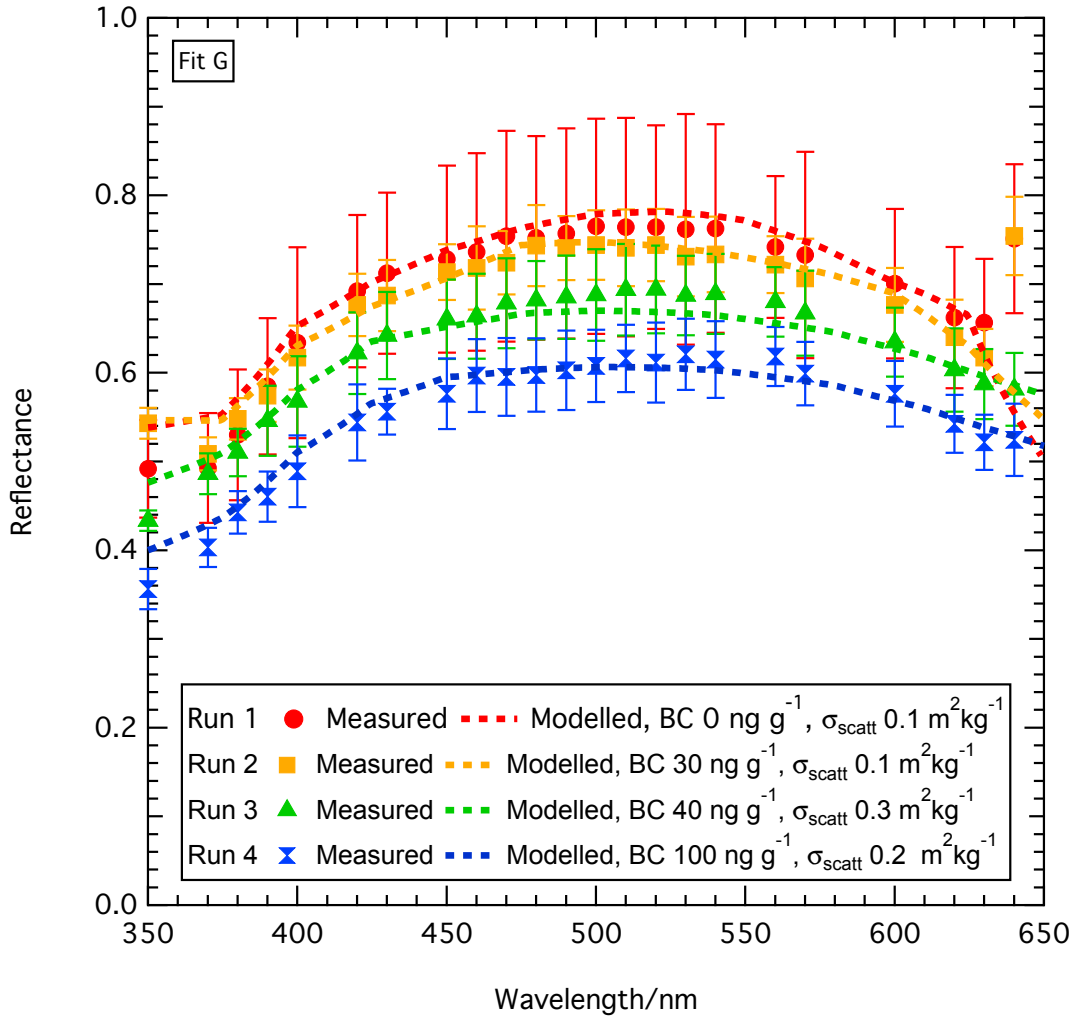

Figure 6.17 *– Fit G: Comparison between measured and calculated (dashed lines) reflectance of simulated sea ice surface due to black carbon in a 5 cm surface layer. Black carbon in the surface layer is decreased to obtain a better fit. Derived absorption by impurities is added to the top and bottom layer, and the bottom layer is fitted with the derived scattering cross-section. Scattering cross-section of the top layer is between fits E and F, being within reasonable limits, but also varying to provide an accurate representation of measured values.*

6.4 Discussion

The discussion section will focus on the possible reasons why calculations with the TUV-snow model require about a factor of three less black carbon to fit the reflectance measured with black carbon in the top 5 cm layer of artificial sea ice. The discussion section will also examine the realism of the simulated scenario including the effect that adding an extra layer of ice to the surface has on the overall ice properties and structure and the presence of other absorbing impurities in the “clean” ice.

6.4.1 Reasons for reduced black carbon mass-ratio to produce fit between modelled and measured reflectance

Section 6.4.1 will examine the causes of the reduced black carbon mass-ratio required to model the artificial sea ice (fit G), for which there are several potential reasons. The most influential causes are a potential difference in the optical and physical properties of the black carbon used in the model compared to the black carbon added to the artificial sea ice and the fact that black carbon may not stay in the surface layer of the sea ice. Other influential factors could include an incorrect asymmetry parameter (g value) used for calculations, variation in thickness of the top and bottom layer, uncertainty in the derived scattering and absorption cross-section and uncertainty in the mass-ratio of black carbon added to the artificial sea ice in the top layer.

6.4.1.1 Black carbon properties

The black carbon optical and physical properties used in the TUV-snow model may differ from those of the black carbon added to the artificial sea ice surface. The black carbon added to the sea ice is a commercially produced standard black carbon which is very similar (according to the manufacturer) to Monarch 71 used by Clarke (1982) and Grenfell et al. (2011). Grenfell et al. (2011) state that the absorption of Monarch 71 at 525 nm is 6 m^2 g^{-1}, which is significantly less than the value of $\sim$10 m^2 g^{-1} used in the radiative-transfer calculations presented in this thesis. Figure 6.18 shows a comparison between the slightly wavelength dependant black carbon absorption used previously, and the suggested black carbon absorption for Monarch 71 of 6 m^2 g^{-1}, based on same parameters as fit G but with the black carbon mass-ratio in the top layer increased to the original amount (0, 75, 150 and 300 ng g^{-1}). Figure 6.18 shows how the decreased absorption cross-section (6 m^2 g^{-1}) for black carbon significantly increases the reflectance at all wavelengths for each run with the same mass-ratio of black carbon. For run 2 (75 ng g^{-1} of black carbon) the reflectance becomes within uncertainty (1 SD) of the measured reflectances. However for runs 3 and 4, although the reflectance increases it is still not within the uncertainty of the measured reflectance values.

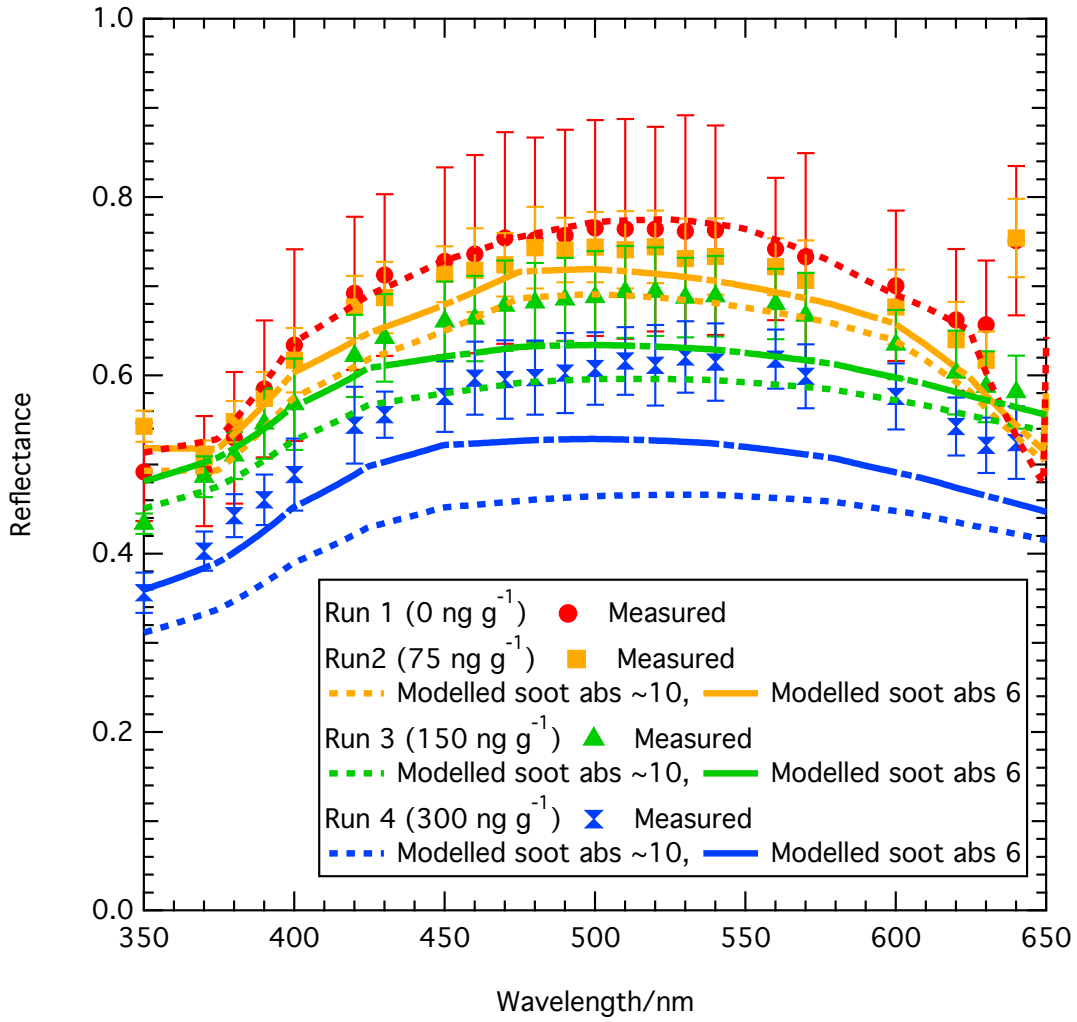

Figure 6.18 *– Modelled reflectance values, based on the same parameters for fit G but full black carbon mass-ratios used for each run (0, 75, 150 and 300 ng g^{-1} respectively) with a black carbon absorption cross-section of ~10 m^2 g^{-1} and 6 m^2 g^{-1}. Measured reflectance values also shown with ±1 SD uncertainty bars.*

The black carbon used for the radiative transfer calculations is assumed to have a particle diameter of 0.2 μm, however this might be unrealistic of the particle size used in the simulator. Figure 6.19 shows the effect of changing particle size from 0.01–0.8 μm on the absorption cross-section of black carbon at a wavelength of 600 nm. As particle size increases the absorption cross-section decreases to less than 50% of the value for a particle diameter of 0.2 μm. Therefore if the particle size is actually around 0.6 μm a factor of ~2.5 more black carbon would be required than for a particle size of 0.2 μm, which could help explain the discrepancy between the calculated and measured values.

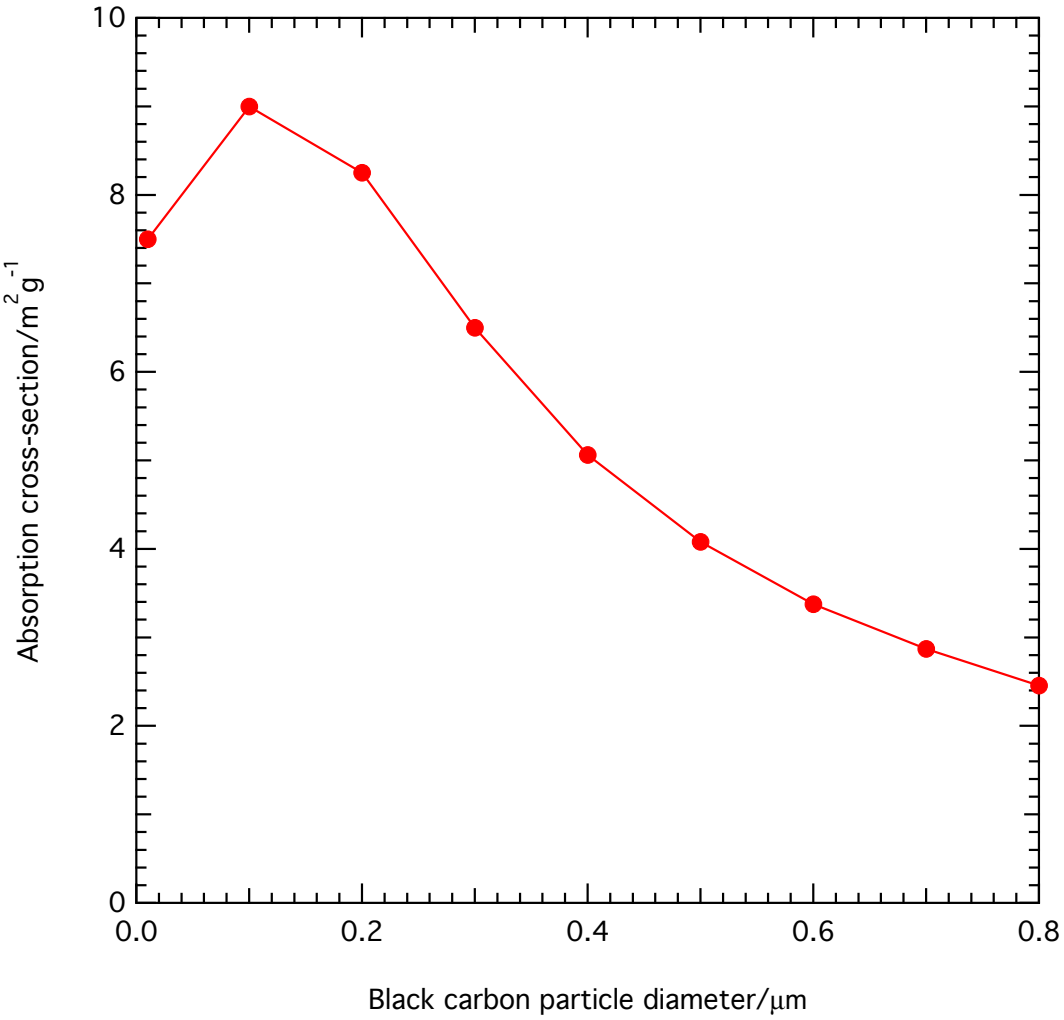

Figure 6.19 *– Absorption cross-section of black carbon in ice for different size black carbon particles at a wavelength of 600 nm, derived by Mie calculation.*

6.4.1.2 Black carbon mobilisation

Sea ice is a dynamic environment constantly seeking equilibrium with its surroundings. The addition of the 75 L of artificial sea water to the surface of the simulated sea ice disturbs the equilibrium by increasing pressure on the ice and disturbing the temperature and salinity gradient through the ice. The seawater added to the surface will have a higher salinity than the underlying sea ice, as observed in the data from ice cores (figures 6.5–6.11 and table 6.3). As the extra layer of seawater freezes brine will drain downwards into the layer of ice below and also be expelled onto the surface. It is unknown whether the black carbon would be frozen into the ice structure or rejected into the brine inclusions within the ice. Eicken (2003) suggest that impurities in seawater are trapped in the brine inclusions as sea ice grows. If black carbon is

situated in brine inclusions then some of it will drain into the underlying layer of sea ice and eventually into the underlying seawater as described in chapter 5 and by Eicken (2003). The loss of black carbon from the surface sea ice layer into the underlying sea ice and seawater may contribute to the need for less black carbon used to give a good fit between modelled and measured reflectance values. Furthermore Doherty et al. (2010) who measured black carbon mass-ratios in sea ice in the Arctic show that black carbon is concentrated at the surface of the sea ice but also found in smaller concentrations throughout the ice, supporting the idea that black carbon deposited onto the surface of sea ice can be mobilised through the ice.

6.4.1.3 Asymmetry parameter

Based on the suggestion by Mobley et al. (1998) for a bubble rich ice an asymmetry parameter, g, value of 0.95 is utilised when both deriving the absorption and scattering cross-section and also for the subsequent modelling. Table 6.6 shows the effect on absorption of impurities other than black carbon and scattering cross-section at 400 nm for changing the value of g within possible values for sea ice; 0.94–0.99 (Mobley et al., 1998).

Run	**g=0.94**		**g=0.95**		**g=0.96**		**g=0.97**		**g=0.98**		**g=0.99**	
number	σ_{abs}	σ_{scatt}	σ_{abs}	σ_{scatt}	σ_{abs}	σ_{scatt}	σ_{abs}	σ_{scatt}	σ_{abs}	σ_{scatt}	σ_{abs}	σ_{scatt}
1	3.32	0.29	3.34	0.35	3.34	0.43	3.27	0.54	3.09	0.74	3.54	1.64
2	2.55	0.19	2.56	0.24	2.59	0.31	2.60	0.40	2.71	0.57	2.76	1.14
3	2.46	0.10	2.35	0.12	2.23	0.16	2.28	0.21	2.32	0.31	2.34	0.63
4	0.95	0.07	0.92	0.08	0.83	0.10	0.93	0.14	0.83	0.21	0.97	0.44

Table 6.6 *– Variation in absorption cross-section ($cm^2\ kg^{-1}$) and scattering cross-section ($m^2\ kg^{-1}$) owing to variation in the asymmetry parameter at 400 nm.*

Table 6.6 shows that change in the g value has very little effect on the absorption cross-section with the average standard deviation being only 0.092. Therefore, an incorrect value of g is unlikely to be a cause for the lack of fit between measured and modelled reflectance values.

In the case of scattering cross-section, the effect of changing g from 0.94–0.99 at 400 nm is also shown in table 6.6. Changing the g value has a much larger effect on the scattering cross-section, with a larger g value giving a larger scattering cross-section. Changing scattering cross-section however would not improve the fit between

modelled and measured reflectance as this would change the shape of the reflectance curve as well as the values, as a sea ice with a larger scattering cross-section means absorbing impurities have less effect, as described in chapter 4.

Overall an incorrect g value is unlikely to be the cause for the lack of fit between measured and calculated values.

6.4.1.4 Layer thickness

The surface onto which the 75 L of seawater containing black carbon was poured, to form the top layer, was not completely smooth/flat, as is shown in figure 6.20. An uneven surface could have resulted in an uneven 5 cm black carbon bearing layer, with possible deviations of ±1 cm over the area were reflectance is measured.

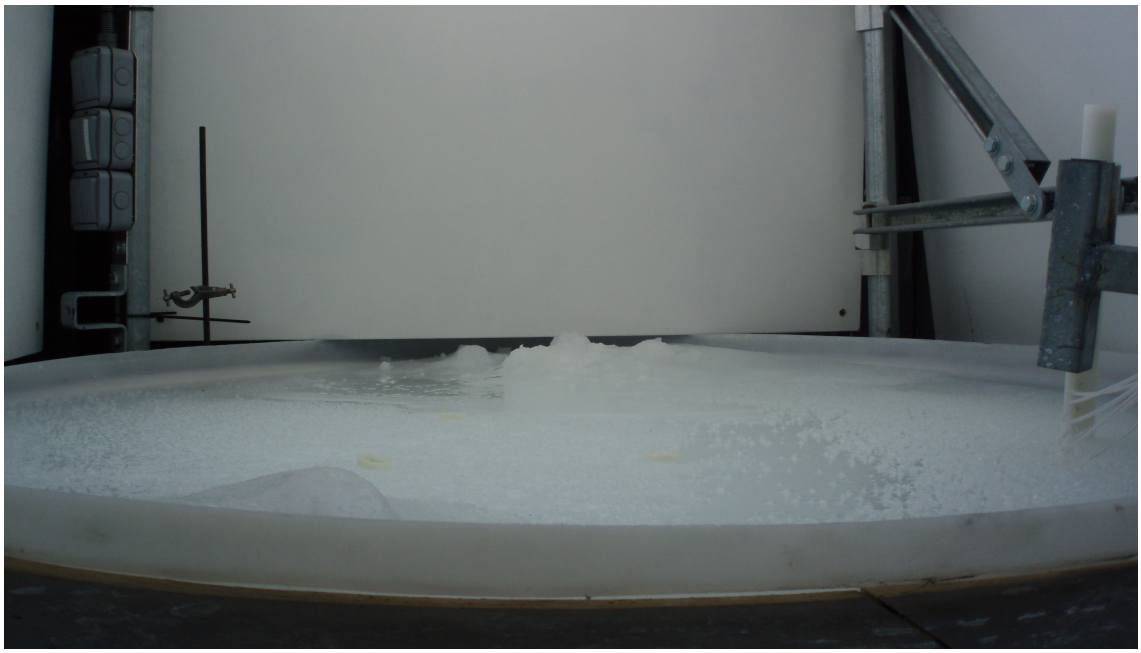

Figure 6.20 *– Example of rough ice surface to which the 75 L of black carbon bearing seawater was added, this could cause deviations from a flat 5 cm layer of ±1 cm.*

Figure 6.21 shows the influence of increasing and decreasing the thickness of the upper black carbon bearing layer by 1 cm, using the same parameters as fit G. However, the black carbon mass-ratio is kept at the original values (0, 75, 150 and 300 ng g^{-1}). Figure 6.21 shows the effect of increasing or decreasing thickness of the top black carbon bearing layer is minimal for all runs. The greatest effect is seen for run 4, 300 ng g^{-1} of black carbon in the top layer, where a 4 cm layer has a slightly higher reflectance at all wavelengths. However the difference is not significant enough to

make up for the difference in reflectance between the measured and modelled values, although could be a contributing factor.

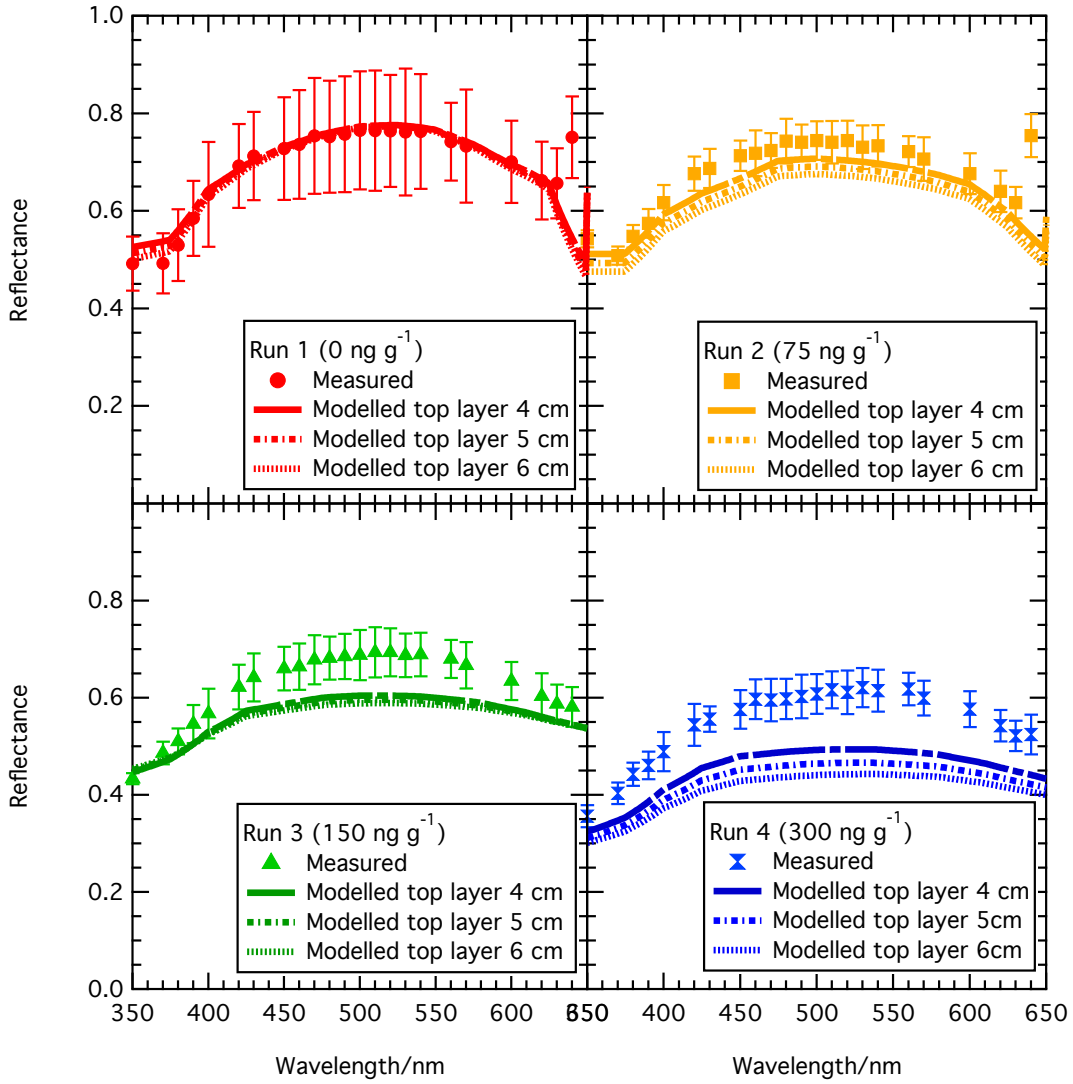

Figure 6.21 *– Comparison between calculated and measured reflectance for runs 1–4. Modelling is based on the parameters for fit G, although black carbon mass-ratios in the top layer of 0, 75, 150 and 300 ng g^{-1} are used for runs 1–4 respectively. The top layer is modelled as 4, 5 and 6 cm thick to understand the role of top layer thickness in calculated reflectance values.*

The thickness of the bottom ice layer is modelled as 40 cm thick, this is based on an average of data from core measurements and depth deduced from temperature measurements. However, as table 6.2 suggests, the whole ice thickness (including the top layer) could be ∼±5 cm of the 45 cm ice layer modelled. Figure 6.22 demonstrates the effect of changing the thickness of the bottom ice layer by ±5 cm, using the same parameters as fit G. The effect of changing the bottom layer thickness is minor for all runs, with the fit still being well within error. As the ice is near “optical

thickness" a small change in the thickness of the bottom layer has limited effect on the surface reflectance.

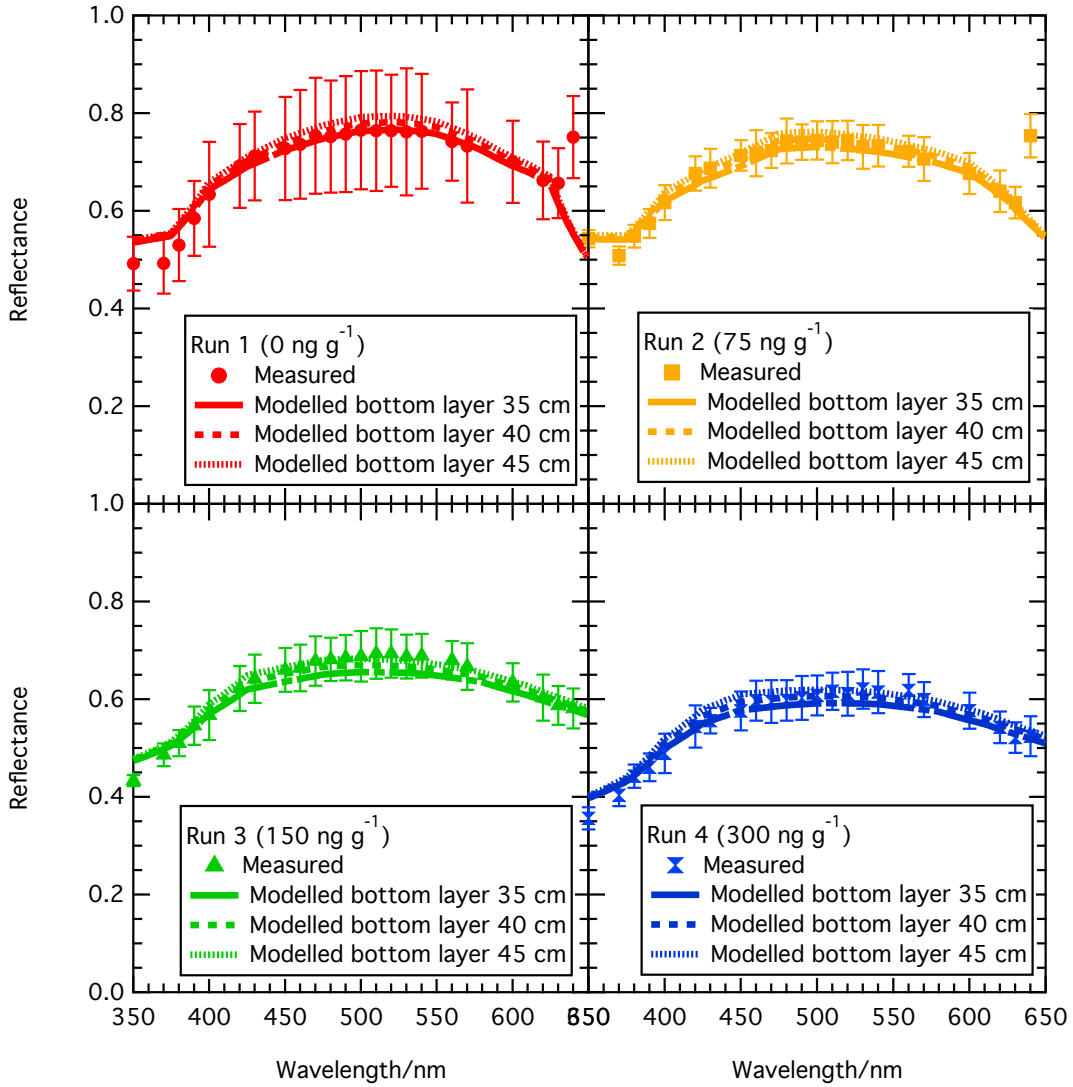

Figure 6.22 *– Comparison between calculated and measured reflectance for runs 1–4. Modelling is based on fit G (see table 6.4). The bottom layer is modelled as 35, 40 and 45 cm thick to understand the role of bottom layer thickness in calculated reflectance values.*

6.4.1.5 Uncertainty in derived scattering and absorption cross-section

As discussed in chapter 3 there is a degree of uncertainty in deriving the scattering and absorption cross-section values from reflectance and *e*-folding depth data. Figure 6.13 shows the uncertainty in the absorption cross-section values calculated for the bottom ice layer. The uncertainty bars are determined by making small changes to the fit of the reflectance and *e*-folding depth data used to obtain the absorption cross-section values, as described in chapter 3. The uncertainty in the derivation of the absorption

cross-section is very low, and thus would have little impact on the cause for the difference between modelled and measured reflectance values.

6.4.1.6 Uncertainty in added black carbon mass-ratio

The method for determining the black carbon mass-ratio in the 75 L of seawater has a high level of uncertainty, shown in table 6.1. Within one standard deviation the mass-ratios of the black carbon in the top 5 cm layer could be as low as 0 ng g^{-1} (run 1), 58.4 ng g^{-1} (run 2), 116.7 ng g^{-1} (run 3) and 243.16 ng g^{-1} (run 4). Although significantly lower these values are not low enough to match the measured reflectance values as the values are still significantly larger than the values used for the best fit (Fit G). Uncertainty in the black carbon mass-ratio added is therefore unlikely to be a cause for the difference between measured and calculated values.

6.4.2 How realistic is the simulated scenario?

To evaluate the TUV-snow model a scenario is created in the sea ice simulator which is as near as possible representation of reality. Grenfell et al. (2002) and Doherty et al. (2010) suggest black carbon is concentrated at a surface layer in sea ice following melting of overlying snow. Thus in the simulator black carbon is distributed in a 5 cm surface layer. To create this scenario a black carbon bearing layer had to be added to the sea ice surface after the clean layer had frozen. Placing black carbon in a solution with seawater ensures a more even distribution of black carbon across the surface of the ice rather than placing black carbon directly on the ice. However, the addition of 75 L of seawater to the ice surface may influence the whole ice properties, which will be discussed in section 6.4.2.1. Section 6.4.2.2 will discuss the presence of an absorbing impurity in the “clean” ice and the effect this has on the realism of the scenario.

6.4.2.1 Effects on ice properties

Adding the 75 L of artificial sea water containing black carbon may alter the overall ice properties and structure unrealistically. Table 6.7 shows a comparison of the average

simulated sea ice properties measured from ice cores taken before and after the black carbon bearing layer was added in each run.

Average ice property	Before black carbon layer added ±1SD	After black carbon layer added ±1SD	Change?
Temperature (°)	-9.83 ± 0.70	-11.03 ± 0.27	Yes
Density (g cm^{-3})	0.90 ± 0.029	0.93 ± 0.029	No
Bulk salinity (PSU)	7.61 ± 1.03	8.28 ± 1.42	No
Brine salinity (PSU)	152.20 ± 9.02	170.44 ± 4.25	Yes
Brine density (g cm^{-3})	1.12 ± 0.0071	1.14 ± 0.034	Yes
Brine fraction (%)	4.31 ± 0.88	4.11 ± 0.79	No
Air fraction (%)	3.84 ± 2.26	1.74 ± 0.99	No

Table 6.7 *– Average ice properties measured from all ice cores before and after the addition of the 5 cm black carbon bearing ice layer.*

The only significant difference in the properties of the ice after the black carbon bearing layer has been added is the temperature and brine salinity, which are both increased slightly with the addition of the 5 cm black carbon bearing layer. It is unsurprising that both of these parameters increase, the addition of a relatively saline layer to the surface will increase the salinity of all the ice until the brine drains out. Photos of ice cores taken after the layer was added and frozen, shown in figures 6.5–6.11, show there is no distinct boundary where the extra layer of ice is added. Therefore it appears overall the addition of the extra layer has limited effect on the overall ice properties and thus remains a realistic scenario with the surface layer becoming integrated with the underlying ice.

6.4.2.2 Presence of other absorbing impurities

Figure 6.13 shows that the “clean” ice has a clear wavelength dependent absorption for every run, suggesting the presence of an absorbing impurity in the clean ice which may be unrealistic of a natural sea ice environment. The absorption in the clean ice is likely to be due to absorption by algae present in the water. Figure 6.23 shows a comparison of the absorption measured for the clean ice from each run compared to absorption of chlorophyll (A) (Bricaud et al., 2004) found in algae. Figure 6.23 shows similar absorption spectra for the clean ice and chlorophyll suggesting that the absorbing impurity present in the clean ice may indeed be algae. The presence of algae in the artificial seawater is not unrealistic of the sea ice environment where

algae is a common component of sea ice, although this may be different to algae found in the simulator which is likely to be sourced from trees surrounding the outside of the simulator.

The algae present in the simulator were not obvious to the naked eye, conditions in the simulator have been adapted to minimise algae growth in the future including limiting light and extended use of the UV steriliser.

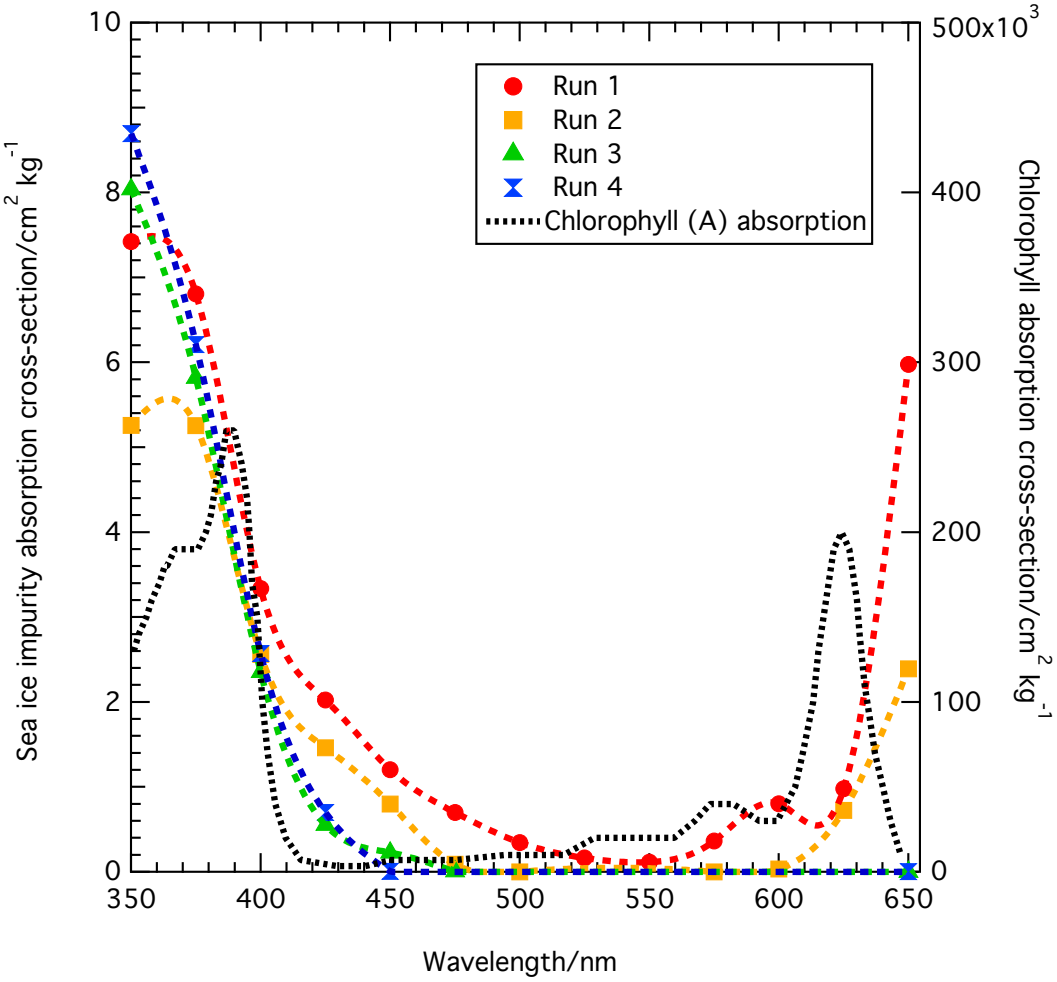

Figure 6.23 *– Comparison between absorption spectra derived for "clean" ice from each run compared to chlorophyll absorption from Bricaud et al. (2004). The values for run 4 are too small to plot clearly.*

6.4.3 Suggestions for future research

The experiments presented in Chapter 6 were limited by the time scale of the project. From the results presented several ideas for future experiments can be suggested in order to better evaluate the TUV-snow model using the sea ice simulator. Firstly, more black carbon mass ratios should be investigated in addition to the three presented

here to understand if the trends presented in this chapter, where black carbon must be reduced by a factor of three, occurs at all black carbon mass ratios. Also to try and find the reason for the factor of three difference, the absorption cross-section of black carbon used in the simulator should be measured to understand if an incorrect black carbon absorption cross-section is the cause of the discrepancy. Black carbon distribution within the sea ice should also be investigated to understand if drainage of black carbon occurs. Lastly algae growth should be eliminated in the sea ice simulator so that the effects of black carbon only on albedo can be determined.

6.5 Conclusions

In order to achieve an optimal fit between reflectance measured due to black carbon mass-ratios of 0, 75, 150 and 300 ng g^{-1} within a top 5 cm layer of artificial ice compared to the TUV-snow model calculations requires three factors. Firstly, absorption by the "clean" ice layer must be considered due to the presence of an absorbing impurity present, most likely algae. Secondly, the scattering cross-section of the upper layer differs slightly from the underlying layer and between each run, although well within a normal sea ice scattering cross-section. Thirdly, and most importantly, the black carbon mass-ratio in the top layer must be reduced by a factor of three to obtain a fit. There are two main reasons for this; an incorrect black carbon absorption cross-section or mobilisation of black carbon from the top 5 cm layer into the below sea ice and underlying seawater. The sea ice simulator can be used for evaluation of the TUV model, however to improve the evaluation presented here further research must be carried out to ascertain the cause of the factor of three difference in black carbon mass ratio.

Chapter 7

Validation of a Gonio Radiometirc Spectrometer System for measuring Polar surface BRDF (HDRF)

The work presented in chapter 7 is a result of a collaboration between UK and Italian researchers to measure multi-angular reflectance of snow surfaces at Dome C for calibration and validation of remote sensing products. The research collaboration included: myself, Martin King (Royal Holloway, University of London), Corrado Fragiacomo (National Institute of Oceanography and Geophysics, Italy), Giuseppe Zibordi (Institute for Environment and Sustainability, Joint Research Centre, Italy), Alasdair MacArthur (NERC Field Spectroscopy Facility, UK) and Nigel Fox (National Physical Laboratory, UK). Corrado Fragiacomo and I undertook 8 weeks of fieldwork at the joint Italian and French Antarctic research base, Dome C, to measure the multi-angular reflectance of snow surfaces using equipment hired from NERC Field Spectroscopy Facility (Alasdair MacArthur). I undertook all subsequent data analysis presented here, with initial data analysis tools provided by Alasdair MacArthur. Thanks go to PNRA (Italian Antarctic Research Institute) for funding the fieldwork at Dome C and also COMNAP (Council of Managers of National Antarctic Programs) for funding travel expenses for myself and equipment to Antarctica.

7.1 Introduction

To enable wide scale measurements of black carbon in snow and sea ice and thus ascertain its potential global climatic influences remote sensing measurements of planetary albedo could be utilised (e.g. Warren (2012)). Warren (2012) suggests the anisotropic reflectance of snow is a major limitation to enabling satellite black carbon measurements. Natural surfaces, including snow, scatter light anisotropically, i.e. reflectance (upwelling irradiance divided by downwelling irradiance over a discrete angle) varies with illumination and viewing angle, thus algorithms are required to convert satellite reflectivity measurements to a measurement of albedo (measure of the upwelling irradiance from the whole hemisphere divided by downwelling irradiance from the whole hemisphere) , as most satellite sensors measure reflectance at a few viewing angles, close to nadir, rather than directly measuring surface albedo. The algorithms require ground-based measurements of the anisotropic reflectance; commonly described by a bi-directional reflectance distribution factor (BRDF), described in further detail in section 7.2.

Dome C, Antarctica (75°S, 123°E), location shown in figure 7.1, was highlighted as an excellent ground-calibration site for measurements of BRDF by Six et al. (2004) for the following reasons. The snow surface is spatially homogeneous with small surface roughness; sastrugi less than 10–20 cm (Petit et al., 1982), and a relatively flat surface (Rémy et al., 1999). The surface at Dome C is also temporally stable due to a small snow accumulation rate, low winds (Keller et al., 2002) and temperatures constantly well below freezing mean snow remains frozen year-round. Owing to the high altitude (>3000 m) and its long distance from the coast (>1000 km) the atmospheric conditions of Dome C favour clear skies with very low column aerosol and a small atmospheric water vapour content. Satellites also frequently overpass the area.

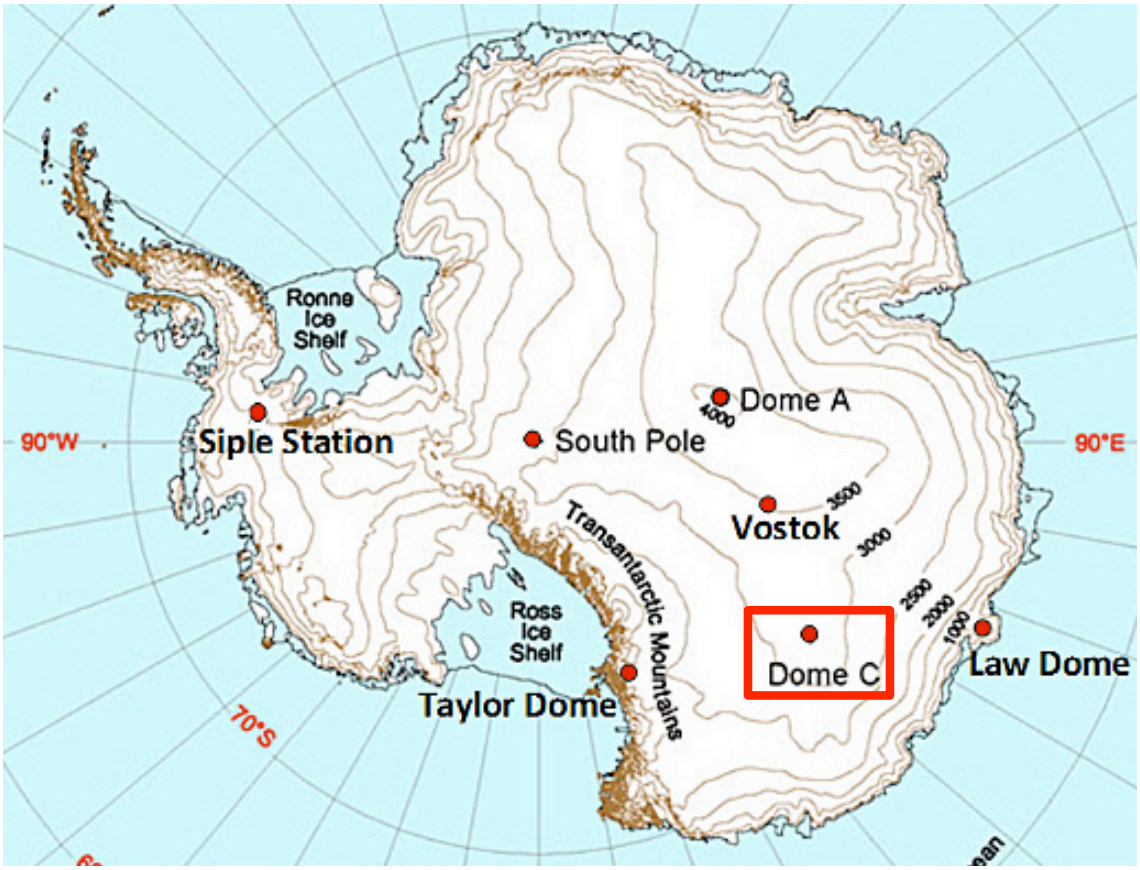

Figure 7.1 *– Location of Concordia base (Dome C) in Antarctica (adapted from CDIAC (http://cdiac.ornl.gov/trends/co2/ice_core_co2.html)).*

Hudson et al. (2006) previously undertook measurements of a quantity relating to BRDF at Dome C from the top of a 32 m tower at wavelengths 350–2400 nm, which they express as an "anisotropic reflectance factor". The set up used for their measurements is shown in figure 7.2. Each observation sequence involved 85 measurements of the surface radiance from the snow surface at viewing zenith angles from 22.5 to 82.5° and azimuth angles from 142.5° to 37.5°. Hudson et al. (2006) show snow is forward scattering with the prominence of forward scattering increasing with wavelength, they also demonstrate surface roughness of the snow surfaces causes anisotropy to be less than that of flat snow.

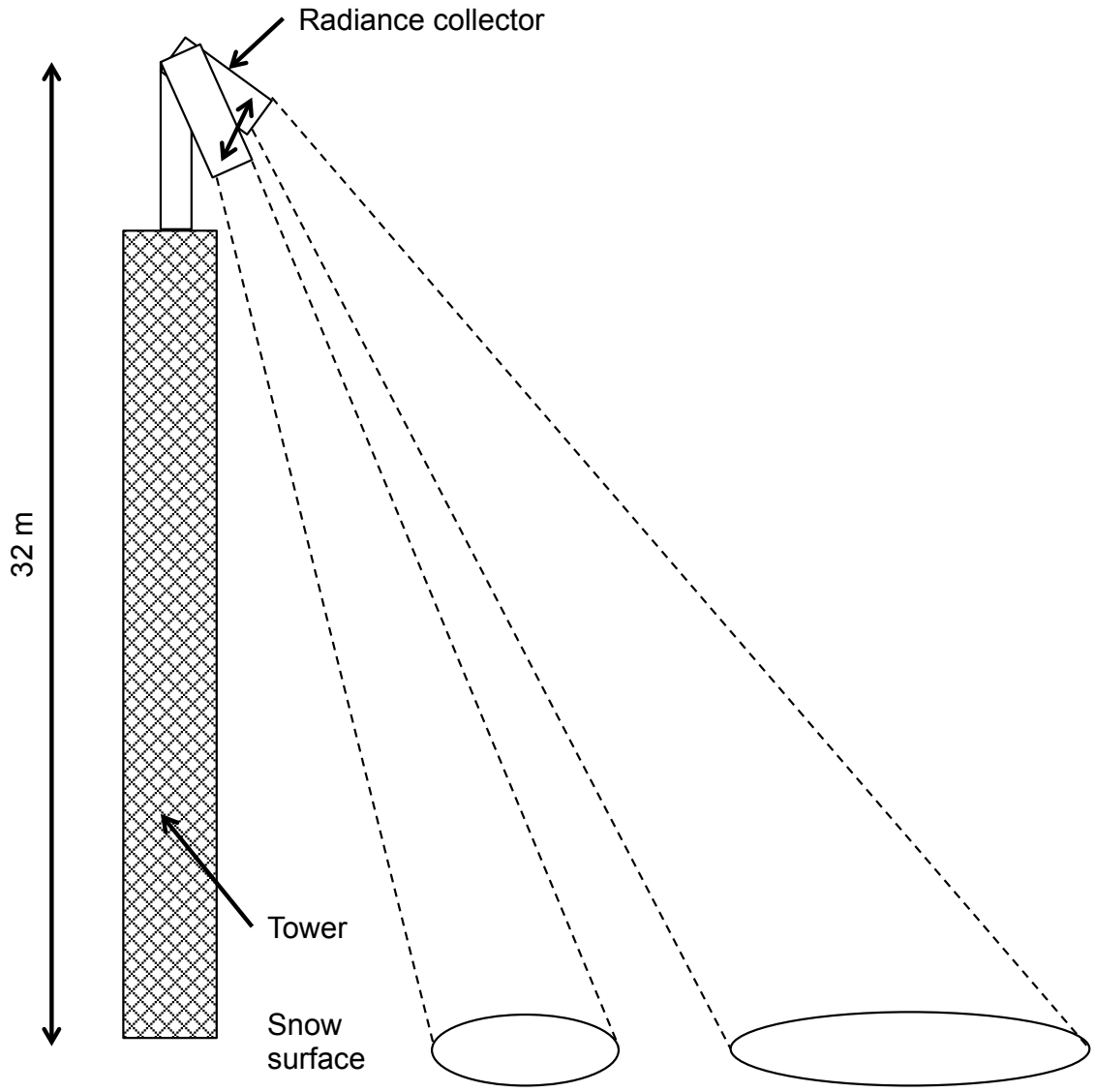

Figure 7.2 *– Technique used by Hudson et al. (2006) to measure BRDF of snow. Surface radiance was measured from the top of a tower. For each angle examined a different snow surface was observed.*

Although comprehensive, the study of Hudson et al. (2006) has several limitations. Firstly for each measurement at a different azimuth/zenith angle a different snow surface was observed. Different snow surfaces may exhibit a different BRDF, although they do use a larger, variable, measurement footprint to account for this. Secondly, Hudson et al. (2006) do not take measurements at viewing zenith angles less than 22.5°. Finally, the study of Hudson et al. (2006) was unable to observe a full 360° of azimuth in one measurement sequence owing to the presence of the station at Dome C.

To address the potential limitations of Hudson et al. (2006), presented in this chapter are new measurements of a quantity relating to BRDF at Dome C using a Gonio

Radiometric Spectrometer system (GRASS), shown in Figure 7.3. A goniometer is an instrument used measuring angles precisely. The purpose of the study is to complement and enhance the data collected by Hudson et al. (2006). GRASS is described in detail in section 7.3.1. Measurements using GRASS observe the same snow surface for each surface radiance measurement taken at different viewing azimuth and zenith angles. Studying the same snow surface at each zenith/azimuth angle and using a smaller viewing footprint enables small-scale differences in individual snow surfaces to be observed. The measurements presented here were taken over viewing zenith angles from 0° (nadir) to 60° providing more detail of BRDF near nadir and also cover all viewing azimuth angles (0–360°) in one measurement. GRASS measurements use a wavelength resolution of every 1 nm from 400–1700 nm.

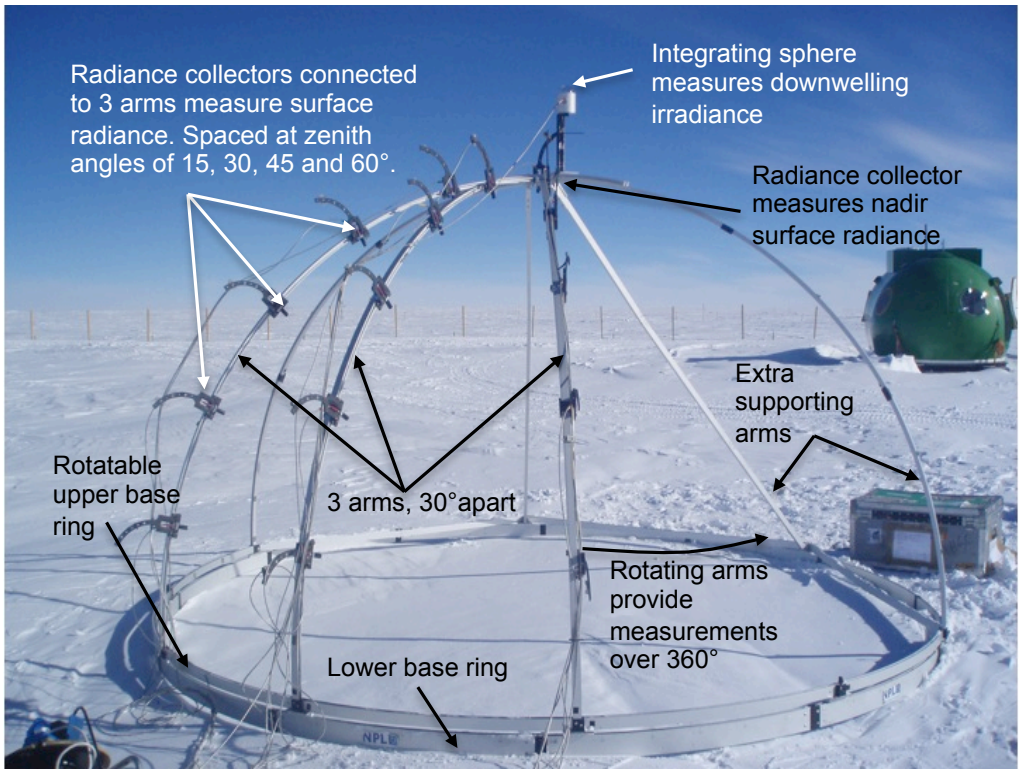

Figure 7.3 *– A picture of GRASS: radiance collectors are attached to three arms spaced 15° apart, a further radiance collector is attached at nadir to record surface radiance. On top of the structure there is an integrating sphere to measure downwelling irradiance. The arms of GRASS can be rotated 360° to record surface radiance at all azimuth angles.*

7.2 Reflectance terminology

The anisotropic reflectance of surfaces is commonly described by the bi-directional reflectance distribution function (BRDF). BRDF is the ratio of incident light at a known zenith, θ_i, and azimuth, ϕ_i, angle, to radiance reflected at a known viewing zenith and azimuth angle (Nicodemus et al., 1977), demonstrated by Figure 7.4.

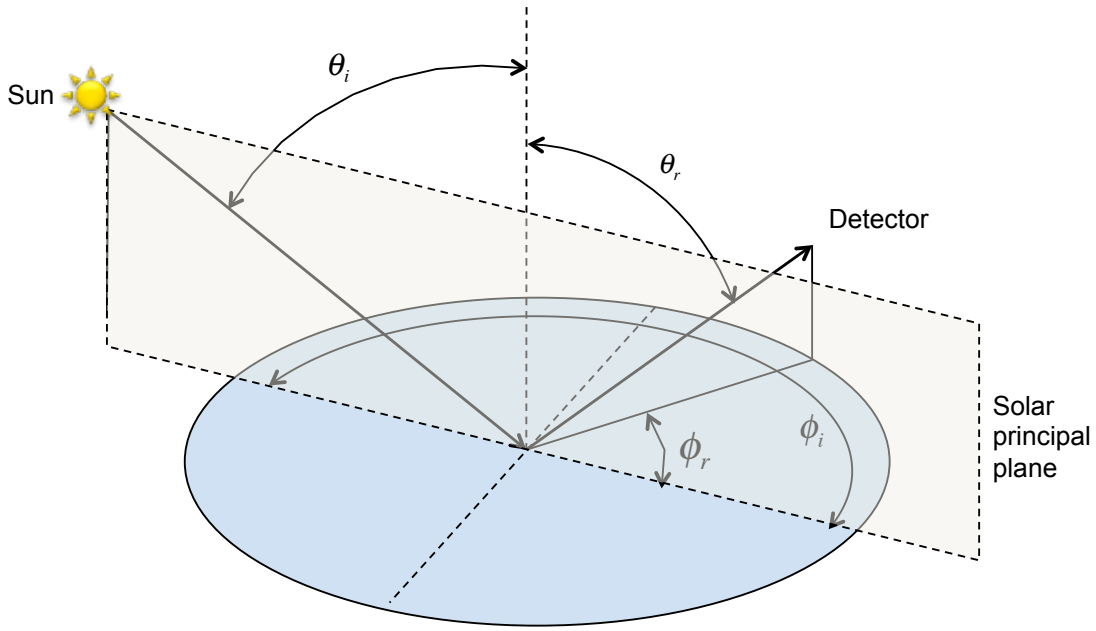

Figure 7.4 *– Definition of angles required for BRDF measurements, where ϕ_i is the azimuth angle of incident light, θ_i is the zenith angle of incidence light, ϕ_r is the azimuth viewing angle and θ_r is the zenith viewing angle.*

The BRDF of a surface cannot be easily measured in the field (Schaepman-Strub et al., 2006) due to difficulties in accurately measuring incident solar radiation. A more practical term is the bidirectional reflectance factor (BRF), which defines the ratio of radiance reflected from the target surface to the reflected radiance from an ideal (Lambertian) reflector under identical illumination and viewing geometries (Schaepman-Strub et al., 2006; Nicodemus et al., 1977), eliminating the need to measure incident solar radiation. A true Lambertian reflector reflects light equally into all zenith and azimuth viewing angles. BRF is defined by equation 7.1, where R is the reflectance factor, Φ_r is the reflected radiant flux and Φ_r^{id} is the reflected radiant flux of an ideal (Lambertian) surface (Schaepman-Strub et al., 2006).

$$BRF = R(\theta_i, \phi_i; \theta_r, \phi_r) = \frac{d\Phi_r(\theta_i, \phi_i; \theta_r, \phi_r)}{d\Phi_r^{id}(\theta_i, \phi_i; \theta_r, \phi_r)} = \frac{d\Phi_r(\theta_i, \phi_i; \theta_r, \phi_r)}{d\Phi_r^{id}(\theta_i, \phi_i)} \tag{7.1}$$

BRF assumes downwelling irradiance comes from a direct source, however in nature downwelling irradiance has a diffuse component due to Rayleigh scattering of solar radiation by atmospheric particles. Rayleigh scattering is more efficient at shorter wavelengths, thus there is a larger diffuse component for shorter wavelengths. The hemispherical-directional reflectance factor (HDRF) is similar to BRF but is determined using measurements of irradiance from the whole downwelling hemisphere (direct and diffuse solar radiation) and thus is dependent on atmospheric conditions and reflectance from the local surrounding area (Schaepman-Strub et al., 2006). HDRF is defined in equation 7.2.

$$HDRF = R(\theta_i, \phi_i, 2\pi; \theta_r, \phi_r) = \frac{d\Phi_r(\theta_i, \phi_i, 2\pi; \theta_r, \phi_r)}{d\Phi_r^{id}(\theta_i, \phi_i, 2\pi)} \tag{7.2}$$

The term HDRF will be subsequently used to describe the snow anisotropic measurements taken at Dome C, as this is what is measured by GRASS. HDRF is still a useful measurement, which can be utilised.

7.3 HDRF measurements at Dome C

The following section will firstly describe the design of the Gonio Radiometric Spectrometer System (GRASS); subsection 7.3.1. Subsection 7.3.2 will describe how GRASS was utilised to acquire values of HDRF. Subsection 7.3.3 will describe the field site at Dome C and subsection 7.3.4 will describe the measurements of the physical properties of snow taken at the HDRF measurement sites from snow pits.

7.3.1 GRASS equipment design

Measurements of HDRF were taken using a Gonio Radiometric Spectrometer System (GRASS) described by Pegrum et al. (2006). GRASS is shown in Figure 7.3, consisting of a hemispherical frame of 2 m radius, which can be lifted and moved over a target surface. The frame can be rotated on a lower base ring, that is aligned with the sun at the start of measurements and the frame kept in the same position throughout each measurement sequence. The hemispherical frame consists of an upper base ring that slots into the lower base ring. Attached to the upper base ring three arms, spaced 30°

of azimuth apart, run vertically from the top of the hemisphere to the base ring. Four radiance collectors (shown in figure 7.5) are attached to each of these arms positioned at zenith angles of 15, 30, 45 and 60° to measure surface radiance. The radiance collectors all focus on the centre of the target surface. A further radiance collector is attached at the top of GRASS facing directly downwards for measuring surface radiance at nadir (0°). The radiance collectors consist of a fibre optic coupled to an optic lens with an 8° cone of acceptance. The viewing footprint of each lens ranges from 491 cm^2 at nadir to 1419 cm^2 at a viewing zenith angle of 60°; eccentricity of the field of view increases as viewing zenith angle increases (from a circular footprint at nadir). The radiance collectors are attached to GRASS via a bracket as shown in figure 7.5.

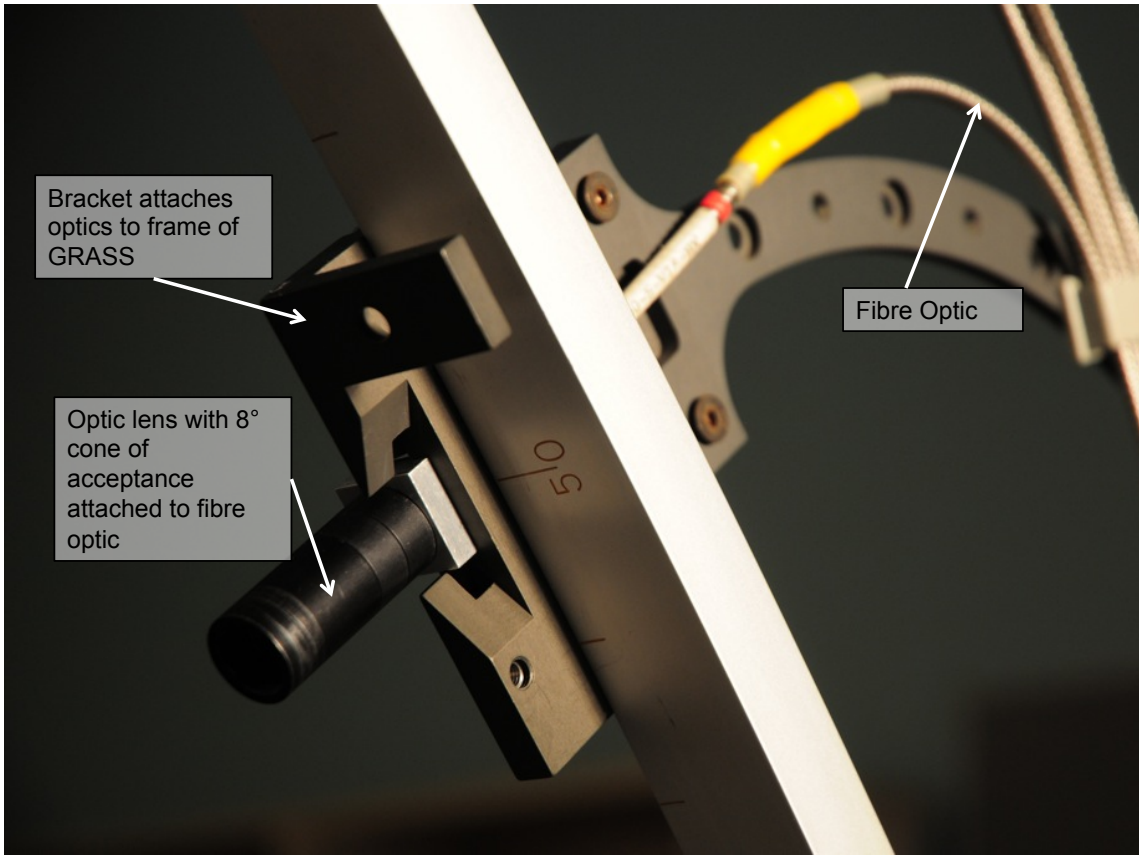

Figure 7.5 *– Example of a radiance collector consisting of an optical lens attached to fibre optic, both of which are fastened to the GRASS frame via a bracket at the desired viewing zenith angle (Photo courtesy of K. D'Souza).*

A further fibre optic is coupled to an integrating sphere, attached to the top of the GRASS hemisphere facing upwards to record downwelling solar irradiance, as shown in figure 7.3. An integrating sphere is an optical device which uniformly scatters and diffuses light. The integrating sphere consists of a hollow spherical cavity with

a diffuse white reflective interior with small holes for light to enter and exit. Light entering the sphere is multiply scattered and evenly distributed to all other points within the sphere before leaving through the exit hole. For the light leaving the sphere the effects of the original direction of light are minimised but the same intensity is maintained.

Four further arms on GRASS provide support to keep the hemispherical shape and ensure the radiance collectors all point at the same target area. The arms and upper base ring of GRASS can be rotated around a full 360° azimuthally enabling surface radiance measurements at a full range of azimuth angles of the same target. The surface radiance through each radiance collector is measured in turn via a fibre optic multiplexer at wavelengths from 400 to 1700 nm by a visible and shortwave infra-red (VSWIR) spectrometer. VSWIR has a resolution of 3 nm at a wavelength of 700 nm and 10 nm at a wavelength of 1400 nm. VSWIR is a one-off special spectrometer built for GRASS, which is not commercially available. The VSWIR spectrometer is a dual field of view portable spectroradiometer enabling near simultaneous measurement of downwelling irradiance from the integrating sphere and surface radiance (via the multiplexer). Both irradiance and radiance can be acquired using the VSWIR spectrometer within 2 seconds (MacLellan and Malthus, 2009). The light is detected by two Ocean Optics (USB 2000) spectrometers (for visible and near infrared) and Sol 1.7, B&WTek spectrometers (for shortwave infrared). The set up of the electrical equipment including the multiplexer, VSWIR spectrometer and Panasonic Toughbook attached to GRASS is shown in figure 7.6

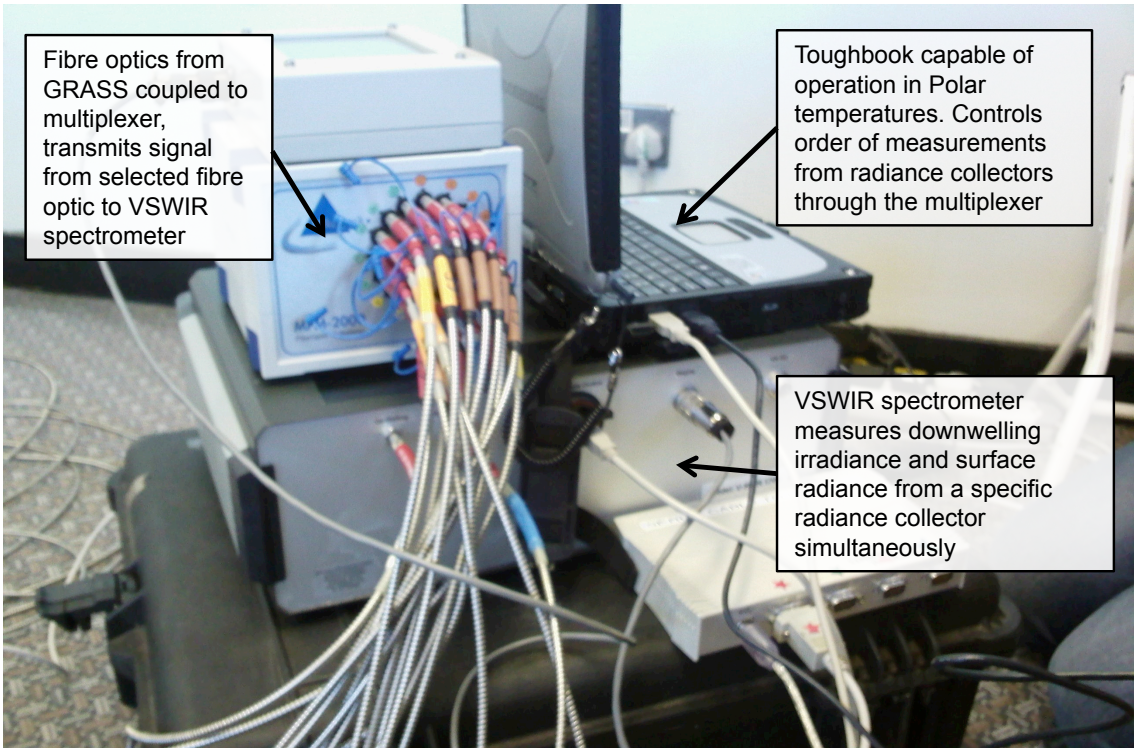

Figure 7.6 *– Set up of electrical equipment attached to GRASS, including coupling of fibre optics to multiplexer, connection to VSWIR spectrometer and connection to a Toughbook used to control GRASS, which can function in cold Polar temperatures.*

7.3.2 Acquiring HDRF measurements with GRASS

7.3.2.1 Raw measurement collection

A complete measurement of the HDRF of a target surface using GRASS entailed measurements of surface radiance at twelve equally spaced azimuth angles, (∼30° apart), achieved by rotating the upper ring of GRASS by three turns ∼90°. At each azimuth angle surface radiance measurements were taken at four viewing zenith angles (15, 30, 45, 60°); a total of 49 azimuth and zenith angle combinations including a surface radiance measurement at nadir (0°). The measurement at nadir was repeated three times for each rotation, giving a total of 64 measurements in each measurement sequence. Downwelling irradiance was measured simultaneously to each surface radiance measurement. When rotating the GRASS structure care was taken to ensure that no part of the structure created a shadow over the measurement area. GRASS was therefore not always rotated exactly 90°, but within 80–100°.

Following a complete hemisphere of radiance measurements (three rotations of GRASS) a ∼0.25 m^2 calibrated Spectralon panel was placed on the target surface and the

radiance from the panel was recorded with the nadir radiance collector. The radiance measurements from the Spectralon panel provide a reference measurement to which the surface radiance measurements from the target surface can be compared to in order to derive HDRF values, as described in the next section 7.3.2.2.

The intensity response of each radiance collector was intercalibrated at the end of each measurement sequence by placing the lens entrance optic in an integrating sphere illuminated by a stable tungsten-halogen lamp providing a constant radiance source. The calibration was performed in ambient cold conditions with GRASS in place. Section 7.3.2.2 describes how these intercalibration values are used in derivation of HDRF values.

Obtaining surface radiance measurements from the whole 360° hemisphere, the Spectralon panel reference measurement and the radiance collector intercalibration took 2–3 hours for each site. Measurements were only taken within four hours of solar noon when solar zenith angle was highest and the change in solar zenith angle with time was smallest. Solar zenith angle varied by less than 3.5° over the course of a measurement of HDRF. The average solar zenith angle for all HDRF measurements was 58.2±5.9°(one standard deviation). Solar zenith angle changes particularly slowly towards the north and south poles, so temporal variation in solar zenith angle was small.

7.3.2.2 Raw measurement processing to generate HDRF plots

The following procedure was used to derive values of HDRF from the measurements of the surface radiances. Firstly, the values of the surface radiance from each radiance collector, $\Phi_{raw}(\theta_r, \phi_r)$, were corrected, to give $\Phi_{cor}(\theta_r, \phi_r)$. The correction accounts for variation in the response of each radiance collector by multiplying by a factor of the radiance measured by a calibration lamp for a specific radiance collector, Φ_i^{cal}, to the average measurement of radiance from the calibration lamp for all radiance collectors, $\overline{\Phi_i^{cal}}$, see equation 7.3.

$$\Phi_{cor}(\theta_r, \phi_r) = \left(\frac{\overline{\Phi_i^{cal}}}{\Phi_i^{cal}} \right) \Phi_{raw}(\theta_r, \phi_r) \tag{7.3}$$

Figure 7.7 shows the variation in the signal from the tungsten-halogen lamp recorded by different radiance collectors on different days. There is a significant degree of

variation in each radiance collector between different days which would be caused by movement of the fibre optics or optical lens during movement of the entire frame, showing the importance of completing the intercalibration after each measurement sequence. The intensity of the tungsten-halogen lamp was measured three times with the nadir radiance collector (number 4.0). Figure 7.8 shows the variation in the three repeats for each day the intercalibration was completed. For the majority of days there is very little variation in the repeats, especially compared to figure 7.7, with an average relative standard deviation of 3.1%. However figure 7.8 does show a clear degradation to the signal over time, likely to be due to degradation of the fibre optics over time in the cold conditions. The degradation would not affect measurements as all the optics are inter-calibrated after each measurement.

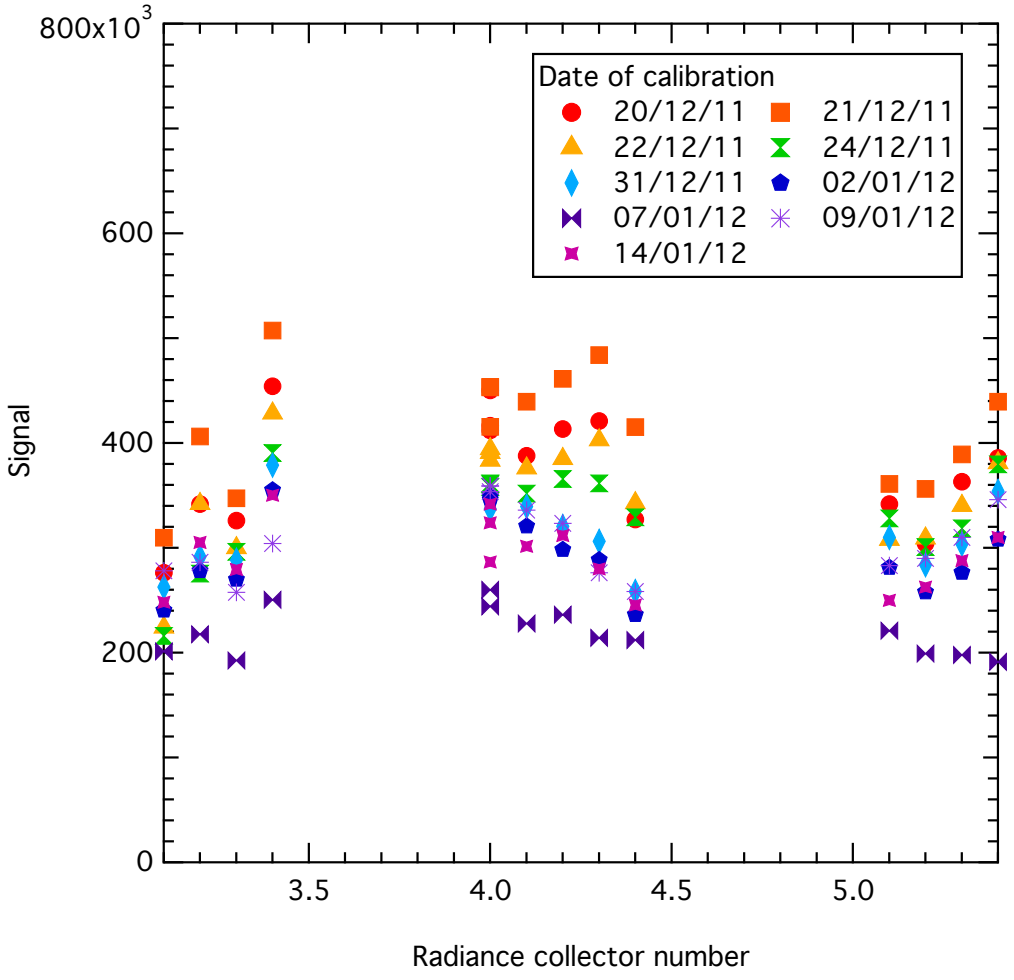

Figure 7.7 *– Variation in raw intensity signal, at 800 nm, recorded from the tungsten-halogen lamp across all days and for all radiance collectors during the intercalibration. "Radiance collector number" refers to a specific azimuth and zenith angle where x.1 is for the smallest zenith angle and x.4 is the largest. 3.x, 4.x and 5.x refers to different azimuth angles. 4.0 is the nadir radiance collector.*

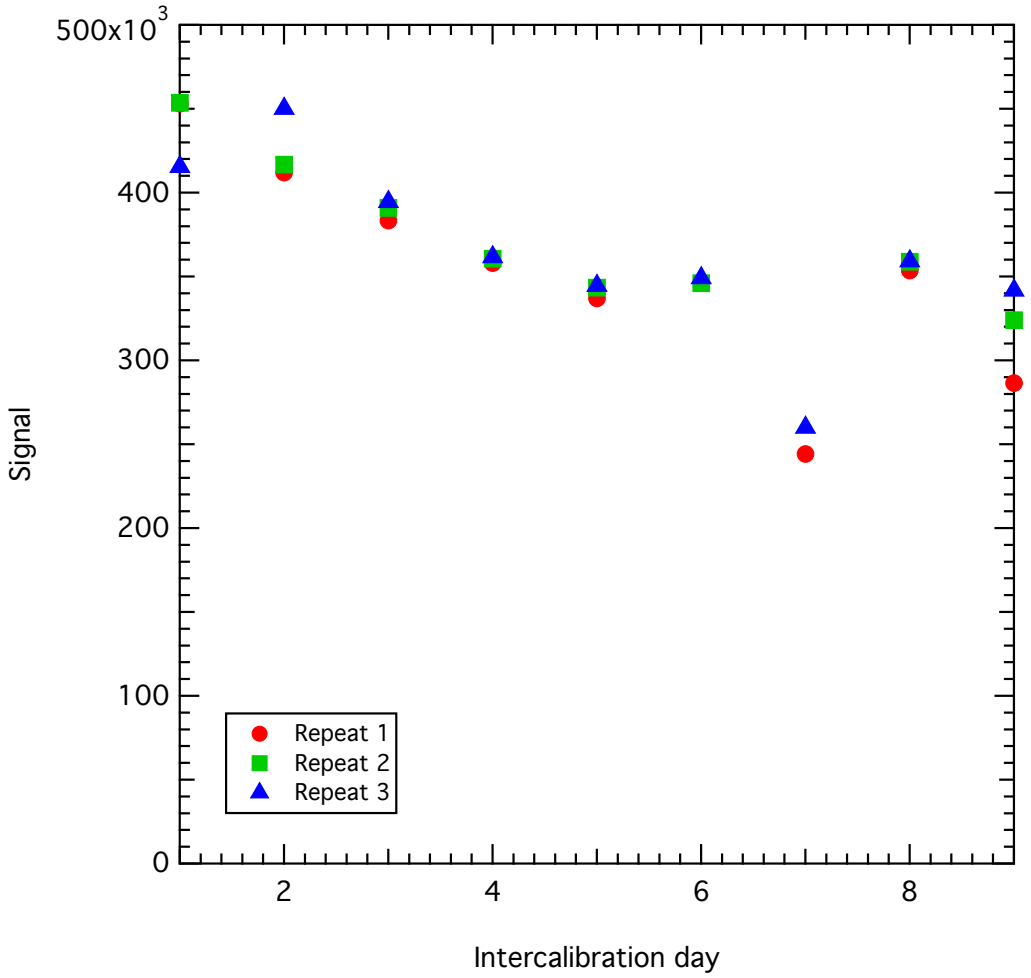

Figure 7.8 *– Variation in the three repeats of the nadir radiance collector raw intensity signal at 800 nm during the intercalibration and day-to-day variation, relative standard deviation of measurements averages 3.1%.*

Following application of the radiance collector intercalibration, HDRF was calculated using equation 7.4. Where $HDRF(\theta_r, \phi_r)$ is HDRF at a particular viewing zenith and azimuth angle, $\Phi_{cor}(\theta_r, \phi_r)$ is a corrected surface radiance for a viewing zenith and azimuth angle, $E(\theta_r, \phi_r)$ is the value of downwelling irradiance recorded simultaneously to an surface radiance value, Φ_{cor}^{id} is the corrected radiance from the Spectralon reference panel, and E^{id} is the downwelling irradiance recorded during the radiance measurement from the Spectralon reference panel.

$$HDRF(\theta_r, \phi_r) = \frac{\left(\frac{\Phi_{cor}(\theta_r, \phi_r)}{E(\theta_r, \phi_r)}\right)}{\left(\frac{\Phi_{cor}^{id}}{E^{id}}\right)} \tag{7.4}$$

Measurements are thus corrected for small changes in downwelling irradiance which occur during a measurement sequence. Figure 7.9 shows two examples (sites 6

and 7) of changes in downwelling irradiance during a measurement sequence at 500 nm; a total of 64 measurements, with 16 measurements per GRASS rotation. Site 6 is nearly consistent with time, while site 7 shows slightly more variation over the measurement sequence. Downwelling irradiance measurements for all sites are shown in appendix C. The "corrected" and "not corrected" downwelling data for each site show the raw downwelling signal ("not corrected") and the raw downwelling signal corrected for changes in signal due to rotating GRASS ("corrected"). In the non-corrected data clear "steps" can be seen in the signal as GRASS is rotated (after each 16 measurements), these are not due to changes in downwelling irradiance but due to the fact the integrating sphere wasn't facing truly upwards. These steps are corrected for in the corrected data by making all data points relative to the first 15 data points (first GRASS rotation), which is achieved by subtracting or adding the difference in signal caused by each rotation. As the downwelling measurements are used for correction only the relative change in downwelling radiation is important, not the absolute values.

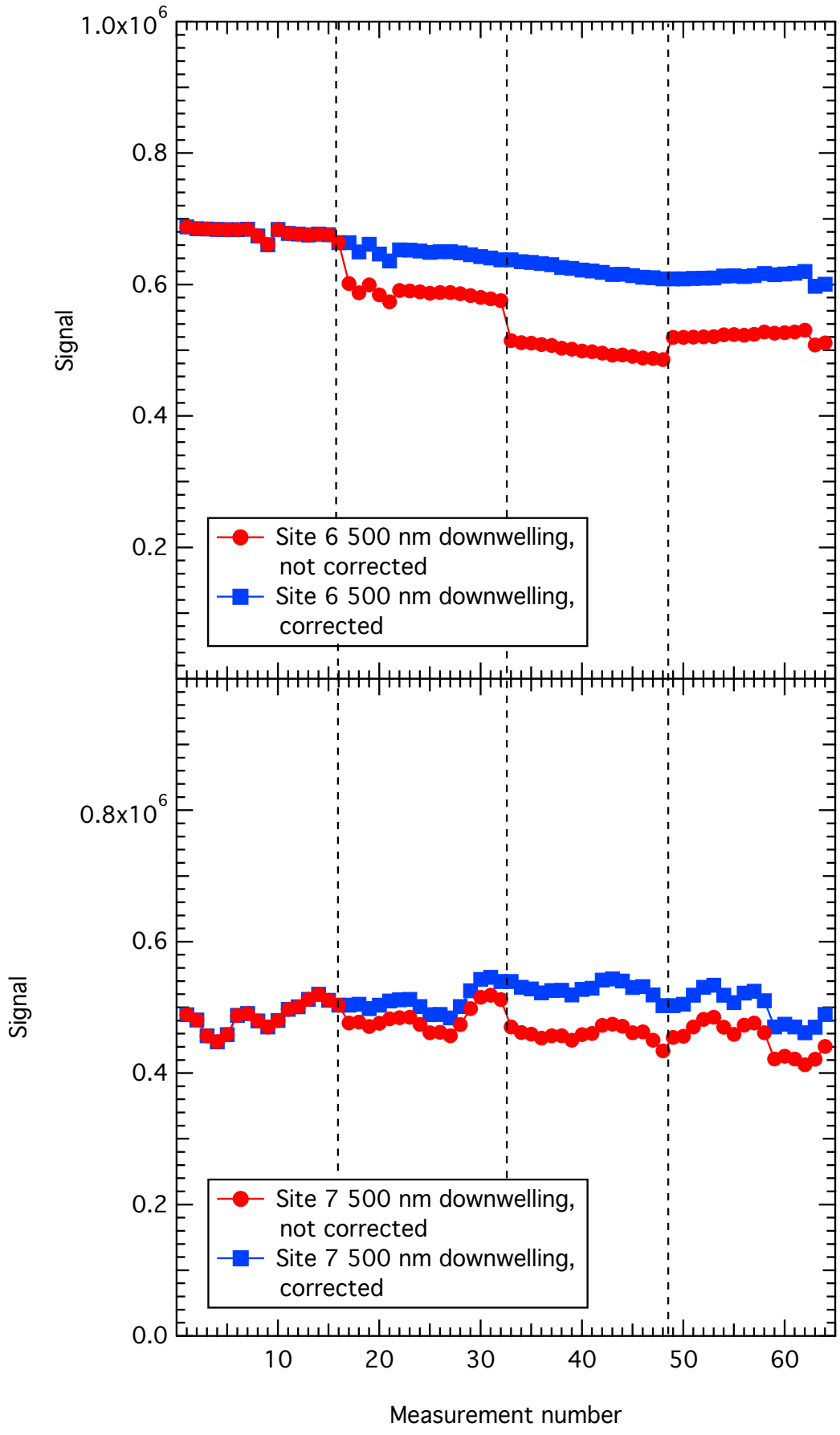

Figure 7.9 *– Examples of change in raw downwelling irradiance signal at 500 nm during a measurement sequence. Site 6 shows very little variation while site 7 shows more variation in downwelling irradiance. The corrected data corrects for the steps which appear in the non corrected data due to rotating GRASS every 16 measurements, shown as dashed lines.*

Application of equations 7.3 and 7.4 to raw surface radiance measurements enables calculation of HDRF values covering π steradians centred on the nadir in 30° azimuth intervals and 15° zenith increments. A HDRF value of 1 means reflectance of the target surface at that angle is equal to the Spectralon panel, a value greater than 1 means more light is reflected at those angles and a value of less than 1 equates to less light being reflected than is reflected by the Spectralon panel. The values of HDRF are represented here as "polar contour plots", to be comparable with those presented by Hudson et al. (2006). Figure 7.10 shows an example polar plot layout with each dot representing a radiance collector. The radius of the plot represents increasing zenith angle (the centre of the plot being 0° and the edge 60°) and the circumference of the plot represents azimuth angle decreasing clockwise. To create the HDRF polar plots the azimuth and zenith angle of each HDRF measurement at a specific wavelength are converted to Cartesian coordinates and then linearly interpolated to a 1000×1000 matrix.

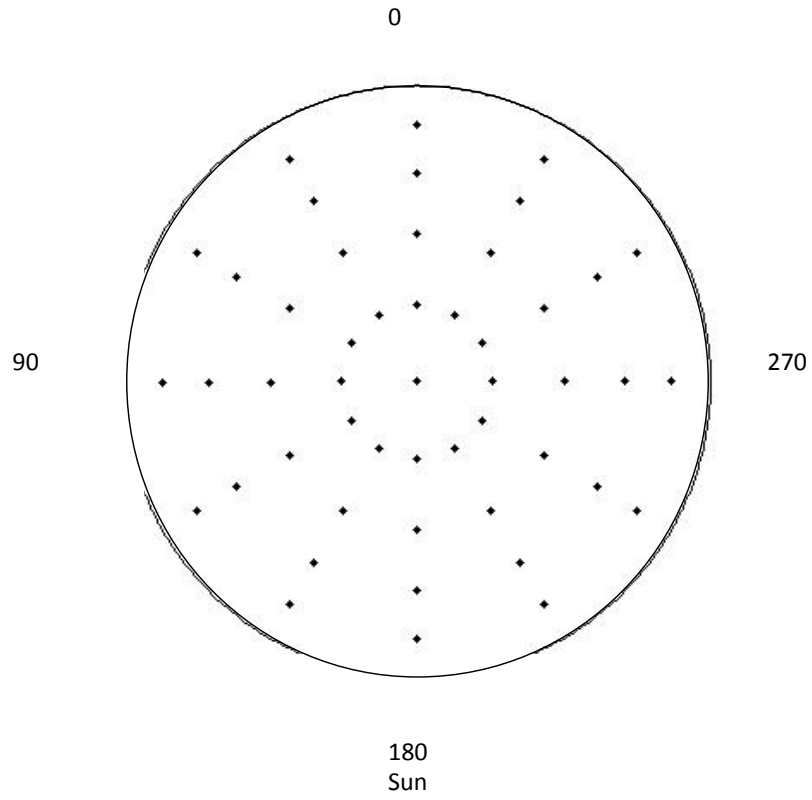

Figure 7.10 *– Example layout of polar plot with each dot representing a radiance collector at a different azimuth/zenith angle. The radius of the plot represents zenith angle (the centre 0°, the edge 60°) and the circumference represents azimuth values (shown on the figure). The solar principle plane runs from 0–180° with the sun positioned at 180°. The HDRF values for each radiance collector are linearly interpolated to form the polar plots in this chapter.*

7.3.3 HDRF measurement location

Dome C is a joint French-Italian research base, situated 75° 06′S and 123° 23′E, at an elevation of 3233 m. The location of Dome C (see figure 7.1), high on the Antarctic plateau, results in relatively low wind speeds, clear skies and small relief surfaces, making it an ideal place for a remote sensing calibration location. Figure 7.11 shows typical Dome C surface conditions. Unfortunately the study described here experienced uncharacteristic poor weather conditions for the measurement period with cloudy skies and high winds. Consequently, far fewer measurements were taken than planned.

Figure 7.11 *– Typical Dome C conditions- clear skies and flat snow surface with small sastrugi. Photo taken from top of the "American Tower" from which the measurements by Hudson et al. (2006) were taken.*

The HDRF of eight snow surfaces were measured in a ∼100 m transect that was both representative of the snowpack around Dome C area and close to the previous measurements of Hudson et al. (2006). A map showing the location of the transect is shown in figure 7.12, and figure 7.13 shows a photo of the transect also depicting the snow conditions of the site. The transect was just east of the "American tower" used in the study of Hudson et al. (2006), and ran at least 30 m north of, and parallel to, the little used access "road" leading from the base to the tower. The location of the transect allows future studies to repeat the study presented here for comparison before considering other sites in the Dome C locale. The measurement

location showed very few sastrugi and most surface features were small; ∼10 cm scale, which was characteristic of the rest of the plateau. There had been no recent (<1 year) anthropogenic ground disturbance.

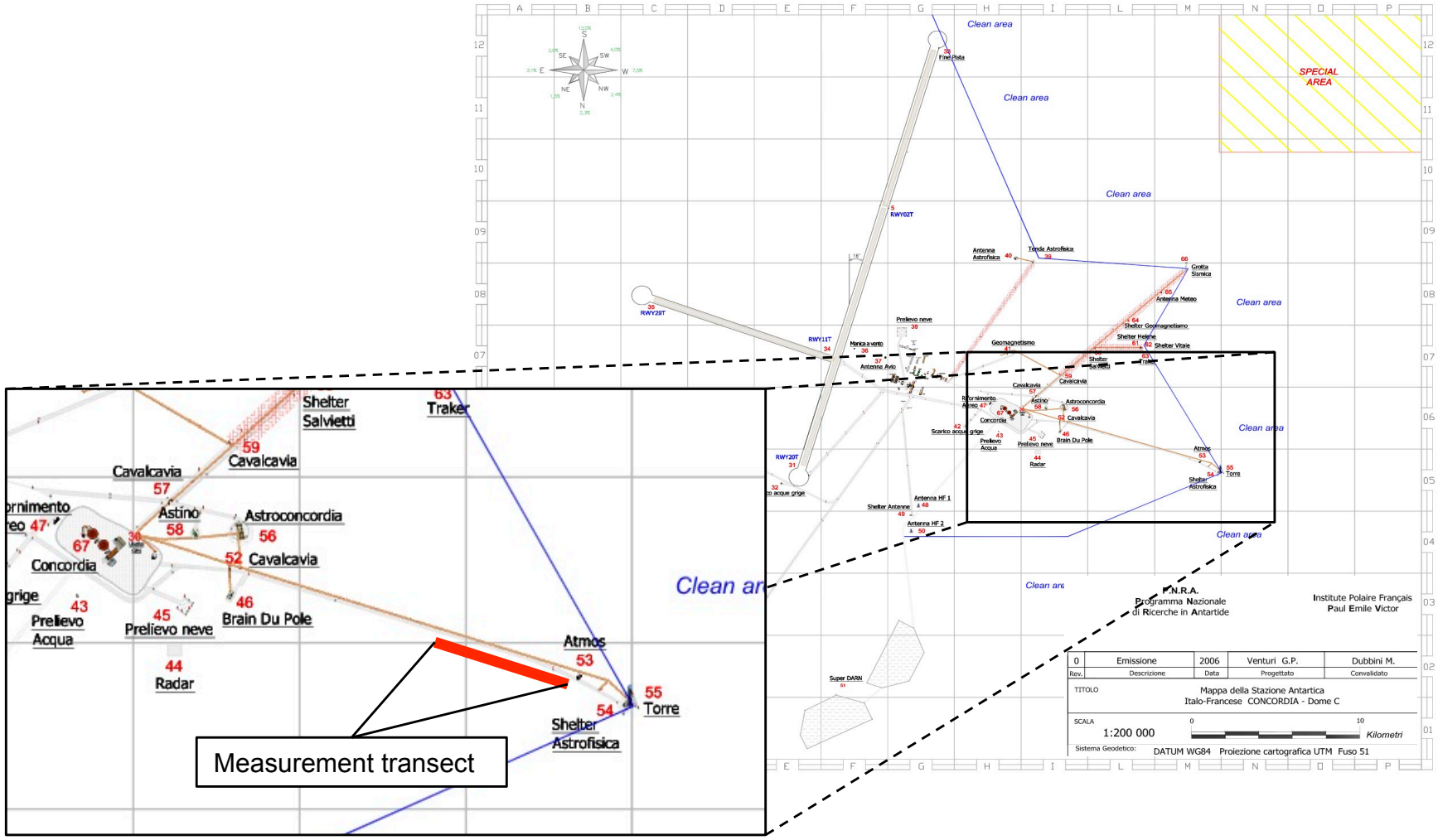

Figure 7.12 *– Map of the location of the measurement transect at Dome C running along the little used access road running from the base to the American Tower (Torre) (Image adapted from PNRA).*

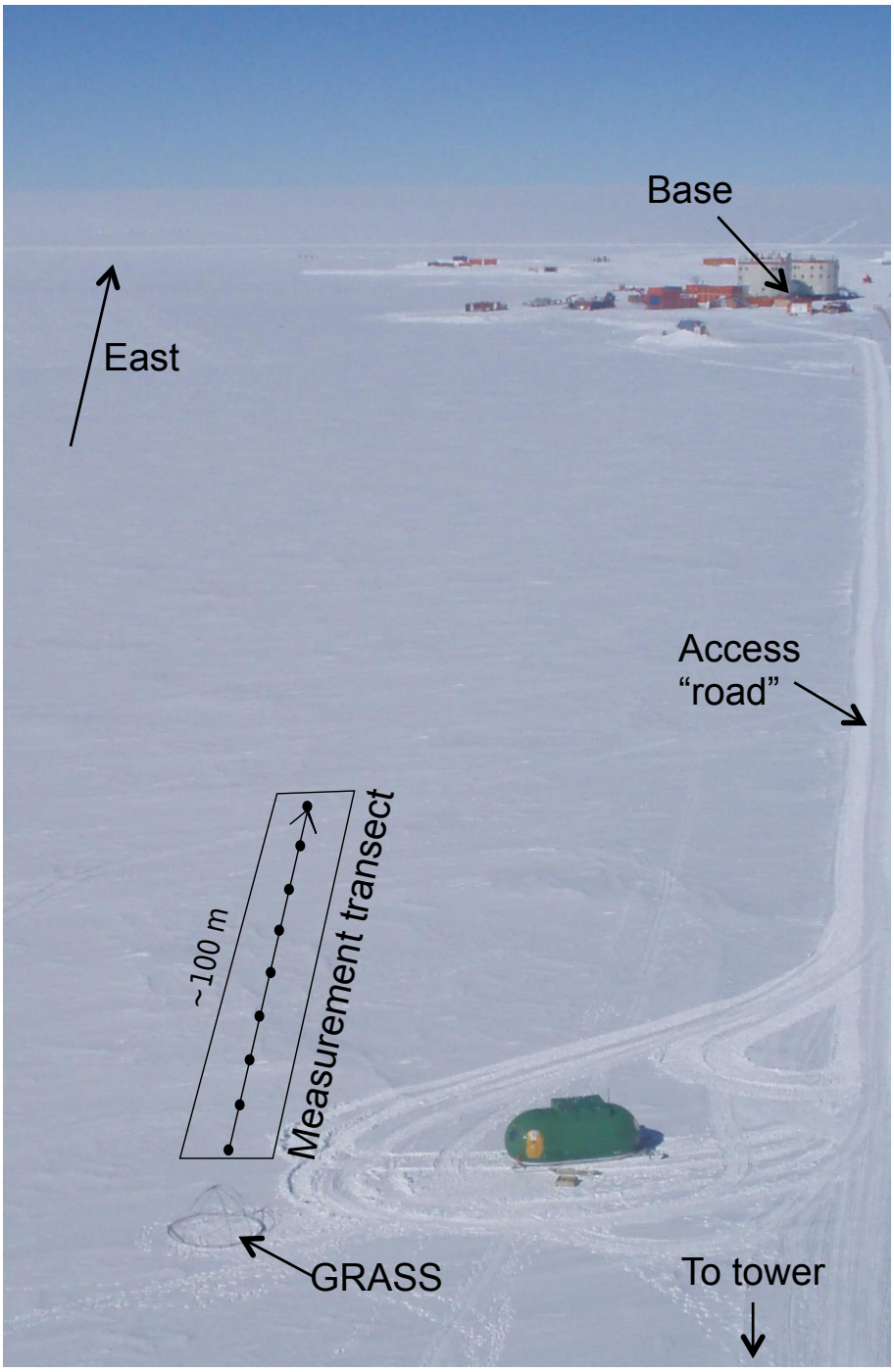

Figure 7.13 *– Location of ∼100 m transect over which GRASS measurements were taken. The transect runs parallel to a little used access “road” running from the main base to the “American tower” from which this photo was taken. The recent disturbed snow was due to tracked vehicles moving GRASS and ancillary equipment into position.*

7.3.4 Snow physical properties from snow pits

At each of the eight measurement sites along the transect a 1 m deep snow pit was dug after recording the HDRF. Snow density, temperature, grain size, grain type, and penetration profiles were taken down the pit wall. Temperature was recorded every 10 cm down the pit by inserting a thermometer into the snow, snow density was recorded every 5 cm by weighing a block of snow of known volume (270 cm^3) cut from the wall. Grain size, grain type and snow penetration were all recorded according to the international classification for seasonal snow on the ground (Fierz et al., 2009). An example snow pit is shown in figure 7.14.

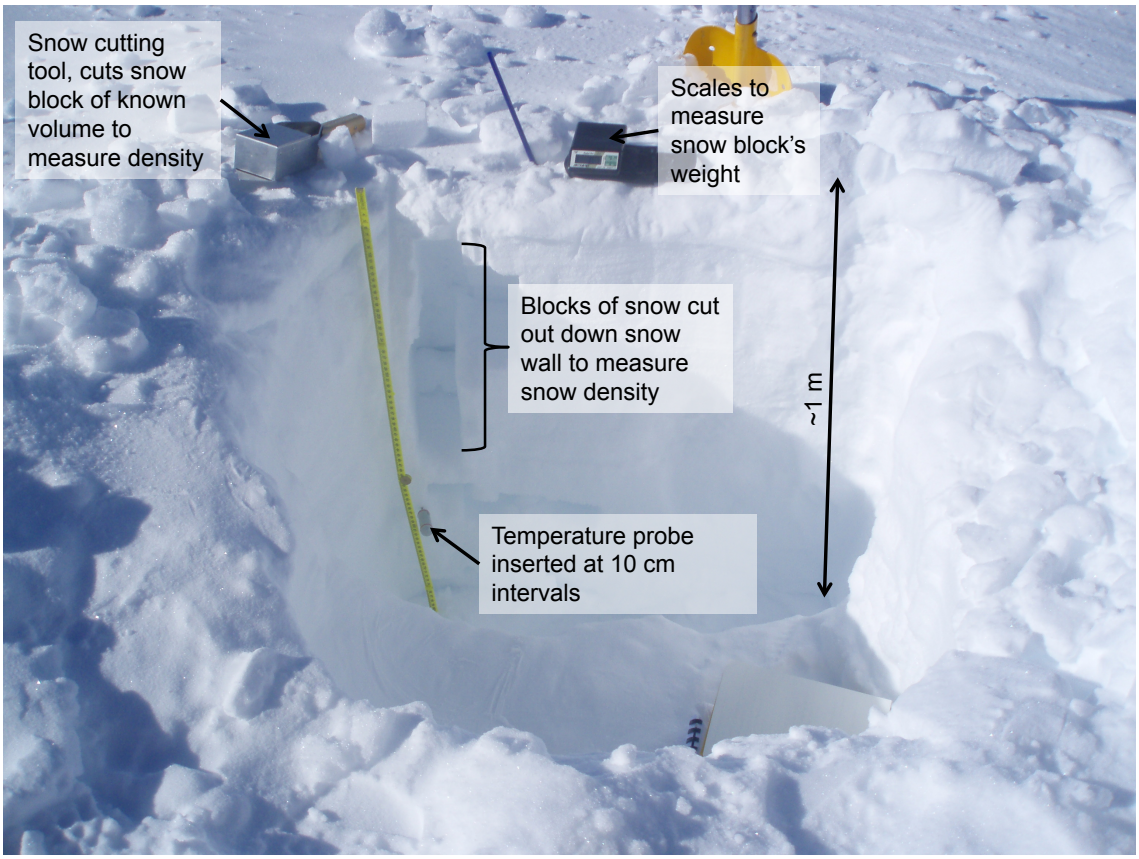

Figure 7.14 *– Example of snow pit ∼1×1×1 m dug after HDRF measurements were complete to measure snow grain size and type, density, temperature and penetration.*

7.4 Results

Polar plots of HDRF, as described in section 7.3.2.2, of individual sites along the transect, for a wavelength of 600 nm, are reported in section 7.4.1 with corresponding snow pit data from each site. An average polar plot of HDRF from all sites along the

transect, creating a representative polar contour plot, for wavelengths of 400, 600, 800, 1000, 1200, 1400 and 1600 nm, is presented in section 7.4.2.

7.4.1 Variation in polar plots of HDRF of individual sites

Figure 7.15 shows polar plots of HDRF for all eight sites along the transect at a wavelength of 600 nm. Snow pit data from each site is also shown including snow grain type, grain size, snow density and penetration/hardness, with a corresponding photograph of the measured surface showing snow topography. A key to the snow pit data is shown in table 7.1. Polar plots for other wavelengths (400, 800, 1000, 1200, 1400 and 1600 nm) for each site are shown in appendix C. Snow topography is important to consider as small scale inhomogeneities of the snow surface will affect the HDRF, especially with the relatively small viewing footprint used with GRASS. Knowledge of snow physical properties below the measurement site is also critical as under snow structure may affect HDRF measurements. France et al. (2011) described the stratigraphy of the top 80 cm of Dome C snow as generally consisting of a surface windpack and a hoar-like layer beneath the windpack. The *e*-folding depths at a wavelength of 400 nm were ∼10 cm for the windpack layers and ∼20 cm for the hoar-like layer, at 600 nm *e*-folding depths decreased to ∼8 cm for the windpacked snow and ∼5 cm for the hoar-like snow. Snow is optically thick after 3–4 *e*-folding depths (France et al., 2011), thus the structure of snow may affect albedo down to ∼80 cm.

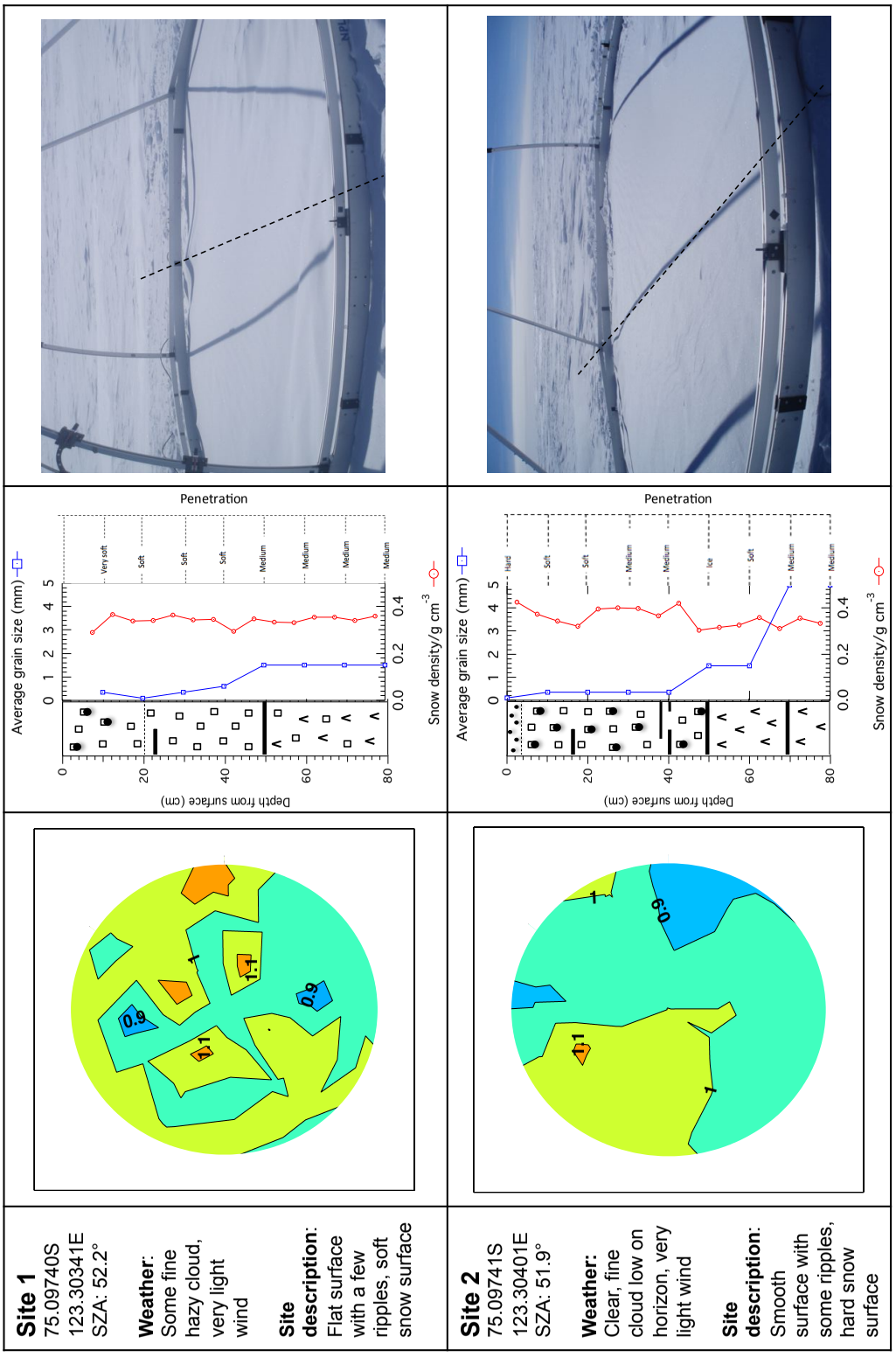
Site 1
75.09740S
123.30341E
SZA: 52.2°
Weather: Some fine hazy cloud, very light wind
Site description: Flat surface with a few ripples, soft snow surface
Penetration
Average grain size (mm)
Snow density/g cm-3
Depth from surface (cm)
Very soft
Soft
Soft
Soft
Medium
Medium
Medium
Medium
0.9
1
1
1.1
0.9
1
Site 2
75.09741S
123.30401E
SZA: 51.9°
Weather: Clear, fine cloud low on horizon, very light wind
Site description: Smooth surface with some ripples, hard snow surface
Penetration
Average grain size (mm)
Snow density/g cm-3
Depth from surface (cm)
Hard
Soft
Soft
Medium
Medium
Ice
Soft
Medium
Medium
1
0.9
1.1
1

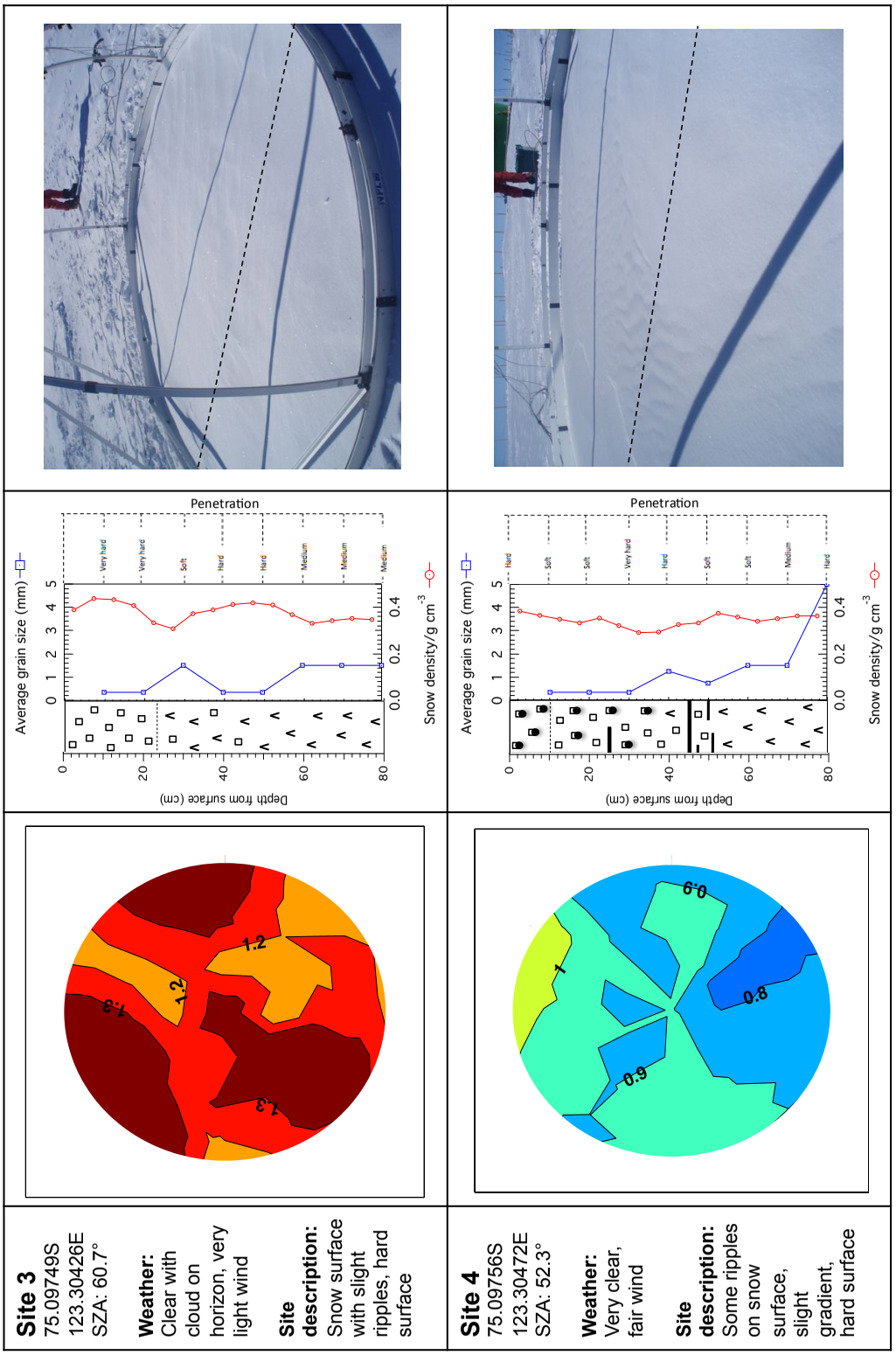
Site 3
75.09749S
123.30426E
SZA: 60.7°
Weather:
Clear with cloud on horizon, very light wind
Site description:
Snow surface with slight ripples, hard surface
Penetration
Average grain size (mm)
Snow density/g cm-3
Depth from surface (cm)
Very hard
Very hard
Soft
Hard
Hard
Medium
Medium
Medium
1.2
1.2
1.3
1.3
Site 4
75.09756S
123.30472E
SZA: 52.3°
Weather:
Very clear, fair wind
Site description:
Some ripples on snow surface, slight gradient, hard surface
Penetration
Average grain size (mm)
Snow density/g cm-3
Depth from surface (cm)
Hard
Soft
Soft
Very hard
Hard
Soft
Soft
Medium
Hard
0.9
1
0.8
0.9

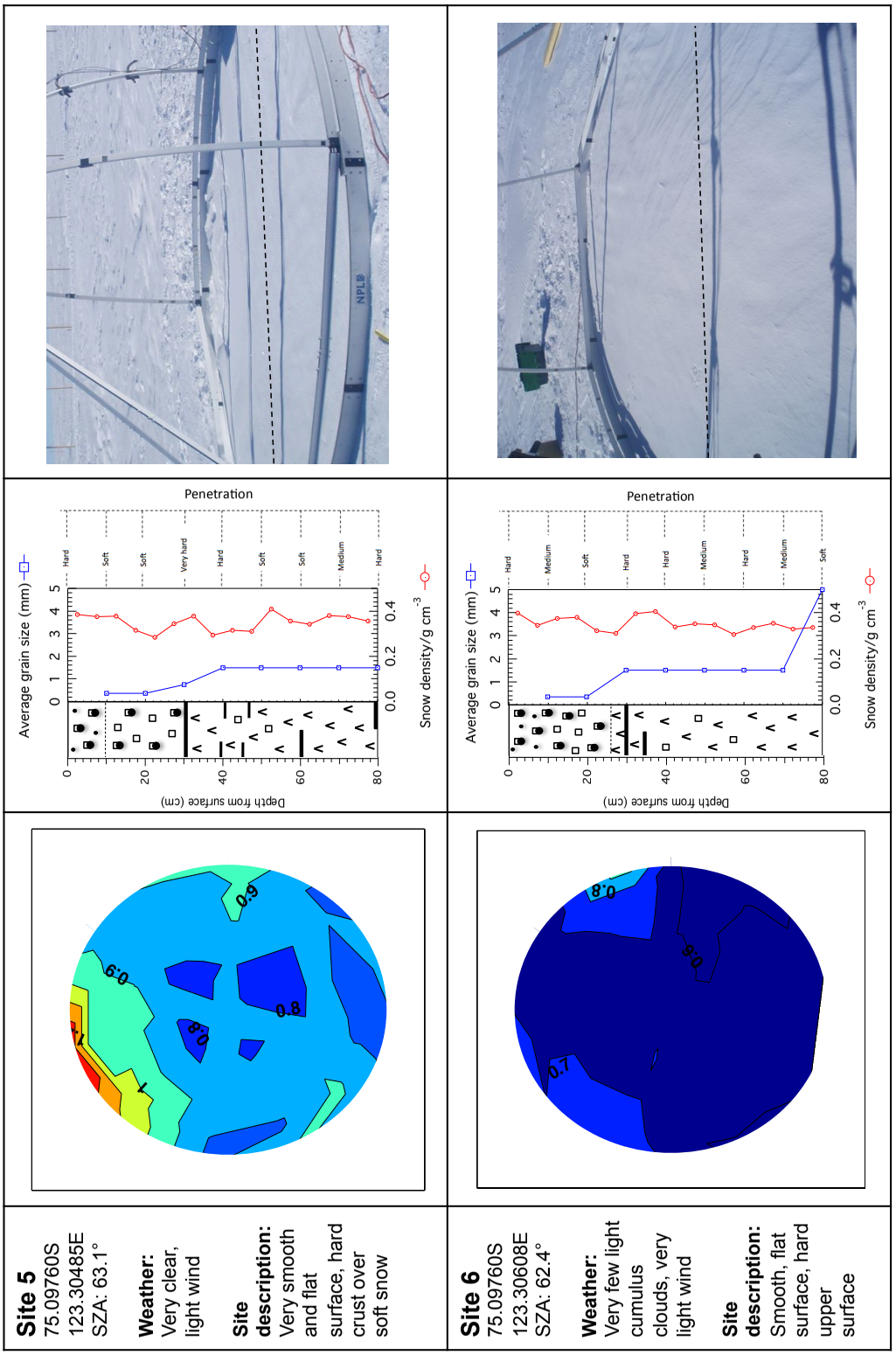
Site 5
75.09760S
123.30485E
SZA: 63.1°
Weather:
Very clear,
light wind
Site
description:
Very smooth
and flat
surface, hard
crust over
soft snow
Penetration
Average grain size (mm)
Snow density/g cm-3
Depth from surface (cm)
Hard
Soft
Soft
Very hard
Hard
Soft
Soft
Medium
Hard
0.9
0.8
0.8
1
1
Site 6
75.09760S
123.30608E
SZA: 62.4°
Weather:
Very few light
cumulus
clouds, very
light wind
Site
description:
Smooth, flat
surface, hard
upper
surface
Penetration
Average grain size (mm)
Snow density/g cm-3
Depth from surface (cm)
Hard
Medium
Soft
Hard
Hard
Medium
Hard
Medium
Soft
0.8
0.8
0.7

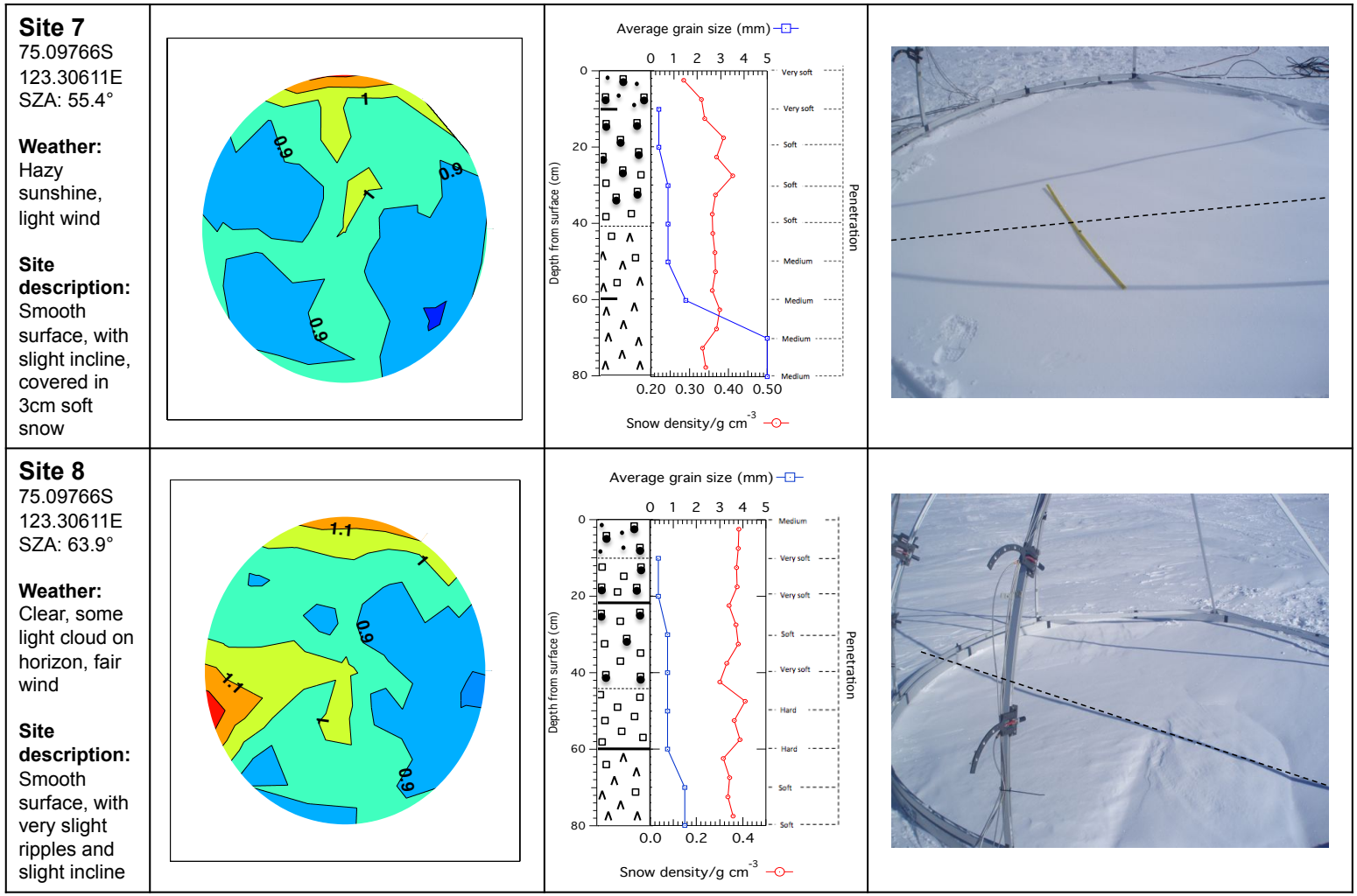

Figure 7.15 *– HDRF polar plots at 600 nm from each of the eight sites with site longitude and latitude (±5 m), average solar zenith angle, weather, surface conditions, selected snow pit data (snow stratigraphy, snow density and grain size) and a photo of each site. The solar principle plane is marked roughly on the photos as a dashed line. On the polar plots the solar principle plane runs from top to bottom with the sun at the base of the plots.*

Snow grain type
 Facetted
 Rounded-facetted
 Rounded
 Depth hoar
 Ice

Grain size	
Size (mm)	**Term**
<0.2	Very fine
0.2–0.5	Fine
0.5–1.0	Medium
1.0–2.0	Coarse
2.0–5.0	Very coarse
>5.0	Extreme

Hardness	
Snow penetration object	**Term**
Fist	Very soft
4 fingers	Soft
1 finger	Medium
Pencil	Hard
Knife blade	Very hard
Ice	Ice

Table 7.1 *– Key to snow pit data including symbols for snow grain types, terms for measured snow grain size and snow hardness/penetration terms for snow penetrated using the tools described.*

Two things are apparent from the HDRF plots presented in figure 7.15. Firstly there is significant variation in the shape of the plots between sites showing that small scale (<1 m) heterogeneity occurs in Dome C HDRF measurements. Secondly the shape of individual plots deviates significantly from symmetrical across the solar principal plane, which it is often assumed the HDRF of snow is (e.g. Hudson et al. (2006); Warren et al. (1998)). Warren et al. (1999) state several causes of variation in snow anisotropic reflectance measurements, including solar zenith angle, snow properties including grain size, grain shape and density and snow topography. The measurements at all sites were taken under similar solar zenith angles 52.8±5.9°, therefore differences in the polar plots which occur between the sites are most likely to be due to small scale differences in snow stratigraphy and topography. Along the transect different snow features and snow types were encountered as seen in figure 7.15, which were representative of the Dome C area.

The surface snow grain size at all sites was very similar, being either “fine” (0.2–0.5 mm) or “very fine” (<0.2 mm). At all sites, at the base of the snow profiles a coarse-grained (>5 mm) depth hoar was found which began at depths ranging from ∼23 cm, at site 3, to ∼60 cm for site 8. The surface ∼0–15 cm layer at sites 5, 6, 7 and 8 consisted of rounded and rounded-faceted grains, while site 1 had a surface ∼0–10 cm layer of round-facetted and facetted grains at the surface, site 2 had only rounded grains in a 5 cm layer, site 3 had facetted grains in a 22 cm surface layer, and site 4 had rounded-facetted grains in a 10 cm surface layer.

The physical penetrability of the surface layer ranged between sites from very hard to

very soft. The hardest surface occurs at site 3 while the softest surface occurs at sites 1 and 8. Unfortunately it is difficult to correlate the different polar plots of HDRF observed with particular snow features.

The photos of snow surfaces in figure 7.15 and the site descriptions give an indication of snow topography for each site. Inhomogeneities in snow topography across a measured snow surface could result in the non-symmetrical plots observed in figure 7.15. The snow surfaces observed at Dome C range from smooth (to the eye) to having small scale ripples or rough surfaces, on ∼5 cm scale. Sites 5 and 7 exhibit the smoothest surfaces, and also exhibit the strongest HDRF forward scattering pattern and the most symmetrical plots, as expected. Sites 3, 6 and 8 show the roughest topography, with a slightly rippled surface. The polar plots of sites 3 and 6 subsequently show the least forward scattering pattern. Site 8 has a raised area of snow in the measurement area (bottom right of photo); the polar plot of figure 8 shows high HDRF values where the raised snow patch is. The decrease in snow anisotropy with increased surface roughness was also noted by Hudson et al. (2006).

Although there are clear differences between the plots, some similarities can also be drawn. The majority of the polar plots of HDRF from individual sites show the snow is forward scattering with values of HDRF peaking at the top the plots with values greater than1. The forwards scattering pattern is most clear in sites 5, 7 and 8 where the forwards scattering peak occurs at zenith angles >55° and azimuth angles ±45° of 90°. For sites 3 and 6 no clear forwards scattering is observed. The forward scattering of snow has been widely reported in previous literature (e.g. Kuhn (1985); Dozier et al. (1988); Warren et al. (1998); Leroux et al. (1999); Aoki and Fukabori (2000); Painter and Dozier (2004); Li and Zhou (2004); Peltoniemi et al. (2005); Dumont et al. (2010)). HDRF values are also generally similar between sites, with most values ranging from 0.8–1.1 (with outliers ranging from 0.6–1.3). These HDRF values are different to other natural surfaces, for example, grass, trees and water (e.g. Sandmeier et al. (1998); Voss et al. (2007); Sayer et al. (2010)).

7.4.2 A spatially averaged HDRF polar contour plot of a Dome C snow surface

The polar plots shown in figure 7.15 clearly show differences in small scale (<1 m) HDRF measurements. However a typical satellite would measure over a larger viewing footprint (>10 m). To obtain an HDRF polar plot which is more representative of a larger viewing footprint the polar plots of individual sites can be spatially averaged. The spatially averaged plot can also be compared to the results from Hudson et al. (2006), who measured anisotropic reflectance of Dome C snow surfaces from the top of a 32 m tower, thus had a much larger viewing footprint which would average over any surface inhomogeneities.

Hudson et al. (2006) reflect their polar plots assuming that values are symmetrical across the solar principle plane. In order to be able to compare the results presented here to those measured by Hudson et al. (2006) the spatially averaged HDRF is made symmetrical across the solar principle plane by reflecting and averaging across the plane. To achieve this firstly the matrix to form the plot is duplicated and all values in one matrix are reflected. The values in both matrices are then averaged to form a plot which is symmetrical around the solar principle plane. Figure 7.16 shows a comparison between the spatially averaged plot at 600 nm for non-symmetrical and symmetrical HDRF values. Figure 7.16 shows the non-reflected spatially averaged plot is not completely symmetrical, this is likely to be due to a few sites showing extreme unsymmetrical HDRF values due to surface roughness which therefore affects the average values. However the average non-reflected plot is much closer to being symmetrical than the majority of plots from the individual sites. If more snow surfaces were included in the average then it is likely the plot would become more symmetrical, suggesting HDRF moves towards being symmetrical across the plane when averaged over sites, but not for individual sites due to small scale homogeneities.

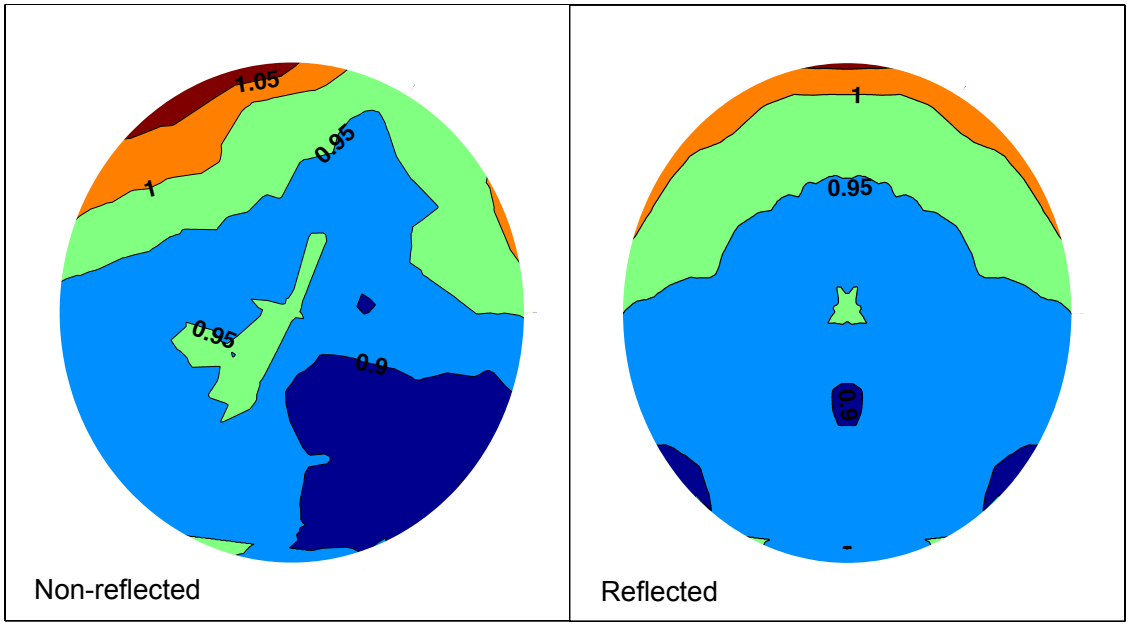

Figure 7.16 *– Comparison between reflected and non-reflected spatially averaged HDRF polar plot at 600 nm. Polar plot is made symmetrical in the right hand plot by reflecting and averaging across the solar principal plane.*

The representative polar plots at wavelengths of 400, 600, 800, 1000, 1200, 1400 and 1600 nm are shown in Figure 7.17. The snow surface is forward scattering at all wavelengths, as expected, with a very similar HDRF pattern at wavelengths from 400–800 nm. A marked decrease in values of HDRF occurs as the wavelength increases to over 800 nm with the value of the prominent forward scattering peak becoming less, decreasing from ∼1.05 at 600 nm down to ∼0.25 at 1600 nm. Therefore showing a decrease in reflectance with wavelength. However the relative change in HDRF values with azimuth and zenith angle becomes larger with wavelength; as a percentage of HDRF at nadir, at 600 nm the HDRF peak is 110% the value at nadir while at 1600 nm it is 167%. Thus snow becomes more forward scattering with increased wavelength as expected (e.g. Hudson et al. (2006)). The HDRF forward scattering pattern remains constant with wavelength occurring at ±60° of the solar principal plane and at a zenith angle of ∼60°.

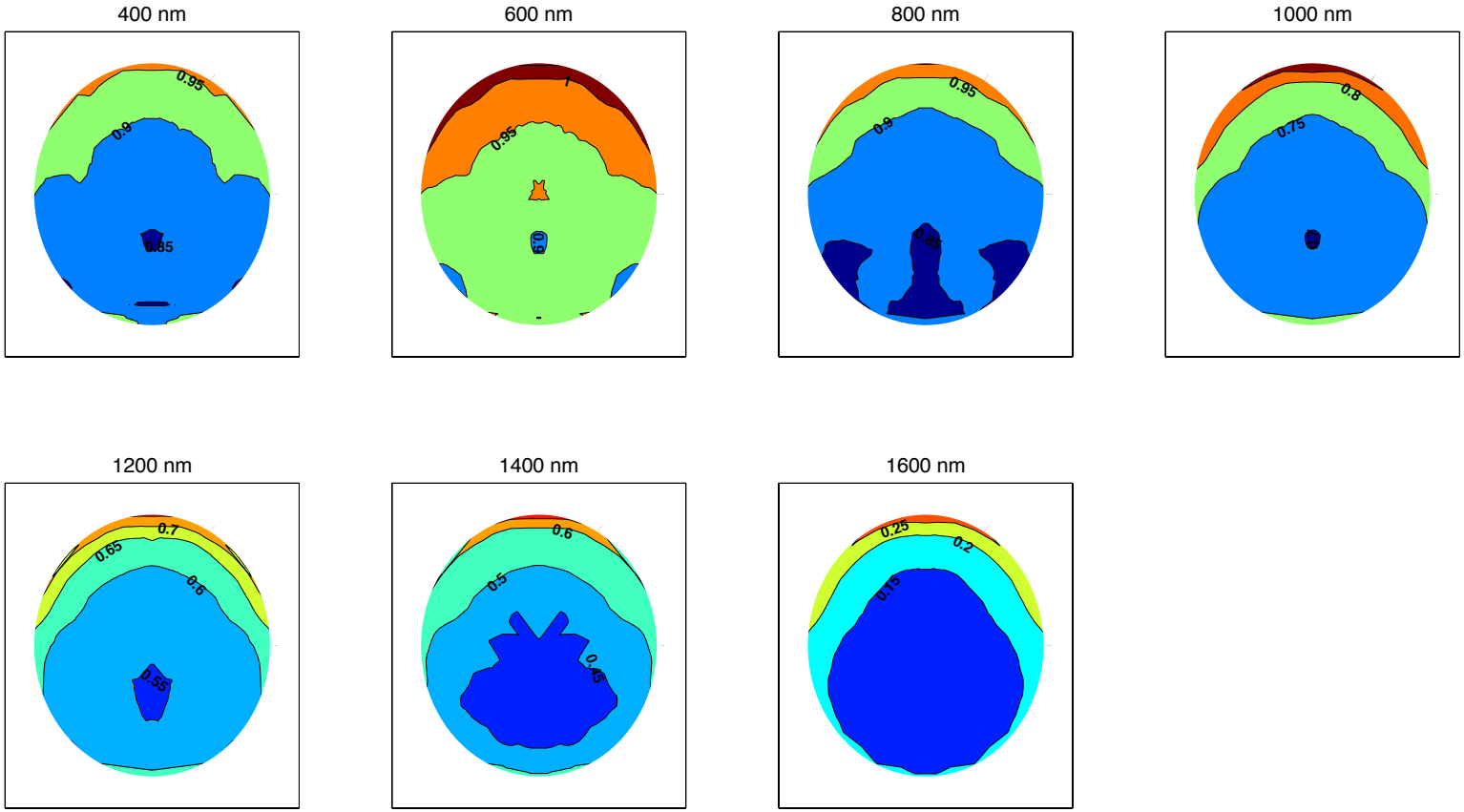

Figure 7.17 *– Representative polar plots from HDRF averaged across all eight sites at wavelengths 400–1600 nm. Average solar zenith angle was 58.2±5.9°(1SD). Note different colour scale for each plot.*

7.5 Discussion

The discussion section will compare how the representative HDRF polar plots presented here correspond with Dome C HDRF values reported by Hudson et al. (2006) and discuss accuracy of GRASS HDRF measurements.

7.5.1 Comparison to previous Dome C measurements

Hudson et al. (2006) measured the anisotropic reflectance of Dome C surfaces in the form of an "anisotropic reflectance factor" at wavelengths 350–2400 nm, by taking measurements from a 32 m tower, at viewing zenith angles from 22.5 to 82.5°. Angles less than 22.5° were not used as the footprint would have been too small for that study to contain a representative snow sample. Each observation sequence involved 85 measurements of different snow surfaces at different viewing azimuth/zenith angles over 255° of azimuth (from 142.5° to 37.5°). The measurement method of Hudson et al. (2006) varies from that presented here as GRASS includes all azimuth angles in one measurement sequence and solar zenith angles to 0°. GRASS also observes the same snow surface with each azimuth/zenith angle observed. The HDRF measurements made by GRASS have a much smaller footprint than the measurements by Hudson et al. (2006), with the GRASS measurement footprints varying from 0.049 m^2 at nadir to 0.142 m^2 at 60° of zenith and the footprint of the measurements of Hudson et al. (2006) varying from 70 to 1170 m^2. The smaller footprint of the measurements made by GRASS means that each measurement is only representative of the snow surface measured. However, the representative HDRF contour plots of figure 5 are considered comparable with the anisotropic reflectance factor measurements of Hudson et al. (2006). To compare the two values, the anisotropic reflectance factor presented by Hudson et al. (2006) must be converted to an HDRF presented here, as subsequently described. The relationship between the BRDF and the anisotropic reflectance factor described by Hudson et al. (2006) is snown in equation 7.5 (their equation 6). Where ψ is the anisotropic reflectance factor measurement and α is albedo (total surface irradiance divided by total downwelling irradiance).

$$\psi = \frac{\pi}{\alpha} BRDF \tag{7.5}$$

BRDF is linked to BRF by equation 7.6 (Schaepman-Strub et al., 2006). Measurements of the HDRF of snow at wavelengths greater than 800 nm are not significantly influenced by diffuse light (Li and Zhou, 2004), as scattering of light in the atmosphere by Rayleigh scattering a ffects shorter wavelengths much more than longer wavelengths. HDRF is therefore a reasonable estimate of BRF at near-infrared wavelengths (800–1400nm).

$$BRF = BRDF\,\pi \tag{7.6}$$

Substituting equation 7.5 into equation 7.6 produces equation 7.7, providing a means of direct comparison between the anisotropic reflectance factor measurements of Hudson et al. (2006) to the HDRF measurements presented here (at near infrared wavelengths where HDRF equates to BRF).

$$BRF = \psi\alpha \tag{7.7}$$

The BRF was calculated from anisotropic reflectance factor data from Hudson et al. (2006) using equation 7.7. Figure 7.18 shows a comparison of a BRF polar contour plot at a wavelength of 1000 nm calculated from Hudson et al. (2006) values, to the representative GRASS HDRF polar plot at a wavelength of 1000 nm. The anisotropic reflectance factor data from Hudson et al. (2006) are for a solar zenith angle of 58.2°, which is the same as the average solar zenith angle for which the HDRF measurements with GRASS were taken. Albedo measurements are taken from Hudson et al. (2006) figure 6. Note, only BRF values for viewing zenith angles measured by Hudson et al. (2006) that are similar to those measured by GRASS are shown for comparative purposes. Figure 7.18 also shows the percentage difference between the GRASS measurements and the Hudson et al. (2006) measurements. The agreement is very good, with over 95% of the zenith and azimuth angle parameter space having less than 4% difference in the values. The best agreement occurs at smaller viewing zenith angles where the difference is less than 2%. The agreement is less good at some larger viewing zenith angles, particularly in the backwards scattering direction (base of the plot) where the difference is around 6%. Both the measurements from GRASS and Hudson et al. (2006) show the snow is forward scattering, peaking in the forwards

direction around 0.8. The shape of the polar contour plot is very similar, with the forward peak occurring at similar azimuth angles, although over a slightly greater range in Hudson et al. (2006). Both GRASS and Hudson et al. (2006) show there is a slight backscattering present. From Figure 7.18 it can be suggested that even though GRASS provides a very different method to that utilised by Hudson et al. (2006) the results produced are very similar, adding strength to both the data presented here and that presented by Hudson et al. (2006).

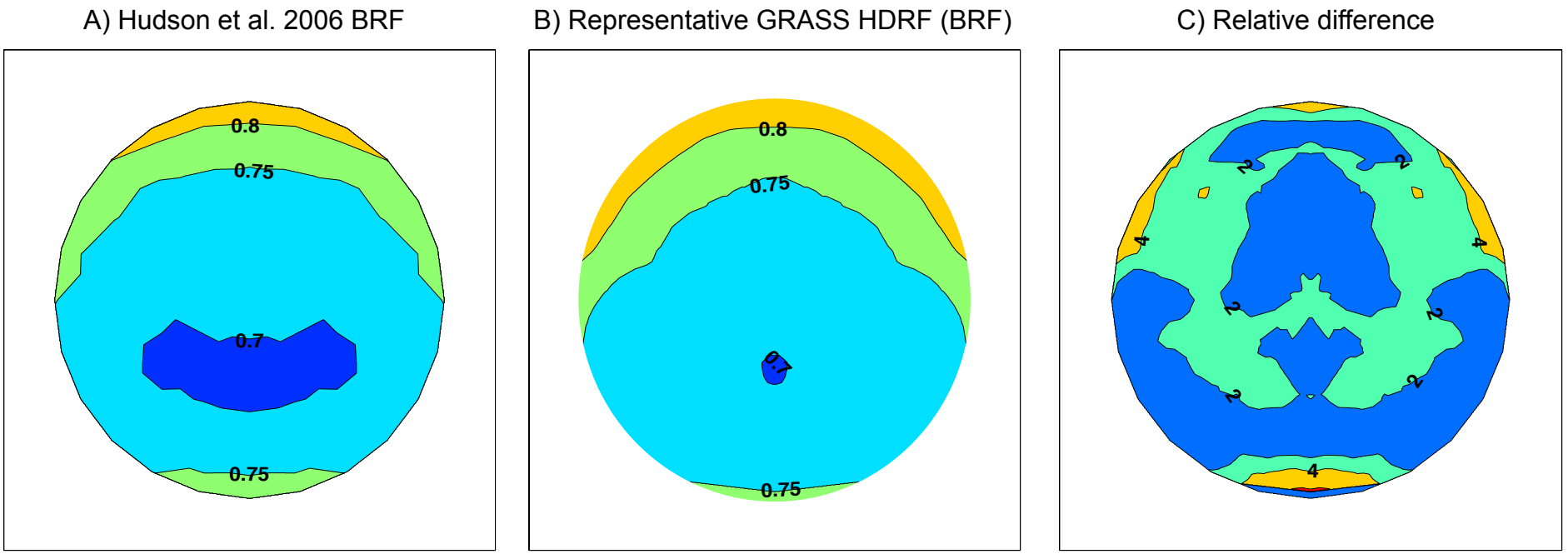

Figure 7.18 *– Comparison between BRF measurements by Hudson et al. (2006) (A) and BRF measurements from GRASS presented here (B) at a wavelength of 1000 nm (BRF approximates to HDRF at near infrared wavelengths). Relative difference (%) between plots A and B is shown in plot C.*

7.5.2 Accuracy and precision of HDRF measurements using GRASS

Sandmeier (2000) reviews uncertainties in BRDF (HDRF) measurements from field goniometers and how these sources of error are best reduced. Sources of error include; geometrical accuracy of the goniometer, atmospheric conditions and the Spectralon reference panel. Section 7.5.2 will ascertain how each of these uncertainties could have impacted the HDRF results presented here.

7.5.2.1 Geometrical accuracy

The geometrical accuracy of the goniometer defines measurement repeatability (Sandmeier, 2000). For geometrically accurate HDRF measurements the centre of a radiance collector viewing footprint should always point at the centre of the hemisphere (Sandmeier, 2000). Variation in the location of the radiance collector viewing footprints on GRASS was recorded by transmitting a laser through each radiance collector attached to GRASS and recording the viewing footprint shown by the laser on the surface under laboratory conditions. Figure 7.19 shows variation in the viewing footprint of the nadir radiance collector as it is rotated into the four 90° of azimuth apart positions. The centre of the viewing footprint for the nadir radiance collector in each position deviates from the centre of the hemisphere surface by an average of 6.8 cm, as shown in figure 7.19.

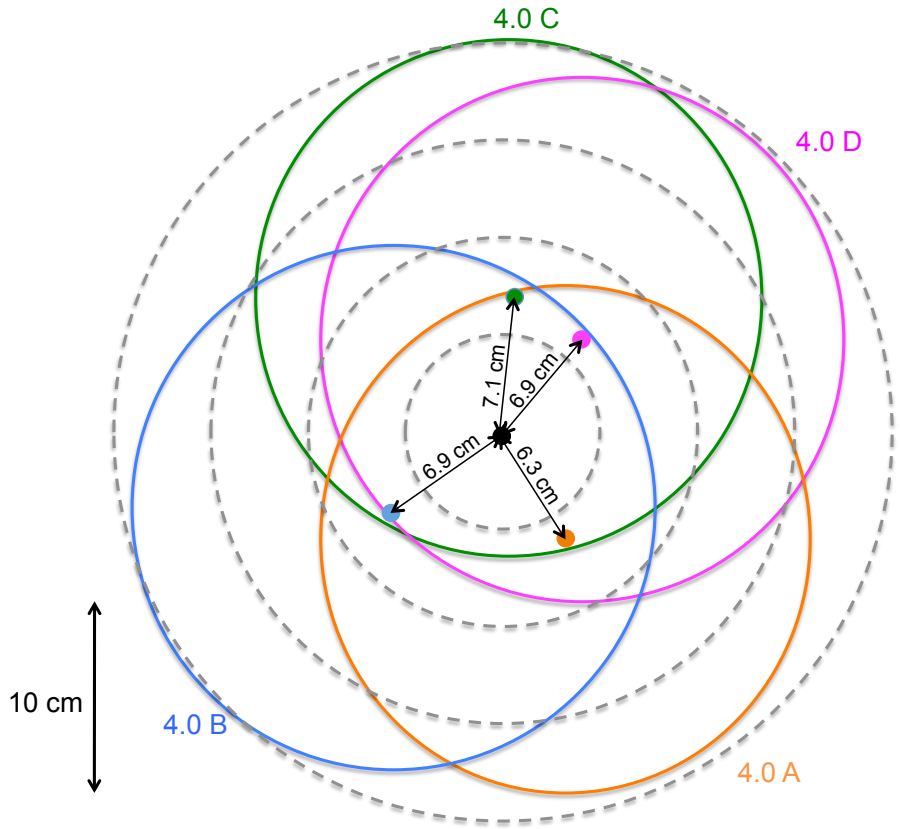

Figure 7.19 *– Variation in the viewing footprint of the nadir radiance collector as GRASS is rotated into four, 90° of azimuth apart, positions, shown as solid circles. Lengths show deviation of the viewing footprint from the centre, averaging 6.8 cm. The dashed circles show distance, each being 5 cm apart.*

Figure 7.20 shows the viewing footprint of all the radiance collectors at different viewing azimuth/zenith angles. All radiance collectors on GRASS focus on the same target surface within the viewing footprint. However there is a significant increase in the size of the viewing footprint as viewing zenith angle increases; 491 cm^2 at nadir to 1419 cm^2 at a zenith angle of 60°. The eccentricity of the viewing footprint also significantly increases.

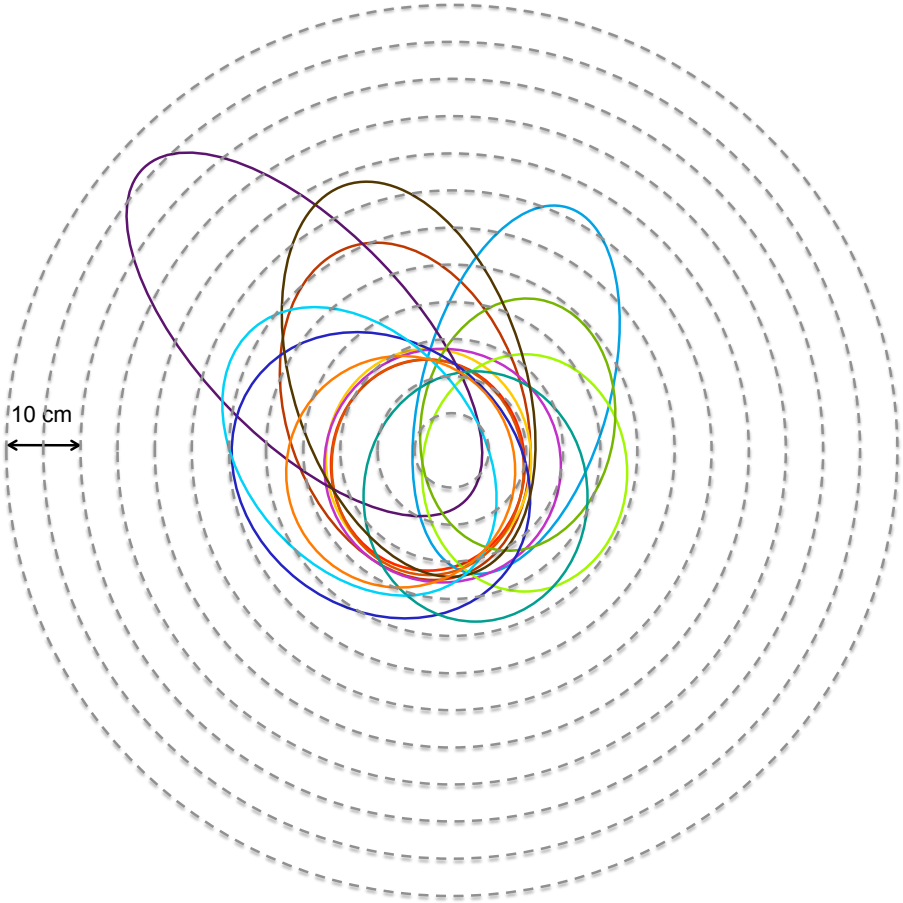

Figure 7.20 *– Variation in the viewing footprint of all radiance collectors on GRASS at different viewing azimuth/zenith angles, with the GRASS frame in one position only (no rotation).*

To test the repeatability of GRASS measurements, HDRF measurements of a white linoleum surface were repeated six times under laboratory conditions and with constant illumination provided by tungsten-halogen lamps placed at a zenith angle of ∼50°. For the majority of measurements, at a specific zenith/azimuth angle, the relative standard deviation is less than 15%, meaning that the measurements presented here of HDRF may have a 15% uncertainty. However, the method presented here for the repeatability experiments is not ideal and subsequent, more stable, repeatability measurements suggest the standard deviation of measurements is about 5%. Figure 7.21 shows the standard deviation in HDRF measurements for the six repeats across the polar plots.

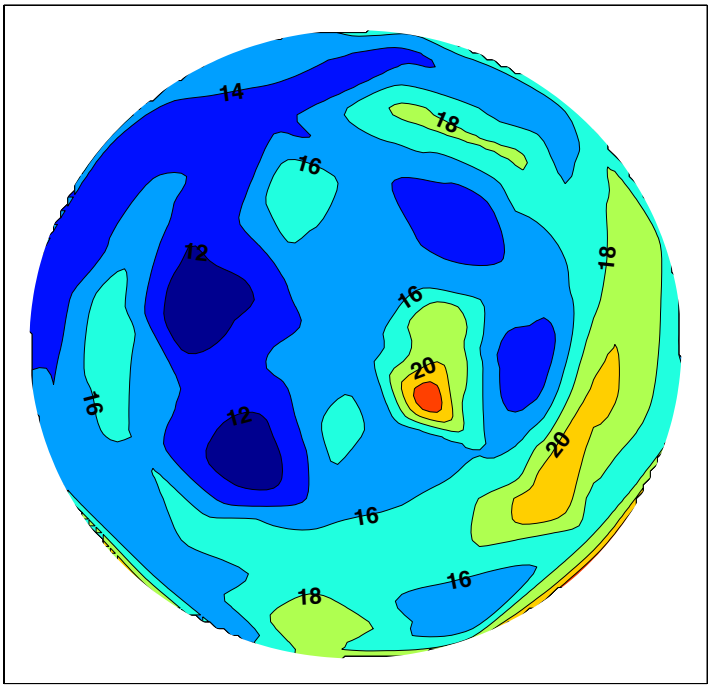

Figure 7.21 *– Variation in the viewing footprint of all optics on GRASS (relative standard deviation (%)).*

7.5.2.2 Effect of varying optic lens cone of acceptance and radiance collector zenith angle position

To test how different zenith angle positions of the radiance collectors and different cone of acceptance may affect the HDRF measurements of GRASS the field of view was measured under four different set ups of GRASS; with the radiance collectors situated at 10° zenith angle increments (0,10, 20, 30, 40, 50°) and 15° increments (0, 15, 30, 45, 60°) and with optical lenses with a 2° and 8° cone of acceptance. Figure 7.22 shows the different viewing footprints for each radiance collector under the four different set ups. Figure 7.22 shows that for the 2° optical lens there is very poor overlap of the viewing footprint for each radiance collector at a different viewing zenith/azimuth angle, thus the size of the viewing footprint of a 2° optical lens is insufficient. Using an optical lens with a cone of acceptance larger than 8° would provide better overlapping of the viewing footprint, but the increased eccentricity and size of the viewing footprint with increased zenith angle would become worse and the viewing footprint would be larger than the Spectralon panel at large zenith

angles.

The 10° separation only includes viewing zenith angles as high as 50°, while the 15° separation covers angles to 60°, the extra 10° enables anisotropy at large zenith angles to be observed, which isn't seen at 50°. Unfortunately it is not possible to go above 60° due to increased eccentricity of the viewing footprint. Indeed in the measurements presented here originally a zenith angle of 75° was also included, but in laboratory experiments it was shown the radiance collector had a viewing footprint overlapping the base ring of GRASS due to the largely increased eccentricity in the viewing footprint at this zenith angle. The measurements at 75° were thus removed for data analysis. The optimum set up is the 15° zenith angle separation and 8° cone of acceptance used in the work presented in this chapter (although ideally an extra radiance collector could be added to each arm enabling 10° zenith separation to 60°, as this would provide better viewing zenith angle resolution).

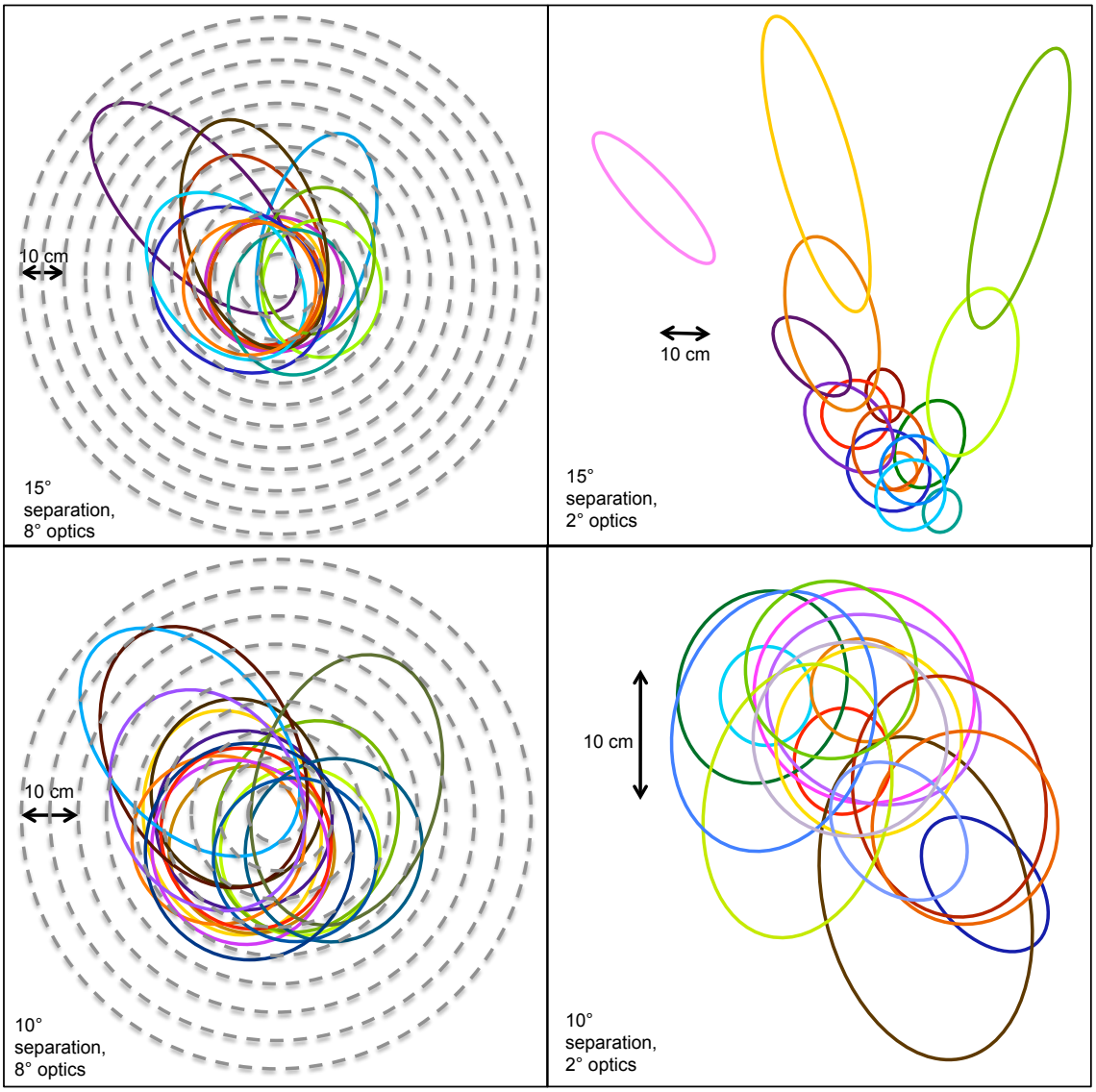

Figure 7.22 *– Variation in the viewing footprint of all radiance collectors on GRASS with the radiance collectors with different viewing zenith angle separation (10 and 15°) and different cone of acceptance (2 and 8°).*

7.5.2.3 Atmospheric conditions

Atmospheric conditions can influence reflectance measurements. In order to minimise the effect of atmospheric interference, measurements were only taken in clear sky conditions, or when there was only a small amount of cloud low on the horizon (sky conditions are noted in figure 7.15). Atmospheric column aerosol at Dome C is minimal. Aerosol optical thickness was measured during each HDRF measurement of a snow surface using a Microtops Sunphotometer. The average values of aerosol optical thickness were 0.037±0.090 (1 SD) at 440 nm and 0.070±0.031 (1SD) at 1200 nm. A value of <0.01 corresponds to an extremely clean atmosphere, a typical

value for Europe is 0.17 (Meij et al., 2012).

7.5.2.4 Spectralon reference panels

The Spectralon reference panel used to calculate HDRF is assumed to be a perfect Lambertian reflector, however several studies (e.g. Kimes and Kirchner (1982); Jackson et al. (1992); Sandmeier et al. (1998)) suggest this is not the case, with deviations of up to 8% from a perfect Lambertian reflectance (Sandmeier et al., 1998). In the measurements presented here reflectance of the reference panel is only measured at the nadir. However the non-ideal reflectance may affect the determination of HDRF as reflectance from the panel may vary as a function of solar zenith angle. The panel was calibrated at the National Physical Laboratory prior to the measurements by GRASS. At nadir, and with a incident radiation angle typical to that under which GRASS measurements were taken, the Spectralon panel was 4% from lambertian at 400 nm, decreasing to <0.02% at 900 nm. Spectralon panels are typically calibrated at room temperature, Ball et al. (2013) showed there was no significant difference between measurements taken at room temperature (∼20°C) and at a polar temperatures despite a phase transition in the panels at 19°C.

7.6 Conclusions

HDRF measurements were taken at eight sites along a ∼100 m transect of snow surfaces at Dome C, Antarctica, using a gonio-radiometric spectrometer system (GRASS). The measurements of HDRF compliment previous Dome C HDRF measurements. The HDRF results from GRASS show snow is forward scattering which is consistent with all previous literature. Polar plots of HDRF from the individual sites show differences in the HDRF patterns, which is likely to be due to snow surface features or snow properties. The small scale (<1 m) heterogeneity was not seen before at Dome C and is important for future satellites, which may have smaller viewing footprints. A representative HDRF polar plot was created by spatially averaging over the transect. As wavelength increases the prominence of the forward scattering increases on the representative plot although overall reflectance decreases. The representative plot shows very good agreement with previous Dome C measurements (within 4% at a

wavelength of 1000 nm) even though the techniques utilised to measure HDRF are significantly different. Improved measurements of snow surface HDRF will improve satellite albedo measurements, by improving conversion of the satellites measurements of surface reflectance over narrow viewing angles to hemispherical albedo requiring understanding of the anisotropic reflectance of surfaces. Improved albedo measurements could enable large scale black carbon measurements.

Chapter 8

Concluding remarks

8.1 Introduction

In the thesis the response of sea ice albedo and *e*-folding depth to increased mass-ratio of black carbon has been examined using both a radiative transfer model, TUV-snow, and through experiments with artificial sea ice which were used to validate the TUV-snow model. This final, concluding remarks, chapter will begin with a summary of the findings of each chapter, discuss the potential importance of black carbon in sea ice on global climate and then move on to suggestions of how the work presented here can be carried forwards, with ideas for future research.

8.2 Key conclusions

The following key conclusions were made from each chapter presented here:

Chapter 2 presented an introduction to radiative-transfer modelling using TUV-snow and investigated how both black carbon and HULIS affect albedo, light penetration and PAR propagation of a snow free ablating first-year sea ice. Black carbon was shown to have a much greater effect than HULIS on albedo and *e*-folding depths, as black carbon has a larger absorption cross-section than HULIS, especially at longer wavelengths. HULIS absorption may still be important at shorter wavelengths, influencing photochemistry. The effect of black carbon and HULIS distribution in the sea ice on albedo was also investigated suggesting the impurities

have a greater effect on albedo of sea ice when they are concentrated at the surface of the sea ice. Black carbon may be concentrated in a surface layer in the sea ice due to overlying snow melt, where black carbon is left behind from snow.

Chapter 3 expanded on the work presented in chapter 2 investigating and comparing the response of an Arctic first year and multi-year sea ice to increasing black carbon. Absorption and scattering cross-sections were derived for a first year and multi-year ice, and dry and wet snow from optical field data from Grenfell and Maykut (1977), suggesting black carbon is the dominating absorbing impurity. Subsequently, radiative-transfer calculations using the derived absorption and scattering cross-sections showed that the albedo of a first-year Arctic sea ice is more responsive to black carbon additions than multi-year sea ice. Chapter 3 also investigated the degree to which a snow cover over sea ice will mitigate the albedo response of increased black carbon in sea ice. A 2–5 cm snow layer is enough to disguise a change in surface albedo owing to additional black carbon in the surface layer of sea ice. Thus effects of black carbon in sea ice are limited to when snow cover is less than 2–5 cm. When snow cover is thin enough for black carbon in the sea ice to affect surface albedo snow melting will be exacerbated leading to longer snow free conditions, and greater sea ice melting. The time of year with snow-free sea ice coincides with the largest solar radiation, thus black carbon's influence on reducing sea ice albedo will be larger.

Chapter 4 further develops the work of chapters 2 and 3 through a thorough investigation of how the albedo and light penetration depth of snow and sea ice with different optical properties responds to increased black carbon by exploring a wide parameter space of scattering and absorption. The albedo and *e*-folding depth response of a multi-year ice, first year ice, melting ice, cold polar snow, windpacked snow and melting snow were compared, showing that the relative response of snow and sea ice to increased mass-ratio of black carbon is highly dependent on the type of snow and sea ice. A snow or sea ice with a larger scattering cross-section, e.g. a cold polar snow or a multi-year sea ice is relatively less responsive to black carbon than a melting snow or sea ice, especially for albedo. The change in albedo owing to black carbon is relatively less in snow than sea ice. Current climate change is causing a decrease in multi-year sea ice and increased first-

year/melting sea ice, which is more responsive to black carbon, thus potentially exacerbating melting rates of sea ice.

Chapter 5 introduces the design and experimental set up of the sea ice simulator showing that the artificial sea ice created in the simulator is representative of a first-year sea ice with accurate growth rates, salinity profiles, and reflectance and *e*-folding depth values. The sea ice simulator creates polar temperatures, shortwave illumination and an artificial ocean.

Chapter 6 describes the use of the artificial sea ice grown in the sea ice simulator to measure the response of artificial sea ice to increased black carbon in a 5 cm surface layer of the sea ice. The results from the simulator are compared to calculations with the TUV-snow model to evaluate the model. To recreate measurements of the artificial sea ice reflectance, with black carbon mass ratios of 0, 75, 150 and 300 ng g^{-1} within a top 5 cm layer, using the TUV-snow model requires three factors. Firstly, absorption by impurities in the "clean" ice layer must be considered. The impurity was most likely algae. Secondly, the scattering cross-section of the top black carbon bearing layer and bottom ice layer have to be altered from each other within a factor of three. Finally the black carbon mass ratio in the top layer must be reduced by a factor of three in the model compared to that added to the artificial ice to obtain a fit. Two reasons are suggested for this; the black carbon absorption cross-section of the black carbon added to the ice is different to that in the TUV-snow model or black carbon is mobilised from the top 5 cm layer to the below sea ice and eventually into the underlying seawater.

Chapter 7 looked at the anisotropic reflectance of polar surfaces through describing results from fieldwork measuring HDRF of snow surfaces at Dome C which can be used for satellite calibration and validation. HDRF measurements were taken at eight sites along a ∼100 m transect of snow surfaces at Dome C, Antarctica, using a gonio-radiometric spectrometer system (GRASS). The measurements show snow is forward scattering being consistent with all previous literature but also show differences in the HDRF patterns from individual sites, which is likely to be due to snow surface features or snow properties, this was not seen before at Dome C. A representative HDRF polar plot was also created by spatially averaging over the transect, which shows very good agreement with

previous Dome C measurements (within 4% at a wavelength of 1000 nm), even though the techniques utilised to measure HDRF are significantly different. The measurements at Dome C can be used for satellite calibration to improve global albedo measurements and potentially measurements of global black carbon concentrations in snow and sea ice.

Table 8.1 provides a summary of the effects on albedo and *e*-folding depth of impurities in snow or sea ice that are investigated in the calculations using the TUV-snow model, particularly focussing on realistic increases in mass-ratios of impurities in the snow or sea ice.

Chapter	Sea ice/snow type investigated	Impurity	Impurity distribution	Effect on albedo	Effect on *e*-folding depth
2	Antarctic melting sea ice	Black carbon	Homogeneous through sea ice	Decreases by 7% for 1-8 ng g^{-1} impurity increase	Decreases by 15% for 1-8 ng g^{-1} impurity increase
2	Antarctic melting sea ice	HULIS	Homogeneous through sea ice	Decreases by 0.5% for 1-8 ng g^{-1} impurity increase	Decreases by 0.5% for 1-8 ng g^{-1} impurity increase
2	Antarctic melting sea ice	Black carbon	In top layer of varying thickness	Greatest effect when black carbon is concentrated at the surface	Not investigated
2	Antarctic melting sea ice	HULIS	In top layer of varying thickness	Greatest effect when black carbon is concentrated at the surface	Not investigated
2	Antarctic melting sea ice	Black carbon	In a layer of varying depth in sea ice	1 cm layer has an effect down to 90 cm	Not investigated
2	Antarctic melting sea ice	HULIS	In a layer of varying depth in sea ice	1 cm layer has an effect down to 50 cm	Not investigated
3	Arctic first year ice	Black carbon	In 5 cm surface layer	Decreases by 1.3% for 1-8 ng g^{-1} impurity increase	Not investigated
3	Arctic multi-year ice	Black carbon	In 5 cm surface layer	Decreases by 0.3% for 1-8 ng g^{-1} impurity increase	Not investigated
3	Arctic first year and multi-year ice ice with wet or dry snow cover	Black carbon	In 5 cm surface layer in sea ice with varying thickness of snow cover	A snow cover of 2-5 cm is required for snow albedo to be uninfluenced by the sea ice albedo;dry snow is more effective than wet snow. First year sea ice requires a greater snow cover than the multi-year ice.	Not investigated
4	Melting sea ice	Black carbon	Homogeneous through sea ice	Decreases by 32% for 1-8 ng g^{-1} impurity increase	Decreases by 65% for 1-8 ng g^{-1} impurity increase
4	First year sea ice	Black carbon	Homogeneous through sea ice	Decreases by 20% for 1-8 ng g^{-1} impurity increase	Decreases by 64.5% for 1-8 ng g^{-1} impurity increase
4	Multi-year sea ice	Black carbon	Homogeneous through sea ice	Decreases by 10% for 1-8 ng g^{-1} impurity increase	Decreases by 64% for 1-8 ng g^{-1} impurity increase
4	Melting snow	Black carbon	Homogeneous through sea ice	Decreases by 3% for 1-8 ng g^{-1} impurity increase	Decreases by 64% for 1-8 ng g^{-1} impurity increase
4	Windpacked snow	Black carbon	Homogeneous through sea ice	Decreases by 0.7% for 1-8 ng g^{-1} impurity increase	Decreases by 64% for 1-8 ng g^{-1} impurity increase
4	Cold polar snow	Black carbon	Homogeneous through sea ice	Decreases by 0.4% for 1-8 ng g^{-1} impurity increase	Decreases by 64% for 1-8 ng g^{-1} impurity increase

Table 8.1 *– Summary table of the effects of impurities on albedo and e-folding depth.*

8.3 The importance of black carbon in sea ice in the global climate system

The results presented in this thesis demonstrate that black carbon in sea ice is of particular importance during Spring when sea ice is melting. There are four reasons for this, firstly as there is no overlying snow cover, secondly black carbon will be concentrated at the surface of sea ice following snow melt, solar irradiance will be larger during spring months thus absorption by black carbon larger, and finally melting sea ice is more responsive to black carbon than frozen first year or multi-year ice. Black carbon in melting sea ice may lead to exacerbated melt rates and subsequently ice free conditions. To comprehend the overall role the exacerbated melt rates would have on global climate change requires the use of global climate models as discussed in section 8.4.2.

To understand the future importance of black carbon in sea ice, projections of black carbon emissions are required. Cofala et al. (2007) estimate a 17% reduction in global anthropogenic black carbon emissions by 2030 compared to present day emissions, while Streets (2007) estimate a decrease of 9–34% over the same time period suggesting some regions where emissions may increase including Africa and South America. Year-to-year changes in black carbon emissions are of increased importance for black carbon in sea ice, as in the case of first year ice, once melted, the black carbon will enter the ocean system. Thus, only the black carbon emitted each year is important and decreased black carbon emissions could have a rapid effect on decreasing sea ice melting rates.

8.4 Future research potential

The work presented in this thesis has improved understanding of the potential impact of black carbon on snow and sea ice albedo and light penetration depths. However a number of further research questions have also arisen, these include: a requirement for improved knowledge of global black carbon concentrations in snow and sea ice; the possibility of incorporating the results presented here into global climate models to improve understanding of the role of black carbon in snow and sea ice on global

climate and working towards more realistic sea ice simulation.

8.4.1 Black carbon concentrations and distribution in sea ice

To fully understand the potential global effects of black carbon in snow and sea ice the global concentrations of black carbon in snow and sea ice need to be understood. Although understanding of global snow mass-ratios of black carbon is good, knowledge of sea ice black carbon mass ratios is very poor. Chapter 2 showed that black carbon is most effective when concentrated at a surface layer as also suggested by Grenfell et al. (2002). Measurements of black carbon distributions in sea ice are also very limited, with, to all knowledge, values only previously reported by Doherty et al. (2010). To increase understanding of global concentrations and distributions of black carbon in sea ice two methods can be used; fieldwork and remote sensing, the benefits and disadvantages of both of these methods will be discussed below.

8.4.1.1 Fieldwork

Fieldwork enables collection of ice cores and subsequent determination of black carbon mass ratios in the ice. Black carbon mass-ratios are determined through filtration of melted samples and using an integrating sandwich spectrometer to measure total absorption by impurities on the filter paper as described by Clarke and Noone (1985). The technique has been attempted for sea ice only by Doherty et al. (2010) and Grenfell et al. (2002). The method can be used for whole core analysis e.g. Grenfell et al. (2002) or the core can be divided in to sections and each analysed individually to provide an idea of black carbon distribution (Doherty et al., 2010). Grenfell et al. (2002) state high uncertainty in their measurements due to small transparent particles in the sea ice which may have obscured black carbon on the filter papers. Although Doherty et al. (2010) present a larger range of results of black carbon concentrations in sea ice ranging from 4 to 67 ng g^{-1}, their conclusions on black carbon distributions in sea ice are inconclusive, suggesting black carbon may be concentrated at a surface layer. There is an evident need for more sampling of sea ice to be done in the field to ascertain black carbon concentrations and distributions. Fieldwork is however inherently expensive, dangerous and has limited scope, thus the sampling range may be unrepresentative of global black carbon concentrations.

8.4.1.2 Remote sensing

To understand global black carbon concentrations in sea ice remote sensing can also be used to take measurements of sea ice albedo and calculate the contribution of black carbon to albedo. Remote sensing would be a highly valuable tool, enabling measurements of expansive and inaccessible areas. The idea has been proposed before for snow but not for sea ice (Warren, 2012). Warren (2012) suggests that for black carbon concentrations in snow to be measured using remote sensing methods progress in accuracy of remote sensing albedo measurements must be made before the contribution of black carbon to albedo can be determined. Current problems include difficulties differentiating snow from thin cloud layers above the snow surface and the effects of snow anisotropic reflectance (BRDF), similar problems would also occur for measuring sea ice black carbon concentrations remotely. The BRDF measurements presented in chapter 7 could help improve satellite measurements of snow albedo. Ground surface measurements of the BRDF of sea ice are very limited. The sea ice simulator could be used for taking BRDF measurements of sea ice which can be applied for satellite calibration.

8.4.2 Incorporating the effects of black carbon in sea ice in to global climate models

To be able to understand the influence of black carbon on sea ice on global climate the radiative forcing caused by black carbon in sea ice must be understood within the global system; to do this global climate models can be used. The results presented in this thesis can be incorporated into global climate models. If black carbon distribution on to snow and sea ice is known during the year then the resultant decrease in albedo for a particular type of snow or sea ice can be deduced using the results in this thesis. These values can then be used in global climate models to understand the effect of the decrease in snow and sea ice albedo owing to black carbon on the global albedo and global energy budget, in order to characterise the extent black carbon on snow or sea ice may influence global albedo and hence the global heat budget.

During the course of this thesis black carbon in sea ice has been added to a few global climate models by others; Holland et al. (2012) used the Community Climate System

Model 4 to investigate the impact of melt ponds and aerosols (black carbon and dust) on Arctic sea ice and Goldenson et al. (2012) used the Community Earth System Model Version 1 (CESM1) to model forcing owing to black carbon and dust in snow and sea ice. Holland et al. (2012) suggest over the 20th century black carbon and dust has caused an annual average 0.2 W m^{-2} increase in shortwave absorption in Arctic sea ice resulting in a decrease of Summer sea ice area of 0.5 million km^2. Goldenson et al. (2012) conclude that black carbon may decrease Arctic sea ice thickness by 0.34 m in September. Black carbon in sea ice thus has a clear effect on global climate which needs to be fully understood through the use of global climate models.

8.4.3 More realistic sea ice simulation

In the work presented in the thesis, apart from chapter 2, black carbon has been considered to be the only other absorbing impurity in both the radiative-transfer calculations using the TUV-snow model and measurements with artificial sea ice using the sea ice simulator. Although with the measurements of artificial sea ice it was clear another absorbing impurity was present, most likely to be algae. The inclusion, in principle, of only black carbon as an absorbing impurity enabled the albedo and light penetration depth reduction due to black carbon alone to be deduced. In reality, other natural absorbing impurities are likely to be present, mainly sediment and algae (e.g. Larssen:1987, Nurnberg:1994, Zebbe:1996, Perovich:1998, Light:1998, Mundy:2005). Light et al. (1998) investigated the albedo reduction due to sediment in sea ice showing that sediment loadings in sea ice of 5–10 g m^{-3} could reduce albedo by 5–10%. Decreased ice thickness in the Arctic has led to a longer sea ice algae growing season as photosynthetically active radiation (PAR) at the base of sea ice is now high enough to allow algae growth for extended periods of the year (Arrigo et al., 2008). Increased algae productivity will increase absorption and decrease sea ice albedo, further exacerbating melting. Thus for a more accurate representation of a sea ice environment absorption by sediment and algae should also be taken into consideration.

8.5 Final conclusions

The work presented here has greatly increased knowledge of how black carbon in sea ice and snow will affect albedo and light penetration depths. The effect of black carbon distribution in the sea ice, sea ice and snow properties and snow cover on the response of snow and sea ice to black carbon have all been quantified. The key results from the work show that black carbon is most effective when situated at the surface of sea ice which would occur following melting of an overlying snow cover. Melting snow and sea ice is the most responsive to black carbon while multi-year sea ice and cold polar snow are least responsive. Sea ice is also more responsive than snow to black carbon. The work also shows that a thin snow cover would "mask" black carbon in sea ice. Therefore overall black carbon in sea ice would have most influence when it is situated at the surface of melting sea ice following snow melt, the time of year this occurs would coincide with times of greatest solar irradiance thus exacerbating the influence of black carbon in sea ice. During the ice melting season black carbon in sea ice may have important global climatic consequences, potentially increasing melt rates. A reduction in global black carbon concentrations could thus potentially quickly ameliorate the heightened summer sea ice melting rates observed in the Arctic today. The results presented in the thesis are of significant use to climate modellers examining the contribution of black carbon in sea ice to overall climate change and can be incorporated into global climate models to understand the influence of black carbon in sea ice on global albedo.

References

A. Angal, G. Chnader, X. Xiong, T. Choi, and A. Wu. Characterisation of the Sonoran desert as a radiometric calibration target for Earth observing sensors. *Journal of Applied Remote sensing*, 5(1), 2011.

T. Aoki and M. Fukabori. Effects of snow physical parameters on spectral albedo and bidirectional reflectance of snow surface. *Journal of Geophysical Research*, 105(D8): 10,219–10,236, 2000.

T. Aoki, A. Hachikubo, and M. Hori. Effects of snow physical parameters on shortwave broadband albedos. *Journal of Geophysical Research*, 108(D19):4916, 2003.

S. Arcone, A..Gow, and S. McGrew. Microwave dielectric, structural, and salinity properties of simulated sea ice. *Geoscience and Remote Sensing, IEEE Transactions on*, GE-24(6):832–839, 1986.

G. Arnold, S. Tsay, M. King, J. Li, V. Virginia, and P. Soulen. Airborne spectral measurements of surface–atmosphere anisotropy for arctic sea ice and tundra. *International Journal of Remote Sensing*, 23(18):3763–3781, 2002.

K. Arrigo, G. Dijken, and S. Pabi. Impact of a shrinking Arctic ice cover on marine primary production. *Geophysical Research Letters*, 35(19), 2008.

K. Arrigo, T. Mock, and M. Lizotte. *Sea ice*, chapter Primary Producers in Sea Ice, pages 283–325. Blackwell Publishing, Oxford, 2010.

A. Assur. Composition of sea ice and its tensile strength. Technical Report 44, SIPRE Researvh Report, 1960.

M. Atkinson and C. Bingman. Elemental composition of commercial seasalts. *Journal of Aquariculture and Aquatic Sciences*, 8(2):39, 1997.

C. Ball, A. Levick, E. Woolliams, P. Green, M. Dury, R. Winkler, A. Deadman, N. Fox, and M. King. Effect of polytetrafluoroethylene (PTFE) phase transition at 19 °C on the use of Spectralon as a reference standard for reflectance. *Applied Optics*, 52 (20):4806–4812, 2013.

S. Beaven, G. Lockhart, S. Gogineni, A. Hossetmostafa, K. Jezek, A. Gow, D. Perovich, A. Fung, and S. Tjuatja. Laboratory measurements of radar backscatter from bare and snow-covered saline ice sheets. *Remote Sensing Letters*, 16(5):851–876, 1995.

H. Beine, A. Amoroso, F. Domine, M. King, M. Nardino, A. Ianniello, and J. France. Surprisingly small HONO emissions from snow surfaces at Browning Pass, Antarctica. *Atmospheric Chemistry and Physics*, 6:2569–2580, 2006.

H. Beine, C. Anastasio, G. Esposito, K. Patten, E. Wilkening, F. Domine, D. Voisin, M. Barret, S. Houdier, and S. Hall. Soluble, light-absorbing species in snow at Barrow, Alaska. *Journal of Geophysical Research*, 116(D00R05), 2011.

C. Belzile, S. Johannessen, M. Gosselin, M. Demers, and W. Miller. Ultraviolet attenuation by dissolved and particulate constituents of first-year ice during late spring in an Arctic polynya. *Limnology and Oceanography*, 45(6):1265–1273, 2000.

M. Birch and R. Cary. Elemental carbon-based method for monitoring occupational exposures to particulate diesel exhaust. *Aerosol Science and Technology*, 25(3):221–241., 1996.

L. Bjorn. *Photobiology: The Science of Life and Light*. Springer, 2007.

C. Bohren. Applicability of effective-medium theories to problems of scattering and absorption by nonhomogeneous atmospheric particles. *Journal of Atmospheric Sciences*, 43(5):468–475, 1986.

T. Bond and R. Bergstrom. Light absorption by carbonaceous particles: An investigative review. *Aerosol Science and Technology*, 40(1):27–67, 2006.

T. Bond, S. Doherty, D. Fahey, P. Forster, T. Berntsen, B. DeAngelo, M. Flanner, S. Ghan, B. Kärcher, and D. Koch. Bounding the role of black carbon in the climate system: A scientific assessment. *Journal of Geophysical Research: Atmospheres*, 118(11): 5380–5552, 2013.

T. Boyer, J. Antonov, O. Baranova, C. Coleman, H. Garcia, A. Grodsky, D. Johnson, R. Locarnini, A. Mishonov, T. O'Brien, C. Paver, J. Reagan, D. Seidov, I. Smolyar, and M. Zweng. World ocean database 2013. Technical Report NOAA Atlas NESDIS 72, National Oceanic and Atmospheric Administration, 2013.

R. Brandt, S. Warren, A. Worby, and T. Grenfell. Surface albedo of the Antarctic sea ice zone. *Journal of Climate*, 18(17):3606–3622, 2005.

R. Brandt, S. Warren, and A. Clarke. A controlled snowmaking experiment relating black-carbon content to reduction of snow albedo. *Journal of Geophysical Research*, 116(D08109), 2011.

C. Brest and S. Goward. Deriving surface albedo measurements from narrow band satellite data. *International Journal of Remote Sensing*, 8(3):351–367, 1987.

A. Bricaud, H. Claustre, J. Ras, and K. Oubelkheir. Natural variability of phytoplanktonic absorption in oceanic waters: Influence of the size structure of algal populations. *Journal of Geophysical Research*, 109(C11), 2004.

I. Buist, S. Potter, T. Nedwed, and J. Mullin. Herding surfactants to contract and thicken oil spills in pack ice for in situ burning. *Cold regions science and technology*, 67(1–2):3–23, 2011.

H. Cachier and M. Pertuisot. Particulate carbon in Arctic ice. *Analusis*, 22(7):M34–M37, 1994.

J. Chow, J. Watson, L. Pritchett, W. Pierson, C. Frazier, and R. Purcell. The DRI thermal/optical reflectance carbon analysis system: Description, evaluation and applications in U.S. air quality studies. *Atmospheric Environment*, 27A(8):1185–1201, 1993.

J. Chow, J. Watson, D. Crow, D. Lowenthal, and T. Merrifield. Comparison of IMPROVE and NIOSH carbon measurements. *Aerosol Science and Technology*, 34 (1):23–34, 2001.

C. Chung, V. Ramanathan, D. Kim, and I. Podgorny. Global anthropogenic aerosol direct forcing derived from satellite and ground-based observations. *Journal of Geophysical Research*, 110(D24), 2005.

P. Chýlek, V. Ramaswamy, and V. Srivastava. Albedo of soot-contaminated snow. *Journal of Geophysical Research*, 88(C15):10837–10843, 1983.

P. Chýlek, V. Srivastava, L. Cahenzli, R. Pinnick, R. Dod, T. Novakov, T. Cook, and B. Hinds. Aerosol and graphitic carbon content of snow. *Journal of Geophysical Research*, 92(D8):9801–9809, 1987.

A. Clarke. Integrating sandwich: a new method of measurement of the light absorption coefficient for atmospheric particles. *Applied Optics*, 21(16), 1982.

A. Clarke and K. Noone. Soot in the arctic snowpack: A cause for perturbations in radiative transfer. *Atmospheric Environment (1967)*, 19(12):2045–2053, 1985.

J. Cofala, M. Amann, Z. Klimont, K. Kupiainen, and L. Hoglund-Isaksson. Scenarios of global anthropogenic emissions of air pollutants and methane until 2030,. *Atmospheric Environment*, 41(38):8486–8499, 2007.

G. Cota. Photoadaptation of high Arctic ice algae. *Nature*, 315:219–222, 1985.

G. Cota and C. Sullivan. Photoadaptation, growth and roduction of bottom ice algae in the antarctic. *Journal of Phycology*, 26, 1990.

G. Cox and W. Weeks. Equations for determining the gas and brine volumes in sea-ice samples. *Journal of Glaciology*, 29(102), 1983.

T. Dauphinee, E. Lewis, J. Ancsin, H. Klein, and J. Phillips. Background papers and supporting data on the practical salinity scale 1978: Unesco/ICES/SCOR/IAPSO Joint Panel on Oceanographic Tables and Standards. *Unesco technical papers in marine science*, 37, 1981.

R. Dickinson. *Advances in Geophysics*, volume 25, chapter Land surface processes and climate- surface albedos and energy balance. Academic Press, 1983.

G. Dieckmann and H. Hellmer. *Sea ice*, chapter The importance of sea ice: An overview, pages 1–22. Blackwell Publishing, Oxford, 2010.

T. Dittmar. The molecular level determination of black carbon in marine dissolved organic matter. *Organic Geochemistry*, 39(4):396–407, 2008.

S. Doherty, S. Warren, T. Grenfell, A. Clarke, and R. Brandt. Light-absorbing impurities in Arctic snow. *Atmospheric Chemistry and Physics*, 10(8):18807–18878, 2010.

J. Dozier, R. Davis, A. Chang, and K. Brown. The spectral bidirectional reflectance of snow. In T. Guyenne and J. Hunt, editors, *Spectral Signatures of Objects in Remote Sensing, Proceedings of the conference held 18-22 January, 1988 in Aussois (Modane), France*, page 87, 1988.

M. Dumont, O. Brissaud, G. Picard, B. Schmitt, J. Gallet, and Y. Arnaud. High-accuracy measurements of snow bidirectional reflectance distribution function at visible and nir wavelengths-comparison with modelling results. *Atmospheric Chemistry and Physics*, 10(5):2507–2520, 2010.

H Eicken. *Sea ice-an introduction to its physics, biology, chemistry and geology*, chapter From the microscopic, to the macroscopic, to the regional scale: growth, microstructure and properties of sea ice. Blackwell Science, London, 2003.

H. Eicken, J. Weissenberger, I. Bussmann, J. Freitag, W. Schuster, F. V. Delgado, K. Evers, P. Jochmann, C. Krembs, R. Gradinger, F. Lindemann, F. Cottier, R. Hall, P. Wadhams, M. Reisemann, H. Kuosa, J. Ikävalko, G. Leonard, H. Shen, S. Ackley, and L. Smedsrud. *Ice in surface waters*, chapter Ice-tank studies of physical and biological sea-ice processes. Baikema, Rotterdam, 1998.

H. Eicken, J. Kolatschek, J. Freitag, F. Lindemann, I. Dmitrenko, and H. Kassens. Key source area and constraints on entrainment for basin-scale sediment transport by Arctic sea ice. *Geophysical Research*, 27(13):1919–1922, 2000.

H. Eicken, R. Gradinger, A. Gaylord, A. Mahoneya, I. Rigord, and H. Melling. Sediment transport by sea ice in the Chukchi and Beaufort Seas: Increasing importance due to changing ice conditions? *Deep-Sea Research Part II*, pages 3281–3302, 2005.

H. Eicken, R. Gradinger, M. Salganek, K. Shirasawa, D. Perovich, and M. Leppäranta, editors. *Field techniques for sea ice research*. University of Alaska Theatre Dept, Fairbanks, Alaska, 2010.

C. Fierz, R.L. Armstrong, Y. Durand, P. Etchevers, E. Greene, D. McClung, K. Nishimura, P. Satyawali, and S. Sokratov. *The International Classification of Seasonal Snow on the Ground*. ICSI-UCCS-IACS Working Group on Snow Classification, 2009.

F. Fisher, M. King, and J. Lee-Taylor. Extinction of UV-visible radiation in wet midlatitude (maritime) snow: Implications for increased NO_x emission. *Journal of Geophysical Research*, 110(D21301), 2005.

M. Flanner, C. Zender, J. Randerson, and P. Rasch. Present-day climate forcing and response from black carbon in snow. *Journal of Geophysical Research*, 112(D11202), 2007.

M. Flanner, C. Zender, P. Hess, N. Mahowald, T. Painter, V. Ramanathan, and P. Rasch. Springtime warming and reduced snow cover from carbonaceous particles. *Atmospheric Chemistry and Physics*, 9(7):2481–2497, 2009.

S. Forsström, J. Ström, C. Pedersen, E. Isakson, and S. Gerland. Elemental carbon distribution in Svalbard snow. *Journal of Geophysical Research*, 114(D19,16), 2009.

J. France. *Chemical Oxidation in Snowpacks*. PhD thesis, Royal Holloway, University of London, 2008.

J. France, M. King, and J. Lee-Taylor. Hydroxyl (OH) radical production rates in snowpacks from photolysis of hydrogen peroxide (H_2O_2) and nitrate (NO_3^-). *Atmospheric Environment*, 41:5502–5509, 2007.

J. France, M. King, and J. Lee-Taylor. The importance of considering depth-resolved photochemistry in snow: a radiative-transfer study of NO_2 and OH production in Ny-Alesund (Svalbard). *Journal of Glaciology*, 56(198):655–663, 2010a.

J. France, M. King, and A. MacArthur. A photohabitable zone in the martian snowpack? A laboratory and radiative-transfer study of dusty water-ice snow. *Icarus*, 207:133–139, 2010b.

J. France, M. King, M. Frey, J. Erbland, G. Picard, S. Preunkert, A. MacArthur, and J. Savarino. Snow optical properties at Dome C (Concordia), Antarctica; implications for snow emissions and snow chemistry of reactive nitrogen. *Atmospheric Chemistry and Physics*, 11(18):9787–9801, 2011.

J. France, H. Reay, M. King, D. Voison, H. Jacobi, F. Domine, H. Beine, C. Anastasio, A. MacArthur, and J. Lee-Taylor. Hydroxyl Radical and NO_x producion rates, black carbon concentrations and light-absorbing impurities in the snow from field

measurements of light penetration and nadir reflectivity of on-shore and off-shore coastal Alaskan snow. *Journal of Geophysical Research*, 117(21), 2012.

K. Fung. Particulate carbon speciation by MnO_2 oxidation. *Aerosol Science and Technology*, 12:122–127, 1990.

N. Galin, A. Worby, T. Markus, C. Leuschen, and P. Gogineni. Validation of Airborne FMCW Radar Measurements of Snow Thickness Over Sea Ice in Antarctica. *IEE Transactions on Geoscience and Remote Sensing*, 50(1):3–12, 2012.

S. Gerland, J. Winther, J. Ørbæk, G. Liston, N. Øritsland, A. Blanco, and B. Ivanov. Physical and optical properties of snow covering Arctic tundra on Svalbard. *Hydrological Processes*, 13(14–15):2331–2343, 1999.

M. Giani, F. Rampazzo, and D. Berto. Humic acids contribution to sedimentary organic matter on a shallow continental shelf (northern Adriatic Sea). *Estuarine, Coastal and Shelf Science*, 90:103–110, 2010.

N. Goldenson, S. Doherty, C. Bitz, and M. Holland. Arctic climate response to forcing from light-absorbing particles in snow and sea ice in CESM. *Atmospheric Chemistry and Physics*, 12(17):7903–7920, 2012.

E. Graber and Y. Rudich. Atmospheric HULIS: How humic-like are they? A comprehensive and critical review. *Atmospheric Chemistry and Physics*, 6:729–753, 2006.

A. Grannas, A. Jones, J. Dibb, M. Ammann, C. Anastasio, H. Beine, M. Bergin, J. Bottenheim, C. Boxe, and G. Carver. An overview of snow photochemistry: evidence, mechanisms and impacts. *Atmospheric chemistry and physics*, 7(16): 4329–4373, 2007.

T. Grenfell and G. Maykut. The optical properties of ice and snow in the Arctic Basin. *Journal of Glaciology*, 18(80), 1977.

T. Grenfell, S. Warren, and P. Mullen. Reflection of solar radiation by the Antarctic snow surface at ultraviolet, visible, and near-infrared wavelengths. *Journal of Geophysical Research: Atmospheres*, 99(D9):18669–18684, 1994.

T. Grenfell, B. Light, and M. Sturm. Spatial distribution and radiative effects of soot in the snow and sea ice during the SHEBA experiment: The surface heat budget of Arctic ocen (SHEBA). *Journal of Geophysical Research*, 107(C10), 2002.

T. Grenfell, S. Neshyba, and S. Warren. Representation of a non-spherical ice particle by a collection of independent spheres for scattering and absorption of radiation: 3. Hollow columns and plates. *Journal of Geophysical Research*, 110(D17), 2005.

T. Grenfell, S. Doherty, A. Clarke, and S. Warren. Light absorption from particulate impurities in snow and ice determined by spectrophotometric analysis of filters. *Applied Optics*, 50(14):2037–2048, 2011.

S. Grossmann and M. Gleitz. Microbial responses to experimental sea-ice formation: implications for the establishment of Antarctic sea-ice communities. *Journal of Experimental Marine Biology and Ecology*, 173:273–289, 1993.

C. Haas, F. Cottier, L. Smedsrud, and D. Thomas. Multidisciplinary ice tank study shedding new light on sea ice growth processes. *EOS, Transactions*, 80(43):507–513, 1999.

O. Hadley and T. Kirchstetter. Black carbon reduction of snow albedo. *Nature Climate Change*, 2:437–440, 2012.

O. Hadley, C. Corrigan, T. Kirchstetter, S. Cliff, and V. Ramanathan. Measured black carbon deposition on the Sierra Nevada snow pack and implication for snow pack retreat. *Atmospheric Chemistry and Physics*, 10(15):7505–7513, 2010.

G. Hagler, M. Bergin, E. Smith, and J. Dibb. A summer time series of particulate carbon in the air and snow at Summit, Greenland. *Journal of Geophysical Research*, 112(D21):D21309, 2007a.

G. Hagler, M. Bergin, E. Smith, J. Dibb, C. Anderson, and E. Steig. Particulate and water-soluble carbon measured in recent snow at Summit, Greenland. *Geophysical Research Letters*, 34(16):L16505, 2007b.

J. Hansen and L. Nazarenko. Soot climate forcing via snow and ice albedos. *Proceedings of the National Academy of Sciences of the United States of America*, 101 (2):423, 2004.

J. Hansen, M. Sato, and R. Ruedy. Radiative forcing and climate response. *Journal of Geophysical Research*, 102(D6):6831– 6864, 1997.

J. Hansen, M. Sato, R. Ruedy, L. Nazarenko, A. Lacis, G. A. Schmidt, G. Russell, I. Aleinov, M. Bauer, S. Bauer, N. Bell, B. Cairns, V. Canuto, M. Chandler, Y. Cheng, A. Del Genio, G. Faluvegi, E. Fleming, A. Friend, T. Hall, C. Jackman, M. Kelley, D. Koch N. Kian and, J. Lean, J. Lerner, K. Lo, S. Menon, R. Miller, P. Minnis, T. Novakov, V. Oinas, J. Perlwitz, J. Perlwitz, D. Rind, A. Romanou, D. Shindell, P. Stone, S. Sun, N. Tausnev, D. Thresher, B. Wielicki, T. Wong, M. Yao, and S. Zhang. Efficacy of climate forcings. *Journal of Geophysical Research*, 110(D18), 2005.

J. Hansen, J. Sato, P. Kharecha, G. Russell, D. Lea, and M. Siddall. Climate change and trace gases. *Philosophical Transactions: Mathematical, Physical and Engineering Sciences*, 365(1856):1952–1954, 2007.

A. Hare, F. Wang, D. Barber, N. Geilfus, and R. Galley. pH evolution in sea ice grown at an outdoor experimental facility. *Marine Chemistry*, 154:46–54, 2013.

J. Haywood and V Ramaswamy. Global sensitivity studies of the direct radiative forcing due to anthropogenic sulfate and black carbon aerosols. *Journal of Geophysical Research*, 103(D6):6043–6058, 1998.

M. Haywood and M. Shine. The effect of anthropogenic sulfate and soot aerosol on the clear sky planetary radiation budget,. *Geophysical Research Letters*, 22(5): 603–606, 1995.

J. Hedges and R. Keil. Sedimentary organic matter preservation: an assessment and speculative synthesis. *Marine chemistry*, 49(2–3):81–115, 1995.

J. Hedges, R. Keil, and R. Benner. What happens to terrestrial organic matter in the ocean? *Organic Geochemistry*, 27(5–6):195–212, 1997.

E. Highwood and R. Kinnersley. When smoke gets in our eyes: The multiple impacts of atmospheric black carbon on climate, air quality and health. *Environment international*, 32(4):560–566, 2006.

A. Hoffer, A. Gelencsér, P. Guyon, G. Kiss, O. Schmid, G. Frank, P. Artaxo, and M. Andreae. Optical properties of humic-like substances (HULIS) in biomass-burning aerosols. *Atmospheric Chemistry and Physics*, 6(11):3563–3570, 2006.

M. Holland, D. Bailey, B. Breigleb, B. Light, and E. Hunke. Improved sea ice short wave radiation physics in CCSM4: The impact of melt ponds and aerosols on Arctic sea ice. *Journal of Climate*, 25:1413–1430, 2012.

R. Hubley. Measurements of diurnal variations in snow albedo on Lemon Creek Glacier, Alaska. *Journal of Glaciology*, 2(18):560–563, 1955.

S. Hudson, S. Warren, R. Brandt, T. Grenfell, and D. Six. Spectral bidirectional reflectance of Antarctic snow: Measurements and parameterization. *Journal of Geophysical Research*, 111(D18):106, 2006.

IPCC. IPCC Working Group 1 Fifth Assessment Report Summary for Policy Makers - Climate Change 2013: The Physical Science Basis. Technical report, IPCC, 2013.

D. Isleifson, R. Galley, D. Barber, J. Landy, A. Komarov, and L. Shafai. A study on the C-band polarimetric scattering and physical characteristics of frost flowers on experimental sea ice. *Geoscience and Remote Sensing, IEEE Transactions on*, PP(99), 2012.

R. Jackson, T. Clarke, and M. Moran. Bidirectional calibration results for 11 spectralon and 16 $BaSO_4$ reference reflectance panels. *Remote Sensing of Environment*, 40(3): 231–239, 1992.

M. Jacobson. Strong radiative heating due to the mixing state of black carbon in atmospheric aerosols. *Nature*, 409(6821):695–697, 2001.

M. Jacobson. Climate response of fossil fuel and biofuel soot, accounting for soot's feedback to snow and sea ice albedo and emissivity. *Journal of Geophysical Research*, 109(D21201), 2004.

M. Jacobson, W. Colella, and D. Golden. Cleaning the air and improving health with hydrogen fuel-cell vehicles. *Science*, 308(5730):1901–1905, 2005.

M. Jeffries, H. Krouse, B. Hurst-Cushing, and T. Maksym. Snow-ice accretion and snow-cover depletion on Antarctic first-year sea ice floes. *Annals of Glaciology*, pages 51–60, 2001.

T. Jenk, S. Szidat, M. Schwikowski, H. Gaggeler, S. Brutsch, L. Wacher, H. Synal, and M. Saurer. Radiocarbon analysis in an Alpine ice core: record of anthropogenic and

biogenic contributions to carbonaceous aerosols in the past. *Atmospheric Chemistry and Physics*, 6:5381–5390, 2006.

M. Johnston and G. Timco. Temperature Changes in First Year Arctic Sea Ice During the Decay Process. In *Proceedings of the 16th IAHR International Symposium on Ice*, volume 2, pages 194–202, 2002.

J. Joseph, W. Wiscombe, and J. Weinman. The delta-eddington approximation for radiative flux transfer. *Journal of the Atmospheric Sciences*, 33(12):2452–2459, 1976.

P. Kanagaratnam, T. Markus, V. Lytle, B. Heavey, P. Jansen, G. Prescott, and S. Gogineni. Ultrawideband radar measurements of thickness of snow over sea ice. *IEE Transactions on Geoscience and Remote Sensing*, 45(9):2715–2724, 2007. doi: 10.1109/TGRS.2007.900673.

L. Keller, Weidner G., Stearns C., Whittaker M., and Holmes R. Antarctic automatic weather station data for the calendar year 1998. Madison, WI, University of Wisconsin-Madison, Space Science and Engineering Center, 2002. Call Number: UW SSEC Publication No.02.07.K1., 2002.

D. Kimes and J. Kirchner. Irradiance measurement errors due to the assumption of a lambertian reference panel. *Remote Sensing of Environment*, 12:141–149, 1982.

M. King and W. Simpson. Extinction of UV radiation in Arctic snow at Alert, Canada (82°N). *Journal of Geophysical Research*, 106(D12):12499, 2001.

M. King, J. France, F. Fisher, and H. Beine. Measurement and modelling of UV radiation penetration and photolysis rates of nitrate and hydrogen peroxide in Antarctic sea ice: An estimate of the production rate of hydroxyl radicals in first-year sea ice. *Journal of Photochemistry and Photobiology A: Chemistry*, 176:39–49, 2005.

S. Kinne. An aerocom initial assessment—optical properties in aerosol component modules of global models. *Atmospheric Chemistry and Physics*, 6:1815–1834, 2006.

J. Kirk. *Light and Photosynthesis in Aquatic Ecosystems*. Cambridge University Press, Cambridge, United Kingdom and New York, NY, USA, 2000.

D. Koch and A. Del Genio. Black carbon semi-direct effects on cloud cover: Review and synthesis. *Atmospheric Chemistry and Physics*, 10(16):7685–7696, 2010.

D. Koch, M. Schulz, S. Kinne, C. McNaughton, J. Spackman, Y. Balkanski, S. Bauer, T. Berntsen, T. Bond, O. Boucher, M. Chin, A. Clarke, N. De Luca, F. Dentener, T. Diehl, O. Dubovik, R. Easter, D. Fahey, J. Feichter, D. Fillmore, S. Freitag, S. Ghan, P. Ginoux, S. Gong, L. Horowitz, T. Iversen, A. Kirkevaring, Z. Klimont, Y. Kondo, M. Krol, X. Liu, R. Miller, V. Montanaro, N. Moteki, G. Myhre, J. Penner, J. Perlwitz, G. Pitari, S. Reddy, L. Sahu, H. Sakamoto, G. Schuster, J. P. Schwarz, Ø. Seland, P. Stier, N. Takegawa, T. Takemura, C. Textor, J. Van Aardenne, and Y. Zhao. Evaluation of black carbon estimations in global aerosol models. *Atmospheric Chemistry and Physics*, 9(22):9001–9026, 2009. doi: 10.5194/acp-9-9001-2009.

A. Kokhanovsky and E. Zege. Scattering optics of snow. *Applied Optics*, 43(7):1589–1602, 2004.

C. Krembs, T. Mock, and R. Gradinger. A mesocosm study of physical-biological interactions in artificial sea ice: effects of brine channel surface evolution and brine movement on algal biomass. *Polar Biology*, 24(5):356–364, 2001.

J. Kristjansson. Studies of the aerosol indirect effect from sulfate and black carbon aerosols. *Journal of Geophysical Research*, 107(D15), 2002.

Z. Krivácsy, G. Kiss, D. Ceburnis, G Jennings, W. Maenhaut, I. Salma, and D. Shooter. Study of water-soluble atmospheric humic matter in urban and marine environments. *Atmospheric Research*, 87(1):1–12, 2008.

M. Kuhn. Bidirectional reflectance of polar and alpine snow surfaces. *Annals of Glaciology*, 6:164–167, 1985.

R. Kwok and G. Cunningham. ICESat over Arctic sea ice: Estimation of snow depth and ice thickness. *Journal of Geophysical Research: Oceanss*, 113(C8):C08010, 2008.

R. Kwok, B. Panzer, C. Leuschen, S. Pang, T. Markus, B. Holt, and S. Gogineni. Airborne surveys of snow depth over arctic sea ice. *Journal of Geophysical Research: Oceans*, 116:C11018, 2011.

B. Larssen, B. Elverhoi, and P. Aagaard. Study of particulate material in sea ice in the Fram Strait- A contribution to paleoclimatic research. *Polar Research*, pages 313–315, 1987.

V. Lavanchy, H. Gäggeler, U. Schotterer, M. Schwikowski, and U. Baltensperger. Historical record of carbonaceous particle concentrations from a European high-alpine glacier (Colle Gnifetti, Switzerland). *Journal of Geophysical Research*, 104 (D17):21227–21236, 1999.

K. Law and A. Stohl. Arctic air pollution: Origins and impacts. *Science*, 2007.

T. Ledley and S. Thompson. Potential effect of nuclear war smokefall on sea ice. *Climatic Change*, 8:155–171, 1986.

J. Lee-Taylor and S. Madronich. Calculation of actinic fluxes with a coupled atmosphere-snow radiative transfer model. *Journal of Geophysical Research*, 107 (D24), 2002.

M. Legrand and H. Puxbaum. Summary of the CARBOSOL project: Present and retrospective state of organic versus inorganic aerosol over Europe. *Journal of Geophysical Research: Atmospheres (1984–2012)*, 112(D23), 2007.

C. Leroux, J. Lenoble, G. Brogniez, J. Hovenier, and J. De Haan. A model for the bidirectional polarized reflectance of snow. *Journal of Quantitative Spectroscopy and Radiative Transfer*, 61(3):273–285, 1999.

S. Li and X. Zhou. Modelling and measuring the spectral bidirectional reflectance factor of snow-covered sea ice: an intercomparison study. *Hydrol Process*, 18(18): 3559–3581, 2004.

B. Light, H. Eicken, G. Maykut, and T. Grenfell. The effect of included particulates on the spectral albedo of sea ice. *Journal of Geophysical Research*, 103(C12):27739–27752, 1998.

B. Light, T. Grenfell, and D. Perovich. Transmission and absorption of solar radiation by Arctic sea ice during the melt season. *Journal of Geophysical Research*, 113: C03023, 2008.

B. Light, R. Brandt, and S. Warren. Hydrohalite in cold sea ice: Laboratory observations of single crystals, surface accumulations, and migration rates under a

temperature gradient, with application to “snowball earth”. *Journal of Geophysical Research*, 114(C07):018, 2009.

M. Lizotte. The contributions of sea ice algae to Antarctic marine primary production. *Integrative and Comparative Biology*, 41:57–73, 2001.

C. MacLellan and T. Malthus. High performance dual field of view spectroradiometer with novel input optics for autonomous reflectance measurements over an extended spectral range. In *International Geoscience and Remote Sensing Symposium*, 2009.

S. Madronich and S. Flocke. *Hanbook of Environmental Chemistry*, chapter The role of solar radiation in atmospheric chemistry. Springer-Verlag, New York, 1998.

F. Malgrem, G. Institutt, S. Forskningsfond, and N. Fond. *The Norwegian Polar Expedition ‘Maud,’ 1918–1925:Scientific Results*, volume 1, chapter On the properties of sea-ice, pages 1–67. Gofys. Inst., Bergen, Norway, 1927.

O. Mangoni, G. Carrada, M. Modigh, G. Catalano, and V. Saggiiomo. Photoacclimation in Antarctic bottom ice algae: an experimental approach. *Polar Biology*, 32(325–335), 2009.

A. Marks and M. King. The effects of additional black carbon on the albedo of Arctic sea ice: variation with sea ice type and snow cover. *The Cryosphere*, 7:1193–1204, 2013.

C. Masiello. Black carbon in deep-sea sediments. *Science*, 280(5371):1911–1913, 1998.

R. Massom, H. Eicken, C. Hass, M. Jeffries, M. Drinkwater, M. Sturm, A. Worby, X. Wu, V. Lytle, S S. Ushio, K. Morris, P. Reid, S. Warren, and I. Allison. Snow on Antarctic sea ice. *Reviews of Geophysics*, pages 413–445, 2001.

J. McConnell and R. Edwards. Coal burning leaves toxic heavy metal legacy in the Arctic. *Proceedings of the National Academy of Sciences of the United States of America*, 105(34):12140–12144, 2008.

J. McConnell, R. Edwards, G. Kok, M. Flanner, C. Zender, E. Saltzman, J. Banta, D. Pasteris, M. Carter, and J. Kahl. 20th-century industrial black carbon emissions altered Arctic climate forcing. *Science*, 317(5843):1381, 2007.

A. McMinn and K. Ryan. Diurnal changes in photosynthesis of Antarctic fast ice algal communities determined by pulse amplitude modulation fluorometry. *Marine Biology*, 143:359–367, 2003.

A. McMinn, C. Ashworth, and K. Ryan. In situ net primary productivity of an Antarctic fast ice bottom algal community. *Aquatic Microbial Ecology*, 21:177–185, 2000.

A. Medalia and F. Heckman. Morphology of aggregates—ii. size and shape factors of carbon black aggregates from electron microscopy,. *Carbon*, 7:569–582, 1969.

A. Meij, A. Pozzer, and J. Lelieveld. Trend analysis in aerosol optical depths and pollutant emission estimates between 2000 and 2009. *Atmospheric Environment*, 51:75–85, 2012. doi: 10.1016/j.atmosenv.2012.01.059.

J. Middelburg, J. Nieuwenhuize, and P Breugel. Black carbon in marine sediments. *Marine Chemistry*, 65(3–4):245–252, 1999.

W. Middleton and A. Mungal. The luminous directional reflectance of snow. *Journal of the Optic Society of America*, 42(8), 1952.

J. Ming, H. Cachier, C. Xiao, D. Qin, S. Kang, S. Hou, and J. Xu. Black carbon record based on a shallow Himalayan ice core and its climatic implications. *Atmospheric Chemistry and Physics*, 8:1343–1352, 2008.

J. Ming, C. Xiao, H. Cachier, D. Qin, X. Qin, Z. Li, and J. Pu. Black Carbon (BC) in the snow of glaciers in west China and its potential effects on albedos. *Atmospheric Research*, 92(1):114–123, 2009.

C. Mobley, G. Cota, T. Grenfell, R. Maffione, W. Pegau, and D. Perovich. Modeling light propagation in sea ice. *Geoscience and Remote Sensing, IEEE Transactions on*, 36(5):1743–1749, 1998.

T. Mock and D. Thomas. Recent advances in sea-ice microbiology. *Environmental Microbiology*, 7(5):605–619, 2005.

T. Mock, G. Dieckmann, C. Haas, A. Krell, J. Tison, A. Belem, S. Papadimitriou, and D. Thomas. Micro-optodes in sea ice: a new approach to investigate oxygen dynamics during sea ice formation. *Aquatic Microbial Ecology*, 29:297–306, 2002.

C. Mundy, D. Barber, and C. Michel. Variability of snow and ice thermal, physical and optical properties pertinent to sea ice algae biomass during spring. *Journal of Marine Systems*, 58(3-4):107–120, 2005. doi: 10.1016/j.jmarsys.2005.07.003.

M. Nakawo and N. Sinha. Growth rate and salinity profile of first-year sea ice in the high Arctic. *Journal of Glaciology*, 27(96), 1981.

F. Nicodemus, J. Richmond, J. Hsia, I. Ginsberg, and T. Limperis. Geometrical considerations and nomenclature for reflectance. *U.S. Department of commerce, National Bureau of Standards*, 1977.

D. Nomurai, H. Yoshikawa-Inoue, and T. Toyota. The effect of sea-ice growth on air–sea CO_2 flux in a tank experiment. *Tellus B*, 58(5), 2006.

D. Nurnberg, I. Wollenburg, D. Dethleff, H. Eicken, H. Kassens, T. Letzig, E. Reimnitz, and J. Thiede. Sediments in Arctic sea ice-implications for entrainment, transport and release. *Marine Geology*, 119:185–214, 1994.

T. Painter and J. Dozier. The effect of anisotropic reflectance on imaging spectroscopy of snow properties. *Remote Sensing of Environment*, 89(4):409–422, 2004. doi: 10.1016/j.rse.2003.09.007.

T. Painter, A. Bryant, and M. Skiles. Radiative forcing by light absorbing impurities in snow from modis surface reflectance data. *Geophysical Research Letters*, 39(L1), 2012.

S. Papadimitriou, H. Kennedy, G. Kattner, G. Dieckmann, and D. Thomas. Experimental evidence for carbonate precipitation and CO_2 degassing during sea ice formation. *Geochemica et Cosmochimica Acta*, 68(8):1749–1761, 2003.

R. Payne. Albedo of the sea surface. *Journal of Atmospheric Sciences*, 29(5), 1972.

H. Pegrum, N. Fox, M. Chapman, and E. Milton. Design and testing a new instrument to measure the angular reflectance of terrestrial surfaces. In *IEEE International Conference on Geoscience and Remote Sensing Symposium, 2006. IGARSS 2006.*, pages 1119–1122, 2006.

J. Peltoniemi, S. Kaasalainen, J. Naranen, L. Matikainen, and J. Piironen. Measurement of directional and spectral signatures of light reflectance by snow.

IEE Transactions on Geoscience and Remote Sensing, 43(10):2294–2304, 2005. doi: 10.1109/TGRS.2005.855131.

D. Perovich. Theoretical estimates of light reflection and transmission by spatially complex and temporally varying sea ice covers. *Journal of Geophysical Research*, 95 (C6):9557–9567, 1990.

D. Perovich. The optical properties of sea ice. *US Army Corps of Engineers: Cold Regions Research and Engineering Laboratory*, 96(1), 1996.

D. Perovich. Observations of the polarization of light reflected from sea ice. *Journal of Geophysical Research*, 103(C3):5563–5575, 1998a.

D. Perovich. Complex yet translucent: the optical properties of sea ice. *Physica B: Condensed Matter*, 338(1-4):107–114, 2003a.

D. Perovich. The interaction of ultraviolet light with Arctic sea ice during SHEBA. *Annals of Glaciology*, 44(1):47–52, 2006.

D. Perovich and T. Grenfell. Laboratory studies of the optical properties of young sea ice. *Journal of Glaciology*, 27(96), 1981.

D. Perovich, C. Roesler, and W. Pegau. Variability in Arctic sea ice optical properties. *Journal of Geophysical Research*, 103(C1):1193–1208, 1998b.

D. Perovich, T. Grenfell, B. Light, and P. Hobbs. Seasonal evolution of the albedo of multiyear Arctic sea ice. *Journal of Geophysical Research*, 107(C10):8044, 2002.

J. Petit, J. Jouzel, M. Pourchet, and L. Merlivat. A detailed study of snow accumulation and stable isotope content in Dome C (Antarctica). *Journal of Geophysical Research*, 87(C6):4301–4308, 1982.

G. Petty. *A First Course in Atmospheric Radiation*. Sundog Publishing, Madison, Wisconsin, 2006.

S. Pfirman, I. Wollenburg, J. Theide, and M. Lange. *Paleoclimatology and paleometeorology: modern and past patterns of global atmospheric transport*, chapter Lithogenic sediment on Arctic pack ice: potential aeolian flux and contribution to deep sea sediments, pages 463–493. Kluwer Academic Publishers, Dordrecht, 1989.

G. Phillips and W. Simpson. Verification of snowpack radiation transfer models using actinometry. *Journal of Geophysical Research*, 110(D08306), 2005.

R. Polach, S. Ehlers, and P. Kujala. Model-Scale Ice-Part A: Experiments. *Cold regions science and technology*, 94:74–81, 2013.

B. Rabus and K. Echelmeyer. Increase of 10 m ice temperature: climate warming or glacier thinning? *Journal of Glaciology*, 48(161), 2002.

V. Ramanathan and G. Carmichael. Global and regional climate changes due to black carbon. *Nature Geoscience*, 1:221–227, 2008.

V. Ramanathan, P. Crutzen, J. Lelieveld, A. Mitra, D. Althausen, J. Anderson, M. Andreae, W. Cantrell, G. Cass, C. Chung A. Clarke, J. Coakley, W. Collins W. Conant, F. Dulac, J. Heintzenberg, A. Heymsfield, B. Holben, S. Howell, J. Hudson, A. Jayaraman, J. Kiehl, T. Krishnamurti, D. Lubin, McFarquhar, T. Novakov, J. Ogren, I. Podgorny, K. Prather, K. Priestley, J. Prospero, P. Quinn, K. Rajeev, P. Rasch, S. Rupert, R. Sadourny, S. Satheesh, G. Shaw, P. Sheridan, and F. Valero. Indian Ocean Experiment: An integrated analysis of the climate forcing and effects of the great Indo-Asian haze. *Journal of Geophysical Research*, 106(D22):28371–28398, 2001b.

J. Rand and M. Mellor. Ice-coring augers for shallow depth sampling. Technical Report 85-21, CRREL, Washington, 1985.

J. Raven, J. Kübler, and J. Beardall. Put out the light, and then put out the light. *Journal of the Marine Biological Association of the UK*, 80(01):1–25, 2000.

H. Reay, J. France, and M. King. Decreased albedo, efolding depth and photolytic OH radical and NO_2 production with increasing black carbon content in Arctic snow. *Journal of Geophysical Research*, 117(11), 2012.

C. Reinsch. Smoothing by spline functions. *Numerische Mathematic*, 10:177–183, 1967.

F. Rémy, P. Shaeffer, and B. Legrésy. Ice flow physical processes derived from the ERS-1 high-resolution map of the Antarctica and Greenland ice sheets. *Geophysical Journal International*, 139(3):645–656, 1999.

H. Rhode, C. Persson, and O. Akesson. An investigation into regional transport of soot and sulphate aerosols. *Atmospheric Environment*, 6:675–693, 1972.

D. Roesler and F. Faxvog. Optical properties of agglomerated acetylene smoke particles at 0.5145 μm and 10.6 μm wavelengths. *Journal of the Optic Society of America*, 1980.

K. Rypdal, N. Rive, T. Berntsen, Z. Klimont, T. Mideksa, G. Myhre, and R Skeie. Costs and global impacts of black carbon abatement strategies. *Tellus B*, 61(4):625–641, 2009.

B. Saenz. *Spatial and temporal dynamics of primary production in Antarctic sea ice*. PhD thesis, Stanford University, California, USA, 2011.

S. Sandmeier. Acquisition of bidirectional reflectance factor data with field goniometers. *Remote Sensing of Environment*, 73(3):257–269, 2000.

S. Sandmeier, C. Müller, B. Hosgood, and G. Andreoli. Sensitivity Analysis and Quality Assessment of Laboratory BRDF Data. *Remote Sensing of Environment*, 64(2):176–191, 1998.

A. Sayer, G. Thomas, and R. Grainger. A sea surface reflectance model for (A)ATSR and application to aerosol retrievals. *Atmospheric Measurement Techniques*, 3:813–838, 2010.

G. Schaepman-Strub, M. Schaepman, T. Painter, S. Dangel, and J. Martonchik. Reflectance quantities in optical remote sensing–definitions and case studies. *Remote Sensing of Environment*, 103(1):27–42, 2006.

M. Schulz, C. Textor, S. Kinne, Y. Balkanski, S. Bauer, T. Berntsen, T. Berglen, O. Boucher, F. Dentener, S. Guibert, I. Isaksen, T. Iversen, D. Koch, A. Kirkevag, X. Liu, V. Montanaro, G. Myhre, J. Penner, G. Pitari, S. Reddy, O. Seland, P. Stier, and T. Takemura. Radiative forcing by aerosols as derived from the aerocom present-day and pre-industrial simulations. *Atmospheric Chemistry and Physics*, 6:5225–5246, 2006.

J. Schwarz, R. Gao, D. Fahey, D. Thomson, L. Watts, J. Wilson, J. Reeves, M. Darbeheshti, D. Baumgardner, G. Kok, S. Chung, M. Schulz, J. Hendricks, A. Lauer, B. Kärcher, J. Slowik, K. Rosenlof, T. Thompson, A. Langford,

M. Loewenstein, and K. Aikin. Single-particle measurements of midlatitude black carbon and light-scattering aerosols from the boundary layer to the lower stratosphere. *Journal of Geophysical Research: Atmospheres*, 111(D16), 2006.

H. Shen, S. Ackley, and Y. Yuan. Limiting diameter of pancake ice. *Journal of Geophysical Research: Oceans*, 109(C12), 2004.

D. Six, M. Fily, S. Alvain, P. Henry, and J. Benoist. Surface characterisation of the Dome Concordia area (Antarctica) as a potential satellite calibration site, using Spot 4/Vegetation instrument. *Remote Sensing of Environment*, 89(1):83–94, 2004.

R. Skeie, T. Berntsen, G. Myhre, C. Pedersen, J. Ström J, S. Gerland, and J. Ogren. Black carbon in the atmosphere and snow, from pre-industrial times until present. *Atmospheric Chemistry and Physics*, 11(14):6809–6836, 2011.

S. Solomon, D. Qin, M. Manning, Z. Chen, M. Marquis, K. Averyt, M. Tignor, and H. Miller. *IPCC, 2007: Climate Change 2007: The Physical Science Basis. Contribution of Working Group I to the Fourth Assessment, Report of the Intergovernmental Panel on Climate Change*. Cambridge University Press, Cambridge, United Kingdom and New York, NY, USA, 2007.

K. Stamnes, S. Tsay, K. Jayaweera, and W. Wiscombe. Numerically stable algorithm for discrete-ordinate-method radiative transfer in multiple scattering and emitting layered media. *Applied Optics*, 27(12):2502–2509, 1988.

D. Streets. Dissecting future aerosol emissions: Warming tendencies and mitigation opportunities. *Climatic Change*, 81(3–4):313–330, 2007.

D. Suman, T. Kuhlbusch, and B. Lim. *Sediment Records of Biomass Burning and Global Change*, pages 271–293. Springer-Verlag, Berlin, 1997.

C. Swift, K. Germain, K. Jezek, S.Gogineni, A. Gow, D. Perovich, T. Grenfell, and R. Onsott. Laboratory investigations of the electromagnetic properties of artificial sea ice. *Microwave Remote Sensing of Sea Ice*, 1992.

P. Teilleta, G. Fedosejevsa, R. Gauthiera, N. O'Neillb, K. Thomec, S. Biggarc, H. Ripleyd, and A. Meygrete. A generalized approach to the vicarious calibration of multiple earth observation sensors using hyperspectral data. *Remote Sensing of Environment*, 77(3), 2001.

F. Thevenon, F. Anselmetti, S. Bernasconi, and M. Schwikowskit. Mineral dust and elemental black carbon records from an Alpine ice core (Colle Gnifetti glacier) over the last millennium. *Journal of Geophysical Research: Atmospheres (1984–2012)*, 114(D17), 2009.

D. Thomas and G. Dieckmann. Antarctic sea ice–a habitat for extremophiles. *Science*, 295:641–644, 2002.

G. Timco and R. Frederking. A review of sea ice density. *Cold regions science and technology*, 24(1):1–6, 1996.

J Tison, C Haas, M Gowing, S. Sleewaegen, and A. Bernard. Tank study of physico-chemical controls on gas content and composition during growth of young sea ice. *Journal of Glaciology*, 48(161), 2002.

S. Twomey. Pollution and the planetary albedo. *Atmospheric Environment*, 8(12): 1251–1256, 1974.

D. Voisin, J. Jaffrezo, S. Houdier, M. Barret, J. Cozic, M. King, J. France, H. Reay, A. Grannas, G. Kos, P. Ariya, H. Beine, and F. Domine. Carbonaceous species and humic like substances (HULIS) in Arctic snowpack during OASIS field campaign in Barrow. *Journal of Geophysical Research*, 117(D00R19), 2012.

K. Voss, A. Morel, and D. Antoine. Detailed validation of the bidirectional effect in various case 1 waters for application to ocean color imagery. *Biogeosciences*, 4: 781–789, 2007.

Q. Wang, D. Jacob, J. Fisher, J. Mao, E. Leibensperger, C. Carouge, P. Sager, Y. Kondo, J. Jimenez, and M. Cubison. Sources of carbonaceous aerosols and deposited black carbon in the Arctic in winter-spring: implications for radiative forcing. *Atmospheric Chemistry and Physics*, 11(23):12453–12473, 2011.

S. Warren. Optical properties of snow. *Reviews of geophysics and space physics*, 20(1): 67–89, 1982.

S. Warren. Optical constants of ice from the ultraviolet to the microwave. *Applied Optics*, 23(8):1206–1225, 1984.

S. Warren. Can black carbon in snow be detected by remote sensing? *Journal of Geophysical Research*, 118:779–786, 2012.

S. Warren and R. Brandt. Optical constants of ice from the ultraviolet to the microwave: A revised compilation. *Journal of Geophysical Research*, 113(D14420), 2008.

S. Warren and A. Clarke. Soot in the atmosphere and snow surface of Antarctica. *Journal of Geophysical Research*, 95(D2):1811–1816, 1990.

S. Warren and W. Wiscombe. A model for the spectral albedo of snow. II: Snow containing atmospheric aerosols. *Journal of the Atmospheric Sciences*, 37(12):2734–2745, 1980.

S. Warren and W. Wiscombe. Dirty snow after nuclear war. *Nature*, 313:467–470, 1985.

S. Warren, R. Brandt, and P. Hinton. Effect of surface roughness on bidirectional reflectance of Antarctic snow. *Journal of Geophysical Research*, 103(E11):25, 1998.

S. Warren, I. Rigor, N. Untersteiner, and V. Radionov. Snow depth on Arctic sea ice. *Journal of Climate*, 12:1814–1829, 1999.

W. Weeks. *On sea ice*, chapter Snow, pages 417–433. University of Alaska Press, 2010.

W. Weeks and O. Lee. Observations on the physical properties of sea-ice at Hopedale, Labrador. *Arctic*, 11(3):134–155, 1958.

J. Weissenberger and S. Grossmann. Experimental formation of sea ice: importance of water circulation and wave action for incorporation of phytoplankton and bacteria. *Polar Biology*, 20:178–188, 1998.

H. Welch and M. Bergmann. Seasonal Development of Ice Algae and its Prediction from Environmental Factors near Resolute N.W.T., Canada. *Canadian Journal of Fisheries and Aquatic Sciences*, 46(10), 1989.

B. Wielicki, T. Wong, N. Loeb, P. Minnis, K. Priestley, and R. Kandel. Changes in earth's albedo measured by satellites. *Science*, 308(825), 2005.

J. Williams, M. deReus, R. Krejci, H. Fischer, and J. Ström. Application of the variability-size relationship to atmospheric aerosol studies: Estimating aerosol lifetimes and ages. *Atmospheric Chemistry and Physics*, 2:133–145, 2002.

W. Wiscombe and S. Warren. A model for the spectral albedo of snow. i: Pure snow. *Journal of the Atmospheric Sciences*, 37(12):2712–2733, 1980.

B. Xu, T. Yao, X. Liu, and N. Wang. Elemental and organic carbon measurements with a two-step heating gas chromatography system in snow samples from the Tibetan Plateau. *Annals of Glaciology*, 43(257–262), 2006.

B. Xu, M. Wang, D. Joswiak, J. Cao, T. Yao, G. Wu, W. Yang, and H. Zhao. Deposition of anthropogenic aerosols in a southeastern Tibetan glacier. *Journal of Geophysical Research*, 114(D17209), 2009a.

B. Xu, J. Cao, J. Hansen, T. Yao, D. Joswia, N. Wang, G. Wu, M. Wang, H. Zhao, W. Yang, X. Liu, and J. He. Black soot and the survival of Tibetan glaciers. *Proceedings of the National Academy of Sciences of the United States of America*, 106 (52):22114–22118, 2009b.

M. Zatko, T. Grenfell, B. Alexander, S. Doherty, J. Thomas, and X. Yang. The influence of snow grain size and impurities on the vertical profiles of actinic flux and associated NO_x emissions on the Antarctic and Greenland ice sheets. *Atmospheric Chemistry and Physics*, 13:3547–3567, 2013.

Appendix A

Data for chapter 4 for albedo/*e*-folding depth response to black carbon for different snow/sea ice thicknesses

Appendix A includes tables of the data for albedo of snow and sea ice from chapter 4 at different thicknesses and tables of data for the *e*-folding depth of snow and sea ice at different thicknesses.

Black carbon (ng g^{-1})	Melting snow (0.5 m^2 kg^{-1})	Melting snow (2 m^2 kg^{-1})	Windpacked snow (5 m^2 kg^{-1})	Windpacked snow (10 m^2 kg^{-1})	Cold polar snow (15 m^2 kg^{-1})	Cold polar snow (25 m^2 kg^{-1})
1	0.98532	0.987332	0.974779	0.982063	0.922462	0.960467
2	0.984344	0.986364	0.973123	0.980797	0.917359	0.957762
4	0.982559	0.984711	0.969954	0.978591	0.908039	0.952932
8	0.979302	0.982068	0.964527	0.97479	0.892156	0.944498
16	0.974245	0.977573	0.955775	0.968524	0.866735	0.930935
32	0.966231	0.970699	0.942224	0.95876	0.828729	0.910263
64	0.954461	0.960425	0.922468	0.944501	0.775127	0.880225
128	0.937569	0.945661	0.894336	0.924083	0.703471	0.838259
256	0.913788	0.924871	0.855515	0.89546	0.612693	0.781576
512	0.880986	0.896038	0.803108	0.856263	0.504781	0.707639
1024	0.836437	0.856646	0.734416	0.803614	0.386633	0.615245

a) Albedo with increasing black carbon for 10m of snow

Black carbon (ng g^{-1})	Melting snow (0.5 m^2 kg^{-1})	Melting snow (2 m^2 kg^{-1})	Windpacked snow (5 m^2 kg^{-1})	Windpacked snow (10 m^2 kg^{-1})	Cold polar snow (15 m^2 kg^{-1})	Cold polar snow (25 m^2 kg^{-1})
1	0.912546	0.960129	0.974814	0.982065	0.985319	0.98731
2	0.908746	0.957537	0.973098	0.98078	0.984341	0.986363
4	0.901429	0.952768	0.969994	0.978583	0.982469	0.984673
8	0.888035	0.944448	0.964514	0.974804	0.979269	0.982086
16	0.864898	0.930912	0.955725	0.968521	0.974224	0.977494
32	0.828244	0.910248	0.942238	0.95879	0.966276	0.970702
64	0.775062	0.880219	0.922469	0.944482	0.954458	0.960479
128	0.703471	0.838254	0.894352	0.924051	0.937542	0.945669
256	0.612693	0.781573	0.855506	0.895486	0.913803	0.924889
512	0.504782	0.70764	0.803111	0.856257	0.880977	0.896038
1024	0.386632	0.615243	0.734419	0.803623	0.83644	0.856658

b) Albedo with increasing black carbon for 1 m of snow

Black carbon (ng g^{-1})	Melting snow (0.5 m^2 kg^{-1})	Melting snow (2 m^2 kg^{-1})	Windpacked snow (5 m^2 kg^{-1})	Windpacked snow (10 m^2 kg^{-1})	Cold polar snow (15 m^2 kg^{-1})	Cold polar snow (25 m^2 kg^{-1})
1	0.87708	0.95499	0.974073	0.981979	0.985304	0.987152
2	0.874842	0.952985	0.972524	0.980712	0.984323	0.986338
4	0.870419	0.949187	0.969621	0.978555	0.982449	0.984657
8	0.86189	0.942129	0.964351	0.97477	0.979268	0.982081
16	0.845883	0.929836	0.955677	0.968515	0.974262	0.977496
32	0.817441	0.909941	0.942231	0.958793	0.966284	0.97069
64	0.770904	0.880179	0.922458	0.944479	0.954457	0.960467
128	0.702567	0.838246	0.894352	0.924037	0.937539	0.945665
256	0.612608	0.781572	0.855508	0.895477	0.913801	0.924879
512	0.50478	0.707639	0.803115	0.856257	0.880978	0.896032
1024	0.386632	0.615243	0.734417	0.803623	0.83644	0.856658

c) Albedo with increasing black carbon for 0.5 m of snow

Black carbon (ng g^{-1})	Melting snow (0.5 m^2 kg^{-1})	Melting snow (2 m^2 kg^{-1})	Windpacked snow (5 m^2 kg^{-1})	Windpacked snow (10 m^2 kg^{-1})	Cold polar snow (15 m^2 kg^{-1})	Cold polar snow (25 m^2 kg^{-1})
1	0.639391	0.867508	0.939857	0.967245	0.976795	0.981706
2	0.638962	0.867034	0.939385	0.966735	0.976369	0.981262
4	0.638104	0.866083	0.938417	0.965807	0.975401	0.980301
8	0.636392	0.864183	0.936502	0.963953	0.97364	0.978585
16	0.633002	0.860421	0.932755	0.960405	0.970247	0.975341
32	0.626324	0.853124	0.925617	0.953782	0.96412	0.969591
64	0.613383	0.839197	0.91253	0.942128	0.953616	0.960107
128	0.589046	0.813787	0.889941	0.923346	0.937358	0.945622
256	0.545748	0.770604	0.854244	0.895359	0.913778	0.924878
512	0.475847	0.70447	0.802923	0.856258	0.880971	0.896038
1024	0.378993	0.614774	0.734408	0.80362	0.836445	0.856654

d) Albedo with increasing black carbon for 0.1 m of snow

Figure A.1 *– Data of albedo of snowpacks for different black carbon mass-ratios and snow thickness.*

Black carbon (ng g^{-1})	Melting ice (0.01 m^2 kg^{-1})	Melting ice (0.05 m^2 kg^{-1})	First year ice (0.1 m^2 kg^{-1})	First year ice (0.2 m^2 kg^{-1})	Multiyear ice (0.5 m^2 kg^{-1})	Multiyear ice (1 m^2 kg^{-1})
1	0.742002	0.874818	0.55319	0.656543	0.276497	0.396257
2	0.726954	0.866686	0.531648	0.637975	0.256662	0.373767
4	0.70032	0.852255	0.494603	0.605492	0.224202	0.336093
8	0.656508	0.82772	0.436978	0.553354	0.178441	0.280488
16	0.591062	0.789083	0.358534	0.478444	0.126018	0.211501
32	0.503214	0.732772	0.267389	0.38389	0.07861	0.141738
64	0.398172	0.656473	0.178623	0.280568	0.0442115	0.0846419
128	0.287681	0.560297	0.106865	0.184352	0.0232247	0.0461275
256	0.187356	0.448426	0.0583621	0.10894	0.0117871	0.023758
512	0.110006	0.330572	0.0300451	0.0589994	0.00590609	0.0119252
1024	0.0593235	0.220962	0.0150408	0.0302194	0.00295045	0.0059409

a) Albedo with increasing black carbon for 10 m of sea ice

Black carbon (ng g^{-1})	Melting ice (0.01 m^2 kg^{-1})	Melting ice (0.05 m^2 kg^{-1})	First year ice (0.1 m^2 kg^{-1})	First year ice (0.2 m^2 kg^{-1})	Multiyear ice (0.5 m^2 kg^{-1})	Multiyear ice (1 m^2 kg^{-1})
1	0.170194	0.237555	0.380271	0.520695	0.660401	0.866649
2	0.166217	0.232759	0.374239	0.51382	0.652996	0.859964
4	0.15866	0.22359	0.362632	0.50056	0.638759	0.847462
8	0.144976	0.206815	0.341113	0.475855	0.612265	0.825103
16	0.122298	0.178498	0.30388	0.432666	0.566073	0.788166
32	0.0900724	0.137035	0.246915	0.365117	0.493597	0.732613
64	0.0542731	0.0887746	0.175402	0.276405	0.396161	0.656468
128	0.0264254	0.0481276	0.107125	0.184068	0.287527	0.560297
256	0.0120651	0.0239478	0.0584206	0.108944	0.187353	0.448424
512	0.00590763	0.0119264	0.0300449	0.0589991	0.110006	0.330571
1024	0.00294954	0.00594095	0.0150397	0.0302188	0.0593235	0.220962

b) Albedo with increasing black carbon for 1 m of sea ice

Black carbon (ng g^{-1})	Melting ice (0.01 m^2 kg^{-1})	Melting ice (0.05 m^2 kg^{-1})	First year ice (0.1 m^2 kg^{-1})	First year ice (0.2 m^2 kg^{-1})	Multiyear ice (0.5 m^2 kg^{-1})	Multiyear ice (1 m^2 kg^{-1})
1	0.142647	0.185258	0.285534	0.402675	0.546118	0.828423
2	0.140712	0.182987	0.282686	0.399341	0.542341	0.82421
4	0.136959	0.178565	0.277118	0.39281	0.534944	0.816068
8	0.129883	0.170183	0.266474	0.380259	0.520675	0.800609
16	0.117243	0.155057	0.24697	0.357036	0.494152	0.772592
32	0.0967388	0.130149	0.213984	0.317008	0.447965	0.725521
64	0.0684264	0.095088	0.165497	0.256154	0.376223	0.654536
128	0.0381079	0.0566249	0.108634	0.180495	0.282929	0.560048
256	0.0160051	0.0271458	0.0599825	0.109186	0.187034	0.448414
512	0.00625849	0.0122174	0.0302105	0.0590597	0.11001	0.33057
1024	0.00295215	0.00594206	0.015041	0.0302185	0.0593224	0.220961

c) Albedo with increasing black carbon for 0.5 m of sea ice

Black carbon (ng g^{-1})	Melting ice (0.01 m^2 kg^{-1})	Melting ice (0.05 m^2 kg^{-1})	First year ice (0.1 m^2 kg^{-1})	First year ice (0.2 m^2 kg^{-1})	Multiyear ice (0.5 m^2 kg^{-1})	Multiyear ice (1 m^2 kg^{-1})
1	0.124733	0.149734	0.213142	0.29585	0.414689	0.743081
2	0.123813	0.148688	0.21186	0.29434	0.412933	0.740881
4	0.122005	0.14663	0.20933	0.291357	0.409467	0.736557
8	0.118511	0.142642	0.204403	0.285529	0.402664	0.728092
16	0.111964	0.135133	0.195049	0.274391	0.389602	0.71186
32	0.100393	0.121761	0.178141	0.254014	0.365457	0.681954
64	0.0818663	0.100172	0.150212	0.219629	0.32393	0.630533
128	0.0565693	0.0705547	0.110723	0.169275	0.260996	0.551378
256	0.0297211	0.0390651	0.0670994	0.110545	0.18314	0.446775
512	0.010736	0.0162705	0.0331544	0.0606578	0.110246	0.330458
1024	0.00334767	0.00630327	0.0153153	0.0303899	0.0593862	0.22096

d) Albedo with increasing black carbon for 0.25 m of sea ice

Figure A.2 *– Albedo data for three different types of sea ice with increasing mass-ratio of black carbon and different sea ice thickness*

Black carbon (ng g^{-1})	Melting snow (0.5 m^2 kg^{-1})	Melting snow (2 m^2 kg^{-1})	Windpacked snow (5 m^2 kg^{-1})	Windpacked snow (10 m^2 kg^{-1})	Cold polar snow (15 m^2 kg^{-1})	Cold polar snow (25 m^2 kg^{-1})
1	119.121	59.3557	37.7438	26.6185	22.0661	18.2446
2	101.04	50.7127	31.7737	22.4568	18.3449	15.9066
4	80.989	40.4144	25.6597	18.0435	14.9071	12.6717
8	61.8056	30.9305	19.5309	13.8642	11.3176	9.71473
16	45.6008	22.8206	14.449	10.2199	8.33989	7.19314
32	32.9722	16.5112	10.4403	7.38991	6.05025	5.21831
64	23.5599	11.8116	7.4728	5.28306	4.31482	3.73806
128	16.7021	8.39504	5.31479	3.75917	3.07022	2.65709
256	11.7676	5.94389	3.76755	2.66617	2.17673	1.88534
512	8.22549	4.19534	2.66414	1.88648	1.5411	1.33499
1024	5.67883	2.94896	1.88021	1.33307	1.08953	0.943975

a) *e*-folding depth with increasing black carbon for 10m of snow

Black carbon (ng g^{-1})	Melting snow (0.5 m^2 kg^{-1})	Melting snow (2 m^2 kg^{-1})	Windpacked snow (5 m^2 kg^{-1})	Windpacked snow (10 m^2 kg^{-1})	Cold polar snow (15 m^2 kg^{-1})	Cold polar snow (25 m^2 kg^{-1})
1	68.3823	50.5387	36.2801	26.3738	21.9461	19.0631
2	65.3733	45.5752	31.1434	22.4011	18.3538	15.9379
4	60.2362	38.4776	25.4923	18.1349	14.9043	12.8613
8	52.5035	30.4074	19.5081	13.8684	11.2843	9.70245
16	42.6415	22.7441	14.4467	10.2132	8.34045	7.16456
32	32.3607	16.5096	10.4438	7.39089	6.038	5.22651
64	23.4847	11.8116	7.47161	5.28451	4.31491	3.74066
128	16.6972	8.39554	5.31462	3.75946	3.0701	2.66029
256	11.7676	5.94402	3.76766	2.66533	2.17652	1.88561
512	8.22549	4.19534	2.66434	1.88662	1.54122	1.33505
1024	5.6791	2.94896	1.88025	1.33318	1.0895	0.943988

b) *e*-folding depth with increasing black carbon for 1 m of snow

Black carbon (ng g^{-1})	Melting snow (0.5 m^2 kg^{-1})	Melting snow (2 m^2 kg^{-1})	Windpacked snow (5 m^2 kg^{-1})	Windpacked snow (10 m^2 kg^{-1})	Cold polar snow (15 m^2 kg^{-1})	Cold polar snow (25 m^2 kg^{-1})
1	25.6563	21.593	19.6332	17.6255	16.0658	15.1561
2	25.4815	21.1814	18.8181	16.4488	14.9166	13.6236
4	25.1506	20.4088	17.5125	14.7152	12.9002	11.6984
8	24.5204	19.0663	15.4408	12.3726	10.536	9.31042
16	23.3788	16.9693	12.7938	9.73793	8.11645	7.07649
32	21.4358	14.1724	9.93963	7.27326	5.98585	5.21056
64	18.5712	11.0765	7.35584	5.26417	4.31186	3.73854
128	14.9976	8.22088	5.29584	3.75728	3.06965	2.66012
256	11.3311	5.91436	3.76528	2.6652	2.17663	1.88559
512	8.14799	4.19225	2.66418	1.88648	1.54104	1.33509
1024	5.67106	2.94877	1.88021	1.33319	1.08951	0.943988

c) *e*-folding depth with increasing black carbon for 0.5 m of snow

Black carbon (ng g^{-1})	Melting snow (0.5 m^2 kg^{-1})	Melting snow (2 m^2 kg^{-1})	Windpacked snow (5 m^2 kg^{-1})	Windpacked snow (10 m^2 kg^{-1})	Cold polar snow (15 m^2 kg^{-1})	Cold polar snow (25 m^2 kg^{-1})
1	11.3142	8.33298	7.68337	7.39476	7.24533	7.12584
2	11.2877	8.31181	7.64042	7.32176	7.13529	7.00923
4	11.2622	8.26955	7.55972	7.17126	6.92305	6.7265
8	11.2112	8.1872	7.40338	6.90893	6.56617	6.28162
16	11.1093	8.02735	7.10721	6.44138	5.97581	5.58987
32	10.8861	7.7309	6.59881	5.70035	5.10905	4.65838
64	10.4898	7.20785	5.80893	4.70934	4.05246	3.59868
128	9.80205	6.37935	4.76509	3.62338	3.01989	2.63757
256	8.68108	5.26629	3.64306	2.64529	2.17173	1.88402
512	7.11635	4.03784	2.64782	1.88468	1.54071	1.33469
1024	5.33738	2.92578	1.8787	1.33317	1.08944	0.94401

d) *e*-folding depth with increasing black carbon for 0.1 m of snow

Figure A.3 *– Data for e-folding depth (m) of snow for different snow types, black carbon mass-ratio and snow thickness.*

Black carbon (ng g^{-1})	Melting ice (0.01 m^2 kg^{-1})	Melting ice (0.05 m^2 kg^{-1})	First year ice (0.1 m^2 kg^{-1})	First year ice (0.2 m^2 kg^{-1})	Multiyear ice (0.5 m^2 kg^{-1})	Multiyear ice (1 m^2 kg^{-1})
1	219.659	98.7289	419.009	307.308	737.298	596.835
2	186.693	83.7709	355.926	260.469	624.238	507.398
4	149.218	67.1313	281.471	207.761	484.684	397.964
8	113.342	51.1735	209.642	156.723	342.163	288.136
16	83.1182	37.7469	149.098	113.755	225.952	196.172
32	59.3074	27.2519	101.404	79.7057	140.932	126.959
64	41.3847	19.4084	66.4482	54.2325	84.912	78.6526
128	28.1697	13.6772	41.9377	35.6629	49.7899	47.3121
256	18.5765	9.52725	25.5243	22.5724	28.6448	27.7574
512	11.7885	6.52483	15.0436	13.7357	16.2934	15.963
1024	7.16422	4.35402	8.59493	8.04319	9.10415	8.97105

a) *e*-folding depth with increasing black carbon for 10 m of sea ice

Black carbon (ng g^{-1})	Melting ice (0.01 m^2 kg^{-1})	Melting ice (0.05 m^2 kg^{-1})	First year ice (0.1 m^2 kg^{-1})	First year ice (0.2 m^2 kg^{-1})	Multiyear ice (0.5 m^2 kg^{-1})	Multiyear ice (1 m^2 kg^{-1})
1	260.293	176.598	102.145	69.2211	48.2233	26.9746
2	253.504	173.713	101.195	68.7616	47.9005	26.6839
4	239.522	167.509	99.2949	67.6326	47.2647	26.1389
8	218.283	156.069	95.3497	65.6632	46.0467	25.1252
16	182.146	137.945	88.3077	61.9741	43.7798	23.3473
32	136.42	110.61	76.5997	55.659	39.9008	20.6198
64	90.3968	78.8867	60.2049	46.0427	33.9071	16.9912
128	53.6308	49.7355	41.8764	34.1543	26.2404	13.0215
256	30.0088	28.8651	26.0684	22.6362	18.3454	9.40624
512	16.578	16.2149	15.2163	13.8229	11.8028	6.51189
1024	9.13526	8.99964	8.61678	8.05776	7.17085	4.35326

b) *e*-folding depth with increasing black carbon for 1 m of sea ice

Black carbon (ng g^{-1})	Melting ice (0.01 m^2 kg^{-1})	Melting ice (0.05 m^2 kg^{-1})	First year ice (0.1 m^2 kg^{-1})	First year ice (0.2 m^2 kg^{-1})	Multiyear ice (0.5 m^2 kg^{-1})	Multiyear ice (1 m^2 kg^{-1})
1	260.293	176.598	102.145	69.2211	48.2233	26.9746
2	253.504	173.713	101.195	68.7616	47.9005	26.6839
4	239.522	167.509	99.2949	67.6326	47.2647	26.1389
8	218.283	156.069	95.3497	65.6632	46.0467	25.1252
16	182.146	137.945	88.3077	61.9741	43.7798	23.3473
32	136.42	110.61	76.5997	55.659	39.9008	20.6198
64	90.3968	78.8867	60.2049	46.0427	33.9071	16.9912
128	53.6308	49.7355	41.8764	34.1543	26.2404	13.0215
256	30.0088	28.8651	26.0684	22.6362	18.3454	9.40624
512	16.578	16.2149	15.2163	13.8229	11.8028	6.51189
1024	9.13526	8.99964	8.61678	8.05776	7.17085	4.35326

c) *e*-folding depth with increasing black carbon for 0.5 m of sea ice

Black carbon (ng g^{-1})	Melting ice (0.01 m^2 kg^{-1})	Melting ice (0.05 m^2 kg^{-1})	First year ice (0.1 m^2 kg^{-1})	First year ice (0.2 m^2 kg^{-1})	Multiyear ice (0.5 m^2 kg^{-1})	Multiyear ice (1 m^2 kg^{-1})
1	225.747	158.095	92.334	62.9881	43.5205	23.3762
2	224.847	157.495	91.9655	62.0563	43.0513	23.2161
4	202.769	146.432	89.6296	61.5194	42.3829	22.8958
8	182.996	139.767	86.7117	59.2605	41.6186	22.2808
16	147.047	121.007	78.7286	55.6365	39.6897	21.1049
32	109.331	92.144	66.8888	49.8564	36.2578	19.1673
64	69.81	64.3383	51.644	40.8469	30.924	16.3127
128	42.9625	41.1484	35.6671	29.8385	24.0667	12.8403
256	24.572	23.8995	21.8169	19.6052	16.8209	9.37261
512	13.6277	13.3573	12.6849	11.8931	10.7246	6.48612
1024	7.51126	7.43897	7.25396	6.98901	6.5169	4.32929

d) *e*-folding depth with increasing black carbon for 0.25 m of sea ice

Figure A.4 *– Data for e-folding depth (m) of three sea ice types for different sea ice thickness and black carbon mass-ratio*

Appendix B

Supplementary data for chapter 6 for ice cores taken before and after the addition of a black carbon bearing layer

Appendix B includes extra ice core data from cores taken before and after the black carbon bearing layer is added for each run (1–4) with a different black carbon loading (0, 75, 150 and 300 ng g^{-1}). Salinity, temperature and density is measured for each core and brine salinity, density and brine and air volume are derived using equations by Cox and Weeks (1983). A photograph of each core is also shown. Note that core data from run 2 after the black carbon bearing layer is added is missing.

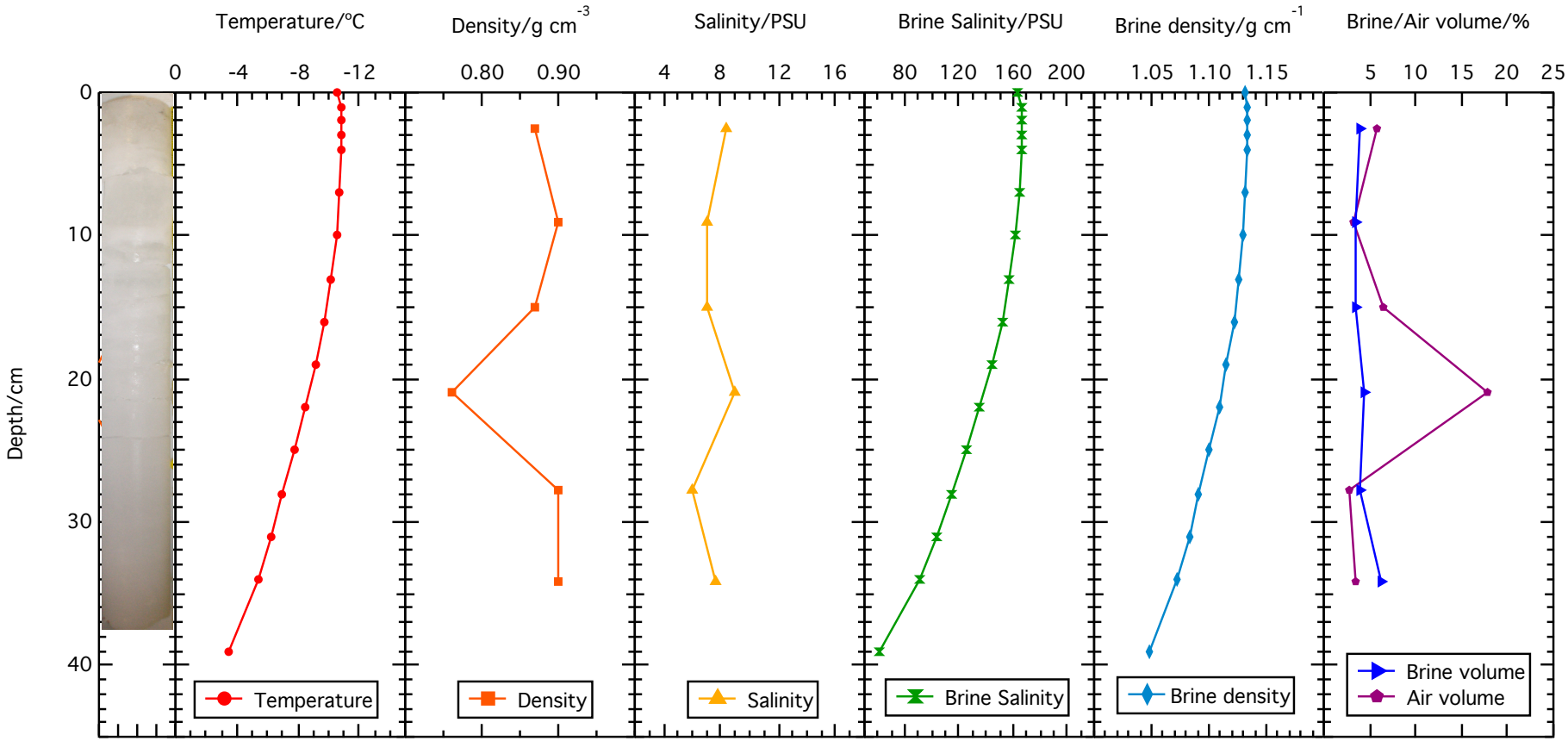

***Figure B.1* – Run 1 before layer added** *Physical ice properties for bottom "clean" ice layer before additional layer added for run 1. Temperatue, density and salinity are measured from core sections, while brine salinity, brine density and brine and air volume are derived from equations of Cox and Weeks (1983). Photo of the ice core is also shown*

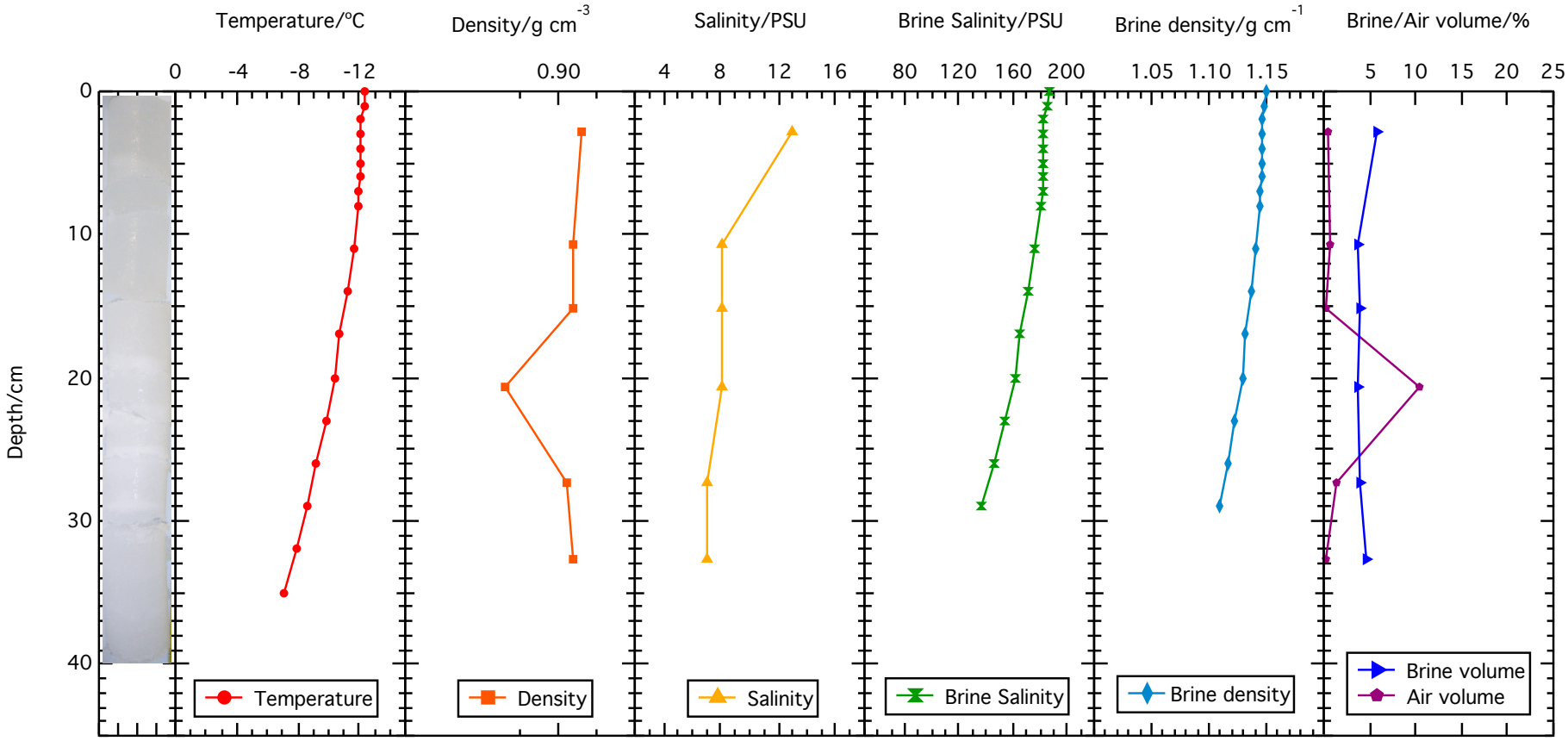

***Figure B.2* – Run 1 after layer added** *Physical ice properties for bottom "clean" ice layer and additional layer added for run 1. Temperature, density and salinity are measured from core sections, while brine salinity, brine density and brine and air volume are derived from equations of Cox and Weeks (1983). Photo of the ice core is also shown*

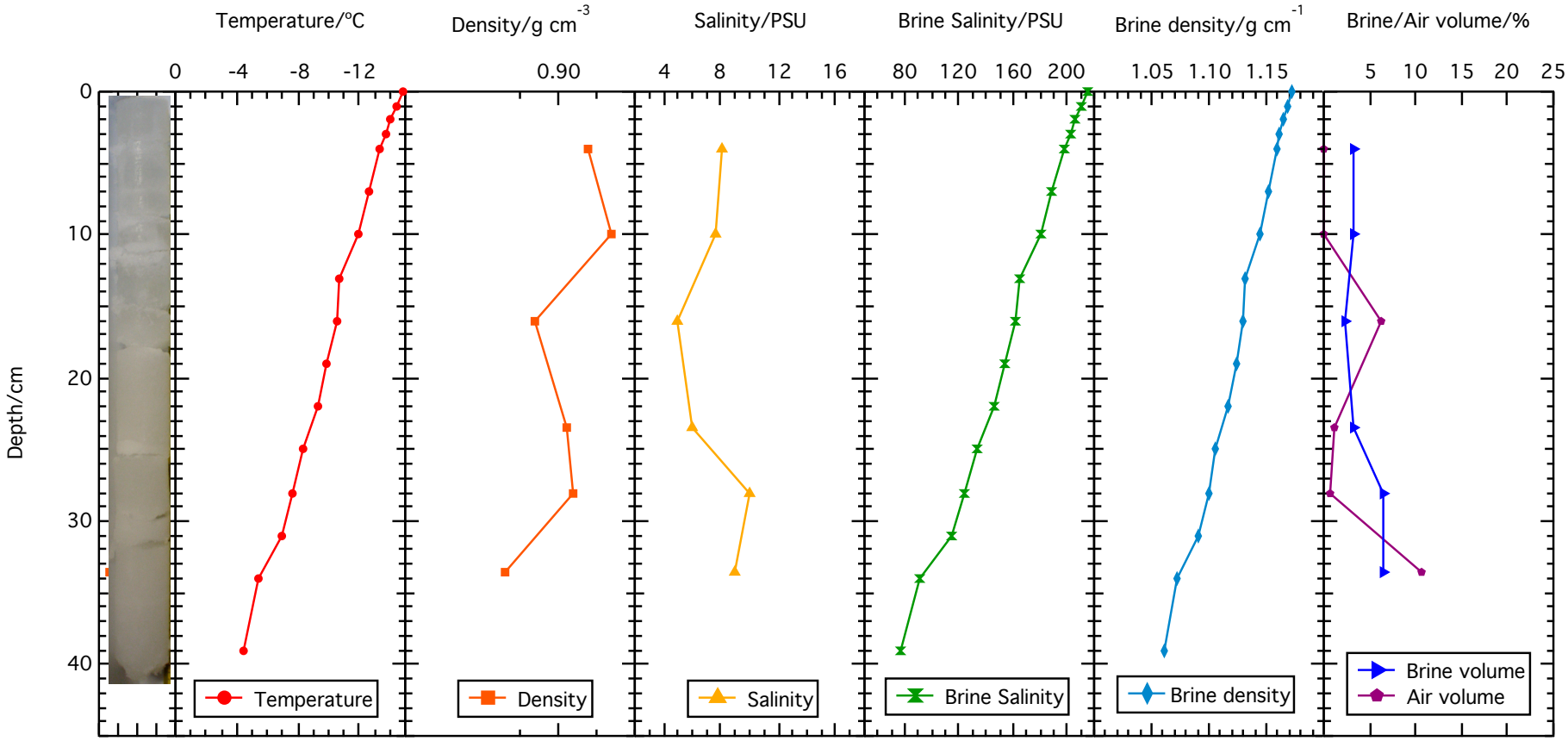

***Figure B.3* – Run 2 before layer added** *Physical ice properties for bottom "clean" ice layer before additional black carbon bearing layer added for run 2. Temperature, density and salinity are measured from core sections, while brine salinity, brine density and brine and air volume are derived from equations of Cox and Weeks (1983). Photo of the ice core is also shown*

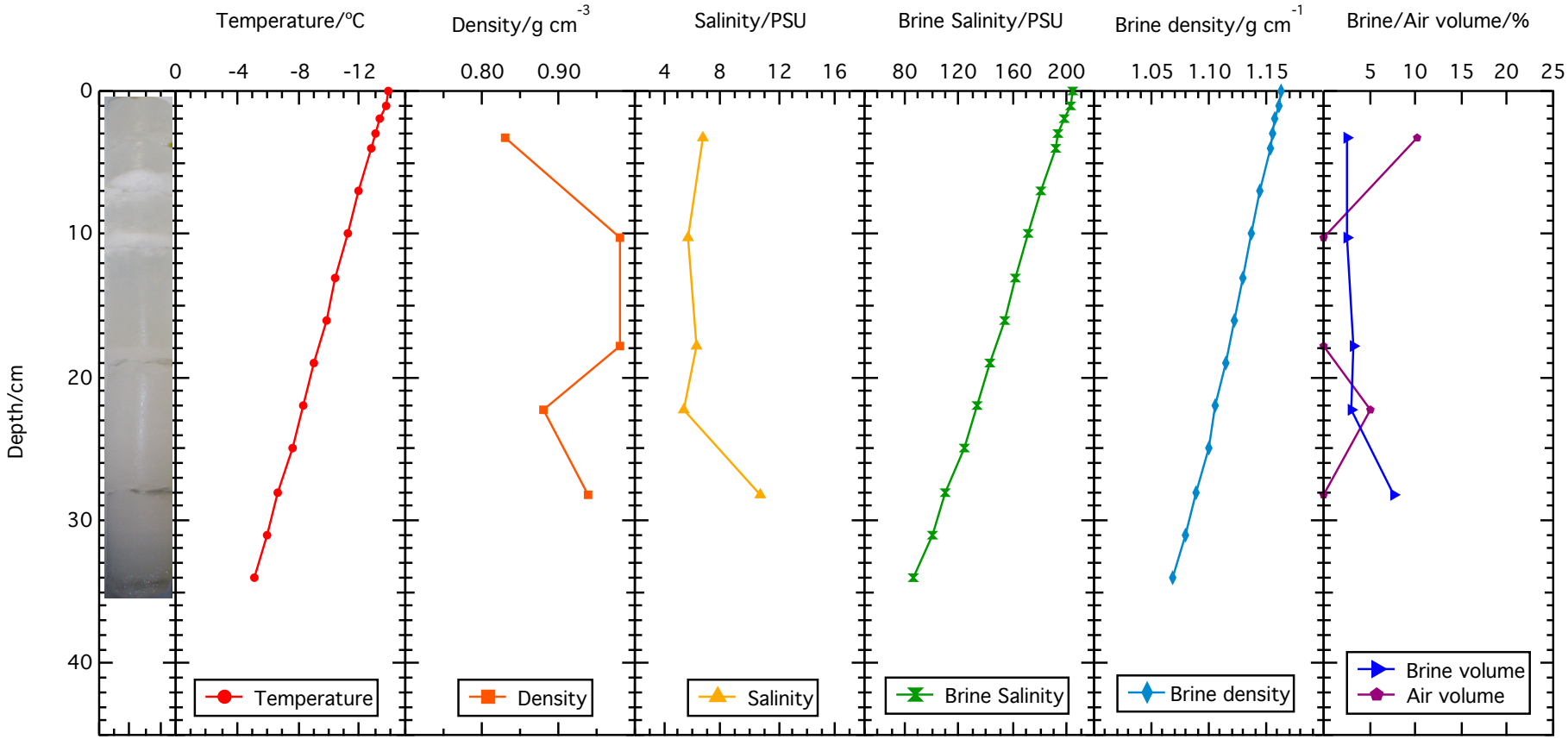

***Figure B.4* – Run 3 before layer added** *Physical ice properties for bottom "clean" ice layer before additional black carbon bearing layer added for run 3. Temperature, density and salinity are measured from core sections, while brine salinity, brine density and brine and air volume are derived from equations of Cox and Weeks (1983). Photo of the ice core is also shown*

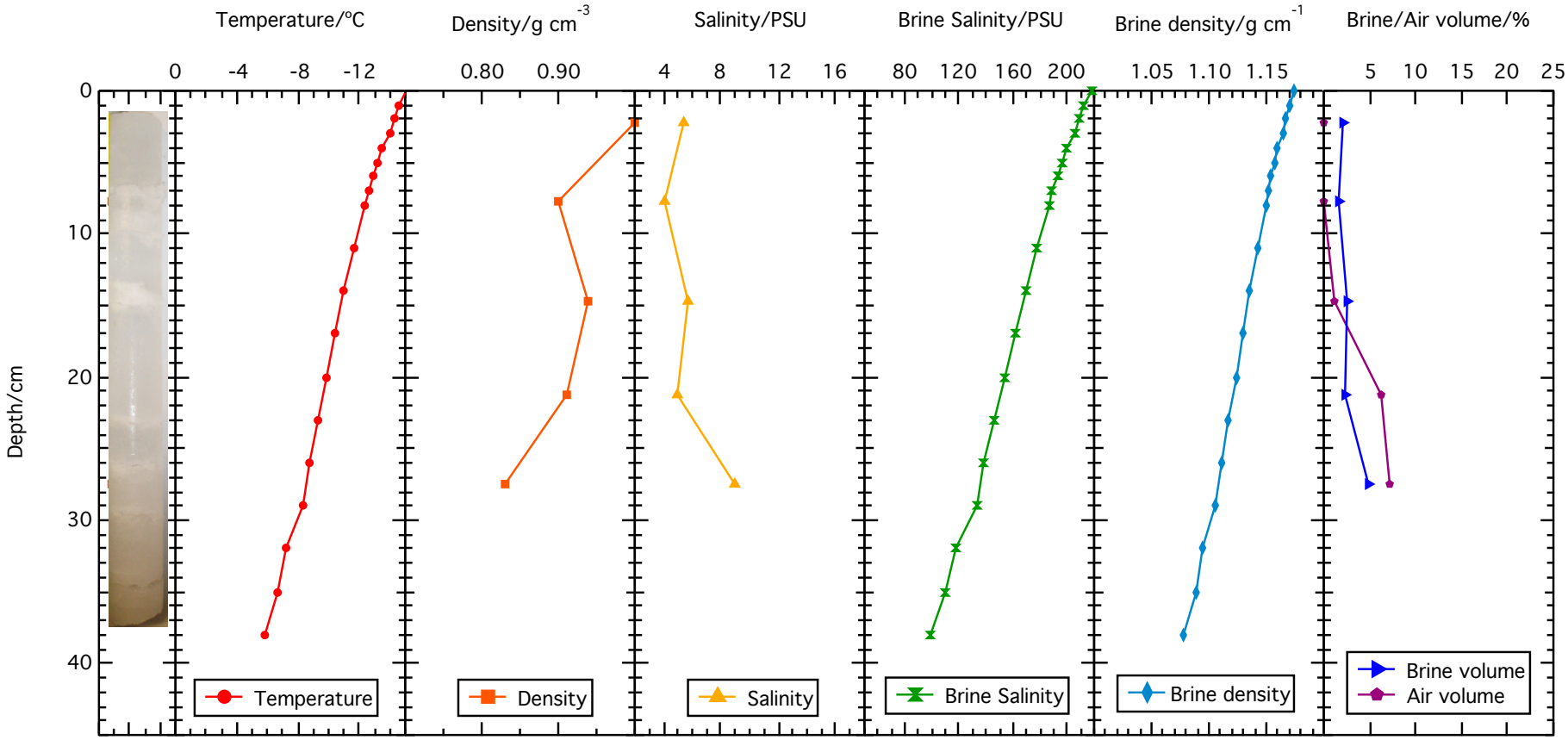

***Figure B.5* – Run 3 after layer added** *Physical ice properties for bottom "clean" ice layer and additional black carbon bearing layer for run 3. Temperature, density and salinity are measured from core sections, while brine salinity, brine density and brine and air volume are derived from equations of Cox and Weeks (1983). Photo of the ice core is also shown*

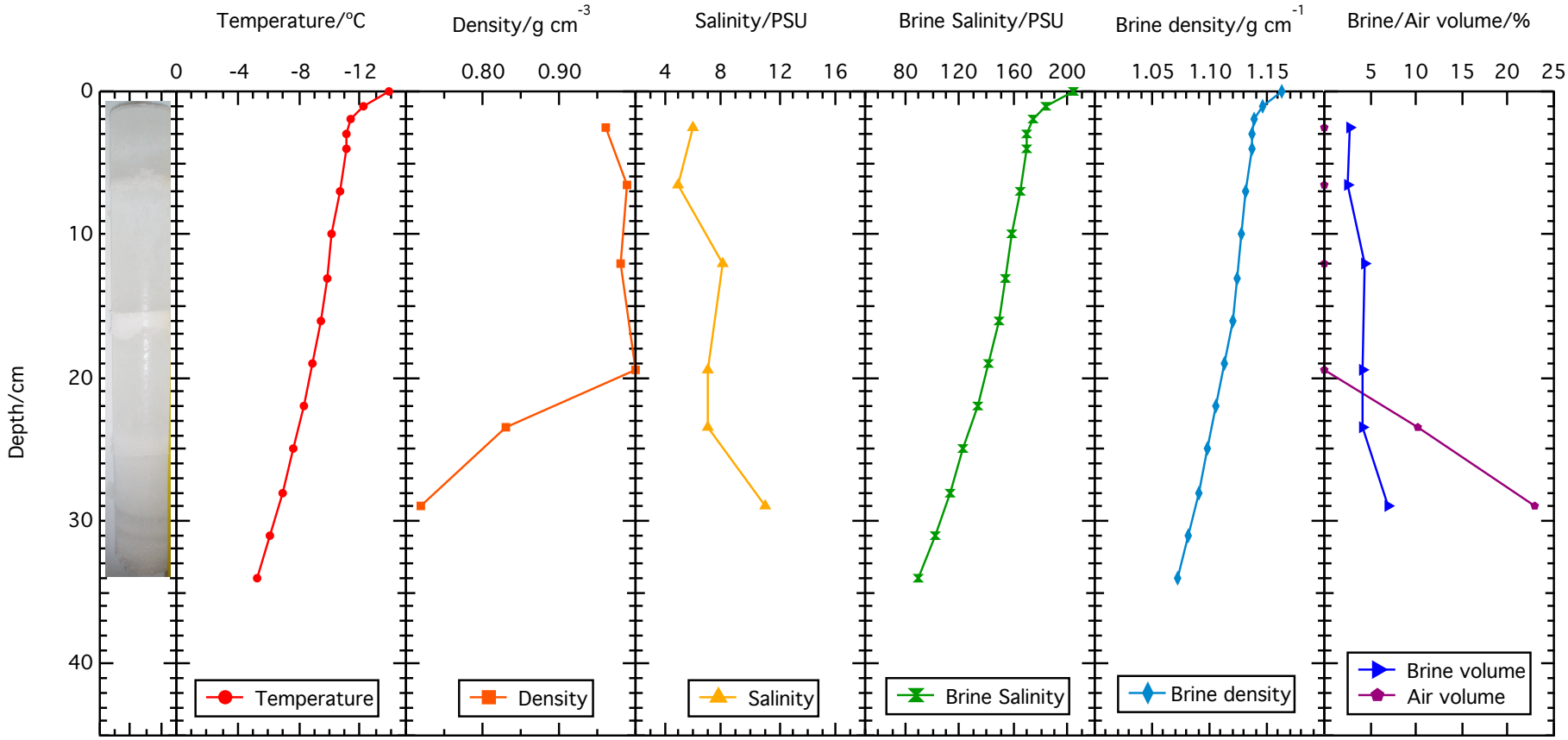

***Figure B.6* – Run 4 before layer added** *Physical ice properties for bottom "clean" ice layer before additional black carbon bearing layer added for run 4. Temperature, density and salinity are measured from core sections, while brine salinity, brine density and brine and air volume are derived from equations of Cox and Weeks (1983). Photo of the ice core is also shown*

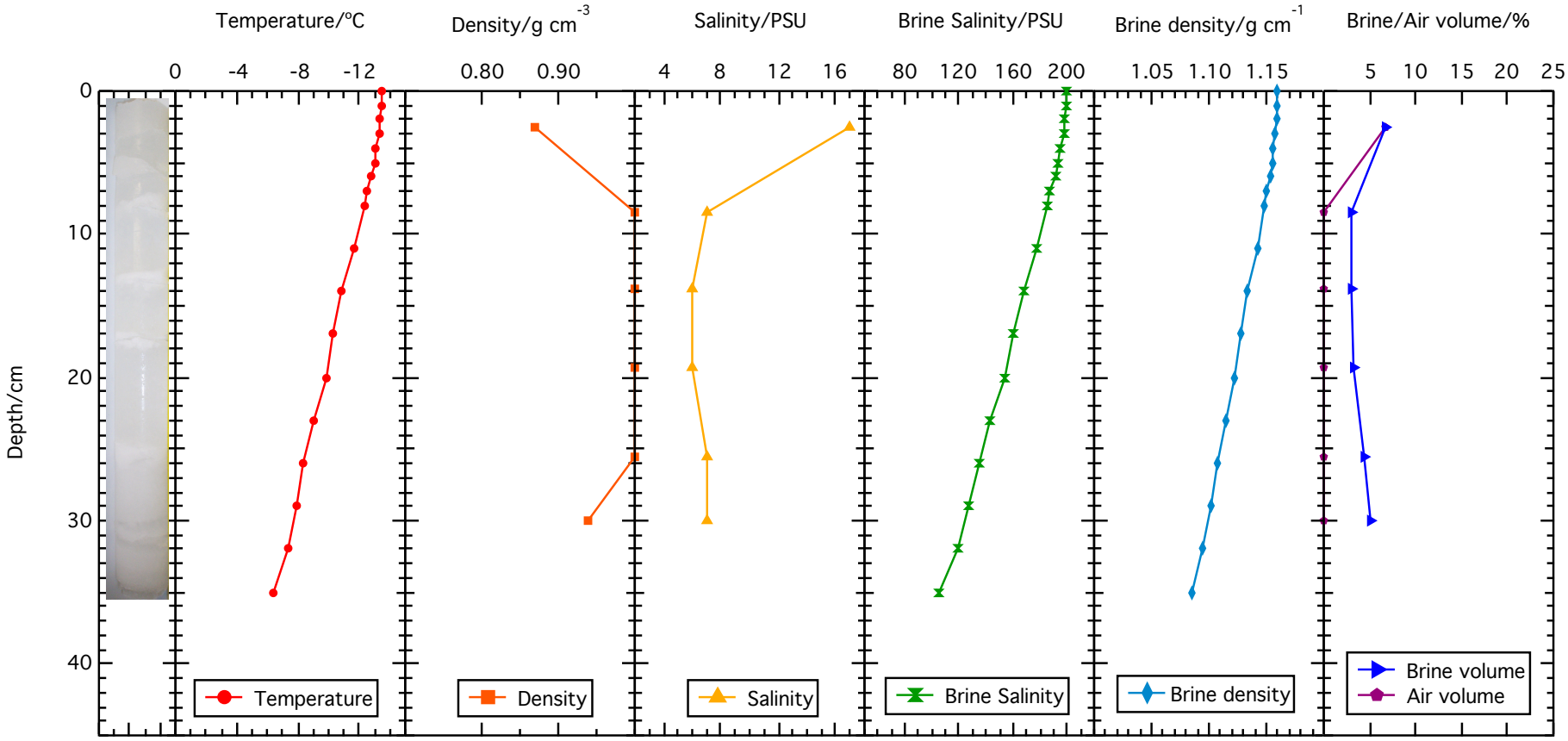

***Figure B.7* – Run 4 after layer added** *Physical ice properties for bottom "clean" ice layer and additional black carbon bearing layer for run 4. Temperature, density and salinity are measured from core sections, while brine salinity, brine density and brine and air volume are derived from equations of Cox and Weeks (1983). Photo of the ice core is also shown*

Appendix C

Supplementary data for chapter 7 for HDRF measurements from individual snow sites at Dome C

Appendix C includes polar plots for individual sites at wavelengths from 400–1600 nm and downwelling data through the entire measurements sequence for each site.

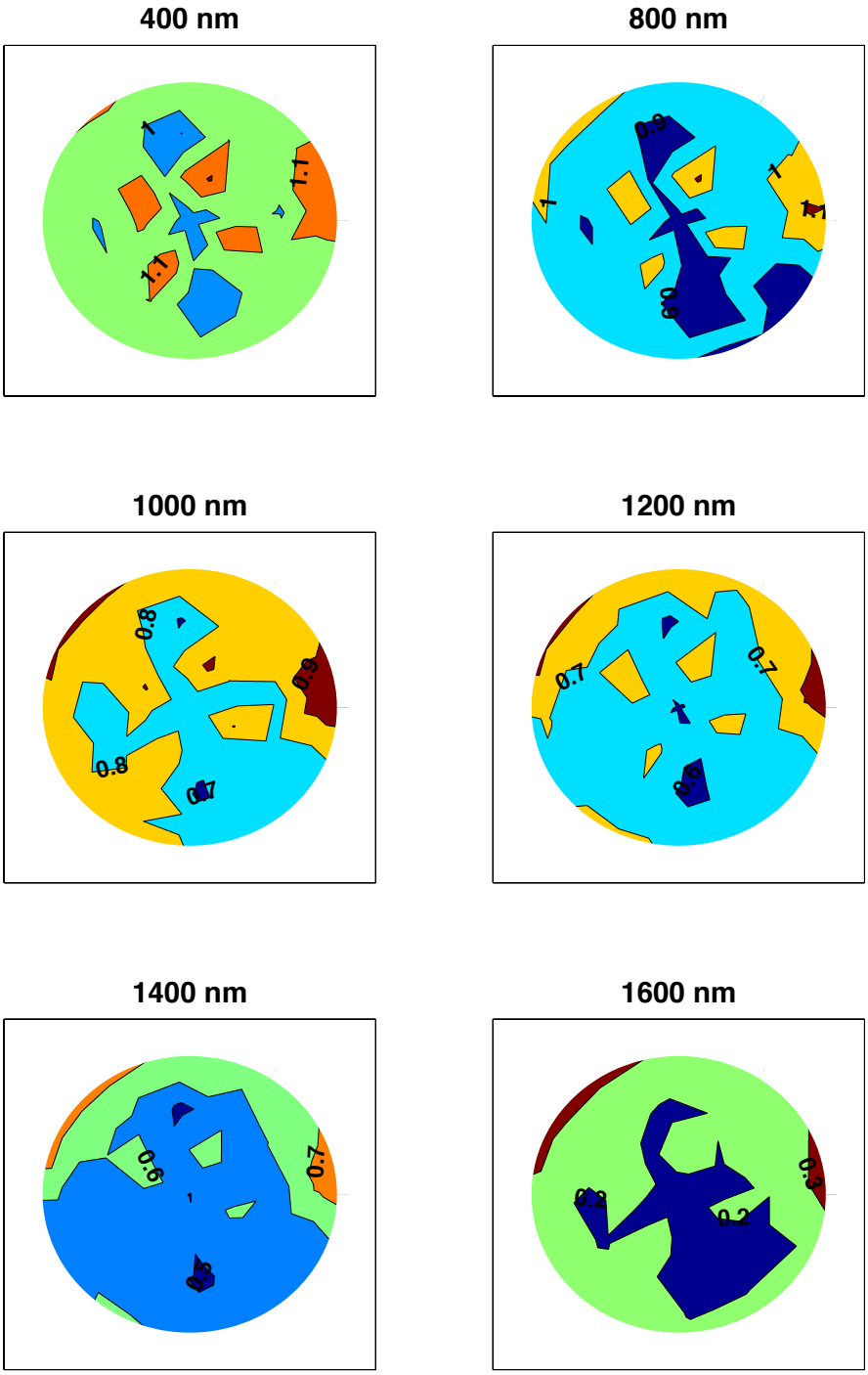

Figure C.1 *– HDRF polar plots at wavelengths of 400, 800, 1000, 1200, 1400 and 1600 nm for site 1. The sun is at the base of each plot*

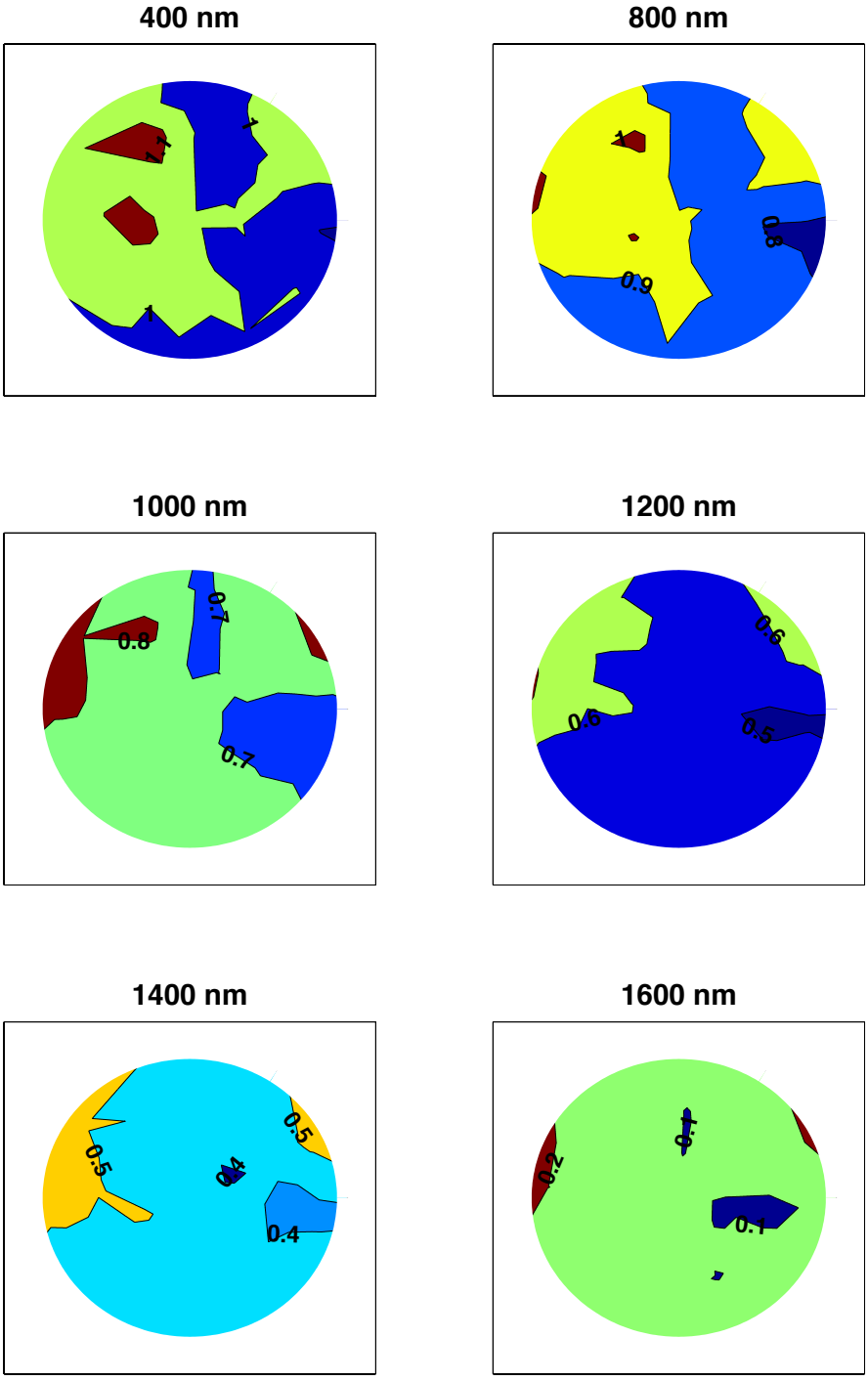

Figure C.2 *– HDRF polar plots at wavelengths of 400, 800, 1000, 1200, 1400 and 1600 nm for site 2. The sun is at the base of each plot*

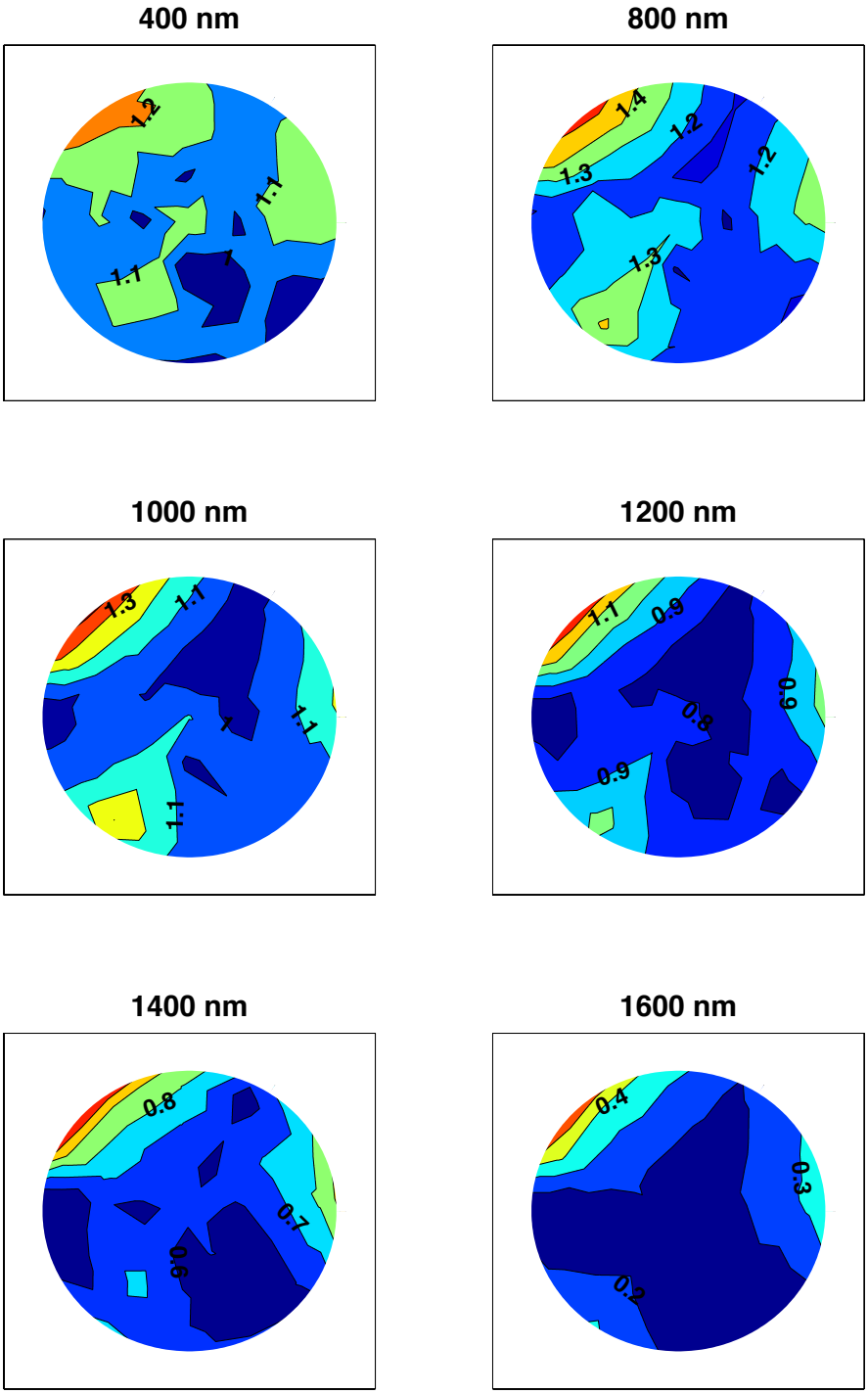

Figure C.3 *– HDRF polar plots at wavelengths of 400, 800, 1000, 1200, 1400 and 1600 nm for site 3. The sun is at the base of each plot*

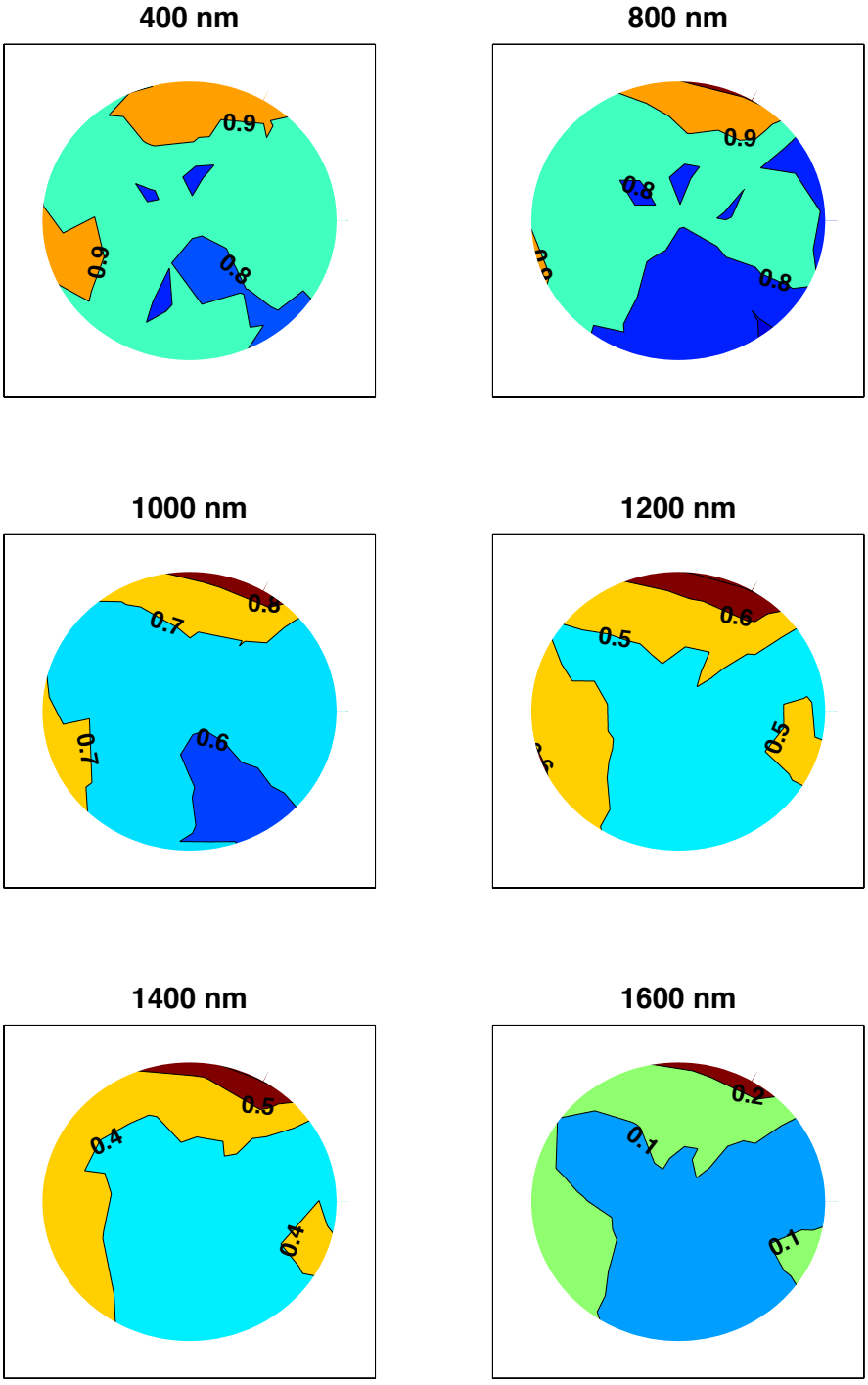

Figure C.4 *– HDRF polar plots at wavelengths of 400, 800, 1000, 1200, 1400 and 1600 nm for site 4. The sun is at the base of each plot*

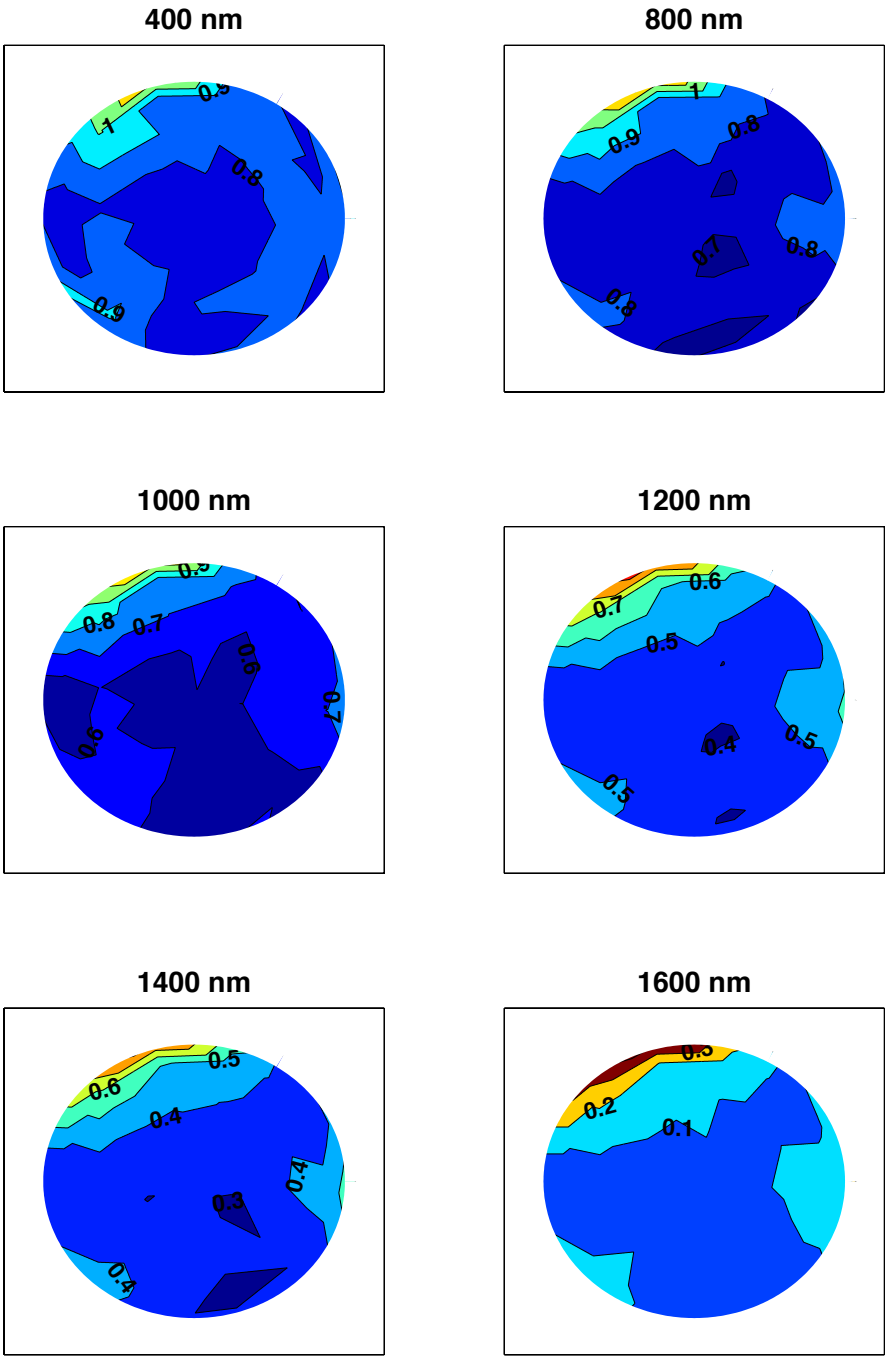

Figure C.5 *– HDRF polar plots at wavelengths of 400, 800, 1000, 1200, 1400 and 1600 nm for site 5. The sun is at the base of each plot*

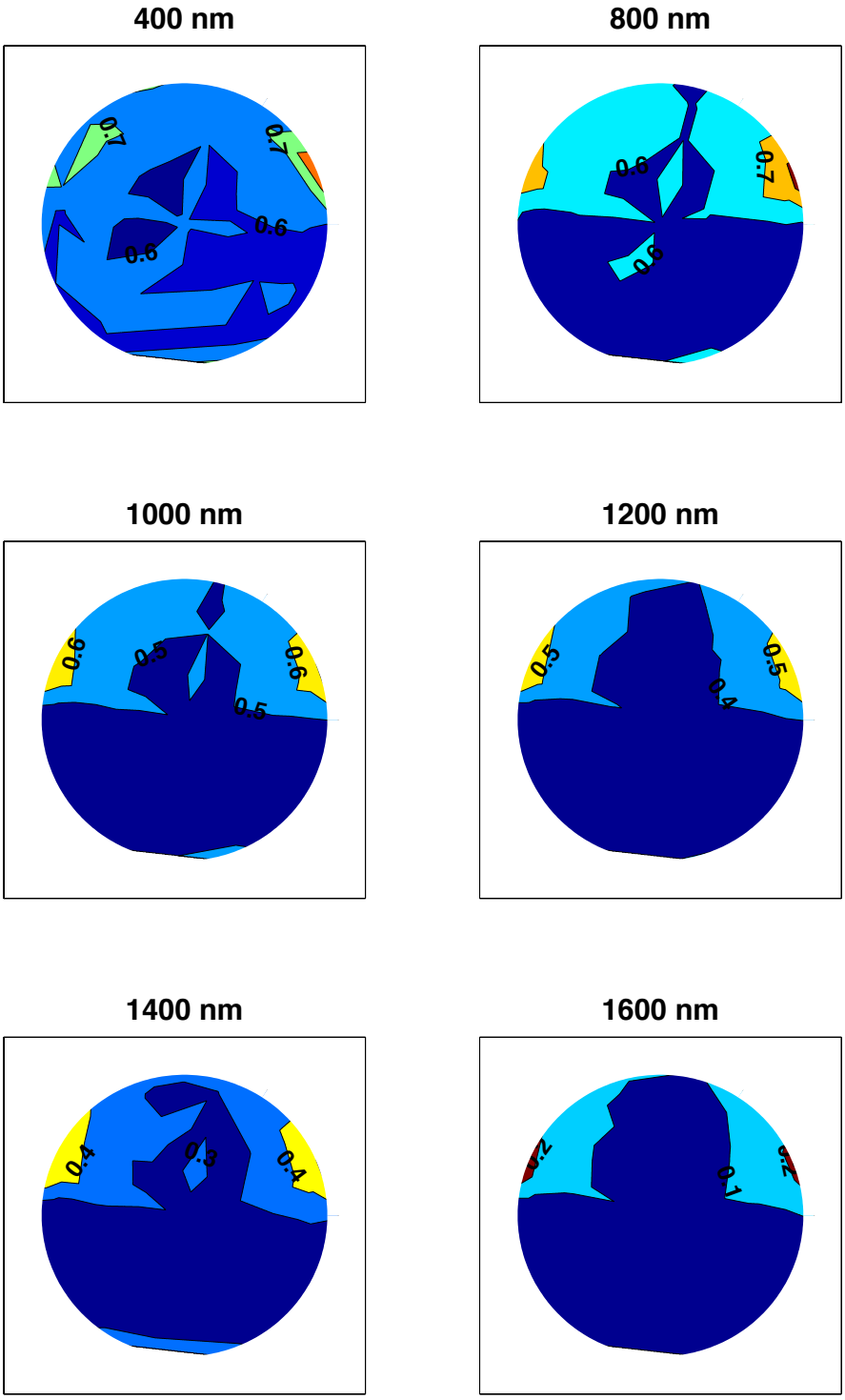

Figure C.6 *– HDRF polar plots at wavelengths of 400, 800, 1000, 1200, 1400 and 1600 nm for site 6. The sun is at the base of each plot*

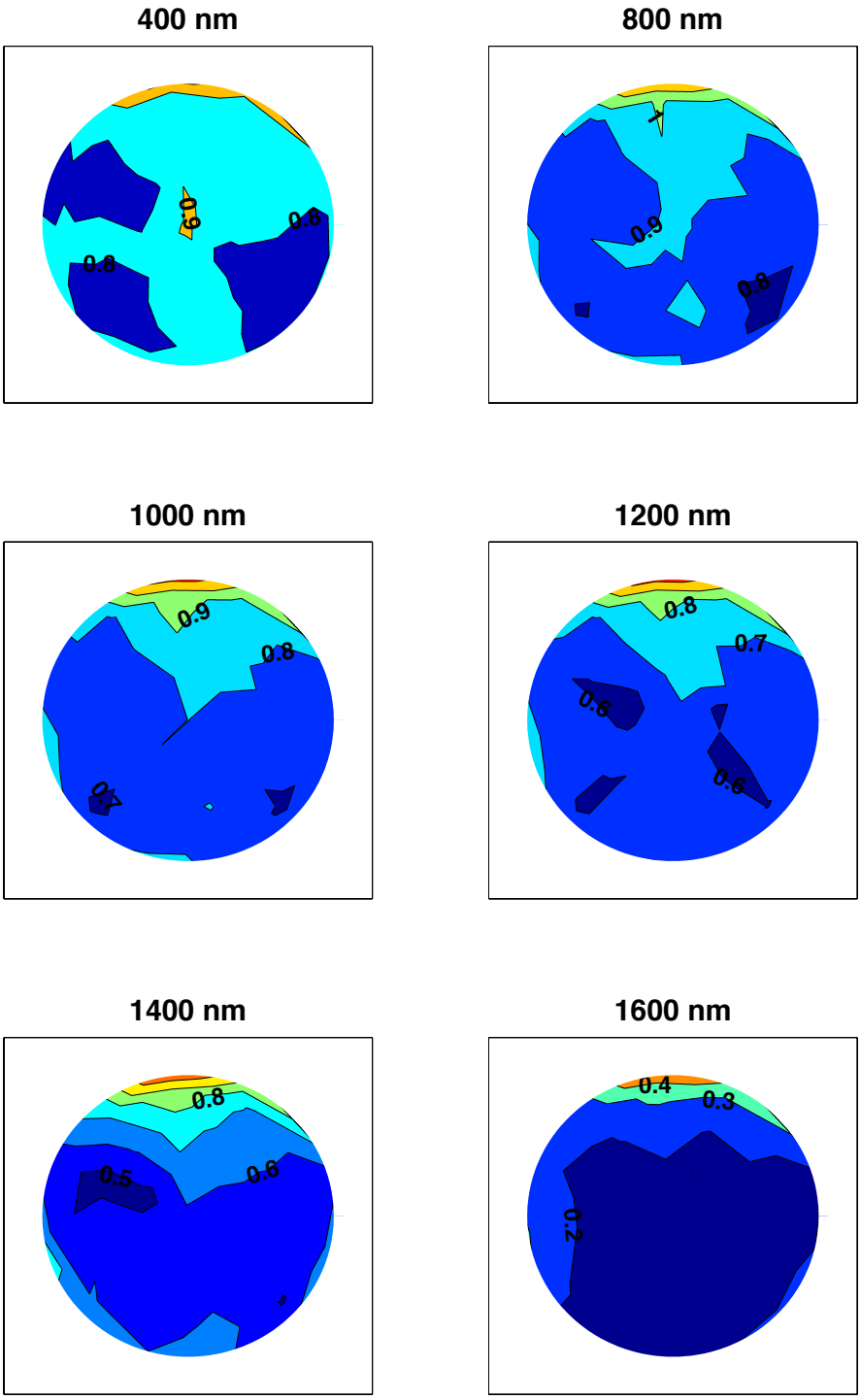

Figure C.7 *– HDRF polar plots at wavelengths of 400, 800, 1000, 1200, 1400 and 1600 nm for site 7. The sun is at the base of each plot*

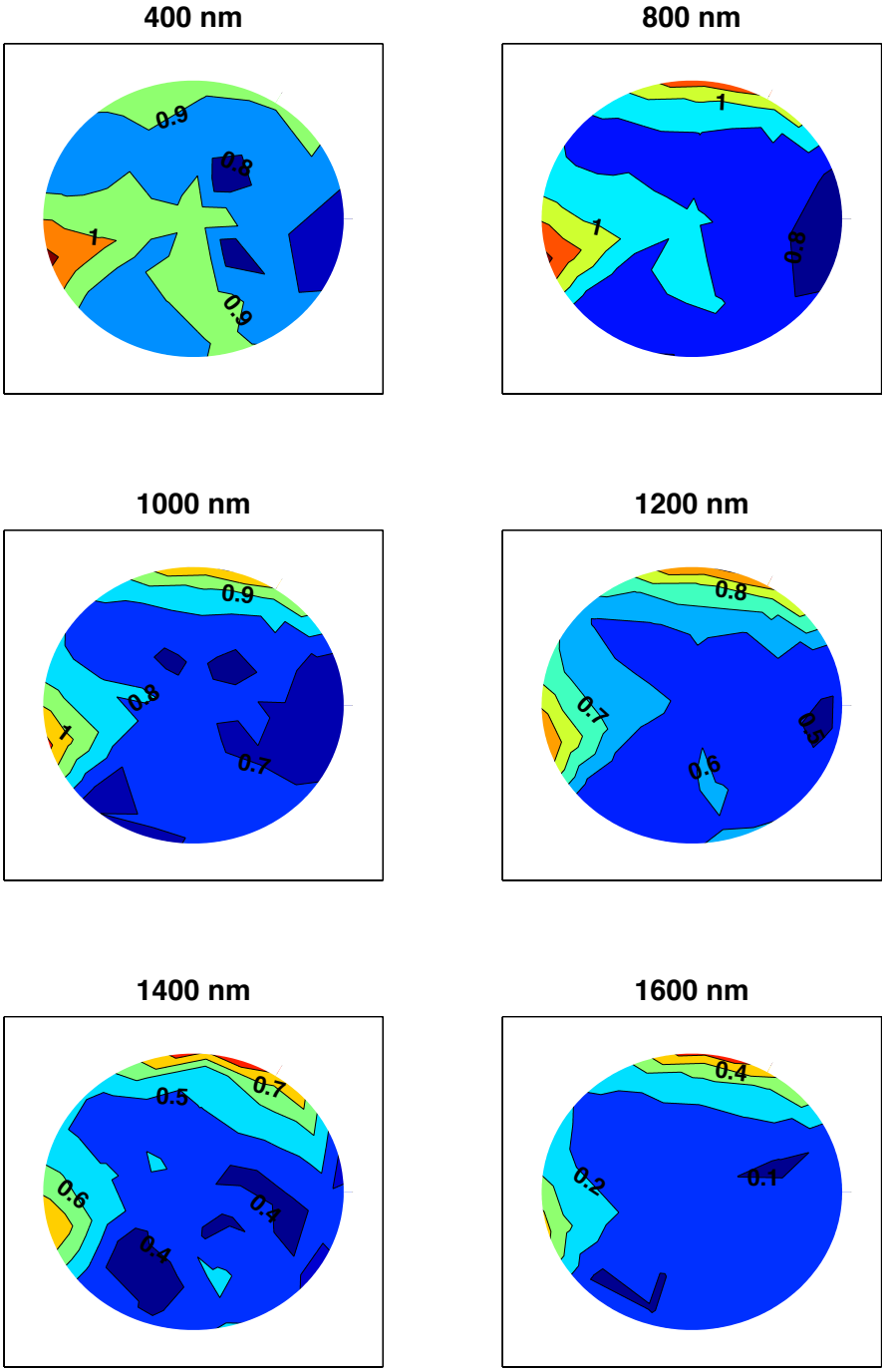

Figure C.8 *– HDRF polar plots at wavelengths of 400, 800, 1000, 1200, 1400 and 1600 nm for site 8. The sun is at the base of each plot*

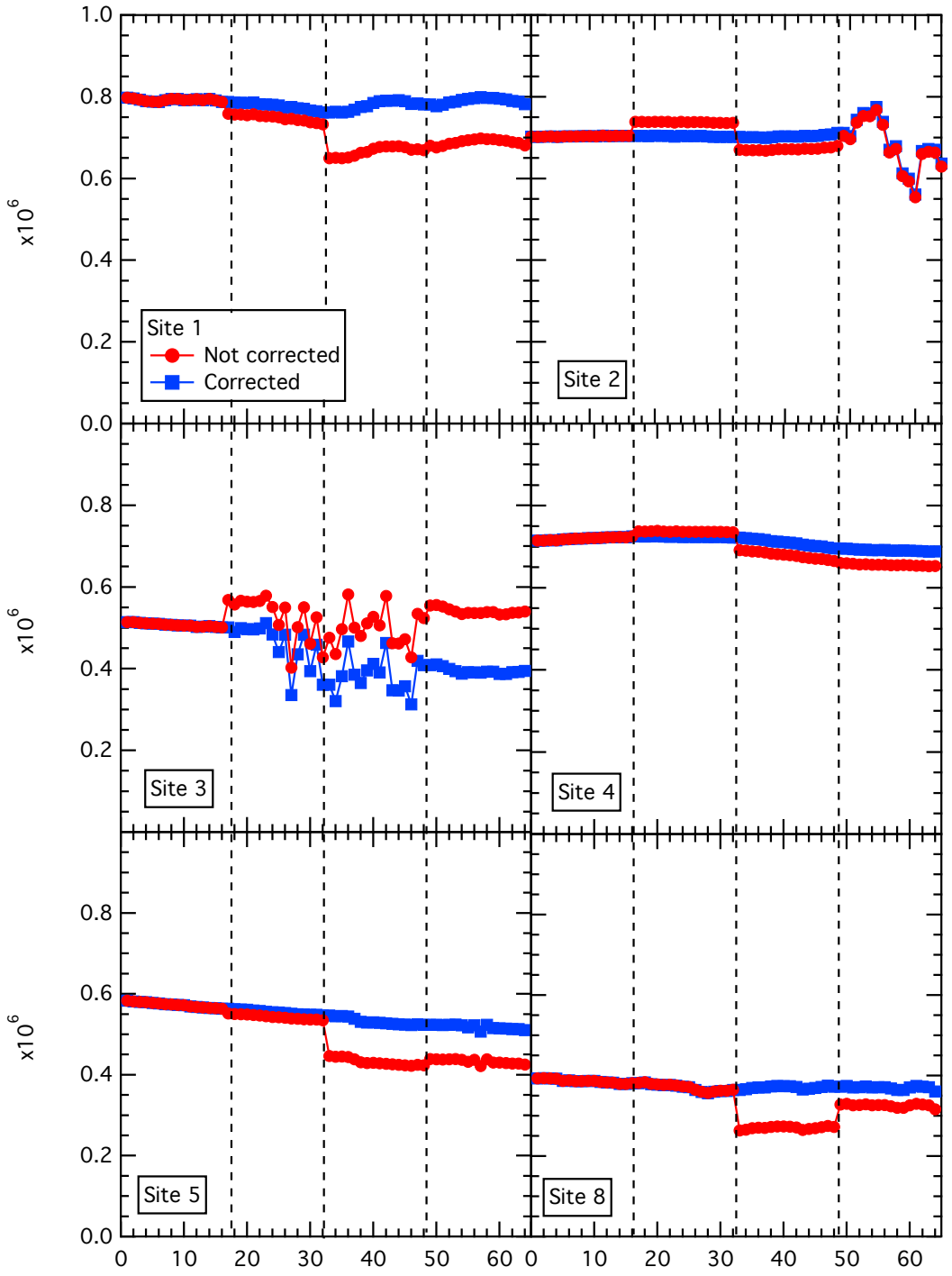

Figure C.9 *– Downwelling data at 500 nm recorded from the integrating sphere on top of GRASS during the course of a measurement sequence, for all sites not included in chapter 7.*